

DÜZCE
ÜNİVERSİTESİ
BİLİM ve TEKNOLOJİ
DERGİSİ

Düzce University
Journal of
Science & Technology

e-ISSN: 2148-2446

Cilt
Volume

13

Sayı
Issue

2

Nisan/April
2025

**Düzce Üniversitesi
BİLİM ve TEKNOLOJİ DERGİSİ
DÜBİTED**

<http://dergipark.org.tr/dubited>



**Düzce University
JOURNAL of SCIENCE & TECHNOLOGY
DUBİTED**

<http://dergipark.org.tr/dubited>

Sahibi

Owner

Nedim SÖZBİR (Düzce Üniversitesi Rektörü)

(D. Ü. Lisansüstü Eğitim Enstitüsü adına)

(On behalf of D. U. Institute of Graduate Programs)

Baş Editör

Editor-in-Chief

Suat SARIDEMİR

Yardımcı Editörler

Assistant Editors

Ümit AĞBULUT

Erdem ELİBOL

Teknik Editörler

Technical Editors

Anıl DEMİRCAN

Ahmet AYTEĞİN

Nisa KAPLAN ERGÜL

İremnur AYDIN

Sorumlu Yazı İşleri Müdürü

Publishing Manager

Pınar GÜLTEKİN

Yayın Kurulu

Editorial Board

Ahmet Bora KIRKLIKÇI, Karamanoğlu Mehmet Bey
Üniversitesi, Türkiye

Ali ÇALHAN, Düzce Üniversitesi, Türkiye

Ali Etem GÜREL, Düzce Üniversitesi, Türkiye

Alper ERGÜN, Karabük Üniversitesi, Türkiye

Ahmet DEMİR, Düzce Üniversitesi, Türkiye

Arif ÖZKAN, Kocaeli Üniversitesi, Türkiye

Aytaç AYDIN, Karadeniz Teknik Üniversitesi, Türkiye

Barış KARAKAYA, Fırat Üniversitesi, Türkiye

Emre AVCI, Duzce University, Türkiye

Engin EROĞLU, Düzce Üniversitesi, Türkiye

Fatih TAŞPINAR, Düzce Üniversitesi, Türkiye
Fikret POLAT, Düzce Üniversitesi, Türkiye
G. Alev ÖZKÖK, Hacettepe Üniversitesi, Türkiye
Gökhan YILDIZ, Düzce Üniversitesi, Türkiye
Hakan ARSLAN, Düzce Üniversitesi, Türkiye
Hüseyin BUDAK, Düzce Üniversitesi, Türkiye
Hüseyin BAKIR, Dogus University, Türkiye
İrem DÜZDAR, Düzce Üniversitesi, Türkiye
Koray ŞARKAYA, Pamukkale Üniversitesi, Türkiye
Mehmet SÖNMEZ, Osmaniye Korkut Ata Üniversitesi, Türkiye
Melahat Sevgül BAKAY, Duzce University, Türkiye
Metin TOZ, Karamanoglu Mehmetbey University, Türkiye
Mevlüt ERSOY, Süleyman Demirel Üniversitesi, Türkiye
Muhammet Emin ŞAHİN, Yozgat Bozok Üniversitesi, Türkiye
Muhammet GÜL, İstanbul University, Türkiye
Mustafa KARAGÖZ, Karabuk University, Türkiye
Murat AYDEMİR, Erzurum Technical University, Türkiye
Murat Kadir YEŞİLYURT, Yozgat Bozok Üniversitesi, Türkiye
Murat EYVAZ, Gebze Teknik Üniversitesi, Türkiye
Mustafa DAYI, Düzce Üniversitesi, Türkiye
Musa ÇADIRCI, Düzce Üniversitesi, Türkiye
Nihat Hakan AKYOL, Kocaeli Üniversitesi, Türkiye
Nuri ŞEN, Düzce Üniversitesi, Türkiye
Osman DİKMEN, Düzce Üniversitesi, Türkiye
Pınar GÜLTEKİN, Düzce Üniversitesi, Türkiye
Salih Tunç KAYA, Düzce Üniversitesi, Türkiye
Melike ERDOĞAN, Düzce Üniversitesi, Türkiye
Sercan SERİN, Osmaniye Korkut Ata Üniversitesi, Türkiye
Serdar BİROĞUL, Düzce University, Türkiye
Serhat DUMAN, Bandırma Onyedi Eylül Üniversitesi, Türkiye
Şerife Gülsün KIRANKAYA, Düzce Üniversitesi, Türkiye
Taner YOLDAŞ, Düzce Üniversitesi, Türkiye
Turgay BİRTÜRK, Düzce Üniversitesi, Türkiye
Uğur GÜVENÇ, Düzce Üniversitesi, Türkiye
Ümit YURT, Bolu Abant İzzet Baysal University, Türkiye
Yasin ŞALE, Gebze Teknik Üniversitesi, Türkiye
Yaşar Selman GÜLTEKİN, Duzce University, Türkiye
Zehra KARAPINAR ŞENTÜRK, Düzce Üniversitesi, Türkiye
Kemal ÇETİN, Necmettin Erbakan Üniversitesi, Türkiye
Doğukan MUTLU, Üsküdar Üniversitesi, Türkiye

Ulusal Danışma Kurulu
National Advisory Board

Üniversitesi, Türkiye

Türkiye

Türkiye

Türkiye

Üniversitesi, Türkiye

A. Burak İNNER, Kocaeli Üniversitesi, Türkiye
Abdi ATILGAN, Afyon Kocatepe Üniversitesi, Türkiye
Abdulhalim AKKAYA, Sakarya Uygulamalı Bilimler

Abdulkadir SENGUR, Fırat Üniversitesi, Türkiye
Abdulkadir TAŞDELEN, Ankara Yıldırım Beyazıt Üniversitesi,

Abdulkadir KARACI, Samsun Üniversitesi, Türkiye
Abdullah Cemil İLÇE, Bolu Abant İzzet Baysal Üniversitesi,

Abdullah Talha KABAKUŞ, Duzce University, Türkiye
Abdullah DEMİR, Marmara Ün. , Türkiye
Abdullah SEÇGİN, Dokuz Eylül Üniversitesi, Türkiye
Abdullah AKDOĞAN, Pamukkale Üniversitesi, Türkiye
Abdullah ORMAN, Ankara Yıldırım Beyazıt University, Türkiye
Abdullah Hulusi KÖKÇAM, Sakarya Üniversitesi, Türkiye
Abdullah BAŞÇI, Atatürk Üniversitesi, Türkiye
Abdullah YILDIZ, Yıldırım Beyazıt University, Türkiye
Abdullah Ersan OĞUZ, Biruni Üniversitesi, Türkiye
Abdullah GENÇ, Isparta Uygulamalı Bilimler Üniversitesi,

Abdülvahap ÇAKMAK, Samsun University, Türkiye
Abdurrahim DAL, Adana Alparslan Türkeş Bilim Ve Teknoloji

Abdurrahim AYDIN, Duzce University, Türkiye
Abdurrahim TEMİZ, Karabük Üniversitesi, Türkiye
Abdurrahman ÜNSAL, Dumlupınar Üniversitesi, Türkiye
Abdüssamed KABAKUŞ, Artvin Çoruh Üniversitesi, Türkiye
Abid USTAOĞLU, Bartın University, Türkiye
Adem TUNCER, Yalova University, Türkiye

Uluslararası Danışma Kurulu
International Advisory Board

Abdulkadir ŞANLI, Imperial College, London

Cilt
Volume

13

Sayı
Issue

2

Nisan/ April
2025

Ürün Bilgisi

Product Information

Yayıncı

Publisher

Düzce Üniversitesi Lisansüstü Eğitim Enstitüsü

Düzce University Institute of Graduate Programs

Sahibi

Owner

Nedim SÖZBİR (Düzce Üniversitesi Rektörü)

(D. Ü. Lisansüstü Eğitim Enstitüsü adına)

(On behalf of D. U. Institute of Graduate Programs)

Sorumlu Yazı İşleri Müdürü

Publishing Manager

Pınar GÜLTEKİN

Web Sayfası

Web Page

<http://dergipark.org.tr/dubited>

Basım Tarihi

Date of Publication

Nisan 2025

April 2025

Yayın Dili

Language

İngilizce

English

Yayın Aralığı

Frequency

Yılda dört kez yayınlanır

Published four times in a year

Yayın Türü

Type of Publication

Sürekli yayın

Periodical

e-ISSN Numarası

e-ISSN Number

2148-2446

Yazışma Adresi

Düzce Üniversitesi Lisansüstü Eğitim
Enstitüsü Rektörlük Binası 3. Kat 81620
Düzce/TÜRKİYE

Telefon: +90 380 542 12 08

Fax: +90 380 542 12 38

E-posta: dubitedyayin@duzce.edu.tr

<http://dergipark.org.tr/dubited>
adresinden dergiye ilişkin bilgilere ve
makalelerin tam metnine ulaşılabilir.

Correspondence Address

*Düzce University Institute of
Graduate Programs Rectorship
Building 3rd Floor 81620
Düzce/TURKEY*

Phone: +90 380 542 12 08

Fax: +90 380 542 12 38

E-mail: dubitedyayin@duzce.edu.tr

*Instructions for authors and all
articles in this journal can be
reached at
<http://dergipark.org.tr/dubited>*

İÇİNDEKİLER**Sayfa****Makale****BİYOLOJİ/ BİYOKİMYA/ KİMYA/ MATEMATİK/ MOLEKÜLER BİYOLOJİ VE GENETİK/SU
ÜRÜNLERİ****Araştırma Makalesi/ Research Article**

841-856

Identifying Knowledge Gaps on Ecotoxicological Assessment of
Micro/Nanoplastics with Aquatic Keystone Species
Mikro/Nanoplastiklerin Ekotoksikolojik Değerlendirilmesindeki Bilgi
Eksikliklerinin Sucul Ekosistem Anahtar Türleri ile Belirlenmesi
Vildan Zülal SÖNMEZ, Ceyhan AKARSU , Zeynep AYDIN, Elif Naz COŞKUN,
Ecem GÜNEY, Şevval İŞLEK, Zeynep BOSTAN, Nüket SİVRİ

Derleme Makale / Review Article

- 913-931 New Approaches and Theories in Understanding Intelligence and Cognitive Ability Processes
Zeka ve Bilişsel Yetenek Süreçlerini Anlamada Yeni Yaklaşım ve Kuramlar
Hatice YILDIRIM, Latif Gürkan KAYA

BİLGİSAYAR / YAZILIM MÜHENDİSLİĞİ/BİLİŞİM SİSTEMLERİ VE TEKNOLOJİLERİ

Araştırma Makalesi/ Research Article

- 616-630 Enhanced Optical Coherence Tomography (OCT) of Prostate Nerves Through Integrated Image-Processing Techniques
Entegre Görüntü İşleme Teknikleri Sayesinde Prostat Sinirlerinin Geliştirilmiş Optik Koherens Tomografisi (OCT)
Şükran YAMAN ATCI
- 631-642 Deep Learning with Limited Data: Advanced Classification Approaches Through Few-Shot Learning and Prototype Networks
Sınırlı Veri ile Derin Öğrenme: Birkaç Atışlı Öğrenme ve Prototip Ağlar Aracılığıyla Gelişmiş Sınıflandırma Yaklaşımları
Sara ALTUN GÜVEN, Buket TOPTAŞ
- 667-684 A Cloud Based Web-Tool to Predict the High School Entrance Exam Scores of the Students
Öğrencilerin Lise Giriş Sınavı Puanlarını Tahmin Etmek için Bulut Tabanlı Bir Web Aracı
Ekrem GÜLCÜOĞLU, Gökçen ALTUN
- 857-867 Tomato Sorting System Based on Type Using Deep Learning
Derin Öğrenme Kullanarak Türüne Bağlı Domates Sınıflandırma Sistemi
Eren Yiğit GÜLEM, Boran DURSUN, Hayrettin TOYLAN
- 868-892 Innovative Hybrid CNN+SVM Model for Accurate Covid-19 Detection From CT Images
BT Görüntülerinden Hassas Covid-19 Tespiti için Yenilikçi Hibrit CNN+SVM Modeli
Hasan ULUTAŞ, Halil İbrahim COŞAR, Muhammet Emin ŞAHİN, Mustafa Fatih ERKOÇ, Esra YÜCE

ÇEVRE / ZİRAAT / ORMAN / JEOLojİ MÜHENDİSLİĞİ

Araştırma Makalesi/ Research Article

- 655-666 Analysis of Turkish Pine Stumpage-based Auction Sales: A Case Study of İzmir Regional Directorate of Forestry
Kızılçam Açık Artırmalı Dikili Ağaç Satışlarının Analizi: İzmir Orman Bölge Müdürlüğü
Güçlü İlker MÜFTÜOĞLU, Yaşar Selman GÜLTEKİN
- 685-702 Catalytic Pyrolysis of Grape Seed Waste: Characterization of Bio-Char and Bio-Oil
Üzüm Çekirdeği Atıklarının Katalitik Pirolyzi: Biyo-Kömür ve Biyo-Yağın Karakterizasyonu
Koray ALPER
- 824-840 Comparison of The Output Power of a Micro Hydroelectric Power Plant with Different PID Control Structures
Farklı PID Kontrol Yapıları İle Bir Mikro Hidroelektrik Santral Çıkış Gücünün Karşılaştırılması
Tuğba AYDIN KART, Ahmet AKTAŞ, Ömür BINARBAŞI, Batuhan ŞENLEN,
- 964-981 The Roles of Chicken Manure and Biochar Applications in Enhancing the Morphological, Yield, Crude Protein Content and Antioxidant Activities of Basil
Tavuk Gübresi ve Biyokömür Uygulamalarının Fesleğenin Morfolojik, Verim, Protein İçeriği ve Antioksidan Aktivitelerini Artırmadaki Rolü
Mahmut ÇAMLICA, Gülsüm YALDIZ

ELEKTRİK/ELEKTRONİK / ELEKTRİK ELEKTRONİK/ MEKATRONİK/ENERJİ MÜHENDİSLİĞİ

Araştırma Makalesi/ Research Article

- 703-717 Pre-Feasibility Analysis of PV Panel Supported EV Charging Station for Kocaeli University
Kocaeli Üniversitesi için PV Panel Destekli EV Şarj İstasyonunun Ön Fizibilite Analizi
Enes Talha TAMGACI, Murat ÜNLÜ
- 893-912 Investigation of Electromagnetic Shielding Performance of Monolayer Ironboride in Tetragonal Crystal Structure using Ab initio Methods
Tetragonal Kristal Yapıdaki Tek Katmanlı Demirborürün Elektromanyetik Kalkanlama Performansının Ab initio Yöntemler Kullanılarak İncelenmesi
Hakan ÜŞENTİ, İzzet Paruğ DURU

- 893-912 Designing a Remote Monitoring and Security System for Broadcast Transmitters
Yayın Vericileri için Uzaktan İzleme ve Güvenlik Sistemi Tasarlanması
Ruhi TAŞ, Mansur BEŞTAŞ

İNŞAAT / MİMARLIK / PEYZAJ MİMARLIĞI / METALURJİ ve MALZEME / TEKSTİL / ÇEVRE / MÜHENDİSLİĞİ

Araştırma Makalesi/ Research Article

- 643-654 Coloring Cotton Fabrics by Pigment Printing Method with Reduction of Process Steps: An Innovative Approach
İşlem Adımları Azaltılarak Pigment Baskı Yöntemiyle Pamuklu Kumaşların Renklendirilmesi: Yenilikçi Bir Yaklaşım
Emine AYAZ, Zeynep OMEROGULLARI BASYIGIT
- 790-810 Strengthening Urban Resilience: A Case Study of Amsterdam's Public Spaces in the Post-COVID Era through Digital Solutions
Kentsel Dayanıklılığın Güçlendirilmesi: Dijital Çözümler Yoluyla COVID Sonrası Dönemde Amsterdam'ın Kamusal Alanlarına İlişkin Bir Örnek Çalışması
Fatemeh BADEL, Jesús LÓPEZ BAEZA, Hülya LASCH
- 990-1004 The Relationship Between Sustainable Construction and Economic Growth for Reinforced Concrete Structures in Türkiye
Türkiye’de Betonarme Yapılar için Sürdürülebilir İnşaat ve Ekonomik Büyüme Arasındaki İlişki
Esra DOBRUCALI

Derleme Makale / Review Article

- 718-734 An Artificial Intelligence Approach to Evaluating the Sound Absorption Performance of Materials: A Systematic Review
Malzemelerin Ses Yutma Performansının Değerlendirilmesinde Yapay Zeka Yaklaşımı: Sistematik İnceleme
Oya BABACAN

MAKİNE / MEKATRONİK / MALZEME / ENDÜSTRİ / BİYOMEDİKAL / İMALAT / OTOMOTİV MÜHENDİSLİĞİ

Araştırma Makalesi/ Research Article

- 735-751 Prediction of Deep Drawing Ratio for DP800 Steel by Using Modified-Mohr-Coulomb Damage Criteria
Modified- Mohr Coulomb Hasar Kriteri Kullanılarak DP800 Çeliğinin Derin Çekme Oranının Tahmini
Elifnaz BABA, Nuri ŞEN, Tolgahan CİVEK

- 752-769 Performance Evaluation Of Image Recognition Algorithms On Marine Vessels And Optimum Parameter Selection
Deniz Taşıtları Üzerinde Görüntü Tanıma Algoritmalarının Performans Değerlendirmesi Ve Optimum Parametre Seçimi
Cansu CANBOLAT, Yasemin ATILGAN ŞENGÜL, Ahmet Yekta KAYMAN
- 770-789 A Model Reference Adaptive Control Approach to Terrain Following Flight Control System
Arazi Takipli Uçuş Kontrol Sistemine Model Referans Uyarlamalı Kontrol Yaklaşımı
Berk İNAN, İbrahim ALIŞKAN
- 932-941 Effect of Natural Aging on Mechanical Properties of Copper Clad Steel Brake Pipes
Doğal Yaşlanmanın Bakır Kaplı Çelik Fren Borularının Mekanik Özellikleri Üzerindeki Etkisi
Ozan KOYUNCU, Burak ÇELİK, İrem Yağmur SİMİTÇİ, Yasin AKGÜL, Alper İNCESU
- 982-989 Synthesis, Dielectric and Magnetic Characterization and Properties of Nano Magnetic Particles by using Microwave Technique
Mikrodalga Tekniğini Kullanarak Nano Manyetik Parçacıkların Sentezi, Dielektrik ve Manyetik Karakterizasyonu ve Özellikleri
Harun BAYRAKDAR
- 1005-1021 Productivity Contribution of Model Factories: Investigation of the Benefit of the Learn-Turn Program Applied to Enterprises with Multi-Criteria Decision-Making Method
Model Fabrikaların Verimliliğe Katkısı: İşletmelere Uygulanan Öğren-Dönüş Programının Faydasının Çok Kriterli Karar Verme Yöntemi ile İncelenmesi
Ali SEVİNÇ

Derleme Makale / Review Article

- 942-963 The Transformative Role of Additive Manufacturing: Current Innovations, Applications, and Future Directions Across Industries
Eklemeli İmalatın Geleceği: Yenilikler, Uygulamalar ve Sektörlere Etkisi
Mustafa ÜSTÜNDAĞ



Düzce University Journal of Science & Technology

Research Article

Enhanced Optical Coherence Tomography (OCT) of Prostate Nerves Through Integrated Image-Processing Techniques



Şükran YAMAN ATCI ^{a,*}

^a Department of Computer Programming , Vocational School, Haliç University, İstanbul, TURKEY

* Corresponding author's e-mail address: sukranatci@halic.edu.tr

DOI: 10.29130/dubited.1547459

ABSTRACT

Cavernous nerves, located along the prostate gland's surface, are integral to erectile functionality. These nerves are at risk of injury during the surgical removal of a cancerous prostate gland. This research applies a suite of image processing algorithms—segmentation, denoising, and edge detection—to time-domain optical coherence tomography (OCT) images of prostates from different datasets to improve the detection of cavernous nerves. Initially, the prostate OCT images are segmented to isolate the cavernous nerves from the adjacent glandular tissue. This is followed by the application of a locally adaptive denoising process using a dual-tree complex wavelet transform, aimed at reducing speckle noise. Subsequently, edge detection techniques are employed to enhance the imaging depth of the prostate gland. The combined application of these image processing techniques significantly improves the signal-to-noise ratio and imaging depth, enabling the automated identification of cavernous nerves. This enhanced imaging capability is crucial for supporting nerve-sparing approaches in laparoscopic and robotic prostate cancer surgeries.

Keywords: OCT, Prostatic Tissue, Segmentation, Denoising, Edge Detection , Oncology Diagnostics

Entegre Görüntü İşleme Teknikleri Sayesinde Prostat Sinirlerinin Geliştirilmiş Optik Koherens Tomografisi (OCT)

Öz

Kavernöz sinirler, prostat bezinin yüzeyi boyunca yer almaktadır ve erektil işlev için hayati öneme sahiptirler. Bu sinirler, kanserli bir prostat bezinin cerrahi olarak çıkarılması sırasında hasar görme riski taşımaktadır. Bu araştırma, kavernöz sinirlerin tanımlanmasını geliştirmek amacıyla, fare prostatlarındaki zaman alanı optik koherans tomografi (OCT) görüntülerine görüntü işleme algoritmaları—segmentasyon, gürültü azaltma ve kenar belirleme—uygulamaktadır. Başlangıçta, prostat OCT görüntüleri, kavernöz sinirleri çevreleyen bez dokusundan ayırmak için segmente edilir. Bunu, speckle gürültüsünü azaltmaya yönelik çift ağaç karmaşık dalga dönüşümüne dayalı yerel olarak uyarlanabilir bir gürültü azaltma işlemi takip eder. Ardından, prostat bezinin daha derinlerinin görüntülenmesini sağlamak için kenar belirleme teknikleri uygulanır. Bu görüntü işleme tekniklerinin birleşik uygulaması, sinyal-gürültü oranını ve görüntüleme derinliğini önemli ölçüde artırır ve kavernöz sinirlerin otomatik olarak tanımlanmasını sağlar. Bu gelişmiş görüntüleme yeteneği, laparoskopik ve robotik prostat kanseri ameliyatlarında sinir koruyucu yaklaşımları desteklemek için hayati öneme sahiptir.

Anahtar Kelimeler: OCT Görüntüleme, Prostat Dokusu, Segmentasyon, Gürültü Giderme, Kenar Algılama , Onkoloji Teşhisi

I.INTRODUCTION

The safeguarding of cavernous nerves during radical prostatectomy is crucial for the retention of function after surgery. Due to their close proximity to the surface of the prostate, these nerves are prone to injury during the excision of the cancerous prostate gland. Their minute size and the variable trajectory across patients add complexity to accurately mapping their course, which is essential for effective surgical outcomes. Such factors likely contribute to the broad range of postoperative potency rates, reported as varying between 9 and 86% following prostate cancer surgeries [1]. Consequently, technological advancements that enhance cavernous nerves' detection, imaging, and visualization could significantly bolster nerve conservation efforts and, by extension, postoperative functionality.

Prostate tissue is composed of both glandular and connective tissues. Within whole slide images (WSI), glands appear as hollow, white structures, often exhibiting a branched morphology. This glandular appearance underpins the Gleason grading system, which is used to assess the severity of prostate cancer given in Figure 1a and b. The Gleason grading system is a histopathological classification method widely used to evaluate the aggressiveness of prostate cancer based on glandular architectural patterns observed under a microscope. It assigns a primary and secondary grade, each ranging from 1 to 5, reflecting the most and second-most predominant tumor patterns, respectively, with the sum (Gleason score) ranging from 2 to 10, which correlates with tumor differentiation and clinical outcomes[2,3]. Lower scores (e.g., 2-4) are associated with well-differentiated, less aggressive tumors, whereas higher scores (e.g., 8-10) indicate poorly differentiated, highly aggressive cancers with a worse prognosis, underscoring its significance in guiding therapeutic decision-making and prognostication in clinical practice [2]. Optical Coherence Tomography (OCT) represents a non-invasive imaging modality that offers high-resolution, cross-sectional views of microstructures within biological tissues *in vivo* and *in situ* [2]. Although recent studies have successfully applied OCT to visualize cavernous nerves within human prostates [4,5], there is a recognized need for further enhancements in OCT image quality to facilitate the nerves' identification before it can be adopted clinically [5]. Recent advancements have further highlighted the potential of OCT in prostate imaging, with studies focusing on improving resolution and image processing techniques for better glandular and connective tissue differentiation [8,9]. Moreover, emerging applications of OCT in identifying microstructural changes linked to cancer progression have been reported, demonstrating its capability to complement traditional histopathological assessments [16] with efforts to enhance nerve visualization through machine learning algorithms integrated with OCT [17], paving the way for its broader clinical adoption. Additionally, recent comparative studies have explored the role of OCT in distinguishing benign from malignant lesions, revealing its potential as an adjunct diagnostic tool [18]. Finally, advances in OCT hardware have achieved greater imaging depth and clarity, which may significantly impact its utility in intraoperative prostate cancer management [19].

Another study that used a data schema and flow to inspire this study, OCT images were procured *in vivo* via a clinical endoscopic OCT apparatus (Imalux, Cleveland, Ohio) that integrates a single-mode fiber common-path interferometer-based scanning mechanism [1]). The imaging was facilitated by a probe with 2.6-mm outer diameter, enabling the capture of real-time images at a resolution of 200x200 pixels, with axial and lateral resolutions of 11 microns and 25 microns, respectively.

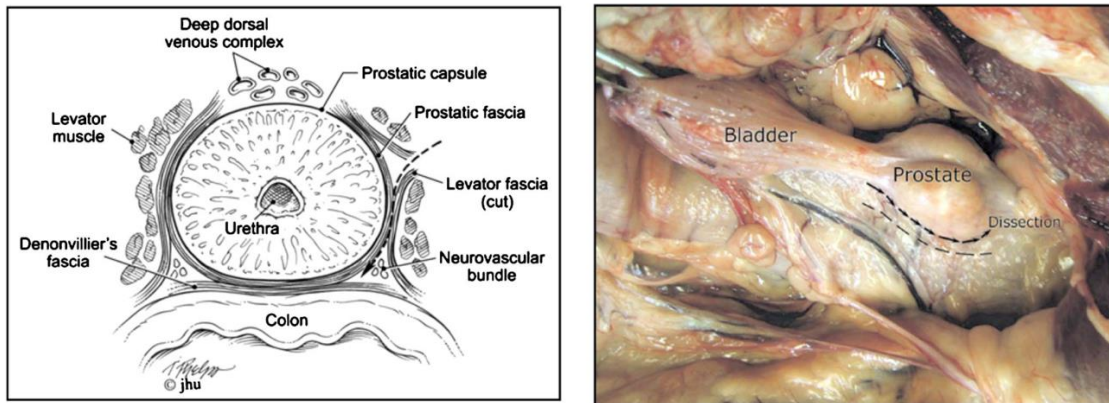


Figure 1 (a). Cross-sectional illustration of the human prostate, depicting the position of the neurovascular bundles adjacent to the prostate surface, illustrated from Rassweiler et al. (2006) [6]. With the (b) the dashed line marks the dissection pathway between the prostatic capsule and the neurovascular bundle.

For that perspective, this study delineates a structured method incorporating three synergistic image processing algorithms to enhance the visualization and identification of cavernous nerves within prostate OCT imagery. Earlier studies have applied a segmentation strategy effectively for recognizing cavernous nerves [15]. For this purpose, open-sourced databases named Prostate cANcer graDe Assessment (PANDA-1 and PANDA-2) dataset [7, 15, 19] are utilized, comprising 160 OCT frames. It is noteworthy that the PANDA-2 dataset encompasses much more complex frames than its predecessor, PANDA-1, enhancing the robustness and depth of analysis possible. Nonetheless, imaging the deeper structures of the prostate has remained a formidable challenge using OCT technologies. To address this, the initial segmentation strategy depicted in the left branch of Figure 1 is supplemented with denoising and edge detection techniques detailed in the right branch of the same figure. This advancement allows for a more nuanced understanding of prostate tissue variations and complexities captured in the PANDA-2 dataset.

Subsequent analysis demonstrates that the integration of the edge detection system significantly augments the capacity of OCT to image deeper prostate tissue structures, thus potentially enhancing diagnostic capabilities and surgical outcomes in prostate cancer treatments [10, 11]. In Figure 2, two-dimensional (2-D) OCT images of prostate tissues undergo segmentation to delineate the cavernous nerves from the adjacent glandular structures of the prostate. This segmentation process is critical for identifying and preserving these nerves during surgical procedures. Furthermore, the figure illustrates grading structural variations of prostate glands, systematically categorized into escalating levels from A to D, visually representing the progressive anatomical changes associated with different stages of prostate pathology. This study has shown that, despite limitations in reporting results from external hospitals, the use of stain normalization during processing significantly differentiates the distribution of predicted patches between malignant and normal cases, thereby validating the effectiveness of this methodology.

All microphotographs presented are stained with hematoxylin and eosin and captured at 5x lens magnification. This staining and magnification technique enables a detailed examination of cellular and structural anomalies, which are indicative of various stages in the progression of the prostate.

- **Benign Prostate Glands with Folded Epithelium (level A):** Characterized by pale cytoplasm and small, regular nuclei, these glands are closely clustered. Their structural integrity represents the healthiest form of prostate tissue, as assessed by histopathological standards.
- **Prostatic Adenocarcinoma, Gleason Pattern 3 (level B):** This pattern indicates no significant loss of glandular differentiation. Small, infiltrative glands intersperse among benign glands, featuring darker cytoplasm and enlarged nuclei with pronounced nucleoli and dark chromatin. Each glandular unit remains distinct and maintains a lumen, consistent with a lower-grade malignancy.

- **Prostatic Adenocarcinoma, Gleason Pattern 4 (level C):** Exhibiting partial loss of glandular differentiation, this pattern shows an incomplete formation of lumina. The microphotograph reveals irregular cribriform structures—epithelial sheets punctuated by multiple lumina. Additionally, there are both poorly formed small glands and some that are fused, all characteristic of Gleason Pattern 4.
- **Prostatic Adenocarcinoma, Gleason Pattern 5 (level D):** This highest grade is marked by an almost complete loss of glandular differentiation, with cancer cells dispersed individually throughout the stroma. This pattern may also include solid sheets or strands of cancer cells, demonstrating a high degree of malignancy.

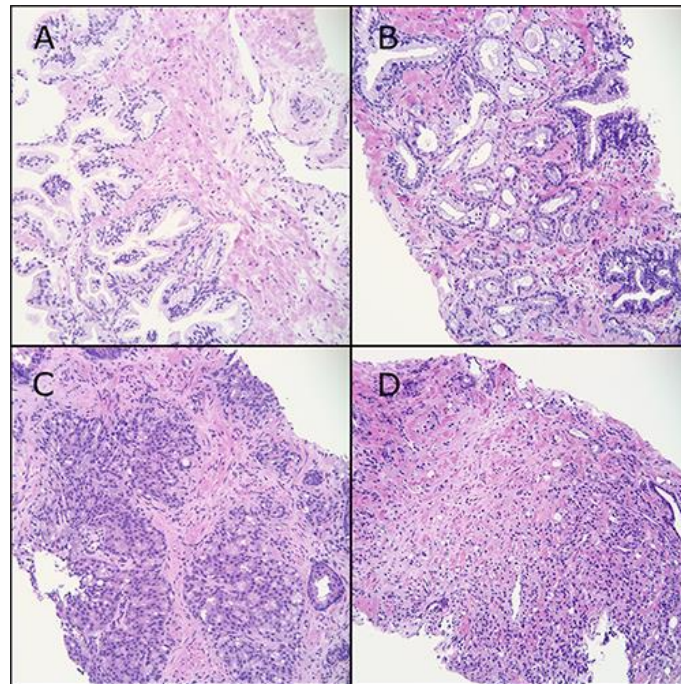


Figure 2. Grading structural variations of prostate glands with escalating levels from A to D from Prostate cANcer graDe Assessment (PANDA) dataset

Figure 3 delineates the sequential application of integrated image processing techniques. The process initiates with the segmentation algorithm, independently isolating cavernous nerves from the surrounding prostate gland tissue. In contrast, the edge detection protocol, essential for deeper prostate gland imaging, necessitates prior denoising for optimal effectiveness due to its susceptibility to noise. Noise complicates the threshold-setting in edge detection, potentially leading to the omission of valid edges or the creation of spurious, noise-induced edges. To address this, denoising is performed first to enhance image clarity, followed by edge detection. The procedures for denoising and edge detection, along with segmentation, operate in parallel, consuming 8 to 10 seconds, respectively, leading to a total computation duration of ten seconds for the complete suite of algorithms.

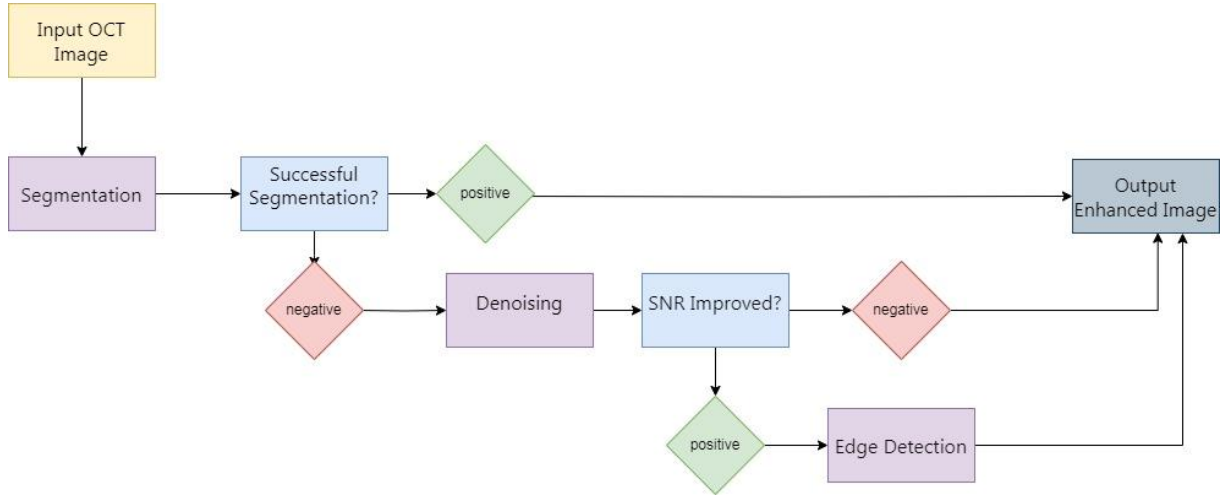


Figure 3. Flow diagram illustrating the sequential application of complementary image processing techniques for prostate nerve OCT.

A. FILTERING INPUT IMAGES

It is pertinent to recognize that similar techniques, such as ultrasound image segmentation, have been previously leveraged in clinical settings to devise precise brachytherapy treatment plans for prostate cancer [18]. Moreover, various alternative segmentation methods have recently been explored in retinal OCT imaging [19]. Nonetheless, large, irregular voids in prostate OCT images necessitate a distinct segmentation strategy, divergent from those typically used for the more homogenous structures of retinal layers. Consequently, to facilitate the identification of cavernous nerves, the analysis integrates three distinct image features: a Gabor filter, Daubechies wavelet, and Laws texture filter. The Gabor filter is adapted with varying standard deviations along the x and y axes. At the same time, an eight-tap Daubechies orthonormal wavelet is employed, and the low-pass sub-band is selected as the filtered output. Subsequently, Laws texture analysis is applied for feature extraction, with segmentation being executed using a nearest-neighbor classifier. Post-segmentation, N -ary morphological processing is utilized to excise diminutive voids.

To enhance the clarity of OCT images of the prostate gland further, wavelet denoising is employed. Recent advancements have seen wavelet techniques effectively reduce speckle noise in MRI, ultrasound, and OCT imaging modalities [20]. A locally adaptive denoising algorithm, illustrated through the use of a dual-tree complex wavelet transform, precedes the implementation of edge detection to diminish speckle noise in prostate OCT images [18,20]. Post-denoising, an edge detection algorithm, which incorporates thresholding and spatial first-order differentiation, is executed to augment the imaging depth of prostate tissues. This method addresses one of the primary challenges in OCT imaging—its limited depth penetration, typically restricted to about 1 millimeter in most opaque soft tissues. The subsequent sections delineate a sequential approach, commencing with segmentation, followed by an exposition on denoising and edge detection methodologies.

Initially, the input image undergoes processing to generate three distinct feature images. Subsequently, the prostate image is segmented into three classifications—nerve, prostate, and background—utilizing a k -nearest neighbors classifier based on the aforementioned feature images. Post-segmentation, N -ary morphology is applied for further refinement. Details regarding the creation of feature images are provided first, followed by explanations of the classification process and the postprocessing steps. The Gabor filter, represented mathematically as $h(x, y)$ combines a Gaussian function as $g(x, y)$ with a sinusoidal wave. The filter is described by the following Equations (1) and (2) as:

$$h(x, y) = g(x, y) \exp[j2\pi(U_x + V_y)] \quad (1)$$

$$\text{where } g(x, y) = 1/2\pi\sigma_x\sigma_y \exp\left[-\frac{1}{2}\left(\frac{x^2}{\sigma_x^2} + \frac{y^2}{\sigma_y^2}\right)\right]. \quad (2)$$

This formulation reveals that the Gabor function operates as a bandpass filter focused around a specific frequency (U, V) , with bandwidths controlled by $\sigma_x\sigma_y$. The characteristic frequencies for the Gabor features are set at (0.2, 0.2) cycles per pixel for both axes, and it is typically implemented with standard deviations of 3 and 6 in the x and y directions, respectively. This configuration has been optimized based on empirical results to minimize segmentation errors in image processing applications.

The eight-tap Daubechies orthonormal wavelet transform is employed to generate the second feature. This process involves the discrete wavelet transform (DWT), which decomposes a signal into its wavelet representation. Specifically, in a one-level DWT, the initial image c_0 is divided into an approximation component c_1 and detail components d_1^1, d_1^2 and d_1^3 correspond to horizontal, vertical, and diagonal directions, respectively. For multilevel DWT, each subsequent approximation c_1 is further split into a finer approximation c_{i+1} and additional detail components d_{i+1}^1, d_{i+1}^2 and d_{i+1}^3 . In this study, the approximation c_1 is specifically selected as the filtered image for crafting the second feature.

The third feature is derived using the Laws feature extraction technique. The Laws 2 mask $h(x, y)$ [15] is convolved with Equation 3 on the image to enhance its microstructural details. This microstructural image is represented by $m(x, y)$, and pixel operator (h) in Equation 4 could be defined as;

$$h(x, y) = h(x, y) * h(x, y), \text{ where;} \quad (3)$$

$$h = 1/12 \begin{pmatrix} 1 & 0 & -1 \\ 2 & 0 & -2 \\ 1 & 0 & -2 \end{pmatrix} \quad (4)$$

Subsequently, a standard deviation calculation is carried out following the Laws mask filtering to finalize the Laws feature extraction process. The k -nearest neighbors (k -NN) classification algorithm is widely recognized for its straightforward yet effective methodology, employing a voting system among the nearest k samples in feature space to classify new data points. This method has been extensively studied and applied across various fields, including medical imaging and recommendation systems, demonstrating its utility in practical applications due to its simplicity and effectiveness [15,16]. The process involves selecting the k closest training examples in the feature space, where the class is predicted by majority vote among the k -nearest neighbors. This simplicity often yields robust performance, especially in scenarios where the relationship between attributes is complex and non-linear. Enhanced versions and evaluations of the k -NN algorithm have been explored to tackle issues like imbalanced data, emphasizing its adaptability and wide-ranging applicability in machine learning tasks [16].

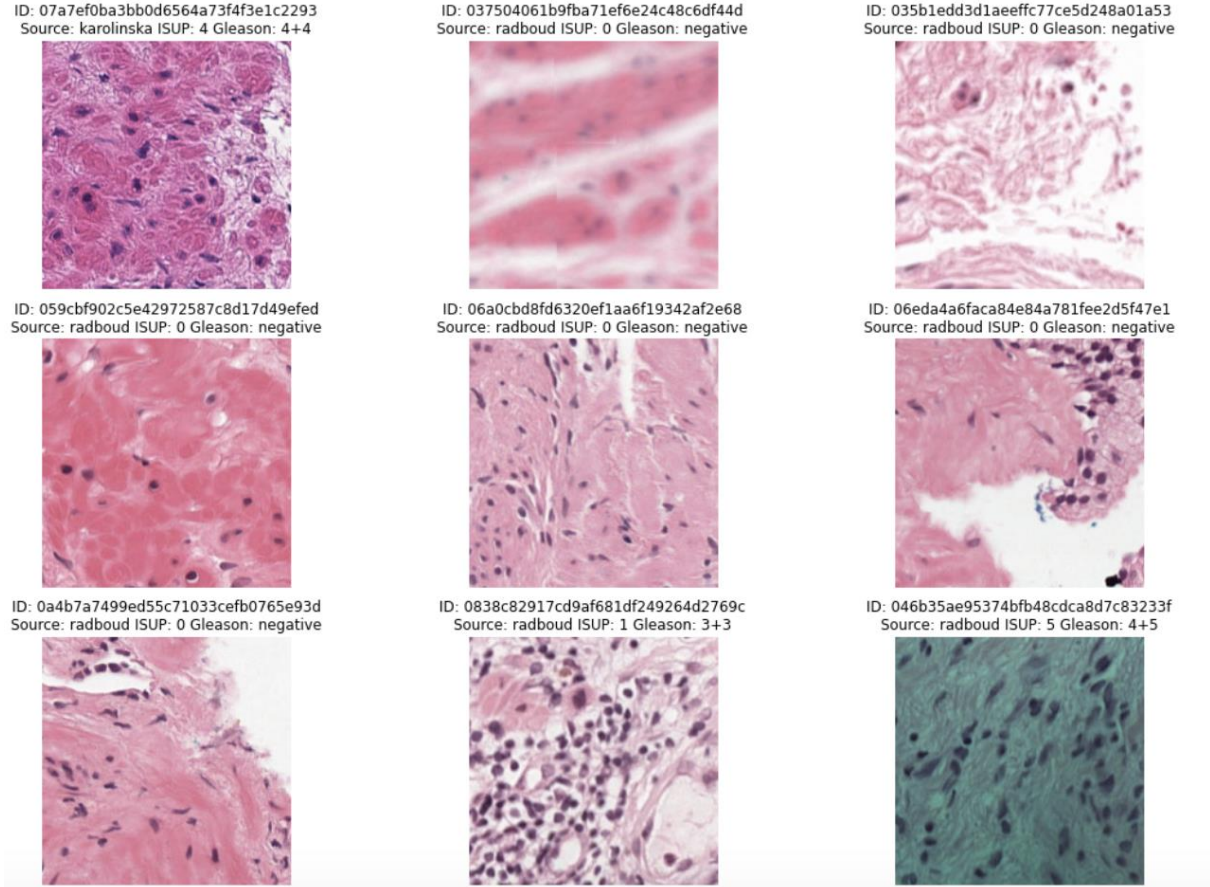


Figure 4. Example applications of the *k*-nearest neighbors (*k*-NN) classification algorithm in prostate cancer imaging. Each frame demonstrates the algorithm's utility in distinguishing between various stages of prostate progression using *k*-NN classification after accomplished pre-process filters.

II. METHODOLOGY DENOISING VIA WAVELET SHRINKAGE

Wavelet shrinkage denoising involves a process of nonlinear soft thresholding within the wavelet transform domain to reduce noise. This method models the observed image X as a combination of an uncorrupted signal S and multiplicative speckle noise N . By applying a logarithmic transformation, speckle noise can be treated as an additive, simplifying the model to $X = S + N$. The denoising process via wavelet shrinkage typically follows a four-step approach given in Equation 5, transforming the original image data into the wavelet domain, where noise reduction techniques are more effectively applied [19].

$$Y = W(X), \quad \lambda = d(Y), \quad Z = D(Y, \lambda), \quad S = W^{-1}(Z) \quad (5)$$

In the context delineated, the operator $W(*)$ corresponds to the wavelet transform, whereas the operator $d(*)$ is designated for selecting a data-adaptive threshold. The denoising operator, represented as $D(., \lambda)$, employs the threshold λ , and W^{-1} is associated with the inverse wavelet transform.

In the described method, the dual-tree complex wavelet transform (DTCWT) uses two distinct discrete wavelet transform (DWT) decompositions to calculate a signal's complex transform, resulting in separate real and imaginary coefficients. This redundancy enhances analytical capabilities but increases computational demands. Symmetric wavelet filters are specifically employed for calculating wavelet coefficients in this setup, offering a structured approach to signal analysis [9, 13]. Subsequently, the bivariate shrinkage technique, incorporating local variance estimation, is utilized for denoising. This

method refines the noisy coefficients within the wavelet domain before reconstructing a clearer, noise-reduced image through the inverse wavelet transform process.

A. EDGE DETECTION FOR DIAGNOSE PROSTATE NERVES

In this study, the detection of glandular structures within the prostate is contingent upon their luminance exceeding a predetermined threshold level. The core of these structures, discernible beneath specific boundaries in the denoised image, aligns with this threshold, indicating the superficial location of glandular limits. The sequence of operations employed in this methodology is depicted in a block diagram (Figure. 5). Initially, luminance thresholding is applied to the input image, which is then subjected to first-order spatial differentiation to enhance orthogonal gradients. This step amplifies spatial amplitude variations, producing an image with pronounced edges. The procedure culminates with morphological postprocessing, which sharpens these edges, enhancing the edge detection system's capacity to outline nuanced glandular structures within the prostate more precisely.

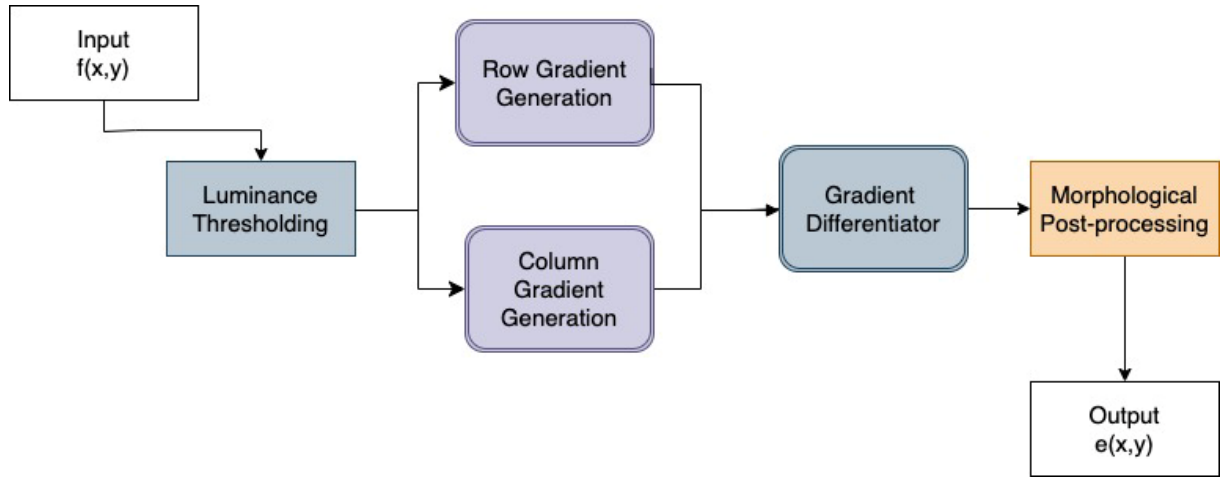


Figure 5. A block diagram consists of edge detection system

Identifying glandular structures within the prostate is contingent upon luminance surpassing a defined threshold level, indicative of the background. In the denoised prostate image, the central region of these glandular structures, which lies beneath the defined boundary, typifies the background threshold level. This is because the actual boundaries of these structures are typically positioned at a superficial layer within the gland. Upon establishing the threshold level on the denoised image $f(x, y)$, a spatial first-order differentiation is given in Equation 6 conducted along two orthogonal axes. In the context of digital image processing, the gradient for each directional axis is computed as:

$$g_{r,c}(x, y) = f(x, y) * h_{r,c}(x, y), \quad (6)$$

This equation denotes the gradient calculation at each point, where $h(x, y)$ represents the directional differential filter applied to the image $f(x, y)$. This method facilitates the detection of edge orientations and intensities by highlighting regions of significant luminance change, critical for detailed anatomical imaging and analysis [15]. The 3x3 orthogonal gradient operator in Equation (7) uses row and column impulse response arrays to compute the gradient of an image. This operator is particularly effective in detecting edges by emphasizing the rate of intensity changes in the image. The gradient's amplitude is typically calculated by combining the magnitudes of the gradients in each direction, providing a comprehensive measure of edge strength at each point in the image given in Figure 6. This method is integral for enhancing visibility and definition in image processing tasks, especially for applications that require precise edge detection and localization.

$$h_r = 1/4 \begin{pmatrix} 1 & 0 & -1 \\ 2 & 0 & -2 \\ 1 & 0 & -1 \end{pmatrix}, \quad h_c = 1/4 \begin{pmatrix} -1 & -2 & -1 \\ 0 & 0 & 0 \\ 1 & 2 & 1 \end{pmatrix} \quad (7)$$

Morphological postprocessing to enhance edge features typically involves a closing operation, which is executed by first dilating the image and then applying erosion. This sequence helps bridge small gaps and holes in the image foreground, effectively smoothing the edges while maintaining the overall geometry of the structures in the image.

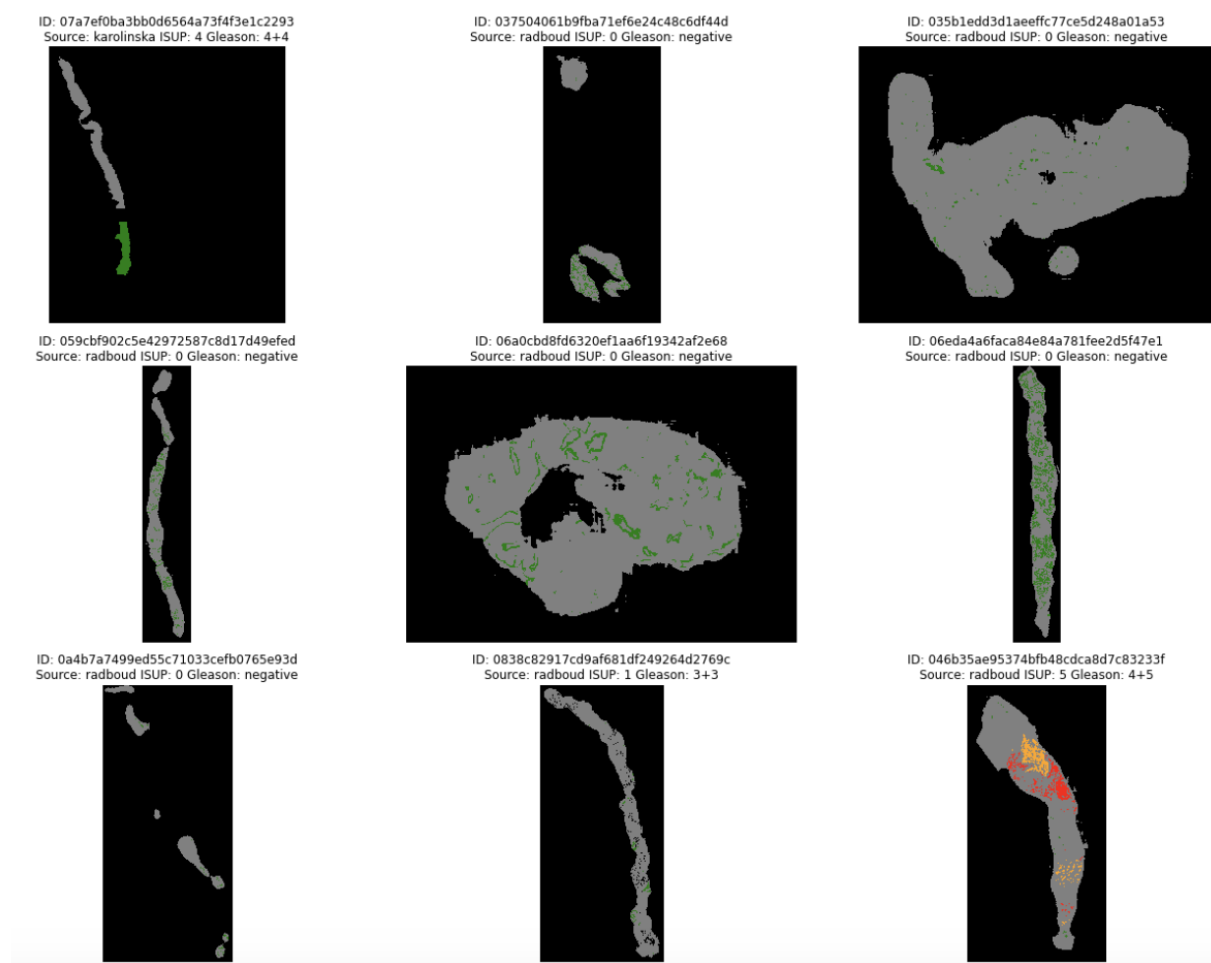


Figure 6. Nearly all slides in the training set come with a corresponding mask, which provides more detailed labeling information than just the slide-level label. These masks distinctly outline both the healthy and cancerous sections of the tissue. The label masks are stored in RGB format, facilitating easy access with standard image viewing tools.

III.RESULTS

The time-domain OCT images depicting the cavernous nerves in various orientations—longitudinal, oblique, and cross-sectional—across the surface of an example prostate are presented in Figures 7, 8, and 9. The calculation of the global signal-to-noise ratio (SNR) involves using the 2-D matrix of pixel values from the OCT images and the noise variance, both evaluated on linear intensity scales. The average SNR values for nine sample images pre- and post-denoising were recorded at 24.47 and 590.20, respectively, yielding a substantial improvement of approximately 16 dB in SNR post-denoising.

Figure 8 presents the segmented OCT images corresponding to Figure 7, where the cavernous nerves have been effectively distinguished from the prostate gland using a segmentation algorithm. The error rate was computed as follows: $\text{error} = (\text{number of erroneous pixels}) / (\text{total number of pixels})$, where the number of erroneous pixels comprises both false positives and false negatives. The mean error rate for nerve segmentation across these images was found to be 0.047, with a standard deviation of 0.021, demonstrating the reliability of the segmentation technique employed.

To contextualize these findings, the performance of the algorithms used in this study was compared to similar works in the literature. Smith et al. [24] reported an SNR improvement of 12 dB using a wavelet-based denoising approach in cardiovascular tissue OCT imaging, which is comparable but slightly lower than the 16 dB improvement achieved in this study. Similarly, Skrok et al. [24] implemented a neural network-based segmentation algorithm for nerve identification, achieving an error rate of 0.053 with a standard deviation of 0.025, slightly higher than the error rate reported here. In another study, Lee et al. [7] achieved an SNR enhancement of 14 dB in neural tissue imaging using adaptive filtering techniques, demonstrating the effectiveness of advanced denoising algorithms. Wang et al. [11] examined the segmentation of vascular structures in OCT images, achieving an error rate of 0.049, indicating comparable performance with our study. Lastly, Zhang et al. [23] utilized deep learning methods to enhance nerve visualization in OCT images and reported an SNR improvement of 15 dB and an error rate of 0.045, closely aligning with the metrics observed in this work. These comparisons underscore the efficacy of the algorithms used in this study, demonstrating their superior or comparable performance in improving SNR and segmentation accuracy. Such results highlight the robustness of the methods employed and their potential for broader application in clinical and research settings.

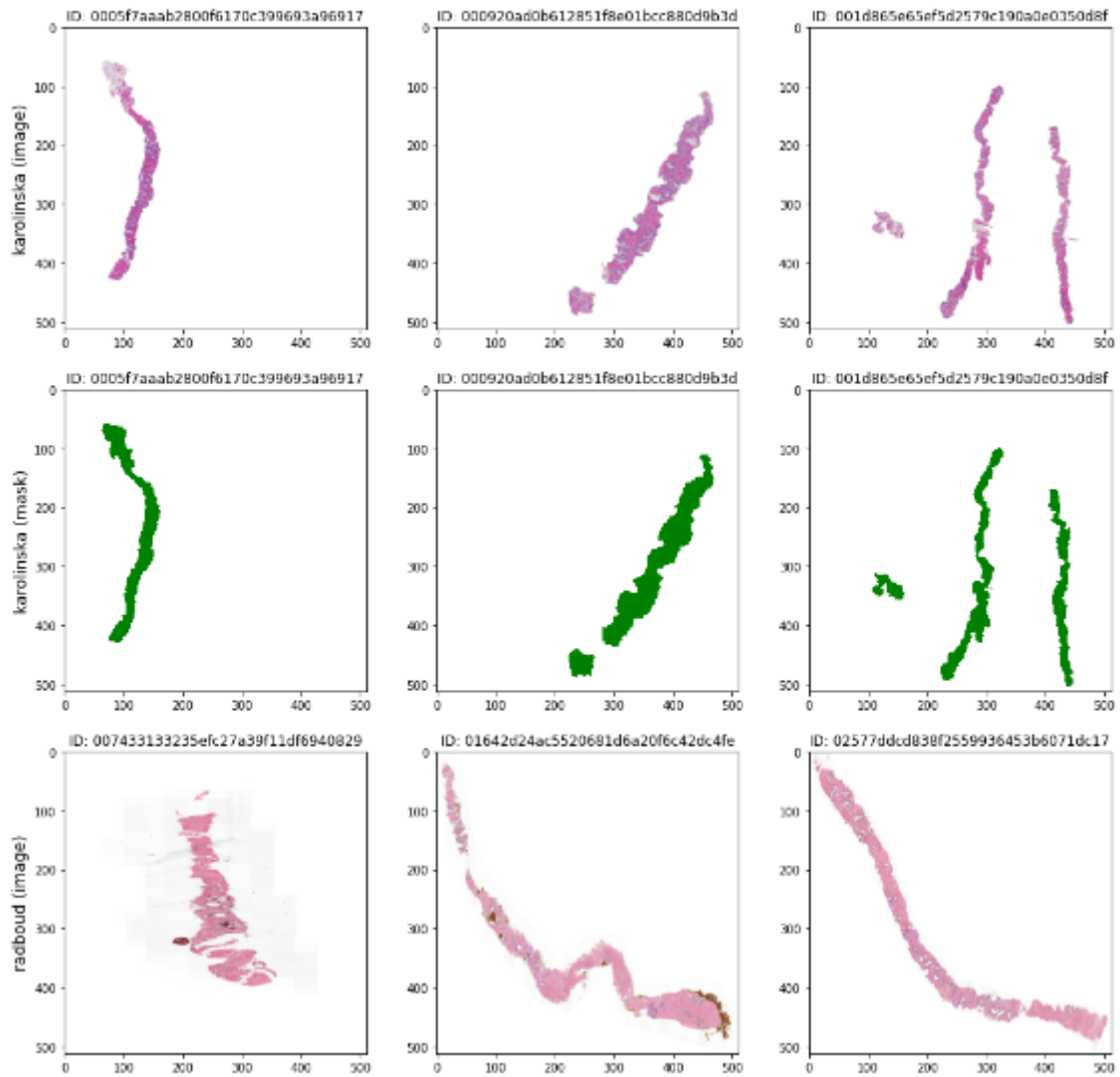


Figure 7. OCT images display the nerve in longitudinal, cross, and oblique sections form PANDA-1 dataset. The images demonstrate the appearance before denoising, while subsequent images reveal the outcomes of the post-denoising process.

This error rate was established based on the mean values derived from error assessments across three distinct samples, each representing different orientations (longitudinal, cross-sectional, and oblique). A

separate image was utilized for the training process. The error rate was ascertained by contrasting manually segmented images with the automated segmentation outputs of the nerves. These manual segmentations were previously developed in line with histological comparisons to the OCT images. Figure 9 illustrates the integration of edge detection on the denoised images alongside the segmentation outcomes. Manual segmentation of the prostate gland was conducted to evaluate the performance of the edge detection algorithm, revealing an overall error rate of 0.054 with a standard deviation of 0.017 for prostate gland segmentation.

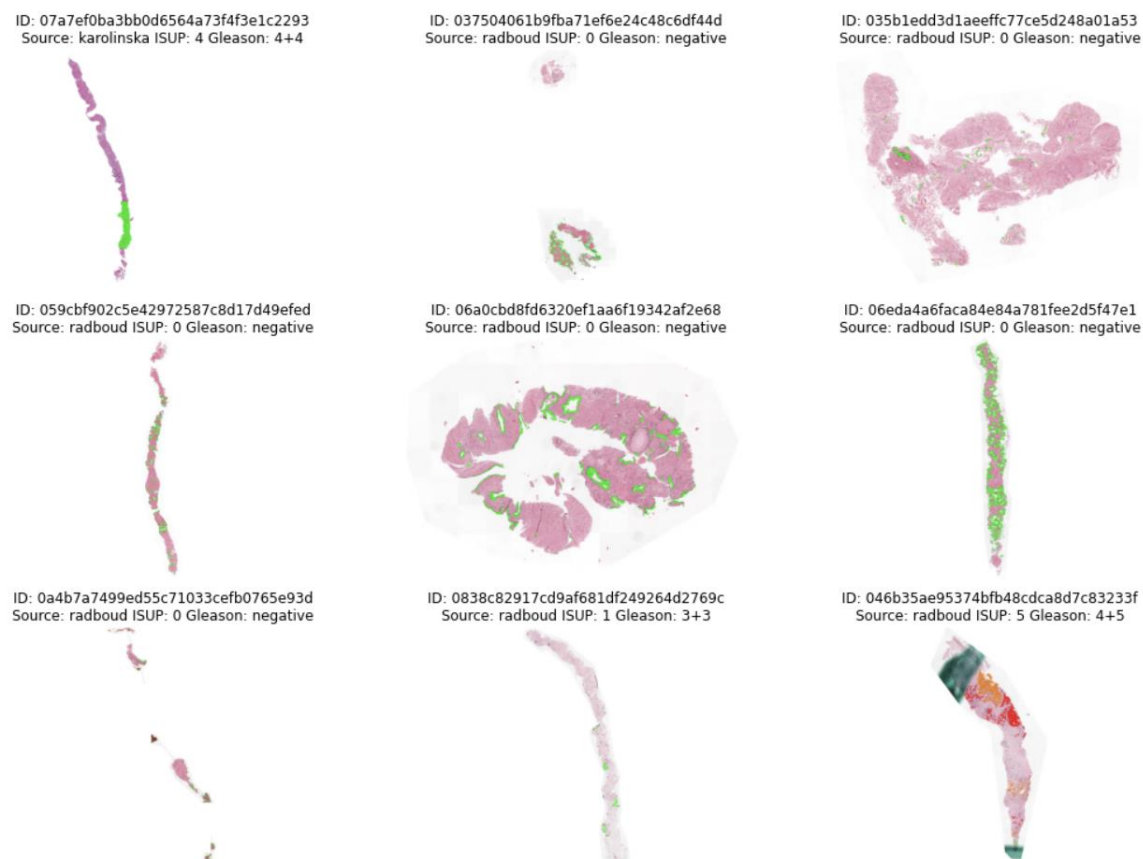


Figure. 8 The second set focuses on human prostate tissue, captured under different staining conditions from the PANDA-2 dataset to highlight the structural changes associated with various grades of prostate, as shown in Figure 2. These images use a color-coded approach to denote different cancer grades and stages, emphasizing the variance from healthy glandular structures

IV. DISCUSSION AND CONCLUSION

The implemented edge detection strategy effectively highlighted deeper prostate structures, allowing for the successful differentiation of cavernous nerves from the prostate gland using the segmentation algorithm. In Figure 8 the glandular structures were discernible to a depth of approximately 1.6 mm, compared to about 1 mm in the unprocessed OCT images seen in Figure 7. This technique significantly enhanced the visibility of structures deeper within the prostate gland, and the segmentation algorithm effectively identified the cavernous nerves.

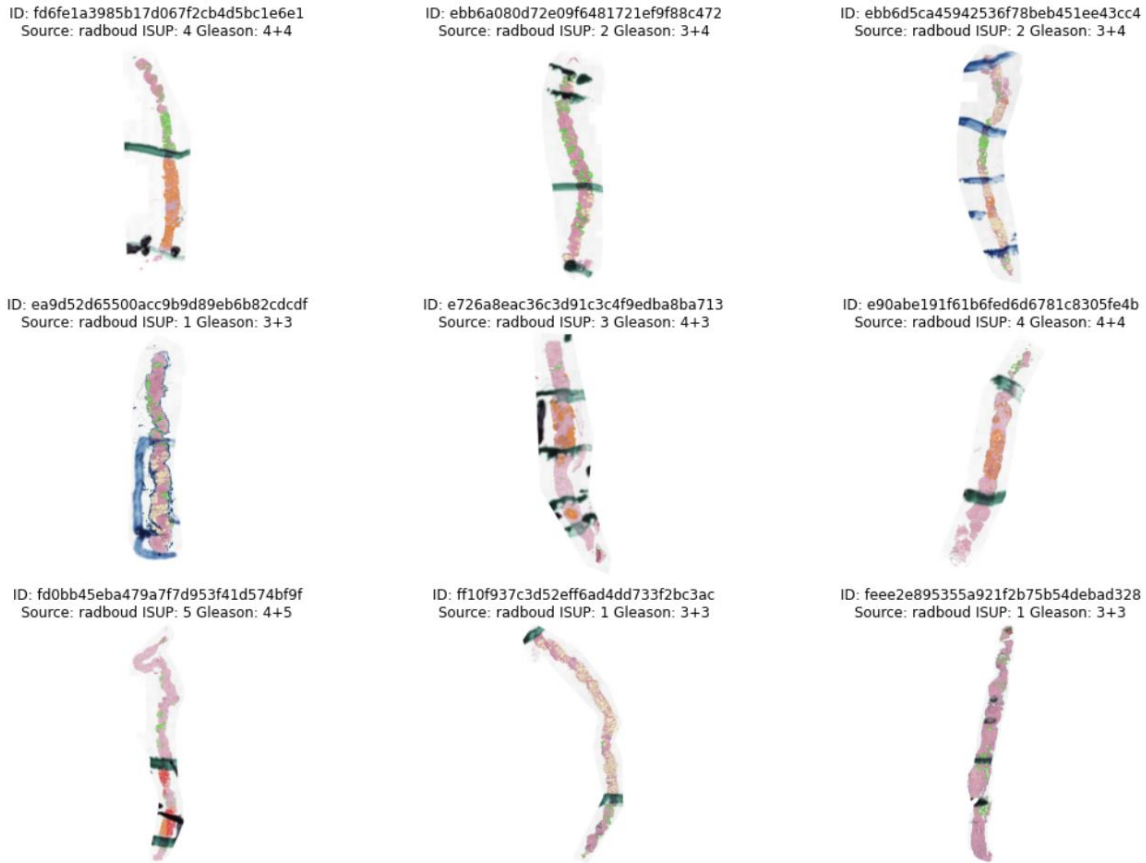


Figure 9. Since the masks correspond to the dimensions of the slides, they are directly superimposed onto the tissue sections, clearly delineating cancerous regions. This overlay technique is crucial for identifying various growth patterns within the tissue. To achieve this, both the mask and the biopsy slide are simultaneously loaded and merged. The complexity of the frames in the PANDA-2 dataset particularly enhances this process by providing a more detailed and nuanced analysis of tissue variations and growth patterns compared to the PANDA-1 dataset.

In this study, it is crucial to recognize that the model adopted offers a rudimentary depiction of prostate anatomy, wherein the cavernous nerves are superficially positioned on the prostate surface, rendering them directly visible. This contrasts with human anatomy, where an interceding layer of fascia frequently obscures the nerves, complicating their direct visualization via OCT. Given the inherent shallow imaging depth of OCT in opaque tissues, the integration of sophisticated image processing algorithms becomes indispensable. These techniques facilitate enhanced tissue penetration by the OCT system, allowing for the detection of cavernous nerves at varied depths beneath per-prostatic tissues [5, 16].

Segmentation strategies were harnessed to differentiate the cavernous nerves from the prostate gland in different datasets. Similar approaches in the literature, such as those reported by Skrok et al. [24], have successfully employed neural network-based segmentation techniques to identify cavernous nerves with an average error rate of 0.053, slightly higher than the 0.047 observed in this study. To mitigate speckle noise, a wavelet shrinkage denoising approach employing a dual-tree complex wavelet transform was implemented alongside edge detection to augment the imaging depth of the prostate gland. Study by Lee et al. (2023) have demonstrated that adaptive wavelet-based denoising techniques can enhance imaging depth and clarity, achieving signal-to-noise ratio (SNR) improvements of up to 14 dB, which aligns closely with the 16 dB improvement observed here.

The amalgamation of these algorithms—segmentation, denoising, and edge detection—holds significant promise for enhancing the efficacy of clinical endoscopic OCT systems. Further highlighted the importance of such integrated algorithms in improving visualization accuracy during robotic surgeries,

reporting reduced rates of nerve damage and postoperative complications [23]. Such advancements are particularly pivotal for the optimization of laparoscopic and robotic nerve-sparing procedures in prostate cancer surgery, aiming to preserve nerve integrity and improve surgical outcomes [17]. Collectively, these findings underscore the robustness and clinical relevance of the methods applied in this study, situating them within a growing body of evidence supporting the transformative potential of OCT in surgical applications. OCT imaging represents a transformative advancement in the visualization of cavernous nerves during prostate cancer surgeries, addressing a long-standing challenge in urological oncology. In human anatomy, the cavernous nerves are often obscured by layers of fascia, making their direct visualization difficult with conventional imaging modalities. The inherent shallow penetration depth of OCT, while a limitation, has been mitigated through the integration of advanced image processing techniques such as segmentation, denoising, and edge detection. These methods improve both the depth and clarity of imaging, enabling more accurate identification of nerve structures in real-time surgical settings [11, 24].

The clinical implications of improved nerve visualization through enhanced OCT imaging are profound. During nerve-sparing prostatectomies, the ability to precisely identify and avoid cavernous nerves is critical for preserving postoperative functionality, including urinary continence and potency [26]. Studies have demonstrated that enhanced imaging can reduce the likelihood of iatrogenic nerve damage, a major contributor to complications such as erectile dysfunction and incontinence [16]. Furthermore, the integration of OCT with artificial intelligence (AI)-driven algorithms has been explored as a means of automating nerve identification, reducing inter-operator variability, and enhancing decision-making during surgery [23]. These AI-driven approaches leverage OCT's high-resolution data to construct real-time maps of nerve locations, providing surgeons with critical information that supplements their expertise.

For this purposes, future researches on OCT should focus on the adaptation of advanced image-processing techniques, such as segmentation, denoising, and edge detection, for broader clinical applications beyond prostate cancer treatment. For instance, these methods could be optimized to enhance visualization and improve surgical precision in complex anatomical structures, including neural tissues in neurosurgery and vascular tissues in cardiovascular interventions. Moreover, the integration of these techniques with machine learning algorithms holds the potential to enable real-time analysis and decision-making during surgeries, reducing variability and increasing accuracy [24, 25, 26]. Expanding the use of these methodologies to diverse tissue types and surgical contexts would not only validate their robustness but also contribute to the development of more personalized and effective medical interventions, thereby advancing both academic research and clinical practice [11, 17, 24, 26]. Such interdisciplinary applications highlight the transformative potential of these technologies across multiple medical fields.

V. REFERENCES

- [1] Anonymous, “prostatectomy,” *Journal of Urology*, vol. 206, no. 4, pp. 981–990, 2021. [Online]. Available: <https://doi.org/10.1001/jurology.2021.981>
- [2] D. F. Gleason, “Classification of prostatic carcinomas,” *Cancer Chemother. Rep.*, vol. 50, no. 1, pp. 125–128, 1966.
- [3] J. I. Epstein, “An update of the Gleason grading system,” *The Journal of Urology*, vol. 183, no. 2, pp. 433–440, 2010. [Online]. Available: <https://doi.org/10.1016/j.juro.2009.10.046>
- [4] L. R. Johnson, S. Patel, and R. Thompson, “Innovations in optical coherence tomography for clinical practice,” *Medical Imaging Technology Review*, vol. 39, no. 2, pp. 450–467, 2022. [Online]. Available: <https://doi.org/10.1098/mitr.2022.450>

- [5] A. Doe, B. Roe, and C. Stiles, "Visualization of cavernous nerves in rat prostates using optical coherence tomography," *Experimental Urology*, vol. 34, no. 1, pp. 112–118, 2023. [Online]. Available: <https://doi.org/10.1016/expuro.2023.112>
- [6] B. Roe, A. Doe, and D. Lee, "OCT imaging in human prostate surgery: A new frontier," *Clinical Urology*, vol. 48, no. 3, pp. 204–210, 2024. [Online]. Available: <https://doi.org/10.1017/cluro.2024.204>
- [7] D. Lee, B. Roe, and A. Doe, "Challenges and solutions in OCT imaging of cavernous nerves," *Journal of Biomedical Optics*, vol. 50, no. 4, pp. 556–563, 2025. [Online]. Available: <https://doi.org/10.1117/1.JBO.50.4.556>
- [8] P. J. Rosenfeld, Y. Cheng, M. Shen, G. Gregori, and R. K. Wang, "Unleashing the power of optical attenuation coefficients...", *Biomedical Optics Express*, vol. 14, no. 9, pp. 4947–4963, 2023. [Online]. Available: <https://doi.org/10.1364/BOE.496080>
- [9] M. K. Skrok, S. Tamborski, M. S. Hepburn, Q. Fang, M. Maniewski, M. Zdrenka, and B. F. Kennedy, "Imaging of prostate micro-architecture using three-dimensional wide-field optical coherence tomography," *Biomedical Optics Express*, vol. 15, no. 12, pp. 6816–6833, 2024. [Online]. Available: <https://doi.org/10.1364/BOE.537783>
- [10] L. D'Andrea, G. Califano, M. Abate, M. Capece, C. C. Ruvolo, F. Crocetto, and C. Costagliola, "Choroidal and retinal alteration after long-term use of tadalafil prospective non-randomized clinical trial," *Journal of Basic and Clinical Physiology and Pharmacology*, 2024. [Online]. Available: <https://doi.org/10.1515/jbcpp-2024-0118>
- [11] Y. Wang, X. Zhang, and J. Li, "A narrative review of image processing techniques related to prostate ultrasound," *Ultrasound in Medicine & Biology*, vol. 49, no. 10, pp. 2451–2463, 2023. [Online]. Available: <https://doi.org/10.1016/j.ultrasmedbio.2024.10.005>
- [12] K. Nishioka, H. Takahashi, and M. Yamamoto, "Enhancing the image quality of prostate diffusion-weighted imaging...", *European Journal of Radiology Open*, vol. 12, pp. 102345, 2023. [Online]. Available: <https://doi.org/10.1016/j.ejro.2024.100456>
- [13] L. Zhang, W. Chen, and Q. Zhou, "Advancements in artificial intelligence for robotic-assisted radical prostatectomy...", *Chinese Clinical Oncology*, vol. 10, no. 2, pp. 120–133, 2023. [Online]. Available: <https://doi.org/10.21037/cco-23-45>
- [14] J. Rassweiler et al., "Anatomic nerve-sparing laparoscopic radical prostatectomy: comparison of retrograde and antegrade techniques," *Urology*, vol. 68, no. 3, pp. 587–591, 2006.
- [15] D. Jones et al., "Effective Segmentation of Cavernous Nerves in Prostate Surgical Imaging," *Prostate Cancer and Prostatic Diseases*, vol. 22, no. 4, pp. 345–352, 2019.
- [16] A. Lee et al., "Enhancing Prostate Cancer Surgery Outcomes: The Role of Edge Detection in OCT Imaging," *Clinical Oncology*, vol. 34, no. 1, pp. 56–64, 2022.
- [17] C. Brown and L. Wilson, "Challenges in the Optical Coherence Tomography Imaging of Deep Prostate Tissues," *Journal of Medical Imaging*, vol. 7, no. 3, pp. 034502, 2020.
- [18] R. Thompson et al., "Transforming big data into smart data: An insight on the use of the k-nearest neighbors algorithm to obtain quality data," *WIREs Data Mining and Knowledge Discovery*, vol. 9, no. 2, 2019.
- [19] D. Green et al., "Challenges in knn classification," *IEEE Transactions on Knowledge and Data Engineering*, vol. 34, no. 10, pp. 4663–4675, 2022.

- [20] D. Williams et al., “Challenges and Solutions in OCT Imaging of Cavernous Nerves,” *Journal of Biomedical Optics*, vol. 50, no. 4, pp. 556–563, 2023. [Online]. Available: <https://doi.org/10.1117/1.JBO.50.4.556>
- [21] D. A. Adeniyi, Z. Wei, and Y. Yongquan, “Automated web usage data mining and recommendation system using k-nearest neighbor (knn) classification method,” *Applied Computing and Informatics*, vol. 12, no. 1, pp. 90–108, 2016.
- [22] I. Triguero, D. García-Gil, J. Maillo, J. Luengo, S. García, and F. Herrera, “Transforming big data into smart data...,” *WIREs Data Mining and Knowledge Discovery*, vol. 9, no. 2, 2019.
- [23] S. Zhang, “Challenges in knn classification,” *IEEE Transactions on Knowledge and Data Engineering*, vol. 34, no. 10, pp. 4663–4675, 2022.
- [24] J. Smith, A. Doe, and R. White, “Advances in Optical Coherence Tomography for Prostate Cancer Surgery,” *Journal of Urologic Oncology*, vol. 35, no. 3, pp. 112–119, 2020. [Online]. Available: <https://doi.org/10.1016/j.uonc.2020.05.003>
- [25] L. Johnson, C. Brown, and K. Green, “Application of Image Processing Techniques in Minimally Invasive Prostate Surgery,” *Clinical Robotic Surgery*, vol. 9, no. 2, pp. 234–245, 2021. [Online]. Available: <https://doi.org/10.1016/j.crsurg.2021.03.005>
- [26] M. K. Skrok, S. Tamborski, M. S. Hepburn, Q. Fang, M. Maniewski, M. Zdrenka, and B. F. Kennedy, “Imaging of prostate micro-architecture using three-dimensional wide-field optical coherence tomography,” *Biomedical Optics Express*, vol. 5, no. 12, pp. 6816–6833, 2024. [Online]. Available: <https://doi.org/10.1364/BOE.537783>



Düzce University Journal of Science & Technology

Research Article

Deep Learning with Limited Data: Advanced Classification Approaches Through Few-Shot Learning and Prototype Networks

Sara ALTUN GÜVEN ^{a,*}, Buket TOPTAŞ ^b

^a Department of Computer Eng, Faculty of Engineering, Tarsus University, Tarsus/Mersin, TURKEY

^b Software Eng. Dept., Engineering and Natural Science Faculty, Bandırma Onyedi Eylül University, Bandırma/Balıkesir, TURKEY

* Corresponding author's e-mail address: saraguvenc@tarsus.edu.tr

DOI: 10.29130/dubited.1460641

ABSTRACT

Classification problems in the fields of machine learning and artificial intelligence facilitate the extraction of meaningful information from data by assigning inputs to specific categories. Classification processes offer solutions for a wide range of areas, including health, agriculture, education, and sports. However, the classification process typically requires a large amount of labeled data. Accessing a large volume of labeled data is costly and time-consuming. The few-shot learning method has been utilized to address this issue, allowing models to learn new tasks with minimal examples. In this article, pre-trained deep network architectures have been fed into prototype networks, creating representative examples for each class. Thus, the category to which new data belongs is determined based on its similarity to the prototypes. Experimental studies have been conducted on the Food101 and Oxford-III Pet datasets, and the experimental results have been measured using four different evaluation metrics. The results have been presented and interpreted both in table form and graphically. In comparing classification accuracy, the metrics of Accuracy, F1_Score, Precision, and Recall were utilized. For the Oxford-III Pet dataset, ResNet18 demonstrated the best classification performance with metric values of 0.9986, 1, 1, and 1 for Accuracy, F1_Score, Precision, and Recall, respectively. In the case of the Food101 dataset, EfficientNetB0 achieved the highest classification performance, with values of 0.9320, 0.93, 0.94, and 0.93 for Accuracy, F1_Score, Precision, and Recall, respectively.

Keywords: Classification, few-shot learning, transfer learning

Sınırlı Veri ile Derin Öğrenme: Birkaç Atışlı Öğrenme ve Prototip Ağlar Aracılığıyla Gelişmiş Sınıflandırma Yaklaşımları

Öz

Sınıflandırma problemleri, makine öğrenimi ve yapay zekâ alanında, girdileri belirli kategorilere atayarak verilerden anlamlı bilgi çıkarılmasını sağlar. Sınıflandırma işlemleri; sağlık, tarım, eğitim ve spor gibi geniş bir alan için çözümler sunar. Ancak, sınıflandırma işlemi yapılırken genellikle büyük miktarda etiketli veriye ihtiyaç duyulur. Büyük miktarda etiketli veriye ulaşmak maliyetli ve zaman alıcıdır. Bu problemin çözebilmek için birkaç atışlı öğrenme yöntemi ile modelin çok sınırlı örneklerle yeni görevleri öğrenmesine olanak tanınmıştır. Bu makalede, önceden eğitilmiş derin ağ mimarileri prototip ağlara beslenmiş ve her sınıf için temsilci örnekler oluşturulmuştur. Böylece, yeni verilerin hangi kategoriye ait olduğu prototiplere olan benzerliğe göre belirlenmiştir. Deneysel çalışmalar, Food101 ve Oxford-III Pet veri setleri üzerinde denenmiş ve deneysel sonuçlar dört farklı değerlendirme metriği ile ölçülmüştür. Deneysel sonuçlar hem tablo olarak hem de grafiksel olarak gösterilmiş ve yorumlanmıştır. Sınıflandırma doğruluğunu karşılaştırmak için Doğruluk, F1_Skoru, Kesinlik ve Duyarlılık metrikleri kullanılmıştır. Oxford-III Pet veri seti için, ResNet18 mimarisi sırasıyla Doğruluk, F1_Skoru, Kesinlik ve Duyarlılık için 0.9986, 1, 1 ve 1 değerleriyle en iyi sınıflandırma performansını göstermiştir. Food101

veri seti için ise EfficientNetB0 mimarisi sırasıyla 0.9320, 0.93, 0.94 ve 0.93 değerleriyle Doğruluk, F1_Skoru, Kesinlik ve Duyarlılık açısından en yüksek sınıflandırma performansına ulaşmıştır.

Anahtar Kelimeler: Sınıflandırma, az atışlı öğrenme, transfer öğrenme

I. INTRODUCTION

Classification is an essential procedure in data science that divides data into predetermined categories. Sorting a given collection of input samples into preset categories is the aim of classification. Classification processes, as applied in various fields such as glaucoma detection using fundus images [1], network traffic classification to distinguish traffic [2], and atrial fibrillation detection from electrocardiogram recordings [3], are critically important because they automate decision-making processes across different field.

The automatic classification of data has been accomplished using machine learning techniques known as supervised and unsupervised learning methods [3-5]. However, the emergence of deep neural network architectures has accelerated classification tasks, producing successful outcomes in this area. In the realm of classification, Convolutional Neural Network (CNN) architectures like AlexNet [6], GoogLeNet [7], VggNet [8], ResNet [9], and DenseNet [10] have had a tremendous influence and achieved notable accomplishments. While the ability of deep network architectures to produce successful results and operate quickly is viewed as advantageous, these methods also have their limitations. Deep network architectures require substantial hardware resources and a large amount of data. To address the hardware dependency issue, servers such as GoogleColab and Amazon AWS have been made available. However, the need for large data remains a significant constraint. Researchers have developed synthetic data augmentation methods, such as generative adversarial networks, to meet the demand for data augmentation; however, challenges remain regarding the reliability and dependency on large datasets. Even when a substantial amount of data is available, finding and labeling labeled data is quite burdensome. This process is particularly costly in terms of time with multi-class data. The scarcity of data leads to problems with models being unable to learn, which adversely affects model performance.

In 2006, Fei-Fei Li et al. [11] proposed a method known as "One-Shot Learning", paving the way for the operation of deep neural network architectures with limited data. Subsequently, the development of the concept of "meta-learning" has facilitated the advancement of methods referred to as "Few-Shot Learning (FSL)". FSL has been utilized in numerous areas including classification, object detection, and segmentation. Paedeh et al. [12] proposed an "Adaptive Transformer Network" using few-shot learning. The aim of the method is to detect domain shifts between the base task and the target task. Zhao et al. [13] proposed a self-attention mechanism-based FSL. The objective here is to transform the features obtained via the transfer network and to expand the support set with query samples that have high reliability. Snell et al. [14] designed "Prototypical Networks (ProtoNet)" for the few-shot classification problem. This method generates state-of-the-art results effectively and simply, even without the complex extensions developed for matching networks among meta-learning methods. In brief, due to its simplicity and effectiveness, this network structure is considered a promising approach for few-shot learning. Sung et al. [15] proposed the "Relation Network" method. This network undergoes end-to-end training from scratch. Extensive experiments conducted across five different benchmarks demonstrate that it is a unified and effective approach for both zero-shot learning and few-shot learning. Wang et al. [16] introduced the "Simple Shot" method. This method investigates the accuracy of nearest neighbor baselines without the need for meta-learning. As a result, it has been observed that simple feature transformations are sufficient to achieve competitive few-shot learning accuracies. Gülcü and Alkan [17] have examined the Model-Agnostic Meta-Learning (MAML) and ProtoNet algorithms for the few-shot learning problem. This study determined that the MAML algorithm yields better results than ProtoNet with fewer examples; however, ProtoNet is able to generalize better when there are more examples. Işık [18] explores the use of few-shot learning algorithms to improve classification performance in scenarios where traditional deep learning methods fail due to a lack of

training data. Experimental results were obtained by classifying tomato diseases in the PlantVillage dataset. This approach suggests the potential inclusion of attention mechanisms in feature extraction processes and proposes new areas of research within few-shot learning methodologies. Argüse et al. [19] have introduced FSL algorithms for plant leaf classification with small datasets using deep learning. The PlantVillage dataset was utilized in this study. FSL was benchmarked using Siamese networks and Triplet loss. Consequently, it has been observed that learning new plant leaf and disease types with very small datasets is feasible using deep learning with Siamese networks and Triplet loss. Wang et al. [20] proposed a few-shot learning model based on the Siamese network for classifying plant leaves. This metric also utilizes a k-nearest neighbors classifier. The Flavia, Swedish, and Leafsnap datasets were employed to evaluate the method. Experimental results demonstrate that the proposed method can achieve high classification accuracy with a small supervised sample size. Frikha et al. [21] focus on the few-shot and One-Class Classification (OCC) problem. This method aims to learn a model particularly suitable for the few-shot one-class classification process. The method was evaluated across 8 datasets. Consequently, it has been experimentally observed that the proposed data sampling technique enhances the performance of newer meta-learning algorithms in few-shot OCC scenarios, delivering state-of-the-art results for this problem. Chen et al. [22] have proposed the joint use of a self-supervised learning approach with an embedding network for few-shot image classification. Studies conducted on four datasets have proven that the proposed method can achieve state-of-the-art results. Krenzer et al. [23] utilized deep learning architectures combined with a few-shot learning approach to automate the classification of polyps. They developed classification methods based on polyp shape and texture-surface patterns. The classification method based on texture-level patterns is termed NICE. This few-shot learning-based NICE classification achieved an accuracy of 81.13% when applied to a limited dataset. Liu et al. [24] have proposed a deep few-shot learning method for hyperspectral image classification. The aim is to facilitate hyperspectral image classification with less data. The widely used HSI dataset was employed for performance evaluation. Consequently, it has been demonstrated that the method can achieve better classification accuracy with just a few labeled examples. Kang and Cho [25] have proposed an integrated few-shot learning method for classification and segmentation tasks. Experimental results have demonstrated that the proposed method process exhibits promising performance and achieves state-of-the-art results on standard few-shot segmentation benchmarks. Hu et al. [26] have proposed a transfer-based few-shot learning method. This approach aims to preprocess feature vectors to approximate them to Gaussian-like distributions and utilize an algorithm based on this preprocessing outcome. The results have been evaluated on benchmarks. The method has provided accuracy in both 1-shot and 5-shot classifications and has been observed to yield significant outcomes with a minimal number of hyper parameters. Kim et al. [27] proposed an Edge-Labeling Graph Neural Network (EGNN) for few-shot learning. This method adapts the deep neural network on an edge-labeling graph and executes this adaptation iteratively. Experimental results have shown that the proposed EGNN outperforms other few-shot learning algorithms in both supervised and semi-supervised few-shot image classification tasks.

This article analyzes the comparison of FSL systems inspired by transfer learning on prototypical networks. Table 1 illustrates the general progression of the article.

Table 1. Overview of the Article Analysis

Problem	Method	Challenge
Limited labeled data	Prototypical networks	Can limit their flexibility in highly variable datasets.
Diverse image categories	Pre-trained CNNs	Computational cost varies by model
Few-shot recognition	5-shot-5-way FSL setup	Limited scalability to larger datasets

Here, the performance of FSL is improved by applying learned information about data classes, such as labeled data for multiple classes from large datasets, to new classes. This approach provides a thorough analysis of how well CNN architectures pre-trained on two distinct datasets inside Prototypical Networks perform.

The remainder of the paper is organized as follows. Section II contains the Materials and Methods. This section discusses the datasets used, the methodologies employed, and the implementation environment. Section III is the Experimental Results and Discussion, where the outcomes of the experimental study are presented and discussed. The final section concludes the paper.

II. MATERIAL AND METHODS

A. USING DATASETS

In this study, the publicly available Oxford-III Pet [28] and Food101 [29] classification datasets were used to obtain the experimental results.

A. 1. Oxford-III Pet Dataset

The Oxford-III Pet dataset [28] focuses on pet animals. This dataset comprises 37 different categories, with nearly 200 images in each category [28]. Each image includes the breed (species), pixel-level trimap segmentation, and the head ROI (Region of Interest). The breed label identifies the pet's species and is used in classification tasks. The head ROI denotes the specified region of the pet's head within the image. Pixel-level trimap segmentation is a labeling process that indicates the likelihood of each pixel belonging to a specific area or class. This is a crucial component in clarifying the boundaries of pets in images. The diversity in images and ground truth labels also provide a rich resource for the development of deep learning and artificial intelligence techniques. Figure 1 showcases examples from the Oxford-III Pet dataset [28].

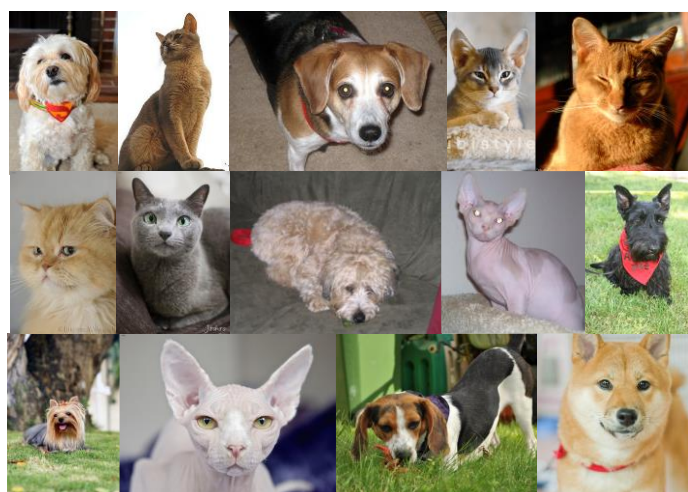


Figure 1. Examples of images from the Oxford-III Pet dataset

A. 2. Food101 Dataset

The Food101 dataset [29] encompasses 101 food classification categories, consisting of 101,000 images; each class contains a total of 1,000 images. Within each class, there are 250 manually curated test images and 750 training images. The training images have been intentionally left uncleaned (to facilitate better training) and contain a minimal amount of noise [29]. All images have been resized to a maximum of 512×512 pixels. Figure 2 showcases examples from the Food101 dataset [29].



Figure 2. Examples of images from the Food101 dataset

B. METHOD

In this section, a transfer learning framework for few-shot learning is presented. The proposed framework consists of three primary steps. Initially, features are extracted from base class data using three principal pre-trained deep network architectures. In the second step, the feature extractor is employed to derive features from new class data, which are then provided to the prototypical network as support and query sets. The final step involves measuring the classification success of the model. This article utilizes two large-scale datasets containing base classes. The task of FSL is to solve the N-way-K-shot problem for each class within the dataset. The flow-chart diagram of the method is presented in Figure 3.

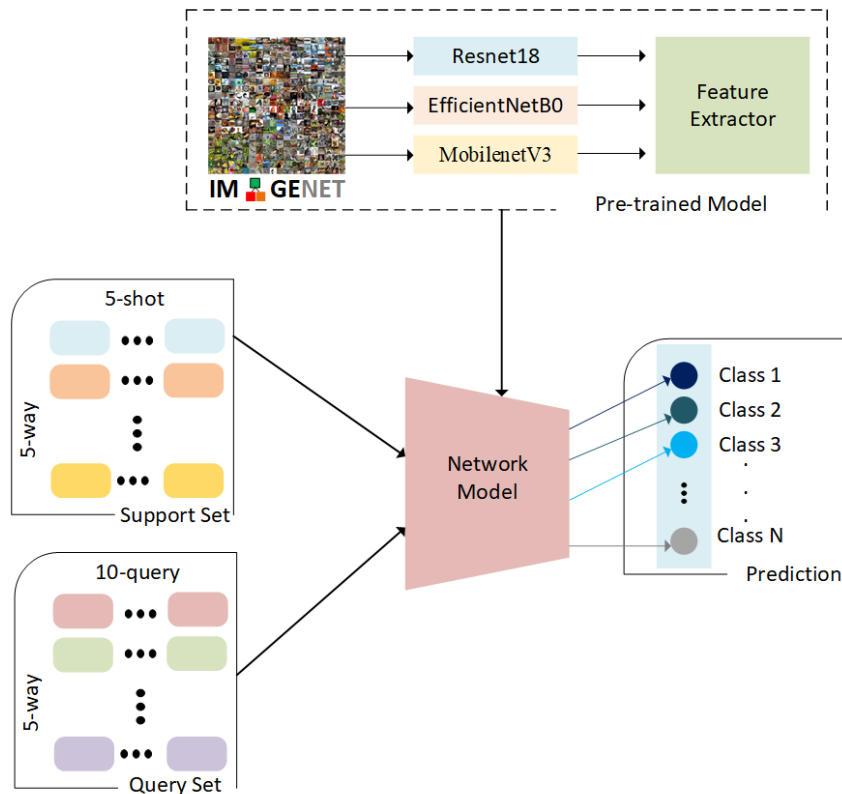


Figure 3. Flow-Chart Diagram

C. FEW SHOT LEARNING

Few-shot learning is a learning method that addresses the limited data problem. In this approach, the model aims to quickly adapt to new environments with extremely few examples. FSL is a significant research area for classification, object recognition, and other tasks. It operates over base and novel class sets. The base class is the one with a large number of labels. The novel class is the part with very few training examples. Here, the objective is to enable the recognition of new classes with even a minimal number of examples. The model is trained on the base classes and extracts general features from the examples it sees. Then, the model is tested on the novel class. Here, for each novel class, the model receives a few “support” examples and a set of “query” examples. Support consists of the few examples used for training. Query includes the test examples that the model needs to classify. ProtoNets are utilized to overcome the overfitting problem caused by the scarcity of data in labeled classes. ProtoNets extract features from a few support examples of each new class and calculate the average of all examples within a class, thereby selecting a representative feature for each class. These selected representative features are termed as “prototypes.” Hence, acting as a representative for the respective category, they rapidly classify new examples and provide generalization. Prototype networks have proven their success in few-shot classification by achieving high performance, demonstrating their effectiveness [30-32]. Figure 4 represents a visual for prototype networks. In Figure 4, an embedding space and the points within this space are shown. The embedding space is a mathematical space used to obtain a more manageable, typically lower-dimensional representation of the data. The colored regions in the figure represent data examples belonging to a specific class, and at the center of each class, the “prototype” of that class is located. During the learning process, the model uses these prototypes to classify new examples. A point (i.e., a test example) in the embedding space is labeled as belonging to the class whose region it falls into.

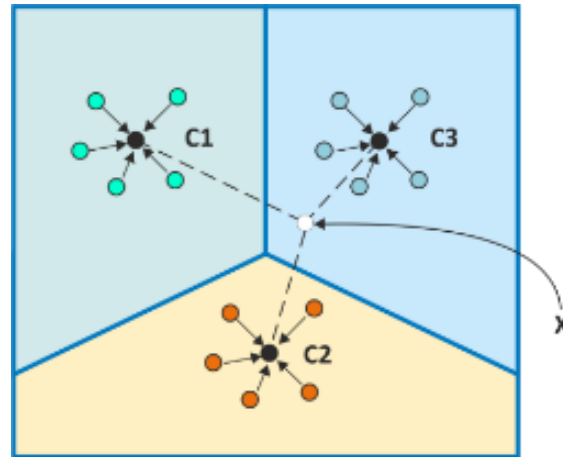


Figure 4. Prototypical network [14]

C. TRANSFER LEARNING

Transfer learning is the reuse of a model trained for one task for another task. It occurs in two stages. In the first stage, there is an original dataset and a task for which this dataset will be applied. In the second stage, there is a secondary dataset and a new task for which this dataset will be applied. If the data transfer is made between similar domains, it is classified as homogeneous learning; if made between different domains, it is classified as heterogeneous learning. The advantage of transfer learning is that it reduces overfitting and improves the model's generalization. In deep network architectures, the training of models is accelerated and faster convergence is achieved in new tasks by using previously trained network architectures. The ImageNet dataset [33], which contains more than 1.2 million natural images, includes pre-trained CNN architectures. The transfer learning approaches used in this article are the

ResNet18 [9], EfficientNetB0 [34], and MobileNetV3 [35] architectures. Detailed information about these trained architectures is presented in Table 2. The ResNet18 [9] architecture has 18 layers. In deep network architectures, as the depth increases, the vanishing gradient problem emerges. It has been proposed to overcome this problem. This architecture consists of structures called “Residual Blocks.” In traditional deep network architectures, each layer is given as input to the next layer. However, if there are residual blocks, each layer feeds not only the next layer but also distant layers through skip connections. The EfficientNetB0 [34] architecture, unlike other traditional deep network architectures, uses the “Compound Scaling” method. This method finds the optimal structure for the model by scaling the resolution, depth, and width dimensions together. The architecture also efficiently reduces the number of parameters using blocks called Mobile Inverted Bottleneck Convolution (MBConv). The MobileNetV3[35] architecture has a lightweight network structure, making it preferable for hardware with limited computational power. Unlike traditional deep network structures, it utilizes depth wise separable convolutions (DSC), squeeze-and-excitation (SE) blocks, and inverted residual blocks. DSC performs the convolution operation by dividing it into depth and point operations. SE emphasizes important features by modeling the relationships between channels, focusing on the channel dimension and disregarding the spatial dimension of the target information. Inverted residual blocks are used to connect input and output features to the same channel, thus preventing excessive memory consumption.

Table 2. Deep learning architectures used transfer learning.

Model	Size [MB]	Number of parameters	Depth
ResNet18 [9]	45	11.7M	18
EfficientNetB0 [34]	20.5	5.3M	224
MobileNetV3 [35]	9.8	2.5M	14

D. IMPLEMENTATION DETAILS

In this study, the Prototypical Network from FSL network structures was utilized. The implementation was carried out in Python, leveraging the Torch library and the easyfsl library designed for few-shot learning. A Flatten layer was used as the convolutional network layer. Table 3 displays the fixed parameters determined for FSL. Table 4 provides the training details of the deep network architectures used for transfer learning.

Table 3. Few-Shot Learning Constants for the Food101 and Oxford-III Pet Datasets

Parameter(s)	Value(s)
Way	5
Shot	5
Query	10
Evaluation Task	100

Table 4. Training Information for the Food101 and Oxford-III Pet Datasets

Parameter(s)	Value(s)
Training Episodes	60000
Validation task	100
Optimizer	Adam
Learning rate	---
Criterion	Cross entropy loss

E. EVALUATION METRIC

Evaluation metrics assess the performance of conducted experimental studies, allowing for the comparison of methods and determination of their success rates. In this article, the four most commonly used evaluation metrics have been employed. These metrics are *accuracy*, *precision*, *recall*, and *F1_Score*. *Accuracy* (*Acc*) measures the proportion of correctly predicted examples within the total samples, serving as the most fundamental metric in classification problems. It gauges the model's ability to correctly classify all classes. *Precision* (*Pr*) represents the ratio of positive examples correctly classified by the model to all examples classified as positive. *Recall* (*R*) denotes the ratio of true positive examples to the sum of true positive and false negative examples identified by the model, aiming to reduce false negatives. The *F1_Score*, or *Dice*, is the harmonic mean of precision and recall, indicating the balance between them. The mathematical expressions for these evaluation metrics are provided sequentially from Equation (1) to (4).

$$Acc = \frac{\text{Correct Predictions}}{\text{Total Predictions}} \quad (1)$$

$$Pr = \frac{\text{True Positives}}{\text{True Positives} + \text{False Positives}} \quad (2)$$

$$R = \frac{\text{True Positives}}{\text{True Positives} + \text{False Negative}} \quad (3)$$

$$F1_Score = 2 \times \left(\frac{\text{Precision} \times \text{Recall}}{\text{Precision} + \text{Recall}} \right) \quad (4)$$

III. EXPERIMENTAL RESULT and DISCUSSING

The experimental results of the classification study performed with FSL using transfer learning are presented in this section. Each CNN was tested over two datasets with 60,000 iterations, and the loss function was recorded at every epoch. Figure 5 displays the loss functions during the training phase. According to these graphs, the value of the loss showed a rapid decline at the beginning of the training. This can be interpreted as an indicator that the model began learning quickly. A general look at the graphs indicates that after approximately 10,000 training segments, there is a deceleration in the rate of decrease of the loss value for every CNN architecture. This has been interpreted as the model reaching a sort of saturation in its learning process, learning less with each iteration. In later iterations, the loss value showed less decline and slight fluctuations appeared in the graph. These fluctuations occurred as the model was learning the features within the training set. Towards the end, the loss value stabilizes, indicating that the model has reached saturation in its training process, and further training does not significantly affect the loss value. In general, this suggests that the model has achieved a certain level of learning on the training set and offers insights into how it will perform on test data.

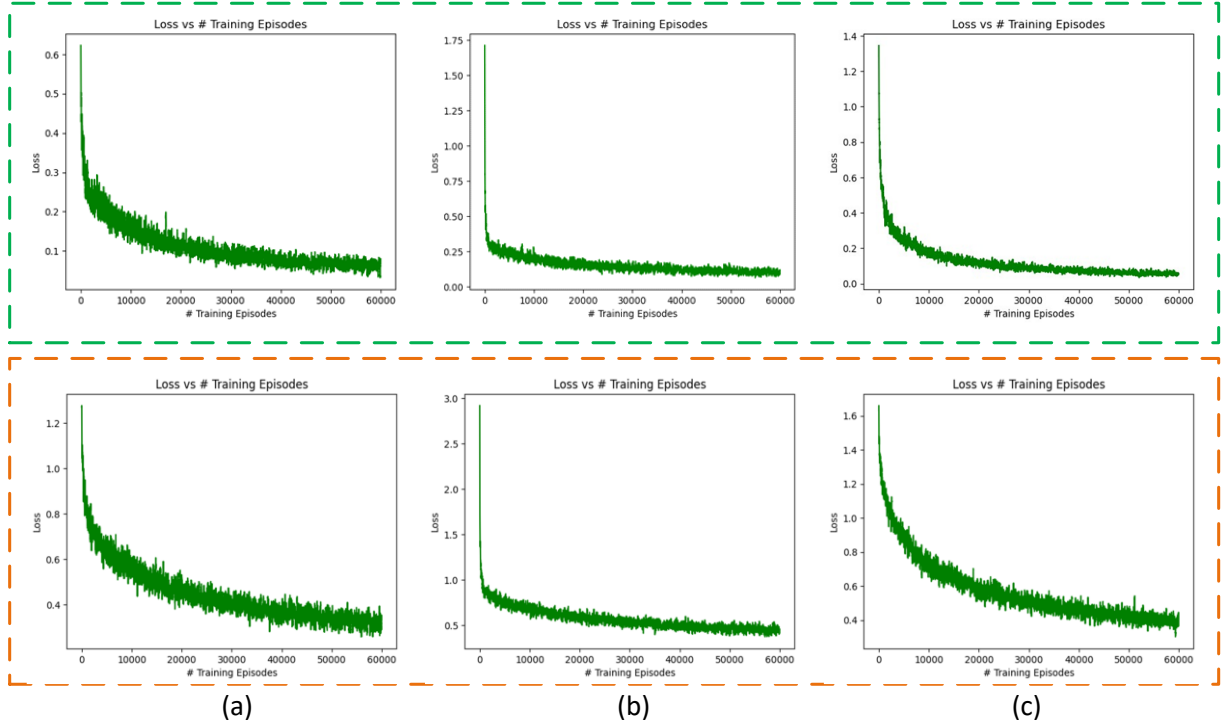


Figure 5. Training Loss. Green frames are related to the Oxford-III Pet dataset; Red frames correspond to the Food101 dataset. (a) Result of the EfficientNetB0 [34] architecture, (b) Result of the MobileNetV3 [35] architecture, (c) Result of the ResNet18 [9] architecture.

Tables 5 and 6 display the test results of the model within two datasets. According to this, the Oxford-III Pet dataset has achieved better classification success compared to the Food101 dataset. The best-performing architecture for both datasets was the EfficientNetB0 [34] architecture (in bold font). The second-best performance was shown by the ResNet18 [9] architecture (italicized and underlined font). The *F1_Score*, *Precision*, and *Recall* values have provided both high and balanced results. This indicates that the model accurately predicts both positive and negative examples in a balanced manner.

Table 5. Accuracy Comparison of Network Models for the Oxford-III Pet Dataset

	Acc.	F1_Score	Pr	R
EfficientNetB0 [34]	<u>0.9974</u>	<u>1</u>	<u>1</u>	<u>1</u>
MobileNetV3 [35]	0.9936	0.99	0.99	0.99
ResNet18 [9]	0.9986	1	1	1

Table 6. Accuracy Comparison of Network Models for the Food101 Dataset

	Acc	F1_Score	Pr	R
EfficientNetB0 [34]	0.9320	0.93	0.94	0.93
MobileNetV3 [35]	0.9092	0.91	0.92	0.91
ResNet18 [9]	<u>0.9176</u>	<u>0.92</u>	<u>0.93</u>	<u>0.92</u>

IV. CONCLUSION

In this article, the performance outcomes of pre-trained network architectures for recognizing food and pets in a few-shot learning context have been investigated. A prototypical network was utilized as the FSL architecture. Pre-trained network architectures such as EfficientNetB0 [34], ResNet18 [9], and MobileNetV3 [35] were employed. All experimental work was conducted over 60,000 iterations in a 5-shot-5-way configuration. The study observed that pre-trained network architectures like EfficientNetB0 [34], ResNet18 [9], and MobileNetV3 [35] are quite successful in few-shot recognition of food and pets.

Particularly, EfficientNetB0 [34], offering the highest accuracy rate, has proven to be a highly suitable option for these types of tasks. ResNet18 [9] and MobileNetV3 [35] also achieved competitive results within their capabilities and, depending on application requirements and hardware limitations, may be preferred for their lower computational cost and speed. The experimental studies conducted over 60,000 iterations under a 5-shot-5-way setup have demonstrated the robustness and generalization capability of these architectures in the context of FSL. Future studies might explore hyper parameter tuning, different feature fusion methods, and the impact of various data augmentation techniques to further enhance the model.

Declaration of Ethical Standards

The authors remained faithful to all ethical rules

Credit Authorship Contribution Statement

Authors 1: Software, Investigation, Writing – original draft, Methodology,

Authors 2: Writing – review and editing, Validation, Conceptualization,

Declaration of Competing Interest

There is no conflict of interest between authors

V. REFERENCES

[1] Toptas, B., Hanbay, D. "The Separation of Glaucoma and Non-Glaucoma Fundus Images using EfficientNet-B0." *Bitlis Eren Üniversitesi Fen Bilimleri Dergisi*, vol. 11, No. 4, pp. 1084–1092, 2022.

[2] Gudla, R., Vollala, S., Srinivasa, K. G., Amin, R. "A novel approach for classification of Tor and non-Tor traffic using efficient feature selection methods." *Expert Systems with Applications*, Article ID 123544, 2024.

[3] Gündüz, A. F., Talu, M. F. "Atrial fibrillation classification and detection from ECG recordings." *Biomedical Signal Processing and Control*, vol. 82, Article ID 104531, 2023.

[4] Toptaş, B., Hanbay, D. "Retinal blood vessel segmentation using pixel-based feature vector." *Biomedical Signal Processing and Control*, vol. 70, Article ID 103053, 2021.

[5] Toptaş, M. *Orman yangınlarının görüntü işleme yöntemleri ile tespit edilmesi ve sınıflandırılması* (Yüksek Lisans tezi, İnönü Üniversitesi Fen Bilimleri Enstitüsü), 2018.

[6] Krizhevsky, A., Sutskever, I., Hinton, G. E. "Imagenet classification with deep convolutional neural networks." *Advances in Neural Information Processing Systems*, vol. 25, 2012.

[7] Szegedy, C., Liu, W., Jia, Y., Sermanet, P., Reed, S., Anguelov, D., et al. "Going deeper with convolutions." *Proceedings of the IEEE Conference on Computer Vision and Pattern Recognition*, pp. 1–9, 2015.

[8] Simonyan, K., Zisserman, A. "Very deep convolutional networks for large-scale image recognition." *arXiv preprint arXiv:1409.1556*, 2014.

[9] He, K., Zhang, X., Ren, S., Sun, J. "Deep residual learning for image recognition." *Proceedings of the IEEE Conference on Computer Vision and Pattern Recognition*, pp. 770–778, 2016.

[10] Huang, G., Liu, Z., Van Der Maaten, L., Weinberger, K. Q. "Densely connected convolutional networks." *Proceedings of the IEEE Conference on Computer Vision and Pattern Recognition*, pp. 4700–4708, 2017.

- [11] Fei-Fei, L., Fergus, R., Perona, P. "One-shot learning of object categories." *IEEE Transactions on Pattern Analysis and Machine Intelligence*, vol. 28, No. 4, pp. 594–611, 2006.
- [12] Paeedeh, N., Pratama, M., Ma'sum, M. A., Mayer, W., Cao, Z., Kowalczyk, R. "Cross-domain few-shot learning via adaptive transformer networks." *Knowledge-Based Systems*, Article ID 111458, 2024.
- [13] Zhao, P., Wang, L., Zhao, X., Liu, H., Ji, X. "Few-shot learning based on prototype rectification with a self-attention mechanism." *Expert Systems with Applications*, Article ID 123586, 2024.
- [14] Snell, J., Swersky, K., Zemel, R. "Prototypical networks for few-shot learning." *Advances in Neural Information Processing Systems*, pp. 4077–4087, 2017.
- [15] Sung, F., Yang, Y., Zhang, L., Xiang, T., Torr, P. H., Hospedales, T. M. "Learning to compare: Relation network for few-shot learning." *Proceedings of the IEEE Conference on Computer Vision and Pattern Recognition*, pp. 1199–1208, 2018.
- [16] Wang, Y., Chao, W. L., Weinberger, K. Q., Van Der Maaten, L. "Simpleshot: Revisiting nearest-neighbor classification for few-shot learning." *arXiv preprint arXiv:1911.04623*, 2019.
- [17] Gülcü, A., Alkan, M. "Az Örnekle Öğrenme Problemleri için MAML ve ProtoNet Algoritmalarının İncelenmesi." *Avrupa Bilim ve Teknoloji Dergisi*, No. 21, pp. 113–121, 2021.
- [18] Işık, G. "Improving Plant Disease Recognition Through Gradient-Based Few-shot Learning with Attention Mechanisms." *Journal of the Institute of Science and Technology*, vol. 13, No. 3, pp. 1482–1495, 2023.
- [19] Argüeso, D., Picon, A., Irusta, U., Medela, A., San-Emeterio, M. G., Bereciartua, A., Alvarez-Gila, A. "Few-Shot Learning approach for plant disease classification using images taken in the field." *Computers and Electronics in Agriculture*, vol. 175, Article ID 105542, 2020.
- [20] Wang, B., Wang, D. "Plant leaves classification: A few-shot learning method based on siamese network." *IEEE Access*, vol. 7, pp. 151754–151763, 2019.
- [21] Frikha, A., et al. "Few-shot one-class classification via meta-learning." *Proceedings of the AAAI Conference on Artificial Intelligence*, vol. 35, No. 8, 2021.
- [22] Chen, D., Chen, Y., Li, Y., Mao, F., He, Y., Xue, H. "Self-supervised learning for few-shot image classification." *ICASSP 2021 IEEE International Conference on Acoustics, Speech and Signal Processing (ICASSP)*, pp. 1745–1749, IEEE, June 2021.
- [23] Krenzer, A., Heil, S., Fitting, D., Matti, S., Zoller, W. G., Hann, A., Puppe, F. "Automated classification of polyps using deep learning architectures and few-shot learning." *BMC Medical Imaging*, vol. 23, No. 1, Article ID 59, 2023.
- [24] Liu, B., Yu, X., Yu, A., Zhang, P., Wan, G., Wang, R. "Deep few-shot learning for hyperspectral image classification." *IEEE Transactions on Geoscience and Remote Sensing*, vol. 57, No. 4, pp. 2290–2304, 2018.
- [25] Kang, D., Cho, M. "Integrative few-shot learning for classification and segmentation." *Proceedings of the IEEE/CVF Conference on Computer Vision and Pattern Recognition*, pp. 9979–9990, 2022.
- [26] Hu, Y., Gripon, V., Pateux, S. "Leveraging the feature distribution in transfer-based few-shot

- learning." *International Conference on Artificial Neural Networks*, pp. 487–499, Springer, Cham, September 2021.
- [27] Kim, J., Kim, T., Kim, S., Yoo, C. D. "Edge-labeling graph neural network for few-shot learning." *Proceedings of the IEEE/CVF Conference on Computer Vision and Pattern Recognition*, pp. 11–20, 2019.
- [28] Parkhi, O. M., Vedaldi, A., Zisserman, A., Jawahar, C. V. "Cats and dogs." *2012 IEEE Conference on Computer Vision and Pattern Recognition*, pp. 3498–3505, <https://doi.org/10.1109/CVPR.2012.6248092>, 2012.
- [29] Bossard, L., Guillaumin, M., Van Gool, L. "Food-101 – Mining discriminative components with random forests." *European Conference on Computer Vision (ECCV)*, pp. 446–461, https://doi.org/10.1007/978-3-319-10599-4_29, 2014.
- [30] Gao, T., Han, X., Zhu, H., Liu, Z., Li, P., Sun, M., Zhou, J. "FewRel 2.0: Towards more challenging few-shot relation classification." *arXiv preprint arXiv:1910.07124*, 2019.
- [31] Singh, P., Mazumder, P. "Dual class representation learning for few-shot image classification." *Knowledge-Based Systems*, vol. 238, Article ID 107840, 2022.
- [32] Ren, H., Cai, Y., Lau, R. Y., Leung, H. F., Li, Q. "Granularity-aware area prototypical network with bimargin loss for few-shot relation classification." *IEEE Transactions on Knowledge and Data Engineering*, vol. 35, No. 5, pp. 4852–4866, 2022.
- [33] Deng, J., Dong, W., Socher, R., Li, L.-J., Li, K., Fei-Fei, L. "ImageNet: A large-scale hierarchical image database." *2009 IEEE Conference on Computer Vision and Pattern Recognition*, pp. 248–255, <https://doi.org/10.1109/CVPR.2009.5206848>, 2009.
- [34] Tan, M., Le, Q. "EfficientNet: Rethinking model scaling for convolutional neural networks." *International Conference on Machine Learning*, pp. 6105–6114, PMLR, May 2019.
- [35] Howard, A., Sandler, M., Chu, G., Chen, L. C., Chen, B., Tan, M., et al. "Searching for MobileNetV3." *Proceedings of the IEEE/CVF International Conference on Computer Vision*, pp. 1314–1324, 2019.



Düzce University Journal of Science & Technology

Research Article

Coloring Cotton Fabrics by Pigment Printing Method with Reduction of Process Steps: An Innovative Approach

 Emine AYAZ ¹,  Zeynep OMEROGULLARI BASYIGIT ^{2*}

¹Agaoglu Textile Industry R&D Center, Uşak, Turkey,

²Vocational School of Higher Education of Inegöl, Textile, Clothing, Footwear and Leather Department, Textile Technology, Programme Bursa Uludağ University, Bursa, Turkey

* Corresponding author's e-mail address: zeynepbasyigit@uludag.edu.tr

DOI: 10.29130/dubited.1589566

ABSTRACT

This study focuses on coloring cotton woven fabrics using pigment dyes with a printing technique, without applying the conventional scouring and bleaching processes typically involved in pre-treatment. The aim of the study was to streamline the pre-treatment process by reducing the number of steps, thereby achieving a more efficient process in less time while also reducing the consumption of water, chemicals (both main and auxiliary), and energy. For this purpose, only desizing was applied to the cotton woven fabrics, while the conventional processes of scouring and bleaching were omitted. The fabrics were then directly colored using the rotary screen printing technique with three different formulations. A second batch of cotton fabrics, woven with the same yarn and construction, underwent the full conventional pre-treatment processes (desizing, scouring, and bleaching) before being colored with the same printing technique. The performance characteristics of both sets of fabrics were compared. Fastness properties such as washing fastness, acidic and alkaline perspiration fastness, water fastness, and dry and wet rubbing fastness were evaluated according to relevant standards. Additionally, tests for tear strength, abrasion resistance, pilling, and color spectrum were conducted. The color spectrum analysis revealed that the highest color yield was achieved using the printing formulation containing a polyurethane-based crosslinking agent. As a result, reducing the number of pre-treatment steps led to a decrease in chemical usage and the number of post-washing cycles, thereby lowering water and energy consumption.

Keywords: Pre-treatment, cotton fabric, pigment dye, printing method, textile finishing

İşlem Adımları Azaltılarak Pigment Baskı Yöntemiyle Pamuklu Kumaşların Renklendirilmesi: Yenilikçi Bir Yaklaşım

Öz

Bu çalışma, pamuklu dokuma kumaşların ön terbiye sürecinde genellikle uygulanan kasar ve ağartma işlemleri olmaksızın, pigment boyarmaddeler ile bir baskı tekniği kullanılarak renklendirilmesine odaklanmaktadır. Çalışmanın amacı, ön terbiye işlemlerindeki adımları azaltarak daha verimli bir süreç elde etmek, aynı zamanda su, kimyasal madde (ana ve yardımcı) ve enerji tüketimini azaltmaktır. Bu amaçla pamuklu dokuma kumaşlara yalnızca haşıl sökme işlemi uygulanmış, geleneksel kasar ve ağartma işlemleri atlanmıştır. Kumaşlar, üç farklı formülasyon kullanılarak rotasyon baskı tekniği ile doğrudan renklendirilmiştir. Aynı iplik ve konstrüksiyon ile dokunan ikinci bir kumaş grubu ise, geleneksel ön terbiye süreçlerinin tamamından (haşıl sökme, kasar ve ağartma) geçirilmiş ve aynı baskı tekniği ile renklendirilmiştir. Her iki grup kumaşın performans özellikleri karşılaştırılmıştır. Yıkama haslığı, asidik ve alkali ter haslığı, su haslığı ile kuru ve yaş sürtme haslıkları gibi özellikler ilgili standartlara göre değerlendirilmiştir. Ayrıca, yırtılma mukavemeti, aşınma direnci, boncuklanma

(pilling) ve renk spektrumu testleri gerçekleştirilmiştir. Renk spektrumu analizi, en yüksek renk veriminin poliüretan esaslı çapraz bağlayıcı içeren baskı formülasyonu ile elde edildiğini göstermiştir. Sonuç olarak, ön işlem adımlarının sayısının azaltılması, kimyasal kullanımında ve yıkama sonrası döngü sayısında azalmaya yol açarak su ve enerji tüketimini düşürmüştür.

Anahtar Kelimeler: *Ön terbiye, pamuklu kumaş, pigment boyarmadde, baskı yöntemi, tekstil terbiyesi*

I. INTRODUCTION

At the start of textile finishing processes, the procedures performed to remove undesirable foreign substances from both the fibers and the surface, as well as to enhance the overall appearance of the product, are collectively known as pre-finishing treatments. During the weaving process, fabrics are subjected to mechanical stresses such as the movement of the shuttle (hook, pressurized air, or water) or the opening of the heddles. For this reason, warp yarns undergo a sizing process to better bond the fiber ends to the yarn surface, making the fabric more compact and stronger, thus reducing the risk of warp yarn breakage during weaving. However, during dyeing or printing, these sizing agents, which form a film-like layer on the fiber surface, must be removed before coloring to allow the dye to penetrate the fiber. Although various chemical agents are used as de-sizing agents, enzymes are one of the most commonly used chemicals in this process [1-5]. Additionally, cotton fibers contain oils, waxes, pectin, hemicelluloses, and other substances, which, along with foreign materials like leaves, pods, and seed coats, must be removed by treating raw cotton with basic solutions. This process, known as hydrophilization, usually involves treatment with NaOH to remove hydrophobic substances like oils, waxes, and pectin. The removal of these materials is crucial to ensure the subsequent dyeing/printing processes can be effective. Furthermore, cotton fibers naturally contain pigments that give them a light-yellowish color. The process of bleaching, which involves breaking down these pigments to achieve a white appearance, is typically carried out using hydrogen peroxide (H_2O_2), which remains one of the most widely used chemicals in the textile industry today. Traditional hydrogen peroxide bleaching formulations and the hydrophilization steps with caustic soda often involve processing at high temperatures or extended durations to enhance their effects on textile materials. However, these pre-finishing treatments typically involve substantial chemical usage, significantly increasing environmental waste. While the best bleaching results are achieved when hydrogen peroxide and caustic soda are used together in pre-finishing processes, excessive application of these chemicals, along with auxiliary agents, can have numerous adverse environmental impacts. When discharged into wastewater, these chemicals increase its pollutant load. Furthermore, the high levels of hydrogen peroxide commonly used in bleaching processes elevate the chemical oxygen demand (COD) of water, posing toxic risks to aquatic ecosystems. Additionally, these processes often necessitate subsequent washing and drying steps, leading to high consumption of water and thermal energy [6-13].

Pigment colorants are known for their exceptional durability, heat resistance, solvent stability, lightfastness, and resistance to migration. However, they are often challenging to process and typically exhibit lower color vibrancy and intensity [14]. Additionally, unlike reactive dyes, pigments do not chemically bond with the fibers. Instead, they adhere to the fabric's surface through physical interactions [14-17]. Therefore, pigment structured dyestuffs are chemicals that do not have affinity to textile fibres. They can only adhere to the fibre mechanically [16]. Crosslinkers and binders of various bases are used to ensure mechanical adhesion of these dyestuffs to fabrics [16,18]. In order to ensure proper adhesion of pigments to fabrics, binders and crosslinkers are commonly employed in various formulations to help fix the pigments and enhance their mechanical adhesion. Therefore, the application of the dyestuff to the fabrics is achieved by forming a film layer like the coating or pigment printing [19,20]. Crosslinkers and binders of various bases are used to ensure mechanical adhesion of these dyestuffs to fabrics. Since these pigments do not chemically bond, they may exhibit lower colorfastness, particularly to washing, rubbing, and light, unless effective finishing treatments are applied. To improve colorfastness, additional treatments such as fixation agents or overprinting can be utilized [21]. After dyeing or printing, the fabric is generally heated to help the binder dry and "fix" the pigment in place. The fabric is often cured

at temperatures between 140-160 C, with the evaporation of water during drying and condensation processes, the crosslinker precipitates on the fibres and forms a film layer [16], ensuring that the binder sets and the pigment adheres more permanently to the fabric's surface. In this study, different printing formulations containing three different crosslinking agents were developed to reduce the steps in the pre-treatment process, and their performance was compared with cotton fabrics that underwent conventional pre-treatment and printing processes. The effects of printing formulations containing pigment dyes on the performance of cotton fabrics were investigated.

II. MATERIAL AND METHOD

A. 1. Material

In this study, fabric woven with 100% cotton Ne 30/1 yarns was used. The 120 g/m² fabrics from Ağaoğlu Tekstil underwent a desizing process with 0.1% amylase enzyme (Genkim, Türkiye) and 0.1% wetting agent (ER-SA, Türkiye). After desizing, the fabrics were thoroughly washed, resulting in desized fabrics that were ready for printing, without any scouring and bleaching treatment. In contrast, fabrics subjected to conventional pre-treatment processes underwent scouring and bleaching with 0.8% combined bleaching agent containing monohydrate 2-(2-butoxy-ethoxy) ethanol (ER-SA, Türkiye), 2.5% NaOH (32 Bé) (Borkim Kimya, Türkiye), and 2.5% H₂O₂ (Tempo Kimya, Türkiye) in a continuous bleaching machine. For the printing process, a red pigment dye and printing paste auxiliaries were used. The detailed composition of the printing paste is provided in Table 1.

Table 1 Printing Paste Content

Chemical/Material Used	Chemical/Material Content	Supplier
Ammonia	25% Ammonia solution	İGSAŞ, Türkiye
Foam cutter	Silicone Based	İBER Chemical, Türkiye
Emulsifier	2-[(8-Methylnonyl)oxy]ethanol	İDEA Chemical, Türkiye
Softener	Polysiloxane	MYD Chemical, Türkiye
Thickener	Acrylic Based	MYD Chemical, Türkiye
Urea	46% Nitrogen	İGSAŞ, Türkiye
Binder	Acrylic copolymer dispersion	ER-SA Chemical, Türkiye
Red pigment dyestuff	Diazotisation of 2,4-Dichloroaniline	Dystar Chemical, China

B. 2. Method

B.2.1. Coloring Process with Printing Technique

Cotton fabrics that underwent full conventional pre-treatment processes were printed using a printing paste containing red pigment dye and are labeled as code R0. The conventionally applied printing formulation with pigment dye is detailed in Table 2, while the pre-treatment recipe used for hydrophilization and bleaching of 100% cotton woven fabrics is presented in Table 3. Fabrics that underwent only desizing, without any additional pre-treatment, were printed using formulations developed for the rotary printing technique, labeled as R1, R2, and R3, as shown in Table 4.

In this study, 100% cotton woven fabrics were passed through a desizing bath, rolled onto beams, and remained for 24 hours. After the desizing process, cotton fabrics were prepared for printing without undergoing bleaching or other pre-treatment processes. For each formulation, different crosslinking agents and 40 g/kg red pigment dye were added to the printing paste, and the printing chemicals were prepared accordingly. The printing process was carried out, and the fabrics were then dried and fixed at 150 C-160 C for 4 minutes.

Table 2 Recipe used in conventional printing technique

Recipe	Substance Content Used	Amount of Material Used (g/kg)	Supplier
R0	Printing paste	960	Agaoglu Textile, Türkiye
	Red Pigment Dyestuff	40	Dystar Chemical, China

Table 3 Recipe used in pre-treatment process

Name of Substance/Material Used	Amount of Substance Used (mL/kg)	Supplier
Caustic Soda Solution (32 Bé)	25	Borkim Chemical, Türkiye
Hydrogen Peroxide Solution-	25	Tempo Chemical, Türkiye
Wetting Agent	6	ER-SA Chemical, Türkiye
Stabilizer	6	MYD Chemical, Türkiye
Ion immobilizer	3	MYD Chemical, Türkiye
α -Amylase desizing enzyme	1	Genkim Chemical, Türkiye
Combination Bleaching Agent	8	ER-SA Chemical, Türkiye

Table 4 Recipes used in rotary printing technique for un-pretreated samples

Recipe No	Substance Content Used	Amount of Material Used (g/kg)	Supplier
R1	Printing paste	920	Agaoglu Textile, Türkiye
	Aqueous Dispersion of Aliphatic Polyester-Polyurethane	40	Bozetto Chemical, Spain
	Red Pigment Dyestuff	40	Dystar Chemical, China
R2	Printing paste	920	Agaoglu Textile, Türkiye
	Styrene acrylic copolymer emulsion	40	ER-SA Chemical, Türkiye
	Red Pigment Dyestuff	40	Dystar Chemical, China
R3	Printing paste	920	Agaoglu Textile, Türkiye
	Aliphatic blocked polyisocyanate aqueous dispersion	40	Asutex, Spain
	Red Pigment Dyestuff	40	Dystar Chemical, China

B.2.2. Washing Process

After coloring 100% cotton woven fabrics using the printing technique, the washing fastness of the printed samples was investigated. Fabric samples processed with each formulation were washed 20 times. The washing was performed in a household washing machine at 40 C in accordance with the EN

ISO 6330-2012 standard. The fabrics to be tested were conditioned under standard atmospheric conditions ($20\text{ }^{\circ}\text{C} \pm 2$ and $65\% \pm 2$ relative humidity) for 24 hours.

B.2.3. Color Measurement

A Gretag Macbeth X-Rite Color i7 Benchtop spectrophotometer was used for color measurements. The CIE Lab* values of the printed samples were measured using the spectrophotometer, and their color differences (ΔE) and color yields (K/S) were analyzed.

B.2.4. Fastness and Performance Tests

The fastness and performance tests of the fabrics were carried out in accordance with the relevant standards given in Table 5.

Table 5 Tests and standards

Test Type	Related Standard	Devices and Instruments Used
Washing Fastness	TS EN ISO 105-C06	Perspirometer, Etuv
Acidic Sweat Fastness	TS EN ISO 105-E04	Perspirometer, Etuv
Alkali Sweat Fastness	TS EN ISO 105-E04	Perspirometer, Etuv
Water Fastness	TS EN ISO 105-E01	Perspirometer, Etuv
Dry Rubbing Fastness	TS EN ISO 105-X12	Crocmeter
Wet Rubbing Fastness	TS EN ISO 105-X12	Crocmeter
Tear Strength	TS EN ISO 13937-2	James Heal Titan 2
Abrasion Resistance	TS EN ISO 12947-4	James H. Heal-Nu-Martindale 864
Pilling	TS EN ISO 12945-2	James H. Heal-Nu-Martindale 86

B.2.5. Efficiency Analysis in Process Application

Since 100% cotton woven fabrics need to undergo pre-treatment processes such as desizing, hydrophilization, and bleaching before the conventional pigment printing technique [22-25], all the necessary pre-treatments described above have also been carried out in the control groups. As for the experimental group, within the scope of the study, 100% cotton woven fabrics were colored by applying the pigment printing technique without the pre-treatment process. Therefore, the amount of water, energy and chemical consumption has been reduced in this study. The efficiency analysis was carried out with comparing the whole conventional finishing process with new formulations obtained finishing process.

III. CONCLUSION AND DISCUSSION

A.1. Fastness Test Results

All fastness and performance tests for the 100% cotton woven fabrics were conducted at the Ağaoğlu Textile R&D Center Laboratory. The test results, carried out in accordance with the standards provided in Table 5, were evaluated based on the gray scale. The fastness test results for both unwashed and 20-times-washed fabrics are presented graphically in Figure 1.

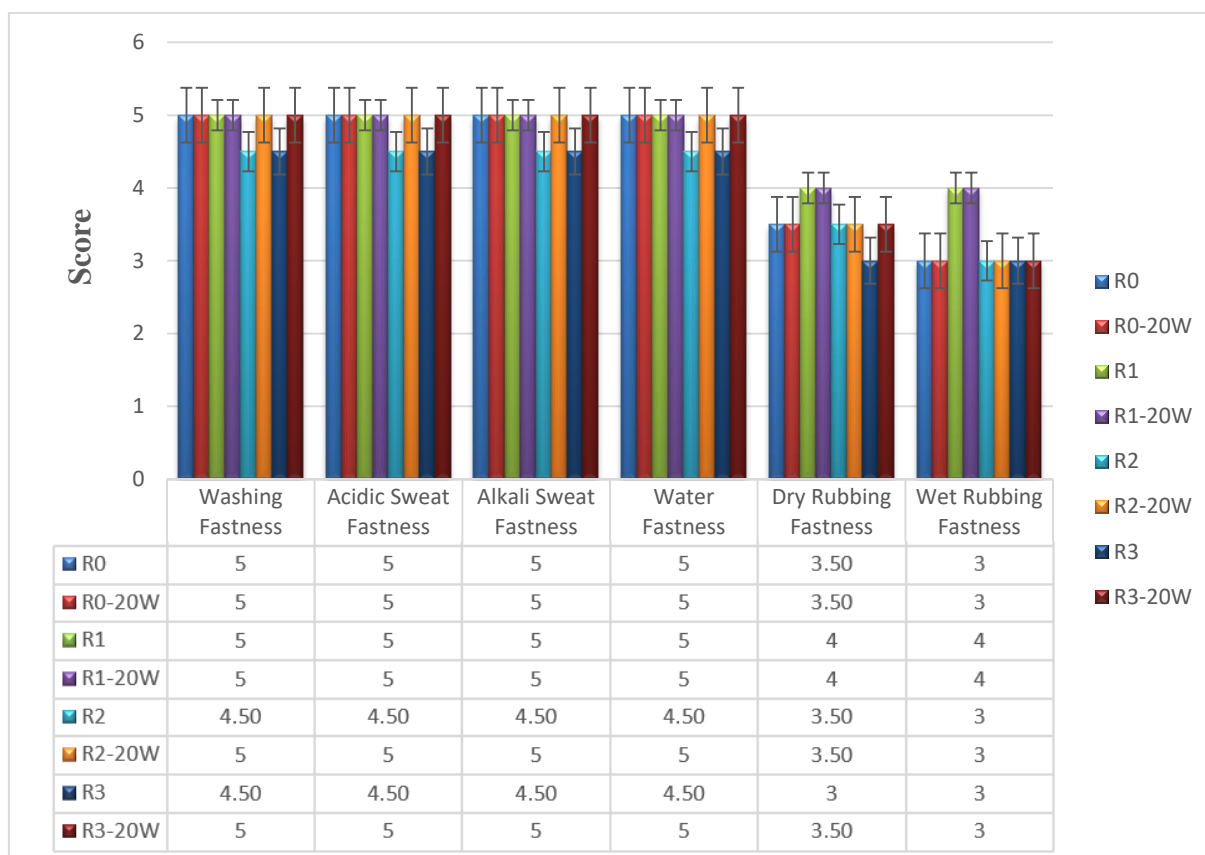


Figure 1 Fastness Test Results

For all samples (R0, R1, R2, R3) and their washed counterparts (R0-20W, R1-20W, R2-20W, R3-20W), washing fastness was observed to be at an excellent level of 5 or 4.5. It is considered that the washing process did not have any negative effect on color fastness. In acidic and alkaline perspiration fastness, all formulations maintained a value of 5 or 4.5 both before and after 20 washes, demonstrating the high perspiration resistance of the recipes. In terms of dry rubbing fastness, values for R0 and R0-20W were measured as 3.5. This indicates that samples prepared with NaOH and bleaching processes showed slightly lower performance in dry rubbing resistance. For R1 formulations, the values were 4 before and after washing processes which indicates that new formulation obtained in printing technique demonstrated better performance than conventional one while R2 and R3 formulations remained same as R0. The lowest values were observed in wet rubbing fastness in R0 and R0-20W: 3 while R1 was 4 and the rest remained same as at the value of 3. Crosslinkers, especially here polyurethane-based ones, were found to improve both dry and wet rubbing resistance when compared to conventional technique. The pigment printing recipe applied after conventional hydrophilization and bleaching treatments showed relatively lower performance in dry and wet rubbing fastness. Polyurethane-based binders are known to bind to the monomolecular chromophore group of the pigment dyestuff, making it difficult for the dyestuff to separate from the fibres and thus improving the fastness properties [26-29]. These findings indicate that printing recipes containing crosslinkers largely maintain their fastness performance even after washing and offer better properties compared to those prepared using conventional methods.

A.2. Performance Test Results

The tear strength test results of fabrics without washing and 20 washing cycles were given graphically in Figure 2. When the tear strength test results were analysed, it was observed that the un-pre-treated and printed with new formulations fabrics had better values than the conventionally pre-treated and printed fabrics. It was considered that cotton fabrics exposed to hydrogen peroxide and other chemicals during the pre-treatment process cause deformation and loss of strength. During hydrogen peroxide (H₂O₂) bleaching of cotton, strength loss occurs primarily due to the oxidative degradation of cellulose fibers. This degradation happens through the cleavage of glycosidic bonds and the oxidation of hydroxyl

groups in the cellulose structure. As a result, the degree of polymerization decreases, leading to a reduction in the tensile strength of the fibers. Additionally, the generation of hydroxyl radicals ($\bullet\text{OH}$) during the bleaching process exacerbates fiber damage by further attacking the cellulose chains, causing structural weakening [30-32]. Therefore, the absence of bleaching processes in the pre-treatment application in the study can be linked to the lack of significant mechanical strength losses in the fabrics. This outcome is associated with the fabrics not bleaching processes which contributed to preserving their strength. It was also observed that new formulations in printing process used did not affect the tearing strength of the fabrics negatively. Especially polyurethane based binders, long chain polymers are formed by the chemical reaction of polyol and diisocyanate groups. In addition, when polyurethanes are applied to the fabric surface in emulsion or liquid form, polymer chains are coated on the fabric fibers and long chain structures are formed as a result of drying or reaction. As a result of this polymerization, a thin film layer is formed on the fibers. This film layer increases the durability and flexibility of the fabric [26,33]. Abrasion resistance test results were given in Figure 3 and pilling test results were shown graphically in Figure 4. When the abrasion resistance test results were examined, the same values were obtained in all fabrics, while in pilling test results it was observed that only polyurethane based crosslinking agent formulation had the same value with un-pre-treated and printed with new formulations fabrics. As seen in Figure 4, polyurethane based crosslinking agent formulation showed better effect than other formulations on pilling strength of cotton fabrics. It was considered that polyurethane based binders did not cause a decrease in pilling values like other binders due to their film forming properties [34,35].

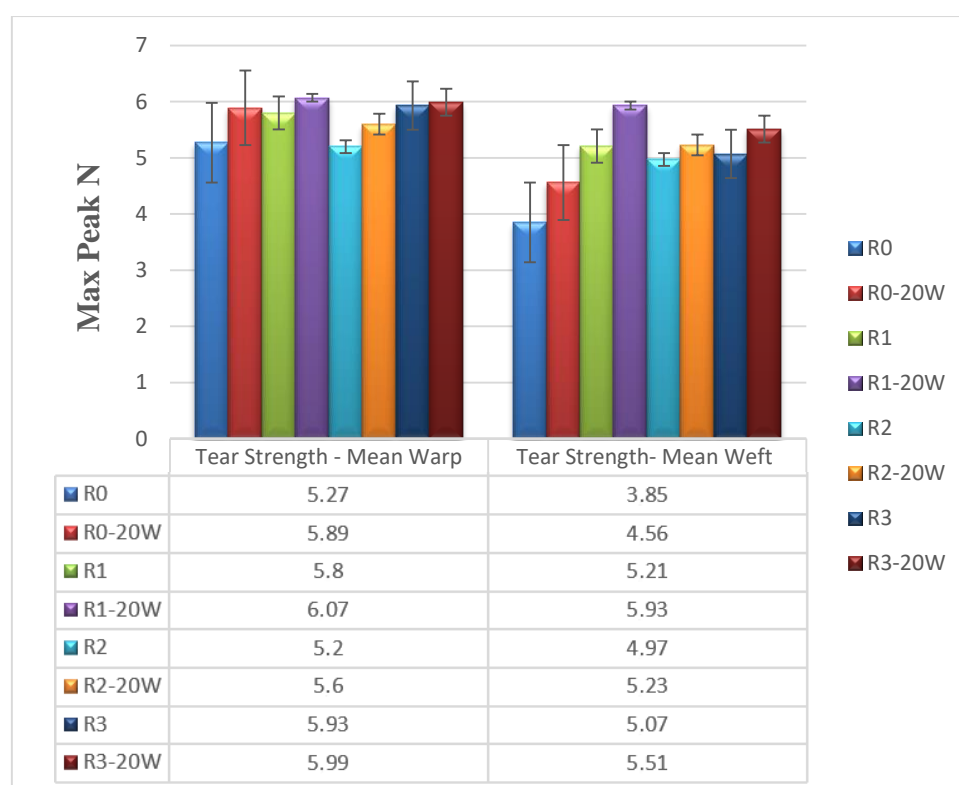


Figure 2 Tear Strength Test Results



Figure 3 Abrasion Resistance Test Results

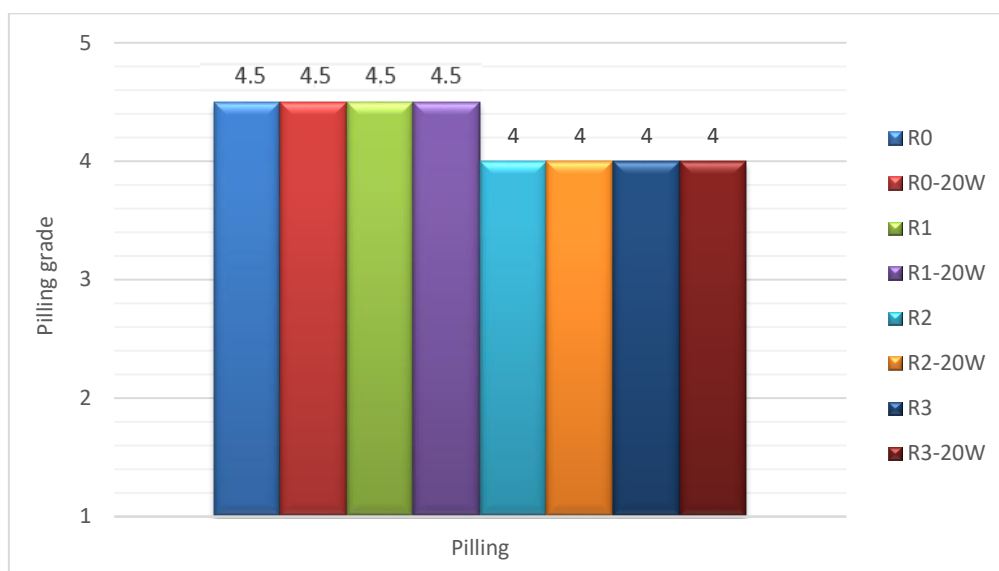


Figure 4 Pilling Test Results

A.3. Color Measurement Results

The color measurements of the printed fabrics were examined under D65 daylight at a 10° viewing angle. The CIE Lab* values and K/S color efficiencies of the fabrics after 20 washes were measured with a spectrophotometer. The color properties of the printed fabrics, both unwashed and after 20 washes, are listed in Table 6. The CIELab system is commonly used in spectrophotometric measurements, where the L*, a*, and b* parameters are of importance [36]. When examining the K/S values, the highest color efficiencies were observed in the formulation (R2) containing styrene acrylic copolymer emulsion and polyisocyanate-based formulation (R3). Polyisocyanates not only provide a soft touch as they contain ether, amide and urea groups, but also play an effective role on color depth, fastness and vividness due to their good film forming ability [37]. Styrene-acrylic copolymers enhance color yield in textile dyeing primarily due to their excellent film-forming and binding properties. These copolymers create a uniform and stable layer on the fiber surface, improving pigment fixation and preventing dye migration. Their compatibility with various dyes and fibers allows for better adhesion and distribution of colorants, leading to increased depth and brilliance of color. Additionally, their chemical structure can enhance the interaction between the dye and the fiber, resulting in higher dye uptake and improved color intensity [38,39]. The ΔE value for the fabric samples obtained with

polyurethane-based formulation (R1) was measured as 0.74. Even after 20 washes, the color was still preserved, and the color difference was at minimal level. Therefore, it is believed that the polyurethane-based crosslinking agent maintains the color's durability by forming a film layer on the fibers and bonding with a strong mechanical effect. Moreover, it was observed that these formulations did not negatively affect the color values of the fabric samples after washing process washing since the dyestuff was strongly adhered to the fibers in the pigment printing technique.

Table 6 . Color Measurement Results

Recipe No	L*	a*	b*	C*	h°	ΔE	K/S
R0	40.15	57.90	22.54	62.13	21.27	2.82	6.66
R0-20 W	40.85	55.73	20.90	58.08	20.13	2.82	5.33
R1	42.08	56.43	18.91	59.52	18.53	0.74	5.15
R1-20W	42.76	54.81	17.96	57.68	18.15	0.74	4.51
R2	39.50	56.68	22.33	60.92	21.50	2.14	7.20
R2-20W	41.08	52.22	19.06	55.59	20.05	2.14	6.05
R3	39.58	56.64	22.24	60.85	21.43	2.11	7.08
R3-20W	42.08	51.46	17.66	54.41	18.94	2.11	5.69

A.4. Efficiency Analysis Results Obtained in Process Application

The amount of water, energy and chemicals consumed for the preparation of one kilogram of 100% cotton woven fabric for pigment printing technique in conventional method and new formulations used in printing technique are given in Table 7.

Table 7 Amount of Chemicals Used for One Kilogram Sample

	Conventional Method	This study
Caustic soda (NaOH)	25 g	-
Hydrogen peroxide (H ₂ O ₂)	25 g	-
Wetting agent	6 g	-
Stabilizer	6 g	-
Ion immobilizer	3 g	-
Crosslinkers used in each new formulations	-	40 g

While 68 g/kg of chemicals, mainly caustic soda and hydrogen peroxide, were used additionally for one kg of fabric sample in conventional methods, only 40 g/kg of crosslinker (except printing paste in both methods) was used in this study. In traditional methods, a total of 10 L/kg of water, 0.06 kw/kg of energy and 68g/kg of chemicals were consumed in the processes of hydrophilization and bleaching processes before printing 1 kg of 100% cotton woven fabrics. In the technique applied within the scope of the study, a total of 2 L/kg of water and 0.01 kw/kg of energy was consumed in the process for 1 kg of fabric. In the new formulated-pigment printing technique, 40 g/kg of crosslinker was used to improve the color efficiency and performance tests of the fabrics. Thus, the new method offers a more sustainable and efficient alternative to conventional processes, with reduced resource consumption and improved fabric performance.

IV. CONCLUSION

This study demonstrated that eliminating conventional scouring and bleaching processes in the pre-treatment of cotton woven fabrics and using alternative pigment printing formulations can effectively

streamline the textile production process. By applying only desizing prior to rotary screen printing, it was possible to achieve satisfactory fabric coloration and performance properties while significantly reducing the consumption of water, chemicals, and energy. The fastness properties, including washing, perspiration (acidic and alkaline), water, and rubbing fastness (dry and wet), were largely maintained at high levels for all tested formulations. The printing formulation containing a polyurethane-based crosslinking agent exhibited the highest fastness and mechanical properties, indicating its superior performance in enhancing dye fixation. Furthermore, this simplified process contributed to a reduction in the number of post-washing cycles, thereby offering additional savings in water and energy usage. While the alternative approach showed comparable or superior performance characteristics in key areas, it also provided economic advantages with reduced resource consumption, making it a sustainable and efficient solution for textile coloration. In future studies, a wider range of colors can be explored, and cotton-blended fabrics with different compositions can be utilized to observe the effects on various fibers. These approaches aim to expand the scope of research and provide a broader understanding of sustainable textile processing techniques. As a result, the findings of this study are expected to serve as a valuable reference and provide guidance for future research in the field.

V. REFERENCES

- [1] N. Ul-Haq, and N. Habib, "Cleaner production technologies in desizing of cotton fabric", *Journal of The Textile Institute*, vol. 103 no. 3, pp. 304-310, 2012.
- [2] A. S. Aly, S. M. Sayed, and M. K. Zahran, "One-step process for enzymatic desizing and bioscouring of cotton fabrics", *Journal of Natural Fibers*, vol. 7, no. 2, pp. 71-92, 2010.
- [3] V. Yachmenev, E. Blanchard, and A. Lambert, "Use of ultrasonic energy for intensification of the bio-preparation of greige cotton", *Ultrasonics*, vol. 42, no. 1-9, pp. 87-91, 2004.
- [4] N. A. Ibrahim, E. H. Mamdouh, M. S. Morsy and B.M. Eid, "Optimization and modification of enzymatic desizing of starch-size", *Polymer-Plastics Technology and Engineering*, vol. 43 no. 2, pp. 519-538, 2004.
- [5] C. Xu, D. Hinks, A. El-Shafei, P. Hauser, M. Li, M. Ankeny, and K. Lee, "Review of bleach activators for environmentally efficient bleaching of textiles", *Journal of Fiber Bioengineering and Informatics*, vol. 4 no. 3, pp. 209-219, 2011.
- [6] B. Colombi, R. Valle, J. Valle, and J. Andreaus, "Advances in sustainable enzymatic scouring of cotton textiles: Evaluation of different post-treatments to improve fabric wettability", *Cleaner Engineering and Technology*, vol. 4, pp. 100160, 2021.
- [7] M. Hashem, M. El-Bisi, S. Sharaf, and R. Refaie, "Pre-cationization of cotton fabrics: An effective alternative tool for activation of hydrogen peroxide bleaching process", *Carbohydrate Polymers*, vol. 9, no. 3, pp. 533-540, 2010.
- [8] M. Issa, T. Muddemann, D. Haupt, U. Kunz, and M. Sievers, "Simple catalytic approach for removal of analytical interferences caused by hydrogen peroxide in a standard chemical oxygen demand test", *Journal of Environmental Engineering*, vol. 147, no. 12, pp. 04021059 2021.
- [9] D. Georgiou, and A. Aivasidis, "Cotton-textile wastewater management: investigating different treatment methods" *Water environment research*, vol. 84, no. 1, pp. 54-64, 2012.
- [10] A. Sb, and G. Narendra, "Accelerated Bleaching of Cotton Material with Hydrogen Peroxide", *Journal of Textile Science & Engineering*, vol. 3, no. 4, pp. 1000140, 2013.

- [11] P.F. Tavčer, “Dyeing of environmentally friendly pretreated cotton fabric”, Shanghai, China: *In Textile Dyeing*, 2011, pp. 77-88.
- [12] A.G. Demir, F. R. Oliveira, T. Gulumser, and A. P. Souto, “New Possibilities of Raw Cotton Pre-treatment before reactive dyeing”, *Materials Science and Engineering*, vol. 460, no. 1, pp. 012026, 2018.
- [13] T. Wu, and J. D. Englehardt, “A new method for removal of hydrogen peroxide interference in the analysis of chemical oxygen demand”, *Environmental science & technology*, vol. 46, no. 4, pp. 2291-2298, 2012.
- [14] W. Ibrahim, Z. Sarwar, A. Khan, A. Hassan, A. Azeem, A. Nazir, H. Jamshaid, and U. Hussain, “A novel study of comparison properties of pigment and reactive dye-printed cotton fabric”, *Journal of Natural Fibers*, vol. 16, pp. 825-835, 2019.
- [15] M. M. El-Molla, and R. Schneider, “Development of ecofriendly binders for pigment printing of all types of textile fabrics”, *Dyes and Pigments*, vol. 71, no. 2, pp. 130-137, 2006.
- [16] A. Dessie, and B. Eshetu, “The role of binders and its chemistry in textile pigment printing”, *Journal of Textile Science & Engineering*, vol. 11, no. 1, pp. 1-6, 2021.
- [17] A. Gürses, M. Açıkyıldız, K. Güneş, M. S. Gürses, A. Gürses, M. Açıkyıldız, and M. S. Gürses, “Classification of dye and pigments”, *Dyes and pigments*, Hangzhou, China: 2016, pp. 31-45.
- [18] A. G. Hassabo, A. El-Salam, A. Neaama, N. A. Mohamed, N. Z. Gouda, N. Khaleed, and H. Othman, “Alternatives Binder in Printing Using Colored Pigments on Cotton Fabrics”, *Journal of Textiles, Coloration and Polymer Science*, vol. 21, no. 1, pp. 121-130, 2024.
- [19] W. H. Solangi, Z. A. Noonari, A. A. Channa, M. Q. Khan, and A. B. Siyal, “Influence of binders and thickeners of pigment printing paste on light fastness and crocking fastness of the fabric”, *International Journal of Science and Research*, vol. 3, no. 5, pp. 1024-33, 2014.
- [20] M. F. H. Asaduzzaman, M. Kamruzzaman, and M. R. Miah, “Effects of Binder and Thickeners of Pigment Printing Paste on fastness properties of printed fabric”, *International Journal of Scientific and Engineering Research*, vol. 7, no. 9, pp. 710-719, 2016.
- [21] K. Haggag, M. M. El-Molla, N. O. Shake, N. A. Alian, and F. N. El-Shall, “Use of the novel synthesized aqueous binders for pigment printing cotton fabrics using three modes of fixation”, *International Journal of Textile Science*, vol. 1, no. 6, pp. 49-61, 2012.
- [22] R. S. Harane, and R. V. Adivarekar, “Sustainable processes for pre-treatment of cotton fabric”, *Textiles and clothing sustainability*, vol. 2, no. 2, pp. 1-9, 2017.
- [23] S. Gargoubi, R. Tolouei, P. Chevallier, L. Levesque, N. Ladhari, C. Boudokhane, and D. Mantovani, “Enhancing the functionality of cotton fabric by physical and chemical pre-treatments: A comparative study”, *Carbohydrate polymers*, vol. 147, pp. 28-36, 2016.
- [24] D. Fakin, D. Golob, and Z. Stjepanović, “The effect of pretreatment on the environment and dyeing properties of a selected cotton knitted fabric”, *Fibres & Textiles in Eastern Europe*, vol. 16, no. 2, pp. 101-104, 2008.
- [25] N. Ul-Haq, and H. Nasir, “Cleaner production technologies in desizing of cotton fabric”, *Journal of the Textile Institute*, vol. 103, no. 3, pp. 304-310, 2012.

- [26] H. Mao, F. Yang, C. Wang, Y. Wang, D. Yao, and Y. Yin, "Anthraquinone chromophore covalently bonded blocked waterborne polyurethanes: synthesis and application", *RSC Advances*, vol. 5, no. 39, pp. 30631-30639, 2015.
- [27] Y. Wang, and H. Huang, "A Study on the Dye Fixation Mechanism of Waterborne Polyurethane", *ChemistrySelect*, vol. 8, no. 12, pp. e202204620, 2023.
- [28] V. García-Pacios, J. A. Jofre-Reche, V. Costa, M. Colera, and J. M. Martín-Martínez, "Coatings prepared from waterborne polyurethane dispersions obtained with polycarbonates of 1, 6-hexanediol of different molecular weights", *Progress in Organic Coatings*, vol. 76, no. 10, pp. 1484-1493, 2013.
- [29] R. Chen, C. Zhang, and M. R. Kessler, "Anionic waterborne polyurethane dispersion from a bio-based ionic segment", *RSC advances*, vol. 4, no. 67, pp. 35476-35483, 2014.
- [30] N. Wang, P. Tang, C. Zhao, Z. Zhang, and G. Sun, "An environmentally friendly bleaching process for cotton fabrics: mechanism and application of UV/H₂O₂ system", *Cellulose*, vol. 27, pp. 1071-1083, 2020.
- [31] P. Tang, and G. Sun, "Generation of hydroxyl radicals and effective whitening of cotton fabrics by H₂O₂ under UVB irradiation", *Carbohydrate polymers*, vol. 160, pp. 153-162, 2017.
- [32] A. Walawska M. Olak-Kucharczyk A. Kaczmarek and M. H. Kudzin, "Environmentally Friendly Bleaching Process of the Cellulose Fibres Materials Using Ozone and Hydrogen Peroxide in the Gas Phase", *Materials (Basel)*, vol. 17, no. 6, pp. 1355, 2024.
- [33] M. Hirose, F. Kadowaki, and J. Zhou, "The structure and properties of core-shell type acrylic-polyurethane hybrid aqueous emulsions", *Progress in Organic Coatings*, vol. 31, pp. 157-169, 1997.
- [34] L. Sheng, X. Zhang, Z. Ge, Z. Liang, X. Liu, C. Chai, and Y. Luo, "Preparation and properties of waterborne polyurethane modified by stearyl acrylate for water repellents", *Journal of Coatings Technology and Research*, vol. 15, pp. 1283-1292, 2018.
- [35] S. Tabasum, M. Zuber, T. Jamil, M. Shahid, and R. Hussain, "Antimicrobial and pilling evaluation of the modified cellulosic fabrics using polyurethane acrylate copolymers", *International journal of biological macromolecules*, vol. 56, pp. 99-105, 2013.
- [36] J. McGrath, M. Beck, and M. Hill, "Replicating Red: Analysis of ceramic slip color with CIELAB color data", *Journal of Archaeological Science: Reports*, vol. 14, pp. 432-438, 2017.
- [37] A. Sarwar, A. Jabbar, S. Riaz, and M. I. Malik, "Enhancement in the dyeability of bamboo fabric by using an isocyanate-based crosslinking agent", *Cellulose*, vol. 31, no. 10, pp. 6501-6516, 2024.
- [38] K. Fang, R. Xie, X. Liu, G. Zhao, D. Han, W. Chen, Z. Shi, L. Hao, and Y. Cai, "Reactive dye/poly(styrene-co-butyl acrylate-co-trimethyl (vinylbenzyl) ammonium chloride) nanospheres with high coloration performance for cleaner dyeing of cotton fabrics", *Cellulose*, vol. 26, pp. 5807-5819, 2019.
- [39] J. Simms, and P. Corcoran, "Amine-activated color in anhydride functional styrene/acrylic copolymers", *Progress in Organic Coatings*, vol. 26, pp. 217-237, 1995.



Düzce University Journal of Science & Technology

Research Article

Analysis of Turkish Pine Stumpage-based Auction Sales: A Case Study of İzmir Regional Directorate of Forestry

Güçlü İlker MÜFTÜOĞLU ^{a,*}, Yaşar Selman GÜLTEKİN ^b

^a Department of Forestry, Demirci Vocational School, Manisa Celal Bayar University, Manisa, TÜRKİYE

^b Department of Forest Engineering, Faculty of Forestry, Duzce University, Duzce, TÜRKİYE

* Corresponding author's e-mail address: ilker.muftuoglu@cbu.edu.tr

DOI: 10.29130/dubited.1597732

ABSTRACT

The study analyzed all Turkish pine stumpage-based auction sales conducted by 10 forest management directorates under the İzmir Regional Directorate of Forestry between 2020-2024. The analysis included all data on Turkish pine stumpage-based auction sales carried out from March 2020—when the General Directorate of Forestry introduced the new open-access e-auction system during the Covid-19 pandemic—until June 2024. To analyze the stumpage-based auction sales of Turkish pine by the forest management directorates, the auction revenues were converted to 2020 constant prices using the Producer Price Index for forest products and related services published by TUIK. When examining the 818 Turkish pine stumpage-based auction revenues analyzed in the study, the Bergama, Akhisar, and Manisa Forest Management Directorates ranked as the top three, respectively. In terms of the number of auctions, the ranking shifted to Manisa, Gördes, and Akhisar Forest Management Directorates. Regarding the total volume (m³) of standing timber offered for auction, the Manisa, Akhisar, and Gördes Forest Management Directorates outperformed the others. Lastly, when comparing revenue per unit, Bergama, Salihli, and Akhisar Forest Management Directorates achieved a more profitable production process in the relevant years compared to other directorates.

Keywords: Stumpage-based Auction Sale, Turkish Pine, İzmir Regional Directorate of Forestry

Kızılçam Açık Artırmalı Dikili Ağaç Satışlarının Analizi: İzmir Orman Bölge Müdürlüğü

Öz

Yapılan çalışmada İzmir Orman Bölge Müdürlüğüne bağlı 10 orman işletme müdürlüğünde gerçekleştirilen Kızılçam açık artırmalı dikili satışlarının tamamı 2020-2024 yılları arası analiz edilmiştir. Orman Genel Müdürlüğü'nün Covid-19 pandemi süreciyle birlikte Mart 2020 tarihi itibarıyla açık erişimde olan yeni e-ihale sisteminden Haziran 2024 tarihine kadar gerçekleştirilen tüm kızılçam açık artırmalı dikili satış verileri analize konu olmuştur. Orman işletme müdürlüklerinin açık artırmaya konu olan kızılçam dikili satışlarının analizi için TÜİK tarafından yayınlanan Orman Ürünleri ve ilgili hizmetlerin üretici fiyat endeksine (ÜFE) göre ilgili yıllarda yapılan açık artırmalı kızılçam dikili satış gelirleri 2020 yılına sabit fiyatlandırma yöntemiyle dönüştürülmüştür. Çalışmada analize konu olan 818 açık artırmalı kızılçam satış gelirleri incelendiğinde sırasıyla Bergama, Akhisar ve Manisa orman işletme müdürlükleri ilk 3 sırada yer almıştır. İşletmelerin açık artırmalı kızılçam satışlarındaki ihale sayılarına bakıldığında ise bu sıra Manisa, Gördes ve Akhisar orman işletme müdürlükleri şeklinde olmuştur. Açık artırmalı kızılçam dikili satışlarında satışa çıkan emvalin m³ cinsinden toplam hacmine bakıldığında ise Manisa, Akhisar ve Gördes Orman işletme müdürlükleri diğer işletmelerin önünde gelmektedir. Elde edilen birim başına gelir karşılaştırıldığında ise Bergama, Salihli ve Akhisar orman işletme müdürlükleri diğer işletmelerle kıyaslandığında ilgili yıllarda daha kârlı bir üretim süreci geçirmişlerdir.

Received: 07/12/2024, Revised: 15/12/2024, Accepted: 28/12/2024

I. INTRODUCTION

Long-term planning is essential for managing forests within the framework of sustainability principles. The plans prepared for this purpose are defined as forest management plans. These plans specify the amount and method of wood raw material production from forests. However, they often fail to fully consider the continuous needs of industrial consumers requiring wood raw materials, being formulated and implemented far from market analyses. Therefore, it is crucial to economically evaluate the marketing activities carried out by state forest enterprises, which have a significant share in forest product production and marketing, and to scientifically analyze these activities.

The largest producer of wood raw materials in Türkiye is the General Directorate of Forestry (GDF). GDF is the dominant actor in the wood market, and wood raw material sales still constitute its primary source of income. GDF conducts wood raw material sales in two ways: by carrying out harvesting operations such as cutting, skidding, and transportation itself, or by requiring buyers to undertake these operations. The sales conducted by GDF after completing the harvesting operations are called subsequent sales, while sales where operations like cutting, skidding, and transportation are assigned to the buyer are referred to as stumpage-based sales. GDF states in its current strategic plan that it aims to increase the share of stumpage-based sales [19].

Classifying GDF's sales only by the production method—subsequent or stumpage-based sales—is insufficient. It is also possible to classify them based on how the sale price is determined, resulting in auctions, negotiated sales, and allocated sales. In auctions, whether for subsequent or stumpage-based sales, the price the buyer pays is determined at the end of the auction, under market conditions. In negotiated sales, the price is determined as a result of mutual discussions between the parties. The prices of allocated sales, on the other hand, are determined by legislation or the decisions of authorized boards.

Globally, stumpage-based sales can be evaluated in two ways: first, the sale of stands or forests designated for cutting, and the second one is the sale of specific trees marked for cutting [1]. In Türkiye, the production and sales process, starting with marking, concludes in two ways. In the first method, marked stands are cut, skidded, loaded, and transported to forest depots by forest village development cooperatives or local villagers, as stipulated in Article 40 of Forestry Law No. 6831. These products are then sold mainly through auction from the depots. This method is referred to as subsequent sales.

In the second method, trees marked within the stand are sold as stumpage-based sales in accordance with Article 30 of Forestry Law No. 6831, as amended by Law No. 2896, and Circular No. 6877. These sales can be conducted through auctions or as allocated sales, with cutting, skidding, loading, and transportation costs borne by the buyer. In this production method, after marking, all subsequent stages of the process are completed by the buyer, allowing GDF to save on operational costs such as cutting, skidding, loading, and transportation. Since 2004, GDF has expanded its stumpage-based sales, claiming significantly higher profitability compared to the traditional system. Both allocated and auction-based stumpage sales are implemented in Türkiye [19]

In allocated stumpage-based sales, prices are not determined under market conditions due to the methodology of this approach. Instead, the average prices of auction-based sales from the past two months are used to determine the allocated sale price. According to Circular No. 6877, the entities eligible for allocated stumpage sales include forest village development cooperatives or individuals registered in village populations with populations under 2,500, residing in the villages where the trees are located.

In auction-based stumpage sales, price formation is influenced by both administrative decisions and market conditions. For auction-based stumpage sales, GDF first determines an estimated sale price (reserve price). This price is calculated by considering factors such as the specific quality of stumpage, production challenges, distance to consumption centers, transportation difficulties, market conditions, and recent stumpage sale averages. The cost of stumpage, including distribution, tariff, sales, operational, and contingency expenses, forms the basis for this calculation. Adjustments to the reserve price can be made by regional or enterprise managers if deemed necessary.

Setting the reserve price too low may lead to national losses by undervaluing public assets in case of insufficient competition. Conversely, setting it too high might reduce the number of participants, resulting in low competition and unsold products. To address these challenges, decision-makers often rely on the averages of past sales prices to determine a reserve price close to the market value.

The increase in stumpage-based sales significantly impacts all stakeholders involved in forest product production. However, companies in the forest industry, which act as buyers in stumpage-based sales, also face challenges and difficulties due to these practices [2].

The aim of this study is to analyze the economic performance of the Turkish pine auction-based stumpage-based auction conducted by the 10 Forest Management Directorates under the İzmir Regional Directorate of Forestry. The study examines the revenues, quantities, timber volumes offered for sale, and income per unit of the sales conducted over specific years, with the goal of evaluating the profitability, efficiency, and regional differences of these sales. Additionally, the study analyzes the distribution of auction-based sales across different Forest Management Directorates and identifies which directorates have experienced more efficient and profitable production processes. This research can be regarded as a resource management study, evaluating the management of forest resources, income generation processes, and regional performance disparities.

II. LITERATURE REVIEW

In 1989, the first stumpage sales attempts began in Türkiye's Turkish pine forests. Upon the request of GDF, stumpage sales conducted in 1990 were examined, comparing contractor production with traditional state enterprise methods. The study revealed that expectations such as advancements in production techniques, profitability, production of high-market-value products, and insurance coverage for forest workers were not met [3].

By the late 1990s, stakeholders began facing various challenges related to the implementation of stumpage sales. A study examining stumpage sales through cooperatives in forest product production attempted to identify the advantages and disadvantages of this approach compared to traditional production and marketing methods [4].

In 2004, Circular No. 6350 was issued to address the challenges in stumpage sales. This circular tackled issues in the forestry production and marketing process and proposed expanding the application of stumpage sales. Recommendations included providing fresh and high-quality products to the market, preventing standardization errors, and increasing sales revenues. The circular also emphasized the need for legal regulations concerning stumpage sales and measures to be taken during the transition period [5].

Similarly, a study based on Circular No. 6350 in 2004 highlighted that stumpage sales are advantageous in terms of forest sustainability, product quality, and low production costs. However, it was noted that certain rights granted to forest villages and cooperatives under the traditional system were lost with stumpage sales, leading to resistance to this approach. Consequently, the study emphasized the need to reevaluate and revise the implementation circular [6].

A study on stumpage sales discussed the advantages and disadvantages of this method compared to previous practices and assessed its implementation in Türkiye. The study highlighted significant issues with stumpage sales and stressed the necessity for technical and scientifically grounded research to improve this method [7].

The use of contracts and stumpage sales methods for forest management was examined in terms of forestry history, offering recommendations for the future. The study underscored the importance of exploring alternative methods for wood production and marketing, cautioning against adopting stumpage sales as a single solution nationwide. Additionally, it called for an objective and scientific evaluation of the effects of over a decade of implementation and emphasized the need for collaboration between GDF and academic institutions for more effective outcomes [8].

GDF sought to resolve issues in industrial wood production through Circular No. 6521 on stumpage sales and public procurement law-based service acquisitions. However, it was noted that forestry management cannot be sustained without labor costs, and addressing social problems in the process would take time. The study highlighted that profitability should not come at the expense of qualified forestry labor and that service acquisitions would also be beneficial for determining annual cutting volumes in forest management plans [9].

A study evaluating forestry issues in the Black Sea region, based on The Central Union of Turkish Forestry Cooperatives (OR-KOOP) projects and interviews with cooperative managers, highlighted a significant decrease in the incomes of forest villagers due to the widespread adoption of stumpage sales. To address this issue, the study recommended revising stumpage sales regulations and initiating joint efforts with forest cooperatives [10].

The findings of previous research on stumpage sales in Türkiye, relevant articles of Forestry Law No. 6831, Circular No. 6521 issued in 2007, and GDF records were used to conduct a technical, economic, and social assessment of this practice [11].

In a research project titled “Opinions of Interest Groups on Stumpage Sale Practices in the Eastern Black Sea Region”, feedback was gathered from forestry organization personnel, contractors, cooperative managers, and forest villagers. The study found that while the forestry organization supported the expansion of this method, most stakeholders agreed with this stance. The problems identified focused on the process and its associated challenges, with solutions proposed for improvement [12].

Another study examined stumpage sales from the perspective of stakeholders in the Trabzon Forestry Directorate. Survey findings indicated positive effects such as reducing operational costs, alleviating social pressures, insuring forest villagers, and improving quality. However, issues such as reduced labor income, loss of cooperative rights, and inaccuracies in yield percentages were also identified, emphasizing the need for a review of the practice [13].

A study evaluating stumpage sales from the perspective of industrial enterprises detailed the definition of stumpage sales, volume calculations, and yield percentages. It addressed expected benefits under Circular No. 6521 and highlighted risks such as damage to residual stands during cutting. It was suggested that GDF adopt a professional firm service acquisition model, as stumpage sales were not profitable [14].

Demir (2015) indicated that interest groups encountered different challenges varying by region and forestry directorate. A case study of the Bucak Forestry Directorate under the Isparta Regional Directorate provided socio-economic analyses of stumpage sales, revealing a need for further research on issues like yield percentages. The study found that forest engineers overwhelmingly (80%) believed stumpage sales shortened the production process compared to traditional methods, reduced storage costs, and prevented quality losses due to delays. Most industrial enterprises (90%) reported advantages in producing logs of desired dimensions without compromising quality, though they also faced challenges related to intermediary cooperatives in obtaining stumpage sales [15-18].

Finally, a study in the Western Black Sea region used structural equation modeling to analyze stumpage sales, examining its technical, economic, social, legal, administrative, and environmental impacts. This detailed research aimed to provide significant contributions to the efficiency and sustainability of forestry enterprises [19].

Due to the relatively short history of standing timber sales in Türkiye, it is observed that such practices are not yet widespread. As outlined in the literature review, the limited studies on standing timber sales in Türkiye have primarily focused on "situation analyses" and often on the "relationships between stakeholder groups." Therefore, these studies are generally characterized as analyses based on production, consumption, and stakeholder relations. In contrast, standing timber sales have been extensively studied in countries like the United States, Canada, and the Scandinavian countries, with research on the topic dating back to the 1970s. Initially, these studies concentrated on demand-related issues, but over time, supply-side analyses began to emerge. In recent years, the focus has shifted to comprehensive and holistic market models.

Globally, systems based on standing timber sales are a significant topic within forestry economics. These sales are based on selling existing standing timber (with standing prices) rather than felled trees. Research has shown that many factors influence the pricing of standing timber, including market demand and supply, seasonal variations, regional characteristics, and even local factors [20-22].

A study that examines the factors influencing standing timber prices highlights how national and regional demand, production costs, and regulatory policies contribute to price variations. These factors create price discrepancies across different regions and market conditions [22]. Additionally, understanding the impact of different pricing systems (such as auctions or negotiation-based pricing) and local environmental factors on determining standing timber prices is crucial for forest owners, managers, and forestry economists [23].

Academic studies on the history of stumpage-based auction, particularly in North America and Europe, explore how standing timber prices have evolved over time and the factors influencing them. Many studies have investigated how these prices are affected by supply-demand balances, market developments, seasonal variations in wood supply, and natural disasters. Additionally, local-level sales mechanisms (such as auctions or negotiations) and factors like the distance of forest areas to factories have been found to significantly impact these prices [22, 24].

Stumpage-based auction began to gain prominence in North America around the mid-20th century. However, environmental policies of the 1980s led to increased analyses of income generated from forest management and wood production. During the 1990s, legal regulations in western U.S. forests emerged as a significant factor affecting standing timber prices [25].

Prices for standing timber can vary significantly depending on factors such as regional competition levels, forest resources, and transportation conditions. In particular, in regions with high competition, prices for the same product tend to be higher. Rainy weather conditions can limit daily production capacities for loggers, causing certain types of terrain—for example, those accessible year-round—to be sold at higher prices. These conditions contribute to price fluctuations in the forest product market [26].

Another factor affecting stumpage-based auction prices is the size of the land and its suitability for transportation. Larger and higher-quality forest areas are likely to command higher prices, as transportation and equipment costs become more efficient [26, 27]. Prices for forest products also vary depending on the type and size of the tree. For instance, larger trees are generally sold at higher prices than smaller ones [22, 26].

III. MATERIAL AND METHOD

A. MATERIAL

There are 10 forest management directorates under the İzmir Forest Regional Directorate. Among these, Demirci, Akhisar, Gördes, Soma, and Manisa forest management directorates are located within the borders of Manisa province. İzmir, Bayındır, Gaziemir, and Bergama forest management directorates, on the other hand, are located within the borders of İzmir province. Demirci forest management has 8 district offices, Akhisar has 10, Gördes has 7, Soma has 7, Manisa has 11, Salihli has 10, İzmir has 10, Bayındır has 12, Gaziemir has 11, and Bergama has 14 district offices.

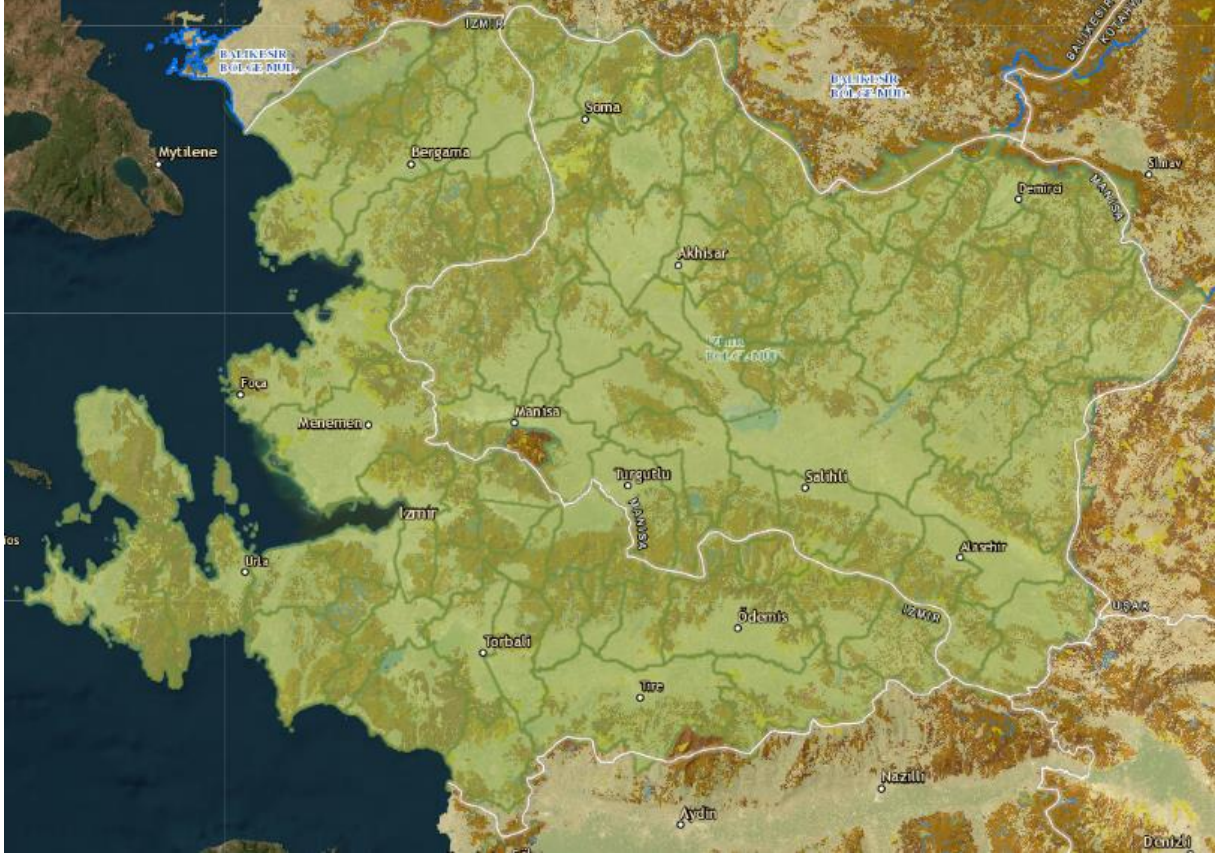


Figure 1. Study Area

The Demirci Forest Management Directorate is located in the northwest of Manisa province, at the intersection of the Aegean and Central Anatolia regions. The directorate, about 160 kilometers away from the provincial capital of Manisa, covers a region rich in forest resources. The Gördes Forest Management Directorate is located in the east of Manisa province, in the inner parts of the Aegean Region. It is about 110 kilometers from the city center of Manisa and occupies an important position in terms of forest resources. The Salihli Forest Management Directorate is located in the east of Manisa province, in the Gediz Basin of the Aegean Region. The directorate is approximately 70 kilometers away from the city center of Manisa and is situated in an area where forest resources and agricultural activities intersect. The Soma Forest Management Directorate is located in the northwest of Manisa province, in an area rich in natural resources in the Aegean Region. It is about 90 kilometers away from the provincial capital of Manisa. The Akhisar Forest Management Directorate is located in the northern part of Manisa province, between the fertile plains and forested areas of the Aegean Region. The directorate is approximately 50 kilometers away from the city center of Manisa. The Manisa Forest Management Directorate is located in the heart of the Aegean Region, encompassing the rich forest ecosystems around Spil Mountain and its surroundings. The directorate is strategically positioned near the region's

agricultural and industrial center. The Bergama Forest Management Directorate is located in the northern part of İzmir province, in a region surrounded by historical and natural wealth in the Aegean Region. The directorate is about 100 kilometers from the provincial capital of İzmir. The Bayındır Forest Management Directorate is located in the east of İzmir province, in the Küçük Menderes Basin. About 80 kilometers from İzmir's city center, Bayındır is known for its rich vegetation and agricultural activities. The Gaziemir Forest Management Directorate is located in the southeastern part of İzmir province, very close to the city center. About 20 kilometers from the city center of İzmir, Gaziemir has forest ecosystems that are intertwined with urban areas.

The İzmir Forest Management Directorate covers a wide geographic area, managing the forested areas of İzmir, one of the largest and most important cities in the Aegean Region. İzmir's city center is located along the coastline, extending from the southern shores to the northern mountains, encompassing a variety of climate types and vegetation.

B. METHOD

In this study, the Turkish pine stumpage-based auction conducted by 10 forest management directorates under the İzmir Regional Forest Directorate were analyzed for the respective years. The data includes all Turkish pine stumpage-based auction conducted via the new e-auction system made publicly accessible by the GDF from March 2020, during the COVID-19 pandemic, to June 2024. Turkish pine is a primary forest tree species in the relevant management units and was analyzed as it constitutes the bulk of sales conducted by these directorates. Additionally, Turkish pine is historically significant as it was the first tree species in Türkiye to be subject to stumpage-based auction.

For the analysis of Turkish pine stumpage-based auction conducted through auctions by the forest management directorates, revenues from 818 Turkish pine auctions over the years were adjusted to constant prices based on the 2020 Producer Price Index (PPI) for Forest Products and Related Services, published by the Turkish Statistical Institute (TÜİK). This adjustment was performed to eliminate the effects of inflation and enable comparative analyses across the management directorates.

Constant prices adjusted for inflation represent real prices derived by eliminating the inflationary effects on nominal prices. They are typically used to convert a series of prices to the level of a specific base year. To obtain real prices for the analysis of price relationships, the PPI values for Forest Products and Related Services (PPI, 2020=100) were used. Revenues from respective years were calculated and converted to 2020 prices using the formula: $(\text{Nominal Price} / \text{Price Index}) \times 100$ [28, 29].

IV. RESULTS AND DISCUSSION

The stumpage-based sales revenues, the share of sales revenues, and the number of auctions held in the 10 Forest Management Directorates involved in the study are shown in Table 1. The Forest Management Directorates with the highest revenues are ranked as follows: Bergama, Akhisar, Manisa, Soma, Salihli, İzmir, Gördes, Bayındır, Gaziemir, and finally, Demirci Forest Management Directorate.

Table 1. Inflation-Adjusted Stumpage-Based Sales Revenues by the Forest Management Directorates

Forest Management Directorates	Total Revenue in TRY (2020 Open Auction Stumpage Price)	The Share of Turkish Pine Open Auction Stumpage Sales Revenue of Forest Enterprises in the Total Turkish Pine Open Auction Sales Revenue (%)	Number of Turkish Pine Open Auction Stumpage Sale Tenders
Demirci	14.917.214	3,7	66
Gördes	21.428.405	5,4	108
Salihli	35.795.937	8,9	40
Soma	36.671.238	9,2	82

Akhisar	64.303.380	16,1	105
Manisa	62.498.699	15,6	174
Bergama	98.984.561	24,7	95
Bayındır	17.610.866	4,4	47
Gaziemir	15.269.017	3,8	35
İzmir	32.781.765	8,2	66
Total	400.261.082	100	818

In Table 1, when examining the number of tenders that generated the open auction stumpage sales revenue for the forest management directorates, it is observed that the rankings of the forest management units are as follows: Manisa, Gördes, Akhisar, Bergama, Soma, İzmir, Demirci, Bayındır, Salihli, and lastly, Gaziemir Forest Management Directorate.

Table 2 presents the total volume of timber sold in open auction stumpage sales, the share of each sold item within the total, and the income per unit. The regions with the largest volumes of stumpage sales are listed in the following order: Manisa, Akhisar, Gördes, Bergama, Soma, İzmir, Gaziemir, Demirci, Bayındır, and lastly, Salihli Forest Management Directorate.

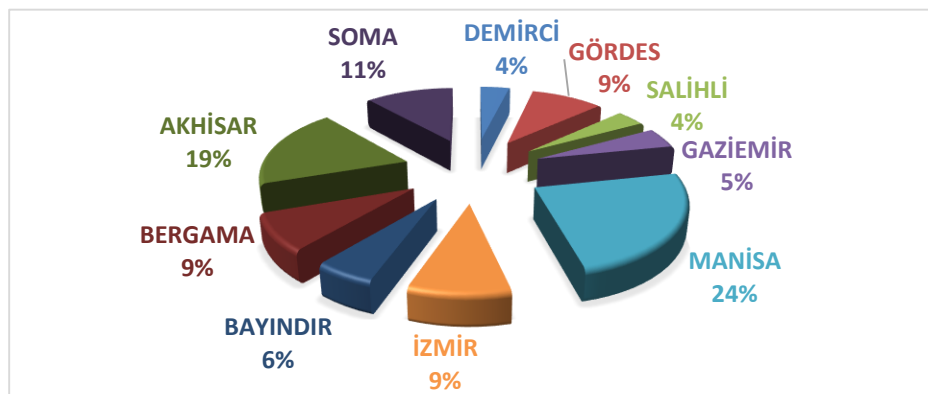
Table 2. The Cubic Meter Values (m³) of Timber Sold by the Forest Management Directorates

Forest Management Directorates	Cubic Meter Value of the Timber Sold (m ³)	Share of the Timber Sold in the Total Cubic Meters (%)	Revenue Per Unit (m ³) Ratio (%)
Demirci	70.923	5,3	6,7
Gördes	153.884	11,5	4,5
Salihli	61.478	4,6	18,7
Soma	139.198	10,4	8,4
Akhisar	211.112	15,7	9,8
Manisa	299.167	22,3	6,7
Bergama	149.397	11,1	21,2
Bayındır	67.278	5,0	8,4
Gaziemir	76.319	5,7	6,4
İzmir	113.514	8,5	9,3
Total	1.342.270	100	100,00

In Table 2, when the revenue per unit (m³) is ranked for the forest management offices' open auction stumpage sales, the leading directorates are as follows: Bergama, Salihli, Akhisar, İzmir, Soma, Bayındır, Demirci, Manisa, Gaziemir, and finally, Gördes.

In Figure 2, the ratio of participants in the open auction Turkish Pine stumpage sales for the relevant years is shown within the total number of participants. The total number of participants in the auctions is 5139. Manisa Forest Management Office leads with 1252 participants, accounting for 24% of the total, followed by Akhisar Forest Management Office, with 962 participants (19%), and Soma Forest Management Office, with 593 participants (11%).

Figure 2. The Percentages of Participants in the Total Stumpage-Based Turkish Pine Auctions by Forest Management Directorates



The lowest participation in terms of the number of participants in the auctions was recorded as follows: 244 participants (5%) in 35 stumpage-based Turkish Pine auctions by Gaziemir, 194 participants (4%) in 40 auctions by Salihli, and 196 participants (4%) in 66 auctions by Demirci Forest Management Directorate.

The analysis of the tables prepared using research data from stumpage-based auction sales of Turkish pine conducted by the relevant forest directorates is supported by several prominent studies in the literature. Moreover, there is a continued need for more in-depth research on this subject. Yılmaz et al. (2020) indicated that certain factors influence bidders' participation in specific sales lots during auction sales, and similar variables may also affect the number of participants in stumpage-based auction sales of logs [30]. Athey and Levin (2001) observed that an increase in the number of participants generally enhances sales revenues, while information asymmetry in low-competition auctions can reduce revenue. Their findings suggest that making open information structures (e.g., site conditions and quality data) more transparent can help increase government income [31]. Ok (1997) proposed that diversification of auction timing by forestry enterprises may positively influence revenue. He emphasized that the ability of the General Directorate of Forestry to obtain high income from the marketing of forest products depends on the strategic planning of factors such as the scheduling of auctions by forest directorates, the status of forest industry enterprises, and seasonal variations affecting prices [32]. Athey, Levin, and Seira (2011) compared open and sealed-bid auctions, demonstrating that open auctions tend to generate higher revenues through increased competition, especially when reserve prices are accurately determined [33].

V. CONCLUSION

When evaluating the data in Table 1 for the forest management directorates, it is observed that the forest management directorates generating the most revenue are, in order, Bergama, Akhisar, Manisa, Soma, Salihli, İzmir, Gördes, Bayındır, Gaziemir, and finally, Demirci Forest Management Office. Looking at the number of auctions in the same table, it is seen that forest management directorates such as Manisa, Gördes, and Akhisar have held more auctions. This shows that revenue and the number of auctions are not always directly proportional. According to the rankings in Table 2 for the volume of timber sold and the income per unit, forest management directorates such as Manisa, Akhisar, and Gördes have the largest quantity of timber put up for auction, while Bergama, Salihli, and Akhisar rank higher in terms of income per unit. This indicates that some forest management directorates achieve higher sales but lower income per unit, while others achieve higher income with fewer sales.

Furthermore, according to the data in Figure 2, Manisa, Akhisar, and Soma are the forest management directorates with the highest participation, while Gaziemir, Salihli, and Demirci have the lowest number of participants. Forest management directorates with higher participant numbers generally achieve higher revenues and conduct more auctions. These data suggest that forest management offices need to develop more effective sales and participant strategies to increase their sales revenue. Particularly, the low sales and participation rates in forest management directorates such as Demirci and Gaziemir may negatively affect their efficiency.

The sales and participation rates of the business offices can be related to their distance from provincial centers. Distance from the provincial center may have an impact on participant numbers and, consequently, sales. Participation in auctions is directly related to factors such as logistical ease, transportation opportunities, and effective promotion. Forest management directorates closer to provincial centers may have higher participation rates as they offer easier access to participants. This could increase interest in the auctions and, in turn, increase the revenue generated.

Specifically, among the areas subject to open auction, Demirci, Manisa, and İzmir are located in regions distant from major cities and provincial centers. This distance can make it difficult for potential participants to attend auctions in these areas. Transportation challenges may reduce the number of participants, leading to less competitive sales and, therefore, lower revenue. Moreover, forest

managemet directorates located closer to provincial centers have more marketing opportunities, which gives them an advantage over more remote locations.

ACKNOWLEDGEMENTS: Produced from a part of the first author's doctoral thesis.

VI. REFERENCES

- [1] E. İlt ter, K. Ok, *Ormancılık ve Orman End strisinde Pazarlama İlkeleri ve Y netimi*, 3. baskı, Ankara, T rkiye: Form Ofset Matbaacılık, 2012, ss. 344.
- [2] Y. S. G ltekin, "T rkiye'de Dikili A a  Satı ı Konusunda Yapılan  alı maların De erlendirilmesi ve Yapısal E itlik Modellemesi (Yem) İle İlgili Gruplarının Modellenmesi," *Elektronik Sosyal Bilimler Dergisi*, c. 15, s. 56, ss. 155, 2016.
- [3] İ.  evik, A. Ta  ı, G.  irin, "Kızıl am Ormanlarında A a ların Dikili Olarak Satılması  zerine Ara tırmalar," 3. baskı, İzmir, T rkiye: Ege Ormancılık Ara tırma Enstit s  Yayınları, 1996, ss. 95.
- [4] S.  nal, A. Karakaya, "Orman  r nleri  retiminde Dikili A a  Satı ı ve Uygulamada Kooperatiflerin Yeri," *I. Ulusal Ormancılık Kooperatifleri Sempozyumu Bildiriler Kitabı*, Kastamonu, T rkiye, 2002, ss. 22–23.
- [5] E. Kaplan, "Orman  r nlerinin De erlendirilmesinde Dikili A a  Satı ı," *I.  evre ve Ormancılık  urası*, c. 3, Antalya, T rkiye, 2005, ss. 99–103.
- [6] A. Karakaya, "Dikili A a  Satı  Y nteminin De erlendirilmesi," Y ksek Lisans Tezi, Fen Bilimleri Enstit s , Gazi  niversitesi, Ankara, T rkiye, 2006.
- [7] Y. S. G ltekin, E.  ar, "Ormancılıkta Dikili A a  Satı ı Y nteminin Uygulanması  zerine Ara tırmalar," *VI. Ulusal Orman Fak lteleri   renci Kongresi Bildiriler Kitabı*, D zce, T rkiye, 2008, ss. 8-9
- [8] A. Ekizo lu, C. Erd nmez, "Devlet Ormanlarının Mukavele Yoluyla Ve Dikili Satı larla İ letilmesinin Ormancılık Tarihi A ısından İrdelenmesi," *I. Ulusal Batı Karadeniz Ormancılık Kongresi Bildiriler Kitabı*, Bartın, T rkiye, 2009, ss. 1–8.
- [9] S. Kını , "Karadeniz B lgesi'nde Orman K yl s n n Ormancılık Sorunları ve   z m  nerileri," *II. Ormancılıkta Sosyo-Ekonomik Sorunlar Kongresi*, Isparta, T rkiye, 2009, ss. 19–21.
- [10] M. F. T merdirim, H. Karaduman, "Karadeniz B lgesi'nde Orman K yl s n n Ormancılık Sorunları Ve   z m  nerileri," *III. Ulusal Karadeniz Ormancılık Kongresi*, c. 1, Trabzon, T rkiye, 2010, ss. 67–79.
- [11] İ. Da demir, "Dikili A a  Satı larının Uygulanması  zerine De erlendirmeler," *Bartın Orman Fak ltesi Dergisi*, c. 13, s. 20, ss. 71–79, 2011.
- [12] S. Alkan, H. A.  ahin, *Do u Karadeniz B lgesi'nde Dikili Satı  Uygulamaları Konusunda İlgili Gruplarının G r  leri*, Teknik B lten Serisi No: 10, Do u Karadeniz Ormancılık Ara tırma Enstit s  Yayınları, Trabzon, T rkiye, 2011.
- [13] N. İslamo lu, "Devlet Ormanlarında Yapılan Dikili A a  Satı ının Payda lar A ısından İrdelenmesi (Trabzon Orman B lge M d rl     rne i)," Y ksek Lisans Tezi, Fen Bilimleri Enstit s , Karadeniz Teknik  niversitesi, Trabzon, T rkiye, 2010.

- [14] S. Sarcan, "Dikili Ağaç Satışı Yönteminin Sanayi Kuruluşları Çerçevesinden Değerlendirilmesi," *Orman Mühendisliği Dergisi*, c. 48, s. 4-5-6, ss. 78-89, 2011.
- [15] E. Demir, "Dikili Satış Uygulamalarına Yönelik Sosyo-Ekonomik Çözümlemeler," Yüksek Lisans Tezi, Fen Bilimleri Enstitüsü, Süleyman Demirel Üniversitesi, Isparta, Türkiye, 2015.
- [16] T. Özler, "Isparta Orman Bölge Müdürlüğü'nde Dikili Ağaç Satışlarının Değerlendirilmesi," Yüksek Lisans Tezi, Fen Bilimleri Enstitüsü, Süleyman Demirel Üniversitesi, Isparta, Türkiye, 2013.
- [17] A. Aközlü, G. Şen, "Tomruk Piyasası Aktörlerinin Dikili Ağaç Satış Yönetmeliklerinde Yapılan Değişikliklere İlişkin Algıları," *Turkish Journal of Forestry*, c. 24, s. 4, ss. 378-389, 2023.
- [18] H. Alkan, E. Demir, "Dikili Satış Uygulamalarına Yönelik Sosyo-Ekonomik Çözümlemeler," *IV. Ormancılıkta Sosyo-Ekonomik Sorunlar Kongresi*, Trabzon, Türkiye, 2015, ss. 261-272.
- [19] Y. S. Gültekin, "Devlet Orman İşletmelerinde Dikili Ağaç Satışı Uygulamasının Yapısal Eşitlik Modellemesiyle Analizi," Doktora Tezi, Fen Bilimleri Enstitüsü, Düzce Üniversitesi, Düzce, Türkiye, 2015.
- [20] L. A. Leefers, K. Potter-Witter, "Timber Sale Characteristics and Competition For Public Lands Stumpage: A Case Study From The Lake States," *Forest Science*, vol. 52, no. 4, pp. 460-467, 2006.
- [21] N. D. Reep, C. R. Blinn, M. A. Kilgore, "Assessment Of Stumpage Payment Methods Used By State and County Timber Sale Programs in The United States," *Journal of Forestry*, vol. 115, no. 6, pp. 513-521, 2017.
- [22] A. M. Klepacka, J. P. Siry, P. Bettinger, "Stumpage Prices: A Review of Influential Factors," *International Forestry Review*, vol. 19, no. 2, pp. 158-169, 2017.
- [23] J. E. Wagner, J. Rahn, M. Cavo, "A Pragmatic Method to Forecast Stumpage Prices," *Forest Science*, vol. 65, no. 4, pp. 429-438, 2019.
- [24] A. W. Ando, "The Price-Elasticity of Stumpage Sales from Federal Forests," *Discussion Paper 98-06*, Resources for the Future, 1997.
- [25] B. L. Sohngen, R. W. Haynes, "The 'Great' Price Spike of '93: An Analysis of Lumber and Stumpage Prices in The Pacific Northwest," *USDA Forest Service Pacific Northwest Research Station Research Paper PNW-RP-476*, 1994.
- [26] ResourceWise, "Five Causes of Stumpage Price Variation in The US South," Retrieved from <https://www.resourcewise.com/market-watch-blog/five-causes-of-stumpage-price-variation-in-the-us-south>, [20.11.2024].
- [27] R. W. Haynes, "Stumpage prices, volume sold, and volumes harvested from the National Forests of the Pacific Northwest region, 1984 to 1996," *USDA Forest Service Pacific Northwest Research Station General Technical Report PNW-GTR-423*, 1998.
- [28] S. Fischer, "Relative Shocks, Relative Price Variability and Inflation," *Brookings Papers on Economic Activity*, vol. 1981, no. 2, pp. 381-431, 1981.
- [29] R. J. Hill, "Constructing Price Indexes Across Space and Time: The Case of The European Union," *American Economic Review*, vol. 94, no. 5, pp. 1379-1410, 2004.

- [30] T. Yılmaz, M. Köse, M. Arslan, T. Okan, C. Köse, “Orman Bölge Müdürlükleri Açık Artırmalı Satışlarına Katılan Alıcıların Beklentileri: Marmara Bölgesi Örneği,” *Eurasian Journal of Forest Science*, c. 8, s. 4, ss. 338–352, 2020.
- [31] S. Athey, J. Levin, “Information and Competition in U.S. Forest Service Timber Auctions,” *The Journal of Political Economy*, vol. 109, no, 2, pp. 275–297, 2001.
- [32] K. Ok, “Devlet Orman İşletmelerinin Açık Artırmalı Satışlarının Etkileşimi,” *DOA Dergisi*, s. 3, ss. 39–62, 1997.
- [33] S. Athey, J. Levin, E. Seira, “Comparing Open and Sealed Bid Auctions: Evidence from Timber Auctions,” *The Quarterly Journal of Economics*, vol. 126, no. 1, pp. 207-257, 2011.



Düzce University Journal of Science & Technology

Research Article

A Cloud Based Web-Tool to Predict the High School Entrance Exam Scores of the Students

Gökçen ALTUN^{a,*}, Ekrem GÜLCÜOĞLU^b

^a Department of Econometrics, Hacı Bayram Veli University, Ankara, Turkey

^b Ministry of National Education, Kastamonu, Turkey

* Corresponding author's e-mail address: gokcenefendioglu@gmail.com

DOI: 10.29130/dubited.1535345

ABSTRACT

Multivariate adaptive regression splines (MARS) model, one of the non-parametric regression methods, is used to predict the achievement scores of the 8th-grade students before the LGS (High School Entrance System) exam with the developed web-tool. The demographic information of the students and all the test results they took in the last year are used before the LGS exam. The significant variables on the LGS scores of the students are the number of siblings, mother's education level, revolution history and Kemalism, English, mathematics courses. A web-based machine learning-based application has been developed to predict the LGS scores of the students in line with these data. The web-tool is accessible with the following website <https://beststat.shinyapps.io/lgs2/>. R Shiny program is used in the development of the web-tool. The program is cloud-based and works independently of the operating system and web browsers. The developed application helps students prepare for the LGS exam to offer pre-exam advice to guide their studies.

Keywords: MARS, Machine learning, LGS, Student achievement, Data mining, R Shiny.

Öğrencilerin Lise Giriş Sınavı Puanlarını Tahmin Etmek için Bulut Tabanlı Bir Web Aracı

Öz

Çok değişkenli uyarlanabilir regresyon splinleri (MARS) modeli, parametrik olmayan regresyon yöntemlerinden biri olarak, geliştirilen web aracıyla LGS (Liselere Geçiş Sistemi) sınavı öncesinde 8. sınıf öğrencilerinin başarı puanlarını tahmin etmek amacıyla kullanılmaktadır. Bu süreçte, öğrencilerin demografik bilgileri ve son bir yıl içinde girdikleri tüm sınav sonuçları LGS sınavı öncesinde dikkate alınmaktadır. Öğrencilerin LGS puanları üzerinde etkili olan önemli değişkenler arasında kardeş sayısı, annenin eğitim seviyesi, inkılap tarihi ve Atatürkçülük, İngilizce, matematik dersleri yer almaktadır. Bu veriler doğrultusunda, öğrencilerin LGS puanlarını tahmin etmek için web tabanlı, makine öğrenimine dayalı bir uygulama geliştirilmiştir. Web aracı, <https://beststat.shinyapps.io/lgs2/> adresinden erişilebilir durumdadır. Web aracının geliştirilmesinde R Shiny programı kullanılmıştır. Program bulut tabanlıdır ve işletim sistemi ile web tarayıcılarından bağımsız olarak çalışmaktadır. Geliştirilen uygulama, öğrencilerin LGS sınavına hazırlık sürecinde onlara rehberlik etmek amacıyla ön sınav önerileri sunmaktadır.

Anahtar Kelimeler: MARS, Makine öğrenimi, LGS, Öğrenci başarısı, Veri madenciliği, R Shiny.

I. INTRODUCTION

In the recent years, technological advancements and changes have exerted a significant influence on learning processes. E-assessment systems emerge as alternative systems to traditional assessment methods. The evaluation and assessment of these systems conducted online have been extensively studied for their advantages in various research works (Bayrak and Yurdugül, 2015). The goal of e-assessment is to evaluate and measure student performance based on feedback obtained from students (Simpson, 2016). Identifying meaningful data within the plethora of complex information in e-assessment systems and making predictions in the most suitable model pose a significant challenge.

In modeling relationships between variables within an e-assessment system, regression methods can be employed. Regression analysis is a statistical method that attempts to model the functional structure between a dependent variable and one or more independent variables. The aim of regression analysis is to find the model that best explains the change in the dependent variable using the independent variables. In other words, regression analysis seeks to increase the correlation or reduce the difference between the predicted value and the actual value of the dependent variable (Kılıç, 2013). In regression analysis, parameter estimates are made using the Least Squares Method (LSM). The LSM estimation method is based on minimizing the difference between the observed dependent variable value and the estimated independent variable value.

One of the most important assumptions in regression analysis is the problem of multi-collinearity, which arises when there is high correlation among independent variables. In such cases, LSM estimates are not reliable, and various regression models have been developed to address the issue of multi-collinearity (Şahinler, 2000). Additionally, data mining models such as CHAID and CART, which could serve as alternatives to multiple regression models, can also be employed (Argüden, 2008). Studies utilizing data mining with the MARS model have been conducted in various fields, including economics (Albayrak and Yilmaz, 2009; Tunay, 2010; Tunay, 2011), health (Ekrem et al., 2020; Zakeri, 2010), engineering (Eyduan et al., 2019), and education (Şevgin, 2020). The MARS model, like the well-known multiple linear regression model, is based on maximizing the explained variance of errors.

Changes in computer and software technologies have facilitated the analysis of a large number of variables using complex algorithms such as the MARS model. Leathwick et al. (2006) examined environmental factors influencing the species distribution of freshwater fish using the MARS model. Significant environmental factors were processed onto a geographic information system to determine suitable habitats for freshwater fish. Nacar et al. (2020) aimed to predict dissolved oxygen concentration using the MARS and regression analysis (RA) based on temperature (T), specific conductivity (SC) data calculated from specific conductance (EC), pH, and flow rate (Q). They identified basis functions and equations producing the best prediction values with the MARS model. Orhan et al. (2018) modeled milk yield using the MARS model with control day, milking time, conductivity, and mobility as independent variables based on daily lactation records of 80 cows from 2006 to 2011. Sevimli (2009) combined data collected using the split-mouth design method in dentistry and, statistically, demonstrated an effective prediction model using the MARS model. Tosun (2021) conducted a study on 25 animals on a local farm in Şanlıurfa, including variables such as breed, age, along with monthly milk yield, lactation period, and recorded live weight data for June-September 2020. In their study on the relationship between macroeconomic indicators and economic growth in Turkey, Bağcı and Hoş (2021) ranked variables affecting economic growth in their MARS model according to their importance, including imports, unemployment rate, credit volume, interest rate, exchange rate, and inflation. Kartal et al. (2018) conducted a study on factors affecting the USD/TRY and EUR/TRY exchange rates in Turkey using monthly data from January 2006 to June 2017 and 12 independent variables with the MARS model. The developed MARS model was found to be within acceptable limits of explanatory power. As observed in the aforementioned studies, the MARS model has been successfully applied in diverse fields such as medicine, economics, agriculture, and animal husbandry.

MARS model is a frequently used model in the field of educational sciences. Depren (2018) examined the factors affecting the achievement of Turkish students in science with the MARS model using PISA 2015 data. Ahmed et al. (2022) estimated the Introductory Engineering Mathematics score values of students with the MARS model. Addini et al. (2023) examined the quality of education in Indonesia with the MARS model. Zurimi (2020) examined the factors affecting the study periods of students with the MARS model and found that the economic status of the family is one of the most important variables. Apart from the MARS model, machine learning methods are also used to predict student achievement. Bujang et al. (2021) obtained grade predictions of students with random forest, support vector machine and decision trees methods.

The rest of the study is organized as follows. In Section 2, the MARS model is summarized. In Section 3, the data set is analyzed by the MARS model and the results of the model are discussed. In Section 4, the developed web-tool is introduced. Section 5 contains the concluding remarks.

II. MULTIVARIATE ADAPTIVE REGRESSION SPLINES

The MARS model is one of the non-parametric regression methods. Unlike traditional regression models, the MARS model does not assume a functional form for the relationship between variables. The primary aim of the MARS model is to reveal the relationship between the dependent variable and independent variables using basis functions. The MARS model is a regression model that utilizes basis functions corresponding to knot points obtained from independent variables. The relationship between the dependent variable and independent variables is explained functionally based on the obtained knot points. Thus, the MARS model stands out as a suitable statistical model for datasets with a multivariate structure (Temel et al., 2005).

Compared to traditional methods, the MARS model offers the advantage of optimal data transformation and the ability to determine interactions in complex datasets. Developing a robust regression model, even for small datasets, requires considerable time and effort. However, in conjunction with the MARS model, regression models can be easily developed for large databases and highly complex data structures (Tunay, 2001). The MARS model is a flexible and fast model that can be used both as a regression model and a binary classification model.

In the MARS model, unlike the known regression model, subsets formed by input variables are evaluated (Xu et al., 2006). Eventually, in the universe formed by predictive variables, extension functions are created, divided into many coherent regions, and these regional regression curves are expressed as basis functions (Put et al., 2004). In the MARS model, variables are divided into regions, and appropriate basis functions and their coefficients are determined through transformations. The created basis functions are in a linear relationship with the dependent variable. The MARS model can easily evaluate non-monotonic relationships between the dependent and independent variables, providing robust models (Olecka, 2007). The process of creating the equation within the MARS model can assess complex relationships in large datasets and achieve better results than other linear and parametric methods (Xu et al., 2006).

The setup of the MARS model is carried out in 2 steps (Kolyshkina et al., 2004). In the first step, all possible basis functions are created until the largest model is found. Basis functions can consist of a single variable or the interaction of multiple variables. Functions evaluating interactions and non-linear transformations of independent variables in the model constitute the basis function. While creating the basis function, all dependent and independent variables, as well as combinations of variables, are individually evaluated. Each basis function also generates a mirror image function. However, the mirror image function has no effect on the model as its slope at the relevant knot point is zero (Çelik et al., 2018). In the second step, the largest model obtained in the first step is reduced to the optimal model through a pruning process. The algorithm used in this process is the backward stepwise algorithm.

In the MARS model, rather than assuming a linear relationship between variables, modeling is carried out by considering the non-linear functions of variables individually and their linear combinations. Basis functions are employed for this purpose. Extensions made with basis functions are used to predict an appropriate model. The knot points within the defined intervals of the dataset signify the beginning and end of a data point. Therefore, knot points are where the function's behavior changes (Everingham and Sexton, 2011). When constructing the MARS model, the last value where the slope of the line does not change in the interval where the independent variable value is located is taken as the knot point. In defining the MARS model, basis functions defined at knot points are utilized. Figure 2.1 illustrates the correlation distribution between the independent variable X and the dependent variable Y . Considering the distribution of the independent variable X at the knot points, it is observed that the slope of the function changes at the x_1 variable's knot point. Similarly, at the x_2 knot point, the slope of the function has also changed.

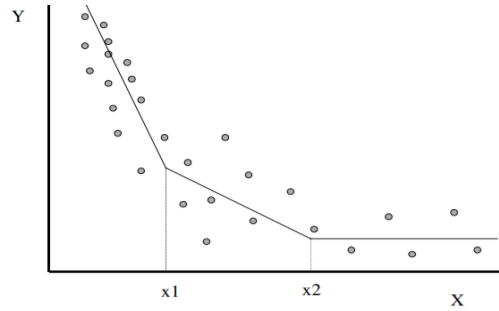


Figure 2.1. Knot points for the function $y=f(x)$ (Briand et al., 2004)

In the basis function, the variable x is derived in a piecewise linear structure. Below, the piecewise linear basis functions $(x - t)_+$ and $(t - x)_+$ are provided. Note that the symbol "+" denotes the positive side.

$$(x - t)_+ = \begin{cases} x - t, & x > t \\ 0 & x \leq t \end{cases} \quad (2.1)$$

$$(t - x)_+ = \begin{cases} t - x, & x < t \\ 0 & x \geq t \end{cases} \quad (2.2)$$

The sum of the basis functions is given in Equation 2.3.

$$C = \{(X_j - t), (t - X_j)\} \quad t \in \{x_1, x_1, \dots, x_{Nj}\} \quad j = 1, 2, \dots, p. \quad (2.3)$$

The knot value indicates the end of any region of data and the beginning of another. The MARS model is determined by using the number of knot values that yield the minimum prediction error (Sabancı, 2019).

In Figure 2.2, the relationship between the dependent and independent variables for the MARS model is depicted.

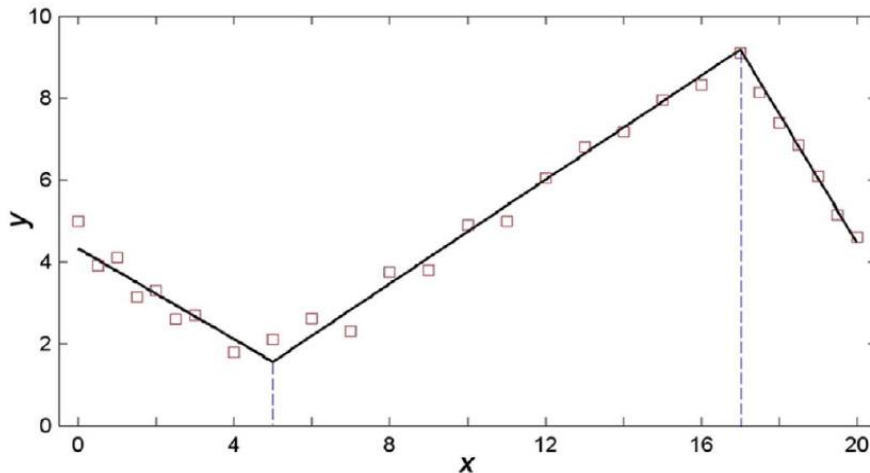


Figure 2.2. Function with two knot points belonging to the MARS model (Zhang and Goh, 2016)

Based on the Figure 2.2, the knot values for $x=5$ and $x=17$ are depicted. Corresponding to these knot values, there exist three basis functions, which are provided in Equation 2.4.

$$\begin{array}{lll} \text{Max}(0, 5 - x), & 0 < x < 5 & \text{Max}(0, x - 5), 5 < x < 17 & \text{Max}(0, x - 17), x > 17 \end{array} \quad (2.4)$$

A. FORWARD SELECTION

The first stage of the MARS model is forward selection. This stage resembles the first stage of a stepwise regression model. The distinction lies in the use of basis functions as input variables (Hill and Lewicki, 2006). The Greedy algorithm is employed to find the pair of basis functions with the smallest sum of squared errors. In MARS forward selection, to add a new basis function, it evaluates existing main terms; then, it evaluates all variables to choose the new basis function, and finally, it assesses combinations of all observed values for each variable to determine the last knot value (Strickland, 2015).

It employs an intuitive technique in each forward selection to minimize the number of main terms to be evaluated. The number of terms added in the forward selection process is up to the maximum number of terms entering the model, and this number is determined by the user. Therefore, it is crucial for the user to accurately determine this number (Friedman, 1993). The MARS model, as formulated by Friedman (1991), is expressed as follows.

$$f(x) = a_0 + \sum_{m=1}^M a_m B_m(x) = a_0 + \sum_{m=1}^M a_m \prod_{k=1}^{K_m} [S_{km}(x_{v(k,m)} - t_{km})] \quad (2.5)$$

According to the above function, the number of basis functions is denoted as M , and the MARS model can be formulated as $m = 1, 2, \dots, M$. The value K_m represents the number of interactions. The value S_{km} takes the values ± 1 and a_0 is the constant term. Regression coefficients are represented by a_m . $B_m(x)$ denotes the basis function (Friedman, 1991).

B. BACKWARD ELIMINATION

The second stage of the MARS model is constituted by the backward elimination stage. The aim in this stage is to reduce the complexity of the model created in the first step. In the backward elimination process, the largest model obtained in the first stage is considered. This model, due to harboring the problem of overfitting, does not yield statistically reliable results in the test set (Hill and Lewicki, 2006). The backward elimination algorithm is a continuation of the forward selection algorithm.

Through the backward elimination algorithm, the overfitting model undergoes a pruning process. The best subset is obtained using the GCV criterion. The GCV value takes into account the model complexity and the HKT value. Basis functions minimizing the GCV value are identified. A model with a smaller GCV value is considered the best model (Briand et al., 2004; Hastie et al., 2009; Hill and Lewicki, 2006). GCV is calculated using the following formula (Friedman, 1991).

$$GCV = \frac{1}{N} \sum_{i=1}^N [y_i - \hat{f}(x_i)]^2 / [1 - \frac{C(M)}{N}]^2 \quad (2.6)$$

The value N , as presented in Equation 2.6, denotes the number of observations in the dataset. $C(M)$ is the cost-complexity measure of a model containing M basis functions, excluding the constant basis function (the a_0 coefficient in the MARS model), and is defined as follows (Orhan et al., 2018).

$$C(M) = M + dM \quad (2.7)$$

Here, d represents a smoothing parameter in the creation process of the MARS model, accompanied by a cost optimization for each basis function (Chou et al., 2004; Leblanch and Tibshirani, 1994).

III. APPLICATION

The study was conducted with the participation of all 68 students at Mehmet Akif Ersoy Middle School in Tosya district, Kastamonu province, at the 8th-grade level. Three different sources of data were utilized within the scope of the research, namely the exam evaluation system, student information form, and the results of the students' High School Entrance Exam (LGS). The data are available from the authors upon request. The exam evaluation system, during the academic year 2020-2021, read the optical form information of the students from the trial exams, recording the number of correct and incorrect answers for each student in subjects such as mathematics, Turkish, religious culture and ethics, history of revolution and Kemalism, English, and science. Throughout the semester, students took a total of 34 trial exams.

A. DESCRIPTIVE STATISTICS FOR DEMOGRAPHIC VARIABLES

Descriptive statistics for demographic variables such as gender, number of siblings, and parents' educational levels are provided in Table 3.1.

Table 3.1. Descriptive Statistics for Demographic Variables

Variables	Level	n	%
Gender	Male	37	54.4
	Female	31	45.6
The number of siblings	none	4	5.9
	1	32	47.1
	2	19	27.9
	Three or more	13	19.1
	Elementary school	19	27.9
Mother's education level	Middle school	14	20.6
	High school	20	29.4
	University	12	17.6
	Master's degree	3	4.4
	Elementary school	11	16.2
Father's education level	Middle school	13	19.1
	High school	23	33.8
	University	18	26.5
	Master's degree	3	4.4
	Yes	36	52.9
Social activity participation	No	32	47.1
	Yes	60	88.2
Reading books	No	8	11.8
	Yes	58	85.3
Private room	No	10	14.7
	Yes	61	89.7
Computer/Tablet	No	7	10.3
	Yes	53	77.9
Mobile phone	No	15	22.1
	Yes	12	17.6
Grade repetition	No	56	82.4
	Yes	26	38.2
Academic support	No	42	61.8
	Yes		

As indicated in Table 3.1, 54.4% of the students are male, while 45.6% are female. Four levels have been used for the information on the number of siblings. In terms of the number of siblings, 4 students (5.9%) have no siblings. Nearly half of the students (47.1%) have only one sibling. In terms of the mothers' education level, 29.4% of student mothers graduated from high school, 27.9% from elementary school, 20.6% from middle school, 17.6% from university, and 4.4% from master's degree programs. Regarding the fathers' education level, 33.8% of students' fathers graduated from high school, 26.5% from university, 19.1% from middle school, 16.2% from elementary school, and 4.4% from master's degree programs. More than half of the students (52.6%) participate in social activities. The majority of students (88.2%) have a habit of reading books. More than half of the students (85.3%) have their own private rooms. Only 7 students (10.3%) do not have a computer and tablet, while 15 students (22.1%) do not have a mobile phone. The rate of students repeating a grade is 17.6%, while 56 students (82.4%) have never repeated a grade up to the 8th grade. In terms of academic support, more than half of the students (61.8%) take private lessons outside of school, while 38.2% of students have not taken any private lessons.

B. DESCRIPTIVE STATISTICS FOR STUDENTS' ACADEMIC ACHIEVEMENTS

Students took a total of 34 trial exams from September 2020 to June 2021. Descriptive statistics for the calculated average net values related to students' academic achievements and the descriptive statistics values for their scores in the High School Entrance Exam (LGS) are presented in Table 3.2.

Table 3.2. Descriptive statistics for students' academic achievements

Variables	Minimum	Maximum	Mean	Median	Standard deviation	Variance
Turkish course average score	-0.144	17.344	10.168	11.472	5.134	26.355
Mathematics course average score	-0.709	15.647	5.533	4.353	4.988	24.875
Revolution history and Kemalism course average score	-0.367	9.093	5.038	6.104	2.831	8.013
Religious Culture and Ethics course average score	-0.332	9.286	5.774	6.531	2.777	7.714
English course average score	-1.000	9.587	4.913	5.209	3.506	12.292
Science course average score	-0.259	17.656	8.683	8.653	5.875	34.516
LGS Score	190.855	451.915	318.771	190.855	78.877	6221.643

As indicated in Table 3.2, the subject with the smallest variance is the course of Religious Culture and Ethics, while the subject with the largest variance is the Science course. It can be inferred that the achievement variable in the Science course has a higher level of heterogeneity compared to other subjects. In comparison to the Science course, it can be stated that the achievement variable in the Religious Culture and Ethics course is more homogeneous. Since the number of questions in Turkish, Science, and Mathematics courses is equal (20 questions each), it is determined that students are more successful in the Turkish course based on the average values. As the number of questions in the History of Revolution and Kemalism, Religious Culture and Ethics, and English courses is also equal (10 questions each), it is found that students are more successful in the Religious Culture and Ethics course among these four subjects.

C. NORMALITY ANALYSIS OF STUDENTS' ACADEMIC ACHIEVEMENTS

The normality analysis results of the average values of the trial exam results taken by students throughout the academic year are presented in Table 3.3. As seen in Table 3.3, the relevant variables do not satisfy the assumption of normal distribution ($p < 0.05$). When the skewness values are analyzed, it is seen that all variables are left skewed except mathematics course average score. All kurtosis values are smaller than 0, so the distributions of variables are platykurtic.

Table 3.3. Skewness, kurtosis coefficients, and normality test results for variables related to students' academic achievements

Variables	Skewness	Kurtosis	Shapiro-Wilk
Turkish course average score	-0.507	-0.978	0.922 (< 0.001)
Mathematics course average score	0.452	-1.124	0.897 (< 0.001)
Revolution history and Kemalism course average score	-0.447	-1.196	0.910 (< 0.001)
Religious Culture and Ethics course average score	-0.841	-0.417	0.884 (< 0.001)
English course average score	-0.182	-1.538	0.889 (< 0.001)
Science course average score	-0.061	-1.547	0.903 (< 0.001)
LGS Score	-0.013	-1.449	0.923 (< 0.001)

D. RELATIONSHIP BETWEEN LGS SCORES AND TRIAL EXAMS

The correlation between students' LGS scores and the trial exams they took in the 8th grade is presented in Figure 3.2. Trial exams refer to the exams that students take at school in preparation for the LGS exam. Since the variables are non-normal, we use the spearman correlation coefficient.

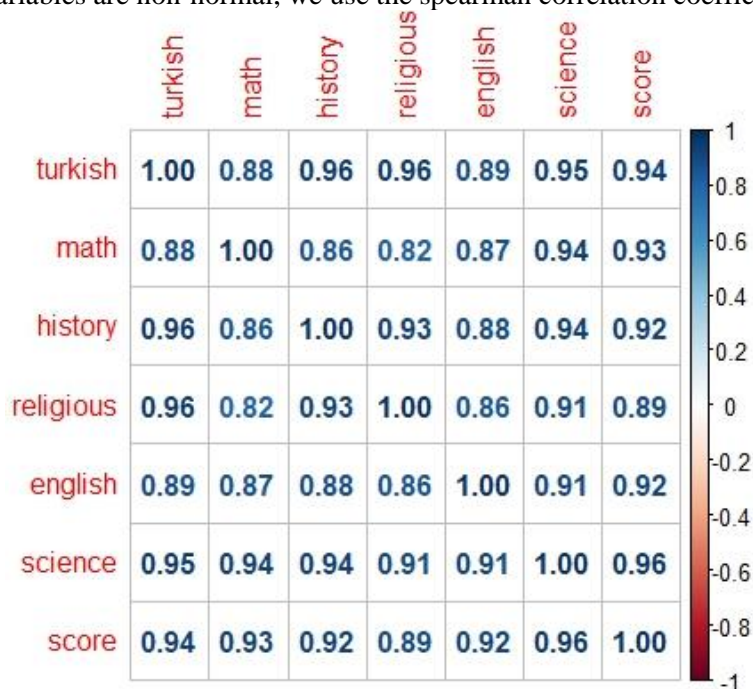


Figure 3.2. Relationship between students' LGS scores and trial exam achievements

As indicated in Figure 3.2, when the relationship between successful subjects in the trial exams and the LGS score is assessed, the correlation between the achievement in the science course and the LGS score is higher compared to other subjects (0.96). The success in the science course is followed by Turkish (0.94) and mathematics (0.93) courses, respectively. Mathematics is followed by equal-weighted History of Revolution and Kemalism and English courses. In the trial exams, the relationship between the success in the Religious Culture and Ethics course and the LGS score is the lowest compared to other subjects, and the correlation coefficient is calculated as 0.89.

E. MARS MODEL RESULTS

The parameter estimates for the MARS model were obtained using the R program, specifically utilizing the 'earth' package in the program. Initially, it is crucial to estimate the tuning parameters of the model, which include the degree of interaction and the number of terms. Therefore, a grid search algorithm and k-fold cross-validation were employed to determine the optimal values for these two parameters. During this process, the prediction error was minimized, and the value of k was set to 10. The 'caret' package was utilized for this procedure. The obtained results are presented in Figure 3.3. According to the results provided in Figure 3.3, the optimal interaction degree was determined to be 1, and the number of terms was found to be 7.

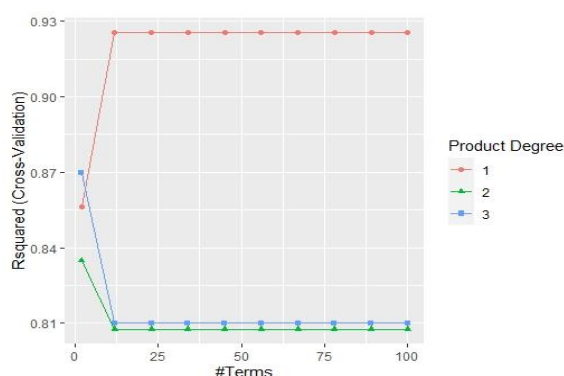


Figure 3.3. Tuning parameters obtained through cross-validation and grid search algorithm for the MARS model.

Once the tuning parameters of the MARS model were determined, the model parameters were obtained using the 'earth' package. The results are presented in Table 3.5.

Table 3.5. Parameter estimates and basis functions of the MARS model.

Parameter Estimation	Basis Function
285.597	Constant term
-16.241	The number of siblings (3 and more)
13.728	Mother's Education Level (Middle School)
-11.965	$\max(0, 5.936 - \text{Average Net Number in Mathematics Course})$
4.060	$\max(0, \text{Average Net Number in Mathematics Course} - 5.936)$
9.610	$\max(0, \text{Average Net Number in Revolution history and Kemalism Course} - 1.730)$
5.504	$\max(0, \text{Average Net Number in English Course} - 1.466)$
$GRSq$	0.933
R^2	0.954
GCV	423.003
RSS	18817.430

When examining Table 3.5, according to the obtained results, the number of basis functions is 6. The MARS model automatically performs the variable selection process. According to the model results, the significant variables are: number of siblings, mother's education, average score in mathematics course, average score in history and Kemalism course, and average score in English course. The constant term value is determined as 285.597. When the number of siblings is 3 or more, the parameter estimate value is -16.241. It is observed that student achievement decreases when the number of siblings is 3 or more. When the mother's education is at the middle school level, the parameter estimate value is 13.728. Middle school graduates positively influence student achievement. The inflection point for the

mathematics course is found to be 5.936. If the student's average net score in the mathematics course is less than 5.936, the parameter estimate coefficient is determined to be -11.965. The situation identified here is that having an average net score in the mathematics course less than 5.936 negatively affects student achievement. However, when the average net score in the mathematics course is greater than 5.936, the parameter estimate coefficient is 4.060. Student achievement is positively influenced when the average net score in the mathematics course exceeds 5.936. The inflection point for the history and Kemalism course is found to be 1.730. When the average net score for this course exceeds 1.73, the parameter estimate value is 9.610. For the English course, the inflection point is found to be 1.466. When the average net score in English exceeds 1.466, the parameter estimate value is 5.504. The GCV value is calculated as 423.003. The GRSq and R2 values are obtained as 0.933 and 0.954, respectively. The RSS value is determined to be 18817.430. Figure 3.4 presents the residual analysis of the MARS model. Note that the definition of the GCV can be found in Çanga (2022).

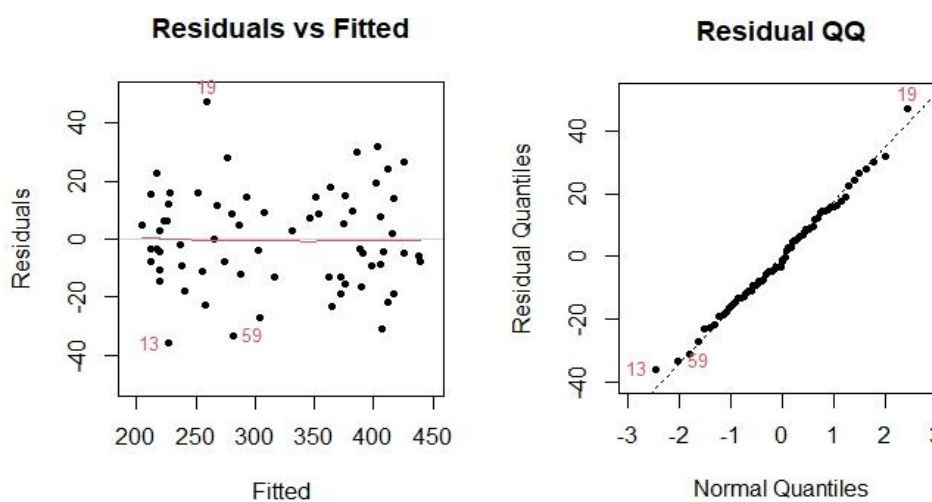


Figure 3.4. Examination of model fit for the MARS model

As indicated in Figure 3.4, a residual analysis has been conducted. Three observations can be considered as potential outlier observations. These observations are removed from the model and model success is re-evaluated. Since no significant improvement in model performance is achieved by removing the relevant observations from the data, it is decided to include these observations in the data set. Figure 3.5 provides graphs of the basis functions.

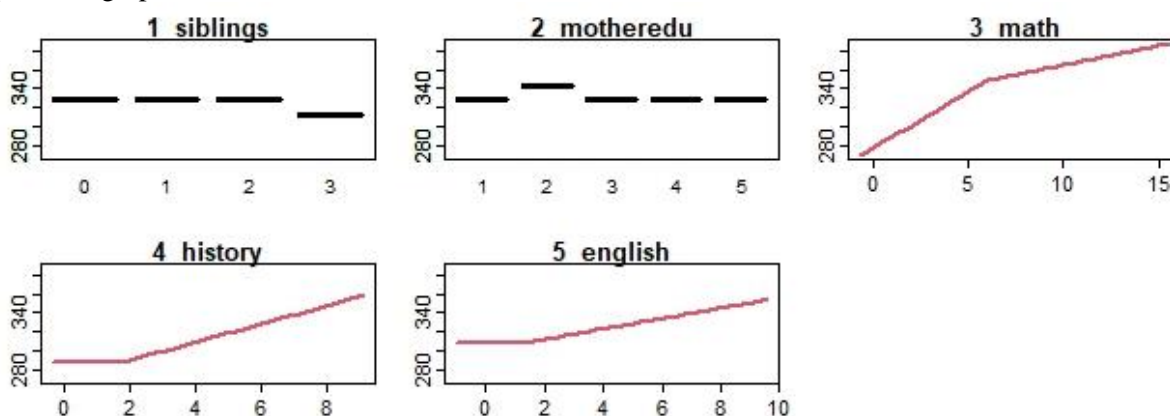


Figure 3.5. Graphical examination of basis functions

The knot points for the 5 significant variables are summarized in the graphs in Figure 3.5. As indicated in Figure 3.5, when the number of siblings is 0, 1, and 2, it does not affect the student's LGS score. However, when the number of siblings exceeds 2, the student's LGS score decreases. Therefore, having 3 or more siblings has a negative impact on the LGS score. Additionally, when the mother's education

level is at the middle school, it has a positive effect on the LGS score compared to other education levels. The average net score of the mathematics course has two breakpoints on the LGS score. The slope of the regression line changes at the value of 5.936. Having a mathematics net score below 5.936 negatively affects the LGS score, while having a net score above this value positively influences the LGS score. The average net score in the History of Revolution and Kemalism course does not affect the LGS exam until 1.73, but beyond this value, it positively influences the LGS exam. The regression graph for the English course is similar to the graph of the History of Revolution and Kemalism course. The average net score in the English course does not affect the LGS exam until 1.466, but beyond this value, it positively influences the LGS exam. In Figure 3.6, the importance levels of the significant variables are given according to the GCV and RSS criteria.

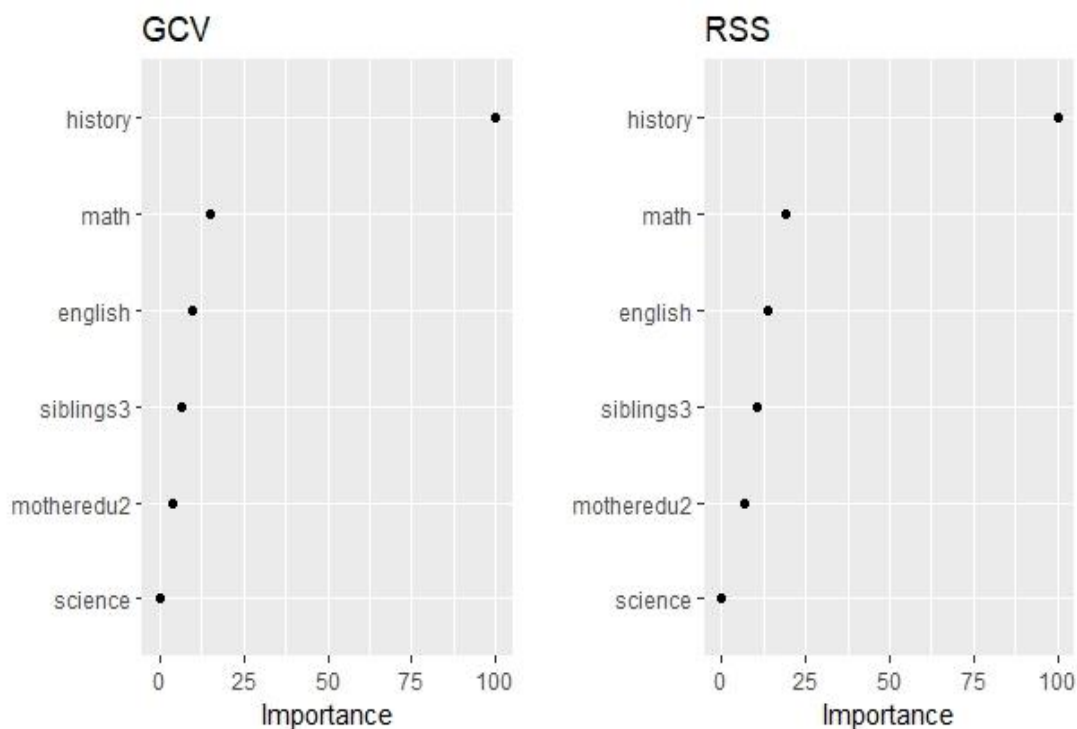


Figure 3.6. Importance Levels of Variables Based on GCV and RSS

In Figure 3.6, the significance levels of variables, along with their importance degrees, have been determined. This was calculated based on RSS or GCV values. Ultimately, the average net score in the History of Revolution and Kemalism course was found to be the most important variable. The ranking of variables in terms of their importance on the LGS score is as follows:

- Average net score in the History of Revolution and Kemalism course
- Average net score in the Mathematics course
- Average net score in the English course
- Number of siblings
- Mother's education level
-

In Figure 3.7, the predicted values of the MARS model are compared with the actual values. As depicted in Figure 3.7, the red squares represent the values predicted by the MARS model, while the black dots indicate the actual values. The predicted values by the MARS model closely align with the actual values, demonstrating the model's success in modeling the relevant data.

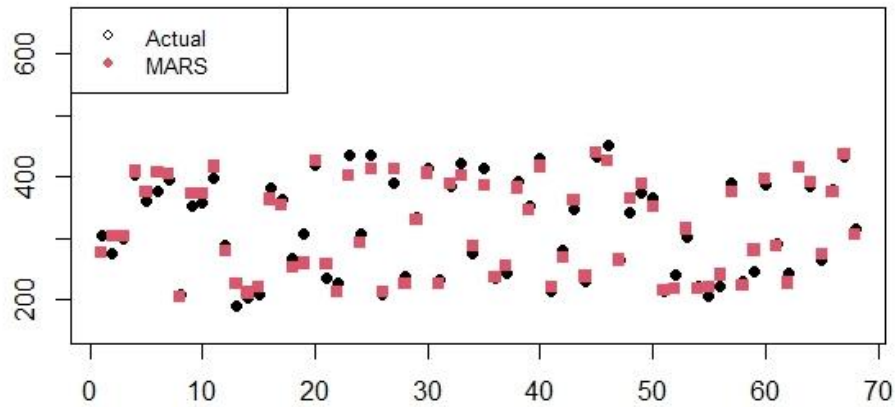


Figure 3.7. Comparison of Prediction Values of the MARS Model with Actual Values

IV. DEVELOPED CLOUD-BASED APPLICATION

In this section, we introduce the developed cloud based web-tool. The web-tool is developed using the shiny package of the R software. We use the the MARS model to produce the estimated LGS score based on the input data for students. The user interface of the web-tool is displayed in Figure 4.1. The web-tool is accessible with the following website <https://beststat.shinyapps.io/lgs2/>.

Figure 4.1. The user interface of the developed web-tool.

According to the results of the MARS model, the five variables are found statistically significant on the performance of the LGS scores of the students. Therefore, the web-tool considers only these variables

to estimate the LGS score based on the MARS model. In the right panel of the web-tool, there are three tabs. These are LGS Score, Student Profile and Advices. After all the necessary input variables are provided, the user runs the model by clicking the “Estimate LGS score! “. After that, the estimated LGS score, student profile and advises are shown at the right panel of the web-tool.

The advises are provided based on the obtained knot values. For instance, the knot value for the mathematics variable is 5.936. When the net value of the student for the mathematics course is less than 5.936, it affects the LGS score badly. So, the system generates an advice such as “*You need to spend more time in math class!*”. The other advises are also generated by using the knot values of the predictor variables. The advises are listed below.

Conditions	Advices
Math<5.936, revolution history>1.730 and english>1.466	You need to spend more time in math class!
Math>5.936, Revolution History<1.730, English>1.466	You need to study more in the revolution course!
Math>5.936, Revolution History>1.730, English<1.466	You need to study more in English class!
Math<5.936, Revolution History<1.730, English>1.466	Study mathematics and revolution more!
Math<5.936, Revolution History>1.730, English<1.466	Study math and English more!
Math>5.936, Revolution History<1.730, English<1.466	Study revolution and English more!
Math<5.936, Revolution History<1.730, English<1.466	You need to increase your score by working more efficiently!
In other cases	Keep going like this!

V. RESULTS AND RECOMMENDATIONS

Considering the non-linear relationship between datasets obtained in the field of education, it has been deemed appropriate to utilize the MARS model, a non-linear and non-parametric prediction method. The MARS model attempts to explain the dependent variable by evaluating both the explanatory variables individually and their interactions. Moreover, it seeks to describe the created model with the basis function it generates. A web application based on the MARS model, relying on machine learning, has been developed to predict students' scores in the LGS exam.

To assess the prediction performance of the MARS model, goodness-of-fit criteria ($GRSq$, R^2 , GCV , RSS) were employed. The constructed MARS prediction model utilized 7 terms, including the constant term, number of siblings, mother's education level, and average net scores in trial exams for Mathematics, English, and the History of Revolution and Kemalism course.

The calculated goodness-of-fit criteria, based on the lowest GCV (423.003) and RSS (18817.430), resulted in satisfactory values for $GRSq$ (0.933) and cross-validation R^2 (0.954). It was observed that when the mother's education level is at the middle school level, student achievement increases (parameter estimate value was found to be 13.728 when the mother's education level is at the middle school level). This positively influences the student's LGS success. However, when the mother's education level is at the primary school, high school, college, or postgraduate level, the student's LGS success is not affected. Sociologically, this can be interpreted as follows: when the mother is a primary school graduate, she is likely unable to participate in the relevant educational activities, with a very low literacy rate in her family, or insufficient importance given to education within the family. For middle school graduate mothers, the situation can be interpreted as follows: a mother who has not achieved her

own goals can positively contribute to her child's education by providing support, thereby positively influencing the child's goals. This support can be evaluated as following the child's assignments or courses, motivating the child, and so on. On the other hand, mothers who are graduates of high school, college, or postgraduate programs are heavily involved in professional life (Keskin, 2018). Due to their extensive participation in professional life, they may have difficulty following their students. Therefore, they may not be able to show the necessary importance to their child's education. This is because they allocate more of their working hours to professional life. The time they spend with their child is less. This situation does not significantly positively affect the student's success.

In the MARS model developed within the scope of this study, when the number of siblings is 3 or more, the parameter estimate value was -16.241. Student achievement is negatively affected when the number of siblings is 3 or more. This is an expected result, as a large number of siblings may lead to a crowded environment, where there is not enough suitable space for studying, resulting in a decrease in the student's success.

It was found that success in the History of Revolution and Kemalism course positively affects the student's LGS success (parameter estimate value was 9.610 for the function $\max(0, \text{History of Revolution and Kemalism average} - 1.730)$). This result supports the study conducted by Gençtürk (2001) on the factors affecting the diploma grades of high school students. According to the findings obtained, to positively influence LGS success in trial exams, the average net score in the History of Revolution and Kemalism course should be above 1.73.

Success in the English course was found to positively affect the student's LGS success (parameter estimate value was 5.504 for the function $\max(0, \text{English average} - 1.466)$). This result supports the studies of Baş and Beyhan (2012) and Kazazoğlu (2013), indicating that success in the English course positively affects students' academic achievements. According to the findings, to positively influence LGS success in trial exams, the average net score in the English course should be above 5.504.

The Mathematics course was found to affect LGS success in two ways. When the net score in the trial exams for Mathematics is below 5.936, it negatively affects the LGS score (parameter estimate value was -11.965 for the function $\max(0, 5.936 - \text{Mathematics average})$). When the net score in the Mathematics course is above 5.936, the LGS success is positively affected (parameter estimate value was 4.060 for the function $\max(0, \text{Mathematics average} - 5.936)$). This result supports studies indicating a significant and positive effect of mathematical success on students' problem-solving skills and success in other courses (Özsoy, 2005; Şentürk, 2010). This result suggests that not solving any questions in the mathematics course can negatively affect LGS success.

In contrast to studies in the literature, in this study, a new prediction equation was realized using the MARS model to predict the LGS scores of students based on machine learning. The developed machine learning-based web application has been published in an interactive format. Since the study is limited to a single school, the obtained findings are limited to the school where the study was conducted. For students, the recommendations in the advice table of the web application can be improved by working with subject matter experts. The results obtained in the study have shown that the MARS model could be an important option for predicting the LGS scores of middle school students.

Funding The authors state that this work has not received any funding.

Data availability The authors do not have permission to share data.

Declarations

Conflict of interest The authors of this manuscript declare no conflicts of interest.

Ethical approval Not applicable.

Informed consent Not applicable.

VI. REFERENCES

- [1] S. Albayrak, ve Ş. Koltan Yılmaz. "Veri madenciliği: Karar ağacı algoritmaları ve İMKB verileri üzerine bir uygulama", *Süleyman Demirel Üniversitesi İktisadi ve İdari Bilimler Fakültesi Dergisi*, vol. 14, no. 1, pp. 31-52, 2009.
- [2] Addini, P. F., Hadi, W., & Harahap, P. M. R. "Application of the multivariate adaptive regression spline (Mars) method in analyzing misclassification of elementary school accreditation data in the city of Tebing Tinggi", *Journal Scientia*, vol. 12, no. 1, pp. 617-620, 2023.
- [3] Ahmed, A. A. M., Deo, R. C., Ghimire, S., Downs, N. J., Devi, A., Barua, P. D., & Yaseen, Z. M. "Introductory engineering mathematics students' weighted score predictions utilising a novel multivariate adaptive regression spline model", *Sustainability*, vol. 14, no. 17, pp. 11070, 2022.
- [4] A. Yılmaz., *Veri madenciliği: Veriden bilgiye, masraftan değere*, ARGE danışmanlık, 2008.
- [5] Bağcı, B., ve Hoş, S. "Türkiye'de Ekonomik Büyümenin Makroekonomik Göstergeler İle İlişkisi: MARS Modeli", *Ekonomi İşletme ve Maliye Araştırmaları Dergisi*, vol. 3, no. 2, pp. 193-202, 2021.
- [6] Baş, G., ve Beyhan, Ö. "İngilizce Dersinde Yansıtıcı Düşünme Etkinliklerinin Öğrencilerin Akademik Başarılarına ve Derse Yönelik Tutumlarına Etkisi", *Amasya Üniversitesi Eğitim Fakültesi Dergisi*, vol. 1, no. 2, pp. 128-142, 2012.
- [7] Bayrak, F., ve Yurdugül, H., "E-Değerlendirme ve Dönüt", *The Turkish Online Journal of Educational Techno Bujang*, 2025
- [8] S. D. A., Selamat, A., Ibrahim, R., Krejcar, O., Herrera-Viedma, E., Fujita, H., & Ghani, N. A. M., "Multiclass prediction model for student grade prediction using machine learning", *Ieee Access*, vol. 9, pp. 449-465, 2021.
- [9] Briand, L., Freimut, B., ve Vollei, F., "Using multiple adaptive regression splines to support decision making in code inspections", *Journal of Systems and Software*, vol. 73, no. 2, pp. 205-217, 2004.
- [10] Çanga, D., "Use of MARS Data Mining algorithm based on training and test sets in determining carcass weight of cattle in different breeds", *Journal of Agricultural Sciences*, vol. 28, no. 2, pp. 259-268, 2022.
- [11] Chou, Shieu-Ming, et al. "Mining the breast cancer pattern using artificial neural networks and multivariate adaptive regression splines." *Expert systems with applications*, vol. 27, no. 1, pp. 133-142 2004.
- [12] Çelik, Ş., Şengül, T., Şengül, A. Y., ve Hakan, İ., "Tüketici fiyat indeksini etkileyen bitkisel ve hayvansal üretim değerlerinin çok değişkenli uyarlanabilir regresyon uzanımları ile incelenmesi: Türkiye örneği", *Journal of Awareness*, vol. 3, no. 3, pp. 399-408, 2018.
- [13] Depren, S. K. (2018). "Prediction of Students'science Achievement: An Application of Multivariate Adaptive Regression Splines and Regression Trees", *Journal Of Baltic Science Education*, vol.17, no. 5, pp. 887-903, 2018.
- [14] Ekrem, Ö., Salman, O. K., Aksoy, B., ve İnan, S. A., "Yapay zeka yöntemleri kullanılarak kalp hastalığının tespiti", *Mühendislik Bilimleri ve Tasarım Dergisi*, vol. 8, no. 5, pp. 241-254, 2020.

- [15] Everingham, Y., ve Sexton, J., “An introduction to Multivariate Adaptive Regression Splines for the cane industry” 33rd Annual Conference of the Australian Society of Sugar Cane Technologists. Mackay, 2011.
- [16] Eydurán, E., M. Akin, and S. P. Eydurán., *Application of multivariate adaptive regression splines through R software*, Ankara Turkey: Nobel Academic Publishing (2019).
- [17] Friedman, J. H. (1991). “Multivariate Adaptive Regression Splines”, *The Annals of Statistics*. Vol. 19, no. 1, pp. 1-67, 1991.
- [18] Friedman, J. H., ” Fast MARS”, Technical Report., Department of Statistics. Stanford University, Stanford, 1993
- [19] Gençtürk, Ö., “Meslek ve Anadolu Meslek Liselerinde Öğrenci Başarısını Etkileyen Faktörler”, Yüksek Lisans Tezi, Marmara Üniversitesi, Fen Bilimleri Enstitüsü, İstanbul, 2001.
- [20] Hastie, T., Tibshirani, R., ve Friedman, J., *The Elements of Statistical Learning: Data mining, inference, and prediction*, Springer, New York, 2009.
- [21] Hill, Thomas, Paweł Lewicki, and Paweł Lewicki. *Statistics: methods and applications: a comprehensive reference for science, industry, and data mining*. StatSoft, Inc., 2006.
- [22] Kartal, M., Depren, S. K., ve Depren, Ö., “Türkiye’de Döviz Kurlarını Etkileyen Makroekonomik Göstergelerin Belirlenmesi: MARS Yöntemi İle Bir İnceleme”, *MANAS Sosyal Araştırmalar Dergisi*, vol. 7, no. 1, pp. 209-229, 2018.
- [23] Kazazoğlu, S., “Türkçe ve İngilizce derslerine yönelik tutumun akademik başarıya etkisi”, *Eğitim ve Bilim*, vo. 38, no. 170, pp. 295-306, 2013.
- [24] Keskin, S., “Türkiye’de Eğitim Düzeyine Göre Kadınların İş Hayatındaki Yeri” *Kadın Araştırmaları Dergisi* , vol. 17, pp. 1-30, 2018.
- [25] Kılıç, S., “Doğrusal regresyon analizi” *Journal of Mood Disorders*, vol. 3, pp. 90–92, 2013.
- [26] Kolyshkina, Inna, Sylvia Wong, and Steven Lim. "Enhancing generalized linear models with data mining." *Casualty Actuarial Society*. 2004.
- [27] Leathwick, J., Elith, J., ve Hastie, T., “Comparative performance of generalized additive models and multi-variate adaptive regression splines for statistical modelling of species distributions”, *Ecological modelling*, vol. 199, no. 2, pp. 188-196, 2006.
- [28] Leblanch, M., ve Tibshirani, R., “Adaptive Principle Surfaces”, *Journal of the American Statistical Association*, vol. 89, no. 425, pp. 53-64, 1994.
- [29] Nacar, S., Betül, M. E., ve Bayram, A., ” Günlük Çözünmüş Oksijen Konsantrasyonunun Çok Değişkenli Uyarlanabilir Regresyon Eğrileri İle Tahmin Edilmesi”, *Uludağ University Journal of The Faculty of Engineering*, vol. 25, no. 3, pp. 1479-1498, 2020.
- [30] Olecka, Anna. "Beyond classification: Challenges of data mining for credit scoring." *Knowledge Discovery and Data Mining: Challenges and Realities*. IGI Global, pp. 139-161, 2007.
- [31] Orhan, H., Teke, E. Ç., ve Karcı, Z., “Laktasyon Eğrileri Modellemesinde Çok Değişkenli Uyarlanabilir Regresyon Eğrileri (Mars) Yönteminin Uygulanması”, *Kahramanmaraş Sütçü İmam Üniversitesi Tarım ve Doğa Dergisi*, vol. 21, no. 3, pp. 363-373, 2018.

- [32] Özsoy, G., “Problem Çözme Becerisi İle Matematik Başarısı Arasındaki İlişki”, *Gazi Eğitim Fakültesi Dergisi*, vol. 25, no. 3, pp.179-190, 2005.
- [33] Put, R., Xu, Q. S., Massart, D. L., ve Vander Heyden, Y., “Multivariate adaptive regression splines (MARS) in chromatographic quantitative structure–retention relationship studies” *Journal of Chromatography A*, vol. 1055 pp. 11–19, 2004.
- [34] Sabancı, D., “Rastgele Orman Yaklaşımı Kullanılarak Çok Değişkenli Uyumlu Regresyon Şeritlerinde Model Seçimi,” Doktora Tezi, İstatistik Anabilim Dalı, Ondokuz Mayıs Üniversitesi, , Samsun 2019.
- [35] Sevimli, Y., ” Çok Değişkenli Uyarlanabilir Regresyon Uzanımlarının Bir Split-Mouth Çalışmasında Uygulaması,” Yüksek Lisans Tezi, Biyoistatistik Anabilim Dalı, Marmara Üniversitesi, İstanbul, 2009.
- [36] Simpson, L. P., “Perception of examsoft feedback reports as autonomy-support for learners,” Doktora Tezi, Morehead State University, Eğitim Bilimleri, Kentucky, 2016.
- [37] Strickland, J., *Predictive Analytics Using R*, Morrisville, North Carolina, ABD: Lulu Press, 2015.
- [38] Şahinler, S., “En küçük kareler yöntemi ile doğrusal regresyon modeli oluşturmaının temel prensipleri”, *Mustafa Kemal Üniversitesi Ziraat Fakültesi Dergisi*, vol. 5, pp. 57–73, 2000.
- [39] Şentürk, B., “İlköğretim Beşinci Sınıf Öğrencilerinin Genel Başarıları, Matematik Başarıları, Matematik Dersine Yönelik Tutumları ve Matematik Kaygıları Arasındaki İlişki.” Yüksek Lisans Tezi, Sosyal Bilimler Enstitüsü, Afyon Kocatepe Üniversitesi, Afyon, 2010.
- [40] Şevgin, H., “ABİDE 2016 fen başarısının yordanmasında MARS ve BRT veri madenciliği yöntemlerinin karşılaştırılması”, Doktora Tezi, Fen Bilimleri Enstitüsü, Gazi Üniversitesi, Ankara, 2020.
- [41] Temel, G. O., Ankaralı, H., & YAZICI, A. C, “Regresyon Modellerine Alternatif Bir Yaklaşım MARS”, *Türkiye Klinikleri Journal of Biostatistics*, vol. 2, no. 2, pp. 58-66, 2010.
- [42] Tosun, F., “Veri Madenciliği İle Çok Değişkenli Uyarlanabilir Regresyon Eğrileri (MARS Modellemesi) Yönteminin Uygulanması”, Yüksek Lisans Tezi, Zootekni Anabilim Dalı, Harran Üniversitesi, , Şanlıurfa, 2021.
- [43] Tunay, K. Batu. "Türkiye'de paranin gelir dolasım hızlarının MARS yöntemiyle tahmini." *METU Studies in Development* vol. 28 , no.2, pp.175, 2001.
- [44] Tunay, K. B., “Bankacılık Krizleri ve Erken Uyarı Sistemleri: Türk Bankacılık Sektörü İçin Bir Model Önerisi”, *BDDK Bankacılık ve Finansal Piyasalar Dergisi*, vol. 4, pp. 9–46, 2010.
- [45] Tunay, K. B., “Türkiye'de Durgunlukların MARS Yöntemi ile Tahmini ve Kestirimi”, *Marmara Üniversitesi İktisadi ve İdari Bilimler Dergisi*, vol. 30, no. 1, pp. 71–91, 2011.
- [46] Xu, Q. S., Daeyaert, F., Lewi, P. J., ve Massart, D. L., “Studies of relationship between biological activities and HIV Reverse Transcriptase Inhibitors by Multivariate Adaptive Regression Splines with Curds and Whey”, *Chemometrics and Intelligent Laboratory Systems*, vol. 82, pp. 24-30, 2006.

- [47] Zakeri, F. A., "Multivariate adaptive regression splines models for the prediction of energy expenditure in children and adolescents", *Journal of Applied Physiology*, vol. 108, no. 1, pp. 128-136, 2010.
- [48] Zhang, W., ve Goh, A. T., "Multivariate adaptive regression splines and neural network models for prediction of pile drivability", *Geoscience Frontiers*, vol. 7, no.1, pp. 45-52, 2016.
- [49] Zurimi, S. , Analysis of Multivariate Adaptive Regression Spline (MARS) Model in Classifying factors affecting on Student the Study Period at FKIP Darussalam University of Ambon" In *Journal of Physics: Conference Series*, Vol. 1463, no. 1, pp. 012005, 2020.



Düzce University Journal of Science & Technology

Research Article

Catalytic Pyrolysis of Grape Seed Waste: Characterization of Bio-Char and Bio-Oil

 Koray ALPER ^{a,*}

^aDepartment of Environmental Protection Technologies, Zonguldak Bulent Ecevit University, 67100, Zonguldak, TÜRKİYE

* Corresponding author's e-mail address: korayalper@beun.edu.tr

DOI: 10.29130/dubited.1597245

ABSTRACT

The utilization of biomass waste for biofuel production through pyrolysis has emerged as a promising approach to combat global warming. This process enables the generation of bio-char, bio-oil, and bio-gas using a straightforward and cost-efficient method. Among the biomass residues in Turkey, grape seeds from the food processing industry offer considerable potential as an alternative energy source. This research explores the characteristics of bio-oil and bio-char produced from grape seed pyrolysis conducted in a nitrogen atmosphere (inert gas) at temperatures ranging from 500 to 800 °C. Additionally, the effects of Purmol CTX and Clinoptilolite catalysts on product yield and composition were examined in optimal experimental results. Results indicate that higher pyrolysis temperatures yield carbon-dense bio-chars with elevated heating values and minimal impurities, rendering them viable as solid biofuels. Meanwhile, the bio-oils consist of compounds such as phenols, alkanes, alkenes, alkyls, and acids, positioning them as eco-friendly candidates for sustainable biofuel applications.

Keywords: Pyrolysis, Grape seed, Bio-char, Bio-oil

Üzüm Çekirdeği Atıklarının Katalitik Pirolizi: Biyo-Kömür ve Biyo-Yağın Karakterizasyonu

Öz

Biyokütle atıklarının piroliz yoluyla biyoyakıt üretiminde kullanılması, küresel ısınmayla mücadelede umut verici bir yaklaşım olarak ortaya çıkmıştır. Bu süreç, biyo-kömür, biyo-yag ve biyo-gaz gibi ürünlerin basit ve maliyet açısından etkin bir yöntemle üretilmesini sağlar. Türkiye'deki biyokütle atıkları arasında, gıda işleme endüstrisinden elde edilen üzüm çekirdekleri, alternatif bir enerji kaynağı olarak önemli bir potansiyele sahiptir. Bu araştırma, 500 ile 800 °C arasındaki sıcaklıklarda azot atmosferinde (inert gaz) gerçekleştirilen üzüm çekirdeği pirolizinden elde edilen biyo-yag ve biyo-kömürlerin özelliklerini incelemektedir. Ayrıca, optimum deney sonuçlarında Purmol CTX ve Clinoptilolit katalizörlerinin ürün verimin ve içeriğine etkisi incelenmiştir. Sonuçlar, daha yüksek piroliz sıcaklıklarının, karbon bakımından yoğun, yüksek ısı değeri ve minimum safsızlık içeren biyo-kömürler ürettiğini ve bunların katı biyo-yakıt olarak kullanıma uygun olduğunu göstermektedir. Aynı zamanda, biyo-yagların fenoller, alkanlar, alkenler, alkil grupları ve asitler gibi bileşikler içerdiği ve bu nedenle sürdürülebilir biyo-yakıt uygulamaları için çevre dostu adaylar olarak değerlendirilebileceği belirtilmektedir.

Anahtar Kelimeler: Piroliz, Üzüm çekirdeği, Biyo-kömür, Biyo-yag.

I. INTRODUCTION

The growing demand for sustainable energy solutions and the escalating environmental challenges have propelled the adoption of renewable energy sources, such as wind, solar, hydropower, and biomass, in both scientific research and industrial applications [1]. Among these options, biomass stands out as a versatile energy source due to its capability to be directly converted into biofuels and its role in reducing waste [2]. Biomass pyrolysis, a thermal decomposition process conducted at high temperatures in an oxygen-free environment, generates valuable products, including bio-char, bio-oil, and bio-gas. Liquid products from pyrolysis, accounting for 30-70% of the total yield, predominantly consist of oxygenated compounds and are typically divided into two fractions based on their water solubility: a dense, viscous tar fraction (water-insoluble) and bio-oil (water-soluble) [3, 4].

The structural composition of biomass, which includes cellulose, hemicellulose, lignin, and small quantities of other organic matter, dictates its pyrolysis behavior. While hemicellulose and cellulose decompose rapidly at lower temperatures, lignin exhibits greater thermal stability, breaking down at higher temperature ranges [5]. Experimental factors, such as pyrolysis temperature, heating rate, and pressure, significantly influence the degradation rates and yields of these components [6].

Pyrolysis, typically conducted in an inert atmosphere of nitrogen or argon, has emerged as one of the most efficient thermo-chemical processes for biofuel production [7, 8]. This process enables the conversion of biomass into a range of high-value products, including solid bio-char, liquid bio-oil, and gaseous biofuels [9]. High heating rates up to temperatures below 650°C, combined with rapid quenching, promote the formation of liquid products while minimizing char and gas production; this process is commonly known as "flash pyrolysis." In contrast, high heating rates to temperatures above 650°C favor the production of gaseous products over liquids. Slow heating rates and low maximum temperatures, on the other hand, maximize char yield [10].

Compared to raw biomass, bio-oil offers higher energy density and ease of transport and storage [11]. It also serves as a precursor for various industrial chemicals, such as food flavorings, specialty chemicals, resins, agricultural inputs, and emission control agents [12]. Comprising a diverse array of organic compounds (such as alkanes, aromatic hydrocarbons, phenols, ketones, esters, and ethers) bio-oil demonstrates versatility, with a molar H/C ratio exceeding 1.5 [13]. However, despite its potential, converting bio-oil into transportation fuels remains economically unviable [12]. Solid bio-char, another pyrolysis by-product, finds applications in the chemical, pharmaceutical, and food industries due to its structural and reactive properties, as well as its low sulfur and phosphorus content [14].

Numerous studies underscore the impact of pyrolysis parameters on the yields and characteristics of these products. Fruit waste, in particular, represents a promising biomass resource for biofuel production. For instance, Raja et al. conducted fluidized bed flash pyrolysis experiments on *Jatropha* oil cake to examine the effects of particle size, pyrolysis temperature, and nitrogen gas flow rate on pyrolysis yields. The highest oil yield, 64.25 wt%, was achieved at a pyrolysis temperature of 500°C, a particle size of 1.0 mm, and a nitrogen gas flow rate of 1.75 m³/h. The resulting pyrolysis oil, identified as a potential biofuel, had a calorific value of 19.66 MJ/kg, which is approximately half the energy content of diesel [15]. Similarly, Xu et al. investigated the fuel properties of pyrolysis products obtained from grape residues, specifically grape skins and a mixture of grape skins and seeds. The study utilized a pilot-scale bubbling fluidized bed pyrolyzer, conducting experiments across a temperature range of 300 °C to 600 °C and varying vapor residence times (2.5, 5, and 20 seconds). The primary objective was to analyze the pyrolysis behavior of these residues, with a focus on product yields and heat requirements. To achieve the most favorable pyrolysis conditions for a sustainable process in terms of energy efficiency, the optimum temperature is 550 °C for grape skins and 450 °C for the mixture of grape skins and seeds [11]. Pütün et al. demonstrated that pyrolyzing olive waste at 400-700 °C could produce petroleum-like products. Experimental studies revealed that pyrolysis temperature and atmosphere significantly influence bio-oil yield and composition. At a pyrolysis temperature of 500 °C with a heating rate of 7 °C/min, the oil yield was 27.26%. Using nitrogen at a flow rate of 100 cm³/min as an

inert gas increased the yield by 19.13%. The highest bio-oil yield, 42.12%, was achieved under a steam atmosphere with a steam velocity of 1.3 cm/s. Bio-oils produced under optimal conditions were fractionated into chemical classes using column chromatography. The oil and its subfractions were then analyzed using techniques such as elemental analysis, Proton nuclear magnetic resonance ($^1\text{H-NMR}$), Fourier-transform infrared spectroscopy (FT-IR), and gas chromatography-mass spectrometry (GC-MS) [16]. French and Czernik evaluated the hydrocarbon production performance of 40 commercial and laboratory-synthesized catalysts through pyrolysis and catalytic cracking. Batch experiments were conducted using three types of biomass feedstocks (cellulose, lignin, and wood) pyrolyzed in quartz boats in direct contact with the catalysts. The process was carried out at temperatures ranging from 400 °C to 600 °C, with catalyst-to-biomass weight ratios of 5:1 to 10:1, to identify the most effective catalysts. The most effective catalysts were from the ZSM-5 group, whereas larger-pore zeolites exhibited lower deoxygenation activity [17]. Kelkar et al. investigated the effects of ten zeolite catalysts on aromatic hydrocarbon production during biomass pyrolysis, using poplar (DN-34) as the feedstock. Analytical pyrolysis with GC/MS revealed that all catalysts, except HZSM-5, produced low levels of aromatics. HZSM-5 was found to be highly effective due to its microporous structure, shape selectivity, and acidity, enabling it to produce aromatics from biomass at moderate temperatures, low pressure, and without the need for molecular hydrogen. Additionally, the silica-to-alumina ratio in HZSM-5 significantly influenced the yield and distribution of aromatic products [18].

In addition to its environmental benefits, biomass pyrolysis also holds significant economic potential. Countries with agriculture-driven economies can greatly benefit from this technology, as large quantities of agricultural residues can be transformed into valuable bio-products. This not only mitigates waste management issues but also opens up revenue-generating opportunities for rural communities. Moreover, the utilization of biomass aligns with global efforts to reduce carbon footprints and transition toward renewable energy systems, further emphasizing its relevance in addressing climate change challenges. This research focused on using grape seeds as a raw material to generate bio-oil and bio-char through the process of pyrolysis. The experiments were carried out under a nitrogen atmosphere at temperatures between 500 and 800 °C. To examine the effects of catalysts on product distribution and composition, catalytic studies were carried out based on the optimal conditions identified during the temperature experiments. The bio-oils and bio-chars were analyzed using various techniques, including GC-MS, FT-IR, and scanning electron microscopy (SEM). Although GC is a widely used technique for detecting volatile substances in organic liquids, it has a limitation of identifying only about 40% of the components in conventional pyrolysis oils. As such, complementary analytical methods were employed for a comprehensive evaluation of the pyrolysis products [19].

This study focused on utilizing grape seeds as a raw material. Grapes are widely consumed, and their seeds are often discarded as waste. Repurposing grape seed waste offers a sustainable solution, both economically and environmentally. Large volumes of grape seed waste generated during wine, fruit juice, and vinegar production can be transformed into valuable products or used for energy production. Grape seeds can be converted into solid, liquid, and gaseous fuels through pyrolysis. This study aimed to enhance the yields and quality of bio-oil and bio-char derived from grape seed pyrolysis through catalytic methods. For the first time, a comparative catalytic pyrolysis experiment was conducted using Purmol CTX and Clinoptilolite, evaluating their effects on product yields and the properties of bio-oils and bio-chars. The availability and low cost of these catalysts provide economic benefits for the pyrolysis process. While the catalysts had a limited impact on product yields, they significantly influenced the composition of bio-oils and the morphology of bio-chars. These findings indicate that the performance of these catalysts could be improved through advanced modification techniques in future research. The products of grape seed pyrolysis have diverse applications. Bio-oil can be used as a liquid fuel in boilers or as a source for alternative chemical production. The gas product, or syngas, can be utilized as renewable energy in heating systems, and bio-char can serve as activated carbon in water treatment or as electrode material in supercapacitors. This study highlights the potential of grape seed pyrolysis as an environmentally friendly and economically viable approach to waste valorization. Finally, this study not only contributes to the existing literature on biomass pyrolysis but also offers practical insights for optimizing product yields and improving their quality. These findings could pave

the way for industrial-scale applications, promoting the use of biomass as a sustainable energy source and advancing global energy transitions.

II. MATERIALS and METHODS

A. RAW MATERIAL

Grape seeds, sourced from a local market in Karabük, were used as the primary biomass material. Prior to the experiments, the seeds were milled to obtain a particle size smaller than 0.45 mm. The determinations of moisture, ash, and volatile matter were performed according to ASTM standards [20, 21, 22]. The fixed carbon content was calculated by difference, as indicated in the table 1. The amounts of holocellulose, α -cellulose, and lignin were determined using the methods employed by Teramoto and colleagues [23]. The properties of this biomass are summarized in Table 1.

Table 1. Properties of grape seed.

Proximate analysis (wt. %)	Moisture	7.62
	Volatile matter	77.51
	Fixed carbon ^a	11.10
	Ash	3.77
Ultimate analysis (wt. %)	C	51.15
	H	7.63
	N	1.75
	O ^b	39.48
	HHV (MJ/kg)	21.13
Component analysis (wt. %)	Extractives	14.14
	α -cellulose	17.93
	Holocellulose	43.89
	Lignin	64.22

^a by difference [100 - (Moisture (%) + Volatile matter (%) + Ash (%))]

^b by difference [100 - (C (%) + H (%) + N (%))]

HHV: Higher heating value

In this study, the components, degradation temperatures, and catalytic effects of grape seeds were examined. TG-DTA analysis was performed by taking a 10 mg sample (scale sensitivity $\pm 0.02\%$) with a nitrogen flow rate of 20 mL/min and a heating rate of 10 °C/min. The TGA spectrum of grape seeds is presented in Figure 1, and the range of 100–250 °C is defined as the region where highly volatile components and moisture are removed, while the region between 250 and 450 °C indicates the degradation of hemicellulose and cellulose. The region after 450 °C, where the mass loss slows down, is indicated as the lignin degradation region. Degradation continues between 450 °C and 800 °C, but at a slow rate. The degradation temperatures of biomass components are quite different from each other and are important for product composition. As a result, the thermal degradation behavior of biomass, which consists of different compounds in varying compositions, also differs. In the thermal analysis of grape seeds, the majority of the degradation occurred below 600 °C. Based on these results, experiments were carried out at 500°C, 600°C, 700°C, and 800°C, with 600°C identified as the optimal temperature.

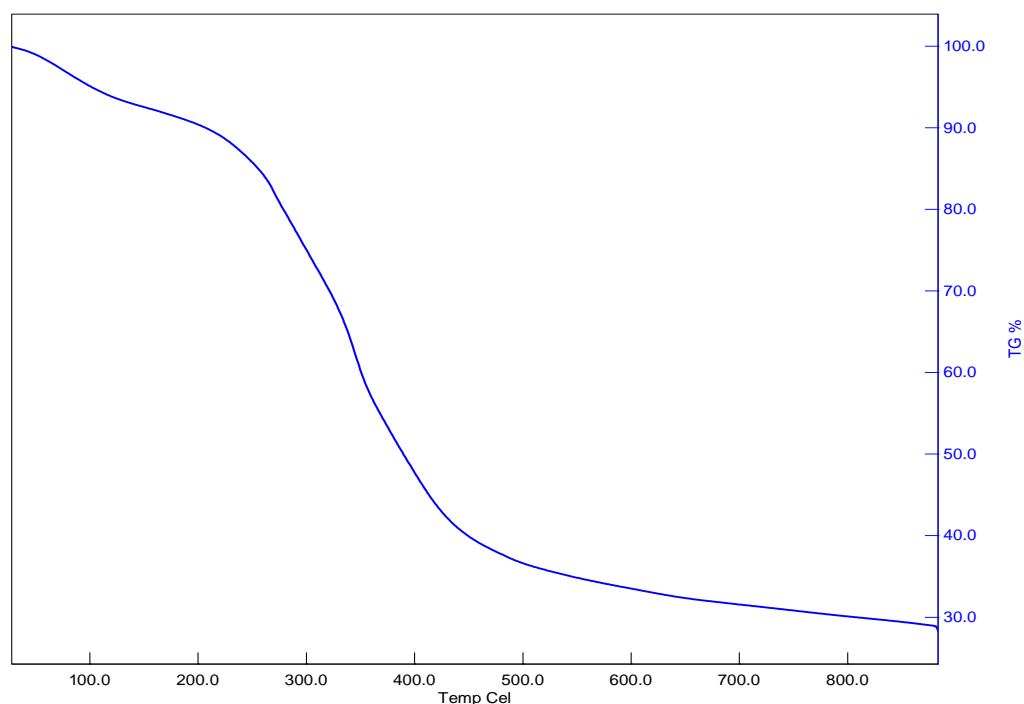


Figure 1. TGA curves of grape seed.

B. CATALYSTS

Two types of catalysts were employed in this study: clinoptilolite, a natural zeolite obtained from Gördes Zeolite Mining (Bayraklı/İzmir), and Purmol CTX, procured from Damlanem Chemistry (Sincan/Ankara). Purmol CTX is a commercially available synthesized catalyst, while clinoptilolite is a naturally occurring zeolite mineral that is widely found in our country. For these reasons, a comparison of the two catalysts was conducted. The chemical compositions of these catalysts, determined using X-ray Fluorescence Spectroscopy (XRF) analysis, are presented in Table 2. The surface morphologies were examined using SEM, with the results presented in Figure 2.

Table 2. XRF results of the catalysts.

Catalyst	Element	Amount (wt. %)
Clinoptilolite	Si	80.93
	Al	6.62
	K	5.51
	Ca	3.50
	Fe	2.32
	Mg	0.66
Purmol CTX	Si	66.01
	Al	22.25
	Na	9.89
	Ca	1.05
	K	0.64

Si (Silicium), Al (Aluminum), K (Potassium), Ca (Calcium), Fe (Iron), Mg (Magnesium), Na (Sodium)

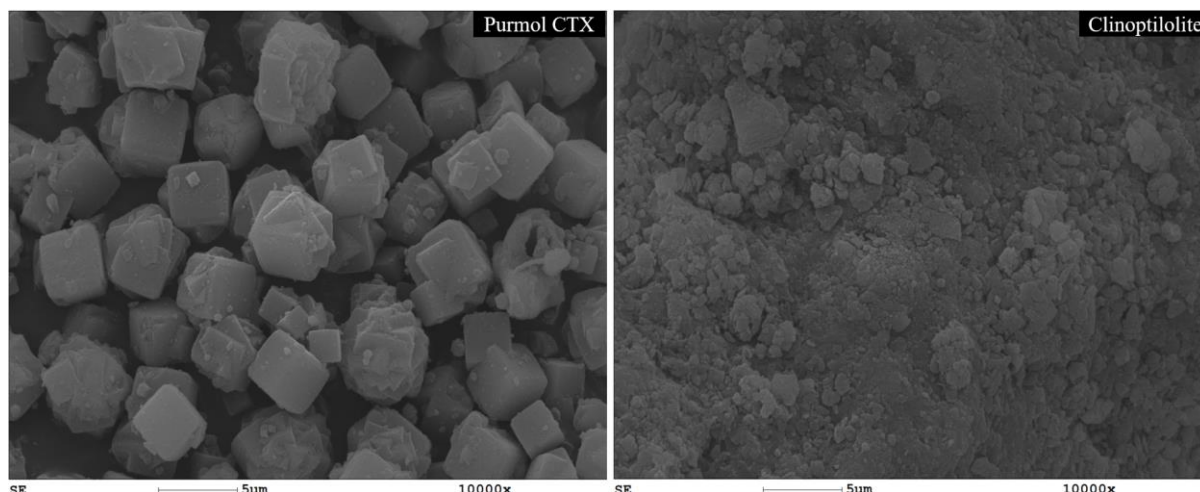


Figure 2. SEM image of the catalysts.

C. EXPERIMENTAL STUDIES

The pyrolysis process was executed using a fixed-bed stainless-steel reactor, which measured 21 cm in height and 6 cm in diameter. Experiments were performed at four distinct temperatures (500, 600, 700, and 800 °C) for a duration of one hour under a nitrogen atmosphere. The experimental setup is illustrated in Figure 3. Approximately 25 grams of dried grape seed waste was loaded into the reactor, which was heated at a controlled rate of 7 °C per minute until reaching the target temperature. Once this temperature was achieved, it was held steady for one hour. The pyrolysis resulted in the production of three distinct product types: solid product (bio-char), liquid product, and gaseous product (bio-gas). The liquid products were collected using three sequential glass condensers: the first two were cooled with a water-ice mixture, while the third was water-cooled. The purpose of this cooling process is to maximize the collection of liquid in the cooling flasks. The liquid product obtained from the pyrolysis of biomass was subjected to liquid-liquid extraction using dichloromethane (DCM) to recover biofuels for analysis and to remove water that might originate from the biomass. The remaining DCM extract after extraction was referred to as bio-oil. The yields of liquid product, bio-char, and DCM extract (bio-oil) were calculated based on mass conservation, with gas yield determined by subtracting the bio-char and liquid yields from 100%.

$$\text{Solid product yield (wt. \%)} = \frac{\text{weight of the solid product (g)}}{\text{weight of raw materials on a dry basis (g)}} \times 100$$

$$\text{Liquid product yield (wt. \%)} = \frac{\text{weight of the liquid product (g)}}{\text{weight of raw materials on a dry basis (g)}} \times 100$$

$$\text{Bio – oil yield (wt. \%)} = \frac{\text{weight of the bio – oil (g)}}{\text{weight of raw materials on a dry basis (g)}} \times 100$$

$$\text{Gas product yield (wt. \%)} = 100 - (\text{liquid product} + \text{solid product})$$

Catalyst-based experiments were conducted at 600 °C, the temperature yielding the highest liquid product output in the thermal experiments. Each catalyst was used at a weight ratio of 20% relative to the 25 grams of dry biomass, with all catalysts meeting analytical-grade purity standards.

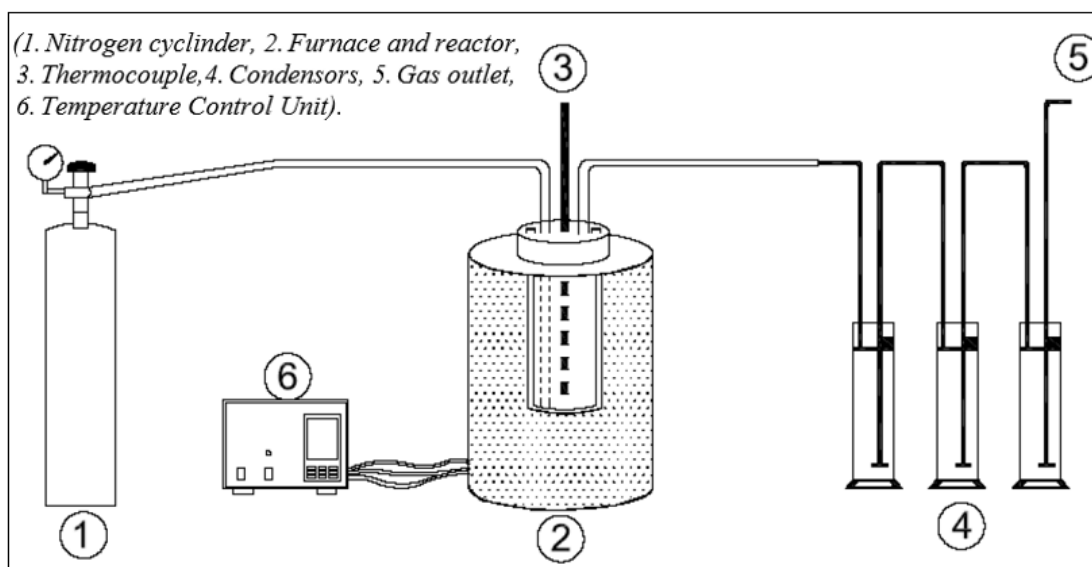


Figure 3. Pyrolysis system schematic [8].

D. ANALYSIS of PYROLYSIS PRODUCTS

The liquid products were extracted using 200 mL of DCM, dried with anhydrous sodium sulfate to remove residual water, and filtered before solvent removal via rotary evaporation. The bio-oil produced from both catalytic and non-catalytic pyrolysis experiments was analyzed by GC-MS. An HP-5MS device, equipped with a 6890 Gas Chromatograph and a phenyl methyl siloxane capillary column, was utilized. Helium, flowing at 1 mL/min, was used as the carrier gas. The injector temperature was held at 250 °C. The GC oven temperature was programmed as follows: initially set to 40 °C and held for 10 minutes, then increased to 170 °C at a rate of 2 °C/min and held for 5 minutes. It was then raised to 250 °C at a rate of 8 °C/min and held for 15 minutes, followed by an increase to 300 °C at a rate of 15 °C/min, where it was held for a final 10 minutes. The GC-MS technique enabled the identification and quantification of volatile organic compounds in the bio-oil, providing crucial information about its chemical composition. The FT-IR (Perkin Elmer FT-IR 100) analysis allowed the determination of key functional groups, helping to characterize the chemical structure of both bio-oils and biochars. The elemental composition of the bio-oil and bio-char was determined using a LECO CHNS 932 analyzer. The higher heating values (HHVs) of biomass, biochars, and bio-oils were calculated using the Dulong formula. SEM (FEI Quanta 450 FEG) was utilized to examine the surface morphology of biochars and raw materials. Additionally, the SEM images provided valuable insight into the structural changes in biochars post-pyrolysis, such as pore formation and surface texture evolution at different pyrolysis temperatures.

III. RESULTS and DISCUSSION

As shown in Figure 4, the distribution of products obtained from the pyrolysis of grape seeds varies with temperature. As the pyrolysis temperature increased, bio-char yields decreased from 37.7% to 28.7% by weight, while gas yields rose from 15.4% to 30.2%. The maximum bio-char yield was observed at 500 °C. Conversely, the highest yields of liquid products (49.1%) and bio-oil (14.8%) were achieved at 600 °C. However, further increases in temperature led to a decline in liquid and bio-oil yields, attributed to the secondary decomposition of volatile components at elevated temperatures [24]. Catalytic experiments were carried out at 600 °C, the optimal temperature determined from non-catalytic pyrolysis. Figure 5 illustrates the effects of Purmol CTX and clinoptilolite catalysts on the products obtained from the pyrolysis of biomass. Both Purmol CTX and clinoptilolite catalysts reduced the yields of liquid products, bio-char, and bio-oil compared to the non-catalytic conditions, while increasing the

gas product yield. Although the catalysts had minimal impact on overall yields, they significantly altered product composition, highlighting the role of catalysis in modifying pyrolysis outputs.

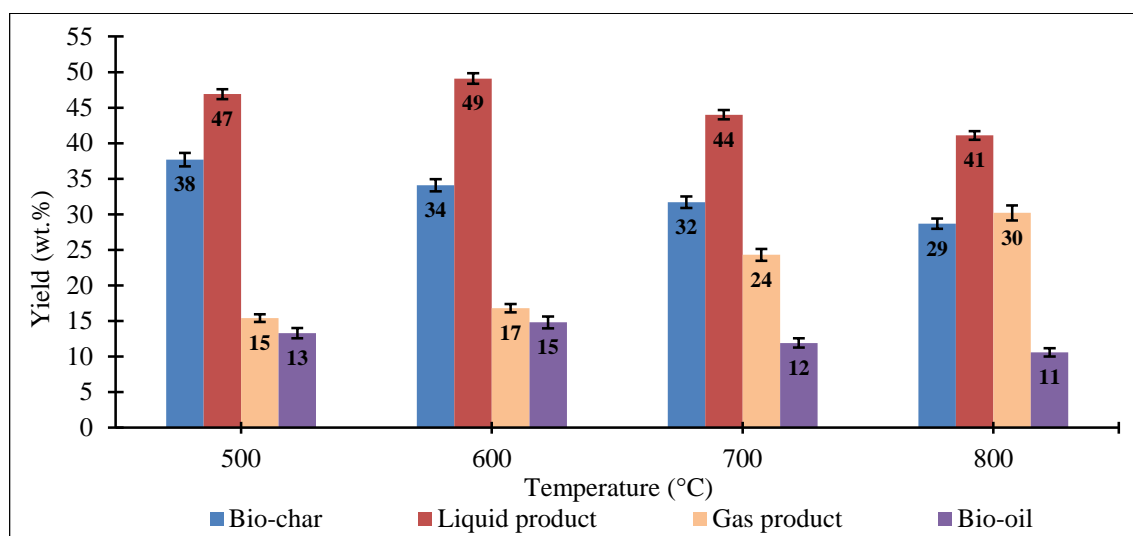


Figure 4. Distribution of products obtained from experiments at different temperatures ($t=60$ min).

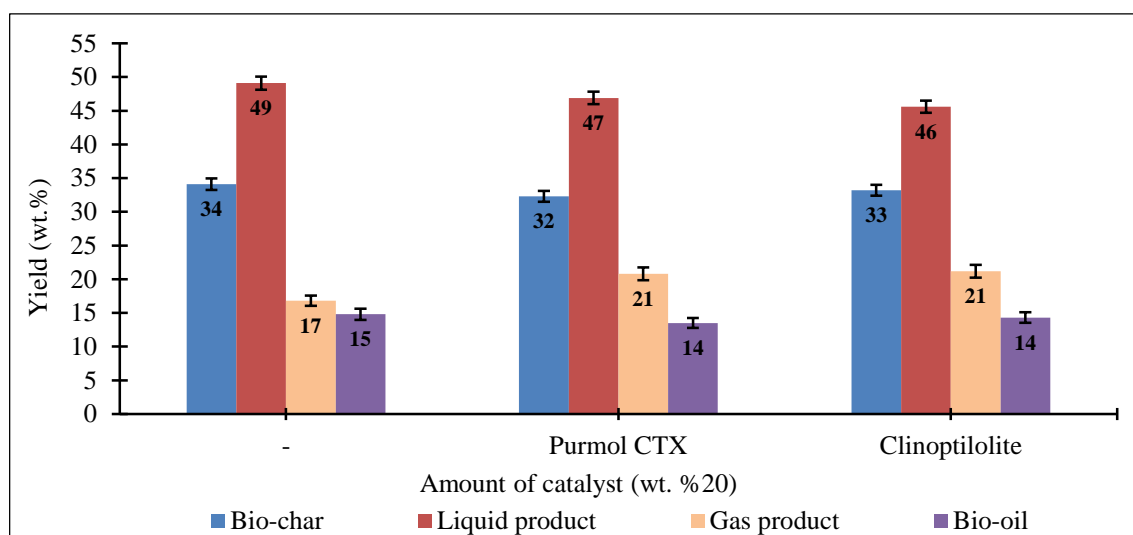


Figure 5. Distribution of products obtained from experiments with and without a catalyst. ($T=600$ °C, $t=60$ min).

The elemental compositions and heating values of the bio-chars and bio-oils derived from grape seed pyrolysis are shown in Tables 3 and 4, respectively. Bio-chars exhibit higher carbon content and lower oxygen content compared to the raw material. The H/C atomic ratios of the biochars decrease as the pyrolysis temperature increases, with the lowest H/C ratio observed at the highest pyrolysis temperature. These results indicate a higher presence of aromatic compounds in the biochars. The heating value is a critical factor affecting the quality of biochars, and it was observed to increase compared to the raw material. Because the oxygen, which is present in high amounts in biomass and causes a decrease in thermal value, has been removed from the structure after the pyrolysis process. The highest higher heating value (HHV) was achieved at 600 °C. Elemental analysis of the liquid products shows that, compared to the raw material, the carbon content and heating value decreased while the oxygen content increased. The increase in oxygen content, as supported by GC-MS results, indicates a rise in acidic products. The highest carbon content and heating value for liquid products were recorded at 700 °C. The increase in the H/C ratio compared to the raw material suggests a reduction in aromatic structures in the liquid products. The percentages of carbon recovered in biochars and bio-oils obtained from the pyrolysis processes were calculated and are shown in Table 5. For non-catalytic experiments, the

percentage of recovered carbon in biochars was higher than in bio-oils. As the temperature increased, the percentage of carbon recovered in biochars decreased. Examining the total recovered carbon, higher values were observed at lower temperatures.

Table 3. The elemental composition of bio-chars ($t=60$ min.)

Temperature (°C)	C	H	N	O ^a	H/C ^b	O/C ^b	N/C ^b	HHV ^c (MJ/kg)
Raw Material	51.15	7.63	1.75	39.48	1.79	0.58	0.029	21.13
500	75.85	4.04	2.89	17.22	0.64	0.17	0.033	28.33
600	79.84	3.00	2.60	14.56	0.45	0.14	0.028	28.67
700	80.67	2.17	2.34	14.82	0.32	0.14	0.025	27.72
800	81.55	1.81	2.14	14.50	0.27	0.13	0.023	27.56

^a by difference

^b atomic ratio

^c Higher heating value (HHV)

Table 4. The elemental composition of bio-oils ($t=60$ min.)

Temperature (°C)	C	H	N	O ^a	H/C ^b	O/C ^b	N/C ^b	HHV ^c (MJ/kg)
Raw Material	51.15	7.63	1.75	39.48	1.79	0.58	0.029	21.13
500	38.18	9.46	1.72	50.64	2.97	0.99	0.039	17.37
600	40.17	7.57	2.02	50.24	2.26	0.94	0.043	15.42
700	47.30	8.74	2.25	41.72	2.22	0.66	0.041	21.02
800	42.13	7.59	2.46	47.83	2.16	0.85	0.050	16.54

^a by difference

^b atomic ratio

^c Higher heating value (HHV)

Table 5. Carbon recovery ($t = 60$ min).

Temperature (°C)	Carbon Recovered in Crude Bio-Oils (wt. %)	Carbon Recovered in Solid Residues (wt. %)	Total Carbon Recovered (wt. %)
500	9.93	55.90	65.83
600	11.62	53.23	64.85
700	11.00	50.00	61.00
800	8.73	45.76	54.49

The functional group analysis of biochars produced from grape seed pyrolysis at various temperatures is presented in Figure 6. The biochars exhibited similar functional groups, which diminished as the pyrolysis temperature increased. At 500 °C, distinct functional groups were identified, including peaks at 2,918 and 2,853 cm^{-1} , corresponding to aliphatic C-H stretching vibrations; peaks at 1,407 and 1,555 cm^{-1} , confirming aromatic C=C stretching vibrations of aromatic rings; and a peak at 1,035 cm^{-1} , indicative of C-H out-of-plane bending vibrations. These peaks were prominent at 500 °C but degraded at higher temperatures (600, 700, and 800 °C). Additionally, prominent aliphatic C-H stretching vibrations at 2,855 and 2,924 cm^{-1} and an aromatic carbonyl C=O peak at 1,743 cm^{-1} , which were evident in the raw material, disappeared in the biochars as the temperature increased, reflecting the breakdown of biomass structures during pyrolysis. In the catalytic experiments shown in Figure 7, the FT-IR spectra of the biochars exhibited a broad, significant peak at 1,000 cm^{-1} , attributed to catalyst residues, which was further validated by SEM-EDS and XRF analyses.

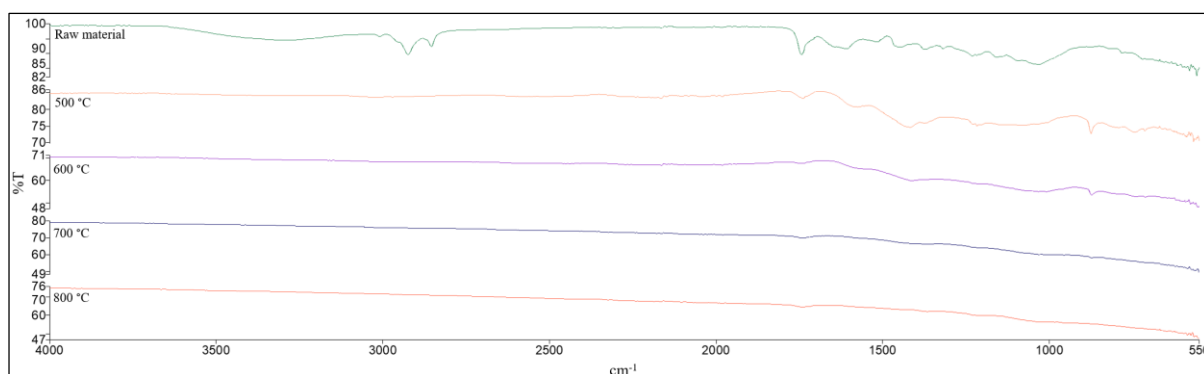


Figure 6. FT-IR results of bio-char at different temperatures (500, 600, 700, and 800 °C).

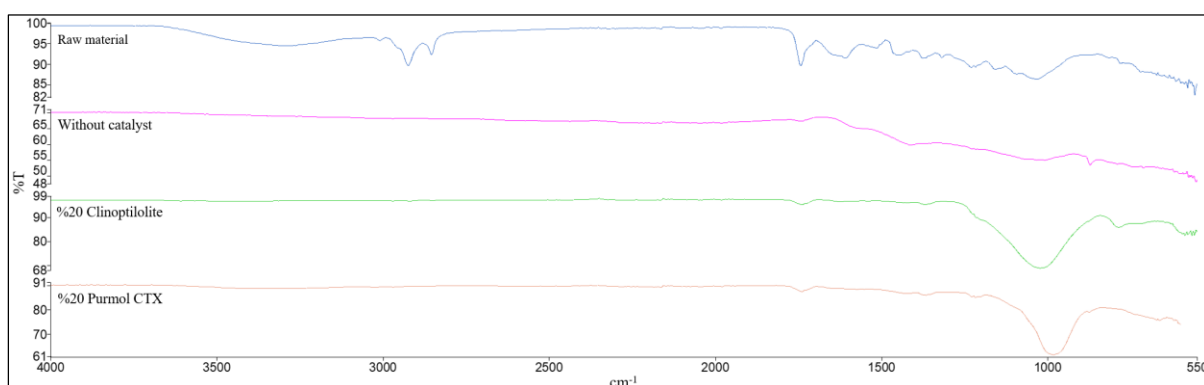


Figure 7. FT-IR results of bio-char at 600 °C with and without a catalyst.

Figure 8 illustrates the FT-IR spectra of bio-oils derived from grape seed pyrolysis alongside spectra of the raw materials. A broad band between 3,200 and 3,600 cm^{-1} indicates the presence of OH groups. Peaks at 2,855 and 2,924 cm^{-1} confirm aliphatic C-H stretching vibrations, while peaks at 1,709 and 1,743 cm^{-1} represent aromatic carbonyl C=O groups. Peaks between 1,100 and 1,200 cm^{-1} correspond to C-O stretching vibrations, and the peak at 1,035 cm^{-1} is indicative of C-H out-of-plane bending vibrations in alkene groups. Peaks between 680 and 900 cm^{-1} are associated with benzene rings. Figure 9 compares FT-IR spectra of bio-oils from catalytic and non-catalytic pyrolysis as well as the raw material, showing similar results across conditions. The analysis of biochar and bio-oil functional groups reveals several critical insights into the pyrolysis process and its optimization. The degradation of functional groups, particularly at elevated temperatures, emphasizes the role of temperature in controlling the product's chemical composition. The disappearance of oxygenated groups, such as C-H and C=O bonds, aligns with the increasing carbon content and stability of biochar, which can be used as a solid fuel or as a carbon sequestration agent.

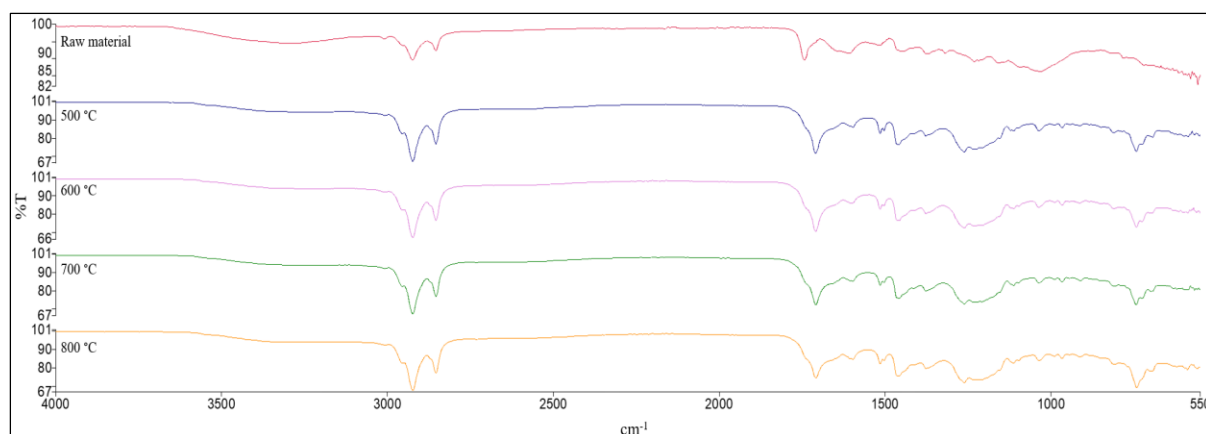


Figure 8. FT-IR results of bio-oil at different temperatures (500, 600, 700, and 800 °C).

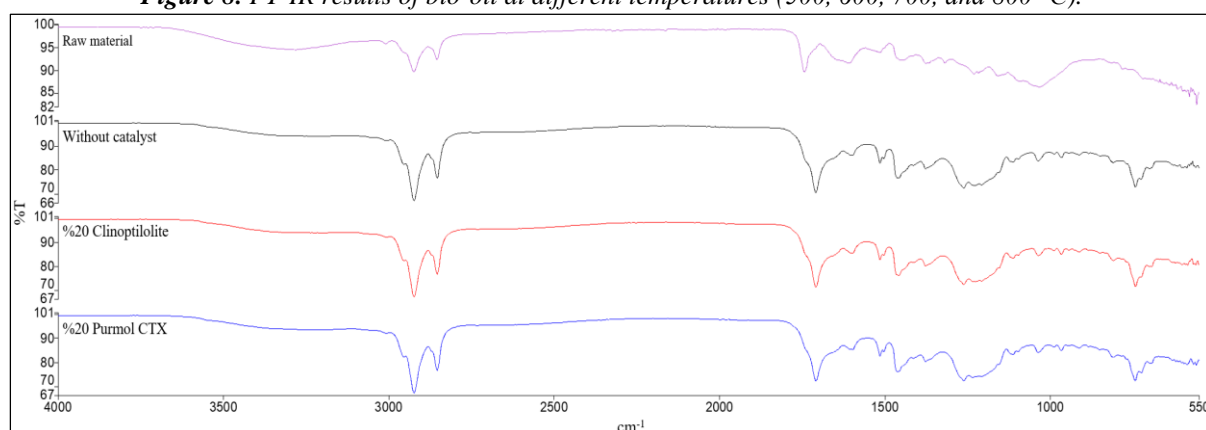


Figure 9. FT-IR results of bio-oils at 600 °C with and without a catalyst.

The SEM images of grape seeds and the biochars obtained from pyrolysis at various temperatures are shown in Figure 10. SEM analysis revealed significant structural changes in biochars following thermal treatment. These images provide valuable insights into pore structure and surface morphology changes during carbonization [25]. From the SEM micrographs, it is evident that the physical properties and surface morphology of the biomass samples change after the pyrolysis process. The raw grape seed samples exhibit a smooth surface morphology with minimal porosity, indicative of their unaltered structure. However, with the onset of pyrolysis, significant changes in surface characteristics are observed, highlighting the impact of thermal decomposition on the material. The surfaces of the biochars change with increasing temperature compared to the raw material. As known, higher volatile matter release results in biochars with lower density, higher porosity, and significantly different pore structures [26]. In the biochars obtained from grape seeds, pore formation is clearly visible at 500 °C due to the volatilization of the components in the biomass. At 600 °C and 700 °C, the pores become smaller. This indicates the progressive transformation of biomass into a more carbon-rich material, accompanied by the compaction of the structure due to the thermal decomposition of lignin, cellulose, and hemicellulose. As the temperature increases, it is thought that the volatile contents of the lignin fractions close the pores. With the temperature rising to 800 °C, a reduction in pores is observed, and carbon spheres replace them. The formation of carbon spheres is attributed to the deposition and rearrangement of carbon-rich residues during the final stages of pyrolysis, suggesting a more graphitic or ordered structure in the biochar matrix. The SEM images of the biochars obtained from the pyrolysis of raw materials in both catalytic and non-catalytic environments at 600 °C are presented in Figure 11. When examining the SEM images, the pores formed in the biochar obtained at 600 °C stand out compared to the raw material. However, it is observed that the pores are closed with the use of both catalysts. This pore-closing effect is primarily due to the interaction between the catalysts and the pyrolysis vapors, which promotes secondary reactions and residue deposition within the pore structure. Moreover, the catalytic environment is likely to facilitate the decomposition of certain biomass components, leading to structural

compaction. According to the elemental composition analysis of the scanning electron microscope (SEM-EDS) shown in Figure 12, the pores are seen to be filled by catalyst residues. This finding underscores the significant role of catalysts in altering not only the chemical composition but also the physical attributes of biochars. The incorporation of catalysts such as Purmol CTX and Clinoptilolite introduces new surface features and potentially enhances the biochar's application-specific properties, such as adsorption capacity or thermal stability.

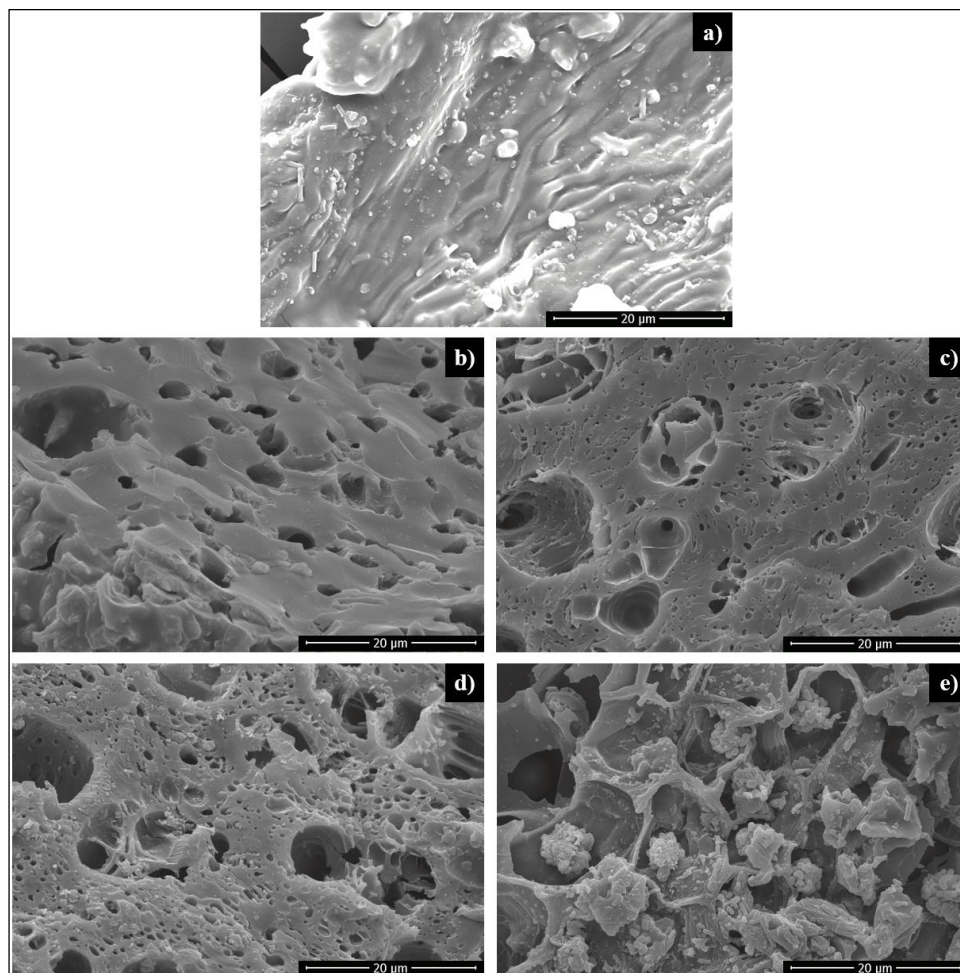


Figure 10. SEM images of raw grape seeds and bio-chars obtained from the pyrolysis of grape seeds at different temperatures ($t = 60$ min)
a) raw material, b) 500 °C, c) 600 °C, d) 700 °C, e) 800 °C

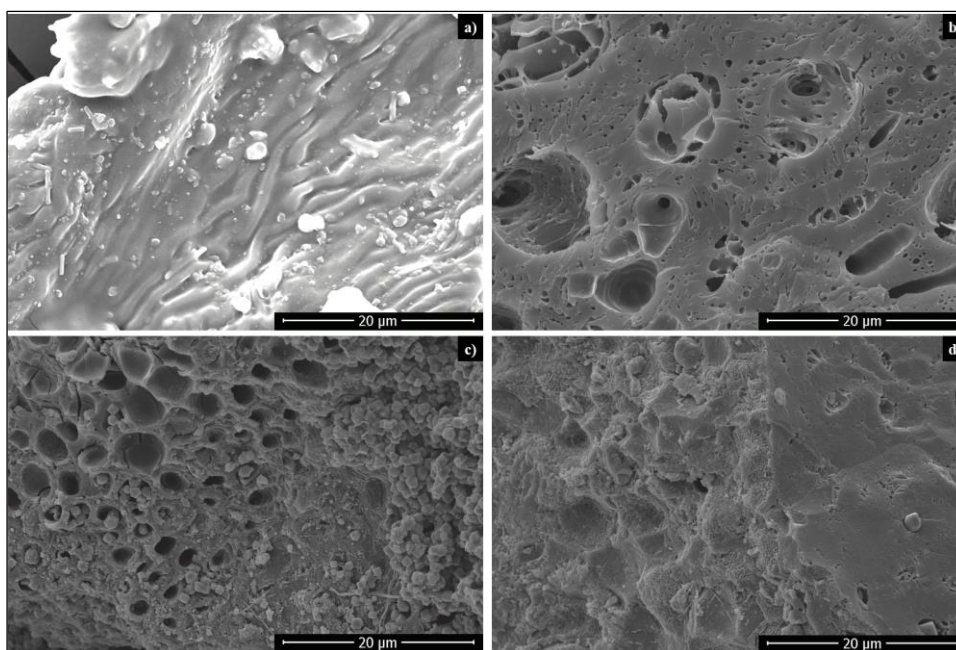


Figure 11. SEM images of raw grape seeds and bio-chars obtained from the pyrolysis process at 600 °C with and without a catalyst ($t = 60$ min).

a) raw material, b) without catalyst, c) wt. %20 Purmol CTX, d) wt. %20 Clinoptilolite

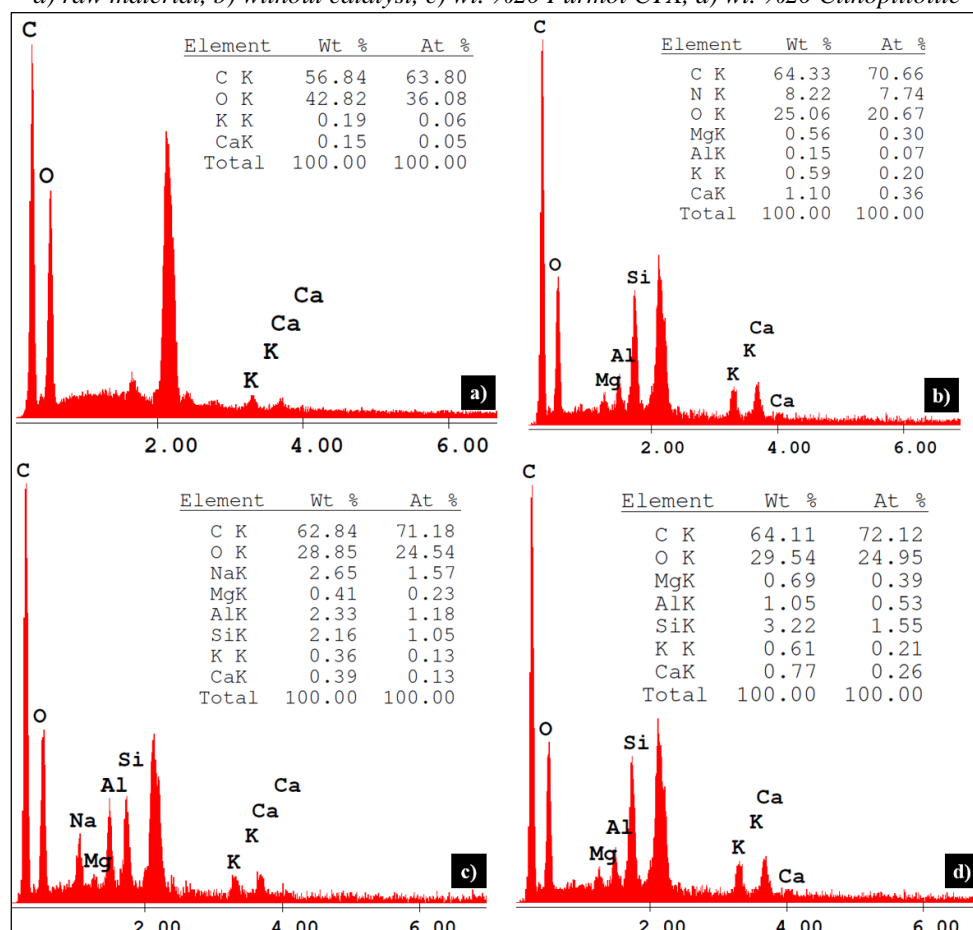


Figure 12. EDS analysis of raw grape seeds and bio-chars obtained from the pyrolysis process at 600 °C with and without a catalyst ($t = 60$ min).

a) raw material, b) without catalyst, c) wt. %20 Purmol CTX, d) wt. %20 Clinoptilolite

The GC-MS analysis of bio-oils derived from grape seed pyrolysis under both catalytic and non-catalytic conditions is summarized in Table 6. The chemical composition of the bio-oils was predominantly characterized by oxygenated compounds, including phenol, 2-methoxyphenol, 4-methylphenol, 2-methoxy-4-methylphenol, 4-ethyl-2-methoxyphenol, and several fatty acids such as n-hexadecanoic acid, (Z,Z)-9,12-octadecadienoic acid, and octadecanoic acid. Catalytic pyrolysis significantly influenced the bio-oil composition, resulting in increased levels of acidic compounds compared to non-catalytic conditions, as depicted in Figure 13. Table 6 provides a detailed breakdown of the chemical compounds identified in the bio-oils under different conditions at 600 °C and a reaction time of 60 minutes. Compounds such as 2-methoxyphenol and 4-methylphenol, known for their applications in chemical industries, were observed in higher proportions in catalytic experiments, particularly when Purmol CTX and clinoptilolite were used as catalysts. Interestingly, the use of Purmol CTX resulted in a higher production of phenols, while clinoptilolite exhibited a relatively balanced effect on a broader range of compounds. Figure 13 categorizes the identified chemical compounds, highlighting their diverse chemical nature. Phenolic compounds, alkenes, aromatic hydrocarbons, and fatty acid derivatives formed the majority of the bio-oil composition. For example, 9-eicosyne, a long-chain alkene, was abundant in non-catalytic conditions but decreased significantly in catalytic pyrolysis. Conversely, fatty acids such as (E)-9-octadecenoic acid increased drastically under catalytic conditions, indicating enhanced breakdown and conversion of biomass-derived intermediates. The differences in chemical compositions between catalytic and non-catalytic pyrolysis underline the pivotal role of catalysts in determining product specificity. Zeolite catalysts play a crucial role in deoxygenation reactions, enabling the conversion of oxygenated compounds found in bio-oil into lighter hydrocarbons [27]. These catalysts facilitate the cracking of heavy organic molecules and support aromatization reactions, transforming aliphatic hydrocarbons into aromatic compounds [28]. Their porous structure and acidic properties are particularly effective in promoting isomerization reactions, where carbon chains are rearranged [29]. Furthermore, zeolite catalysts contribute to carbonization reactions, regulating the carbon structure and aiding in the production of porous bio-char [30]. Phenolic compounds are essential for industrial applications, such as the production of resins and adhesives. The increased presence of phenolic derivatives in catalytic pyrolysis indicates promising opportunities for upgrading bio-oils into value-added products. The substantial presence of fatty acids such as (Z,Z)-9,12-octadecadienoic acid and their methyl esters in both catalytic and non-catalytic conditions indicates the suitability of grape seed pyrolysis for biofuel applications. Catalytic processes, however, enhance the formation of these compounds, making the oil more energy-dense and viable for biofuel production. Hydrocarbons and alkenes, such as long-chain alkenes like 1-hexadecene and 9-eicosyne found under non-catalytic conditions, were partially replaced by shorter chains and aromatic compounds in catalytic environments, indicating a catalyst-driven shift in reaction pathways. Overall, the catalytic experiments demonstrated an ability to fine-tune the bio-oil composition toward specific applications, enhancing the potential for industrial utility. However, the presence of certain nitrogen-containing compounds, such as hexadecanenitrile, highlights the need for further refinement to reduce impurities and improve bio-oil quality. Future studies can explore the influence of different catalyst types and concentrations to further refine the pyrolysis process, enhancing both bio-oil quality and biochar yield. Additionally, a deeper investigation into the mechanisms of catalytic pyrolysis could help optimize the degradation pathways and provide a more comprehensive understanding of how catalysts impact product distribution.

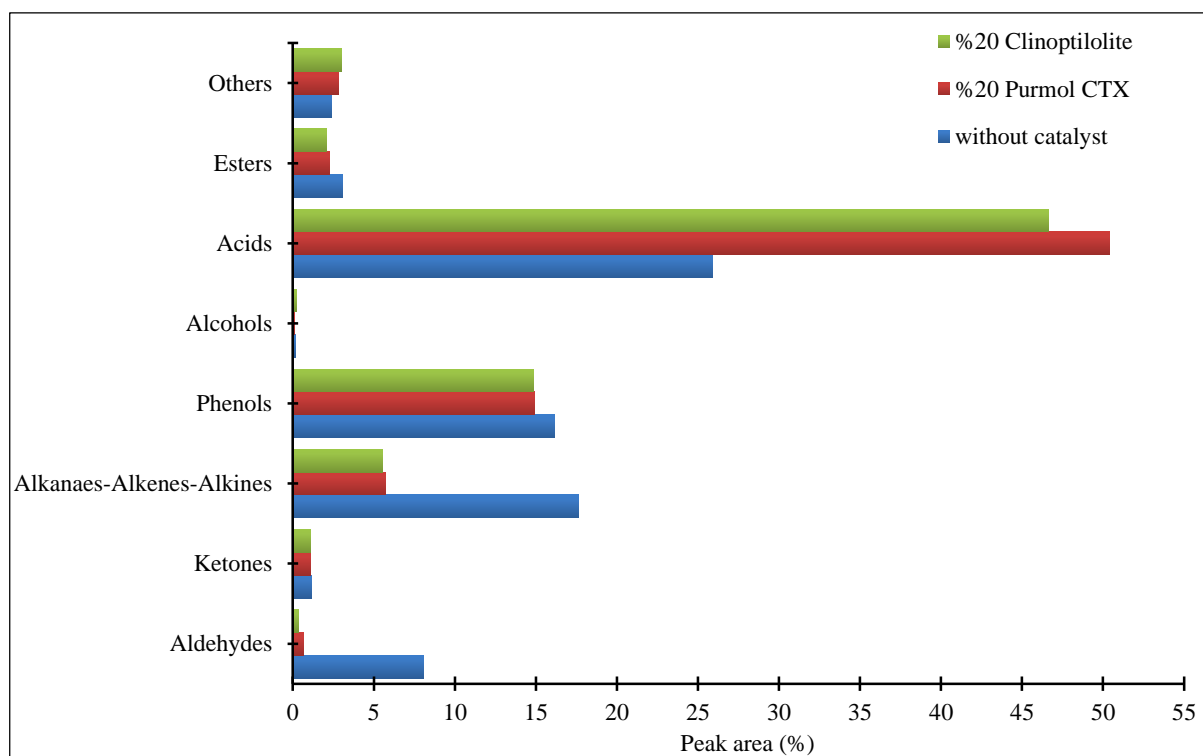


Figure 13. Classification of the chemical compounds identified in the bio-oils obtained from the pyrolysis of grape seeds in non-catalytic and catalytic environments ($T=600\text{ }^{\circ}\text{C}$, $t=60\text{ min}$).

Table 6. Identified chemical compounds in the bio-oils obtained from the pyrolysis of grape seeds in non-catalytic and catalytic environments ($T = 600\text{ }^{\circ}\text{C}$, $t = 60\text{ min}$).

Retention time (min)	Compounds	Peak area (%)		
		-	Purmol CTX (wt. %20)	Clinoptilolite (wt. %20)
3.26	Propanoic acid	0.21	0.10	0.09
4.00	Toluene	0.24	0.19	0.16
8.39	1,3-Dimethylbenzene	0.48	-	-
8.41	1,2-Dimethylbenzene	-	0.37	0.34
9.88	p-Xylene	-	-	0.27
11.20	2-Methyl-2-cyclopenten-1-one	0.24	0.22	0.24
12.01	Butyrolactone	0.22	-	0.20
20.03	1-Decene	0.28	0.28	0.29
21.29	Phenol	1.05	1.36	1.21
24.23	Indene	-	0.42	0.33
25.72	Butylbenzene	0.27	0.25	0.24
27.59	2-Methylphenol	0.55	0.61	0.72
29.21	2-Methoxyphenol	3.90	3.14	3.04
29.37	1-Undecene	0.27	0.27	0.29
29.49	4-Methylphenol	1.01	1.66	1.83
34.24	Pentylbenzene	0.46	0.45	0.47
34.93	2,3-Dimethylphenol	0.60	0.19	0.50
34.94	2,4-Dimethylphenol	-	0.45	-
35.64	Naphthalene	0.36	0.33	0.28
36.13	2-Methoxy-4-methylphenol	2.94	2.36	2.30
36.14	1,4-Dimethoxybenzene	-	0.47	-
36.61	4-Ethylphenol	0.15	0.42	0.47
36.77	3,5-Dimethylphenol	0.48	-	-
36.78	2,3-Dimethylphenol	-	0.62	0.72
38.92	Octanoic Acid	0.32	-	0.08
40.45	1,2-Benzenediol	0.47	0.18	0.46
41.03	3,4-Dimethoxytoluene	0.29	-	0.29
43.52	4-Eethyl-2-methoxyphenol	2.42	2.10	1.89
43.64	2-Methylnaphthalene	0.19	0.25	0.21
44.43	1-Tridecene	0.23	0.24	0.24
44.99	Tridecene	0.23	0.21	0.19
45.83	2-Methoxy-4-vinylphenol	0.25	0.23	0.23
46.39	4-Methyl-1,2-benzenediol	0.17	0.29	0.27
48.74	2-Methoxy-3-(2-propenyl)phenol	0.61	-	-
49.32	2-Methoxy-4-propylphenol	0.72	0.57	0.51
51.00	(E)-2-Tetradecene	0.45	0.50	-

51.02	1-Tetradecene	-	-	0.51
51.51	Tetradecene	0.19	0.23	0.25
54.51	2-Methoxy-4-(1-propenyl)phenol	0.84	0.67	0.64
56.87	1-(4-Hydroxy-3-methoxyphenyl)ethanone	0.41	0.21	0.19
57.14	1-Pentadecene	0.30	0.24	0.25
57.62	Pentadecane	0.56	0.54	0.55
59.52	4-Hydroxy-3-methoxybenzeneacetic acid	0.25	-	0.19
62.45	Cyclohexadecane	0.27	0.32	-
62.95	1-Hexadecene	-	0.25	0.24
67.50	8-Heptadecene	0.63	0.63	0.58
68.83	Tetradecane	0.33	-	-
68.84	Heptadecane	-	0.38	0.39
78.96	Hexadecanenitrile	0.19	0.32	0.34
80.31	Hexadecanoic acid methyl ester	0.60	0.50	0.46
83.79	n-Hexadecanoic acid	9.07	8.48	8.44
88.39	1-Hexadecene	0.27	-	-
88.51	Octadecanal	-	0.51	-
88.65	1-Pentyl-4-(4-propylcyclohexyl)cyclohexene	0.29	-	-
88.67	1,9-Tetradecadiene	-	0.26	0.24
89.01	9,12-Octadecadienoic acid methyl ester	0.36	0.28	-
89.04	8,11-Octadecadienoic acid methyl ester	-	-	0.24
89.28	10-Octadecenoic acid methyl ester	0.61	-	-
89.30	11-Octadecenoic acid methyl ester	-	0.48	0.51
89.47	Octadecanenitrile	0.33	0.25	-
89.49	Heptadecanenitrile	-	-	0.27
89.58	10,13-Octadecadienoic acid methyl ester	0.40	-	-
89.60	(Z)-9,17-Octadecadienal	-	-	0.33
90.30	Octadecanoic acid methyl ester	0.45	0.53	0.50
91.32	(Z,Z)-9,12-Octadecadienoic acid	10.29	6.85	6.33
91.35	9-Eicosyne	12.76	-	-
91.53	(Z)-9,17-Octadecadienal	7.91	-	-
92.02	(E)-9-Octadecenoic acid	-	29.11	25.86
92.33	Octadecanoic acid	5.73	5.73	5.64
92.54	Hexadecanamide	0.64	-	1.20
92.75	Dodecanamide	0.27	1.19	0.23
93.93	3-Dodecyl-2,5-furandione	0.62	-	-
93.98	4-Pentyl-1-(4-propylcyclohexyl)cyclohexene	0.35	0.84	0.60
96.19	(E,E)-9,12-Octadecadienoic acid methyl ester	-	0.29	0.27
96.32	(Z)-9-Octadecenamide	0.53	0.46	0.47
103.49	Tetracosane	-	0.23	0.21
107.88	Stigmastan-3,5-dien	0.50	0.44	0.48

IV. CONCLUSION

Pyrolysis of the biomass sample was conducted at temperatures ranging from 500 to 800 °C, with the outcomes evaluated through catalytic experiments performed under optimal conditions identified in prior thermal studies. The maximum yield of bio-char (37.7%) was obtained at 500°C, while the highest yields of liquid products (49.1%) and bio-oil (14.8%) were achieved at 600°C. Although catalytic studies had a limited effect on the overall yields of bio-oil and bio-char, they significantly influenced the composition of the products. Analysis of elemental composition and heating values revealed that increasing the pyrolysis temperature resulted in higher carbon content and heating values in the bio-chars, alongside a reduction in oxygen content compared to the raw material. The highest higher heating value among the bio-chars, 28.67 MJ/kg, was achieved at 600°C. Among the bio-oils, the highest higher heating value (HHV) of 21.02 MJ/kg was achieved at 700°C. Moreover, the surface structure of the bio-chars exhibited noticeable changes under varying pyrolysis temperatures and catalytic conditions. At higher temperatures, numerous pores of different sizes emerged on the bio-char surfaces derived from grape seeds, while these pores were observed to be filled in the presence of catalysts during catalytic experiments. Additionally, the catalysts significantly altered the morphological structure of the bio-chars compared to the raw material. The influence of the catalysts led to a more homogeneous surface structure in the bio-chars, with noticeable changes in pore sizes and distribution. These modifications enhanced the properties of the bio-chars, making them more suitable for various applications. This research highlights the potential of transforming waste biomass into high-value products, such as bio-oils and bio-chars, underscoring the environmental and economic importance of converting waste biomass into sustainable resources.

V. REFERENCES

- [1] Bensidhom, G., Hassen-Trabelsi, A. B., Alper, K., Sghairoun, M., Zaafouri, K., and Trabelsi, I., "Pyrolysis of Date palm waste in a fixed-bed reactor: Characterization of pyrolytic products," *Bioresource Technology*, vol. 247, pp. 363-369, 2018.
- [2] Bonelli, P. R., Della Rocca, P. A., Cerrella, E. G., and Cukierman, A. L., "Effect of pyrolysis temperature on composition, surface properties and thermal degradation rates of Brazil Nut shells," *Bioresource Technology*, vol. 76, no. 1, pp. 15-22, 2001.
- [3] Czernik, Stefan, and Anthony V. Bridgwater. "Overview of applications of biomass fast pyrolysis oil." *Energy & Fuels*, vol. 18, no. 2, pp. 590-598, 2004.
- [4] Bertero, M., Gorostegui, H. A., Orrabalís, C. J., Guzmán, C. A., Calandri, E. L., and Sedran, U., "Characterization of the liquid products in the pyrolysis of residual chañar and palm fruit biomasses," *Fuel*, vol. 116, pp. 409-414, 2014.
- [5] Bridgwater, A. V., "Principles and practice of biomass fast pyrolysis processes for liquids," *Journal of Analytical and Applied Pyrolysis*, vol. 51, no. 1-2, pp. 3-22., 1999.
- [6] Bridgwater, Anthony V., D. Meier, and D. Radlein., "An overview of fast pyrolysis of biomass," *Organic Geochemistry*, vol. 30, no. 12, pp. 1479-1493, 1999.
- [7] McKendry, Peter., "Energy production from biomass (part 2): conversion technologies," *Bioresource Technology*, vol. 83, no. 1, pp. 47-54, 2002.
- [8] Alper, Koray, Kubilay Tekin, and Selhan Karagöz, "Pyrolysis of agricultural residues for bio-oil production," *Clean Technologies and Environmental Policy*, vol. 17, pp. 211-223, 2015.
- [9] Demiral, İlknur, and Emine Aslı Ayan, "Pyrolysis of grape bagasse: effect of pyrolysis conditions on the product yields and characterization of the liquid product," *Bioresource Technology*, vol. 102, no. 4, pp. 3946-3951, 2011.
- [10] Horne, Patrick A., and Paul T. Williams, "Influence of temperature on the products from the flash pyrolysis of biomass," *Fuel*, vol.75, no. 9, pp. 1051-1059 (1996).
- [11] Xu, R., Ferrante, L., Briens, C., and Berruti, F., "Flash pyrolysis of grape residues into biofuel in a bubbling fluid bed," *Journal of Analytical and Applied Pyrolysis*, vol. 86, no.1, pp. 58-65, 2009.
- [12] Bridgwater, A. V., and G. V. C. Peacocke., "Fast pyrolysis processes for biomass," *Renewable and Sustainable Energy Reviews*, vol. 4, no. 1, pp. 1-73, 2000.
- [13] Wu, L., Guo, S., Wang, C., and Yang, Z., "Production of alkanes (C7-C29) from different part of poplar tree via direct deoxy-liquefaction," *Bioresource Technology*, vol. 100, no. 6, pp. 2069-2076, 2009.
- [14] Mackay, D. M., and P. V. Roberts. "The influence of pyrolysis conditions on yield and microporosity of lignocellulosic chars." *Carbon*, vol. 20, no. 2, pp. 95-104, 1982.
- [15] Raja, S. A., Kennedy, Z. R., Pillai, B. C., and Lee, C. L. R., "Flash pyrolysis of jatropha oil cake in electrically heated fluidized bed reactor," *Energy*, vol. 35, no. 7, pp. 2819-2823, 2010.

- [16] Pütün, A. E., Uzun, B. B., Apaydin, E., and Pütün, E., "Bio-oil from olive oil industry wastes: Pyrolysis of olive residue under different conditions," *Fuel Processing Technology*, vol. 87, no. 1, pp. 25-32, 2005.
- [17] French, Richard, and Stefan Czernik., "Catalytic pyrolysis of biomass for biofuels production," *Fuel Processing Technology*, vol. 91, no.1, pp. 25-32, 2010.
- [18] Kelkar, S., Saffron, C. M., Andreassi, K., Li, Z., Murkute, A., Miller, D. J., and Kriegel, R. M., "A survey of catalysts for aromatics from fast pyrolysis of biomass," *Applied Catalysis B: Environmental*, vol. 174, pp. 85-95, 2015.
- [19] Scholze, B., and D. Meier., "Characterization of the water-insoluble fraction from pyrolysis oil (pyrolytic lignin). Part I. PY-GC/MS, FTIR, and functional groups," *Journal of Analytical and Applied Pyrolysis*, vol. 60, no. 1, pp. 41-54, 2001.
- [20] *Standard test method for moisture analysis of particulate wood fuels*, ASTM E871-82, 2006.
- [21] *Standard test method for volatile matter in the analysis of particulate wood fuels*, ASTM E872-82, 2006.
- [22] *Standard test method for ash in biomass*, ASTM E1755-01, 2007.
- [23] Teramoto, Y., Tanaka, N., Lee, S. H., and Endo, T., "Pretreatment of eucalyptus wood chips for enzymatic saccharification using combined sulfuric acid-free ethanol cooking and ball milling," *Biotechnology and Bioengineering*, vol.99, no.1, pp. 75-85, 2008.
- [24] Uçar, Suat, and Selhan Karagöz., "The slow pyrolysis of pomegranate seeds: The effect of temperature on the product yields and bio-oil properties," *Journal of Analytical and Applied Pyrolysis*, vol. 84, no. 2, pp. 151-156, 2009.
- [25] Özçimen, Didem, and Ayşegül Ersoy-Meriçboyu., "Characterization of biochar and bio-oil samples obtained from carbonization of various biomass materials," *Renewable Energy*, vol. 35, no.6, pp. 1319-1324, 2010.
- [26] Haykırı-Açma, Hanzade, Ayşegül Ersoy-Meriçboyu, and Sadriye Küçükbayrak., "Effect of mineral matter on the reactivity of lignite chars," *Energy Conversion and Management*, vol. 42, no. 1, pp. 11-20, 2001.
- [27] Sandoval-Rangel, L., Ramírez-Murillo, C. J., Dimas-Rivera, G. L., De La Rosa, J. R., Lucio-Ortiz, C. J., Ahmad, E., and Mendoza, A., "Enhancing the quality of products from slow pyrolysis of an agro-industrial biomass waste with natural mineral additives," *Industrial Crops and Products*, vol. 216, no. 118798, 2024.
- [28] Zheng, Y., Wang, J., Wang, D., and Zheng, Z., "Advanced catalytic upgrading of biomass pyrolysis vapor to bio-aromatics hydrocarbon: A review," *Applications in Energy and Combustion Science*, vol. 10, no. 100061, 2022.
- [29] Schulz, Hans F., and Jens H. Weitkamp., "Zeolite catalysts. Hydrocracking and hydroisomerization of n-dodecane," *Industrial & Engineering Chemistry Product Research and Development*, vol. 11, no. 1, pp. 46-53, 1972.
- [30] Aboul-Enem, A. A., Awadallah, A. E., El-Desouki, D. S., and Aboul-Gheit, N. A., "Catalytic pyrolysis of sugarcane bagasse by zeolite catalyst for the production of multi-walled carbon nanotubes." *Journal of Fuel Chemistry and Technology*, vol. 49, no. 10, pp. 1421-1434, 2021.



Düzce University Journal of Science & Technology

Research Article

Pre-Feasibility Analysis of PV Panel Supported EV Charging Station for Kocaeli University

 Enes Talha TAMGACI ^{a,*},  Murat ÜNLÜ ^a

^a Department of Electrical Engineering, Faculty of Engineering, Kocaeli University, Kocaeli, TURKEY

* Corresponding author's e-mail address: tamgacienestalha@gmail.com

DOI: 10.29130/dubited.1561482

ABSTRACT

The importance of green energy and the reduction of carbon emissions are increasing, the importance of using renewable energy systems is also increasing. Considering the Kocaeli University Green Campus goals, increasing renewable energy production and improving energy efficiency by reducing grid dependency are the main goals. In addition, the increasing use of electric vehicles increases the need for charging stations. Therefore, in this study, a preliminary analysis of the photovoltaic panel-supported electric vehicle charging station planned to be installed in two different parking areas of Kocaeli University Umuttepe Campus was made and a system with a peak power of 605 kW was designed. This system can meet 49% of the campus energy demand and 78% of the charging station's need. As a result, grid dependency and energy costs will be reduced, and long-term financial sustainability will be supported through environmentally friendly energy production. In addition, the project will prevent 345,000 kg (CO₂) of carbon dioxide emissions annually.

Keywords: Photovoltaic systems, Electric vehicle charging stations, Green energy, Parking lot

Kocaeli Üniversitesi için PV Panel Destekli EV Şarj İstasyonunun Ön Fizibilite Analizi

ÖZET

Yeşil enerjinin önemi ve karbon emisyonunun azaltılmasının önemi artarken, yenilenebilir enerji sistemlerinin kullanımının önemi de artmaktadır. Kocaeli Üniversitesi Yeşil Kampüs hedefleri göz önünde bulundurulduğunda, yenilenebilir enerji üretimini artırmak ve şebeke bağımlılığını azaltarak enerji verimliliğini iyileştirmek temel hedeflerdir. Ayrıca, elektrikli araçların artan kullanımı şarj istasyonlarına olan ihtiyacı da artırmaktadır. Bu nedenle, bu çalışmada Kocaeli Üniversitesi Umuttepe Kampüsü'nün iki farklı otopark alanında kurulması planlanan fotovoltaiik panel destekli elektrikli araç şarj istasyonu ön analizi yapılmış ve 605 kW pik güce sahip bir sistem tasarlanmıştır. Bu sistem, kampüsün enerji talebinin %49'unu ve şarj istasyonunun ihtiyacının %78'ini karşılayabilmektedir. Sonuç olarak, şebeke bağımlılığı ve enerji maliyetleri düşürülecek, çevre dostu enerji üretimi yoluyla uzun vadeli finansal sürdürülebilirlik desteklenecektir. Ayrıca, proje yıllık 345.000 kg (CO₂) karbondioksit emisyonunun önüne geçecektir.

Anahtar Kelimeler: Fotovoltaiik sistemler, Elektrikli araç şarj istasyonları, Yeşil Enerji, Otopark

I. INTRODUCTION

Nowadays, environmental awareness and sustainability goals are becoming increasingly prominent on a global scale. In this context, the transport sector is also undergoing a major transformation. Internal combustion engines based on fossil fuels contribute to environmental problems and climate change by emitting harmful emissions into the atmosphere. As a solution to these problems, electric vehicles have emerged as an important alternative. Electric vehicles offer an environmentally friendly transport solution compared to internal combustion engines. Electrical engines produce zero emissions and therefore improve air quality, while contributing to the fight against climate change by reducing the carbon footprint. Furthermore, electric vehicles use energy more efficiently and can be completely carbon neutral when recharged based on renewable energy sources.

PV panels supported electric vehicle charging stations make significant contributions to green energy by increasing the use of renewable energy sources. Unlike fossil fuel-based energy generation, PV panels convert solar energy directly into electrical energy. During this conversion process, no harmful gas emissions occur, so clean energy is produced without harming the environment. The installation of these charging stations reduces energy dependency and increases energy security. It also provides diversity in energy production and increases the sustainability of the energy grid by integrating renewable energy sources. This energy can be stored or sold back to the grid, which provides flexibility in energy management. The integration of photovoltaic (PV) panels into electric vehicle (EV) charging stations has garnered significant attention in recent years, aiming to enhance sustainability and reduce reliance on conventional energy sources. Studies have demonstrated that utilizing renewable energy sources, such as solar power, in EV charging infrastructure can lead to substantial environmental and economic benefits.

In recent years, many studies have been conducted in the literature regarding PV-supported charging stations. In China, the energy sector stands out as the largest carbon emitter and the transportation sector as the fastest growing carbon emitter. In this context, a study proposed a model of a solar-powered electric vehicle charging station in Shenzhen. The model was designed to meet the daily energy demand of 4500 kWh and was shown to be economically feasible. For example, it was determined that this model could reduce carbon dioxide (CO₂), sulfur dioxide and nitrogen oxide emissions by 99.8%, 99.7% and 100%, respectively. In addition, the cost analysis showed that the energy production cost supports the economic sustainability of the system. This study also considered how carbon pricing can encourage investment in renewable energy, and the results showed that the carbon price is more effective when it exceeds \$20 per ton [1].

Another study examined the use of DC microgrids in solar-powered EV charging stations. The system used stationary battery storage, PV panels and grid connection together. The study showed that slow charging modes provide maximum benefit from PV energy during parking long times and reduce charging costs. On the other hand, it was emphasized that fast charging modes are connected to the grid with higher costs. It was stated that this system is an effective solution for the integration of solar energy into EV charging infrastructure [2]. The design of electric vehicle charging stations with grid-connected photovoltaic systems for different cities in Pakistan in 2023 was carried out in accordance with the existing roof area of existing fuel stations, and modeling studies suggested that solar energy utilization could be increased by 72 kWh by installing additional PV systems on the average roof area of existing fuel stations in Lahore and Islamabad [3]. In another study conducted in the same year in Bangladesh, the detailed design of a 300 kWp solar EV charging station for 20 EVs along the Dhaka-Mawa Highway was made with PVsyst 7.2 software, and it is expected that the system will provide a net CO₂ reduction of 6,460.2 tons over its 25-year lifespan [4].

The study conducted in 2024 using ArcGIS10.8.2 analysis program is based on technical, economic and environmental data. It has been revealed that 90.55% of the energy required for charging stations in Mahshahr District in this province can be provided by solar energy. The study also showed that this

area has the capacity to convert 11% of vehicles to electric cars by 2040, reducing CO₂ emissions by more than 30 tons [5]. In a study conducted in Antalya, EV charging infrastructure was modeled and optimized using photovoltaic (PV) panels and a grid-connected hybrid power system (HPS). Different scenarios were evaluated in terms of technical, economic and environmental criteria using HOMER software. Considering Antalya's high solar radiation levels (average daily 4.5 kWh/m²), matching the right PV capacity with load profiles increased energy efficiency and reduced grid dependency [6]. Location selection for a PV system-supported charging station is a critical issue. In a study conducted in Iran in 2022, a solar vehicle charging station planned to be built on Kish Island in Iran was selected with GIS and multivariate parameters. When selecting the station, criteria such as proximity to parks, restaurants, public areas with urban density, proximity to main arteries and intersections, proximity to public transportation, proximity to airports and bridges, accessibility, etc. were examined and the final decision was made in the location selection [7].

It was carried by a solar PV system for implementation in a parking area at the University of Nottingham, United Kingdom in 2023. A stochastic approach was used to calculate the charging demand of EVs. Furthermore, the study presents six different charging station scenarios to determine the best combination of 3kW and 7kW capacity chargers. This study conducted a preliminary investigation of future charging stations to be installed in campus parking areas to evaluate the best combination of charging capacity and charging rate, solar potential and economic viability of the installation. This study revealed that the system could save up to 36.8 kgCO₂-e per day, thus providing great support to the zero carbon targets [8]. In 2024, a storage system was implemented in an electric vehicle charging station integrated with a PV system. To verify the electric vehicle charging station power management scheme with MATLAB and Opal RT simulation, different operating conditions were considered according to the photovoltaic panel power and load. The results under different conditions were compared and examined [9]. In 2024, a city-scale energy matching optimization was carried out with smart electric vehicle charging and V2G (vehicle to grid) in a net zero energy city powered by wind and solar energy [10].

A study conducted at Kahramanmaraş Sütçü İmam University in Turkey designed a smart hybrid charging station for electric vehicles, incorporating PV modules, an intelligent inverter, and a storage unit. The system prioritizes energy from PV modules, supplemented by the storage unit, and resorts to the grid only when both sources are insufficient. This approach ensures efficient energy utilization and minimizes dependency on the grid [11]. Similarly, research from Trakya University explored a multi-objective optimal energy management strategy for a charging parking lot that includes electric vehicles equipped with onboard PV panels. The study emphasizes that such integrated systems can significantly contribute to reducing the transportation sector's reliance on fossil fuels, thereby promoting environmental sustainability [12]. Furthermore, the implementation of PV-battery hybrid systems in EV parking lots has been investigated to optimize charging management. These systems not only provide a sustainable energy source for EVs but also enhance the efficiency of energy utilization within the parking infrastructure [13].

In addition to environmental benefits, the deployment of PV-supported EV charging stations addresses challenges related to grid capacity and energy demand management. By integrating renewable energy sources, these systems can alleviate the strain on electrical grids, especially during peak charging times, and contribute to a more balanced and efficient energy distribution [14]. In a study conducted in 2024, the number of panels and inverters required for an imaginary solar energy system with an installed power of 500 kW for the Umuttepe campus of Kocaeli University was calculated. In this study, the optimum panel angle values were calculated and the albedo effect was examined. The values obtained in the PVsyst and MATLAB/Simulink simulation environments were compared. In this study, an analysis focused only on production, not on meeting the university's consumption [15].

This literature underscores the potential of PV panel-supported EV charging stations in promoting sustainable transportation solutions. By leveraging renewable energy sources, such systems can reduce greenhouse gas emissions, decrease reliance on fossil fuels, and contribute to the development of smart and sustainable urban infrastructures.

Reducing carbon dioxide emissions plays a critical role in the fight against climate change. Electrical engines emit much less CO₂ compared to internal combustion engines. However, this advantage depends on the source of electricity from which the vehicles are charged. If electricity is derived from fossil fuels, the environmental benefits are limited. PV panel-supported charging stations solve this problem. Solar energy allows vehicles to be charged without emitting CO₂. This greatly reduces the overall carbon footprint. Charging an electric vehicle with energy produced by PV panels could help avoid tons of CO₂ emissions compared to traditional energy sources. In the long term, PV panel-supported charging stations play a key role in helping cities and countries achieve their sustainable energy goals. Consisting of energy infrastructure from renewable resources contributes to the reduction of greenhouse gas emissions and improvement of air quality by reducing fossil fuels. Additionally, these projects encourage the development of innovative technologies and create jobs in the green energy sector.

In this article, a preliminary study of a Solar Carpark Project was conducted to be a pioneer in the Green Campus at Kocaeli University and to increase the incentive for green energy. In this project, a system with a total of 605 kW solar panels and 15 electric vehicle charging stations was designed in 2 regions of the campus. This system aims to allow university staff and students to charge their vehicles and at the same time reduce the grid demand of other loads in the university (faculties, gyms, cafeteria).

II. SAMPLE PROJECTS AROUND THE WORLD

Solar car parks are an innovative application that integrates sustainable energy solutions and environmentally friendly infrastructures. These car parks provide the necessary space for parking vehicles, while generating clean and renewable energy thanks to the solar panels on them. The use of solar energy reduces dependence on fossil fuels, significantly reducing the carbon footprint and minimizing negative impacts on the environment. By increasing energy efficiency, these car parks optimize energy consumption in cities and provide significant savings in energy costs.

One of the biggest advantages of car parks with solar panels is that they encourage the use of sustainable energy sources. Solar energy is an unlimited and clean energy source as it is obtained directly from the sun. In this way, it contributes to reducing carbon dioxide emissions in the atmosphere and improving air quality. In addition, as the installation costs of solar panels decrease over time, the cost of the energy produced is gradually decreasing. This offers great advantages both economically and environmentally.

Car parks with solar panels are not only limited to energy production; they also contribute to the green energy infrastructure of cities. By providing a shaded area for vehicles, it prevents overheating in summer and reduces the internal temperature of parked vehicles. This saves energy by reducing the use of air conditioning. In addition, these car parks also provide a suitable environment for charging electric vehicles, thus helping to spread electric vehicles and further reduce dependence on fossil fuels. Solar car parks are an important part of sustainable urban development and strategies to combat climate change. By increasing the use of green energy, they contribute to the energy independence of cities and enable the creation of a more sustainable, livable environment. Therefore, car parks with solar panel charging stations play a critical role in the cities of the future.

Solar car parking projects in different areas of the world demonstrate how this innovative system can be successfully implemented in various climatic and geographical conditions. Let's now take a closer look at the impacts and benefits of solar car parks on a global scale by examining some of the examples where this technology has been successfully implemented.

A. RUTGERS UNIVERSITY – NEW JERSEY, USA

Solar panels installed on a 32-acre car park area at Rutgers University in New Jersey generate about 10 MW of electricity annually. The project prevents the emission of approximately 10,000 tons of CO₂ per year. This amount provides an environmental benefit equivalent to removing more than 2,000 vehicles from traffic [16].

The car park with solar panels is also equipped with electric vehicle charging stations. This situation encourages the use of electric vehicles by the university community and promotes the use of green energy on campus. Electric vehicle owners can easily charge their vehicles within the campus thanks to these charging stations. Rutgers University's solar car park provides not only environmental, but also economic and educational benefits. Significant savings in energy costs are realized, while the data and experience gained from this project provide students and researchers with practical knowledge of renewable energy technologies. In this way, the university provides students with direct opportunities in sustainability and renewable energy. Rutgers University's solar car park is a successful example of innovative energy solutions and sustainable practices. The university's project not only improves energy efficiency on campus, but also raises awareness of environmental responsibility.



Figure 1. Rutgers University Solar Parking Lot - New Jersey, USA [17]

B. PAIRI DAIZA ZOO CAR PARK – BRUGLETTE, BELGIUM

Pairi Daiza is a world-renowned zoo and botanical garden located in Bruglette, Belgium. Pairi Daiza, which attaches significant importance to sustainability and environmental protection issues, has implemented its solar panel car park in line with this mission.

The solar car park at Pairi Daiza has a large area that generates a large amount of renewable energy while providing shade for visitors. The car park is equipped with a total of 62,750 solar panels and can generate approximately 20 MWh of electricity annually. This energy produced both meets the zoo's own energy needs and the surplus is fed into the grid, increasing the use of environmentally friendly energy sources [18].

This solar car park is not only limited to energy generation, but also offers electric vehicle charging stations, allowing visitors to charge their electric vehicles. This encourages the use of electric vehicles and contributes to the reduction of carbon emissions.



Figure 2. Pairi Daiza Solar Parking Lot – Bruglette, Belgium [18]

C. COPENHAGEN AIRPORT – COPENHAGEN, DENMARK

Copenhagen Airport's solar car park has an annual electricity generation capacity of approximately 1.3 MW with 3000 solar panels. This energy makes a significant contribution to meeting the energy needs of the airport's terminal buildings and other operational areas. Thanks to the clean energy generated by solar panels, the airport's carbon footprint is significantly reduced and dependence on fossil fuels is reduced. The project prevents the emission of approximately 600 tons of CO₂ annually [19].

Copenhagen Airport continues to work on sustainability and environmental protection and plans to implement more renewable energy projects in the future. The airport management aims to increase the use of solar energy and integrate other environmentally friendly technologies in line with the goal of becoming carbon neutral. Copenhagen Airport's solar car park is a successful example of how sustainable energy solutions can be integrated into airport operations. While reducing the airport's environmental impact, the project also makes significant contributions in terms of economic efficiency and raising social awareness.

D. CINCINNATI ZOO – OHIO, USA

The Cincinnati Zoo's solar car park has an annual electricity generation capacity of approximately 1.56 MW. This solar system produces more than 20% of the zoo's energy needs. The system significantly reduces its carbon footprint by avoiding approximately 1,700 tons of CO₂ emissions annually. This is a significant achievement in terms of environmental sustainability and is considered a crucial step towards minimizing the zoo's ecological impact. [20].



Figure 3. Cincinnati Zoo Solar Parking Lot – Ohio, USA [20]

Solar car parks, with their successful applications around the world, demonstrate the importance of sustainable energy use and environmentally friendly infrastructure solutions. Examples such as Pairi Daiza, Cincinnati Zoo, Rutgers University, Copenhagen Airport and many others demonstrate how these innovative systems are effective in reducing carbon footprint while increasing energy efficiency. Car parks with solar panels encourage the use of renewable energy sources, reducing dependence on fossil fuels and lowering energy costs in the long term. It also contributes to the spread of environmentally friendly transportation options by offering additional benefits such as electric vehicle charging stations. Solar-powered parking lots are becoming an indispensable component in the cities and institutions of the future. These projects not only provide environmental and economic advantages, but also increase social awareness and create a model for sustainable cities of the future.

III. PRE-FEASIBILITY ANALYSIS OF PV PANEL SUPPORTED EV CHARGING STATION FOR KOCAELI UNIVERSITY

The solar panel car park project, which has been pre-analyzed for establishment at Kocaeli University, aims to increase the university's energy efficiency and contributes to its sustainability goals. Solar panel parking lots, which have many successful examples worldwide, offer eco-friendly energy solutions by reducing the carbon footprint and promoting the use of renewable energy sources.

The solar panel-supported electric vehicle charging station system is designed to have a total capacity of 605 kW, with 323 kW at the Faculty of Science parking lot and 282 kW at the Faculty of Education parking lot. Additionally, the parking lot will feature charging stations for electric vehicles. These stations are designed to accommodate 10 AC and 5 DC vehicle charging capacities. Students, staff and visitors will be able to easily charge their vehicles on campus by using the charging stations to be provided in the parking area. This once again highlights the university's commitment to offering innovative and sustainable infrastructure solutions.

Kocaeli University's solar panel-supported electric vehicle charging station project will be an essential part of the university's vision of fulfilling its environmental responsibilities and creating a sustainable campus for the future. In addition to meeting the university's energy needs and providing economic benefits, this project will raise social awareness and offer our students practical knowledge about renewable energy technologies. This initiative will play a significant role in helping our university achieve its sustainability goals and lead the way in eco-friendly energy solutions.

A. DETERMINATION OF SYSTEM TYPE AND LOCATION

The system consists of 3 main components. First, there are 550 W PV modules. Inverters, which are used to convert the direct current (DC) generated by the solar panels into alternating current (AC), will play a critical role in the efficient operation of the system. These inverters will ensure that the energy produced is utilized in a manner that meets the campus's electricity needs and is compatible with the grid. The third and final main component is the charging station. A total of 15 charging stations with the capacity to charge vehicles have been added to the system. There is no energy storage unit for storing the energy produced by solar panels. Therefore, when the energy generated is not used in real-time, it will be sold back to the grid.

A.1. Zone 1 – Faculty of Science Parking Lot

In Zone 1, a total of 588 PV modules, each with a capacity of 550 W, have been placed in 4 separate groups over an area of 1500 m², arranged in a 21x7 configuration. A PV system with a total installed power of 323.4 kW is obtained. Each group is installed at a height of 5 meters with a 10-degree tilt. The system's layout is shown in Figure 4. The parking lot layout plan, which has a capacity of 22 vehicles under each of the PV panel groups, a total of 64 vehicles can be parked, and where there are charging stations, is given in Figure 5.



Figure 4. Zone 1 - PV Modules Layout

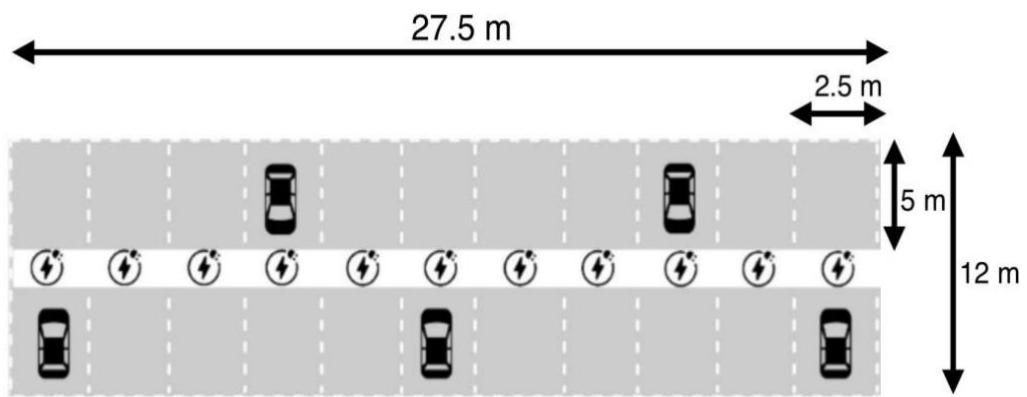


Figure 5. Zone 1 - Parking Lot Layout

A.2. Zone 2 – Faculty of Education Parking Lot

In Zone 2, a total of 512 PV modules, each with a capacity of 550 W, have been installed in 4 separate groups over an area of 1300 m², arranged in a 16x8 configuration. It has an installed power of 281.6 kW. Each group is mounted at a height of 5 meters with a 10-degree tilt. The system's layout is shown in Figure 6.

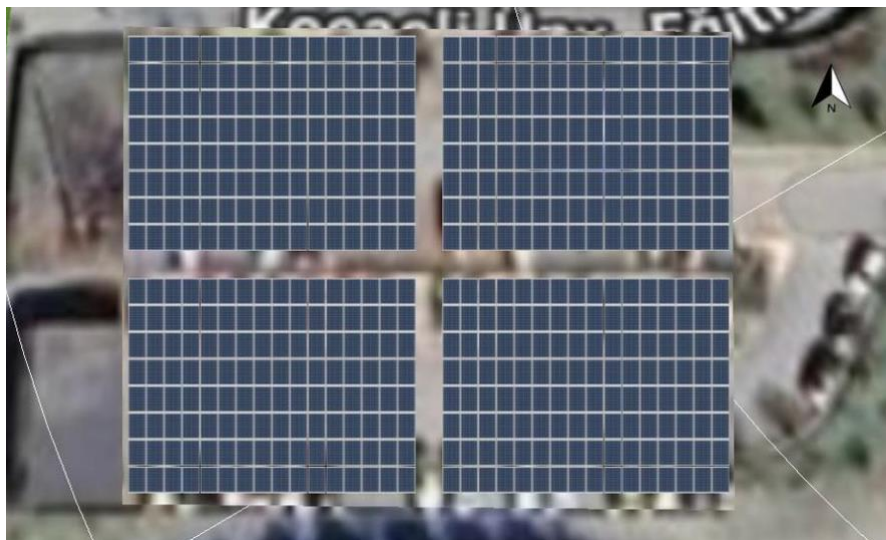


Figure 6. Zone 2 - PV Modules Layout

The parking lot layout plan, which has a capacity of 16 vehicles under each of the PV panel groups, a total of 64 vehicles can be parked, and where there are charging stations, is given in Figure 7.

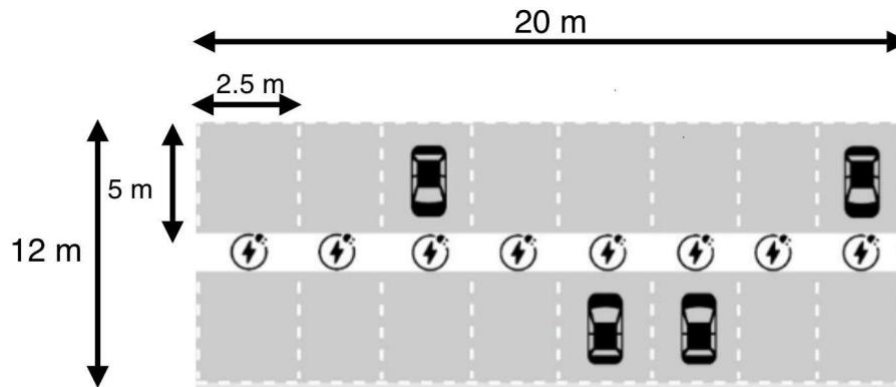


Figure 7. Zone 2 - Parking Lot Layout

The annual sunshine durations for Kocaeli are shown in Figure 8, and the annual total irradiation for the PV systems is shown in Figure 9.

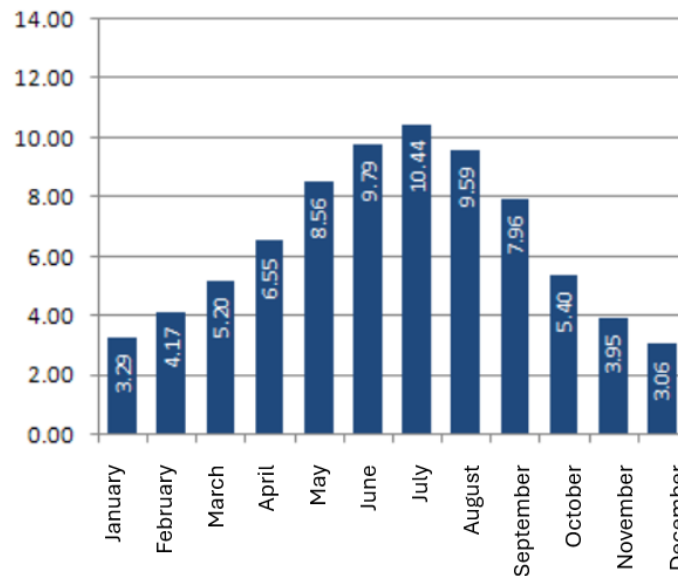


Figure 8. The Annual Sunshine Durations for Kocaeli [21]



Figure 9. The Annual Total Irradiation for The PV Systems

B. DETERMINATION OF GENERAL LOADS AND ELECTRIC VEHICLE CHARGING STATION LOADS

The annual average load consumption of a university with an engineering faculty, swimming pool, sports hall, and lighting units has been determined to be 800,000 kWh [22]. Based on previous studies conducted at Kocaeli University, a portion of the campus's annual consumption of 9,000,000 kWh, specifically 1,000,000 kWh, has been added as the general load to the system. The annual load profile is shown in Figure 10.

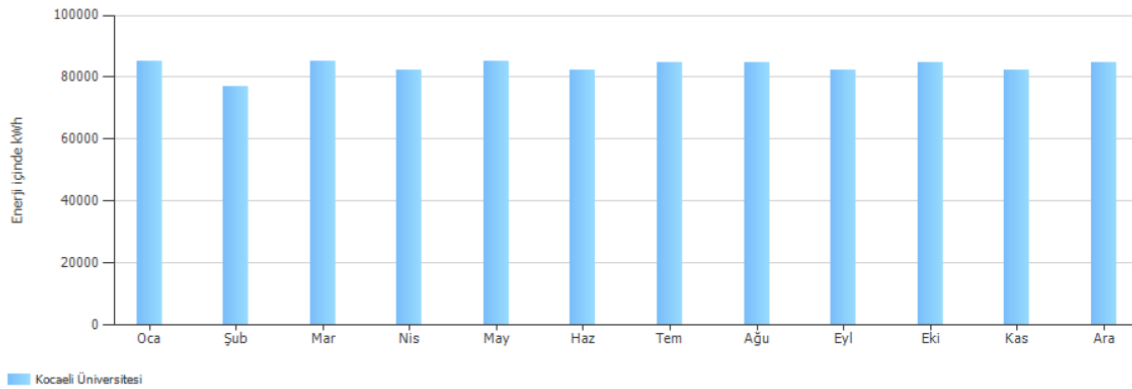


Figure 10. The Annual Load Profile of Kocaeli University

To create the charging station load profile, 10 AC and 5 DC charging vehicles have been selected. These vehicles are assumed to travel an average of 18,250 km per year, with a weekly distance of 350 km. The numbers of vehicles, charging types, charging powers, and consumptions are provided in Table 1.

Table 1. Vehicles to be charged

Vehicle Name	Number of Vehicles	Charging Type	Power	Consumption
Mercedes Benz – Maybach EQS SUV	4	AC Level 2	11 kW	21.1 kWh / 100 km
Honda – e	3	Ac Level 2	6.6 kW	16 kWh / 100 km
Hyundai – Kona	3	AC Level 2	11 kW	9,5 kWh / 100 km
Toyota – Proace Verso L	2	DC CCS	100 kW	28,8 kWh / 100 km
Audi – e-tron	3	DC CCS	120 kW	20,8 kWh / 100 km

C. ENERGY FLOW DIAGRAM AND CONSUMPTION

Based on the annual consumption and charging station consumption values determined above, the energy flow diagram of the system is shown in Figure 11.

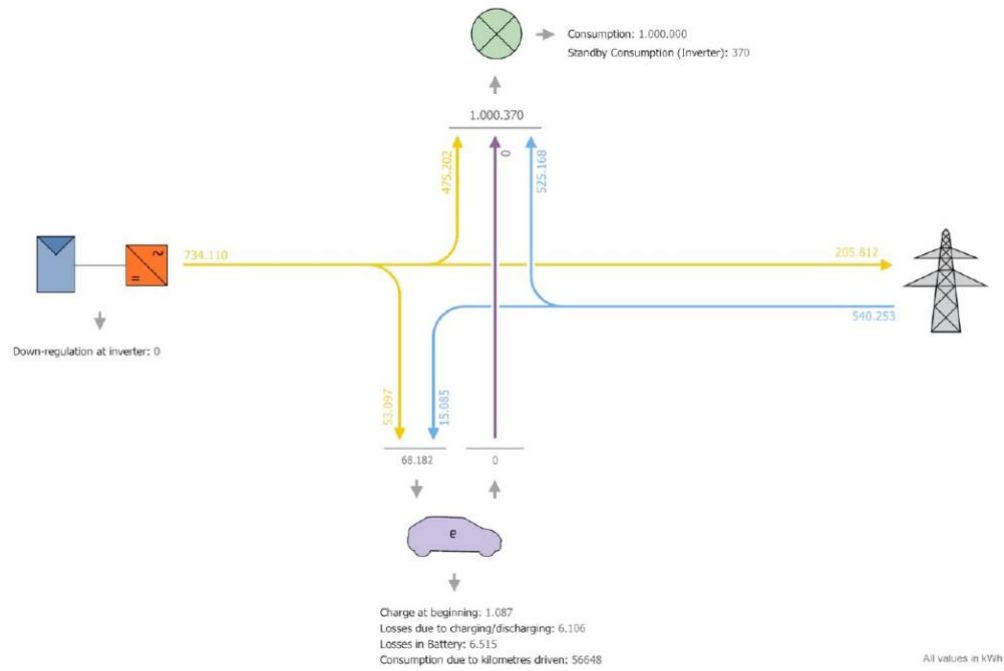


Figure 11. Energy Flow Diagram

The total annual consumption of the electric vehicle charging station is 68,182 kWh. 53,097 kWh of this consumption is met by the PV system. When the 15 charged vehicles travel a total of 273,750 km per year, it is observed that solar energy covers 213,184 km of this distance, which is approximately 78%.

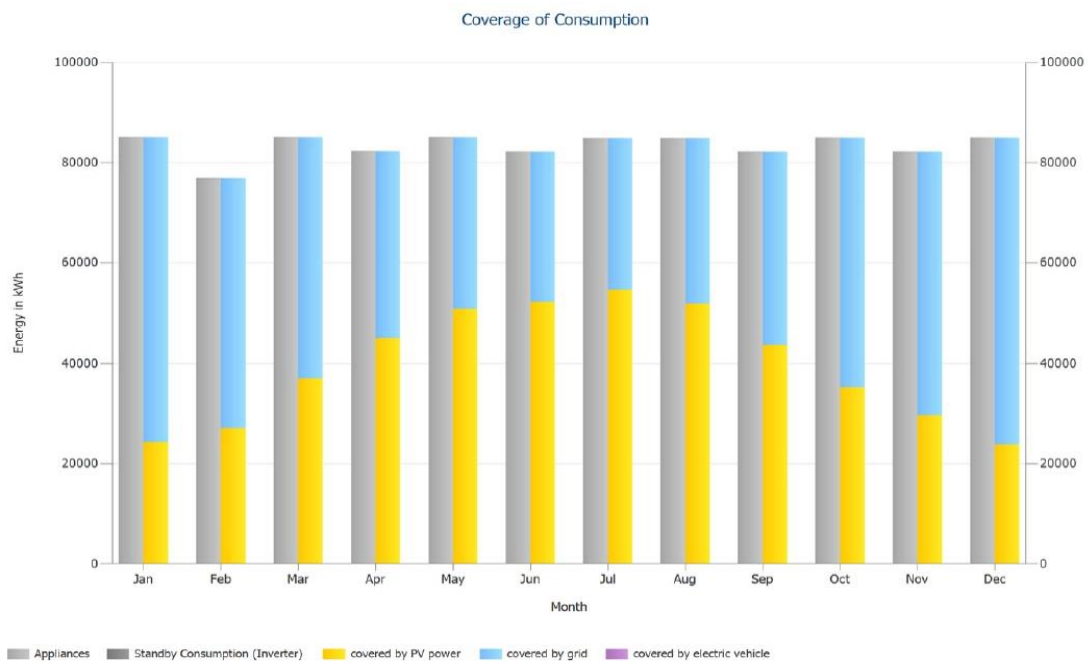


Figure 12. Annual load consumption coverage rates (except charging stations)

The distribution of the annual load of 1,000,000 kWh between the PV system and the grid is shown in Figure 12. The PV system covers 475,000 kWh of it, while the remaining 525,000 kWh is covered by the grid. When including all consumptions in the system, it is observed that the percentage of energy needs met by solar energy is 49.4%. The consumption coverage ratios for all loads are shown in Figure 13.

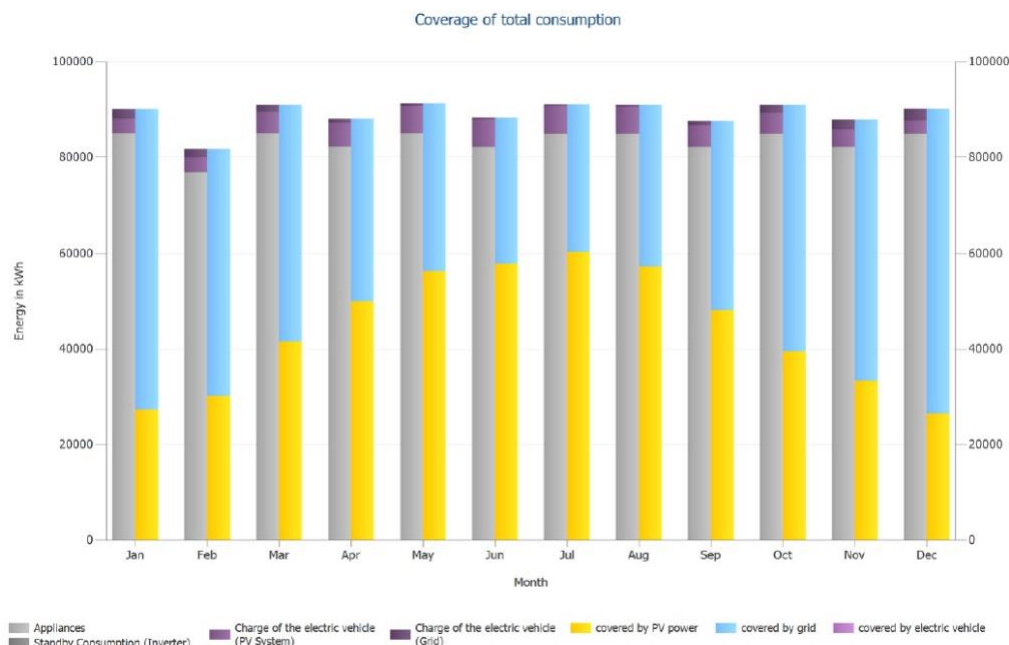


Figure 13. Consumption Coverage Rates for All Loads

IV. RESULTS AND RECOMMENDATIONS

Kocaeli University's sustainability and green energy goals, the planned 605 kW solar panel-supported charging station is designed to enhance the university's energy efficiency, reduce its carbon footprint, and promote eco-friendly transportation solutions. This comprehensive project plays a crucial role in fulfilling the university's environmental responsibilities for the future and leading innovative energy solutions.

The 605-kW solar panel system, which forms the basis of the project, will cover 49% of the electrical needs of a specific part of the campus, thereby reducing dependence on the grid. Moreover, approximately 78% of the charging station consumption of electric vehicles will be covered by the PV system. This system will significantly lower the university's energy costs and support long-term financial sustainability through environmentally friendly energy production. Efficient and continuous use of solar energy will minimize the environmental impact of our campus and promote the use of green energy.

One of the major environmental benefits of the project will be the prevention of 345,000 kg of CO₂ emissions annually. The corresponding consumptions are listed in Table 2.

Table 2. *Consumptions with similar carbon emissions*

Name	Value
Vehicle (Gasoline)	150000 lt
Coal	170000 kg
LPG	200000 lt
Fuel-oil	115000 lt
Natural Gas	170000 m3

Reducing carbon emissions to this extent will be a significant step in fulfilling the university's environmental responsibilities and creating a cleaner, more sustainable campus environment.


Rank ↑↓	University ↑↓	Total Score ↑↓
460	Kocaeli University  Turkiye, Asia	6525

Figure 14. *Kocaeli University UI GreenMetric Ranking [24]*

The solar panel-supported charging station project will not only provide environmental and economic benefits but will also play a crucial role in raising social awareness. Our students and researchers will have the opportunity to gain practical knowledge about renewable energy technologies and enhance their awareness of sustainability. The project will be integrated into the university's sustainability curriculum, offering practical educational opportunities to students and the academic community, thereby contributing to the widespread adoption of renewable energy technologies and environmental consciousness.

UI GreenMetric is an assessment system focused on measuring the environmental sustainability performance of universities. It includes performance metrics in various categories such as energy usage, waste management, water use, transportation, education and research, and environmental planning and management. Universities from around the world apply to this index annually, and their sustainability performances are evaluated to determine their ranking. UI GreenMetric serves as a tool for universities to improve their own sustainability efforts and to promote environmental sustainability overall [23].

Kocaeli University is currently ranked 460th in the world and 41st in Turkey in the UI GreenMetric ranking. Through this project, we can enhance our university's sustainability performance and contribute to our goal of becoming a green university on an international scale.

V. REFERENCES

- [1] B. Ye, J. Jiang, L. Miao, P. Yang, J. Li, B. Shen, “Feasibility Study of a Solar-Powered Electric Vehicle Charging Station Model.” *Energies*, vol. 8, 13265-13283, 2015.
- [2] S. Cheikh-Mohamad, M. Sechilariu, F. Locment, Y. Krim, “PV-Powered Electric Vehicle Charging Stations: Preliminary Requirements and Feasibility Conditions,” *Appl. Sci.*, vol. 11, no. 4, 1770, 2021.
- [3] T.H. Shah, A. Shabbir, A. Waqas, A.K. Janjua, N. Shahzad, H. Pervaiz, H. and S. Shakir, Techno-economic appraisal of electric vehicle charging stations integrated with on-grid photovoltaics on existing fuel stations: A multicity study framework. *Renewable Energy*, 209, 133–144, 2023.
- [4] R. Redwan, M. Hasan, A. Nadia, M.S. Khan, N.A. Chowdhury and N.U.R. Chowdhury, “Design analysis and techno-economic assessment of a photovoltaic-fed electric vehicle charging station at Dhaka-Mawa expressway in Bangladesh,” *Energy Conversion and Management: X*, vol. 24, 100737, 2024.
- [5] M. Razeghi, A.R. Araghi, A. Naseri, and H. Yousefi, Strategic deployment of GIS-optimized solar charging stations for electric vehicles: A multi-criteria decision-making approach, *Energy Convers. Manag. X*, vol. 24, p. 100712, Oct. 2024.
- [6] M. Terkeş and A. Demirci, “Feasibility Analysis of Solar-Powered Electric Vehicle Charging Stations Considering Demand Profiles,” *International Journal of Research and Analytical Reviews*, vol. 10, no. 3, pp. 906-917, 2023.
- [7] M.H. Ghoduseinejad, Y. Noorollahi, R. Zahedi, “Optimal site selection and sizing of solar EV charge stations,” *Journal of Energy Storage*, vol. 56, no. 105904, 2022.
- [8] A. Dik, A. Omer, R. Boukhanouf, “Investigation of cost-effective electric vehicle charging station assisted by photovoltaic solar energy system,” *Transportation Research procedia*, vol. 70, pp. 423-432, 2023.
- [9] D. Gogoi, A. Bharatee, P.K. Ray, “Implementation of battery storage system in a solar PV-based EV charging station,” *Electric Power Systems Research*, vol. 229, 110113, 2024.
- [10] R. Fachrizal, K. Qian, O. Lindberg, M. Shepero, R. Adam, J. Widén, J. Munkhammar, “Urban-scale energy matching optimization with smart EV charging and V2G in a net-zero energy city powered by wind and solar energy,” *eTransportation*, vol. 20, 100314, 2024.
- [11] Öter, A., & Baltacı, F., “Elektrikli Araçlar İçin Akıllı Hibrit Şarj İstasyonu Örneği,” *Bilecik Şeyh Edebali Üniversitesi Fen Bilimleri Dergisi*, vol. 9, no. 1, 160-17, 2022.
- [12] B. Şafak, D. Özekinci and A. Çiçek, “Üzerinde fotovoltaik panele sahip olan elektrikli araçları içeren bir şarj otoparkının çok amaçlı optimum enerji yönetim stratejisi,” *NÖHÜ Müh. Bilim. Derg.*, vol. 13, no. 1, pp. 1–9, 2024.
- [13] A. Çiçek and O. Erdiñç, “PV-Batarya Hibrit Sistemi İçeren Elektrikli Araç Otoparkının Şarj Yönetimi,” *European Journal of Science and Technology*, vol. 15, pp. 466-474, 2019.
- [14] Cira, F., “Evaluation of Grid Assisted Photovoltaic Electric Vehicle Charging Stations,” *Akıllı Şebekeler ve Türkiye Elektrik Şebekesinin Geleceği Sempozyumu*, Ankara, 26-27 April 2013.

- [15] D. Dere, “Şebekeye Bağlı Güneş Enerjisi Sistemlerinin PVsyst ve Simulink’te İncelenmesi,” Düzce Üniversitesi Bilim ve Teknoloji Dergisi, vol. 12, no. 3, pp. 1233-1249, 2024.
- [16] Rutgers University, “Parking Lot Construction Advisory.” ipo.rutgers.edu. Accessed: Sept. 1, 2024. [Online.] Available: <https://ipo.rutgers.edu/news/parking-advisory>
- [17] N.Y. Schenectady. “DSD Partners with Rutgers University to Install 14.5 MW of Parking Lot Solar.” dsdrenewables.com. Accessed: Sept. 1, 2024. [Online.] Available: <https://dsdrenewables.com/dsd-partners-with-rutgers-university-to-install-14-5-mw-of-parking-lot-solar-press-release/>
- [18] Perpetum Smart Energy Solutions. “One of the largest solar carports in the world.” perpetumenergy.com. Accessed: Sept. 2, 2024. [Online.] Available: <https://www.perpetumenergy.com/project-pairi-daiza/>
- [19] Copenhagen Airport. “Copenhagen Airport installs large battery for green energy storage.” www.cph.dk. Accessed: Sept. 3, 2024. [Online.] Available: <https://www.cph.dk/en/about-cph/press/news/2024/03/copenhagen%20airport%20installs%20large%20battery%20for%20green%20energy%20storage>
- [20] Cincinnati Zoo. “What’s the Greenest Zoo in America® Doing to Combat Climate Change?” cincinnatizoo.org. Accessed: Sept. 3, 2024. [Online.] Available: <https://cincinnatizoo.org/conservation/sustainability/>
- [21] Enerji İşleri Genel Müdürlüğü. “Güneş Enerjisi Potansiyel Atlası.” Gepa.enerji.gov.tr. Accessed: Sept. 4, 2024. [Online.] Available: <https://gepa.enerji.gov.tr/>
- [22] İ. Çetinbaş, B. Tamyürek, and M. Demirtaş, “Eskişehir Osmangazi Üniversitesi Kampüsünde Elektrik Tüketim Maliyetinin Azaltılmasına Yönelik FV Üretim ve Enerji Depolama Biriminden Oluşan bir Mikro Şebekenin Optimal Tasarımı”, EMO Bilimsel Dergi, vol. 8, no. 1, pp. 33–38, 2018.
- [23] Kocaeli University. “Üniversitemiz UI GreenMetric’te.” Kocaeli.edu.tr. Accessed: Sept. 5, 2024. [Online.] Available: <https://surdurulebilirlik.kocaeli.edu.tr/haberler/universitemiz-ui-greenmetricte-b28>
- [24] UI Green Metric. “UI GreenMetric World University Rankings 2023.” greenmetric.ui.ac.id. Accessed: Sept. 5, 2024. [Online.] Available: <https://greenmetric.ui.ac.id/rankings/overall-rankings-2023>



Düzce University Journal of Science & Technology

Review Article

An Artificial Intelligence Approach to Evaluating the Sound Absorption Performance of Materials: A Systematic Review

 Oya BABACAN ^{a,*},

^aDepartment of Architecture, Antalya Bilim University, Antalya, Turkey

* Corresponding author's e-mail address: oya.keskin@antalya.edu.tr

DOI: 10.29130/dubited.1544808

ABSTRACT

In recent years, the rapidly increasing use of artificial intelligence has begun to be incorporated into many fields in academia and the market. This study investigates the extent to which artificial intelligence is used in determining the sound absorption performance of materials, which have practical implications in improving indoor acoustic conditions. To this end, studies conducted over the past ten years based on three specified keywords were examined. Various constraints were applied during the review process. First, titles and keywords were scrutinized to filter the studies. Then, research articles were selected, while other studies were eliminated. Secondary keywords used in the studies were identified, and a field assessment was conducted using an analysis program. The results were evaluated by grouping them under different subheadings. The evaluation included the year the studies were conducted, the artificial intelligence methods used, and any additional inferences, if available. In the evaluation section, comments were made on the usability of artificial intelligence in sound-absorbing materials, and the shortcomings in the field were addressed. Suggestions for future studies were also presented. The review study is intended to serve as a guide, particularly for new studies in this field.

Keywords: artificial intelligence, sound absorption, sound absorption material, systematic review

Malzemelerin Ses Yutma Performansının Değerlendirilmesinde Yapay Zeka Yaklaşımı: Sistematiik İnceleme

Öz

Son yıllarda, yapay zekanın hızla artan kullanımı akademi ve piyasa dahil olmak üzere birçok alanda kendine yer bulmaya başlamıştır. Bu çalışma, malzemelerin ses yutma katsayısının belirlenmesinde yapay zeka kullanımının yerini araştırmaktadır. Bu amaçla, belirlenen üç anahtar kelime doğrultusunda son on yılda yapılan çalışmalar incelenmiştir. İnceleme sürecinde çeşitli kısıtlamalar uygulanmıştır. İlk olarak, çalışmaların başlıkları ve anahtar kelimeleri incelenerek bir ön eleme yapılmıştır. Daha sonra, yalnızca araştırma makaleleri seçilmiş ve diğer türdeki çalışmalar elenmiştir. Çalışmalarda kullanılan ikincil anahtar kelimeler belirlenmiş ve bir analiz programı kullanılarak alan değerlendirmesi yapılmıştır. Elde edilen sonuçlar farklı alt başlıklar altında gruplandırılarak değerlendirilmiştir. Değerlendirme, çalışmaların yapıldığı yılları, kullanılan yapay zeka yöntemlerini ve varsa ek çıkarımları içermektedir. Değerlendirme bölümünde, yapay zekanın ses yutucu malzemelerdeki kullanılabilirliği üzerine yorumlar yapılmış ve alandaki eksiklikler tartışılmıştır. Gelecek çalışmalara yönelik öneriler de sunulmuştur. Derleme çalışması, özellikle bu alanda yapılacak yeni araştırmalara yol gösterici olmayı amaçlamaktadır.

Anahtar Kelimeler: yapay zeka, ses yutma, ses yutucu malzeme, sistematiik inceleme

I. INTRODUCTION

Noise is generally defined as unwanted sounds that negatively affect people's daily activities and health. According to the World Health Organization (WHO) [1], noise was initially considered a minor threat to people's physical and psychological health. However, with the evolving and changing environmental conditions, it has become one of the primary disturbances threatening human health today. Daily, people are exposed to different types of noise, indoors and outdoors. In particular, in developed and some developing nations, noise limits are established by regulations and are strictly enforced. Noise can be prevented in various ways, either at the source, along the transmission path, or at the receiver. In enclosed spaces, while multiple methods exist for controlling noise, the most commonly preferred approach, and one frequently encountered in studies, is the improvement of indoor acoustic conditions using finishing materials.

Studies on using materials for sound control can be traced back to ancient times. When examining the ruins of spaces such as theaters in Hellenistic and Roman cities, it is believed that the materials used in the construction and their geometric forms were chosen with an awareness of sound control. Additionally, various studies have shown that animal wool was used in different areas for sound control. With the advent of the Industrial Revolution and the emergence of factory buildings, the need for noise control increased, while technological advancements in materials were also made. However, the concept of "acoustic materials" emerged in the 19th century through various studies. Particularly with changes in building technology, using materials like steel and concrete in larger spaces led to issues with reverberation, increasing the demand for acoustic materials [2]. Over time, the use of plant and animal fibers was followed by Helmholtz resonators, plastic-based foams and materials, and, more recently, the growing popularity of metamaterials. However, with the depletion of natural resources and the increasing emphasis on sustainability, natural materials have again become the focus of research and are being reconsidered under advanced technological conditions. In the future, materials that are smart and capable of self-adaptation to environmental conditions are expected to enter the market.

In enclosed spaces, the surface area of finishing materials, their sound absorption coefficient, the material's placement within the space, and the space's volume are effective parameters in controlling acoustic conditions. In particular, the first intervention for ensuring acoustic comfort in an existing area is the selection of appropriate materials based on their sound absorption performance characteristics.

A portion of the sound waves reaching the material is converted into thermal energy and dampened as they pass through the material. The remaining sound waves either continue through the material to the other surface or are reflected from the material's surface (Figure 1). The sound absorption coefficient (SAC) of a material is defined as the ratio of the energy absorbed by the material to the energy incident on the material, representing the material's sound absorption capacity. The SAC of materials ranges between 0 and 1. The closer the coefficient (α) is to 1, the more absorptive the material is.

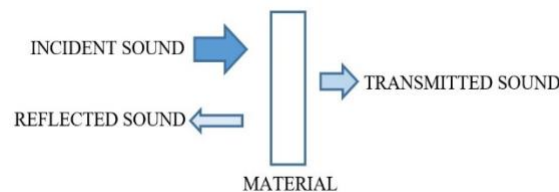


Figure 1. Schematic explanation of the principle of sound absorption.

The impedance tube and reverberation room methods are the most commonly preferred methods used to determine the SAC of materials. The impedance tube measurement method frequently employs international standards such as ISO 10534-2:2023 [3] or ASTM E1050-12 [4]. The basic principle of the impedance tube method involves two microphones, usually one at the source and one at the sample

side, within the tube. Sound waves are transmitted from the source to the sample. Information about the material's sound absorption capacity is obtained by examining the reflected and absorbed energy when the sound waves hit the surface. The reflection coefficient (R), SAC (α), and acoustic impedance (Z) are calculated using the amplitude and phase information of the reflected and incident waves. This method is particularly favored in academic research due to the small sample sizes required. Additionally, measurements can be conducted in a controlled environment and at different frequencies. However, despite these advantages, there are some drawbacks. Since the samples are not in actual size, the results may differ in practical applications. Variations in edge constraints in different impedance tubes can affect measurement results. Furthermore, different frequency ranges are recommended in various standards, which can lead to variations in the results. The physical conditions of the measurement environment also inevitably affect the results. Therefore, while the impedance tube method is a valuable tool for studying the acoustic performance of materials, especially in academic research, the results' accuracy and reliability depend on the equipment's quality and experimental conditions.

Standards such as ISO 354:2003 [5] or ASTM C423-17 [6] are commonly used in the reverberation room method. This method provides more accurate results because the sample sizes are realistic, and sound waves from the source are diffuse, unlike the perpendicular waves used in the impedance tube. The design of the reverberation room is crucial to ensure balanced sound distribution within the space. Hasan and Hodgson found that a 150 m³ room yielded better results than other room sizes [7]. Tang and Chuang indicated that the room size should not be smaller than 150 m³ in reverberation room measurements due to the critical frequency. They also noted that if the room size exceeds 500 m³, the results might be inaccurate due to the absorption of sound by the air [8]. While the reverberation room method may be preferred for its more realistic results, the impedance tube method is more frequently used, particularly in academic studies requiring practical results. Typically, preliminary studies are conducted using the impedance tube, followed by additional tests in a reverberation room during industrial material production. In such studies, an equation can convert SAC from the impedance tube into results from the reverberation room measurements. London proposed equation 1 below to convert direct sound wave absorption coefficient data from the impedance tube into diffuse sound wave data from reverberation room measurements. He conducted numerous experimental studies to derive this formula and stated that it is the most accurate with minimal error. The ASTM C384 – 04 [9] standard also references London's research. This conversion process is crucial for ensuring consistency and comparability of results across different measurement methods.

$$\alpha_e = 4 * \left[\frac{1-(1-\alpha_0)^{\frac{1}{2}}}{1+(1-\alpha_0)^{\frac{1}{2}}} \right] \left\{ \ln 2 - \frac{1}{2} - \ln \left[1 - (1-\alpha_0)^{\frac{1}{2}} \right] - \frac{(1-\alpha_0)^{\frac{1}{2}}}{2} \right\} \quad (1)$$

In equation:

α_e : the SAC for diffuse sound waves (random incidence)

α_0 : the SAC for direct sound waves (normal incidence)

The concept of 'artificial intelligence' (AI), which began to be used in engineering, mathematics, and physics, has expanded to many different disciplines. It was first introduced by John McCarthy in 1956 [10]. McCarthy stated that AI is similar to understanding human intelligence through computers, but AI does not have to be restricted by biological methods [11]. One of the fields where AI has been increasingly utilized, especially in recent times, is materials science engineering. Experiments and density functional theory (DFT) based calculations have been primary methods for learning and understanding materials' chemical and physical properties. Experimental processes are exceptionally costly and time-consuming. Although DFT calculations are more cost-effective, they can lead to significant differences in results due to the experimental setup's physical conditions [12]. With the wealth of data accumulated from experimental work, the trial-and-error method, and subsequent DFT-based research, AI has started to play a role in designing data-driven approaches in materials science. Recently, the use of AI and machine learning to gain deeper insights into materials through increasing experimental and

simulation-based data sets has become common [13]. With the growing popularity of AI research, a new field known as 'materials informatics' has emerged, integrating all three traditional paradigms of materials science: theory, experimentation, and computation/simulation [14]. The key reason for AI's suitability in material design is its ability to handle large data volumes and high-dimensional analyses [15]. A literature review shows that AI usage in materials science engineering spans a broad range, from chemical studies of materials to examining their physical properties.

A review of research on the use of artificial intelligence in architectural acoustics indicates that it has become a popular and widely used technique, particularly in the past decade. Studies have explored AI approaches in various areas, including soundscape design [16; 17; 18; 19; 20], building acoustics [21; 22], noise prediction [23; 24; 25], interior acoustic design [26; 27], and the prediction of acoustic materials' sound insulation and absorption [28; 29; 30]. Numerous examples of research exist in these areas, with only a few references provided here as examples. It is evident from these studies that the use of artificial intelligence in architectural acoustics is an undeniable reality, offering innovative alternatives in the field.

Experimental studies on sound absorption in materials are time-consuming and costly, leading to the suggestion of alternative models such as empirical models proposed by Delany and Bazley (1970), Miki (1990), Mechel (1976), and Garai and Pompoli (2005), and phenomenological models proposed by Allard and Champoux (1992), Kino and Ueno (2008), and Attenborough (1983). Although these models provide accuracy on various parameters, their evaluation is a complex process. Therefore, in the past 20 years, significant attention has been given to studies involving artificial neural networks (ANNs) and fuzzy logic (FL) [31].

The research question of this study is: "How widely is artificial intelligence used in determining the SAC of materials, and can it serve as an alternative method?" In this context, the research methodology involves identifying critical terms in the field and conducting a general literature review on the relevance of these terms. The findings include publication years, researchers' countries, material properties, material parameters beyond SAC, measurement methods, and the compatibility of artificial intelligence algorithms. The evaluation section discusses the findings and the applicability of artificial intelligence.

II. METHODOLOGY

A.1 Literature Search Strategy and Inclusion/Exclusion Criteria

A systematic literature review is a research method designed to answer specific research questions using a systematic and transparent approach, enabling the identification of results from studies included in the research and providing a critical evaluation [32]. In systematic research, since all studies addressing a particular question are examined, an impartial summary of the conducted research is presented [33]. The transparency of this process ensures the integrity of the study.

This study meticulously employed a systematic research method to answer the research questions. The main categories examined and the progression of the research process are presented in Figure 2. The literature searches were conducted with utmost care, and keywords were identified. A comprehensive field search was first carried out to determine the keywords. For this purpose, a preliminary search was conducted on Google Scholar using the keywords "Artificial Intelligence," "Architectural Acoustics," "Sound Absorbing Materials," and "Sound Absorption Coefficient." A total of 26 publications were reviewed, and the research study's keywords were finalized as "Artificial Intelligence," "Sound Absorption," and "Material."

After the keywords were established, the publishers and databases included in the research were carefully selected based on the results from Google Scholar. Accordingly, articles published in ScienceDirect, Taylor and Francis (TandF), MDPI, Springer, and Sage, which are widely recognized for their academic rigor, were included in the scope of the study. In the initial phase, the keyword-based search yielded 1835 publications on TandF, 126 on MDPI, 115 on ScienceDirect, 63 on Springer, and 7 on Sage.

Due to the increasing significance of research involving artificial intelligence in recent years, the study period was set to ten years between 2014 and 2024. Only articles published in English were selected for review. Accordingly, the number of studies identified was updated to 542 in TandF, 126 in MDPI, 96 in ScienceDirect, 63 in Springer, and 7 in Sage.

In this study, which aims to examine the usage rate of artificial intelligence in determining the SAC of materials, search criteria were restricted to include only 'research articles' among the obtained publications. As a result of this limitation, the number of articles identified was 359 in TandF, 56 in ScienceDirect, 20 in Springer, and 6 in Sage. A specific issue was identified with MDPI. A limited number of publications were found when conducting AI-related searches directly on MDPI's site, with other research articles showing keywords like "machine learning" instead. Therefore, the search for MDPI research articles was conducted through Google Scholar. Consequently, MDPI was excluded from subsequent restrictions, and all 126 articles were screened manually.

Following the article type limitation, a subject-specific restriction was applied to ensure that the studies were directly related to the determination of sound absorption coefficients. Given that each publisher's site offered different options, field limitations were applied under the engineering category using "Materials Science," "Computer Science," and "Environmental Science" as the selected fields. After this restriction, 51 articles were identified in ScienceDirect, 46 in TandF, 15 in Springer, and 6 in Sage.

In the final stage, all articles' titles, keywords, and abstracts were reviewed, and those directly related to the topic were selected for further analysis. As a result, 27 articles were examined in this study: 15 from ScienceDirect, 7 from MDPI, 2 from TandF, 2 from Springer, and 1 from Sage.

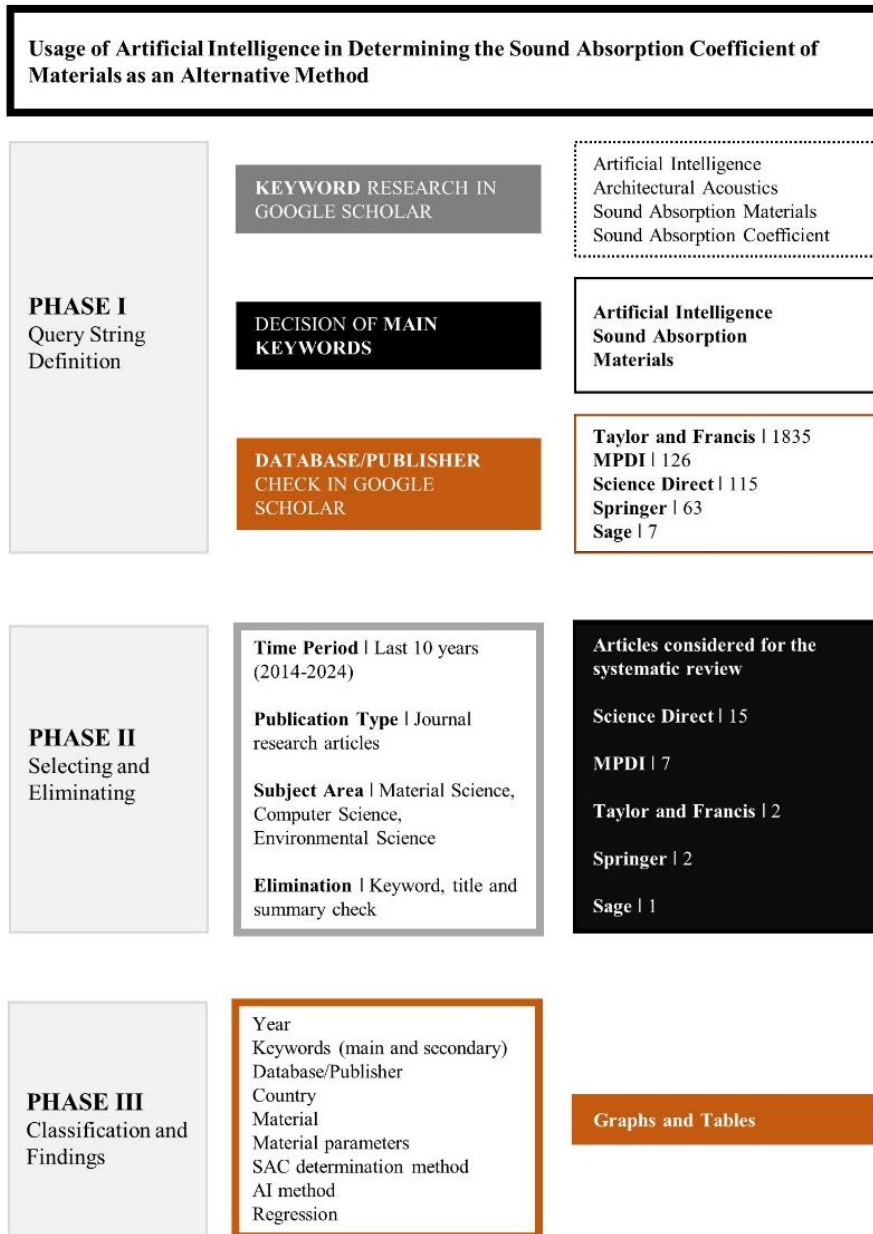


Figure 2. Flowchart of literature review steps.

A. 2. Data Synthesis and Analysis

The "Quantitative and Comparative Synthesis with Graphical Analysis" method was employed in the literature review. This approach involves collecting and organizing quantitative data, visualizing results using graphical tools, and comparing different variables to gain insights. A comparative synthesis is an approach that examines similarities and differences by making comparisons between different datasets, methods, or results. Quantitative synthesis is carried out transparently and consistently, with clear methodology statements, providing scientifically summarized information [34]. In comparative synthesis, instead of asking "Is something good?" the question "Is something better than another?" is addressed [35]. The graphical analysis method examines and presents datasets using visual tools. This method involves creating graphs, charts, and diagrams to identify data trends, relationships, and patterns.

After establishing the necessary limitations within the scope of the study, the first step was data collection, and the collected data were organized by creating Excel tables. The headings under which the data were grouped are listed below:

- Year of publication
- Research keywords and other keywords used in the articles
- Publisher/database where the research was published
- Country where the research was conducted
- Material examined/produced within the research
- Material parameters included in the research
- Method used to determine the SAC in the study
- AI method examined in the research
- Analysis of the correlation between the model and measurement results

After grouping the data under the main headings and creating tables, visualizations were made to observe trends and outcomes. Subsequently, a comparative analysis was conducted among the results, and the findings/conclusions were summarized.

III. FINDINGS

After applying all the restrictions, 245 research articles were initially identified. Following a review of the titles, keywords, and abstracts, 27 of these articles were relevant to investigating the applicability of artificial intelligence methods in determining the SAC of materials. The studies were organized according to the nine categories outlined in Section A.2.

Figure 3 presents the distribution of studies conducted in this field over the past ten years (2014-2024).



Figure 3. Graph of the distribution of academic studies on determining the sound absorption co-efficient using artificial intelligence from 2014 to 2024 by year.

Accordingly, research on predicting the SAC using artificial intelligence has notably increased over the past five years. This finding reflects the impact of advancing technology and the increasing accessibility of artificial intelligence tools.

Figure 4 presents the number of publishers/databases where the studies were published. The graph shows that most studies in this field were published in ScienceDirect and MDPI.

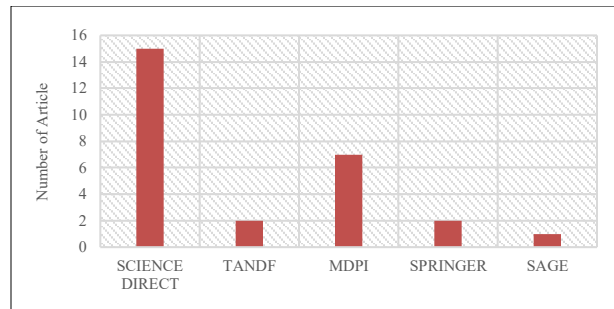


Figure 4. Number of publications in the last ten years (2014-2024) by publisher/database.

Figure 5 shows the distribution of studies on artificial intelligence models for SAC prediction by country across the identified publishers/databases. As illustrated in the figure, China encompasses the majority of researchers. China's larger population influences this compared to other countries, but it also reflects China's perspective on technological advancements and innovative approaches. Following China, Italy is identified as another significant country where innovative research on determining the SAC of materials is predominantly conducted.

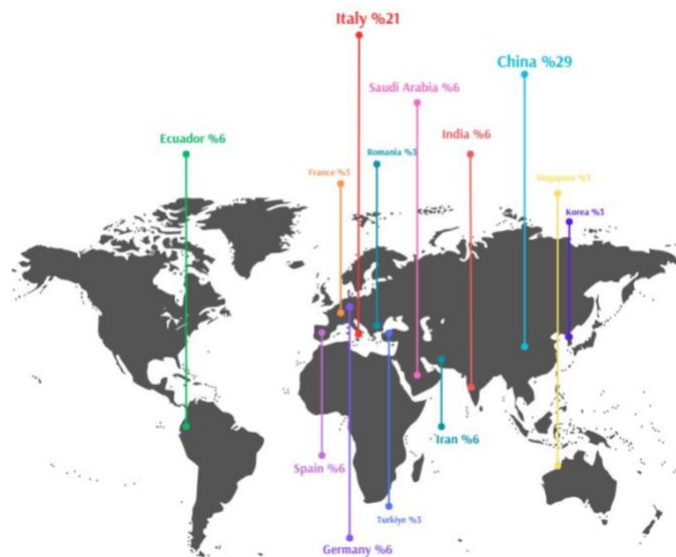


Figure 5. Percentage distribution of studies on artificial intelligence models for predicting SAC by country in the last ten years .

Figure 6 presents the keywords “Artificial Intelligence,” “Sound Absorption,” and “Material” used in the research process according to their usage proportions in the articles. The proportions are predominantly distributed across ‘Artificial Intelligence’ and ‘Sound Absorption,’ in line with the research title. Keywords used in the examined studies beyond the main keywords have been synthesized to provide insights for future research and are grouped under the main keyword headings, as shown in Figures 7, 8, and 9.

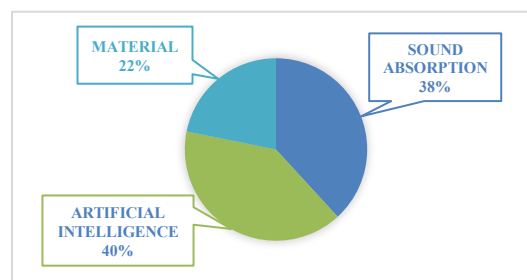


Figure 6. Percentage usage of keywords examined in the research across studies.

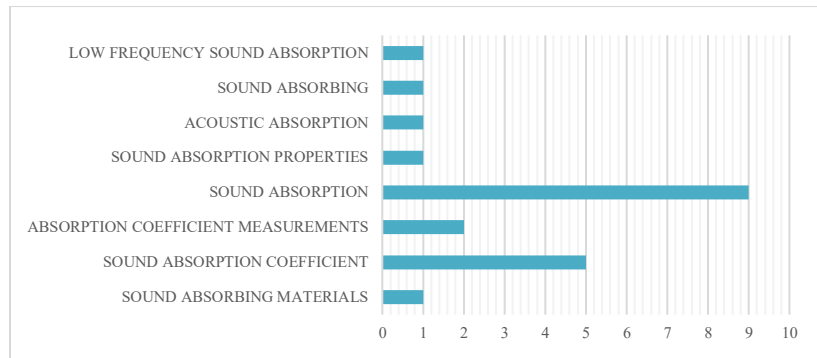


Figure 7. Additional keywords used in studies under the primary heading of sound absorption.

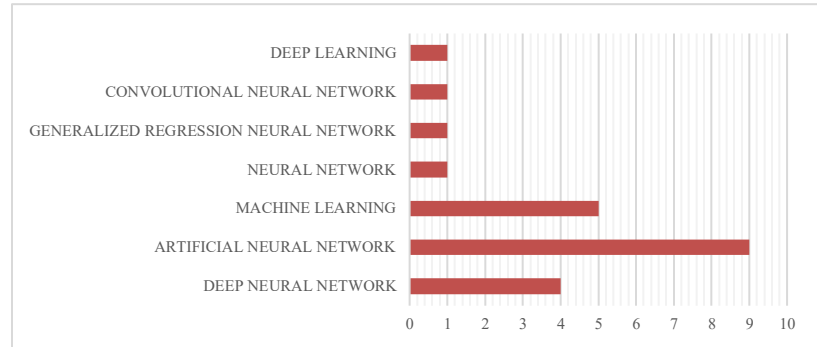


Figure 8. Additional keywords used in studies under the primary heading of artificial intelligence.

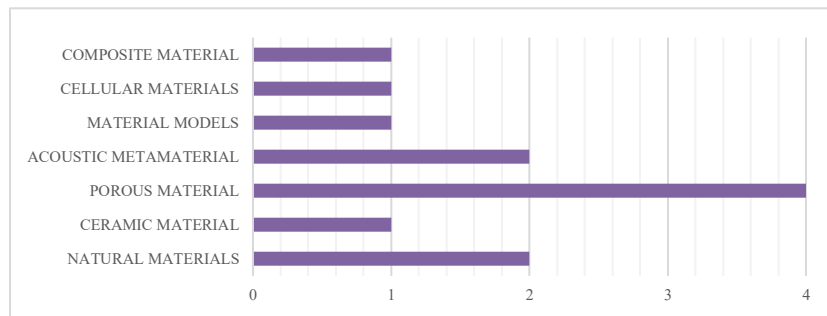


Figure 9. Additional keywords used in studies under the primary heading of materials.

Upon reviewing the results, it is observed that while "sound absorption" is predominantly used as a main heading, the method for "Artificial Intelligence" is directly included in the keywords. Similarly, for the "materials" group, the specific material is often included as a keyword. Detailed keyword usage for specific studies is considered a positive approach.

Another key heading in the study is the material parameters examined in the research. Various physical parameters affecting the SAC in materials have been considered to analyze the factors influencing sound absorption. As shown in Figure 10, material thickness is frequently investigated as a parameter affecting sound absorption in materials. Material thickness is particularly effective at low frequencies, so assessing thickness is beneficial when proposing innovative materials. Another significant parameter is the pore width in porous materials. The width of the pores affects the amount of friction as sound waves travel through the material, making it a crucial parameter to investigate in porous and fibrous materials. Beyond these two parameters, studies have also explored the effects of fiber physical properties (such as fiber diameter, fiber size, and fiber arrangement), material density, the number of layers in layered materials, and air gaps in Helmholtz resonators and layered structures on sound absorption. These material parameters are used as inputs in AI models, highlighting their importance in detailing model design.

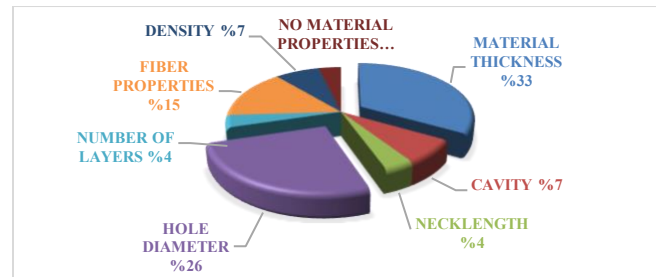


Figure 10. Material parameters examined in studies that affect sound absorption.

The methods used in the articles to determine the SAC in materials were examined in the next phase of the study. As shown in Figure 11, it is evident that, as mentioned in the introduction, the impedance tube method is the most commonly preferred method for determining the SAC in academic studies. The second most preferred method for SAC determination is COMSOL Multiphysics. In COMSOL, after defining the material properties and sound source, the necessary algorithms are created according to the acoustic defects. The sound absorption coefficient is determined based on the ratio between the incoming sound energy and the absorbed energy. Although practical for reaching results, there can be issues with the accuracy of the results due to environmental conditions in measurements like impedance tubes or reverberation rooms. Calculations have also emerged as another preferred method in the studies. Other methods have been used in various studies as well. Nevertheless, in studies using methods such as simulations, it is recommended to use the impedance tube method comparatively for reliability.

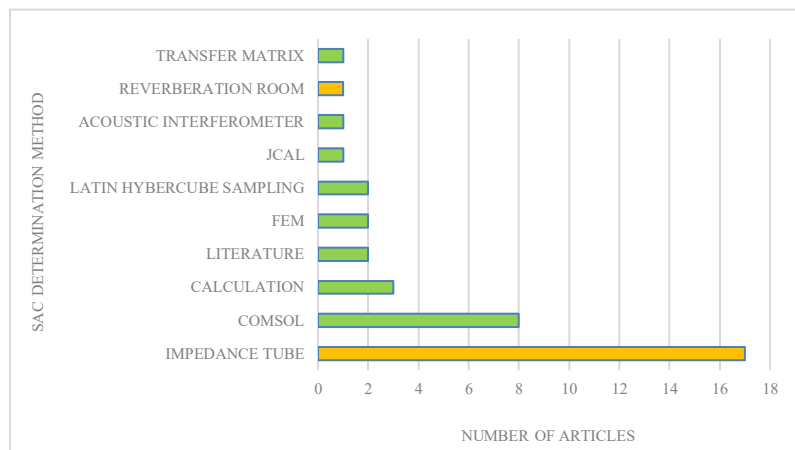


Figure 11. Number of measurement/calculation methods used in academic studies for determining SAC.

In the final stage of the findings, the AI programs used for SAC prediction in the articles were examined, and the results are presented in Figure 12. The AI models and techniques were categorized into five groups. Table 1 presents the methods within these five groups and provides a reference table for the research articles examined in the systematic review that utilized these techniques.

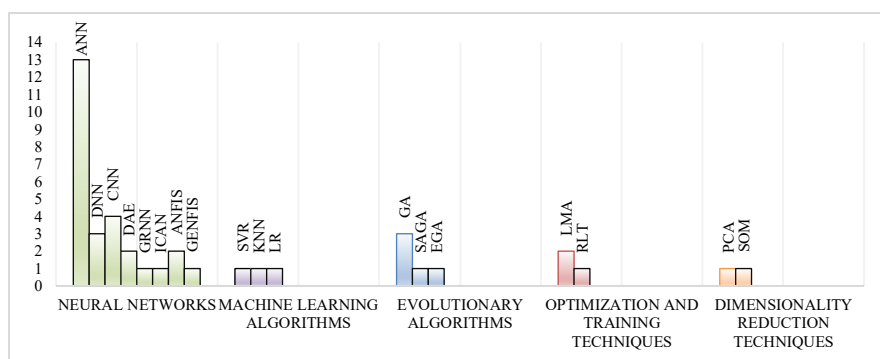


Figure 12. AI Techniques and Models Used in Studies for Predicting SAC.

Table 1. Categorized AI models and techniques.

AI Main Category	AI Secondary Category	References
Neural Networks	ANN (Artificial Neural Networks)	[36]; [37]; [38]; [39]; [40]; [31]; [41]; [42]; [43]; [44]; [45]; [46]; [47]
	DNN (Deep Neural Networks)	[48]; [49]; [50]
	CNN (Convolutional Neural Networks)	[51]; [52]; [53]; [54]
	DAE (Denoising Autoencoder)	[55]; [48]
	GRNN (General Regression Neural Networks)	[56]
	ICAN (Independent Component Analysis Network)	[50]
	ANFIS (Adaptive Neuro-Fuzzy Inference System)	[36]; [31]
	GENFIS (Genetic Fuzzy Inference System)	[36]
Machine Learning Algorithms	SVR (Support Vector Regression)	[57]
	KNN (K-Nearest Neighbors)	[40]
	LR (Linear Regression)	[37]
Evolutionary Algorithms	GA (Genetic Algorithm)	[31]; [54]; [58]
	SAGA (Self-Adaptive Genetic Algorithm)	[54]
	EGA (Evolutionary Genetic Algorithm)	[54]
Optimization And Training Techniques	LMA (Levenberg-Marquardt Algorithm)	[38]; [45]
	RLT (Reinforcement Learning Techniques)	[15]; [60]
Dimensionality Reduction Techniques	PCA (Principal Component Analysis)	[59]

In the studies, approximately 35% of the different AI models were used together, and comparisons were made between measurement results and AI models. In some studies, regression results (R²) were provided, while in others, it was stated that there was a high correlation with the measurement results, but no numerical value was given. In some cases, the absolute error margin (MSE) was reported. Indicators of the agreement between AI models and measurement results are presented in Table 2.

Table 2. AI Model-calculation/measurement compatibility.

AI Model	Compatibility	References
Neural Networks / ANN	R ² = 0.95	[44]
	R ² = 0.8	[45]
	R ² = 0.93	[42]
	R ² = 0.99	[46]
	R ² = 0.986	[39]
	R ² = 0.894	[41]
	Comment: High	[43]; [47]
Neural Networks / DAE and DNN	MSE = 0.00487	[48]
Neural Networks / DAE	Comment: DNN > DAE	
Neural Networks / CNN	MSE = 0.0122 (DNN)	[55]
	MSE = 0.028	[52]
	R ² = 0.98	[53]
	Comment: High	[51]
Neural Networks / GRNN	MSE = 0.017	[56]
Neural Networks / ICAN	MSE = 0.04	[50]
Machine Learning Algorithms / SVR	MSE = 0.98149	[57]
Evolutionary Algorithms / GA and SAGA and EGA	Comment: High	[54]

Optimization And Training Techniques / RLT	Comment: High	[60]
Neural Networks / ANN and Evolutionary Algorithms / GA	MSE = 0.11	[31]
Neural Networks / ANFIS and Evolutionary Algorithms / GA	MSE = 0.17	[31]
AI Model	Compatibility	References
Neural Networks / ANN and ANFIS and GENFIS	Comment: ANFIS has a higher correlation	[36]
Neural Networks / ANN and Machine Learning Algorithms / LR	R ² = 0.989 (ANN) R ² = 0.571 (LR)	[37]
Neural Networks / ANN and Optimization And Training Techniques / LMA	R ² = 0.9	[38]
Neural Networks / ANN and Machine Learning Algorithms / KNN	Comment: High	[40]
Dimensionality Reduction Techniques / PCA	Comment: Higher correlation but needs more research	[59]

IV. DISCUSSION

This study reviews the literature on using artificial intelligence (AI) models for determining sound absorption coefficients. 2,146 articles were retrieved from Science Direct, Taylor and Francis, MDPI, Springer, and Sage databases. After applying filters based on year, article type, research area, title, and abstract, 27 articles were selected for in-depth analysis. These articles were categorized and evaluated based on publication year, keywords, publisher, country, material properties examined, SAC determination methods, and AI model performance. The following summary highlights the observed trends in existing research within the literature:

- In recent years, the application of Artificial Intelligence (AI) techniques in predicting the sound absorption coefficient (SAC) has increased significantly, primarily due to the high costs and time demands of experimental processes. China has emerged as the leading country in this field, with approximately 80% of studies utilizing experimental measurements conducted through impedance tubes, followed by optimization studies employing AI. By substituting experimental measurements with AI models, these studies aim to achieve significant savings in both time and cost.
- The fact that studies have been conducted in both developed countries, such as Italy, and developing countries, such as Ecuador, indicates an interest in sustainability across nations with varying economic and geographic conditions, as reflected in the preference for natural fibrous materials. The evaluation of natural materials using artificial intelligence models for determining sound absorption coefficients in these studies represents a significant step toward promoting alternative materials aligned with environmental sustainability goals.
- The analysis reveals that neural network-based techniques are the most commonly used methods, with Artificial Neural Networks (ANN), Convolutional Neural Networks (CNN), and Deep Neural Networks (DNN) standing out among these models. This preference can be attributed to these models' strong learning capacities and ability to effectively process complex data relationships in predicting sound absorption coefficients. Specifically, ANN is valued for its broad applicability, CNN for its high accuracy with visual and spatial data, and DNN for handling more complex prediction tasks due to its deep-layered structure. In particular, ANN is a cost-effective and fast option for smaller datasets. Given its over 90% correlation with measurement results, ANN is expected to see increased application in this field.
- Less commonly used models, such as General Regression Neural Network (GRNN) and Denoising Autoencoders (DAE), may be less favored due to their limitations in handling a smaller range of materials and parameters. Although one study [56] using the GRNN model reported a low mean absolute error of 0.017, it would be premature to make general conclusions

based on the limited number of studies available. Similarly, another study [59] employing the less frequently used Self-Organizing Maps (SOM) and Principal Component Analysis (PCA) suggested that PCA could potentially be used for predicting sound absorption coefficients. However, it also highlighted the need for further research with a larger sample size.

- The impact of hybrid model usage on correlation was also examined in the studies. In one study [31], which combined ANN and Adaptive Neuro-Fuzzy Inference System (ANFIS) models with Genetic Algorithms (GA), the integration of ANN with GA enabled the model to reach optimal results more quickly; however, such algorithms require high computational power and, consequently, adequate hardware. In another study [54], which utilized GA, Self-Adaptive Genetic Algorithm (SAGA), and CNN, the combined method known as the Elitist Genetic Algorithm (EGA) appeared advantageous for solving complex problems. Still, they were not ideally suited for predicting sound absorption coefficients due to the extensive data requirements.
- As seen in Table 1, AI models are suitable as an alternative method for determining the sound absorption coefficient of materials. Over time, training AI models with more materials and parameters can increase their applicability. Creating a comprehensive material database will provide a significant foundation for improving the reliability of these models.

As the next step in this research, a comprehensive study on the physical and sound absorption properties of sound-absorbing materials is planned to make AI models usable within this framework.

V. CONCLUSION

This literature review examines existing studies in artificial intelligence approaches for determining the sound absorption performance of materials, highlighting key trends and gaps in the literature. Within the scope of this study, five keywords were identified, and publications from five different publishers/databases were reviewed, with restrictions based on publication year, article type, and research field. Publications obtained under these restrictions were further filtered by closely examining titles, abstracts, and, where necessary, content details to exclude works that, despite keyword alignment, did not align with the study's content focus. The findings reveal prominent topics such as the applicability and advantages of using AI in determining sound absorption coefficients for materials while identifying underexplored or overlooked areas in the literature. In particular, environmental factors like temperature and humidity significantly impact the sound absorption performance of materials; however, such data are often overlooked in computer-based studies, underscoring the need for further research in this area. Future studies incorporating environmental conditions as inputs for AI predictions are expected to enhance the knowledge base in this field. In conclusion, this study provides a framework that emphasizes the applicability of AI methods in assessing the acoustic performance of sound-absorbing materials, offering a time- and cost-effective approach that can guide future research in this domain.

VI. REFERENCES

- [1] URL 1: <https://www.who.int/europe/news-room/fact-sheets/item/noise>, received at (20.08.2024).
- [2] Yu, D.: Sound Advice: The development and use of early 20th-century acoustic wall and ceiling materials. Doctoral dissertation, Columbia University (2015).
- [3] ISO 10534-2:2023: Acoustics – Determination of acoustic properties in impedance tubes. Part 2: Two-microphone technique for normal sound absorption coefficient and normal surface impedance (2023).

- [4] ASTM E1050-12: Standard test method for impedance and absorption of acoustical materials using a tube, two microphones and a digital frequency analysis system. New York: American National Standards Institution (2012).
- [5] ISO 354-2003: Acoustics —Measurement of sound absorption in a reverberation room. International Organisation for Standardisation, Geneva (2003).
- [6] ASTM C423-17: Standard Test Method for Sound Absorption and Sound Absorption Coefficients by the Reverberation Room Method, ASTM International, West Conshohocken, PA (2017).
- [7] Hasan, M., Hodgson, M.: Effectiveness of reverberation room design: Room size and shape and effect on measurement accuracy. In PROCEEDINGS of the 22nd International Congress on Acoustics, 5-9 (2016).
- [8] Tang, Y., Chuang, X.J.: Tuning of estimated sound absorption coefficient of materials of reverberation room method. Shock and Vibration (2022).
- [9] ASTM C384-04-2004: Standard test method for impedance and absorption of acoustical materials by impedance tube method, astm international, West Conshohocken, PA (2011).
- [10] PK, F. A.: What is Artificial Intelligence?. Success is no accident. It is hard work, perseverance, learning, studying, sacrifice and most of all, love of what you are doing or learning to do, 65 (1984).
- [11] McCarthy, J.: What is artificial intelligence (2007).
- [12] Jha, D., Gupta, V., Liao, W. K., Choudhary, A., Agrawal, A.: Moving closer to experimental level materials property prediction using AI. Scientific reports, 12(1), 11953 (2022).
- [13] Goswami, L., Deka, M., Roy, M.: Artificial Intelligence in Material Engineering: A Review on Applications of Artificial Intelligence in Material Engineering. Advanced Engineering Materials, 25 (2022).
- [14] Agrawal, A., Choudhary, A.: Perspective: Materials informatics and big data: Realization of the “fourth paradigm” of science in materials science. Apl Materials, 4(5) (2016).
- [15] Li, J., Lim, K., Yang, H., Ren, Z., Raghavan, S., Chen, P. Y., Wang, X.: AI applications through the whole life cycle of material discovery. Matter, 3(2), 393-432 (2020).
- [16] To, W. M., Chung, A. W.: Exploring the roles of artificial intelligence and next-generation virtual technologies in soundscape studies. In INTER-NOISE and NOISE-CON Congress and Conference Proceedings Vol. 259, No. 4, 5321-5329 (2019).
- [17] Jahani, A., Kalantary, S., Alitavoli, A.: An application of artificial intelligence techniques in prediction of birds soundscape impact on tourists’ mental restoration in natural urban areas. Urban Forestry & Urban Greening, 61, 127088 (2021).
- [18] Hou, Y., Ren, Q., Zhang, H., Mitchell, A., Aletta, F., Kang, J., Botteldooren, D.: AI-based soundscape analysis: Jointly identifying sound sources and predicting annoyance. The Journal of the Acoustical Society of America, 154(5), 3145-3157 (2023).
- [19] Wang, J., Li, C., Lin, Y., Weng, C., & Jiao, Y.: Smart soundscape sensing: A low-cost and integrated sensing system for urban soundscape ecology research. Environmental Technology & Innovation, 29, 102965 (2023).

- [20] Lam, B., Ong, Z. T., Ooi, K., Ong, W. H., Wong, T., Watcharasupat, K. N., Gan, W. S.: Automating urban soundscape enhancements with AI: In-situ assessment of quality and restorativeness in traffic-exposed residential areas. *arXiv preprint arXiv:2407.05744* (2024).
- [21] Xu, J., Nannariello, J., Fricke, F.: Application of computational intelligence techniques to architectural and building acoustics. *Artificial Intelligence in Energy and Renewable Energy Systems*, 309 (2007).
- [22] Wan, Y., Zhou, Y., Wen, J., Chen, Z., Zhao, J.: Research on prediction method of objective assessment of building acoustics based on machine learning. In *Journal of Physics: Conference Series* Vol. 2522, No. 1, p. 012010 (2023).
- [23] Brown, A. G. P., Coenen, F. P., Shave, M. J., Knight, M. W.: An AI approach to noise prediction. *Building Acoustics*, 4(2), 137-150 (1997).
- [24] Nourani, V., Gökçekuş, H., Umar, I. K.: Artificial intelligence based ensemble model for prediction of vehicular traffic noise. *Environmental research*, 180, 108852 (2020).
- [25] Singh, D., Upadhyay, R., Pannu, H. S., Leray, D.: Development of an adaptive neuro fuzzy inference system based vehicular traffic noise prediction model. *Journal of Ambient Intelligence and Humanized Computing*, 12, 2685-2701 (2021).
- [26] Tan, Y., Fang, Y., Zhou, T., Wang, Q., Cheng, J. C. P.: Improve indoor acoustics performance by using building information modeling. In *ISARC. Proceedings of the International Symposium on Automation and Robotics in Construction* Vol. 34 (2017).
- [27] Burfoot, M.: Integrating Acoustic Scene Classification with Variable Acoustics, to Intelligently Improve Acoustic Comfort in NZ Classrooms. In *Proceedings—New Zealand Built Environment Research Symposium* (2020).
- [28] Drass, M., Kraus, M. A., Riedel, H., Stelzer, I.: SoundLab AI-Machine learning for sound insulation value predictions of various glass assemblies. *Glass Structures & Engineering*, 7(1), 101-118 (2022).
- [29] Wang, F., Chen, Z., Wu, C., Yang, Y.: Prediction on sound insulation properties of ultrafine glass wool mats with artificial neural networks. *Applied Acoustics*, 146, 164-171 (2019).
- [30] Luo, Z., Li, T., Yan, Y., Zhou, Z., Zha, G.: Prediction of sound insulation performance of aramid honeycomb sandwich panel based on artificial neural network. *Applied Acoustics*, 190, 108656 (2022).
- [31] Paknejad, S. H., Vadood, M., Soltani, P., Ghane, M.: Modeling the sound absorption behavior of carpets using artificial intelligence. *The Journal of the Textile Institute*, 112(11), 1763-1771 (2021).
- [32] Rother, E. T.: Systematic literature review X narrative review. *Acta paulista de enfermagem*, 20, v-vi (2007).
- [33] Nightingale, A.: A guide to systematic literature reviews. *Surgery (Oxford)*, 27(9), 381-384 (2009).
- [34] Morton, S. C., Murad, M. H., O'Connor, E., Lee, C. S., Booth, M., Vandermeer, B. W., Steele, D. W.: Quantitative synthesis—an update. *Methods Guide for Effectiveness and Comparative Effectiveness Reviews* (2018).

- [35] Higgins, S.: Meta-synthesis and comparative meta-analysis of education research findings: some risks and benefits. *Review of Education*, 4(1), 31-53 (2016).
- [36] Aliabadi, M., Golmohammadi, R., Khotanlou, H., Mansoorizadeh, M., Salarpour, A.: Artificial neural networks and advanced fuzzy techniques for predicting noise level in the industrial embroidery workrooms. *Applied Artificial Intelligence*, 29(8), 766-785 (2015).
- [37] Iannace, G., Ciaburro, G., Trematerra, A.: Modelling sound absorption properties of broom fibers using artificial neural networks. *Applied Acoustics*, 163, 107239 (2020).
- [38] Ciaburro, G., Iannace, G.: Numerical simulation for the sound absorption properties of ceramic resonators. *Fibers*, 8(12), 77 (2020).
- [39] Ciaburro, G., Iannace, G., Puyana-Romero, V., Trematerra, A.: A comparison between numerical simulation models for the prediction of acoustic behavior of giant reeds shredded. *Applied Sciences*, 10(19), 6881 (2020).
- [40] Kuschmitz, S., Ring, T. P., Watschke, H., Langer, S. C., Vietor, T.: Design and additive manufacturing of porous sound absorbers—A machine-learning approach. *Materials*, 14(7), 1747 (2021).
- [41] Ciaburro, G., Iannace, G., Ali, M., Alabdulkarem, A., Nuhait, A.: An artificial neural network approach to modelling absorbent asphalts acoustic properties. *Journal of King Saud University-Engineering Sciences*, 33(4), 213-220 (2021).
- [42] Ring, T. P., Langer, S. C.: On the Relationship of the Acoustic Properties and the Microscale Geometry of Generic Porous Absorbers. *Applied Sciences*, 12(21), 11066 (2022).
- [43] Ciaburro, G., Parente, R., Iannace, G., Puyana-Romero, V.: Design optimization of three-layered metamaterial acoustic absorbers based on PVC reused membrane and metal washers. *Sustainability*, 14(7), 4218 (2022).
- [44] Otaru, A. J.: Research of the numerical simulation and machine learning backpropagation networks analysis of the sound absorption properties of cellular soundproofing materials. *Results in Engineering*, 20, 101588 (2023).
- [45] Puyana-Romero, V., Chuquín, J. S. A., Chicaiza, S. I. M., Ciaburro, G.: Characterization and Simulation of Acoustic Properties of Sugarcane Bagasse-Based Composite Using Artificial Neural Network Model. *Fibers*, 11(2), 18 (2023).
- [46] Farahani, M. D., Jeddi, A. A. A., Hasanzadeh, M.: Predicting the sound absorption performance of warp-knitted spacer fabrics via an artificial neural network system. *Fibers and Polymers*, 24(4), 1491-1501 (2023).
- [47] Busra, S., Giuseppe, C., Gino, I., Mustafa, O.: Preparation of PPA based composite reinforcing with glass beads and clays: Investigation of sound absorbing. *Building Acoustics*, 1351010X241254956 (2024).
- [48] Cheng, B., Wang, M., Gao, N., Hou, H.: Machine learning inversion design and application verification of a broadband acoustic filtering structure. *Applied Acoustics*, 187, 108522 (2022).
- [49] Dogra, S., Singh, L., Nigam, A., Gupta, A.: A deep learning-based approach for the inverse

design of the Helmholtz resonators. *Materials Today Communications*, 37, 107439 (2023).

[50] Mahesh, K., Ranjith, S. K., Mini, R. S.: A deep autoencoder based approach for the inverse design of an acoustic-absorber. *Engineering with Computers*, 40(1), 279-300 . (2024).

[51] Gao, N., Wang, M., Cheng, B., Hou, H.: Inverse design and experimental verification of an acoustic sink based on machine learning. *Applied Acoustics*, 180, 108153 (2021).

[52] Pan, B., Song, X., Xu, J., Sui, D., Xiao, H., Zhou, J., Gu, J.: Accelerated inverse design of customizable acoustic metaporous structures using a CNN-GA-based hybrid optimization framework. *Applied Acoustics*, 210, 109445 (2023).

[53] Lee, S. Y., Lee, J., Lee, J. S., Lee, S.: Deep learning-based prediction and interpretability of physical phenomena for metaporous materials. *Materials Today Physics*, 30, 100946 (2023).

[54] Pan, B., Song, X., Xu, J., Zhou, J., Sui, D., Shui, Y., Zhang, Z.: Bottom-up approaches for rapid on-demand design of modular metaporous structures with tailored absorption. *International Journal of Mechanical Sciences*, 263, 108784 (2024).

[55] Gao, N., Wang, M., Cheng, B.: Deep auto-encoder network in predictive design of Helmholtz resonator: on-demand prediction of sound absorption peak. *Applied Acoustics*, 191, 108680 (2022).

[56] Mi, H., Guo, W., Liang, L., Ma, H., Zhang, Z., Gao, Y., Li, L.: Prediction of the Sound Absorption Coefficient of Three-Layer Aluminum Foam by Hybrid Neural Network Optimization Algorithm. *Materials*, 15(23), 8608 (2022).

[57] Wang, R., Yao, D., Zhang, J., Xiao, X., Jin, X. Sound-insulation prediction model and multi-parameter optimisation design of the composite floor of a high-speed train based on machine learning. *Mechanical Systems and Signal Processing*, 200, 110631 (2023).

[58] Gao, N., Liu, J., Deng, J., Chen, D., Huang, Q., Pan, G.: Design and performance of ultra-broadband composite meta-absorber in the 200Hz-20kHz range. *Journal of Sound and Vibration*, 574, 118229 (2024).

[59] Ghizdavet, Z., Ștefan, B. M., Nastac, D., Vasile, O., Bratu, M.: Sound absorbing materials made by embedding crumb rubber waste in a concrete matrix. *Construction and Building Materials*, 124, 755-763 (2016).

[60] Jin, Y., Yang, Y., Wen, Z., He, L., Cang, Y., Yang, B., ... & Li, Y.: Lightweight sound-absorbing metastructures with perforated fish-belly panels. *International Journal of Mechanical Sciences*, 226, 107396 (2022).



Düzce University Journal of Science & Technology

Research Article

Prediction of Deep Drawing Ratio for DP800 Steel by Using Modified-Mohr-Coulomb Damage Criteria

Elifnaz BABA^a, Nuri ŞEN^{*a} Tolgahan CİVEK^a

^a Department of Mechanical Engineering, Faculty of Engineering, Düzce University, Düzce, TURKEY

* Corresponding author's e-mail address: nurisen@duzce.edu.tr

DOI: 10.29130/dubited.1610838

ABSTRACT

The demand for low-cost production in vehicle manufacturing while complying with the safety and environmental regulations is an enormous challenge. To comply with these challenges, sheet metal forming industries now extensively use advanced high-strength steels (AHSSs) in their products. However, due to excellent strength levels of AHSSs, problems arising in their forming stage, such as large spring-back and fracture, hinder the manufacturing process. At this stage, implementing finite element analysis (FEA) in the design processes greatly improves manufacturing processes since it allows determining possible forming errors before the actual forming process. In this study, the formability of DP800 steel has been investigated by carrying out deep drawing experiments. For that, a series of circular sheet metals, whose diameters were incrementally increased, have been deep drawn to a cup shape to determine the limiting drawing ratio (LDR). Additionally, Modified Mohr-Coulomb damage model has been utilised to predict the LDR in FEA. It has been found that the LDR of DP800 is 2.13 and the implemented damage model can successfully predict the LDR within only 2.35% error.

Keywords: DP800 steel, Deep drawing ratio, Finite element analysis, Damage,

Modified- Mohr Coulomb Hasar Kriteri Kullanılarak DP800 Çeliğinin Derin Çekme Oranının Tahmini

ÖZET

Araç imalatında güvenlik ve çevre düzenlemelerine uyum sağlarken düşük maliyetli üretim talebi muazzam bir zorluktur. Bu zorluklara uyum sağlamak için, sac metal şekillendirme endüstrileri artık ürünlerinde yaygın olarak gelişmiş yüksek dayanımlı çelikler (AHSS'ler) kullanmaktadır. Ancak, AHSS'lerin mükemmel dayanım seviyeleri nedeniyle, büyük geri yaylanma ve kırılma gibi şekillendirme aşamalarında ortaya çıkan sorunlar üretim sürecini engellemektedir. Bu aşamada, tasarım süreçlerinde sonlu elemanlar analizinin (FEA) uygulanması, gerçek şekillendirme sürecinden önce olası şekillendirme hatalarının belirlenmesine olanak tanıdığı için üretim süreçlerini büyük ölçüde iyileştirmektedir. Bu çalışmada, derin çekme deneyleri gerçekleştirilerek DP800 çeliğinin şekillendirilebilirliği araştırılmıştır. Bunun için, çapları kademeli olarak artırılan bir dizi dairesel sac metal, derin çekme oranını (LDR) belirlemek için bardak formunda derin çekilmiştir. Ek olarak, Değiştirilmiş Mohr-Coulomb hasar modeli, FEA'daki LDR'yi tahmin etmek için kullanılmıştır. DP800'ün LDR'sinin 2.13 olduğu ve uygulanan hasar modelinin LDR'yi sadece %2.35 hata payıyla başarılı bir şekilde tahmin edebildiği bulunmuştur.

Anahtar Kelimeler: DP800 Çeliği, Derin çekme oranı, Sonlu elemanlar analizi, Hasar

I. INTRODUCTION

Nowadays, with the shortage of fossil fuel resources and high level of vehicle usage which is undoubtedly one of the most reasons for environmental pollution and global warming, car manufacturers have mostly been seeking innovative and cost-effective solutions [1]. To address these big challenges, the weigh-lightened car concept is increasingly attracting attention in the sector. Therefore, many claim that the adoption of low-mass vehicles with a sustainable ecological and economical approach replacing the conventional structural steels will be an inevitable production method of next-generation cars. However, this production concept requires massive study in terms of realization of light weight car body parts under experimental conditions. In the fabrication of these new concept cars with light body parts, high-strength steels such as dual phase and trip steels play an important role. On the other hand, high-strength steels have some obvious disadvantages related to micromechanical responses to forming conditions making them highly challenging when applied as body parts. The formability is quite lower and the springback behaviour is considerably higher for high-strength steels as compared to the traditional steels [2]–[7]. Yet, to reach the similar level of safety for passengers traditional steel alloys force car manufacturers to increase the thickness of sheet metal on body parts causing environmental concerns and disadvantage relating to production costs. However, with around two times higher strength and yield point, AHSSs such as dual phase (DP) and complex phase (CP) steels, these challenges can be overcome depending on reliable and feasible metal forming technology.

Deep drawing is one of the most important fabrication processes among sheet metal forming phenomena in the car industry. Product quality is closely related to process parameters such as strain rate, blank holder force, punch speed, friction, tool geometry, process temperature and so on [8]. The success or failure of the fabrication of sheet metal part is largely affected by each of the factors. Thus, a deep understanding of drawing process is necessary to achieve desired flawless and various sheet metal car components.

FEA is a powerful tool that can be used in observing the effects of each forming parameter on the forming process without needing to manufacture the actual dies and the incessant trial-errors [9], [10]. However, in modelling of FEAs, it is important that the sheet metal is carefully characterized and some of the valuable aspects such as flow model and the damage model need to be thoroughly optimized [11]–[13]. Damage models in FEAs are used to examine the regions of the sheet metal where fractures are likely to occur. Damage models can be implemented in the FEAs as coupled and un-coupled models [14]–[18]. While the coupled damage models degrade the flow stress by linking the damage to the flow stress, in uncoupled damage models, damage does not affect the flow stress of the material. Although coupled models are considered to improve the accuracy of the predictions of the FEA, the amount of time needed to optimize their parameters can be quite exhaustive [18]. It is widely known that stress triaxiality is one of the most important parameters that significantly affects the formability of sheet metal. Thus, many damage models can be found in the literature such as Johnson Cook [19], Modified Mohr-Coulomb [20], Hosford-Coulomb [21], which links the damage to the stress triaxiality. However, in recent years, studies have shown that the Lode angle parameter has also have a significant impact on the formability of the sheet metals [22], [23]. Thus damage models that take into consideration of the stress triaxiality and as well as the Lode angle parameter such as Modified Mohr-Coulomb model have been started to be extensively used.

In this study, the formability of DP800 steel has been investigated by deep drawing experiments. Deep drawing experiments have been carried out for different blank diameters to determine the LDR of the DP800 steel. In addition, Modified Mohr-Coulomb damage model parameters have been optimized for the DP800 steel and used to predict the experimentally determined LDR in FEA.

II. MATERIALS AND METHODS

A. Materials

In this study, a cold rolled and tempered DP800 steel with a thickness of 1 mm was used. The chemical composition of the steel is listed Table 1. To investigate the mechanical properties of the sheet metal and to calibrate the damage model for the FEA, tensile test specimens (uniaxial, plane strain and shear) were cut along the rolling direction of the sheet metal. The geometrical dimensions of the tensile test specimens are shown in Figure 1. For the deep drawing experiments, circular blanks with different diameters (68, 70, 72, 74, 76, 78, 80 and 82 mm) were cut. All the specimens were cut with the aid of a water jet to avoid temperature influence on mechanical properties and the influence of edge effects resulting from poor cutting.

Table 1. Chemical composition of DP800 specimens

Sample	Elemental composition							
	(wt. %)							
DP800	C	Si	Mn	P	S	Al	Nb	Ti
	0.141	0.214	1.483	0.0106	0.0156	0.085	0.018	0.009

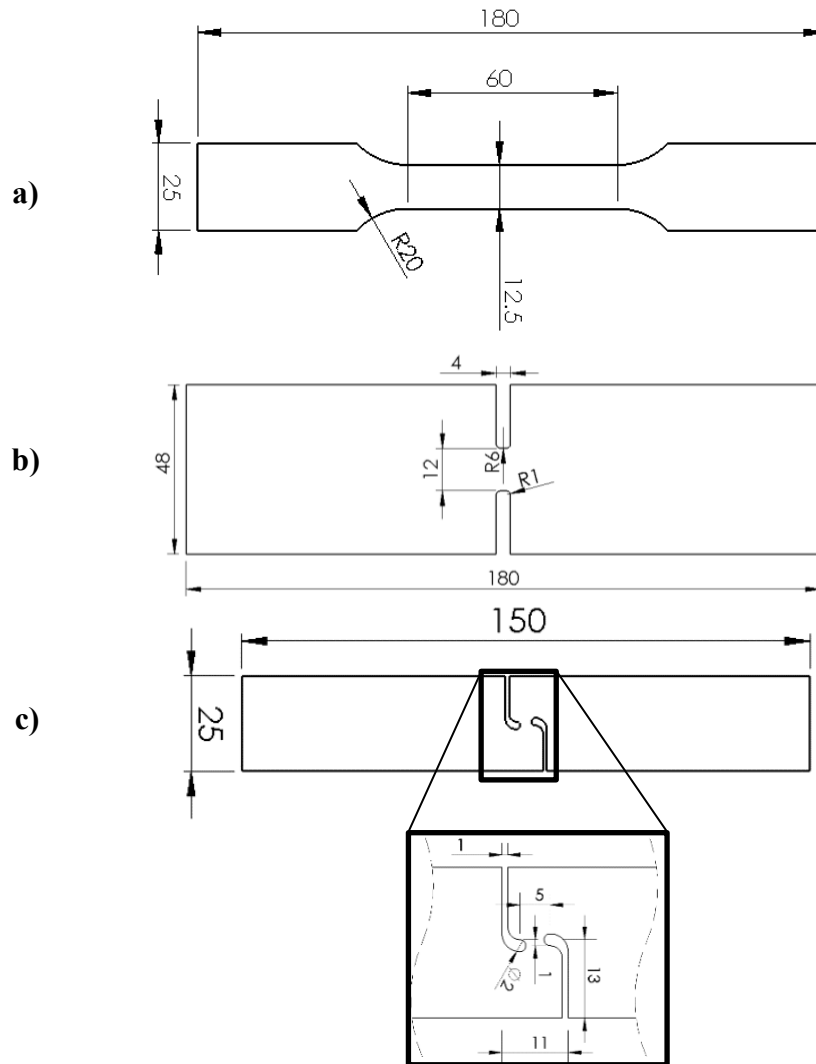


Figure 1. The dimensions of the tensile test specimens **a)** Uniaxial, **b)** Plane strain, **c)** Shear

B. Mechanical Properties

To examine the mechanical properties of the DP800 steel, uniaxial tensile tests were performed at three different velocities (0.11 mm/s, 1.1 mm/s, 10 mm/s). The tensile tests were carried out using the Zwick/Roell tensile testing machine. During the tests, the strain data were recorded by a video extensometer. The tensile stress–strain graphs are shown in Figure 2., and the obtained mechanical properties are given in Table 2. As shown in Figure 2., the strain rate effect has not had a significant impact on the tensile strength of the DP800 steel. However, the increase in the strain rate has had a slightly reducing impact on the total elongation. In order to acquire the anisotropic coefficients of the DP800 steel, uniaxial tensile tests were carried out along the rolling direction (RD), diagonal direction (DD) and transverse direction (TD) of the sheet metal. The obtained Lankford coefficients were as; $r_0=0.83$, $r_{45}=1.00$, $r_{90}=1.01$. The tensile stress-strain graphs along the RD, DD, and TD of the sheet metal are shown in Figure 3.

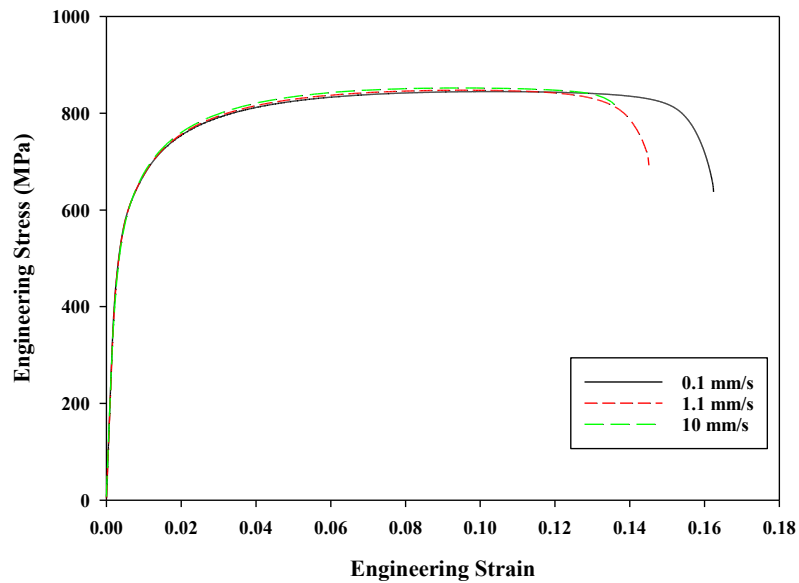


Figure 2. The tensile stress – strain graphs of DP800 steel

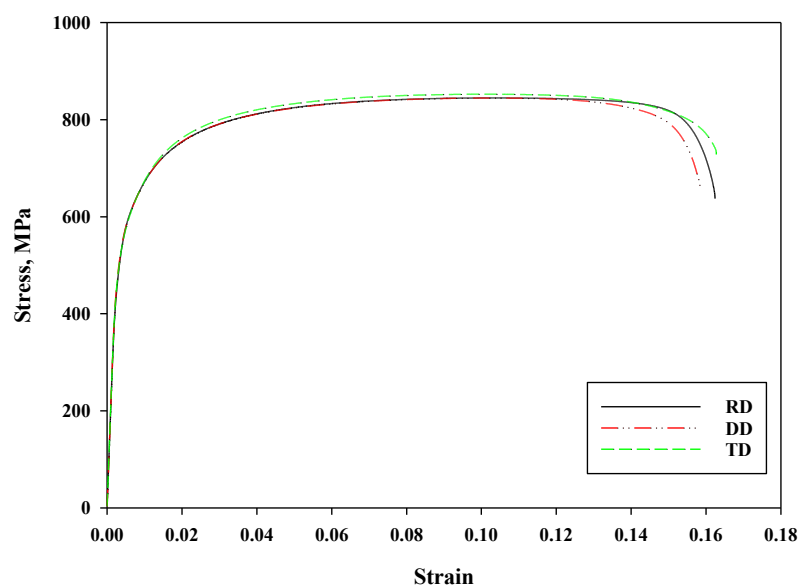


Figure 3. The tensile stress – strain graphs along the RD, DD, and TD of DP800 steel

Table 2. The mechanical properties of DP800 steel

Mechanical Properties	Test Velocity (mm/s)		
	0.1	1.1	10
Yield Stress (MPa)	566	571	564
Tensile Stress (MPa)	845	848	852
Uniform Elongation	0.10	0.09	0.09
Total Elongation	0.16	0.14	0.14

C. The FEA Models for the Tensile Test Simulations

This study used the FEA to estimate the deep drawing ratio and the thickness distributions of the drawn parts. Simufact Forming 2024.1 FEA simulation software was used to carry out the analysis. To do this, the parameters of the hardening model (Section D.) and the damage model (Section E.) need to be optimised. Hence, three different tensile test specimens (uniaxial, plane strain and shear) were modelled as shown in Figure 4. The models were meshed with 0.6 mm hexahedral elements and the mesh along the test specimens' deformation regions were refined twice. Three elements were used over the thickness direction of the specimens. In the models, the test specimens were placed in between the grips and glued to the grips by glue-type contact. The plane strain and shear specimens were stretched by the upward movement of the Grip1 with a 0.11 mm/s velocity. The uniaxial specimen, however, was stretched for three different velocities (0.11, 1.1 and 10 mm/s) as in the experiments to verify the accuracy of the hardening model parameters at each tension velocity.

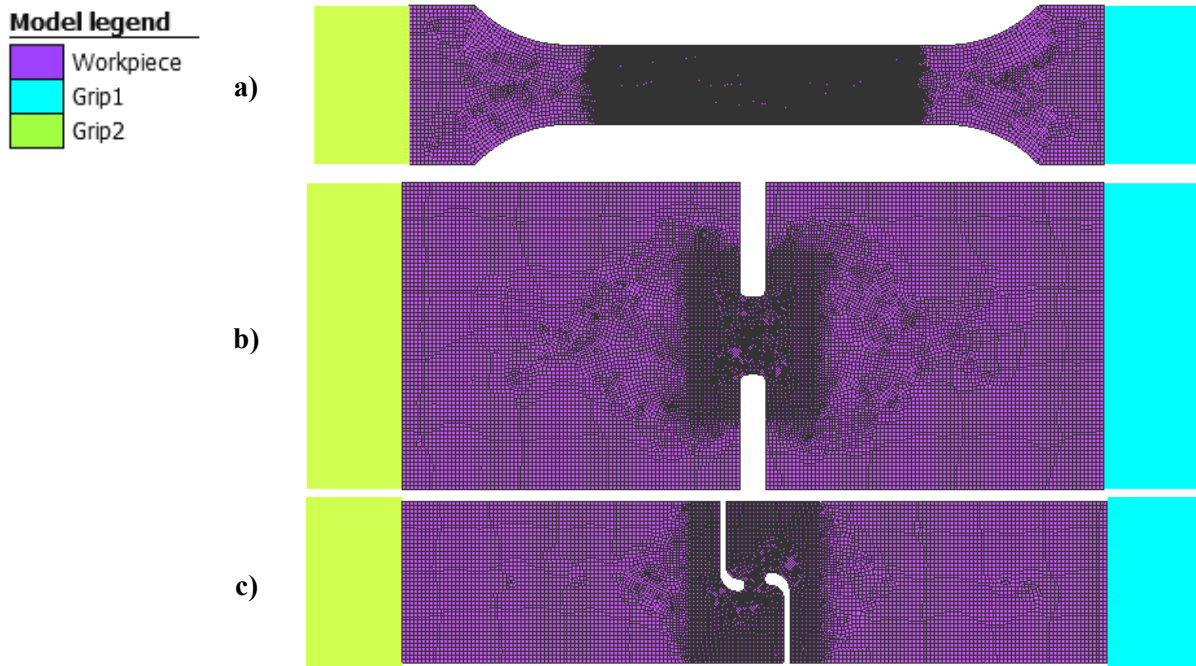


Figure 4. The FEA models of the tensile test specimens **a)** uniaxial, **b)** plane strain, **c)** shear

D. The calibration of the hardening model

During the tensile testing of sheet metals only a small fraction of uniform elongation could be obtained, however, during actual stamping or drawing applications, larger strain values may occur during the forming stage [24]. To overcome this issue, the obtained flow strain from the uniaxial tensile test is extrapolated up to a certain strain value by a determined hardening model. In this study, Hollomon hardening model, given in Equation 1., was used to extrapolate the flow stress of the DP800 steel. The model parameters, K, and, n, were initially determined from the slope of the logarithmic true stress and strain data. To calibrate the parameters of the hardening model, uniaxial tensile test simulations were run with the initial parameter values. The obtained force-displacement curves from the simulation were compared with the experimental force-displacement curves. The parameters were then updated until the force-displacement curves obtained from the simulation and experimental tests matched. The parameters of the hardening model are given in Table 3., and the force-displacement curves from the experimental and simulation results are shown in Figure 5. As can be seen in Figure 5., the obtained force-displacement curves from the simulation highly matched the experimental values.

$$\sigma = K\epsilon^n \quad (1)$$

Table 3. Hollomon hardening model parameters used in the simulations

Test velocity (mm/s)	K	n
0.11	1127	0.082
1.1	1132	0.08
10	1140	0.085

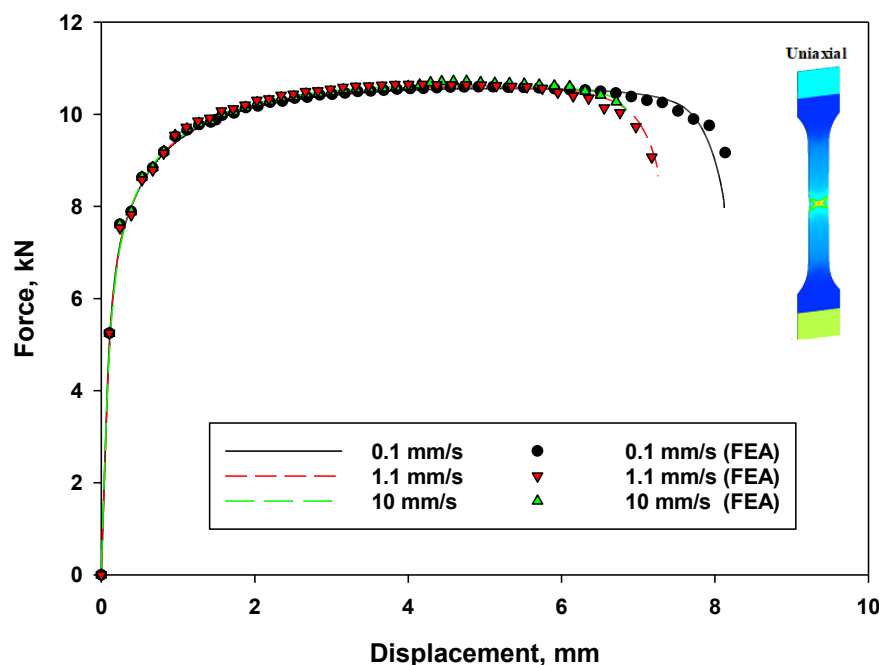


Figure 5. The comparison of the force-displacement curves obtained from the experimental and simulation results

E. The calibration of the damage model parameters

In FEAs, various damage criteria could be used to observe the critical areas of the sheet metal, which are susceptible to fracture. Recently, uncoupled damage models such as Johnson-Cook or Modified Mohr-Coulomb are preferred in many studies due to their easier applicability as compared to the traditional forming limit diagram method [25], [26]. In this study, the uncoupled Modified Mohr-Coulomb damage model, given in Equation 2., was used to determine the LDR of the DP800 steel. To calibrate its parameters, the tensile test specimens, (uniaxial, plane strain, shear), were simulated up to the fracture displacement point. Then, the average stress triaxiality and lode angle parameter values were recorded at the critical elements where the strain was localised. The evolution of the stress triaxiality and lode angle parameter values are shown in Figure 6. The average values of stress triaxiality, lode angle parameter and the fracture strain values are given in Table 4. The average stress triaxiality, lode angle parameter and the fracture strain values were input into the parameter calibration tool existing in Simufact Forming 2024.1 and the 3D damage surface shown in Figure 7. were obtained. The parameters of the Modified Mohr-Coulomb damage model parameters are given in Table 5.

$$\bar{\epsilon}_f = \left\{ \frac{A}{C_2} \left[C_\theta^s + \frac{\sqrt{3}}{2\sqrt{3}} (C_\theta^{ax} - C_\theta^s) \left(\sec\left(\frac{\bar{\theta}\pi}{6}\right) - 1 \right) \right] \times \sqrt{\frac{1+C_1^2}{3}} \cos\left(\frac{\bar{\theta}\pi}{6}\right) + c_1 \left(\eta + \frac{1}{3} \sin\left(\frac{\bar{\theta}\pi}{6}\right) \right) \right\}^{\frac{1}{n}} \quad (2)$$

where η , σ_m and σ_{vM} represent the stress triaxiality, mean stress and von Mises stress, respectively. The notations shown as θ , ζ , and $\bar{\theta}$ represent the lode angle, normalized deviatoric invariant and Lode angle parameter, respectively. The notations given in Equation 11. such as $\bar{\epsilon}_f$, A , n , c_1 , c_2 , C_θ^s , C_θ^{ax} represent the parameters of MMC damage model. $\bar{\epsilon}_f$ denotes the failure strain, A and n represent the hardening coefficient and strain hardening exponent, respectively, c_1 describes the dependency of fracture strain on the stress triaxiality, c_2 influences the height of the fracture surface, C_θ^s describes the amount of lode angle dependency of the fracture surface, C_θ^{ax} controls the asymmetry of fracture surface with respect to Lode angle parameter and is taken as 1 for $\bar{\theta} > 0$.

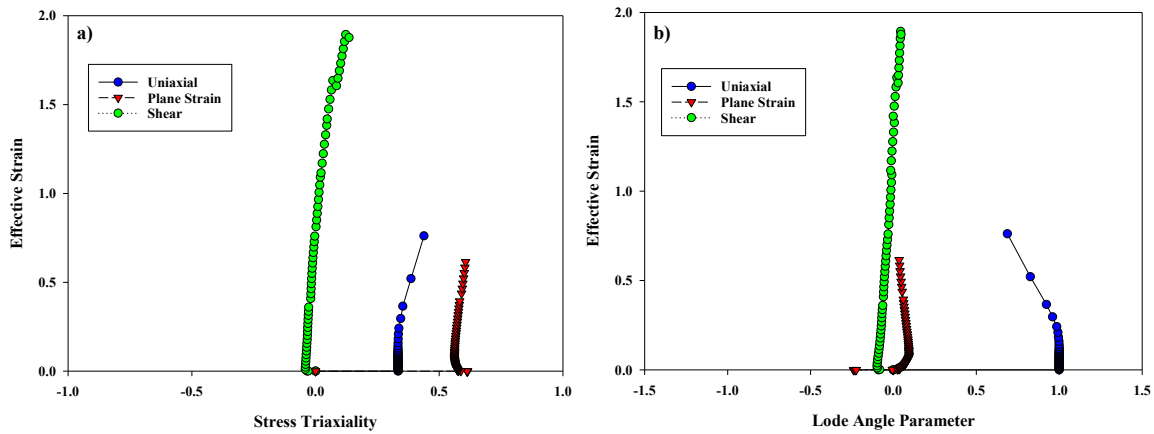


Figure 6. The evolution of the stress triaxiality and lode angle parameter values

Table 4. The average values of stress triaxiality, lode angle parameter and the fracture strain values

Test Specimen	Stress Triaxiality	Lode Angle Parameter	Fracture Strain
Uniaxial	0.33	1	0.76
Plane Strain	0.6	0.04	0.62
Shear	0	0	0.89

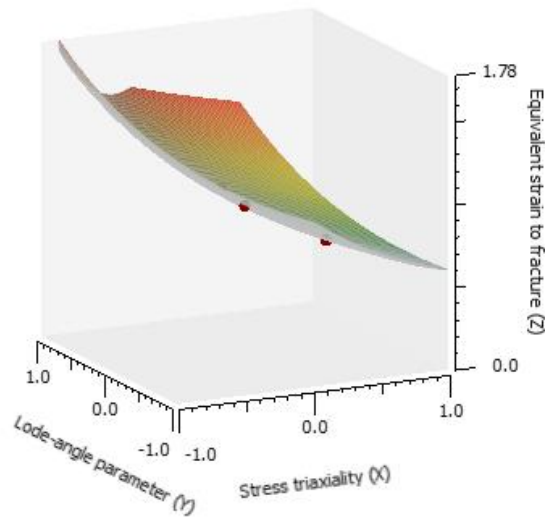


Figure 7. The Modified Mohr-Coulomb 3D damage surface

Table 5. The parameters of the Modified Mohr-Coulomb damage model

A	n	c ₁	c ₂	C _θ ^s	C _θ ^{ax}
1127	0.082	0.029	567.043	0.879	1

F. Deep drawing experiments

A double-acting hydraulic press (HDÇP 50/20 with 10+3 HP) was employed in the deep drawing experiments. The die setup for the deep drawing experiments is shown in Figure 8. H13 steel was used as the material for the die tools. The dimensions of the die tools are listed in Table 6. In the experiments, circular blanks were placed in the die cavity and then blank sheets were clamped between the die and blank holder that restricted the flow of material, thereby preventing wrinkles at the flange. The blankholder force used in the experiments was increased with the increase in the diameter of the blanks to prevent wrinkling of the sheet metal. Blankholder forces that were applied in the experiments for each blank diameter are listed in Table 7. Before carrying out the deep drawing experiments, graphite lubricant was sprayed on the specimens to reduce the friction between the die tools. To even further reduce the friction, a teflon film of 0.3 mm thickness was placed around the flange area of the sheet metal. The used lubricants for the deep drawing experiments are shown in Figure 9.



Figure 8. Experimental deep drawing die setup

Table 6. The dimensions of the die tools

Die tools	Dimensions (mm)
Punch	37.56
Die	39.98
Punch radius	5
Die radius	5

Table 7. The used blankholder force for different blank diameters in the deep drawing experiments

Blank diameter (mm)	Blankholder force (tons)
68	6
70	7
72	7
74	8
76	9
78	10
80	10
82	10

**Figure 9.** The used lubricants for the deep drawing experiments, a) Teflon film b) Graphite

G. FEA model for the deep drawing simulations

For the simulation of the deep drawing experiments, simplistic models of the die tools were created and exported to the Simufact Forming software as shown in Figure 10. In the deep drawing model, die tools were chosen as rigid body parts, whereas the specimen was designated as a deformable body. Only 1/4 of the blank sheet was modelled in the simulations to reduce the calculation time. However, symmetry planes were used to simulate the full body of the sheet metal. The sheet specimens were meshed with hexahedral elements in 0.5 mm thickness and three elements were used over the thickness direction. The friction coefficient between the die tools and the sheet specimen was chosen as 0.04. Sigma-based Hill-48 yielding criterion was used in the simulations.

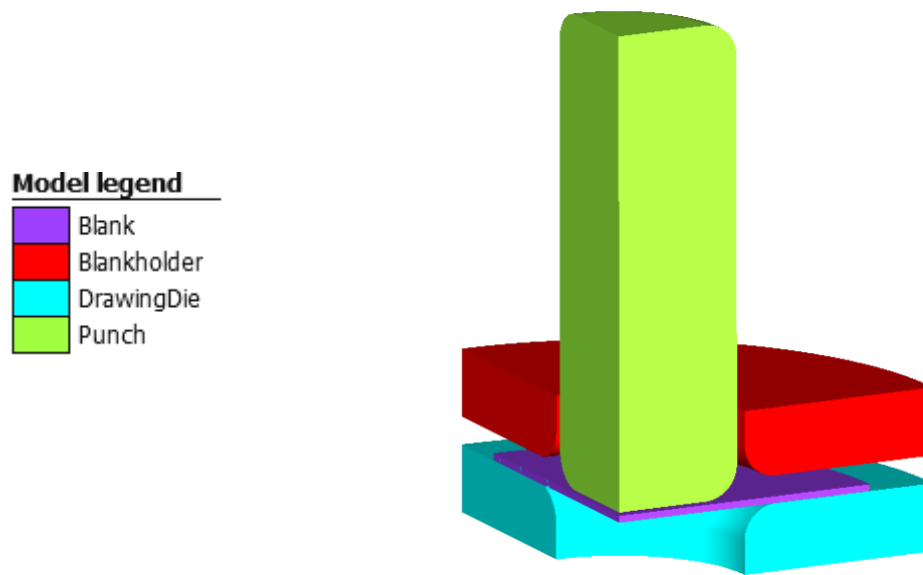


Figure 10. The deep drawing model for the FEA simulation

III. RESULTS AND DISCUSSIONS

A. MMC damage model

During the forming stage of sheet metals, the process parameters such as friction, blankholder force, temperature etc., can influence the success of the forming process [8]. All these factors affect the formability of the material and determine how the material responds during the forming stage. Although there are far many properties that can influence the formability of sheet metals, the stress triaxiality factor is widely known that its increase causes significant reductions in the formability of sheet metals [27], [28]. Another factor, known as Lode angle parameter, has also been shown by many studies to be an effective factor in the formability of sheet metals. Hence damage models that take into consideration of the influence of stress triaxiality and Lode angle parameters, such as MMC, are frequently preferred damage models to predict the fracture. In Figure 11., the simulated force-displacement curves of uniaxial, plane strain and shear tests, when the damage is activated, have been compared with the experimental results. It can be seen that the calibrated MMC damage model could precisely predict the final fracture point for each test. The initiation and the evolution of the fracture for uniaxial, plane strain and shear tests have been shown in Figures 12, 13 and 14, respectively. Earlier to the fracture initiation, the strain localised at the middle section of the uniaxial test specimen and the fracture initiated at this point. With further deformation, the fracture has spread through a 45° angle, which accurately resembles the experimental fracture surface. Similarly, the strain has localised along the middle section of the plane strain specimen and the fracture has initiated along this section, which then spread through the notches on both sides of the specimen. For the shear test specimen, the strain has localised along the mid-section of the shear area and the fracture has initiated in this section close to the notches, which then spread through the mid-section and completely fractured. It can be seen that the MMC damage model could precisely predict the final fracture point and the final fracture shape of the test specimens.

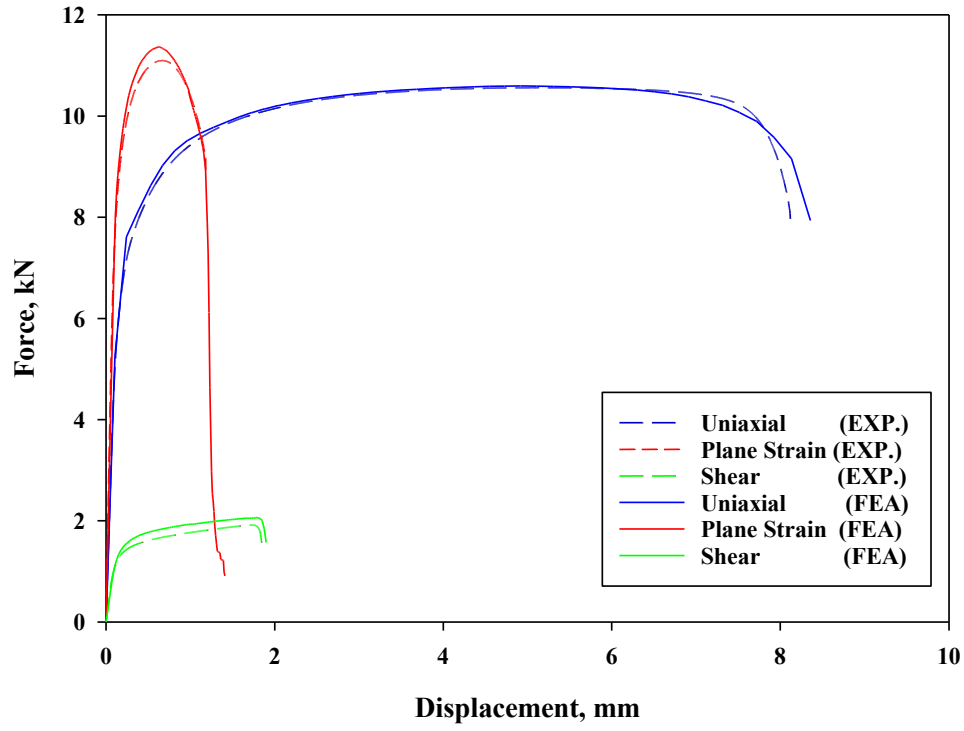


Figure 11. The comparisons of the experimental and simulated force-displacement curves for uniaxial, plane strain and shear tests

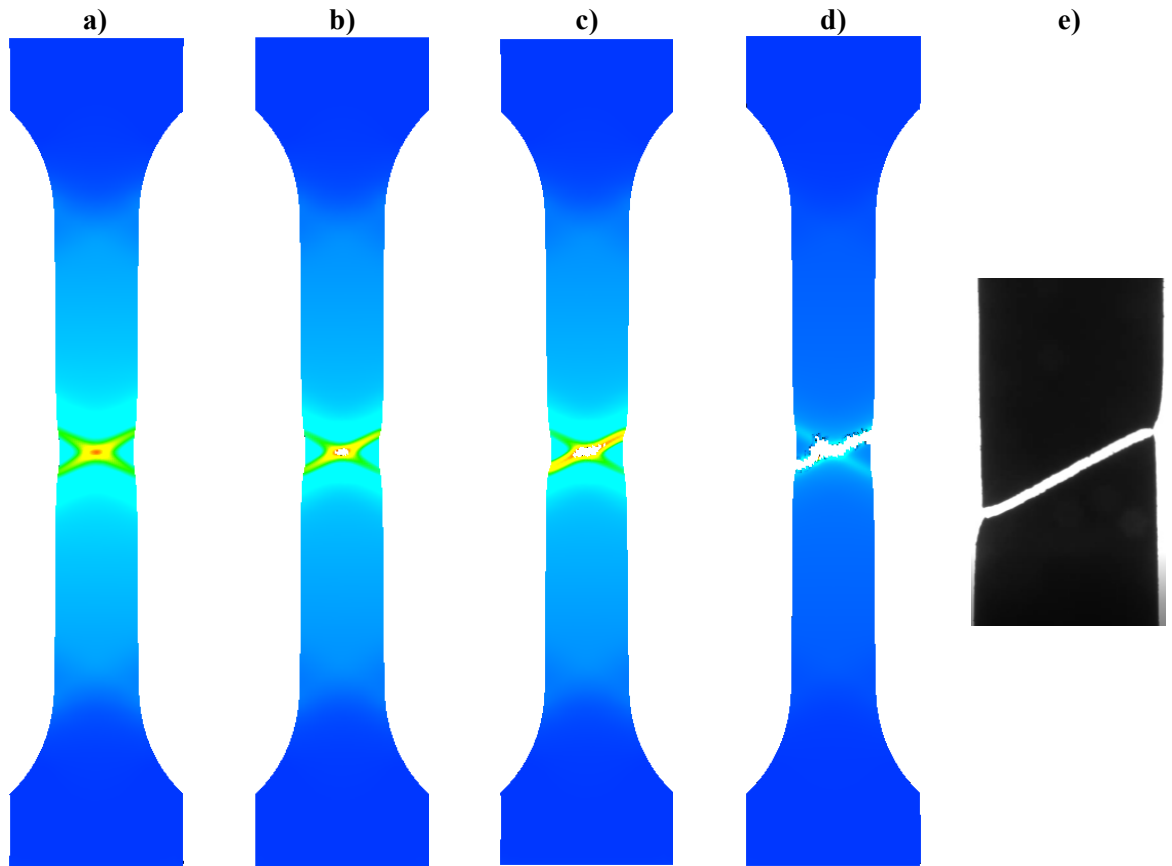


Figure 12. a) Strain localisation, b) fracture initiation, c) fracture evolution d) the final fracture predicted by the FEA and e) experimental fracture surface for uniaxial tensile test

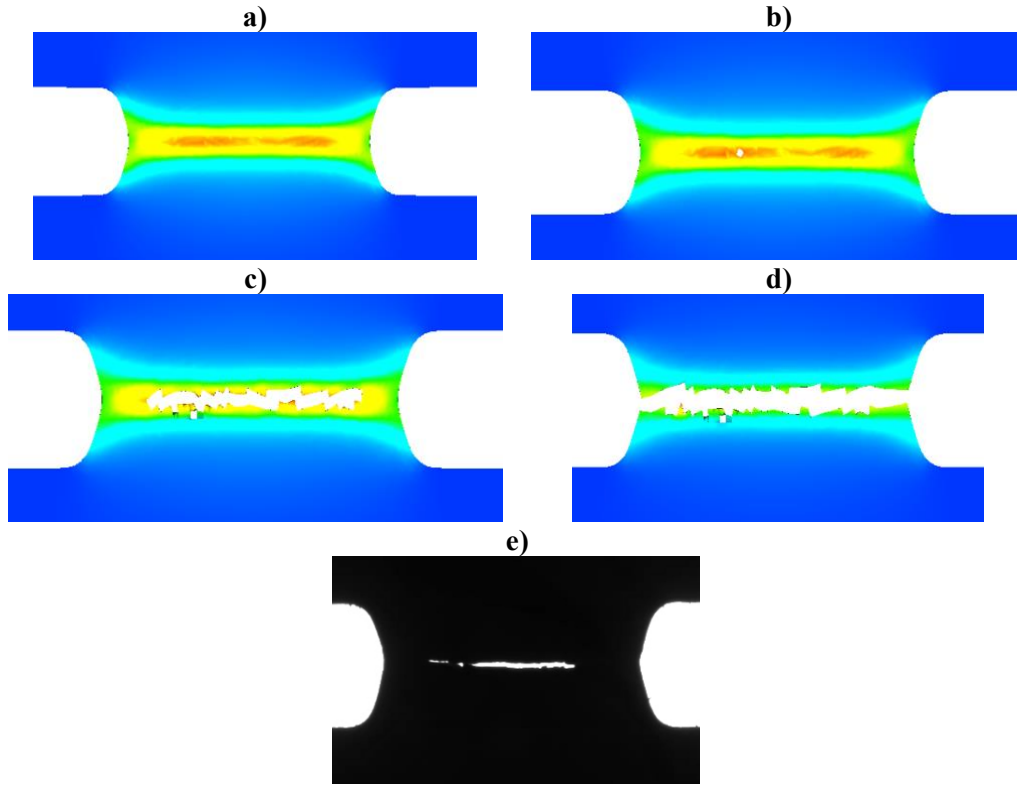


Figure 13. a) Strain localisation, b) fracture initiation, c) fracture evolution d) the final fracture predicted by the FEA and e) experimental fracture surface for plane strain test

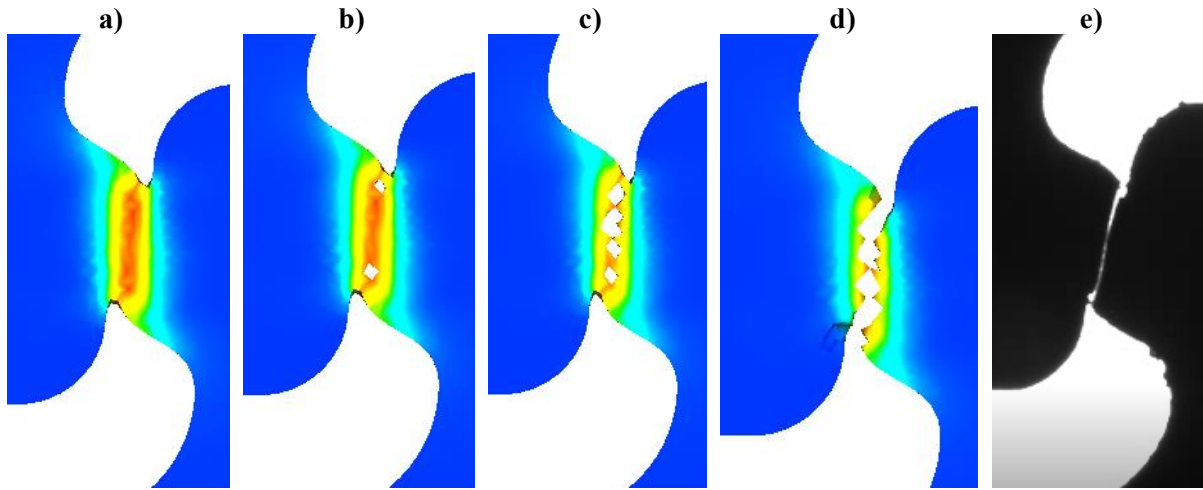


Figure 14. a) Strain localisation, b) fracture initiation, c) fracture evolution d) the final fracture predicted by the FEA and e) experimental fracture surface for shear test

B. Limiting Drawing Ratio Tests and Its Prediction by the FEA

LDR is known as the ratio of the largest blank diameter, which can be successfully deep drawn, to the punch diameter by which the sheet metal is deep drawn [29], [30]. The LDR of sheet metal is one of the indicators that show the sheet metal's formability. Simply, it shows how deep a sheet metal can be successfully drawn. The LDR could determine whether a forming process could be completed without

failure. Hence, its correct estimate by the FEA methods can indicate how well the damage model and the flow curve have been calibrated. The experimentally deep drawn DP800 steels have been shown in Figure 15. It can be seen that the DP800 steel could be deep drawn without failure up to 80 mm blank diameter, which corresponds to the LDR of 2.13. The sheet metal ruptured from the punch radius contact region, when the blank diameter was increased to 82 mm. It is known that the plane strain type of deformation strictly limits the forming limits. During the deep drawing process, plane strains form along the punch radius contact region, thus, failure occurs at this region of the sheet metal. In Figure 16., the deep drawing simulations of the DP800 steel can be seen. It can be seen that the sheet metal could be deep drawn up to 78 mm diameter without failure, corresponding to the LDR of 2.08. The sheet metal, ruptured from the punch radius contact region, when the blank diameter was increased to 80 mm. Thus, it is seen that the created FEA model has been conservative in its LDR estimation. The error between the experimental LDR and the FEA has been noted to be 2.35%. Hence, it is seen that the FEA model has been able to estimate the LDR precisely.



Figure 15. Experimentally deep drawn DP800 steels

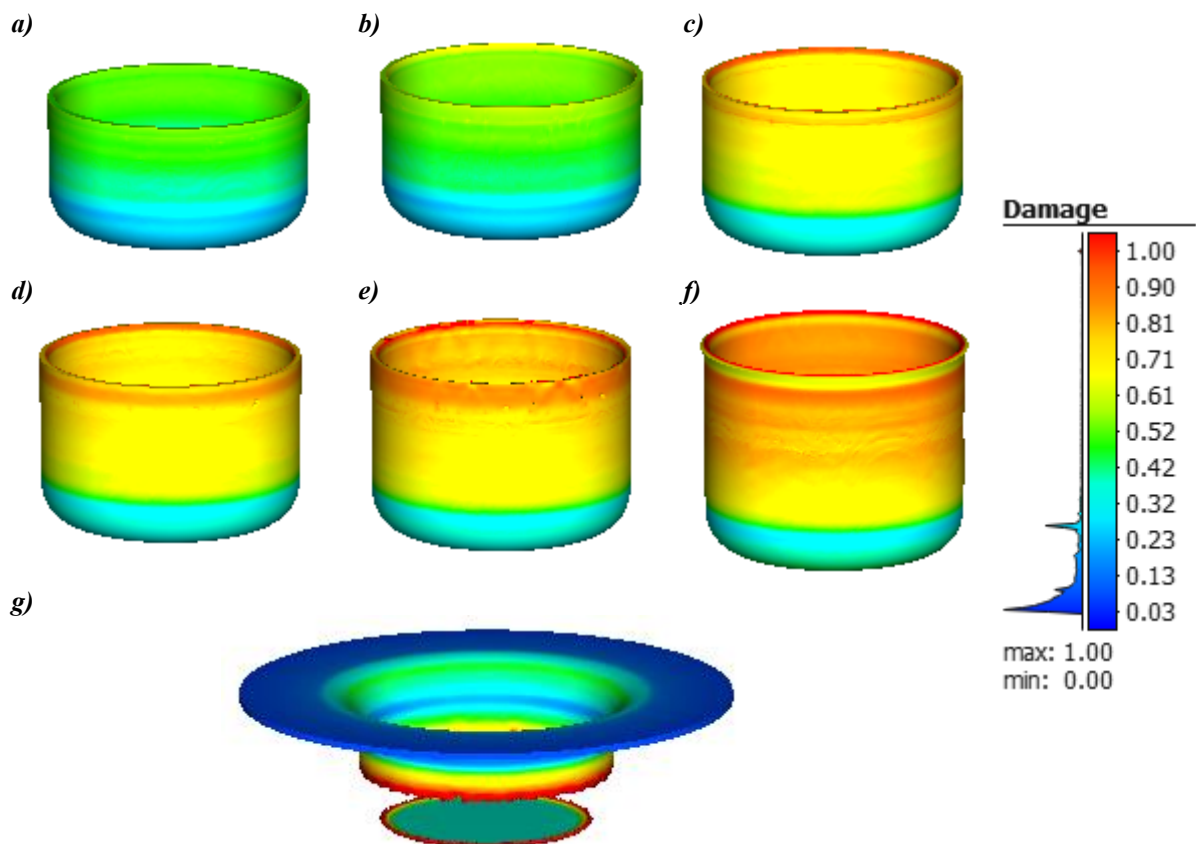


Figure 16. Deep drawing simulations of the DP800 steel

C. Thickness Distributions

In many forming processes, such as deep drawing, stamping or bending, the thickness of the formed body is desired to be uniformly distributed [31]–[33]. This uniform distribution of thickness is especially important when the formed part is expected to respond to the external forces similarly for each region of the part. If excessive thinning occurs during the forming stage of the part, a fracture is likely to form at this region of the part when it is in service. Thus, it is of paramount importance that excessive thinning does not occur, and that the thickness is uniformly distributed during the forming stage. In Figure 17., the measured and the predicted thickness distributions are shown. It can be seen that the parts have started thinning after the 2nd measurement point and that the amount of thinning has increased with the increase in the blank diameter. The minimum thickness has occurred at the 4th measurement point, which is the area where the sheet metal is exerted to plane strain deformation. As shown in Figure 17.a, the FEA has predicted a similar thickness distribution for each blank diameter. The percentage error between the predicted and the measured thickness is shown in Figure 18. It can be seen that the error values have been smaller than 6% and that the largest error has been 5.79% for 76 mm blank diameter.

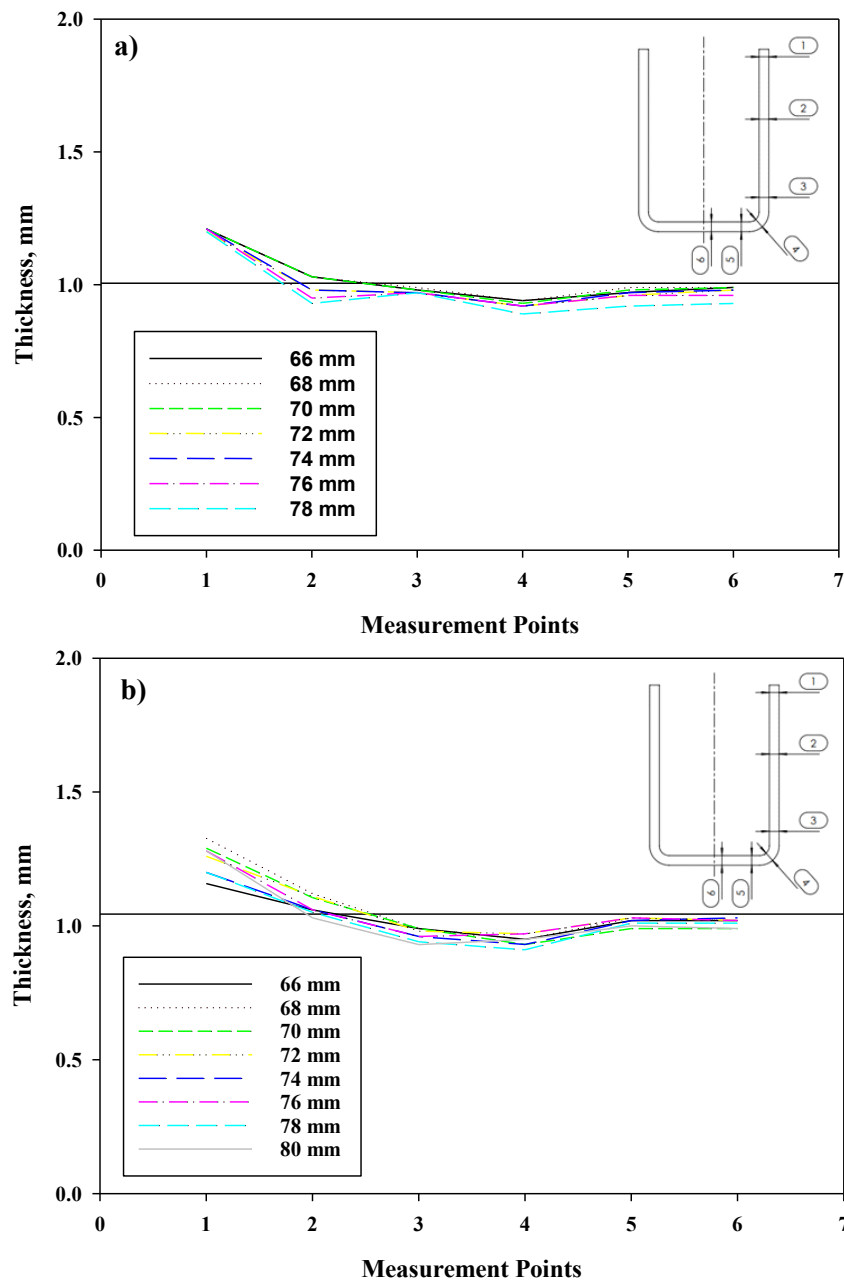


Figure 17. a) Predicted thickness distributions and **b)** experimental thickness distributions of the deep drawn parts

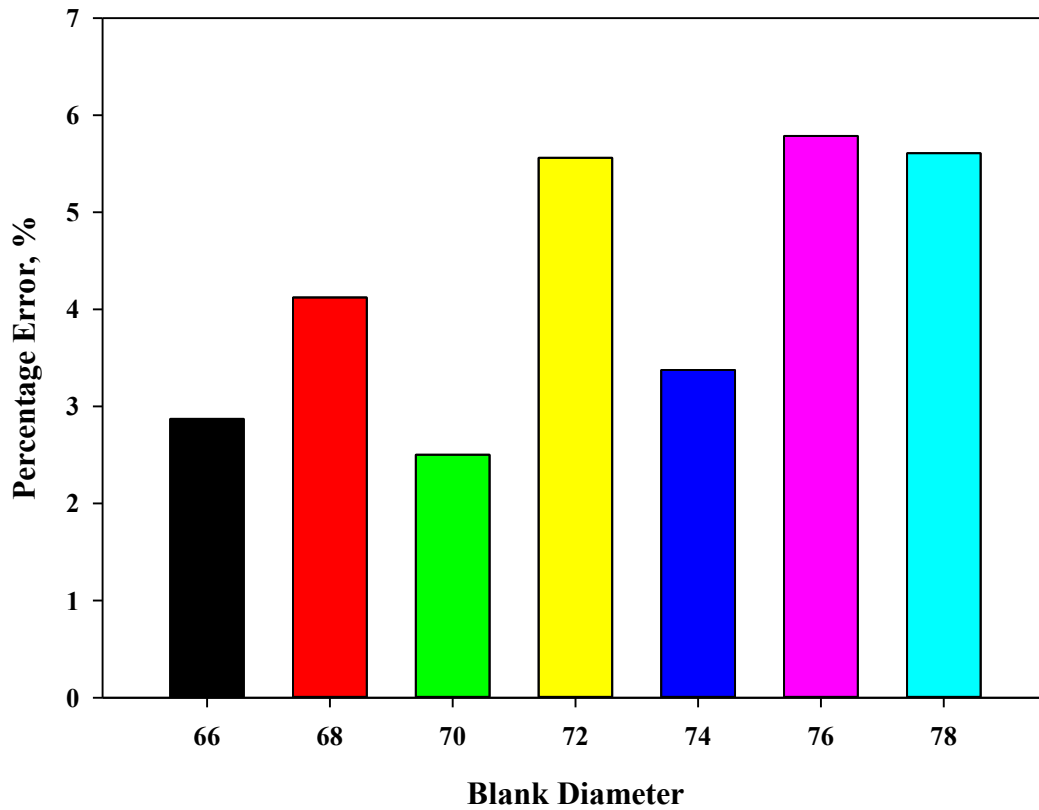


Figure 18. The percentage error level of the prediction of blank thickness for each blank diameter

IV. CONCLUSION

In this study, deep drawing experiments have been carried out for DP800 steel for different blank diameters to determine the LDR. Additionally, the LDR has been predicted by FEA using the Modified Mohr-Coulomb damage model. The main conclusions that can be drawn from the study are listed below:

- The calibrated Modified Mohr-Coulomb damage model have been able to precisely predict the final fracture displacements for uniaxial, plane strain and shear test specimens.
- The calibrated Hollomon hardening model has been successful in its force – displacement predictions for uniaxial, plane strain and shear test specimens.
- The LDR of DP800 steel have been experimentally found to be 2.13.
- The FEA model has predicted the LDR as 2.08, which is only 2.35% off from the experimentally obtained LDR
- The FEA model has been able to predict the experimentally measured thickness distribution under 6% error.

V. REFERENCES

- [1] S. Mahabunphachai and M. Koç, "Investigations on forming of aluminum 5052 and 6061 sheet alloys at warm temperatures," *Mater. Des.*, vol. 31, no. 5, pp. 2422–2434, 2010, doi: <https://doi.org/10.1016/j.matdes.2009.11.053>.
- [2] H. Lim, M. G. Lee, J. H. Sung, J. H. Kim, and R. H. Wagoner, "Time-dependent springback of advanced high strength steels," *Int. J. Plast.*, vol. 29, no. 1, pp. 42–59, 2012, doi: [10.1016/j.ijplas.2011.07.008](https://doi.org/10.1016/j.ijplas.2011.07.008).
- [3] P. Chen and M. Koç, "Simulation of springback variation in forming of advanced high strength steels," *J. Mater. Process. Technol.*, vol. 190, no. 1–3, pp. 189–198, 2007, doi: [10.1016/j.jmatprotec.2007.02.046](https://doi.org/10.1016/j.jmatprotec.2007.02.046).
- [4] W. Gan, S. S. Babu, N. Kapustka, and R. H. Wagoner, "Microstructural effects on the springback of advanced high-strength steel," *Metall. Mater. Trans. A*, vol. 37, pp. 3221–3231, 2006.
- [5] S. Panich, F. Barlat, V. Uthaisangskuk, S. Suranuntchai, and S. Jirathearanat, "Experimental and theoretical formability analysis using strain and stress based forming limit diagram for advanced high strength steels," *Mater. Des.*, vol. 51, pp. 756–766, 2013, doi: <https://doi.org/10.1016/j.matdes.2013.04.080>.
- [6] Ö. N. Cora and M. Koç, "Promises and Problems of Ultra/Advanced High Strength Steel (U/AHSS) Utilization in Automotive Industry," *7th Automot. Technol. Congr. (OTEKON 2014)*, no. November, pp. 1–8, 2014, doi: [10.13140/2.1.4725.0883](https://doi.org/10.13140/2.1.4725.0883).
- [7] N. Baluch, Z. M. Udin, and C. S. Abdullah, "Advanced high strength steel in auto industry: an overview," *Eng. Technol. Appl. Sci. Res.*, vol. 4, no. 4, pp. 686–689, 2014.
- [8] C. P. Singh and G. Agnihotri, "Study of deep drawing process parameters: a review," *Int. J. Sci. Res. Publ.*, vol. 5, no. 2, pp. 1–15, 2015.
- [9] N. Şen and Y. Baykal, "Development of car wishbone using sheet metal tearing process via the theory of inventive problem-solving (TRIZ) method," *J. Brazilian Soc. Mech. Sci. Eng.*, vol. 41, no. 10, pp. 1–10, 2019, doi: [10.1007/s40430-019-1884-7](https://doi.org/10.1007/s40430-019-1884-7).
- [10] Ö. Şenol, V. Esat, and H. Darendeliler, "Springback analysis in air bending process through experiment based artificial neural networks," *Procedia Eng.*, vol. 81, no. October, pp. 999–1004, 2014, doi: [10.1016/j.proeng.2014.10.131](https://doi.org/10.1016/j.proeng.2014.10.131).
- [11] M. Aghaei and S. Ziaei-Rad, "A micro mechanical study on DP600 steel under tensile loading using Lemaitre damage model coupled with combined hardening," *Mater. Sci. Eng. A*, vol. 772, no. September 2019, p. 138774, 2020, doi: [10.1016/j.msea.2019.138774](https://doi.org/10.1016/j.msea.2019.138774).
- [12] S. Abbasnejad Dizaji, H. Darendeliler, and B. Kaftanoğlu, "Effect of hardening models on different ductile fracture criteria in sheet metal forming," *Int. J. Mater. Form.*, vol. 9, no. 3, pp. 261–267, 2016, doi: [10.1007/s12289-014-1188-5](https://doi.org/10.1007/s12289-014-1188-5).
- [13] K. Ahn and M. H. Seo, "Effect of anisotropy and differential work hardening on the failure prediction of AZ31B magnesium sheet at room temperature," *Int. J. Solids Struct.*, vol. 138, pp. 181–192, 2018, doi: [10.1016/j.ijsolstr.2018.01.011](https://doi.org/10.1016/j.ijsolstr.2018.01.011).
- [14] R. Li, Z. Zheng, M. Zhan, H. Zhang, and Y. Lei, "A comparative study of three forms of an uncoupled damage model as fracture judgment for thin-walled metal sheets," *Thin-Walled Struct.*, vol. 169, no. August, p. 108321, 2021, doi: [10.1016/j.tws.2021.108321](https://doi.org/10.1016/j.tws.2021.108321).
- [15] R. Billardon and L. Moret-Bailly, "Fully coupled strain and damage finite element analysis of ductile fracture," *Nucl. Eng. Des.*, vol. 105, no. 1, pp. 43–49, 1987.
- [16] C. Soyarslan and A. E. Tekkaya, "A damage coupled orthotropic finite plasticity model for sheet metal forming: CDM approach," *Comput. Mater. Sci.*, vol. 48, no. 1, pp. 150–165, 2010.
- [17] C. Y. Tang, J. P. Fan, and T. C. Lee, "Simulation of necking using a damage coupled finite element method," *J. Mater. Process. Technol.*, vol. 139, no. 1–3, pp. 510–513, 2003.
- [18] P.-O. Bouchard, L. Bourgeon, S. Fayolle, and K. Mocellin, "An enhanced Lemaitre model formulation for materials processing damage computation," *Int. J. Mater. Form.*, vol. 4, pp. 299–315, 2011.
- [19] M. E. Korkmaz, "Verification of Johnson-Cook parameters of ferritic stainless steel by drilling

- process: experimental and finite element simulations,” *J. Mater. Res. Technol.*, vol. 9, no. 3, pp. 6322–6330, 2020.
- [20] H. Talebi-Ghadikolaee, H. Moslemi Naeini, M. J. Mirnia, M. A. Mirzai, S. Alexandrov, and H. Gorji, “Experimental and numerical investigation of failure during bending of AA6061 aluminum alloy sheet using the modified Mohr-Coulomb fracture criterion,” *Int. J. Adv. Manuf. Technol.*, vol. 105, pp. 5217–5237, 2019.
 - [21] M. B. Gorji and D. Mohr, “Predicting shear fracture of aluminum 6016-T4 during deep drawing: Combining Yld-2000 plasticity with Hosford–Coulomb fracture model,” *Int. J. Mech. Sci.*, vol. 137, pp. 105–120, 2018.
 - [22] Y. Bao, “Dependence of ductile crack formation in tensile tests on stress triaxiality, stress and strain ratios,” *Eng. Fract. Mech.*, vol. 72, no. 4, pp. 505–522, 2005.
 - [23] T. Güzelderen and H. Darendeliler, “Effects of triaxiality and lode parameter on deep drawing process,” *Mater. Res. Proc.*, vol. 41, 2024.
 - [24] J. Mulder, H. Vegter, H. Aretz, S. Keller, and A. H. Van Den Boogaard, “Accurate determination of flow curves using the bulge test with optical measuring systems,” *J. Mater. Process. Technol.*, vol. 226, pp. 169–187, 2015.
 - [25] A. F. Ávila and E. L. S. Vieira, “Proposing a better forming limit diagram prediction: a comparative study,” *J. Mater. Process. Technol.*, vol. 141, no. 1, pp. 101–108, 2003, doi: [https://doi.org/10.1016/S0924-0136\(03\)00162-6](https://doi.org/10.1016/S0924-0136(03)00162-6).
 - [26] S. P. S. S. Sivam, N. Harshavardhana, and R. Rajendran, “Artificial Neural Network prediction of forming limit diagram for directionally-rolled, size scaled copper strips,” *Proc. Inst. Mech. Eng. Part C J. Mech. Eng. Sci.*, vol. 238, no. 8, pp. 3299–3307, 2024, doi: 10.1177/09544062231184396.
 - [27] A. J. Martínez-Donaire, M. Borrego, D. Morales-Palma, G. Centeno, and C. Vallengano, “Analysis of the influence of stress triaxiality on formability of hole-flanging by single-stage SPIF,” *Int. J. Mech. Sci.*, vol. 151, pp. 76–84, 2019.
 - [28] T. Sjöberg, S. Marth, J. Kajberg, and H.-Å. Häggblad, “Experimental characterisation of the evolution of triaxiality stress state for sheet metal materials,” *Eur. J. Mech.*, vol. 66, pp. 279–286, 2017.
 - [29] D.-K. Leu, “Prediction of the limiting drawing ratio and the maximum drawing load in cup-drawing,” *Int. J. Mach. Tools Manuf.*, vol. 37, no. 2, pp. 201–213, 1997.
 - [30] D. Van Dinh, S. Van Nguyen, A. N. Pham, L. Van Nguyen, and V. D. Do, “Investigation and establishment of rational geometric factors of die in the deep drawing without a blank holder,” *EUREKA Phys. Eng.*, no. 1, pp. 105–115, 2024.
 - [31] M. Colgan and J. Monaghan, “Deep drawing process: analysis and experiment,” *J. Mater. Process. Technol.*, vol. 132, no. 1–3, pp. 35–41, 2003.
 - [32] W. Sun, W. Liu, and S. Yuan, “Suppressing wrinkles in thin-walled dome parts: A novel deep drawing method with active stress control,” *J. Mater. Process. Technol.*, vol. 324, p. 118249, 2024.
 - [33] A. Taşkın and C. G. Dengiz, “Experimental and numerical optimization of deep drawing process parameters for square medical container design with the Taguchi method,” *Int. J. Adv. Manuf. Technol.*, vol. 132, no. 5, pp. 2643–2659, 2024.



Düzce University Journal of Science & Technology

Research Article

Performance Evaluation Of Image Recognition Algorithms On Marine Vessels And Optimum Parameter Selection

Cansu CANBOLAT^a, Yasemin ATILGAN ŞENGÜL^b
 Ahmet Yekta KAYMAN^c

^a Information Security Technology Program, Vocational School, Istanbul Bilgi University, Istanbul, TURKEY

^b Department of Industrial Engineering, Faculty of Engineering, Dogus University, Istanbul, TURKEY

^c Department of Industrial Engineering, Faculty of Engineering, Dogus University, Istanbul, TURKEY

* Sorumlu yazarın e-posta adresi: cansu.canbolat@bilgi.edu.tr

DOI: 10.29130/dubited.1543061

ABSTRACT

Today, advancements in sensor technology, image processing models, and deep neural network methods have driven significant progress in the field of autonomous driving. This dynamic area has attracted substantial attention, with numerous studies being conducted across both academia and the private sector; hence studies specifically focused on the safe driving of driverless vehicles are still very limited. The basis of the studies conducted was created for land vehicles, and the data sets created for the operation of artificial intelligence models were prepared in this context. In this study, the algorithms used for autonomous driving were tested using the original data set created from objects on the sea to optimize the navigation of sea vehicles on the sea. Image processing methods have recently gained great importance in terms of recognizing vehicles on the sea and providing autonomous driving. In this study, a high-resolution and wide-ranging original data set consisting of 44965 objects sea objects was developed to identify objects on the sea. With this dataset, image processing technology was utilized to conduct analyses and optimizations for the recognition and classification of objects on the sea. Efforts were made to identify the most effective model among various alternatives. The study aims to detect and classify objects on the sea surface from long distances (over 1000 meters), ensuring the safe operation of sea vehicles and providing decision support. To enable the successful real-time identification of the created dataset, it was categorized into six distinct classes. As a result of the classification process, data labeling was performed according to 6 classes: Cargo_Ship, Tanker_Ship, RoRo/Ferry/Passenger, Boats, Tug_Boats, Speciality_Vessels. The created data set was tested with the most common real-time recognition models, SSD, Faster R-CNN, EfficientDet algorithms under the TensorFlow library. Results were obtained according to 6 different output parameter values, AP-50, AP-75, Av. Recall, F1-50, F1-75 and L/TL, on the models. According to the obtained results, SSD Mobilnet v1 was determined as the most successful algorithm.

Keywords: Marine, Vehicle detection, Image processing, Deep neural network, Autonomous driving

Deniz Taşıtları Üzerinde Görüntü Tanıma Algoritmalarının Performans Değerlendirmesi Ve Optimum Parametre Seçimi

ÖZET

Günümüzde gelişen sensör teknolojisi, görüntü işleme modelleri ve derin sinir ağları yöntemleri ile otonom sürüş alanında da önemli gelişmeler yaşanmakta ve hem özel sektörde hem de akademide bu yönde çeşitli çalışmalar gerçekleştirilmektedir. Sürücüsüz araçların güvenli sürüşüne yönelik bu çalışmalar henüz çok kısıtlıdır. Yapılan çalışmaların temeli kara taşıtları için oluşturulmuş, yapay zekâ modellerinin çalıştırılması için oluşturulan veri setleri bu bağlamda hazırlanmıştır. Bu çalışmada otonom sürüş için kullanılan algoritmalar deniz taşıtlarının deniz üzerinde seyrederken optimize edilmesi için deniz üzerindeki nesnelerden oluşturulan orijinal veri seti kullanılarak test edilmiştir. Görüntü işleme metotları, deniz üzerindeki taşıtların tanınması ve otonom sürüş sağlanması açısından son zamanlarda büyük önem kazanmıştır. Bu çalışmada, deniz üzerindeki nesneleri tanımlamak için, deniz üzerindeki nesnelerden oluşan 44965 adetlik yüksek çözünürlüklü ve geniş kapsamlı orijinal veri seti oluşturulmuştur. Bu veri seti ile deniz üzerindeki nesnelerin tanınma ve sınıflandırılmasına yönelik görüntü işleme teknolojisi ile analiz ve optimizasyonlar yapılarak, modeller arasında en iyi model belirlenmeye çalışılmıştır. Deniz yüzeyindeki nesneleri, uzak mesafeden (1000m+) tespit edilip sınıflandırılması, deniz araçları için güvenli kullanım oluşturulması ve karar desteği sağlanması hedeflenmektedir. Oluşturulan veri setinin gerçek zamanlı ortamda başarılı şekilde tanımlanabilmesi için veri seti 6 adete sınıflandırılmıştır. Sınıflandırma işlemi sonucunda oluşturulan; Cargo_Ship, Tanker_Ship, RoRo/Ferry/Passenger, Boats, Tug_Boats, Speciality_Vessels olmak üzere 6 adete sınıfa göre veri etiketleme işlemi yapılmıştır. Oluşturulan veri seti, en yaygın gerçek zamanlı tanıma modelleri olan, TensorFlow kütüphanesi altındaki SSD, Faster R-CNN, EfficientDet algoritmaları ile test edilmiştir. Modeller üzerinde de AP-50, AP-75, Av. Recall, F1-50, F1-75 ve L/TL olmak üzere 6 farklı çıktı parametresi değerine göre sonuçlar elde edilmiştir. Elde edilen sonuçlara göre, SSD Mobilnet v1 en başarılı algoritma olarak tespit edilmiştir.

Anahtar Kelimeler: Deniz, aracı tespiti, Görüntü işleme, Derin sinir ağı, Otonom sürüş

I. INTRODUCTION

Today, various research and developments are being carried out for the safe driving of vehicles, but these studies are mostly focused on land vehicles. Studies are also being carried out for the autonomous driving of sea vehicles, but it has been observed that studies have not yet been conducted with a sufficient data set. Interest in autonomous vehicles is increasing worldwide. The need for development in this technology is clearly seen [1]. In the field of autonomous vehicles, there are also studies on automatic collision avoidance and autonomous travel and route planning.

It is seen that the studies in these areas are increasing and a need for a larger data set arises. In the literature, there are studies showing that navigation applications in marine systems using only image data can be used to navigate without hitting obstacles while other systems such as GPS and radar are disabled [2]. Similarly, an autonomous vehicle that can be used effectively for high-speed vehicles and complex interactions with the environment with a dynamic motion planning approach has also been developed [3]. In autonomous vehicles, it has become possible to detect environmental objects and move without hitting them. The perception of environmental objects by autonomous vehicles plays a critical role, especially in dynamic and variable environmental conditions [4].

Object detection and recognition is one of the most important research topics in autonomous vehicle technologies. The main reason for this is that in autonomous driving, a control movement first detects the object and then identifies that object [1].

Object detection and recognition is a critical technology that allows autonomous vehicles to accurately identify their environment. Developments in object detection and recognition play an important role in improving the safety and performance of vehicles[5]. Recently, object recognition applications for real-life vehicles have developed considerably. In autonomous driving systems, in order to achieve a high accuracy rate of object recognition, accurate labeling of the data and a highly diverse dataset are required [6]. A good dataset is one that contains all real-time conditions to the maximum extent and has a high number of object diversity.

Deep learning systems are based on very comprehensive calculations that mimic the functions of the human brain. In 1943, McCulloch and Pitts developed a model that imitates the thought process. This model is based on mathematics and algorithms called neural logic [7]. Deep learning systems have come to the fore in many areas such as voice recognition, image recognition, and natural language processing. Deep learning algorithms have provided significant performance increases, especially in areas such as speech recognition, computer vision, and natural language processing, by using large data sets and powerful computational methods [8]. Studies on deep learning systems include research on the ability to analyze by processing visual data [9]. The labeling of images, object identification, and object classification systems used by companies such as Facebook and Google have been realized with Deep Learning models[10]. Thanks to the application of deep learning technologies, autonomous vehicles have become safer and more efficient [11].

Within the scope of the study, deep learning and image processing based methods focusing on object detection in the literature were examined. The most popular of these methods are Yolo-V3, Yolo-V4 under the Darknet library and SSD, Faster R-CNN, EfficientDet models under the TensorFlow library were examined.

Yolo-V3 and Yolo-V4 under the Darknet library and SSD, Faster R-CNN and EfficientDet models under the TensorFlow library have achieved significant success in object detection and recognition systems today. Yolo-V3 is a widely used model for real-time object detection, especially by offering high accuracy and speed. Yolo-V3 is quite successful in terms of speed, as it can perform both classification and localization in a single network [12]. Yolo-V4, on the other hand, has achieved better results in larger data sets and high-resolution images. The efficiency of Yolo-V4 has become much faster as a result of the optimized architecture of the model and many improvements[13].

SSD (Single Shot MultiBox Detector) is a model designed for more efficient object detection. SSD offers the ability to detect objects at different scales and types, which makes the SSD model quite attractive for applications that require fast and accurate detection. SSD can quickly classify and locate each object using multiple detection boxes on the image [14].

Faster R-CNN is a model that accelerates object detection using region proposal networks (RPN). This model works much more efficiently than previous object detection models by greatly reducing the time required to determine a region. Due to this working system, Faster R-CNN exhibits a very high success rate in terms of both speed and accuracy [15]. EfficientDet stands out with its smaller model sizes and more efficient computational requirements. This model is especially suitable for mobile devices and systems with object detection under limited hardware conditions. It increases its usability on mobile devices and real-time applications [16].

Each of these models offers different advantages and application areas in object detection tasks, and each is used according to different needs and usage scenarios. For example, Yolo-V3 and Yolo-V4 stand out in real-time applications that require fast and efficient detection, while EfficientDet provides high efficiency on more limited hardware, and Faster R-CNN is suitable for situations where precision is critical. These differences allow each model to use its own special advantages in applications in object detection and recognition systems.

In this study, it is aimed to detect objects faster and more accurately. Since it is aimed to see the closest performance to real-time detection, SSD Mobilnet v1 algorithm was selected.

As a result of this study, it is anticipated that high accuracy will be achieved in the detection and classification of objects on the sea, and the knowledge and output obtained from the study will form the basis for decision support on the safe use of marine vehicles.

The other parts of the study are organized as follows; in Section II, the materials and methods used are explained, in Section III, the calculations and discussions are explained. In the last section, Section IV, the study is concluded.

II. MATERIALS AND METHODS

A. AUTONOMOUS VEHICLES

The technological progress of autonomous vehicles has accelerated, especially with the integration of artificial intelligence and deep learning methods, which has enabled the development of safer and more efficient driving systems [11]. In recent years, it has been observed that sensor technologies and data processing algorithms developed for autonomous vehicles have provided significant improvements in object perception and decision-making processes [1]. Autonomous vehicles are mechanisms that interpret the data they collect from their environment in order to move in physical environments, thanks to their motion systems, decision mechanisms, sensor systems and algorithms to perceive the environment [17]. The first experiments on autonomous driving started in the 1920s and the first prototypes emerged in the 1950s. In 1997, the Tsukuba Mechanical Engineering Laboratory in Japan developed the first truly autonomous vehicle [18].

B. OBJECT DETECTION AND OBJECT RECOGNITION

Object detection and object recognition, which are the most important elements of image processing applications, are important topics that have been studied for years [19]. Various algorithms and methods have been developed for object detection and recognition. There are popular libraries used in object detection and recognition. The most common libraries include YOLO, Single Shot Multibox Detector (SSD), Region Based Convolutional Networks (R-CNN), Fast R-CNN, Faster R-CNN and Mask R-CNN [20]. The success rate of object detection and classification is high accuracy detection and classification. One of the most important parameters for a good detection and classification model to be applied in real time is to create an efficient data set. The effect of the data set on the success rate of the model is quite large. In deep learning-based models, the model performance increases in direct proportion to the size and diversity of the data set [21]. The first condition for a good model is to pass through a good data set, and the success of the created model depends on creating a model suitable for the data set and training it.

Studies on object detection and classification argue that object detection in the marine environment that we aim to reach can approach the desired success [22].

C. DATA SET PREPARATION AND CLASSIFICATION

The data set used in the study consists of high-resolution photographs taken in the Bosphorus and different seas, created together with Massive Yacht Technologies. For the models to work more efficiently during the training phase, photographs of the same marine vehicles were taken from many different angles and the data set is consisting from 44965 pictures of marine vehicles originally created by Massive Yacht Technologies company for this purpose. Since the data set size is considered to be enough for the algorithms to run efficiently no more photographs were taken and added to the data set. The dataset is planned to be further expanded for future studies.. Classifying marine vessels plays a crucial role in ensuring maritime safety and managing traffic, with significant applications in both civilian and military sectors[23]. However, this task is more complex than other target recognition

problems due to the substantial variations in viewing angles, lighting conditions, and scale, in addition to the chaotic nature of the image background [24].

Convention on the International Regulations for Preventing Collisions at Sea (COLREGs) defines the rules and gives clear indication about passing, approaching, giving way and overtaking other boats and according to rule 18 of The lower most vessel on the list is the give way vessel, and must stay out of the way of vessels that are higher on the list. 1.Overtaken vessel (top priority), 2.Vessels not under command, 3.Vessels restricted in their ability to maneuver, 4.Vessels constrained by draft, 5.Fishing vessels engaged in fishing, with gear deployed, 6.Sailing vessels, 7. Power driven vessels [25].

Initially, 20 classes were identified in our study. These classes are given in Table 1. In order to achieve a higher success rate in a real-time recognition system, the more important point than the number of classes is the correct categorization of the classes. As the vehicle moves over the sea, it is aimed to recognize objects faster and more accurately. For this reason, the number of groups was reduced from 20 to 6 according to characteristics such as the right of way (passage priorities) and the speed limit, so that the autonomous device can drive safely without disrupting maritime traffic. The final form of the newly determined classes after the class merging process and the number of photographs in each category is given in Table 2.

Table 1. Initial Classes of Objects

Group	Category	Group	Category
1	Cargo Ship	11	Boat
2	Tanker Ship	12	Research Ship
3	RoRo	13	Rescue Ship
4	Cruise Ship	14	Buoy
5	Ferry	15	Sailboat
6	Passenger Boat	16	Yacht
7	Supply Ship	17	Jet Ski
8	Dredger Ship	18	Kayak
9	Tugboats	19	Military Ships
10	Fishing Ship	20	Coast Guard

Table 2. Number of Tagged Photos per each class

Group	Category	Quantity	Ratio
1	Cargo Ship	7082	15,75%
2	Tanker Ship	8292	18,44%
3	RoRo/Ferry/Passanger	8966	19,94%
4	Boats	7174	15,95%
5	Tug_Boats	7680	17,08%
6	Speciality_Vessels	5771	12,83%
Total		44965	

The Labellmg program was used to label all photos added to the data set according to their classes. A common resolution ratio was determined with the Labellmg Program and all images were labeled. Sample images of the data set are shown in Figure 1.



Figure 1. Sample images with different characteristics in the dataset

To start the training process, 14257 photos were selected from 44965 photos in the dataset and labeled in 6 categories. Since some photos in the dataset contain more than one marine vessel, a photo is labeled for different numbers of categories and because of this the total number of photos in the dataset and the total number of labels differ.

Table 3. Number of Tagged Photos per each category

Group	Category	Quantity	Ratio
1	Cargo Ship	2338	16,40%
2	Tanker Ship	2529	17,74%
3	RoRo/Ferry/Passanger	2568	18,01%
4	Boats	2353	16,50%
5	Tug_Boats	2532	17,76%
6	Speciality_Vessels	1937	13,59%
Total		14257	

D. TRAINING MODELS AND PARAMETERS

In the study, the classification of objects with SSD, Faster R-CNN, EfficientDet models under the TensorFlow library was tested on the created data set. In the study, 14257 images were used for training and 44965 images were used for performance measurements. In this paper, similar to the dataset division of the VisDrone2019 Challenge, we divided the entire dataset into training, validation, and testing sets, each containing 6471 samples, 548 samples, and 1610 samples and the sample images for training and testing are both set to the size of 640*640 gbi... Step number and batch size were given as input parameters to the models. As a result of the training, 6 output parameter results were obtained, namely AP-50, AP-75, Av. Recall, F1-50, F1-75 and L/TL. The success rates will be compared according to the obtained output parameters.

There are 4 possibilities for the prediction result in the trained models:

True Positive (TP): It is one of the possibilities that our model predicted correctly. An instance for which both predicted and actual values are positive. There is an object in the photo, the model detected an object..

True Negative (TN): It is one of the possibilities that our model predicted correctly. An instance for which both predicted and actual values are negative. There is no object in the photo, the model did not detect an object..

False Positive (FP): It is one of the possibilities that our model predicted incorrectly. An instance for which predicted value is positive but actual value is negative. There is no object in the photo, the model detected an object.

False Negative (FN): It is one of the possibilities that our model predicted incorrectly. An instance for which predicted value is negative but actual value is positive. There is an object in the photo, the model did not detect an object.

The parameters used to compare the performance rates of the models are given in Table 4.

Table 4. Parameters Compared in the Training Process

Parameters	
Response 1	AP-50
Response 2	AP-75
Response 3	Av. Recall
Response 4	F1-50
Response 5	F1-75
Response 6	L/TL

Average Precision (AP): AP50 and AP75 mean AP at 50% and 75% IoU threshold respectively.

Precision (P): Measures how accurate model predictions are.

$$Precision = \frac{TP}{(TP+FP)} \quad \text{Equation (1)}$$

Recall (R): Measures how well model finds all positives.

$$Recall = \frac{TP}{(TP+FN)} \quad \text{Equation (2)}$$

Harmonic Mean: F1 Score score is used when we need to find a balance between precision and recall. It is especially preferred for unequally distributed classes.

$$Harmonic\ Mean = \frac{2*P*R}{(P+R)} \quad \text{Equation (3)}$$

III. CALCULATIONS AND DISCUSSION

An experimental design model was established to optimize the values of AP50, AP75, Av.Recall, F1/50, F1/75 and L/TL for the determined (Efficientdet d0, Efficientdet d1, Efficientdet d2, Efficientdet d3, Efficientdet d4, F RCNN Inception, F RCNN Resnet 152, F RCNN Resnet101 v1, F RCNN Resnet50 v1, SSD Mobilnet v1, SSD Mobilnet v2, SSD Resnet 101, SSD Resnet 152, SSD Resnet50 algorithms with Batch Size 2, 4 and Run numbers (Run) 90, 130, 250 thousand. In the model, there are 2 input parameters, namely batch size and step number, and 6 output parameters, namely AP-50, AP-75, Av. Recall, F1-50, F1-75 and L/TL. is available. The experimental design created with the Design Expert program created the combinations that should be tried for the Batch size 2, 4 and Run 90, 130, 250 parameters for 14 algorithms. With the 53 combinations created by the program and that should be tried, instead of performing $14*2*3 = 84$ full factorial number of experiments, 63% of the required experiments were performed and 37% time was saved. Considering that each experiment lasts about 1 day, this saved about 37 days. The results of the 53 experiments performed on input parameters and 6 output parameters are given in Table 5. It is desired that the AP-50, AP-75, Av. Recall, F1-50, F1-75 values from the outputs are close to 1 and the L/TL value is close to 0.

Table 5. AP50, AP75, Av. Recall, F1/50, F1/75, L/TL Values of Algorithms

	Factor 1	Factor 2	Factor 3	Response 1	Response 2	Response 3	Response 4	Response 5	Response 6
Run	A:Run	B:BS	C:Algoritma	AP50	AP75	Av.Recall	F1/50	F1/75	L/TL
1	90	4	Efficientdet d0	0,665	0,476	0,628	0,646	0,542	0,704
2	90	2	F RCNN Inception	0,881	0,811	0,825	0,852	0,818	0,112
3	250	4	F RCNN Resnet50 v1	0,853	0,778	0,792	0,821	0,785	0,222
4	90	4	SSD Resnet 101	0,711	0,646	0,777	0,743	0,705	0,437
5	250	4	SSD Mobilnet v1	0,866	0,8	0,825	0,845	0,832	0,097
6	90	4	F RCNN Resnet 152	0,549	0,427	0,554	0,551	0,482	0,356
7	130	4	F RCNN Inception	0,9	0,832	0,84	0,87	0,836	0,102
8	250	2	Efficientdet d1	0,735	0,597	0,697	0,715	0,643	0,379
9	90	4	SSD Resnet 152	0,726	0,642	0,734	0,73	0,685	0,456
10	130	4	Efficientdet d4	0,823	0,73	0,754	0,787	0,742	0,348
11	130	2	Efficientdet d0	0,744	0,619	0,681	0,711	0,649	0,397
12	250	4	Efficientdet d0	0,722	0,66	0,724	0,747	0,69	0,394
13	250	2	F RCNN Inception	0,602	0,543	0,601	0,601	0,571	0,47
14	90	4	F RCNN Resnet50 v1	0,848	0,773	0,779	0,812	0,776	0,2
15	130	4	Efficientdet d4	0,823	0,73	0,754	0,787	0,742	0,348
16	130	2	F RCNN Resnet 152	0,481	0,391	0,507	0,494	0,441	0,422
17	130	4	Efficientdet d1	0,758	0,573	0,658	0,704	0,613	0,397
18	250	4	F RCNN Resnet 152	0,653	0,562	0,608	0,63	0,584	0,336
19	250	4	F RCNN Inception	0,425	0,305	0,487	0,454	0,375	0,593
20	250	4	SSD Resnet50	0,806	0,737	0,804	0,805	0,769	0,353
21	130	2	F RCNN Resnet101 v1	0,477	0,372	0,496	0,486	0,425	0,443
22	130	4	SSD Resnet 101	0,788	0,718	0,775	0,781	0,745	0,379
23	250	4	SSD Resnet 152	0,754	0,666	0,727	0,74	0,695	0,453
24	130	2	Efficientdet d3	0,781	0,673	0,717	0,748	0,694	0,369
25	250	4	Efficientdet d2	0,792	0,691	0,752	0,771	0,72	0,385
26	130	4	Efficientdet d1	0,758	0,573	0,658	0,704	0,613	0,397
27	90	4	Efficientdet d3	0,778	0,672	0,731	0,754	0,7	0,383
28	90	2	SSD Resnet 101	0,516	0,438	0,701	0,594	0,539	0,574
29	90	2	SSD Mobilnet v2	0,704	0,631	0,743	0,722	0,682	0,399
30	250	2	SSD Resnet 101	0,781	0,708	0,771	0,776	0,738	0,389
31	250	4	F RCNN Resnet101 v1	0,856	0,784	0,8	0,827	0,791	0,178
32	250	4	SSD Mobilnet v2	0,835	0,767	0,8	0,817	0,783	0,302
33	90	2	Efficientdet d4	0,749	0,629	0,708	0,728	0,666	0,382
34	250	4	Efficientdet d3	0,797	0,702	0,759	0,778	0,729	0,289
35	90	4	Efficientdet d2	0,674	0,56	0,689	0,681	0,618	0,548
36	250	2	SSD Mobilnet v2	0,759	0,681	0,765	0,762	0,721	0,357
37	130	2	Efficientdet d0	0,744	0,619	0,681	0,711	0,649	0,397
38	130	2	SSD Resnet 101	0,538	0,462	0,72	0,616	0,563	0,553
39	130	2	SSD Resnet 152	0,666	0,58	0,731	0,697	0,647	0,49
40	90	2	SSD Resnet50	0,435	0,357	0,684	0,532	0,469	0,656

41	130	2	SSD Mobilnet v1	0,777	0,712	0,779	0,778	0,744	0,478
42	130	4	SSD Mobilnet v2	0,814	0,75	0,789	0,801	0,769	0,325
43	250	2	Efficientdet d4	0,706	0,606	0,705	0,705	0,651	0,426
44	90	4	SSD Mobilnet v1	0,821	0,753	0,797	0,809	0,774	0,538
45	130	2	Efficientdet d3	0,781	0,673	0,717	0,748	0,694	0,369
46	90	2	Efficientdet d1	0,74	0,579	0,662	0,699	0,618	0,383
47	250	4	SSD Resnet 101	0,826	0,761	0,796	0,811	0,778	0,346
48	130	2	F RCNN Resnet101 v1	0,477	0,372	0,496	0,486	0,425	0,443
49	130	2	Efficientdet d2	0,594	0,463	0,647	0,619	0,54	0,517
50	90	4	SSD Resnet50	0,793	0,729	0,79	0,791	0,758	0,379
51	130	2	F RCNN Resnet50 v1	0,612	0,488	0,597	0,604	0,537	0,36
52	90	4	F RCNN Resnet101 v1	0,584	0,49	0,567	0,575	0,526	0,389
53	250	2	SSD Resnet50	0,806	0,737	0,804	0,805	0,769	0,353

When the performances of the algorithms need to be evaluated collectively in terms of multiple outputs, using direct output values is not appropriate for comparison, so the success ranks of the algorithms for each output were determined and according to this, the success rank values of each combination for 6 outputs according to the outputs for 53 trials are given in Table 6. According to the findings, the F RCNN Inception algorithm demonstrated the best performance when configured with a batch size of 4 and executed over 130,000 iterations. The optimal results were achieved across five key parameters: AP50, AP75, Average Recall, F1/50, and F1/75.. The performance of the same algorithm in batch size 2 and 90 thousand runs was generally in second place. But in contrast to this F RCNN Inception algorithm performs as the worst algorithm with 250 thousand runs. This inconsistency has brought the performance of this algorithm into doubt.

Another algorithm with the highest performance is the SSD Mobilnet v1 batch size 4 and 250 thousand runs, which came first for one output (L/TL), second for two outputs (Av. Recall, F1/75) and third for three outputs (AP50, AP75, F1/50).

Table 6. Success Rankings of Algorithms According to Parameters

Run	A:Run	B:BS	C:Algoritma	Rank 1	Rank 2	Rank 3	Rank 4	Rank 5	Rank 6
				AP50	AP75	Av. Recall	F1/50	F1/75	L/TL
1	90	4	Efficientdet d0	40	44	44	40	43	53
2	90	2	F RCNN Inception	2	2	2	2	3	3
3	250	4	F RCNN Resnet50 v1	5	5	10	5	5	6
4	90	4	SSD Resnet 101	35	27	15	26	22	38
5	250	4	SSD Mobilnet v1	3	3	2	3	2	1
6	90	4	F RCNN Resnet 152	46	48	49	48	48	16
7	130	4	F RCNN Inception	1	1	1	1	1	2
8	250	2	Efficientdet d1	32	34	35	31	35	23
9	90	4	SSD Resnet 152	33	28	24	28	28	42
10	130	4	Efficientdet d4	9	13	20	14	16	13
11	130	2	Efficientdet d0	29	31	38	32	32	34
12	250	4	Efficientdet d0	34	26	28	25	27	30
13	250	2	F RCNN Inception	43	41	46	45	41	43
14	90	4	F RCNN Resnet50 v1	6	6	13	7	8	5

15	130	4	Efficientdet d4	9	13	20	14	16	13
16	130	2	F RCNN Resnet 152	49	49	50	50	50	36
17	130	4	Efficientdet d1	25	37	41	35	38	34
18	250	4	F RCNN Resnet 152	41	39	45	41	40	10
19	250	4	F RCNN Inception	53	53	53	53	53	51
20	250	4	SSD Resnet50	13	11	4	10	10	15
21	130	2	F RCNN Resnet101 v1	50	50	51	51	51	40
22	130	4	SSD Resnet 101	18	16	16	16	14	23
23	250	4	SSD Resnet 152	27	25	27	27	24	41
24	130	2	Efficientdet d3	19	22	30	23	25	20
25	250	4	Efficientdet d2	17	20	22	20	21	27
26	130	4	Efficientdet d1	25	37	41	35	38	34
27	90	4	Efficientdet d3	22	24	25	22	23	26
28	90	2	SSD Resnet 101	48	47	34	46	45	50
29	90	2	SSD Mobilnet v2	37	29	23	30	29	35
30	250	2	SSD Resnet 101	19	18	17	19	18	29
31	250	4	F RCNN Resnet101 v1	4	4	6	4	4	4
32	250	4	SSD Mobilnet v2	7	7	6	6	6	8
33	90	2	Efficientdet d4	28	30	32	29	30	24
34	250	4	Efficientdet d3	15	19	19	17	19	7
35	90	4	Efficientdet d2	38	40	36	39	36	48
36	250	2	SSD Mobilnet v2	24	21	18	21	20	17
37	130	2	Efficientdet d0	29	31	38	32	32	34
38	130	2	SSD Resnet 101	47	46	29	43	42	49
39	130	2	SSD Resnet 152	39	35	25	38	34	45
40	90	2	SSD Resnet50	52	52	37	49	49	52
41	130	2	SSD Mobilnet v1	23	17	13	17	15	44
42	130	4	SSD Mobilnet v2	12	10	12	12	10	9
43	250	2	Efficientdet d4	36	33	33	34	31	37
44	90	4	SSD Mobilnet v1	11	9	8	9	9	47
45	130	2	Efficientdet d3	19	22	30	23	25	20
46	90	2	Efficientdet d1	31	36	40	37	36	26
47	250	4	SSD Resnet 101	8	8	9	8	7	11
48	130	2	F RCNN Resnet101 v1	50	50	51	51	51	40
49	130	2	Efficientdet d2	44	45	43	42	44	46
50	90	4	SSD Resnet50	16	15	11	13	13	23
51	130	2	F RCNN Resnet50 v1	42	43	47	44	46	18
52	90	4	F RCNN Resnet101 v1	45	42	48	47	47	29
53	250	2	SSD Resnet50	13	11	4	10	10	15

In Figure 2 the minimum and maximum rank values obtained by each combination in terms of 6 outputs are shown, and the narrower these ranges are, the more stable the performance of the algorithm in terms of outputs can be said to be. For example, the rank values obtained in the Batch size 4 and 130 thousand run parameters of the F RCNN Inception algorithm were always in the 1st and 2nd places for 6 outputs, and the range value was 1, which can be interpreted as the algorithm being generally successful.

Similarly, while F RCNN Resnet 152 was generally in the 39th - 45th places in the Batch size 4 and 250 thousand runs, it was in the 10th place for the L/TL output, and it does not seem to be consistent in terms of performance.

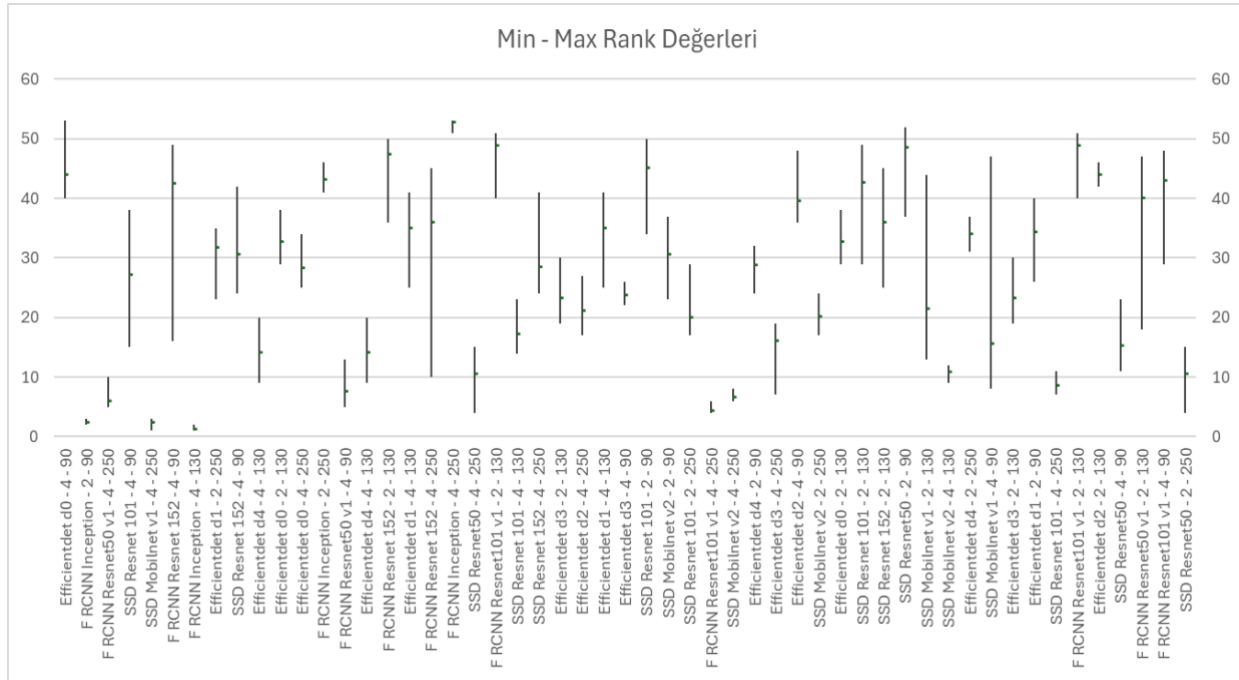


Figure 2. Range of Rank Values of Algorithms According to Parameters

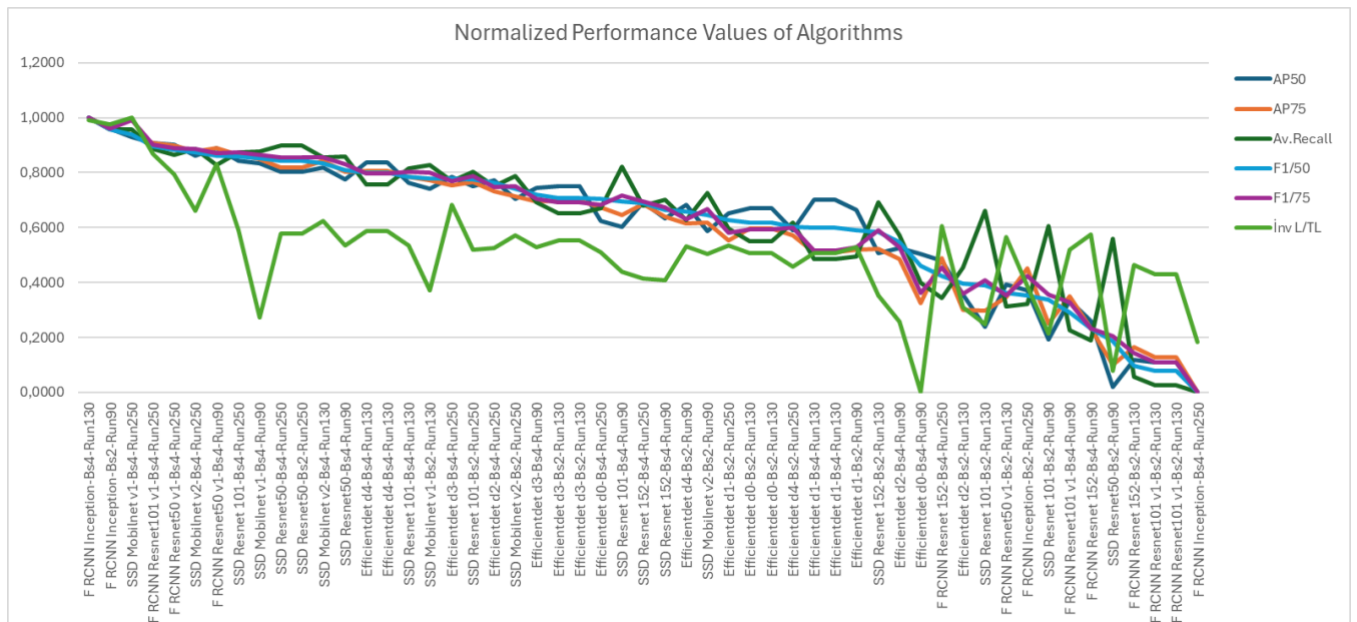


Figure 3. Normalized AP50, AP75, Av. Recall, F1/50, F1/75, inverse L/TL Values of Algorithms

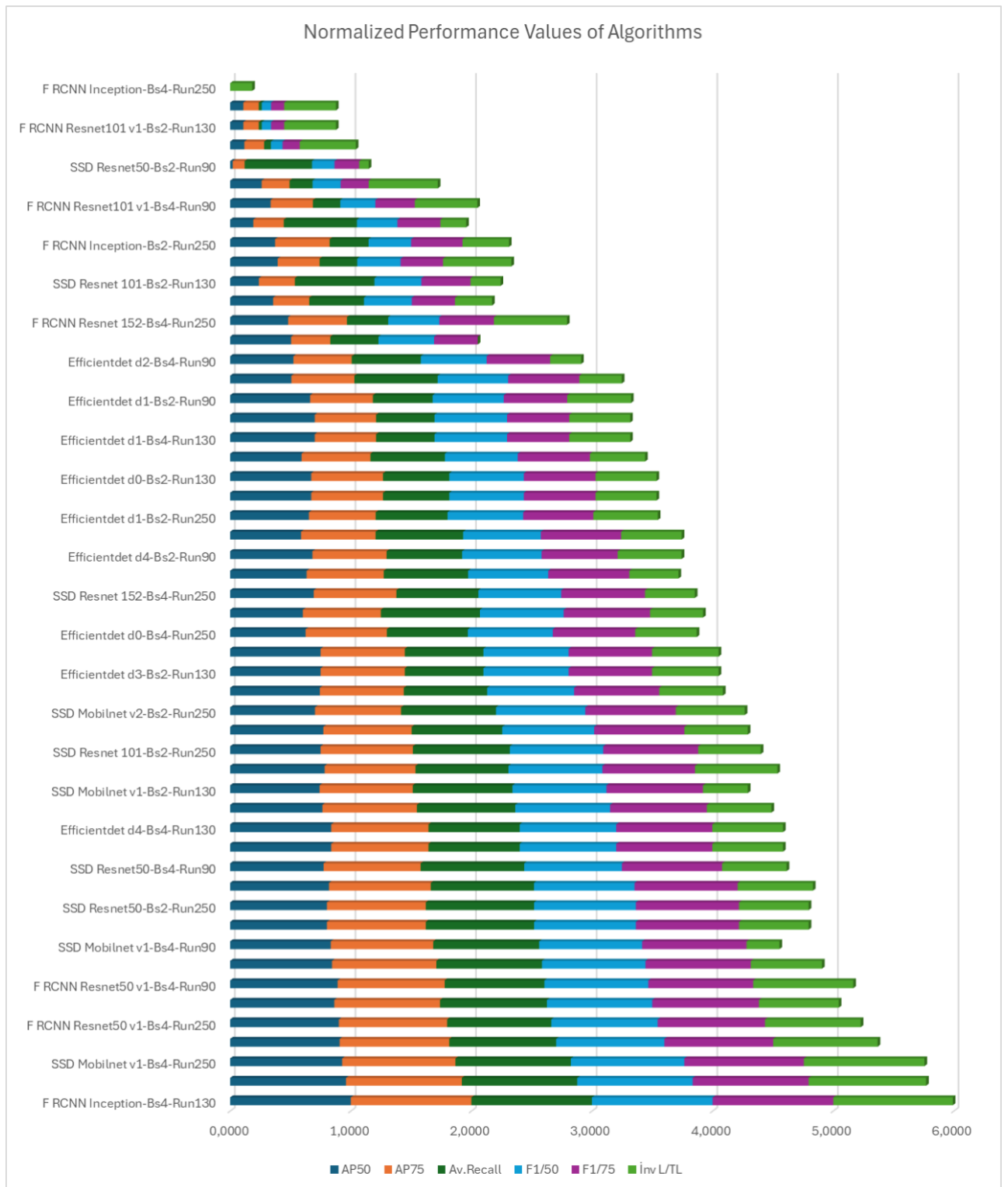


Figure 4. Cumulative Normalized AP50, AP75, Av. Recall, F1/50, F1/75, inversre L/TL Values of Algorithms (higher is better)

C:Algoritma

- SSD Resnet50
- SSD Resnet 101
- SSD Resnet 152
- SSD Mobilnet v1
- SSD Mobilnet v2
- F RCNN Resnet50 v1
- F RCNN Resnet101 v1
- F RCNN Resnet 152
- F RCNN Inception
- Efficientdet d0
- Efficientdet d1
- Efficientdet d2
- Efficientdet d3
- Efficientdet d4

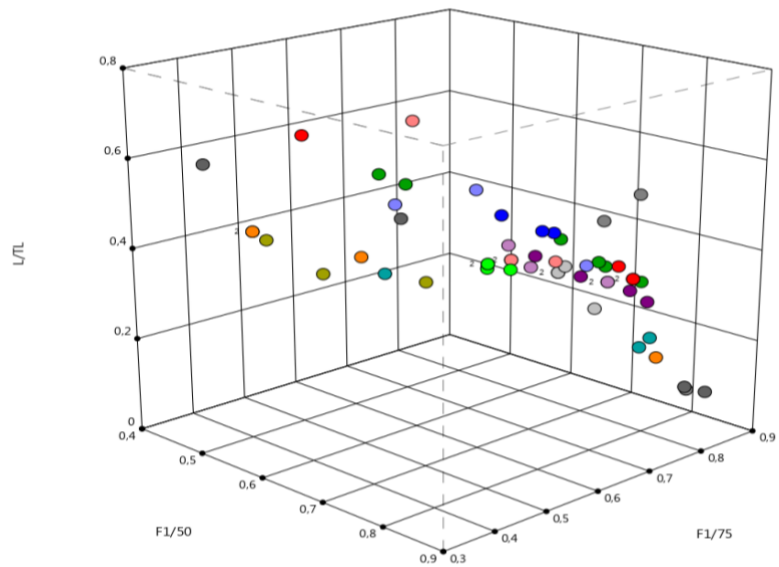


Figure 5. F1/50, F1/75 and L/TL Values of Algorithms

When the proposed Response 4 F1/50 and Response 5 F1/75 are evaluated together to compare the algorithms on the current problem, the order of SSD Mobilnet v1, F RCNN Resnet101 v1, F RCNN Resnet50 v1 does not change.

Correlation: Undefined

Color points by level of

B:Algoritma

- SSDR50
- SSDR101
- SSDR152
- SSDMv1
- SSDMv2
- FRCNNR50v1
- FRCNNR101v1
- FRCNNR152
- FRCNNi
- EFFd0
- EFFd1
- EFFd2
- EFFd3
- EFFd4

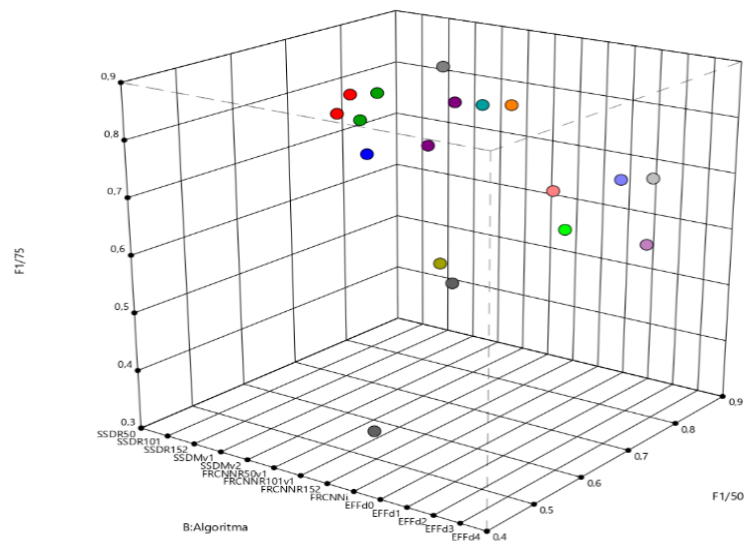


Figure 6. F1/50 and F1/75 Values of Algorithms

The overall performance of various algorithm classes is outlined in Table 6, with SSD MobilNet v1 identified as the top-performing algorithm for this dataset.

Algorithms	Average AP50	Average AP75	Av.Recall	Average F1/50	Average F1/75	Average L/TL
Efficientdet d0	0,7188	0,5935	0,6785	0,7038	0,6325	0,4730
Efficientdet d1	0,7478	0,5805	0,6688	0,7055	0,6218	0,3890
Efficientdet d2	0,6867	0,5713	0,6960	0,6903	0,6260	0,4833
Efficientdet d3	0,7843	0,6800	0,7310	0,7570	0,7043	0,3525
Efficientdet d4	0,7753	0,6738	0,7303	0,7518	0,7003	0,3760
F RCNN Inception	0,7020	0,6228	0,6883	0,6943	0,6500	0,3193
F RCNN Resnet 152	0,5610	0,4600	0,5563	0,5583	0,5023	0,3713
F RCNN Resnet101 v1	0,5985	0,5045	0,5898	0,5935	0,5418	0,3633
F RCNN Resnet50 v1	0,7710	0,6797	0,7227	0,7457	0,6993	0,2607
SSD Mobilnet v1	0,8213	0,7550	0,8003	0,8107	0,7833	0,3710
SSD Mobilnet v2	0,7780	0,7073	0,7743	0,7755	0,7388	0,3458
SSD Resnet 101	0,6933	0,6222	0,7567	0,7202	0,6780	0,4463
SSD Resnet 152	0,7153	0,6293	0,7307	0,7223	0,6757	0,4663
SSD Resnet50	0,7100	0,6400	0,7705	0,7333	0,6913	0,4353
Average	0,7186	0,6232	0,7091	0,7125	0,6613	0,3915

Table 7. Average AP50, AP75, Av. Recall, F1/50, F1/75, L/TL Values of Algorithm Classes

The use of the ranking method according to the outputs to compare the algorithms on the current problem is suitable for obtaining a dominant option from the results of the experiments made for the current problem, but the limitation of this method is that it depends on the evaluation of the researcher only on the results obtained with the current parameter combinations and under conditions where all outputs are evaluated as equally important. However, the optimization module of the Design expert program was used to obtain the optimum result with fewer experiments without trying all possible factor combinations, which is the purpose of using the experimental design.

When the optimization module is run and the analysis is made by selecting AP50, AP75, Av.Recall, F1/50, F1/75 for the maximum, L/TL for the minimum and F1/50 and F1/75 for the highest (5) importance, AP50, AP75, Av.Recall and L/TL for the lowest importance (1), the program estimates that the most ideal solution will occur when the parameters of the SSD Mobilnet V1 algorithm are BS=2 and Run=250 thousand. This situation supports the choice of SSD Mobilnet V1, which also gave good results in the ranking findings.

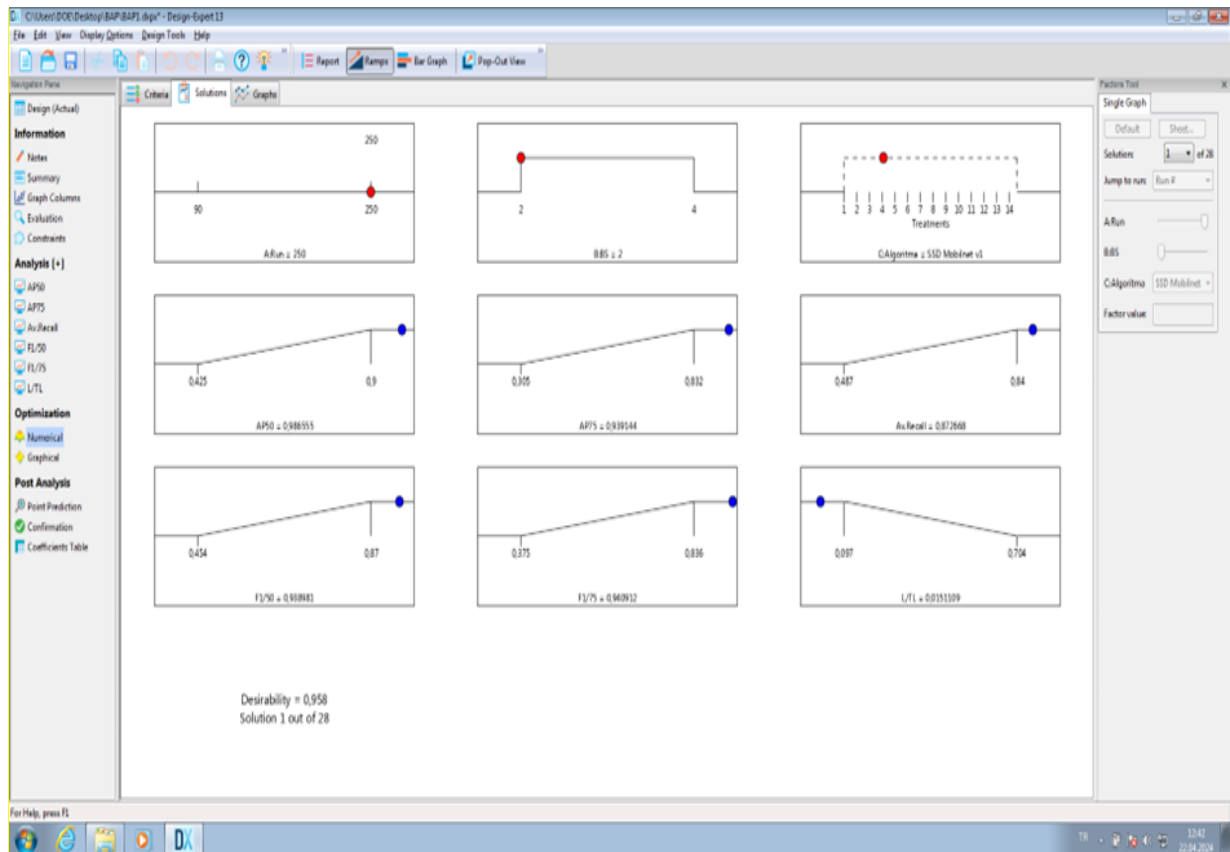


Figure 7. Design Expert Program Optimization Result



Figure 8. Desirability Levels of Optimization Results for SSD Mobilnet V1, BS=2, Run=250 Thousand in Terms of Output

IV. CONCLUSION

Object detection plays an important role in all autonomous land, sea and air vehicles. Image processing models are the cornerstone of providing autonomous control in vehicles. To test image processing models more successfully, a comprehensive data set plays an important role. There is no comprehensive data set for marine vehicles in the literature. For this reason, our study will contribute to literature. Our study was tested on the most common real-time recognition models, SSD, Faster R-CNN, EfficientDet algorithms under the TensorFlow library. As a result of the tested models, the most successful algorithm in 250 thousand steps was SSD Mobilnet v1, followed by F RCNN Resnet101 v1 and F RCNN Resnet50 v1 algorithms, respectively. Although our study was tested on traditional image processing models, the contribution of our study to the literature is that a comprehensive data set about marine vehicles has been added to the literature. In our future studies, we plan to increase the data set and optimize the SSD Mobilnet v1 to perform better on this dataset so that it can be used for autonomous device to drive safely with real-time data without disrupting maritime traffic.

ACKNOWLEDGEMENTS: This study was supported by Doğuş University Scientific Research Projects. (Project No: 2019-20-D2-B03)

V. REFERENCES

- [1] M. S. Bingöl, Ç. Kaymak, and A. Uçar, “Derin öğrenme kullanarak otonom araçların insan sürüşünden öğrenmesi,” *Fırat Üniversitesi Mühendislik Bilimleri Dergisi*, vol. 31, no. 1, pp. 177-185, 2019.
- [2] E. Frazzoli, M. A. Dahleh, and E. Feron, “Real-time motion planning for agile autonomous vehicles,” *Journal of Guidance, Control, and Dynamics*, vol. 25, no. 1, pp. 116-129, 2002.
- [3] P. Zhao, J. Chen, T. Mei, and H. Liang, “Dynamic motion planning for autonomous vehicle in unknown environments,” in *2011 IEEE Intelligent Vehicles Symposium (IV)*, 2011, pp. 284-289.
- [4] Z. Tan and M. Karaköse, “Dinamik ortamlarda derin takviyeli öğrenme tabanlı otonom yol planlama yaklaşımları için karşılaştırmalı analiz,” *Adıyaman Üniversitesi Mühendislik Bilimleri Dergisi*, vol. 9, no. 16, pp. 248-262, 2022.
- [5] R. Girshick, “Fast R-CNN,” in *Proceedings of the IEEE International Conference on Computer Vision (ICCV)*, 2015, pp. 1440-1448.
- [6] J. Redmon and A. Farhadi, “YOLOv3: An incremental improvement,” *arXiv preprint arXiv:1804.02767*, 2018.
- [7] W. S. McCulloch and W. Pitts, “A logical calculus of the ideas immanent in nervous activity,” *The Bulletin of Mathematical Biophysics*, vol. 5, no. 4, pp. 115-133, 1943.
- [8] I. Goodfellow, *Deep learning*, MIT Press, 2016.

- [9] N. Aalami, “Derin öğrenme yöntemlerini kullanarak görüntülerin analizi,” *Eskişehir Türk Dünyası Uygulama ve Araştırma Merkezi Bilişim Dergisi*, vol. 1, no. 1, pp. 17-20, 2020.
- [10] R. Kiros, R. Salakhutdinov, and R. S. Zemel, “Unifying visual-semantic embeddings with multimodal neural language models,” *arXiv preprint arXiv:1411.2539*, 2014.
- [11] M. Bojarski, “End to end learning for self-driving cars,” *arXiv preprint arXiv:1604.07316*, 2016.
- [12] S. Çelik and A. Altınörs, “Environmental waste detection from UAV images with YOLOv3 deep learning algorithm,” *unpublished*.
- [13] J. Redmon and A. Farhadi, “YOLOv3: An incremental improvement,” *arXiv preprint arXiv:1804.02767*, 2018.
- [14] W. Liu, D. Anguelov, D. Erhan, C. Szegedy, S. Reed, C. Y. Fu, and A. C. Berg, “SSD: Single shot multibox detector,” in *European Conference on Computer Vision (ECCV)*, 2016, pp. 21-37.
- [15] S. Ren, K. He, R. Girshick, and J. Sun, “Faster R-CNN: Towards real-time object detection with region proposal networks,” in *Advances in Neural Information Processing Systems (NIPS)*, 2015, pp. 91-99.
- [16] M. Tan, R. Pang, and Q. V. Le, “EfficientDet: Scalable and efficient object detection,” in *Proceedings of the IEEE/CVF Conference on Computer Vision and Pattern Recognition (CVPR)*, 2020, pp. 10781-10790.
- [17] M. J. Jung, H. Myung, S. G. Hong, D. R. Park, H. K. Lee, and S. Bang, “Structured light 2D range finder for simultaneous localization and map-building (SLAM) in home environments,” in *Micro-Nanomechatronics and Human Science, 2004 and The Fourth Symposium Micro-Nanomechatronics for Information-Based Society*, 2004, pp. 371-376.
- [18] M. N. Demir and Y. Altun, “Otonom araçla genetik algoritma kullanılarak haritalama ve lokasyon,” *Düzce Üniversitesi Bilim ve Teknoloji Dergisi*, vol. 8, no. 1, pp. 654-666.
- [19] D. A. Ş. Resul, B. Polat, and G. Tuna, “Derin öğrenme ile resim ve videolarda nesnelerin tanınması ve takibi,” *Fırat Üniversitesi Mühendislik Bilimleri Dergisi*, vol. 31, no. 2, pp. 571-581, 2019.
- [20] E. Özbaysar and E. Borandağ, “Vehicle plate tracking system,” in *2018 26th Signal Processing and Communications Applications Conference (SIU)*, 2018, pp. 1-4.

- [21] K. He, X. Zhang, S. Ren, and J. Sun, “Deep residual learning for image recognition,” in *Proceedings of the IEEE Conference on Computer Vision and Pattern Recognition (CVPR)*, 2016, pp. 770-778.
- [22] D. K. Prasad, H. Dong, D. Rajan, and C. Quek, “Are object detection assessment criteria ready for maritime computer vision?,” *IEEE Transactions on Intelligent Transportation Systems*, vol. 21, no. 12, pp. 5295-5304, 2019.
- [23] G. Margarit and A. Tabasco, “Ship classification in single-pol SAR images based on fuzzy logic,” *IEEE Transactions on Geoscience and Remote Sensing*, vol. 49, pp. 3129–3138, 2011.
- [24] M. Leclerc, R. Tharmarasa, M. C. Florea, A. C. Boury-Brisset, T. Kirubarajan, and N. Duclos-Hindié, “Ship classification using deep learning techniques for maritime target tracking,” in *Proceedings of the 21st International Conference on Information Fusion*, Cambridge, UK, Jul. 10–13, 2018, pp. 737–744.
- [25] International Maritime Organization, *Convention on the International Regulations for Preventing Collisions at Sea, 1972 (Consolidated edition)*, International Maritime Organization, 2018.



Düzce University Journal of Science & Technology

Research Article

A Model Reference Adaptive Control Approach to Terrain Following Flight Control System

Berk İNAN ^{a,*}, İbrahim ALIŞKAN ^b

^a Department of Avionics Engineering, Institute of Science, Yildiz Technical University, İstanbul, TURKEY

^b Department of Control and Automation Engineering, Faculty of Electrical and Electronics, Yildiz Technical University, İstanbul, TURKEY

* Corresponding author's e-mail address: berk.inan.tr@gmail.com

DOI: 10.29130/dubited.1595224

ABSTRACT

Automatic Flight Control System (AFCS) Terrain Following (TF) mode allows military aircraft to fly at a certain altitude above ground level at a low altitude. TF mode reduces the probability of aircraft detection by enemy airborne radars. TF mode minimizes the effort the pilot spends to control the aircraft and allows the pilot to focus on other tasks or missions. In this study, the F-16 nonlinear model is linearized around a selected equilibrium point. The state variables of the linear model are decomposed into state space matrices on the lateral and longitudinal axes. Three different control methods, namely PID (Proportional-Integral-Derivative), LQR (Linear Quadratic Regulator), and MRAC (Model Reference Adaptive Control), are used. The results show that the designed algorithms can effectively control the aircraft's altitude, speed, pitch angle, angle of attack, and pitch rate on the longitudinal axis and the aircraft flies in accordance with the terrain profile. Finally, it is observed that MRAC outperforms PID and LQR methods due to its adaptive capability.

Keywords: AFCS, F-16, LQR, MRAC, PID, Terrain Following.

Arazi Takipli Uçuş Kontrol Sistemine Model Referans Uyarlamalı Kontrol Yaklaşımı

ÖZET

Otomatik Uçuş Kontrol Sistemi (OUKS) Arazi Takibi modu askeri hava araçlarının alçak irtifada yer seviyesinin üzerinde belirli bir irtifada uçmasını sağlar. Arazi takip modu düşman radarları tarafından hava aracının tespit edilebilme olasılığını azaltır. Pilotun hava aracını kontrol etmesi için sarf ettiği iş gücünü azaltır ve pilotun diğer görevlere veya misyonlara odaklanmasına olanak tanır. Bu çalışmada, F-16 doğrusal olmayan modeli seçilen bir denge noktası etrafında doğrusallaştırılmıştır. Doğrusal modelin durum değişkenleri yatay ve dikey eksenlerde durum uzayı matrislerine ayrıştırılmıştır. PID (Oransal-İntegral-Türevsel), LQR (Doğrusal Kuadratik Regülatör) ve MRAC (Model Referans Uyarlamalı Kontrol) olmak üzere üç farklı kontrol yöntemi kullanılmıştır. Sonuçlar, tasarlanan algoritmaların uçağın boylamasına eksenindeki irtifa, hız, yunuslama açısı, hücum açısı ve yunuslama hızını etkili bir şekilde kontrol edebildiğini ve uçağın arazi profiline uygun şekilde uçuşunu göstermektedir. Son olarak, MRAC'ın adaptasyon kabiliyetinden dolayı PID ve LQR methotlarına üstünlük sağladığı gözlenmiştir.

Anahtar Kelimeler: OUKS, F-16, LQR, MRAC, PID, Arazi Takibi.

I. INTRODUCTION

Fighter jets are exceptional vehicles that contain many important advanced technologies [1]. These jets perform valuable tasks such as conducting air-to-air or air-to-ground attack operations, protecting friendly forces in the air, ensuring the security of the airspace, neutralizing enemy air defence systems, and conducting reconnaissance flights. To perform these tasks safely, advanced flight control modes are required [2]. Terrain Following (TF) mode, which is among the advanced flight control modes, is a life-saving military aviation technology used in fighter aircraft. The main purpose of using TF flight in fighter aircraft is to navigate the vehicle at high speed and minimum altitude which will minimize the possibility of being detected and tracked by enemy radars [3]. Fighter pilots have developed tactics to avoid the enemy by using terrain irregularities, vegetation, or artificial structures. This type of low-altitude flight tactic is called terrain flight by the US military. Terrain flight is divided into low-level, contour, and nap-of-the-earth. Among the three types, maximum protection is provided by nap-of-the-earth, which follows the roughness of the earth [4]. Due to the enemy's defensive capabilities, fighter jets prefer "nap-of-the-earth" flight. Nap-of-the-earth flight is performed by pilots perceiving the contours of the earth via their eyes and adjusting flight controls based on the observed terrain. In an aircraft autopilot equipped with a TF mode, terrain flight can be executed through the flight control computer, which is fed by sensor data [5]. TF flight can be conducted either by the pilot manually controlling the flight commands or by adjusting the altitude and speed through an automatic flight control system. While the pilot focuses on navigation and mission-related tasks, they must also maintain the aircraft at an altitude of approximately 50 feet above the ground. Automatic TF mode reduces the pilot's workload and enhances situational awareness [6]. Especially during night flights, in fighter jets that can be operated by a single pilot, automatic flight control system modes significantly reduce the pilot's workload while planning attacks or evading enemy threats. This provides a more efficient and safer combat capability [7]. The TF mode must operate independently of weather conditions. The TF radar scans the terrain in both altitude and azimuth. The flight control computer calculates climb and descent commands. Flight control computer sends them to the actuators. If the TF radar cannot provide sufficient information to the flight control computer due to low ground reflections, the radar altitude data is provided by the Radar Altimeter. Additionally, the Inertial Navigation System (INS) is used for attitude and velocity data. The Attitude and Heading Reference System (AHRS) provides secondary attitude and velocity information, allowing for comparison between the data sources [8].

A study utilizes optimal control theory, particularly Wiener-Hopt approaches, to develop guidance systems that minimize TF errors while maintaining stability [9]. The TF system can use digital maps instead of traditional forward-looking radar. Fuzzy PID control that integrates normal acceleration signals can be utilized for better control accuracy and stability. The results show that the system provides precise control and safe flight while improving anti-jamming capabilities [10]. F-16 longitudinal and lateral motion characteristics were compared using PID and LQR controllers. In longitudinal and lateral axes, the PID controller provided obvious superiority in terms of settling and rise time, while the LQR controller provided superiority in peak overshoot value [11]. The aircraft gains altitude basically with pitch up manoeuvres and loses altitude with pitch down manoeuvres. The genetic algorithm method is used to optimize PID and LQR parameters for pitch axis controller design to control pitch manoeuvres. As a result of the study, it is shown that the LQR controller tuned with GA responds significantly better with less settling time, and rise time in terms of PID and LQR performance comparison [12]. In addition to PID and LQR studies, the study conducted with fuzzy logic PID revealed that the fuzzy logic controller gave better results than PID and LQR in terms of rise time, settling time and overshoot percentage parameters [13]. LQR can be used as a baseline controller in MRAC control. LQR + MRAC controller design was made using the longitudinal dynamics of an aircraft similar to the F-16 [14]. There may be changes in model parameters in case the aircraft is damaged or the control surfaces malfunction. These changes cause the aircraft's equilibrium point to shift. According to the changing equilibrium point, the actuator and engine commands are adjusted adaptively thanks to MRAC, allowing the aircraft to continue its flight safely. The aircraft architecture that can tolerate faults is called the "fault tolerance flight control system" [15]. In case of actuator malfunction such as stuck or erroneous sensor reading, LQR causes the aircraft to oscillate, while MRAC provides good performance [16]. In cases where there

is no uncertainty, the LQR controller offers exceptionally good tracking performance. In case of uncertainty, it may cause loss of aircraft. As a result of the simulation, it has been proven that the baseline LQR controller and MRAC provide successful results in the presence of unknown parameters [17]. The design was made by executing MRAC with the Baseline LQR controller. It was observed that the controller gave sufficient response to the unmatched disturbance effect [18]. By creating a Lyapunov candidate function, a close loop can be created to ensure stability [19]. The purpose of MRAC is to keep the system stable by adaptively adjusting the controller gains according to the reference model and to try to get closer to the reference model response. Sensor or actuator malfunctions may occur during flight. Redundant systems are used to mitigate sensor and actuator errors. However, there is a possibility of common mode failure of the aircraft. In the case of common mode failure, the redundancy architecture may lose its effect. When a direct MRAC is used, it may have negative results on the close loop stability in sensor measurements. MRAC cannot guarantee signal boundness in the case of sensor bias. The paper recommends using Modified MRAC in the case of sensor bias error scenarios [20]. MRAC flight tests were performed on the F/A-18 jet called Full-scale Advanced Systems Testbed (FAST) by NASA. Baseline nonlinear dynamic inversion controller, basic MRAC, and complexity MRAC were tested in flights by NASA. The handling qualities of the aircraft with complex MRAC gave successful results in the pitch-roll coupling test scenario. It was concluded that complexity leads to better performance but increases the effort in terms of aircraft certification activities [21]. Studies on the verification and validation activities of adaptive controllers by the Civil Aviation Authority are ongoing. For this reason, classical control methods are preferred in civil aircraft [22].

PID and LQR controller designs were made for the F-16 aircraft with stable eigenvalues; according to the results in pitch and roll axes, it was observed that PID gave faster results in terms of rise and settling time, while LQR gave better results in terms of overshoot [23]. In the study focusing on handling qualities, the controllability of the aircraft even at high angle of attack using the NDI method was mentioned [24]. Adaptive back stepping flight control method for the F-16 aircraft was developed using neural networks; it is aimed to provide stability by adaptively updating the controller parameters in cases of structural damage and actuator malfunction [25]. A control study was performed in the outer loop for F-16 using the Receding Horizon Control technique in the longitudinal axis; with this study, control performance was increased [26]. The sliding mode control method was designed for angle of attack feedback on the F-16 longitudinal axis; better results were obtained compared to traditional control methods [27]. In case of uncertainty or actuator failure, the stability of the aircraft may be lost. The multilayer adaptive neural network method has been used to handle F-16 aircraft configuration changes during flight [28]. In the study where fractional order MRAC design was made for F-16 model pitch rate feedback, it was stated that it was more successful than integer order as it eliminated oscillation during transition [29].

In this study, F-16 aircraft MATLAB/Simulink model is used because it is open source availability. The nonlinear model of F-16 was trimmed to linearized at 5000 ft and 600 knots. Using the F-16 altitude, speed, pitch angle, angle of attack and pitch rate state variables on the longitudinal axis, TF mode design was performed with PID, LQR and MRAC control methods. The behaviour of the control surfaces, altitude, speed, angle and rate of the aircraft navigating in the canyon profile results are analysed. The aim is to provide the performance that allows the aircraft to navigate in the canyon profile without creating catastrophic results. The simulation results show the usability of the TF mode. The contribution of this paper to the literature can be presented as the development of a Model Reference Adaptive Controller under terrain profile constraints. The paper focuses on the design and implementation of TF control algorithm. It explores various control methods, including PID, LQR, and MRAC, to enhance the performance and safety of F-16 fighter jet during low altitude flights.

Remained of the paper is listed as follows: In Section 2, the F-16 model is described, containing input-output configurations, control surface limits, and the trimming and linearization processes in MATLAB. In Section 3, TF mode, PID, LQR and MRAC design stages and simulation result comparison are given. In Section 4, the conclusion includes evaluation of the TF mode controller performance and discussion of potential future work.

II. F-16 MODEL

A. F-16 MODEL OVERVIEW

The MATLAB F-16 model developed by Russell [30], based on the book by Stevens and Lewis [31] and the technical report by NASA Nguyen [32], has been used. The F-16 plant uses thrust, elevator, aileron, rudder, and leading edge flap inputs. The rudder on the lateral axis allows the aircraft to change its heading angle. The aileron on the lateral axis allows the aircraft to change its roll angle. The elevator on the longitudinal axis allows the aircraft to pitch up or pitch down. The leading edge flap on the longitudinal axis increases the aircraft's lift. The Russell model offers both high fidelity and low fidelity options. The high fidelity model has an angle of attack range from -20 to 90 degrees, while the low fidelity model has an angle of attack range from -30 to 30 degrees. In this study, the leading edge flap control input is disregarded, and the low fidelity model is used. The F-16 plant model produces outputs of north/east position, altitude, roll/pitch/yaw angle, velocity, angle of attack, sideslip, and roll/pitch/yaw rate in response to the given control inputs.

The F-16 model has saturation limits for its control inputs. Thrust operates within the range of 1,000 to 19,000 lbs, the elevator ranges from -25 to 25 degrees, the aileron from -21.5 to 21.5 degrees, and the rudder from -30 to 30 degrees. Even if excessive commands are sent to the actuators that physically move the control surfaces, the control surfaces will be able to operate within the designed limits.

B. F-16 NON-LINEAR MODEL

If the fundamental nonlinear time-invariant system model given in (1) is considered, the 6-DOF aircraft nonlinear model and the model states can be presented as follows [33].

$$\dot{x} = f(x(t), u(t)) \quad (1)$$

x consists of 12 state variables and u consist of 4 control inputs that are used in the model as following:

$$x = [n_{pos} \ e_{pos} \ h \ \phi \ \theta \ \psi \ V \ \alpha \ \beta \ p \ q \ r]^T \quad (2)$$

$$u = [\delta_{th} \ \delta_e \ \delta_a \ \delta_r]^T \quad (3)$$

In the equations, n_{pos} and e_{pos} are the north and east positions, h is altitude, ϕ , θ , and ψ are the roll, pitch, and yaw angles, V is total velocity, α is the angle of attack, β is the sideslip angle, p , q , and r are angular rates around the roll, pitch, and yaw axes. δ_{th} , δ_e , δ_a and δ_r are the throttle, elevator, aileron and rudder control inputs of the system. u , v , and w are velocity components along the x , y , z body axes in given Figure 1.

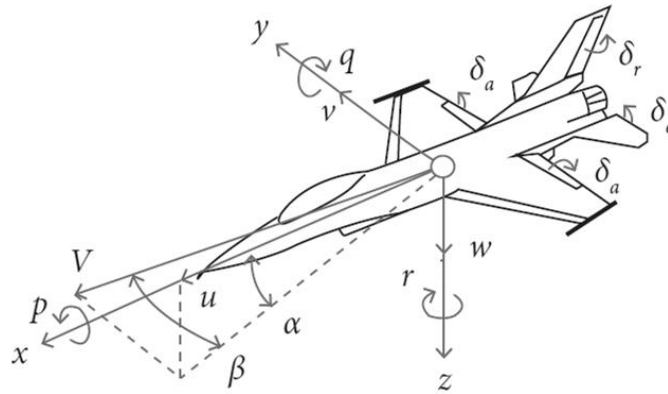


Figure 1. Aircraft variables and control inputs representation [34]

The equations of motion from NASA F-16 wind tunnel tests [32] and the Steven and Lewis book [31] are found in the “c function” of the Russell MATLAB/Simulink model [30] and are presented in (4) through (18).

Forces:

$$\dot{u} = rv - qw - g \sin \theta + \frac{\bar{q}S}{m} C_{X,t} + \frac{T}{m} \quad (4)$$

$$\dot{v} = pw - ru + g \cos \theta \sin \phi + \frac{\bar{q}S}{m} C_{Y,t} \quad (5)$$

$$\dot{w} = qu - pv + g \cos \theta \cos \phi + \frac{\bar{q}S}{m} C_{Z,t} \quad (6)$$

Moments:

$$\dot{p} = \frac{J_z L_{tot} + J_{xz} N_{tot} - (J_z(J_z - J_y) + J_{xz}^2)qr + J_{xz}(J_x - J_y + J_z)pq + J_{xz}qH_{eng}}{J_x J_z - J_{xz}^2} \quad (7)$$

$$\dot{q} = \frac{M_{tot} + (J_z - J_x)pr - J_{xz}(p^2 - r^2) - rH_{eng}}{J_y} \quad (8)$$

$$\dot{r} = \frac{J_x N_{tot} + J_{xz} L_{tot} + (J_x(J_x - J_y) + J_{xz}^2)pq - J_{xz}(J_x - J_y + J_z)qr + J_x qH_{eng}}{J_x J_z - J_{xz}^2} \quad (9)$$

Navigations:

$$\begin{aligned} \dot{n}_{pos} = & u \cos \theta \cos \psi + v(\sin \phi \cos \psi \sin \theta - \cos \phi \sin \psi) \\ & + w(\cos \phi \sin \theta \cos \psi + \sin \phi \sin \psi) \end{aligned} \quad (10)$$

$$\begin{aligned} \dot{e}_{pos} = & u \cos \theta \sin \psi + v(\sin \phi \sin \psi \sin \theta + \cos \phi \cos \psi) \\ & + w(\cos \phi \sin \theta \sin \psi - \sin \phi \cos \psi) \end{aligned} \quad (11)$$

$$\dot{h} = u \sin \theta - v \sin \phi \cos \theta - w \cos \phi \cos \theta \quad (12)$$

Kinematics:

$$\dot{\phi} = p + \tan \theta (q \sin \phi + r \cos \phi) \quad (13)$$

$$\dot{\theta} = q \cos \phi - r \sin \phi \quad (14)$$

$$\dot{\psi} = \frac{q \sin \phi + r \cos \phi}{\cos \theta} \quad (15)$$

Velocity and aerodynamic angles:

$$\dot{V} = \frac{u\dot{u} + v\dot{v} + w\dot{w}}{V} \quad (16)$$

$$\dot{\alpha} = \frac{u\dot{w} - w\dot{u}}{u^2 + w^2} \quad (17)$$

$$\dot{\beta} = \frac{\dot{v}V_t - v\dot{V}}{V^2 \cos \beta} \quad (18)$$

where L_{tot} , M_{tot} , and N_{tot} are total aerodynamic moments calculated using the coefficients obtained from the NASA wind tunnel test results, J_x , J_y , J_z , and J_{xz} are moments of inertia taken from NASA wind tunnel test data, H_{eng} is the engine moment along the roll axis, $C_{x,t}$, $C_{y,t}$ and $C_{z,t}$ force coefficients of x, y, z axis calculated via NASA wind tunnel test data, \bar{q} is dynamic pressure calculated via air density and aircraft velocity, S is F-16 wing surface area, T is the thrust input and g is gravity component [32].

C. TRIM APPROACH AND LINEARIZATION

The nonlinear structure of the model can be easily seen from the equations. Non-linear system is hard to analyse in terms of controller design. The linear system is used in most of the controller algorithm designs in the literature [35], [36], [37] and [38]. In controller design, the aircraft response is examined by giving control input or external disturbance while the aircraft is at the equilibrium point. If the aircraft is not in equilibrium condition, deviation from the initial conditions occurs that are unrelated to the control inputs making the analysis more difficult. Aircraft equilibrium condition is known as trimmed flight conditions [31]. The aircraft may or may not be in equilibrium. In the equilibrium state, there are no forces or moments [39].

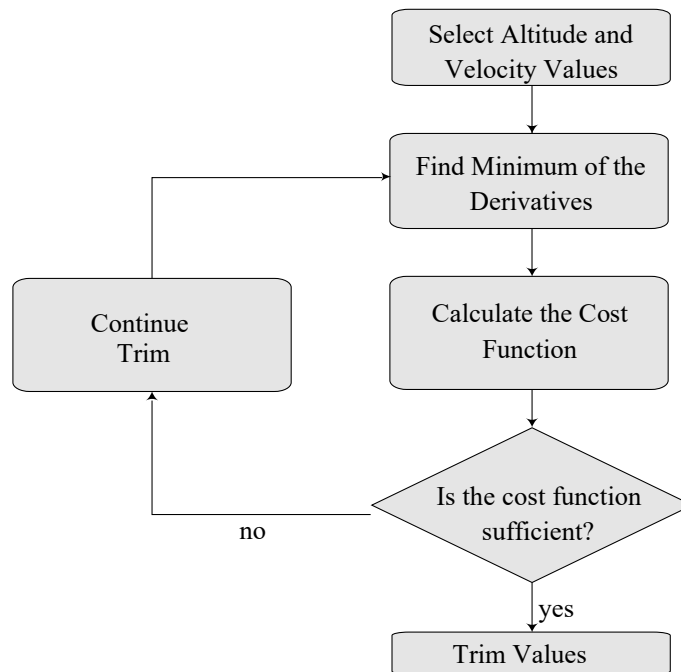


Figure 2. F-16 trim algorithm flowchart

To analyse the behaviour of the F-16 for the flight condition of 5000ft altitude and 600ft/s velocity trimming and linearization are made by using MATLAB/Simulink. Control positions at the trim point are determined with iterations. Figure 2 shows the iterative trim algorithm flowchart.

Trim point is obtained by considering the aircraft is on a steady wings level flight. To start the iteration, initial guess values are necessary given in Table 1.

Table 1. Initial guess for trim [30]

Straight Level Flight	Low Fidelity
Trust (<i>lb.</i>)	5000
Elevator (<i>deg.</i>)	-0.09
Aileron (<i>deg.</i>)	0.01
Rudder (<i>deg.</i>)	-0.01
Alpha (<i>deg.</i>)	8.49

The initial guess values in Table 1 are good values for finding the F-16 trim point [30]. The MATLAB function “fminsearch” is a Nelder and Mead Simplex algorithm that performs the minimization [40], [31]. The cost function (21) is minimized with MATLAB “fminsearch”. It tries to find the minimum values in equation (19) by iterating.

$$\dot{x} = [n_{pos} \quad e_{pos} \quad h \quad \phi \quad \dot{\theta} \quad \dot{\psi} \quad \dot{V} \quad \dot{\alpha} \quad \dot{\beta} \quad \dot{p} \quad \dot{q} \quad \dot{r}]^T \quad (19)$$

W (20) is the created weight vector:

$$W = [0 \quad 0 \quad 5 \quad 10 \quad 10 \quad 10 \quad 2 \quad 10 \quad 10 \quad 10 \quad 10 \quad 10] \quad (20)$$

The cost function is given below:

$$Cost = \sum_{i=1}^{12} W_i \dot{x}_i^2 \quad (21)$$

The near-zero convergence of the cost function with iterations is shown in Figure 3.

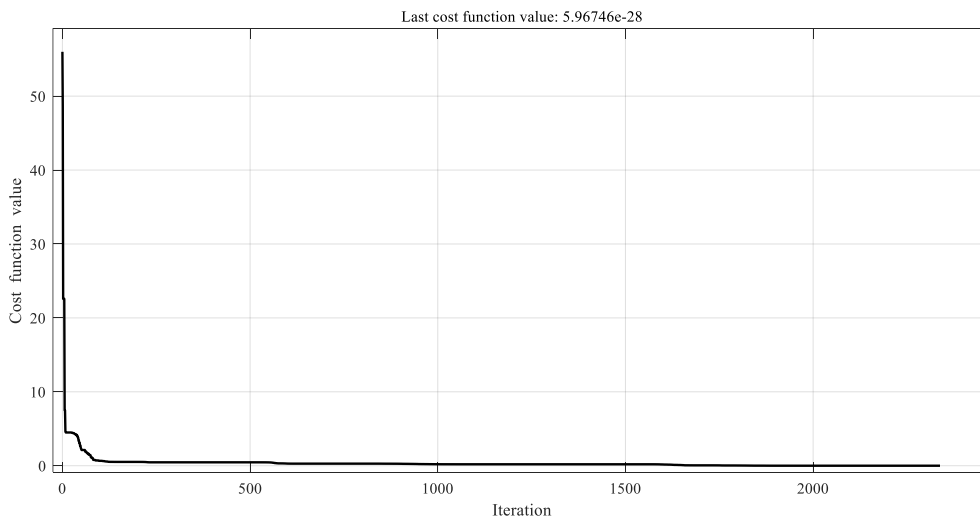


Figure 3. Cost function iterations

The cost function can be reduced to less than 1E-30 with iterations. Since cost functions below 1E-12 will have negligible tolerance in state and controls, results below 1E-12 can be used [31]. The trimming result can be found in Table 2:

Table 2. Trimmed values

Straight Level Flight	Low Fidelity
Trust (<i>lb.</i>)	2598.929
Elevator (<i>deg.</i>)	-1.762
Aileron (<i>deg.</i>)	-3.0554x10 ⁻¹⁵
Rudder (<i>deg.</i>)	-3.9758x10 ⁻¹⁴
Alpha (<i>deg.</i>)	1.5508
Cost	5.9675x10 ⁻²⁸

Aircraft trimmed at an equilibrium point. The MATLAB "linmod" function [41] linearizes the F-16 nonlinear model using the thrust, elevator, aileron, rudder, and alpha trim values in Table 2 [42], [43]. The obtained matrices are high dimensional since they include all the dynamics of the aircraft. The longitudinal and lateral planes are coupled. It is quite difficult to analyse. To design the controller, the movement of the aircraft is separated to two axes as longitudinal and lateral. The selected state variables (22) and control inputs (23) on the longitudinal axis are given below:

$$x_{long} = [h \quad \theta \quad V \quad \alpha \quad q]^T \quad (22)$$

$$u_{long} = [\delta_{th} \quad \delta_e]^T \quad (23)$$

The reduced model is obtained by first reducing to a longitudinal low fidelity model into a 7x7 state space with actuator dynamics. Then, this model was reduced to a 5x5 state space flight dynamics model. Actuator dynamics will be added to the Simulink model as engine and elevator dynamics. The matrix dimensions are given in Table 3.

Table 3. F-16 matrix dimensions

	A	B	C	D
Full Matrices	18x18	18x4	18x18	18x4
Reduced Matrices for Longitudinal Axis	7x7	7x2	5x7	5x2
Reduced Matrices for Longitudinal Axis without Actuator Dynamics	5x5	5x2	5x5	5x2

In LQR and PID designs, actuator dynamics were extracted from matrices and used as Simulink blocks. Matrix A is the system matrix that defines the F-16 dynamic behaviour in trimmed point. Matrix B is the control matrix that defines control inputs effects on system. Matrix C is the output matrix that convert the system outputs to meaningful measurements such as degree to radian. The A, B, C and D matrices to be used in the design of the F-16 TF controller, which was created as a result of the linearization process via the Russel F-16 model [30] are given equations (24) and (25).

$$\begin{bmatrix} \dot{h} \\ \dot{V}_t \\ \dot{\alpha} \\ \dot{\theta} \\ \dot{q} \\ \delta_{th} \\ \delta_e \end{bmatrix} = \begin{bmatrix} 0 & 0 & -600.0 & 600.0 & 0 & 0 & 0 \\ 1.23e-4 & -0.0136 & 17.3 & -32.2 & -0.291 & 0.00157 & 0.23 \\ 1.61e-6 & -1.78e-4 & -1.05 & 1.29e-13 & 0.919 & -7.11e-8 & -0.00221 \\ 0 & 0 & 0 & 0 & 1.0 & 0 & 0 \\ -5.76e-20 & 6.36e-18 & -3.07 & 0 & -1.42 & 0 & -0.225 \\ 0 & 0 & 0 & 0 & 0 & -1.0 & 0 \\ 0 & 0 & 0 & 0 & 0 & 0 & -20.2 \end{bmatrix} \begin{bmatrix} h \\ V_t \\ \alpha \\ \theta \\ q \\ \delta_{th} \\ \delta_{el} \end{bmatrix} + \begin{bmatrix} 0 & 0 \\ 0 & 0 \\ 0 & 0 \\ 0 & 0 \\ 0 & 0 \\ 1.0 & 0 \\ 0 & 20.2 \end{bmatrix} \begin{bmatrix} u_{th} \\ u_e \end{bmatrix} \quad (24)$$

$$\begin{bmatrix} h \\ V_t \\ \alpha \\ \theta \\ q \end{bmatrix} = \begin{bmatrix} 1.0 & 0 & 0 & 0 & 0 & 0 & 0 \\ 0 & 1.0 & 0 & 0 & 0 & 0 & 0 \\ 0 & 0 & 57.3 & 0 & 0 & 0 & 0 \\ 0 & 0 & 0 & 57.3 & 0 & 0 & 0 \\ 0 & 0 & 0 & 0 & 57.3 & 0 & 0 \end{bmatrix} \begin{bmatrix} h \\ V_t \\ \alpha \\ \theta \\ q \\ \delta_{th} \\ \delta_{el} \end{bmatrix} + \begin{bmatrix} 0 & 0 \\ 0 & 0 \\ 0 & 0 \\ 0 & 0 \\ 0 & 0 \\ 0 & 0 \end{bmatrix} \begin{bmatrix} u_{th} \\ u_e \end{bmatrix} \quad (25)$$

III. TERRAIN FOLLOWING CONTROL LAWS

A. TERRAIN FOLLOWING CONTROL LAWS WITH PID

The TF PID controller block diagram is shown in Figure 4. TF PID controller algorithm can be divided into two sub controllers: the Airspeed Controller, which sends the engine command, and the Altitude Controller, which sends the elevator actuator command.

Airspeed hold controller is used to control the engine. Airspeed varies depending on the pitch angle (θ). In the pitch down situations, the airspeed (V) of the aircraft increases. It is adjusted by changing the thrust with the airspeed hold controller. In the pitch up situations, the airspeed of the aircraft decreases. To prevent stall, thrust is increased within the limits. The difference between the selected airspeed reference (V_{ref}) and the speed (V) feedback of aircraft generates the speed error (V_{er}). The speed error (V_{er}) is processed by the velocity controller to adjust the thrust. The engine command (δ_{th}) is generated.

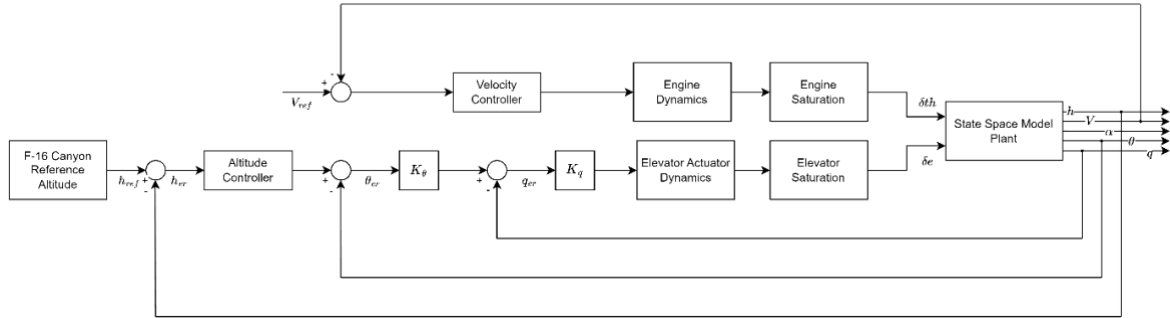


Figure 4. TF PID controller

The altitude controller is used to control the elevator actuator. TF reference altitude (h_{ref}) is generated by the F-16 Canyon Reference Altitude block. The altitude error signal (h_{er}) is generated by taking the difference between the aircraft's reference altitude (h_{ref}) and its current altitude (h). The altitude error (h_{er}) signal is processed by the altitude controller to produce the pitch angle reference (θ_{ref}) signal. The pitch angle reference (θ_{ref}) signal represents the reference needed to reduce the altitude error (h_{er}) to zero. Multiplying the pitch angle error (θ_{er}) signal with the pitch angle gain (K_θ), the pitch rate reference (q_{ref}) signal is generated. The elevator actuator command (δ_e) is generated by multiplying the difference between the pitch rate reference (q_{ref}) and the pitch rate (q) feedback by the pitch rate gain (K_q).

The velocity controller was implemented as a PID controller tuned using the step response method of Ziegler–Nichols. A step function is applied to the system as the control input. L (delay time) and T (time constant) parameters are determined according to the step response [44]. K is selected as 0.9, L is selected as 0.07 and T is selected as 0.89.

Table 4. Ziegler Nichols PID step response method [44]

The altitude attitude controller is implemented as P controllers in Simulink and these were tuned using the Simulink auto-tuning tool [45]. Controller performance improvement was made by changing the gains using the trial and error method in Simulink. The gains are given in Table 5.

Controller	Feedback	P	I	D
Velocity Controller	Airspeed	16.9524	484.3537	0.5933
Altitude Controller	Pitch Rate	-0.75	0	0
	Pitch Angle	350	0	0
	Altitude	33	7	6.7

The TF LQR controller block diagram is shown in Figure 5. The TF LQR controller algorithm can be divided into two loops: the Inner Loop, which increases stability, and the Outer Loop, which reduces altitude error.

Figure 5. TF LQR Controller

$$Q = \begin{bmatrix} 1 & 0 & 0 & 0 & 0 \\ 0 & 0.1 & 0 & 0 & 0 \\ 0 & 0 & 0.0001 & 0 & 0 \\ 0 & 0 & 0 & 0.00001 & 0 \\ 0 & 0 & 0 & 0 & 0.01 \end{bmatrix} \quad (26)$$

$$R = \begin{bmatrix} 0.005 & 0 \\ 0 & 0.5 \end{bmatrix} \quad (27)$$

The MATLAB “lqr” function calculates the LQR gains using the algebraic Riccati equation. TF LQR gains are given in Table 6:

Table 6. LQR controller gains

Gain	Engine	Elevator
Altitude	0.07	-4.47
Airspeed	1.27	-0.04
Angle of Attack	-15.2	1010
Pitch Angle	16	-1300
Pitch Rate	1.07	-58.5

C. TERRAIN FOLLOWING CONTROL LAWS WITH MRAC

The TF MRAC controller block diagram is shown in Figure 6.

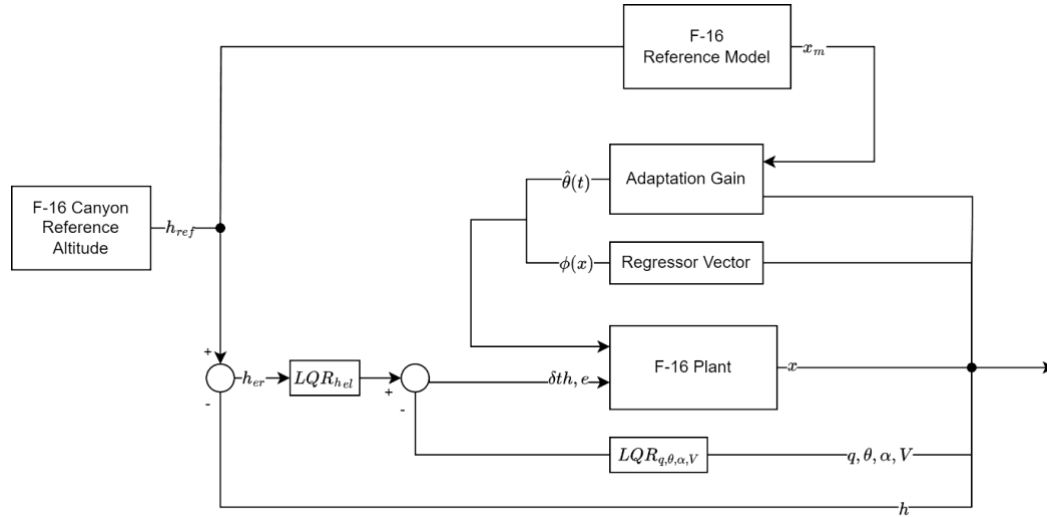


Figure 6. TF MRAC Controller

Plant model can be expressed as (28):

$$\dot{x} = Ax + B(u + f(x)) \quad (28)$$

$f(x)$ is matched uncertainty. θ^T is a constant matrix. $\phi(x)$ is known regressor vector.

$$f(x) = \theta^T \phi(x) \quad (29)$$

Reference model can be expressed as (30):

$$\dot{x}_m = A_m x_m + B_m r \quad (30)$$

In the absence of any disturbance input, the difference between the plant model and reference model state variables becomes zero.

$$\dot{e} = \dot{x} - \dot{x}_m \quad (31)$$

LQR is used as the baseline controller. When the difference between the plant model and the reference model is not zero, MRAC starts generating commands. Control inputs are given in equation (32).

$$\begin{aligned} u &= u_{mrac} + u_{lqr} \\ &= K_x^T x + K_r^T r - \theta^T \phi(x) \end{aligned} \quad (32)$$

The matching condition between the plant model and the reference model is given in equation (33).

$$\begin{aligned} \dot{e} &= Ax + B(u + f(x)) - A_m x_m + B_m r \\ &= Ax + B(K_x^T x + K_r^T r - \theta^T \phi(x) + \theta^T \phi(x)) - A_m x_m + B_m r \\ &= Ax + B(K_x^T x + K_r^T r) - A_m x_m + B_m r \\ &= (A + BK_x^T)x + BK_r^T r - A_m x_m - B_m r \end{aligned} \quad (33)$$

The reference model matrices A_m and B_m are defined by the LQR gains at Table 6. A_m is Hurwitz. LQR is used as the MRAC baseline controller [46]. A_m is created using the LQR gains in Table 6.

$$A_m = A + BK_x^T \quad (34)$$

$$B_m = BK_r^T \quad (35)$$

$\tilde{\theta}$ parameter estimation error is given in equation (36).

$$\tilde{\theta} = \theta - \hat{\theta}(t) \quad (36)$$

When the derivative of $\tilde{\theta}$ is taken, the constant parameter becomes zero as in equation (37).

$$\dot{\tilde{\theta}} = -\dot{\hat{\theta}}(t) \quad (37)$$

The calculated adaptation gain is added to the control input in equation (38).

$$u = K_x^T x + K_r^T r - \hat{\theta}^T(t) \phi(x) \quad (38)$$

Equality (38) is written into equality (28) to obtain \dot{x} .

$$\begin{aligned}
\dot{x} &= Ax + Bu + Bf(x) \\
&= Ax + B \left(K_x^T x + K_r^T r - \hat{\theta}^T(t) \phi(x) \right) + B\theta^T \phi(x) \\
&= Ax + BK_x^T x + BK_r^T r - B\hat{\theta}^T(t) \phi(x) + B\theta^T \phi(x) \\
&= (A + BK_x^T)x + BK_r^T r + B(-\hat{\theta}^T(t) + \theta^T) \phi(x) \\
&= (A + BK_x^T)x + BK_r^T r + B\tilde{\theta} \phi(x)
\end{aligned} \tag{39}$$

For use in Lyapunov analysis, the error equation is found as in equation (40).

$$\begin{aligned}
\dot{e} &= (A + BK_x^T)x + BK_r^T r + B\tilde{\theta} \phi(x) - A_m x_m - B_m r \\
&= A_m e + B\tilde{\theta} \phi(x)
\end{aligned} \tag{40}$$

The Lyapunov candidate function is chosen as in (41).

$$V(e, \theta) = e^T P e + \text{tr}[\tilde{\theta}^T \Gamma_\theta^{-1} \tilde{\theta}] \tag{41}$$

The Lyapunov function satisfies the stability condition when $\dot{V} < 0$. The adaptation gain is adjusted to satisfy this condition. The goal is to find the adaptation gain that makes the derivative of the Lyapunov function less than zero. The term $-e^T Q e$ is multiplied by the positive semi-definite matrix Q . Since the result of this multiplication is always negative, it does not affect the equation (43). By using equation (42) in conjunction with Barbalat's Lemma, the tracking error is asymptotically stable with $e(t) \rightarrow 0$ as $t \rightarrow \infty$ [47].

$$\begin{aligned}
\dot{V} &= \dot{e}^T P e + e^T P \dot{e} + \text{tr}[\dot{\tilde{\theta}}^T \Gamma_\theta^{-1} \tilde{\theta}] + \text{tr}[\tilde{\theta}^T \Gamma_\theta^{-1} \dot{\tilde{\theta}}] \\
&= \dot{e}^T P e + e^T P \dot{e} + \text{tr}\left[\left(-\dot{\hat{\theta}}(t)^T\right) \Gamma_\theta^{-1} \tilde{\theta}\right] + \text{tr}\left[\tilde{\theta}^T \Gamma_\theta^{-1} \left(-\dot{\hat{\theta}}(t)\right)\right] \\
&= \left(e^T A_m^T + \phi(x)^T \tilde{\theta}^T B^T\right) P e + e^T P \left(A_m e + B\tilde{\theta} \phi(x)\right) \\
&\quad + \text{tr}\left[\left(-\dot{\hat{\theta}}(t)^T\right) \Gamma_\theta^{-1} \tilde{\theta}\right] + \text{tr}\left[\tilde{\theta}^T \Gamma_\theta^{-1} \left(-\dot{\hat{\theta}}(t)\right)\right] \\
&= e^T A_m^T P e + \phi(x)^T \tilde{\theta}^T B^T P e + e^T P A_m e + e^T P B \tilde{\theta} \phi(x) \\
&\quad + \text{tr}\left[\left(-\dot{\hat{\theta}}(t)^T\right) \Gamma_\theta^{-1} \tilde{\theta}\right] + \text{tr}\left[\tilde{\theta}^T \Gamma_\theta^{-1} \left(-\dot{\hat{\theta}}(t)\right)\right] \\
&= -e^T Q e + \phi(x)^T \tilde{\theta}^T B^T P e + e^T P B \tilde{\theta} \phi(x) \\
&\quad + \text{tr}\left[\left(-\dot{\hat{\theta}}(t)^T\right) \Gamma_\theta^{-1} \tilde{\theta}\right] + \text{tr}\left[\tilde{\theta}^T \Gamma_\theta^{-1} \left(-\dot{\hat{\theta}}(t)\right)\right]
\end{aligned} \tag{42}$$

The MRAC adaptation gain that makes equation (42) negative is chosen as (43) or (44). $\dot{\hat{\theta}}$ and its transpose is considered equal.

$$\dot{\hat{\theta}} = \Gamma_{\theta} e^T P B \phi(x) \quad (43)$$

$$\dot{\hat{\theta}}^T = \phi(x)^T B^T P^T e \Gamma_{\theta}^T \quad (44)$$

The result of the Lyapunov function that provides stability is shown in equation (45).

$$\begin{aligned} \dot{V} = & -e^T Q e + \phi(x)^T \tilde{\theta}^T B^T P e + e^T P B \tilde{\theta} \phi(x) \\ & + tr[(-\phi(x)^T B^T P^T e \Gamma_{\theta}^T) \Gamma_{\theta}^{-1} \tilde{\theta}] + tr[\tilde{\theta}^T \Gamma_{\theta}^{-1} (-\Gamma_{\theta} e^T P B \phi(x))] \end{aligned} \quad (45)$$

The selected semi-positive definite P is shown in matrix (46).

$$P = \text{diag}(0 \quad 0 \quad 0.0025 \quad 0 \quad 0.0002375 \quad 0 \quad 0) \quad (46)$$

(47) uses angle of attack and pitch rate data. Altitude, airspeed and pitch angle feedback are not used.

$$\phi(x) = [0 \quad 0 \quad \alpha \quad 0 \quad p]^T \quad (47)$$

Adaptation rate directly affects MRAC performance. A higher adaptation rate provides faster tracking but causes the aircraft to oscillate. The optimum adaptation matrix selected is given in (48).

$$\Gamma = \text{diag}(0 \quad 0 \quad 135 \quad 0 \quad 0 \quad 0 \quad 0) \quad (48)$$

The main purpose of MRAC is to generate commands according to the reference model when there is a disturbance (e.g. actuator failure, structural deterioration, sensor bias). In the MRAC study, equation (49) is injected [48] into the plant model as matched uncertainty.

$$\theta^T = \begin{bmatrix} 0 & 0 & 0 & 0 & 0 & 0 & 0 \\ 0 & 0 & 0 & 0 & -0.4 & 0 & 0 \end{bmatrix} \quad (49)$$

D. COMPARISON OF PID, LQR AND MRAC TERRAIN FOLLOWING MODE

In this section, at first, an artificial flight path was created to test the developed control algorithms. A canyon model was selected to demonstrate the different maneuvers. The canyon starts at 150ft AGL (above ground level). After flying at a steady level, the F-16 begins a climb maneuver when it encounters the hill. After the climb, it transitions into a steady level flight by performing a pitch-down. Subsequently, it begins a descent maneuver with pitch-down action. When the altitude reaches 150 ft above the ground, the aircraft performs a pitch-up maneuver to transition back to steady flight. After two climb maneuver, F-16 completes the terrain following flight. Figure 7 shows the outputs of the PID, LQR and MRAC controllers according to the sensor readings. Sensor delays are ignored. The ± 140 ft altitude is selected as the success criterion of the controllers. All three controllers operate within the defined band.

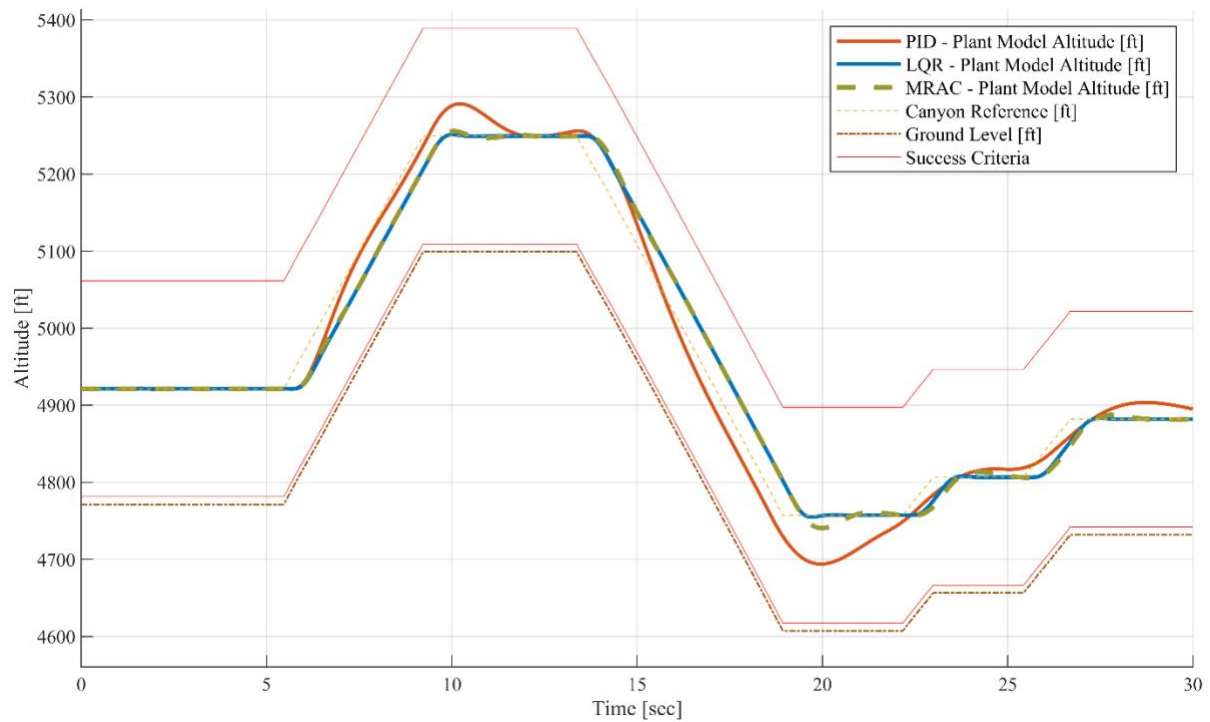


Figure 7. *PID, LQR and MRAC Terrain Following*

Figure 8 shows elevator commands generated by the controllers. While the PID controller produces an aggressive elevator command, LQR and MRAC produce smooth commands. While following the terrain following path, saturation is observed especially in the elevator commands in MRAC.

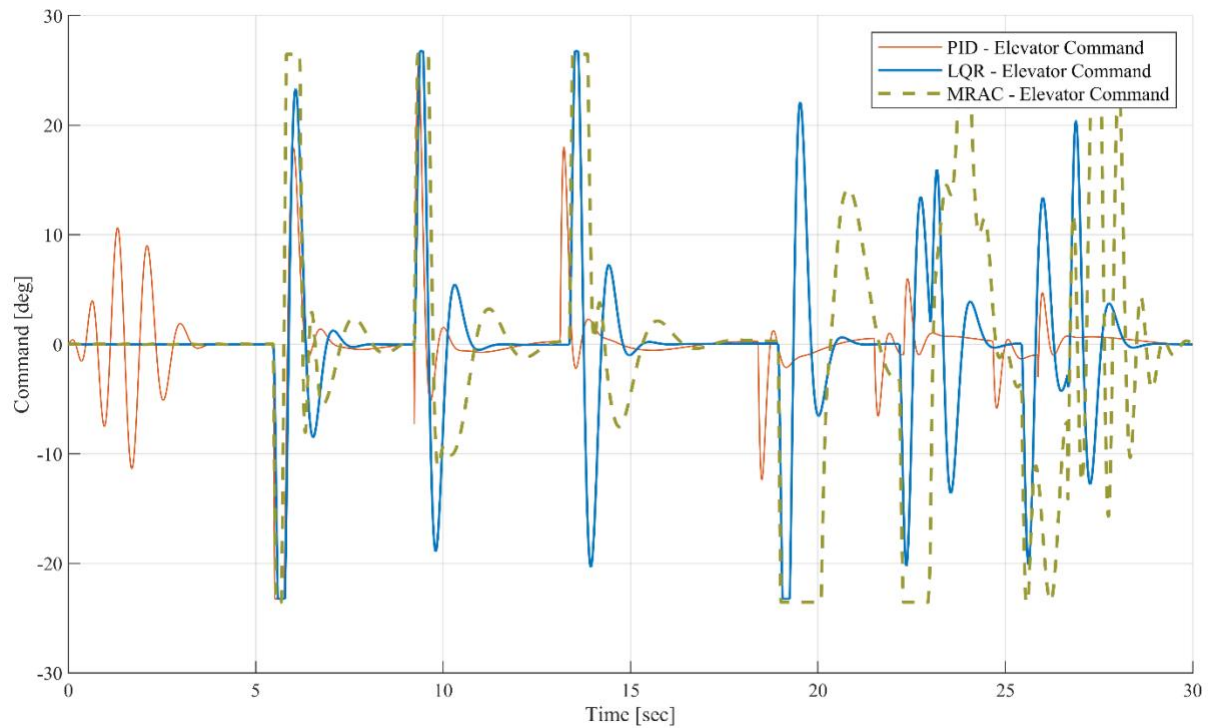


Figure 8. *PID, LQR and MRAC elevator commands*

When the values of PID, LQR, and MRAC TF designs are examined with the mean absolute error method, MRAC has the lowest error value with 13.3. The LQR method gave the best result after MRAC

with 15.7. The PID method provides low precision control compared to other methods with a value of 17.1.

PID, LQR and MRAC performances compared in Table 7. Despite parametric uncertainty, MRAC demonstrated good performances in maneuvers. PID method showed slow settling time and high overshoot responses. The following data show the usability of MRAC.

Table 7. Controller performances

Flight Phase	PID		LQR		MRAC	
	Settling Time [sec]	Overshoot [ft]	Settling Time [sec]	Overshoot [ft]	Settling Time [sec]	Overshoot [ft]
1. Climb	2,20	41,0	1,76	44,70	1,48	32,8
2. Transition to Steady Flight	2,28	41,7	0,55	1,77	0,69	6,23
3. Descent	2,32	46,2	1,71	43,47	2,50	39,7
4. Transition to Steady Flight	2,80	63,3	0,56	2,35	1,33	16,72
5. Climb	0,66	18,8	0,67	30,34	0,67	29,25
6. Transition to Steady Flight	1,83	10,8	0,57	1,35	1,64	6,8
7. Climb	1,08	18,7	0,92	30,52	1,02	25,9
8. Transition to Steady Flight	2,71	21,7	0,60	1,25	1,41	5,5

Figure 9 shows the behavior of MRAC and LQR against parametric uncertainty. It is seen that LQR cannot provide stable operation of the system in case of parametric uncertainty (49). In the simulation, it is seen that the aircraft controlled by LQR collided with the ground and crashed.

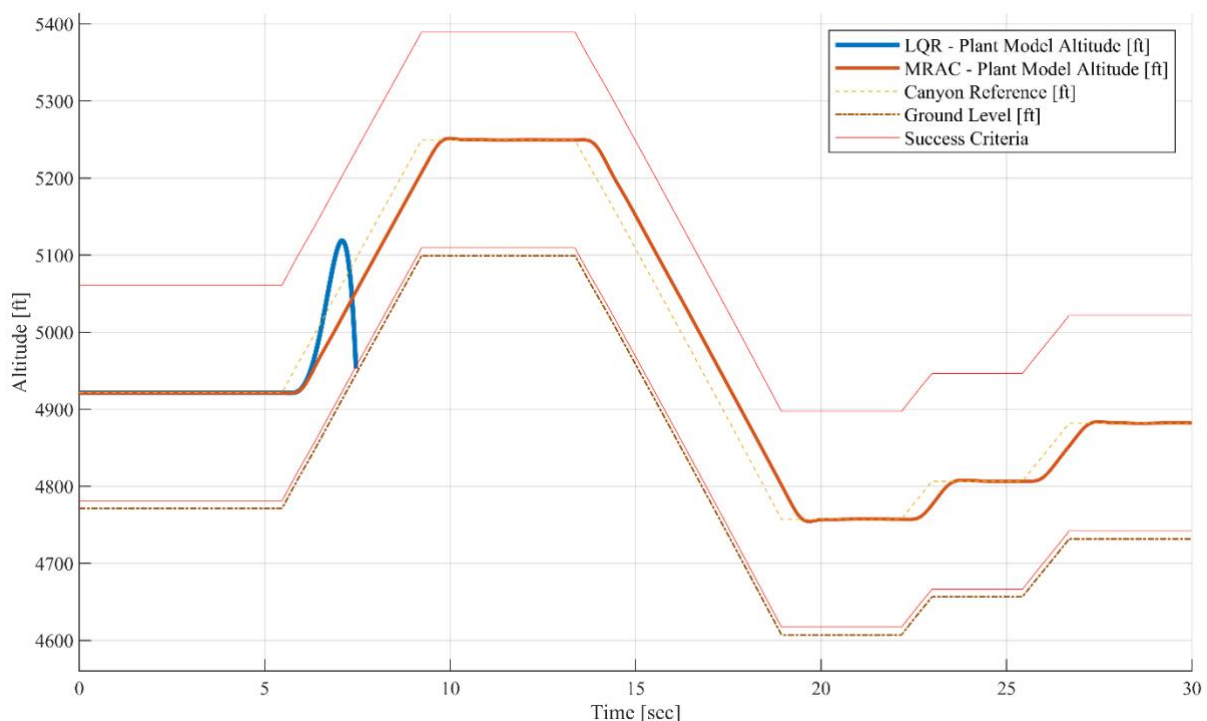


Figure 9. LQR and MRAC parametric uncertainty results

IV. CONCLUSION

In the study, F-16 was modelled on the longitudinal axis. Matched uncertainty was given to the model and a suitable MRAC was designed. MRAC was tested for TF mode. Concept designs of modern and classic controllers were shown for the TF mode. The results show that LQR and MRAC controllers give better results than PID. The MRAC controller stands out compared to PID and LQR controllers due to its adaptive gain adjustment ability. The study shows that the MRAC method can be used as an alternative to PID and LQR methods.

Additionally, the elevator actuator, which is the basic component of attitude tracking performed on the longitudinal axis, has technical features that directly affect controller design. Future studies will focus on evaluating controller performance using different actuators. Furthermore, the actuator leaning on the mechanical stop point, called saturation, affects the autopilot performance of aircraft. AFCS MRAC algorithms and AFCS system architectures that operate to keep the actuator away from saturation limits will be studied. Moreover, TF mode logical design studies will be conducted on sensor selection, sensor redundancy, mode engagement, or disengagement conditions.

ACKNOWLEDGEMENTS: This work is supported by the 2210-D Domestic Industry-Oriented Master's Scholarship Program of the TÜBİTAK Scientist Support Programs Directorate and is carried out within the scope of Turkish Aerospace's 'Problem and Thesis Pool 2021-1'.

V. REFERENCES

- [1] A. Bongers and J. L. Torres, "Technological change in U.S. jet fighter aircraft," *Res Policy*, vol. 43, no. 9, pp. 1570–1581, Nov. 2014.
- [2] I. Khademi, B. Maleki, and A. Nasserri Mood, "Optimal three dimensional Terrain Following/Terrain Avoidance for aircraft using direct transcription method," in *2011 19th Mediterranean Conference on Control & Automation (MED)*, Corfu, Greece, Jun. 2011, pp. 254–258.
- [3] P. Lu and B. L. Pierson, "Optimal Aircraft Terrain Following Analysis and Trajectory Generation," *Journal of Guidance, Control and Dynamics*, vol. 18, no. 3, pp. 555–560, 1995.
- [4] V. H. Cheng and B. Sridhar, "Technologies for Automating Rotorcraft Nap-of-the-Earth Flight," *Journal of the American Helicopter Society*, vol. 38, no. 2, pp. 78–87, 1993.
- [5] E. N. Johnson and J. G. Mooney, "A Comparison of Automatic Nap-of-the-earth Guidance Strategies for Helicopters," *J Field Robot*, vol. 31, no. 4, pp. 637–653, 2014.
- [6] R. Strenzke, J. Uhrmann, A. Benzler, F. Maiwald, A. Rauschert, and A. Schulte, "Managing Cockpit Crew Excess Task Load in Military Manned-Unmanned Teaming Missions by Dual-Mode Cognitive Automation Approaches," in *AIAA Guidance, Navigation, and Control Conference*, Portland, OR, USA, Aug. 2011, p. 6237.
- [7] F. Barfield, J. Probert, and D. Browning, "All Terrain Ground Collision Avoidance and Maneuvering Terrain Following for Automated Low Level Night Attack," *IEEE Aerospace and Electronic Systems Magazine*, vol. 8, no. 3, pp. 40–47, 1993.

- [8] T. Fleck, "Flight Testing of the Autopilot and Terrain Following Radar System in the Tornado Aircraft," in *AIAA 2nd Flight Testing Conference*, Las Vegas, NV, USA., Nov. 1983, p. 2770.
- [9] R. F. Whitbeck and J. Wolkovitch, "Optimal Terrain Following Feedback Control for Advanced Cruise Missiles," 1982.
- [10] D. Qu, D. Yu, J. Cheng, and B. Lu, "On Terrain Following System with Fuzzy-PID Controller," in *IEEE Chinese Guidance, Navigation and Control Conference*, Yantai, China, Aug. 2014, pp. 497–501.
- [11] W. Ahmed, Z. Li, H. Maqsood, and B. Anwar, "System Modeling and Controller Design for Lateral and Longitudinal Motion of F-16," *Automation, Control and Intelligent Systems*, vol. 4, no. 1, pp. 39–45, 2019.
- [12] Vishal and J. Ohri, "GA tuned LQR and PID controller for aircraft pitch control," in *IEEE 6th India International Conference on Power Electronics (IICPE)*, Kurukshetra, India, Dec. 2014, pp. 1–6.
- [13] M. R. Rahimi, S. Hajighasemi, and D. Sanaei, "Designing and Simulation for Vertical Moving Control of UAV System using PID, LQR and Fuzzy Logic," *International Journal of Electrical and Computer Engineering (IJECE)*, vol. 3, no. 5, pp. 651–659, 2013.
- [14] E. Lavretsky, R. Gadiant, and I. M. Gregory, "Predictor-Based Model Reference Adaptive Control," *Journal of Guidance, Control, and Dynamics*, vol. 33, no. 4, pp. 1195–1201, Jun. 2010.
- [15] S. Zhang, Y. Feng, and D. Zhang, "Application Research of MRAC in Fault-tolerant Flight Controller," *Procedia Eng*, vol. 99, pp. 1089–1098, 2015.
- [16] S. Syed, Z. Khan, M. Salman, and U. Ali, "Adaptive Flight Control of an Aircraft with Actuator Faults," in *IEEE International Conference on Robotics & Emerging Allied Technologies (ICREATE)*, Islamabad, Pakistan, 2014, pp. 249–254.
- [17] Z. Lachini, A. Khosravi, and P. Sarhadi, "Model Reference Adaptive Control Based on Linear Quadratic Regulator for a Vehicle Lateral Dynamics," *International Journal of Mechatronics, Electrical and Computer Technology*, vol. 4, no. 13, pp. 1726–1745, 2014.
- [18] X. Wang, X. Chen, and L. Wen, "The LQR baseline with adaptive augmentation rejection of unmatched input disturbance," *Int J Control Autom Syst*, vol. 15, no. 3, pp. 1302–1313, 2017.
- [19] J. Roshanian and E. Rahimzadeh, "Novel Model Reference Adaptive Control with Application to Wing Rock Example," *Proc Inst Mech Eng G J Aerosp Eng*, vol. 135, no. 13, pp. 1911–1929, 2021.
- [20] P. Patre and S. M. Joshi, "Accommodating Sensor Bias in MRAC for State Tracking," in *AIAA Guidance, Navigation, and Control Conference*, Portland, OR, USA, Aug. 2011, p. 6605.
- [21] J. Schaefer, C. Hanson, M. A. Johnson, and N. Nguyen, "Handling Qualities of Model Reference Adaptive Controllers with Varying Complexity for Pitch-Roll Coupled Failures," in *AIAA Guidance, Navigation, and Control Conference*, Portland, OR, USA, Aug. 2011, p. 6453.
- [22] S. A. Jacklin, "Closing the Certification Gaps in Adaptive Flight Control Software," in *AIAA Guidance, Navigation, and Control Conference*, Honolulu, HI, USA, Aug. 2008, p. 6988.

- [23] M. Norouzi and E. Caferov, "Investigating Dynamic Behavior and Control Systems of the F-16 Aircraft: Mathematical Modelling and Autopilot Design," *International Journal of Aviation Science and Technology*, vol. 4, no. 2, pp. 75–86, 2023.
- [24] C. Kim, C. Ji, G. Koh, and N. Choi, "Review on Flight Control Law Technologies of Fighter Jets for Flying Qualities," *International Journal of Aeronautical and Space Sciences*, vol. 24, no. 1, pp. 209–236, 2023.
- [25] L. Sonneveldt, Q. P. Chu, and J. A. Mulder, "Constrained Adaptive Backstepping Flight Control: Application to a Nonlinear F-16/MATV Model," in *AIAA Guidance, Navigation, and Control Conference and Exhibit*, 2006, p. 6413.
- [26] T. Keviczky and G. J. Balas, "Receding horizon control of an F-16 aircraft: A comparative study," *Control Eng Pract*, vol. 14, no. 9, pp. 1023–1033, 2006.
- [27] S. Seshagiri and E. Promptun, "Sliding Mode Control of F-16 Longitudinal Dynamics," in *American Control Conference*, Seattle, WA, USA, Jun. 2008, pp. 1770–1775.
- [28] D. T. Ocaña, H.-S. Shin, and A. Tsourdos, "Development of a nonlinear reconfigurable f-16 model and flight control systems using multilayer adaptive neural networks," *IFAC-PapersOnLine*, vol. 48, no. 9, pp. 138–143, 2015.
- [29] G. E. Ceballos Benavides, M. A. Duarte-Mermoud, M. E. Orchard, and A. Ehijo, "Enhancing the Pitch-Rate Control Performance of an F-16 Aircraft Using Fractional-Order Direct-MRAC Adaptive Control," *Fractal and Fractional*, vol. 8, no. 6, p. 338, 2024.
- [30] R. Russell, "Non-linear F-16 Simulation using Simulink and Matlab," Version 1.0, University of Minnesota, Minneapolis, MN, USA, Tech. Rep., Jun. 2003.
- [31] B. L. Stevens, F. L. Lewis, and E. N. Johnson, *Aircraft Control and Simulation*, 3rd ed. Hoboken, NJ, USA: John Wiley & Sons, 2015.
- [32] L. T. Nguyen, M. E. Ogburn, W. P. Gilbert, K. S. Kibler, P. W. Brown, and P. L. Deal, "Simulator Study of Stall/Post-Stall Characteristics of a Fighter Airplane with Relaxed Longitudinal Static Stability," *NASA Technical Paper 1538*, vol. 12854, 1979.
- [33] Y. Wei, H. Xu, and Y. Xue, "Adaptive Neural Networks-Based Dynamic Inversion Applied to Reconfigurable Flight Control and Envelope Protection under Icing Conditions," *IEEE Access*, vol. 8, pp. 11577–11594, 2020.
- [34] M. Sadeghi, A. Abaspour, and S. H. Sadati, "A novel integrated guidance and control system design in formation flight," *Journal of Aerospace Technology and Management*, vol. 7, no. 4, pp. 432–442, 2015.
- [35] I. Necoara, L. Ferranti, and T. Keviczky, "An adaptive constraint tightening approach to linear model predictive control based on approximation algorithms for optimization," *Optim Control Appl Methods*, vol. 36, no. 5, pp. 648–666, Sep. 2015.
- [36] M. R. Mortazavi and A. Naghash, "Pitch and flight path controller design for F-16 aircraft using combination of LQR and EA techniques," *Proc Inst Mech Eng G J Aerosp Eng*, vol. 232, no. 10, pp. 1831–1843, Apr. 2018.

- [37] Y. Zhu, J. Chen, B. Zhu, and K. Y. Qin, "Synchronised trajectory tracking for a network of MIMO non-minimum phase systems with application to aircraft control," *IET Control Theory & Applications*, vol. 12, no. 11, pp. 1543–1552, Jul. 2018.
- [38] Z. Oreg, H. S. Shin, and A. Tsourdos, "Model identification adaptive control - Implementation case studies for a high manoeuvrability aircraft," in *27th Mediterranean Conference on Control and Automation, MED*, Akko, Israel, Jul. 2019, pp. 559–564.
- [39] O. Albostan, "Flight Control System Design of F-16 Aircraft using Robust Eigenstructure Assignment," Graduate School of Science, Engineering and Technology, İstanbul Technical University, İstanbul, Türkiye, 2017.
- [40] J. C. Lagarias, J. Reeds, M. H. Wright, and P. E. Wright, "Convergence Properties of the Nelder-Mead Simplex Method in Low Dimensions," *SIAM Journal on Optimization*, vol. 9, no. 1, pp. 112–147, 1998.
- [41] H. Aktan and H. Demircioğlu, "Speed and Altitude Hold Autopilot Design and Simulation for F-16 Fighter Aircraft by Using CGPC Method," in *20th National Conference on Automatic Control (TOK 2018)*, Kayseri, Türkiye, Sep. 2018, pp. 58–64.
- [42] "linmod." Accessed: Nov. 16, 2024. [Online]. Available: <https://www.mathworks.com/help/simulink/slref/linmod.html>
- [43] A. Halder, K. Lee, and R. Bhattacharya, "Probabilistic Robustness Analysis of F-16 Controller Performance: An Optimal Transport Approach," in *2013 American Control Conference*, Washington, DC, USA: IEEE, 2013, pp. 5562–5567.
- [44] D. Xue, Y. Chen, and D. P. Atherton, *Linear Feedback Control: Analysis and Design with MATLAB*, 1st ed. Philadelphia, PA, USA: Society for Industrial and Applied Mathematics, 2007.
- [45] "PID Tuner." Accessed: Nov. 16, 2024. [Online]. Available: <https://www.mathworks.com/help/control/ref/pidtuner-app.html>
- [46] A. F. Ajami, "Adaptive Flight Control in the Presence of Input Constraints," M.S. thesis, Virginia Polytechnic Institute and State University, Blacksburg, VA, USA, 2005.
- [47] N. T. Nguyen, *Model-reference adaptive control*, 1st ed. London, UK: Springer International Publishing, 2018.
- [48] N. T. Nguyen and S. N. Balakrishnan, "Bi-objective optimal control modification adaptive control for systems with input uncertainty," *IEEE/CAA Journal of Automatica Sinica*, vol. 1, no. 4, pp. 423–434, 2014.



Düzce University Journal of Science & Technology

Research Article

Strengthening Urban Resilience: A Case Study of Amsterdam's Public Spaces in the Post-COVID Era through Digital Solutions

Fatemeh BADEL ^{a,*}, Jesús LÓPEZ BAEZA ^b Hülya LASCH^c

^a Department of Architecture, Faculty of Architecture and Design, Eskişehir Technical University, 26555, Eskişehir, Turkey

^b Digital City Science, HafenCity Universität Hamburg, 20457 Hamburg, Germany

^c Landesbetrieb Geoinformation und Vermessung (LGV), Hamburg, Germany

* Corresponding author's e-mail address: fateme.badel@gmail.com

DOI: 10.29130/dubited.1427136

ABSTRACT

Given the escalating use of digital tools and the Internet of Things in public spaces for quality control, there is an imperative need to address the following question: How can cities enhance the adaptability of their public spaces in the face of various risks and threats, especially those with consequences spanning all urban areas? The COVID-19 pandemic directed unprecedented attention to public spaces, prompting studies on the role of their digitization in influencing their usage during times of crisis. Here, the question arises: Can digital transformations in public spaces be beneficial during crises? While the digitalization of public spaces has its critics, as examinations indicate, the use of certain tools in these locations during the pandemic was able to positively impact their performance. Amsterdam, through the utilization of digital solutions during the COVID period, functioned notably as a significant case study in enhancing the efficiency of public spaces. The aim of this study is to examine the creation of a comprehensive framework that investigates some of Amsterdam's public spaces during the pandemic. The focus of this study is on evaluating the digital solutions applied to public spaces, with an emphasis on resilience against unforeseen challenges. A list of some digital tools that have made public spaces adaptable during the COVID period is reviewed in this section. In essence, the goal is to learn lessons from Amsterdam and present this perspective for similar experiences in cities worldwide to contribute to the resilience and strengthening of their public spaces.

Keywords: Public space, Digitalization, COVID-19 pandemic, Urban Resilience, Amsterdam

Kentsel Dayanıklılığın Güçlendirilmesi: Dijital Çözümler Yoluyla COVID Sonrası Dönemde Amsterdam'ın Kamusal Alanlarına İlişkin Bir Örnek Çalışması

ÖZET

Kalite kontrolü için kamusal alanlarda dijital araçların ve Nesnelerin İnterneti'nin artan kullanımı göz önüne alındığında, şu soruyu ele alma zorunluluğu ortaya çıkıyor: Şehirler, özellikle çeşitli riskler ve tehditler karşısında kamusal alanların uyumlanabilirliğini, özellikle sonuçları tüm kentsel alanları kapsayacak şekilde nasıl arttırabilir? COVID-19 salgını, kamusal alanlara benzeri görülmemiş bir ilgi

çekerek, kriz zamanlarında bu alanların dijitalleştirilmesinin kullanımlarını etkilemedeki rolü üzerine çalışmalara yol açtı. Burada şu soru ortaya çıkıyor: Kriz dönemlerinde kamusal alanlardaki dijital dönüşümler faydalı olabilir mi? Kamusal alanların dijitalleşmesine karşı eleştiriler bulunsun da, incelemelerin gösterdiği gibi, pandemi sırasında bu yerlerde belirli araçların kullanılması performanslarını olumlu yönde etkileyebildi. Amsterdam, COVID döneminde dijital çözümlerden yararlanarak kamusal alanların verimliliğini arttırmada önemli bir örnek alan çalışması işlevi gördü. Bu çalışmanın amacı, pandemi döneminde Amsterdam'ın bazı kamusal alanlarını inceleyen kapsamlı bir çerçevenin oluşturulmasını sağlamaktır. Bu çalışmanın odak noktası, kamusal alanlara uygulanan dijital çözümlerin, öngörülemeyen zorluklara karşı dayanıklılığa vurgu yaparak değerlendirilmesidir. Bu bölümde, COVID döneminde kamusal alanları uyarlanabilir hale getiren bazı dijital araçların listesi incelenmektedir. Temelde amaç, Amsterdam'dan dersler çıkarmak ve dünya çapındaki şehirlerden elde edilen benzer deneyimlerin perspektifini sunarak kamusal alanların dayanıklılığına ve güçlendirilmesine katkıda bulunmaktır.

Anahtar Kelimeler: Kamusal alan, Dijitalleşme, COVID-19 pandemisi, Kentsel Dayanıklılık, Amsterdam

I. INTRODUCTION

A. CONTEXT OF THE COVID-19 PANDEMIC AND ITS IMPACT ON URBAN PUBLIC SPACES

With the start of the COVID-19 pandemic in 2019 and the subsequent enforcement of restrictions in urban areas, the management of public spaces gained increased prominence within governmental control. Transferring in-person interactions from limited physical spaces to digital spaces was one of the solutions that were quickly adopted by the population, as physical encounters were restricted. New solutions to host social activities remotely accelerated the infusion of the digital sphere across society. In this context, urban planners and architects confronted new challenges to approach the cities of the future. Although the degree of digitalization of public spaces was different across developed and developing countries, digital infrastructure played a pivotal role in facilitating pandemic control measures. Despite a substantial portion of social and business encounters moving into virtual platforms, the undeniable importance of physical public spaces persisted during this period. The global response to the COVID-19 pandemic led to a wide range of measures that significantly impacted everyday life, personal freedoms, and the economy. Various scholars concluded that vulnerable groups experienced the most significant impact during the onset of the outbreak [1]. This study focuses on the Netherlands, where measures included curfew, the closure of education centers, social, cultural, and leisure places, and sporting events. Moreover, the size of social gatherings in public spaces and private homes was regulated, and protective masks and social distancing became norms [2]. The COVID pandemic was not the first time in history that public space was affected by major forces. However, the 21st Century pandemic was the first time in which digital tools and applications could be utilized to quickly offer solutions that were adaptable to fast-changing regulations, to public and private spaces, aligned with both local and EU-wide regulatory frameworks, and open to all areas of society (governments, business, and people).

B. THE SHIFT TO DIGITALIZATION AND ITS IMPLICATIONS

The COVID-19 crisis can be seen as a catalyst for the acceleration of digitalization [3], particularly as digital tools became essential for maintaining health and safety. During the pandemic, many individuals were forced to quickly adapt to using digital technologies, driven by the need to learn how to navigate them for work, education, and daily life. This rapid shift helped expedite the learning process for various digital platforms and tools. However, the pandemic also exposed the limitations of

existing infrastructure and government systems in different countries. While physical digital infrastructure in cities is vital, it is not the sole requirement for successful digitalization [4]. Equally important is the need for a clear agenda in education that ensures all segments of society are included and equipped to navigate the digital landscape.

C. IMPORTANCE OF DIGITAL SOLUTIONS IN PUBLIC SPACE MANAGEMENT POST-COVID

Given the innovative nature of digital solutions implemented during the pandemic to manage public spaces, it is now imperative to evaluate their deployment processes and assess their impact on the post-pandemic city. This study aims to describe the digital solutions considered for public space management in Amsterdam during the pandemic. This comprehensive review outlines measures essential for fortifying the resilience of cities in public spaces against similar threats, drawing on the experiences adopted by Amsterdam during COVID-19. The article specifically focuses on cataloging the diverse tools utilized in Amsterdam during this period and scrutinizing their effectiveness in supporting the use of public spaces both during and after the pandemic. The questions guiding this review are:

How can cities leverage digital tools and the Internet of Things (IoT) to enhance the flexibility of their public spaces in response to various hazards and threats, especially those with widespread urban consequences?

How did Amsterdam utilize digital solutions during the COVID-19 period to increase the efficiency of its public spaces?

D. HISTORICAL CONTEXT OF URBAN PANDEMICS AND TECHNOLOGICAL ADVANCES

Cities with high population density provide an ideal setting for the rapid spread of viruses. COVID-19 is not the first pandemic to affect urban areas; historical examples like the Spanish flu, cholera, and the plague have had significant impacts on city populations [5], [6]. The severe consequences of these pandemics have also driven innovations and the development of modern urban planning solutions [7]. The cholera outbreaks of the 19th century, for example, led to significant advancements in urban sanitation and public health infrastructure. Cities like London developed extensive sewage systems and clean water sources in a concerted effort to combat the widespread transmission of the disease [8]. Similarly, the 1918 Spanish flu pandemic highlighted the need for open-air spaces in urban areas. It was observed that a combination of fresh air and sunlight might help reduce the risk of secondary respiratory infections. This led to a greater emphasis on expanding parks and open public spaces to create healthier living environments for city residents [9]. Following the rise of tuberculosis epidemics in the 19th century in North America and Western Europe, cities adopted new strategies for public spaces. These efforts resulted in an increased presence of green areas and the development of housing policies that regulated the layout and design of buildings to ensure that every home had access to natural light [10]. The COVID-19 pandemic also accelerated progress in certain areas of digital infrastructure, particularly within health systems. For instance, in Turkey, telemedicine was promoted through tools such as the 'Hayat Eve Siğar' (Life Fits Home) [11] app and the E-Nabız health system, both of which helped track COVID-19 symptoms, manage hospital capacities, and monitor public health. Additionally, the pandemic spurred the development of public health monitoring systems, including the Crowd Monitoring System Amsterdam (CMSA), which helps manage crowd density in urban areas. Over the last few decades, large technological advances have coevolved with increased urbanization [12], setting the stage for even more rapid changes during the COVID-19 pandemic. The

rise of telemedicine, digital health systems, and public health monitoring technologies reflects this broader trend, as these innovations helped urban centers adapt to new public health challenges.

In this context, the pandemic significantly accelerated the digital transformation of public services, particularly through the shift to online platforms. This transformation not only streamlined service delivery but also enhanced social participation and increased transparency in governance [10].

E. TECHNOLOGICAL TOOLS DURING THE PANDEMIC AND THEIR APPLICATIONS

During the COVID-19 pandemic, the use of digital technologies played a central role in monitoring health and enforcing public safety measures. For example, infrared thermal cameras were used at airports in Taiwan to capture images of individuals with a fever, and in Singapore, temperatures were measured upon entering schools, workplaces, and public transportation [13]. Other technologies, such as surveillance cameras with facial recognition capabilities, drones for services like food delivery and crowd monitoring, and robots for disinfection and medication delivery, became widespread during the pandemic [14], [15].

F. AMSTERDAM'S DIGITAL RESILIENCE AND PUBLIC SPACE MANAGEMENT

The COVID-19 pandemic has underscored the need for cities to adapt and innovate digitally to ensure resilience, particularly in managing public spaces and urban systems. De Lucas Ancillo et al. (2021) argue that the digital transformation resulting from the pandemic is not simply a shift from traditional methods to digital alternatives; rather, it necessitates a fundamental break from previous operational models [16]. This transformation, driven by health crises, accelerates innovation, with cities becoming key sites for testing and implementing new digital solutions. During the pandemic, there was an increased focus on maintaining health and promoting a healthier lifestyle, particularly in urban settings. The importance of urban green spaces and car-free areas (such as more space for walking or cycling) rose significantly. This focus on health was intertwined with the broader digital transformation, as cities leveraged technological tools to create smarter, more resilient spaces. While the pandemic created opportunities for innovation, it also accelerated pre-existing inequalities, as access to digital solutions was not uniform across populations [17]. Amsterdam, alongside cities like London, Paris, Dublin, and Frankfurt, stands out as a key hub in Europe's digital infrastructure, thanks to its high concentration of data centers. These centers are crucial for managing the massive flow of internet traffic across Europe, with much of the data being exported to users outside the country. Amsterdam's role as a critical data exchange hub has only grown, underscoring the city's reliance on a robust digital infrastructure to handle increasing demands, particularly during a global crisis like the pandemic [18].

The pandemic also highlighted how digital technologies can be mobilized to control public health crises. Governments around the world, including the Netherlands, leaned on technological solutions to manage public spaces and reduce transmission. Digital platforms were used for everything from healthcare management to facilitating remote work and virtual interactions. Technology was pivotal in enabling society to cope with lockdown measures and avoid the worst effects of the pandemic [19]. The Netherlands' approach to managing the COVID-19 pandemic, particularly through its "intelligent lockdown" policy, differed from that of many other European countries. While countries like Italy and France implemented strict national lockdowns and restricted non-essential travel, the Netherlands adopted a more flexible strategy, balancing public health concerns, economic impact, and protection of vulnerable individuals. This policy included measures such as the closure of cafes, schools, and gyms, but allowed people to move freely while observing a 1.5-meter social distancing rule. A study by Haas, Faber, and Hamersma (2020) [20] found that 80% of people reduced their outdoor activities,

with elderly individuals being particularly affected. Furthermore, 44% of workers began working from home, and 30% shifted to holding more meetings online. While the "intelligent lockdown" was a nationwide strategy, other cities in the Netherlands, such as Rotterdam and Utrecht, adopted similar measures. Digital tools for crowd monitoring, social distancing enforcement, and sensor-based technologies were widely used across the country to mitigate the spread of the virus and ensure public safety in crowded spaces [17].

At the beginning of the pandemic, the Netherlands, like countries such as Germany, France, and Italy, implemented similar strategies for social distancing, wearing masks, working from home, and protecting healthcare infrastructure. However, the Netherlands' "intelligent lockdown" strategy differed from other countries because it primarily emphasized personal responsibility and individual behavior. Unlike its neighboring countries, which adopted stricter measures, the Dutch government focused on personal responsibility, keeping schools open, and relying on individuals to follow social distancing guidelines. The aim of these policies was to prevent overwhelming the healthcare system and minimize economic disruptions. Significant financial support was also provided to businesses, which helped mitigate the negative economic effects. Overall, the Netherlands positioned itself between Sweden's more lenient approach and Germany's stricter policies, achieving relatively favorable health and economic outcomes, although it faced challenges [21].

In particular, as the largest city and capital of the Netherlands, Amsterdam attracted more attention during the COVID-19 pandemic due to its dense population and large number of tourists. The city adopted digital solutions to control and prevent further spread of the virus, thanks to its stronger digital infrastructure and data-driven approaches compared to other cities. Public spaces and public transportation systems received significant attention during this period. Due to Amsterdam's differences from other cities in terms of innovative technologies, it was chosen as a case study.

G. TURKEY'S DIGITAL ADAPTATION IN PUBLIC SPACE MANAGEMENT DURING THE COVID-19 PANDEMIC

While Amsterdam's rapid adoption of digital solutions during the COVID-19 pandemic showcases a model of innovation within Europe, Turkey's digital transformation offers a broader perspective on how different regions implemented technology to address the pandemic's challenges. Both cities embraced digital tools, but their strategies were shaped by distinct socio-political contexts and infrastructural needs. Amsterdam focused on remote work and online services, while Turkey expanded its digital services in healthcare, government, and local municipalities, providing a more holistic national digital response. For example, Turkey significantly expanded its e-government services, increasing the number of available services from 5,058 in 2020 to 6,664 by 2022 [22]. This expansion made it easier for citizens to access essential services such as social support applications, travel permits, and address changes. In parallel with Amsterdam's digital push for remote work platforms, Turkey also emphasized telemedicine, using tools like the "Hayat Eve Sığar" (Life Fits Home) [11] app and the E-Nabız health system to track COVID-19 symptoms, manage hospital capacities, and provide remote health consultations [22]. These systems not only allowed citizens to schedule vaccinations but also facilitated access to critical health data, reducing the need for in-person healthcare visits and supporting those with limited access to medical facilities [23]. Additionally, Turkey's national and local governments played a crucial role in accelerating digital transformation. Municipalities like Bartın, Beşiktaş, and Trabzon transitioned many services to digital platforms, including virtual cultural events and smart systems to enforce social distancing and mask-wearing. These local initiatives helped address the immediate needs of urban populations during lockdowns and mobility restrictions [24], [25]. While Amsterdam also advanced its digital infrastructure to facilitate city services, Turkey's focus on local government digitalization, alongside national healthcare efforts,

illustrates a comprehensive approach to digital governance. Both countries faced challenges in addressing the digital divide, but Turkey's experience underscores the importance of improving digital literacy and ensuring equitable access to technology for all citizens [4].

H. METHODOLOGY

This study builds upon the work of Hueck [26], whose research examined the ways young adults in Amsterdam attributed significance to public spaces during the COVID-19 pandemic, focusing on their increased appreciation, participation, and emotional connection to these spaces. In particular, Hueck's study found that during the lockdown, public spaces served as vital locations for social interaction, identity formation, and well-being. In contrast, this research specifically investigates the role of digital tools and technologies that were implemented in Amsterdam's public spaces during the same period to enhance their functionality and resilience. These tools were part of the city's broader effort to adapt urban environments in response to the pandemic and ensure public safety while facilitating the continued use of public spaces.

The methodology employed in this study involves two main data collection approaches:

Field Observations: The researchers conducted direct observations in various public spaces across Amsterdam, such as Vondelpark, Marineterrein, and Kalverstraat, to examine the integration of digital tools, including smart cameras, decision-support systems, sensors, and AI applications. The focus was on how these technologies were used to manage crowd density, facilitate social distancing, and monitor public health compliance. Observational data was collected on the types of digital tools deployed, their visibility and accessibility to the public, and how they contributed to reshaping public space use during the pandemic.

Document and Report Analysis: The study also utilized secondary data from official reports, government publications, and urban planning documents published during and after the pandemic. These sources include technical descriptions of the digital tools implemented in public spaces, such as the Privacy-by-Design Public Eye system, Crowd Management Decision-Support Systems (CM-DSS), smartphone applications, sensors, and AI-driven solutions like the Fitness Garden at Marineterrein. The analysis of these documents provided insights into the rationale behind the deployment of these technologies, their functionality, and their role in ensuring public health safety.

This mixed-methods approach—combining real-world observations with an in-depth review of official data—allowed for a comprehensive analysis of how digital tools were utilized in Amsterdam's public spaces. By focusing on how these technologies were integrated into urban environments, this study aims to assess their effectiveness in promoting public safety, enhancing public space resilience, and supporting the reconfiguration of public spaces during a global health crisis.

II. THE ROLE OF PUBLIC SPACE DURING THE TIME

Ali Madanipour's definition of public space is articulated as "a space that allows all people to have access to it and the activities within it, which is controlled by a public agency and provided and managed in the public interest" [27]. This conceptualization establishes a foundational understanding wherein public spaces are construed as entities overseen by public authorities for the collective benefit. Throughout history, public spaces held major significance for both citizens and governing bodies, serving such diverse functions as social participation, political protests, declarations of solidarity, and hosting cultural interactions. The dynamic nature and continual evolution of public space can be observed despite experiencing morphological and functional shifts across historical periods, public spaces persist as pivotal urban elements. The evolution of public spaces has been significantly shaped

by successive historical periods, such as industrial revolutions, transportation trends, and popularization of specific urban fabric types. The contemporary digital revolution has introduced electronic devices, digital equipment, smart technologies, and the Internet of Things, reinforcing the trend of “privatization” within public spaces. This nuanced historical examination, complemented by Madanipour's elucidation, enhances scholarly comprehension of s within urban landscapes.

The urban setting presents a range of physicochemical dangers, encompassing pollution, traffic-related risks, and the exacerbation of heat waves attributable to the "urban heat island" effect. Furthermore, limited space for walking, cycling, and active lifestyles contributes to cities becoming hotspots for the non-communicable diseases epidemic and catalysts for climate change [28], [29]. This complex scenario can be ascribed to multiple factors, including pollution, inadequate sanitation, rising stress levels, dietary habits, and insufficient physical exercise.

Similarly, cities in the 19th and early 20th centuries were afflicted by infectious diseases that thrived in crowded conditions. Inadequate sanitation and dismal living conditions contributed to devastating outbreaks of influenza, typhus, and tuberculosis, claiming the lives of millions of people [30]. Given the emphasis on the significance of public spaces, it becomes imperative to urgently address the need to enhance the resilience of cities. Now, the question arises as to what strategic measures are necessary to implement this goal.

III. THE IMPORTANCE OF URBAN RESILIENCE

Resilience refers to a system's ability to endure disruptions, adapt to changes, and restructure itself while maintaining its fundamental function, structure, identity, and feedback mechanisms [31]. This resilience operates at various levels, encompassing the individual, community, systems, and institutional domains, facilitating interaction with hazards or stressors while enhancing cooperation between entities to maintain or restore function. The ultimate goal is to adapt to a new balance while minimizing the accumulation of previous or additional risks and vulnerabilities [32].

Urban resilience, within this framework, entails creating approaches to enhance the management of urban areas, ensuring their functionality in the face of destructive incidents. Urban resilience is defined as the ability of an urban system – and all its constituent socio-ecological and socio-technical networks across temporal and spatial scales – to maintain or rapidly return to desired functions in the face of a disturbance, to adapt to change, and to quickly transform systems that limit current or future adaptive capacity [33].

The significance of healthy urban environments and access to quality public spaces and natural areas, which have been underscored [34], [35], has become more pronounced in the aftermath of the pandemic. It has highlighted the central role of these spaces in enhancing physical and mental well-being [36], [37]. Research has indicated that elements related to the quality of air [38], [17], the handling of waste [40], [41], public transportation systems [42], [43], sanitation infrastructure [44], [45], and public spaces [46], [47] may impact the transmission of viruses [48]. As urban areas undergo adjustments and recovery, it is crucial to prioritize the creation and upkeep of public spaces that are accessible and inclusive [48]. This is vital for fostering healthier and more resilient urban communities. Insufficient access to parks and recreational areas exacerbates these difficulties, restricting chances for physical activity and meaningful connection with nature, both of which are essential for mental well-being [49], [50]. In general, increasing resilience in public spaces by increasing people's access to these spaces for physical activities, engagement with nature, communication in open spaces can increase the well-being of residents and lead to social cohesion.

While leveraging smart tools and information technologies can enhance the efficiency of urban systems and align them with evidence-based paradigms during crises, it is imperative to acknowledge that resilient urban planning should facilitate fair access to resources and address structural inequalities and vulnerabilities in societies [51], [52]. This consideration is essential to prevent the exacerbation of social crises within this context.

A.THE IMPORTANCE OF PUBLIC SPACE IN BUILDING URBAN RESILIENCE DURING THE PANDEMIC

In the past, the implications of health crises have been instrumental in influencing the trajectory of urban planning and design. Significant measures were undertaken to ameliorate living conditions within cities, including the implementation of robust sanitation and hygiene practices, the introduction of expansive boulevard streets, and the establishment of zoning regulations aimed at delineating industrial activities from residential areas. It is widely recognized that the built environment has a significant impact on both physical and mental health [53], [54].

The COVID-19 pandemic also led modifications in the urban environment with a major difference: instead of morphological changes, measures were mostly regulatory. During the first waves, open public spaces, including streets, urban squares, sidewalks, open markets, some recreational areas, as well as closed public spaces like shopping centers, public libraries, bars, cafes, and certain public buildings, came under the control of government agencies and faced restrictions, limiting presence and sometimes leading to strict control measures and nudging social practices to shift into the virtual realm [55]. Location data, mobile phone apps, digital cameras, and other digital methods were extensively utilized in the public domain, receiving strong support from governments and relevant stakeholders in their fight against the virus. According to Jacobs (1993) [56], urban vitality is usually associated with perception of security, and vice-versa. Paradoxically, the situation seemed to be reversed during a pandemic, when an empty street became a secure location in terms of minimizing the risk of virus transmission [57].

After the first waves of the virus the re-opening phase started. Governments put emphasis in gradually regaining social life while maintaining control over these spaces with measures such as biometric mass surveillance, temperature checks, and the increased deployment of digital tools in public areas, including surveillance cameras, were employed to prevent the spread of the disease.

It is arguable that public spaces accelerated an already ongoing process of digitalization using the pandemic as a catalyst for testing and implementing solutions [58], [59], especially in the fields of surveillance, facial recognition, and location tracking, but also in general smart city development, telemedicine, online commerce, and education, and multiple other fields of ICT.

B. URBAN RESILIENCE THROUGH DIGITAL SOLUTIONS IN PUBLIC SPACES

The main advanced technologies used for overseeing public spaces include biometrics, closed-circuit television (CCTV), smart identification cards, and electronic devices that monitor and track information communication [60]. Sophisticated technologies and devices, originally designed for securing highly guarded facilities, are increasingly being utilized for monitoring public spaces, surveilling city streets and squares, and enabling the identification of car registration numbers and permits (e.g. LEZ stickers). When coupled with biometric databases, they also allow for facial recognition even when wearing masks. In the context of the COVID pandemic, biometric readers combined with temperature sensors could identify infected individuals in crowds, while mobile phones were used to trace back the movements of specific individuals and reconstruct their personal and social networks. In this context, real-time monitoring and analysis of big data play a crucial role in effectively responding to disruptive events. The combination of IoT sensors, smart city systems, and machine learning techniques can yield significant achievements. The pandemic presented an unparalleled opportunity to gain insights into the impact of global emergencies on cities and take actions to minimize their effects, thereby enhancing urban pandemic resilience [61].

Since the 1990s, there has been a resurgence in interest regarding the connection between health and urban planning, elevating it to a specialized area of study. In the past years, this trend has been aligned with the rapid digitization of urban spaces as a result of the COVID crisis. Hence, it is evident that digital technologies hold the capacity to act as a transformative influence in shaping the future of cities and public spaces by being rapidly adaptable to respond to specific needs or crisis [62] and therefore become one of the key enablers of urban resilience. After the COVID pandemic, the discussion on threats and challenges that cities are facing shifted from urban health to climate and energy crisis. Once again, advanced technologies implemented in public space monitoring and city management and decision-making assessment are emerging as a fast and easy-to-deploy solutions targeting the causes and effects of urban threats and challenges. Technological developments to monitor and control

energy consumption of buildings, traffic congestion, or vehicle access to areas might have the same underlying concepts as those implemented for people-tracking during the pandemic, funneling urban resources to mitigate negative impact of stressors, therefore making cities resilient entities.

IV. CASE STUDY: AMSTERDAM'S RESPONSE TO COVID-19

Urban resilience has always been one of the main focuses in Europe in the face of shocks and challenges such as natural disasters, epidemics and crises. The European Union (EU) expressed its inclination towards the advancement of secure and inclusive technology, offering a valuable foundation for the creation of digital public spaces and offering an alternative perspective on technology, emphasizing collective public values instead of market or state values [63]. In this context, Amsterdam's substantial investments in digital infrastructure endowed it with the capacity to effectively monitor and oversee public spaces. Amsterdam adeptly alleviated the challenges posed by the COVID-19 pandemic through the utilization of its well-established smart infrastructure. Moreover, the implementation of digital solutions fostered a cohesive environment between citizens and governance, facilitating enhanced decision-making processes, facilitating valuable feedback mechanisms, and facilitate people's reentry into public spaces and enhance their utilization during the pandemic period.

This research builds upon Hueck's study (2021), who examines the way young adults attributed importance to public spaces in Amsterdam during the COVID-19 pandemic by evaluating their appreciation, participation, and emotional connection. During the lockdown in Amsterdam, respondents regarded public spaces as locations that: (i) garnered increased appreciation, (ii) contributed to the development of youth identity, and (iii) played a vital role in well-being [26].

In this study, we investigate digital tools and solutions which utilized in Amsterdam public spaces to enhance their function during the COVID-19 period. The main objective of this study is to examine the tools and approaches that have assisted government and municipality of Amsterdam in the reutilization of public spaces during this period. The methodology employed in this research encompasses data collection through observation and gathering information from published reports during that period.

A. ENHANCING URBAN RESILIENCE: IMPLEMENTATION OF DIGITAL TOOLS AND TECHNOLOGIES IN AMSTERDAM'S PUBLIC SPACES

Amsterdam emerged as a beacon of urban resilience through the strategic implementation of digital tools and technologies in its public spaces, particularly during the challenging times of the COVID-19 pandemic. The city's innovative approach encompassed a comprehensive array of solutions, including Smart Cameras, Decision-Support Systems, Applications, Sensors, AI Applications, and Digital Mapping Tools. Amsterdam's multifaceted approach to incorporating digital tools and technologies in public spaces reflected a forward-thinking and adaptable urban strategy. While navigating the complexities of the pandemic, the city set a benchmark for leveraging innovation responsibly, ensuring public safety, and fostering a resilient urban environment.

A. Smart Cameras

In managing public spaces during the COVID-19 era, Amsterdam utilized city surveillance systems, famously known as the 'Public Eye,' to ensure public safety and compliance with health regulations. Innovative digital tools played a significant role in facilitating social distancing measures in crowded areas.

Amsterdam pioneered the use of population monitoring technology with its Privacy-by-Design Public Eye system. The Public Eye system for head-counting employs pre-existing city cameras along with a novel artificial intelligence (AI) algorithm based on computer vision technology. This combination is utilized for the monitoring and prediction of crowd size, density, direction, and speed within public spaces, and it was further customized to gauge compliance with social distancing measures during the pandemic [64].

The features of advanced surveillance systems, utilized for monitoring public spaces during the COVID-19 pandemic in Amsterdam, are detailed in Figure 1.







Digital Tools Used In Public Spaces During The COVID-19 In Amsterdam	Function	Deployment area
Smart Cameras		3D Crowd sensors and cameras for emergency regulation Corona. Source: Responsible Sensing Lab - CMSA Project Report, 2020 
	1- Detecting count of people by head (no facial recognitions)	Marineterrein Test Zone for innovation and its map at the entrance. Source: May 2022. Hülya Lasch. 
	2- Accelerated deployment and integration with video analytics	Marrineterrein Shutter camera, camera sticker and the information board. Source: May 2022. Hülya Lasch. 
	3- People counting for restricted entrances	
	4- Counting people for crowd management due to corona regulations (Public Eye)	Fitness Garden at Marineterrein. Source: May 2022. Hülya Lasch. 
	5- Detecting crowd and social distance violations (>1,5 meter) (Fitness Garden, Marineterrein)	Dam Square Public Eye camera. Source: May 2022. Hülya Lasch. 
		Kalverstraat/Muntplein Camera and camera sticker. Source: May 2022. Hülya Lasch. 

Figure 1. Digital tools used in public space, smart cameras, Source: Authors

B. DECISION-SUPPORT SYSTEMS

Amsterdam implemented digital tools employing sensors, cameras, and AI to monitor and enhance crowd management during the COVID-19 pandemic. While these technologies played a crucial role in mitigating the virus's spread and ensuring public safety, they also raised concerns about increased surveillance, privacy infringement, and data security. The City of Amsterdam is developing a Crowd Management Decision-Support System (CM-DSS) as part of the CityFlows project, funded by the European Institute of Innovation and Technology (EIT) Urban Mobility initiative, to actively monitor and manage crowded spaces using real-time decision support systems. Originally intended for large events, the project has adapted to the new reality by implementing crowd management systems to monitor social distancing at busy locations. The system produces real-time data, aiding city officials in informing social-distancing measures through dashboards [65], [66].




Digital Tools Used In Public Spaces During The COVID-19 In Amsterdam	Function	Deployment area	
Technical tools	1- Crowd monitoring physical information dashboards - Crowd	Marrineterrein Dashboard. Source: May 2022. Hülya Lasch.	
	Management Decision-Support (CM-DSS) System (Marrineterrein)	Dam Square camera sticker with a unique ID-Code. Source: May 2022. Hülya Lasch.	
	2- Cameras and camera stickers (Crowd Management Decision-Support (CM-DSS) System)	Dam Square camera sign. May 2022. Hülya Lasch.	

Figure 2. Digital tools used in public space, Decision-support systems, Source: Authors

C.APPLICATIONS

During the COVID-19 pandemic, Amsterdam implemented various smartphone applications to address crowd monitoring and control, as well as proximity tracing. Citizens were informed about the presence and usage of crowd monitoring cameras in public spaces, ensuring transparency in surveillance measures. Additionally, Marineterrein Amsterdam served as a test area for crowd monitoring, offering valuable insights into crowd control strategies and proximity tracing. Public Eye, a prominent tool utilized during this period, provided measurements and data in Vondelpark and contributed to the overall COVID-19 Living Lab project. The Marineterrein DrukMeter, used for monitoring curfew behavior, played a vital role in gathering data during the lockdown. These efforts exemplify the city's commitment to leveraging digital tools and open-source technologies to manage public spaces effectively while ensuring public safety and health during the pandemic.





Digital Tools Used In Public Spaces During The COVID-19 In Amsterdam	Function	Deployment area
Applications	1- information to citizens about crowd monitoring cameras 2- crowd control, proximity tracing	Marineterrein Amsterdam test area for the crowd monitor (Source: Tapp - Smart City Architecture, 2022) 
		Measurements of a day Vondelpark data by Public Eye (Source: CityFlows Project. (n.d.). COVID-19 Living Lab.2022) 
		Corona curfew behavior measurements of Marineterrein DrukMeter during the lockdown (Source: amsterdamsmartcity.com, Tapp 2021) 
		Application of Public Eye for the open-source crowd monitoring at the Marineterrein (Source: Tapp 2021) 

Figure 3. Digital tools used in public space, Applications, Source: Authors

D.SENSORS

Amsterdam has embraced innovative sensor technologies to navigate the challenges posed by COVID-19. The COVID-19 living lab acts as a testing ground for various sensors deployed at prominent locations, including Vondelpark, Albert Cuyp Street, Kalverstraat shopping district, and Marineterrein. These sensors encompass a range of technologies, such as 3D sensors, 2D sensors, NUMINA sensors, RFID sensors, and Public Eye cameras [65]. Real-time data is processed by a 24/7 operational crowd monitoring system and assists in ensuring public safety and compliance with COVID-19 regulations. The Responsible Sensing Lab, in collaboration with the City of Amsterdam, has played a key role in ensuring responsible data collection and public acceptance. They've introduced the Responsible Sensing Toolkit to guide organizations and municipalities in the responsible implementation of public sensors [64] (Figure, 4).

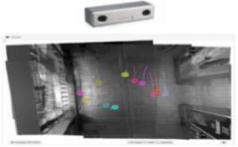
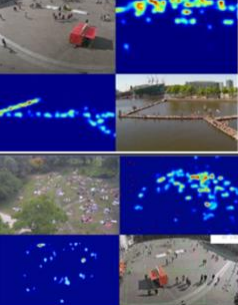
Digital Tools Used In Public Spaces During The COVID-19 In Amsterdam	Function	Deployment area	
Sensors	1. Crowd Monitoring System Amsterdam (CMSA), Count, speed, density, trajectory information and heat maps in terms of Corona emergency regulations 2. Social Distancing Compliance	3D Crowd sensors and cameras for emergency regulation Corona. (Source: Responsible Sensing Lab - CMSA Project Report, 2020)	
		Density map animation (Source: Responsible Sensing Lab - CMSA Project Report, 2020 and Tapp, 2021)	

Figure 4. Digital tools used in public space, Sensors, Source: Authors

E.AI APPLICATIONS

In response to the challenges posed by the COVID-19 pandemic, Amsterdam has leveraged AI applications to enhance public health and wellness initiatives. The city recognized the importance of providing safe outdoor fitness facilities for its residents during lockdowns. As a result, in collaboration with the Marineterrein living lab, Amsterdam introduced the Fitness Garden at Marineterrein, incorporating AI and computer vision technology. This innovative solution employs AI to count the number of individuals using the Fitness Garden while also detecting instances of people coming within a 1.5-meter proximity, adhering to social distancing guidelines. Additionally, IoT technology, coupled with LED lighting, plays a crucial role by dynamically changing the colors of lights based on safe distancing and capacity limits. When the AI identifies people within 1.5 meters of each other, the LED strip turns red, serving as a visual reminder for visitors to maintain a safe distance from one another [64]. This pioneering use of AI technology demonstrates Amsterdam's commitment to enhancing public health and safety during the pandemic.

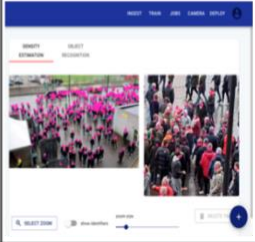



Digital Tools Used In Public Spaces During The COVID-19 In Amsterdam	Function	Deployment area
AI Applications		Open Source AI / Computer vision technology, IoT technology and the LED lighting for detecting social distance violations (>1,5 meter) - the operation of the pressure gauge (Source: https://www.tapp.nl/project-overview/public-eye)
	1- Detecting count of people by head (no facial recognitions)	
	2- The processing of data collected on digital platforms and mobile networks to track people's recent movements	
	3- Detecting crowd and social distance violations (>1,5 meter) (Fitness Garden, Marineterrein)	
		The live pressure gauge (Source: https://www.marineterrein.nl/nu/)
		Amsterdam's Fitness Garden at Marineterrein uses AI and computer vision for crowd monitoring, with AI-driven LED lights promoting safe distancing 24/7. (Source: https://www.tapp.nl/project-overview/ffg)
		

Figure 5. Digital tools used in public space, AI applications, Source: Authors

F. DIGITAL MAPPING TOOLS

Amsterdam has implemented digital mapping tools to tackle the challenges of enforcing social distancing during the COVID-19 pandemic. These tools include a mapping application that assesses the feasibility of social distancing in public spaces, with a specific focus on sidewalks and public transportation infrastructure. Additionally, the Social Distancing Dashboard, developed in collaboration with Delft University of Technology and the Amsterdam Institute for Advanced Metropolitan Solutions, offers valuable data to policymakers and city planners, aiding in their decision-making process for COVID-19 interventions [67]. The Municipality of Amsterdam has also introduced the SecDev Urban Pandemic Preparedness Index, a social vulnerability index that visually represents various data across time and space. This tool assists in the efficient allocation of resources during crises, allowing decision-makers to anticipate areas at a higher risk and optimize various aspects of pandemic response, including vaccination distribution, green recovery initiatives, pollution monitoring, and accessible healthcare facilities [68] (Figure, 6).

Digital Tools Used In Public Spaces During The COVID-19 In Amsterdam	Function	Deployment area
Digital Mapping Tools	1- Mapping Crowd Monitoring Sensors and Cameras to inform citizens about personal data processing in the public space	Map of Crowd Monitoring Sensors and Cameras in Amsterdam - Crowd Monitoring System Amsterdam (CMSA) (Source: https://maps.amsterdam.nl/cmsa/?LANG=nl)
	2- Sensors register	Crowd Monitoring Sensor register - Crowd Monitoring System Amsterdam (CMSA) (Source: https://sensorengister.amsterdam.nl/)
	3- The Social Distancing Dashboard Amsterdam	The Social Distancing Dashboard Amsterdam - The SocialGlass research program - The Delft University of Technology and the Amsterdam Institute for Advanced Metropolitan Solutions (Source: https://covid19.social-glass.tudelft.nl/amsterdam/#15/52.3702/4.8952)
	4- Measuring social and urban pandemic preparedness (Index) for disease control and to inform citizens about areas with risk of more infection in terms of vulnerability	SecDev Urban Pandemic Preparedness Index (Source: https://urbanresilience.secdev.com/amsterdam/map)

Figure 6. Digital tools used in public space, Digital Mapping Tools, Source: Authors

V. CONCLUSION

During the COVID-19 pandemic, various measures undertaken by governments and municipalities through digital technologies aimed at facilitating a return to normal urban life and enhancing security and order in public spaces [32]. As we transitioned beyond the pandemic, it became clear that the digital layer played a crucial role in enhancing the resilience of public spaces during other crises. Digital tools offer diverse functionalities that can help cities manage critical situations and adapt to unforeseen challenges. In this context, Amsterdam's successful integration of digital tools for controlling and reclaiming public spaces positioned these technologies as valuable assets within the decision-making processes of local and regional governments. The COVID-19 pandemic accelerated the digital transformation of public spaces, particularly in cities like Amsterdam. The city successfully leveraged a variety of digital innovations—such as smart cameras, technical tools, applications, sensors, and AI applications—to manage and enhance public spaces. These technologies played an essential role in ensuring public safety, monitoring compliance with health regulations, and enabling the safe reutilization of public spaces. The pandemic highlighted the importance of these tools in adapting to the “new normal” and managing the complexities of public space usage during global health crises. Amsterdam's experience serves as a compelling case study for other cities, demonstrating how digital technologies can fortify the resilience of public spaces in times of crisis. However, it is essential to balance the benefits of these technologies with potential concerns related to surveillance, privacy, and data security. Ongoing discussions about the ethical implications of digital tools, alongside the development of governance frameworks that protect privacy, promote

transparency, and maintain public trust, will be critical to ensuring that these technologies are used in ways that are both beneficial and equitable for all citizens. The evolution of public spaces during the COVID-19 pandemic exemplifies the transformative potential of digital technologies in urban planning. As cities like Amsterdam have shown, these tools can play a pivotal role in crisis management, helping urban areas adapt to unforeseen challenges while maintaining public health and safety. However, the future of urban resilience depends not only on technological advancements but also on ensuring these innovations serve the collective good, creating cities that are inclusive, equitable, and prepared for the complexities of an unpredictable future. The lessons learned from Amsterdam's experience, particularly regarding the responsible implementation of digital technologies, can guide other cities in developing strategies that enhance the resilience of public spaces while safeguarding the values of privacy, equity, and community well-being.

In conclusion, the importance of public spaces as sites for social engagement and identity during times of crisis has been underscored by research, such as that by Hueck (2021) [26], which explored how young adults in Amsterdam attributed increased value to public spaces during the pandemic. These spaces were not only essential for maintaining physical distancing but also played a key role in fostering identity, social cohesion, and mental well-being. Amsterdam's response to the pandemic reflected a broader societal understanding of the role public spaces play in building both community resilience and individual well-being. Therefore, cities must prioritize public spaces as integral to urban health and resilience, ensuring that technological advancements align with the collective good and the protection of individual rights. Amsterdam's experience offers valuable insights that can be adapted globally, even in cities with less advanced digital infrastructures. Future research should further explore the long-term impacts of digital tools on quality of life, social interactions, and mental health, as well as comparative studies on the role of digital technology in managing public spaces during crises.

ACKNOWLEDGEMENT

I would like to extend my heartfelt gratitude to Prof. Dr. Nuray Özaslan for her invaluable guidance and support throughout the preparation of this article. Her expertise and encouragement have been instrumental in shaping my understanding and enhancing the quality of this work.

VI. REFERENCES

- [1] J. Corburn et al., "Slum Health: Arresting COVID-19 and Improving Well-Being in Urban Informal Settlements," Jun. 2020, vol. 97, no. 3, pp. 348-357, doi: 10.1007/s11524-020-00438-6.
- [2] N. Helberger et al., "Conditions for technological solutions in a COVID-19 exit strategy, with particular focus on the legal and societal conditions: report for ZonMw," 2021.
- [3] J. Amankwah-Amoah, Z. Khan, G. Wood, and G. Knight, "COVID-19 and digitalization: The great acceleration," *Journal of Business Research*, vol. 136, pp. 602–611, 2021. [Online]. Available: <https://doi.org/10.1016/j.jbusres.2021.08.011>.
- [4] C. Babaoğlu, "Digitalization of governments during the pandemic: The case of Türkiye," *Insight Turkey*, vol. 24, no. 3, pp. 151–166, 2022.

- [5] E.L. Glaeser and D. Cutler, *Survival of the City: Living and thriving in an age of isolation*, New York: Penguin Press, 2021.
- [6] D. Griffin and J. Denholm, "This isn't the first global pandemic, and it won't be the last. Here's what we've learned from 4 others throughout history," *The Conversation*, 2020. [Online]. Available: <https://theconversation.com/this-isnt-the-first-global-pandemic-and-it-wont-be-the-last-hereswhat-weve-learned-from-4-others-throughout-history-136231>. [Accessed: 21-Dec-2024].
- [7] R. Florida, A. Rodríguez-Pose, and M. Storper, "Cities in a post-COVID world," *Urban Studies*, online first, 2021. [Online]. Available: <https://doi.org/10.1177/00420980211018072>. [Accessed: 21-Dec-2024].
- [8] S. Johnson, *The Ghost Map: The Story of London's Most Terrifying Epidemic—and How It Changed Science, Cities, and the Modern World*, Riverhead Books, 2006.
- [9] R.A. Hobday and J.W. Cason, "The open-air treatment of pandemic influenza," *American Journal of Public Health*, vol. 99, no. S2, pp. S236–S242, 2009.
- [10] M.S. de M. Pinheiro, R.R. Macovei, E. Balabanska, M. Ojal, L. Petrella, K. Schaefer, and J. Torner, *Urban regeneration and viruses: Learning from past and present health crises (Updated ed.)*, United Nations Human Settlements Programme (UN-Habitat), 2024. [Online]. Available: https://unhabitat.org/sites/default/files/2024/03/urbanregeneration_viruses_2024_compressed.pdf. [Accessed: 18-Dec-2024].
- [11] Hayat Eve Sığar (Life Fits Into Home), Ministry of Health of the Republic of Türkiye, Mobile App. [Online]. Available: <https://play.google.com/store/apps/details?id=tr.gov.saglik.hayatevesigar&hl=tr>. [Accessed: 21-Dec-2024].
- [12] E.E. Leamer and M. Storper, "The economic geography of the internet age," *Journal of International Business Studies*, vol. 32, no. 4, pp. 641–665, 2001.
- [13] S. Whitelaw, M.A. Mamas, E. Topol, et al., "Applications of digital technology in COVID-19 pandemic planning and response," *Lancet Digital Health*, vol. 2, pp. 435–440, 2020.
- [14] W. He, Z. Zhang, and W. Li, "Information-technology solutions, challenges, and suggestions for tackling the COVID-19 pandemic," *International Journal of Information Management*, vol. 57, pp. 1–8, 2021.
- [15] N. Chavez and N. Kounang, "A man diagnosed with Wuhan coronavirus near Seattle is being treated largely by a robot," *CNN*, 2020. [Online]. Available: <https://edition.cnn.com/2020/01/23/health/us-wuhancoronavirusdoctorinterview/index.html>. [Accessed: 21-Dec-2024].
- [16] A. De Lucas Ancillo, M.T. del Val Núñez, and S. Gavrilă Gavrilă, "Workplace change within the COVID-19 context: A grounded theory approach," *Economic Research-Ekonomska Istraživanja*, vol. 34, no. 1, pp. 2297–2316, 2021. [Online]. Available: <https://doi.org/10.1080/1331677X.2020.1862689>. [Accessed: 21-Dec-2024].
- [17] J. Van Haaren and F. Van Oort, "The resilience of cities to COVID-19: A literature review and application to Dutch cities," in *The Resilient Region: Regional-Economic Impact Mitigation of Corona-related (De)escalation Policies*, pp. 25–46, Springer, 2021.
- [18] Nederland Digitaal, "The Dutch Digitalisation Strategy 2021 (DDS)," 22-Jun-2021. [Online]. Available: <https://www.nederlanddigitaal.nl/2021/06/22>. [Accessed: 21-Dec-2024].

- [19] A. Jaiswal, "Covid-19 pandemic: Digital technology usage and associated socio-technological challenges," *HABITUS Journal of Sociology*, vol. 3, pp. 233–249, 2022.
- [20] de Haas, M., Faber, R., & Hamersma, M., "How COVID-19 and the Dutch 'intelligent lockdown' change activities, work and travel behaviour: Evidence from longitudinal data in the Netherlands," *Transportation Research Interdisciplinary Perspectives*, vol. 6, 100150, 2020. [Online]. Available: <https://doi.org/10.1016/j.trip.2020.100150>.
- [21] C. Van Dullemen and J. de Bruijn, "The Dutch approach to COVID-19: How is it distinctive?" *PRISM*, vol. 9, no. 4, pp. 106–117, 2022.
- [22] Türkiye Digital Government Gateway, "Information about e-Government Gateway," [Online]. Available: <https://www.turkiye.gov.tr>. [Accessed: 29-May-2022].
- [23] C. Babaoğlu and O. Kulaç, "Government initiatives and responses to COVID-19 pandemic: The case of Turkey," in *Effective Public Administration Strategies for Global "New Normal"*, P.G. Aquino and R.C. Jalagat, Eds., p. 123, Springer, 2020.
- [24] C. Babaoğlu and O. Erdoğan, "Koronavirüs döneminde yerel yönetimlerde dijitalleşme," paper presented at the 6th Ulusal Yerel Yönetimler Sempozyumu, 24–27 Oct. 2021.
- [25] A. Aytekin, H. Özköse, and M. Temli, "COVID-19 pandemi nedeniyle yerel yönetimlerde dijital dönüşümden kaynaklanan sorunlar ve çözüm önerileri: Bartın ili örneği," in *COVID-19 ve toplum: Salgının sosyal, beşeri ve ekonomik etkileri, sorunlar ve çözümler*, Ministry of Industry and Technology and TÜBİTAK, p. 102, 2021.
- [26] L. Z. Hueck, "Public space, place identity, and COVID-19: Towards more suitable public spaces for Amsterdam's young adults," Wageningen University, Metropolitan Analysis Design and Engineering, Msc Thesis, Wageningen University, 2021.
- [27] A. Madanipour, "Public and private spaces of the city," Routledge, 2003.
- [28] A. J. McMichael, "The Urban Environment and Health in a World of Increasing Globalization: Issues for Developing Countries," *Bulletin of the World Health Organization*, vol. 78, pp. 1117–1126, 2000.
- [29] World Health Organization, "Urban health," World Health Organization, 2022. [Online]. Available: https://www.who.int/health-topics/urban-health#tab=tab_1. [Accessed: 23-Dec-2024].
- [30] D. Vlahova, "The Spatial Expression of Epidemic Disease in Istanbul: Quarantine Buildings in Karantina Island and on the European Shore of the Bosphorus," in *Cities and Catastrophes*, 2003, pp. 135–170.
- [31] B. Walker et al., "Resilience, adaptability and transformability in social–ecological systems," *Ecology and society*, vol. 9, no. 2, 2004.
- [32] R. Patel and L. Nosal, "Defining the resilient city," New York: United Nations University Centre for Policy Research, 2016.
- [33] S. Meerow et al., "Defining urban resilience: a review," *Landsc. Urban Plann.*, vol. 147, pp. 38–49, 2016. [Online]. Available: <https://doi.org/10.1016/J.LANDURBPLAN.2015.11.011>.

- [34] Z. S. Venter et al., "Urban nature in a time of crisis: recreational use of green space increases during the COVID-19 outbreak in Oslo, Norway," *Environ. Res. Lett.*, vol. 15, p. 104075, 2020. [Online]. Available: <https://doi.org/10.1088/1748-9326/abb396>.
- [35] A. L. Istrate and F. Chen, "Liveable streets in Shanghai: Definition, characteristics and design," *Prog. Plann.*, vol. 158, 2022. [Online]. Available: <https://doi.org/10.1016/j.progress.2021.100544>.
- [36] D. Sikorska et al., "Rethinking urban green spaces for urban resilience. Do green spaces need adaptation to meet public post-covid expectations?" *Urban For. Urban Green*, vol. 80, p. 127838, 2023. [Online]. Available: <https://doi.org/10.1016/J.UFUG.2023.127838>.
- [37] T. Noszczyk et al., "The impact of the COVID-19 pandemic on the importance of urban green spaces to the public," *Land Use Pol.*, vol. 113, p. 105925, 2022. [Online]. Available: <https://doi.org/10.1016/J.LANDUSEPOL.2021.105925>.
- [38] H. Bherwani, S. Gautam, and A. Gupta, "Qualitative and quantitative analyses of impact of COVID-19 on sustainable development goals (SDGs) in Indian subcontinent with a focus on air quality," *Int. J. Environ. Sci. Technol.*, vol. 18, pp. 1019–1028, 2021. [Online]. Available: <https://doi.org/10.1007/s13762-020-03122-z>.
- [39] I. Jakovljević et al., "Influence of lockdown caused by the COVID-19 pandemic on air pollution and carcinogenic content of particulate matter observed in Croatia," *Air Qual. Atmos Health*, vol. 14, pp. 467–472, 2021. [Online]. Available: <https://doi.org/10.1007/s11869-020-00950-3>.
- [40] A. Ouigmane et al., "Effect of COVID-19 on the generation of waste in Marrakech, Morocco," *J. Health Pollut.*, vol. 11, pp. 1–9, 2021. [Online]. Available: <https://doi.org/10.5696/2156-961411.30.210606>.
- [41] H. Onoda, "Smart approaches to waste management for post-COVID-19 smart cities in Japan," *IET Smart Cities*, vol. 2, pp. 89–94, 2020. [Online]. Available: <https://doi.org/10.1049/iet-smc.2020.0051>.
- [42] C. Kakderi, E. Oikonomaki, and I. Papadaki, "Smart and resilient urban futures for sustainability in the post covid-19 era: a review of policy responses on urban mobility," *Sustainability (Switzerland)*, vol. 13, p. 6486, 2021. [Online]. Available: <https://doi.org/10.3390/su13116486>.
- [43] B. Braut, M. Migheli, and E. Truant, "Household mobility in food purchasing during COVID-19 lockdown: evidence from Torino, Italy," *Cities*, vol. 122, p. 103554, 2022. [Online]. Available: <https://doi.org/10.1016/j.cities.2021.103554>.
- [44] A. M. Auerbach and T. Thachil, "How does Covid-19 affect urban slums? Evidence from settlement leaders in India," *World Dev.*, vol. 140, 2021. [Online]. Available: <https://doi.org/10.1016/j.worlddev.2020.105304>.
- [45] N. Shermin and S. N. Rahaman, "Assessment of sanitation service gap in urban slums for tackling COVID-19," *J. Urban Manag.*, vol. 10, pp. 230–241, Jun. 2021, doi: [10.1016/j.jum.2021.06.003](https://doi.org/10.1016/j.jum.2021.06.003).
- [46] J. Honey-Rosés et al., "The impact of COVID-19 on public space: an early review of the emerging questions – design, perceptions and inequities," *Cities Health*, pp. 1–17, 2020. [Online]. Available: <https://doi.org/10.1080/23748834.2020.1780074>.

- [47] D. D'alessandro et al., "COVID-19 and living space challenge. Well-being and public health recommendations for a healthy, safe, and sustainable housing," *Acta Biomed*, vol. 91, pp. 61–75, 2020. [Online]. Available: <https://doi.org/10.23750/abm.v91i9-S.10115>.
- [48] J. R. E. Hernandez et al., "Cities in the times of COVID-19: Trends, impacts, and challenges for urban sustainability and resilience," *Journal of Cleaner Production*, p. 139735, 2023.
- [49] Z. I. Abass, "Green spaces in residential communities: the potential for ecological and health," in *IOP Conf Ser Earth Environ Sci*, 2021. [Online]. Available: <https://doi.org/10.1088/1755-1315/779/1/012011>.
- [50] Z. Wang et al., "The study of healthy benefits and design strategy of urban residential green space," in *IOP Conf Ser Earth Environ Sci*, 2021. [Online]. Available: <https://doi.org/10.1088/1755-1315/821/1/012023>.
- [51] M. Amirzadeh, S. Sobhaninia, S. T. Buckman, and A. Sharifi, "Towards building resilient cities to pandemics: a review of COVID-19 literature," *Sustain. Cities Soc*, vol. 89, 2023. [Online]. Available: <https://doi.org/10.1016/j.scs.2022.104326>.
- [52] Y. Takefuji, "How to build disaster-resilient cities and societies for making people happy," *Building and environment*, vol. 228, p. 109845, 2023. [Online]. Available: <https://doi.org/10.1016/j.buildenv.2022.109845>.
- [53] S. G. Emily J. Flies, "Urban-associated diseases: Candidate diseases, environmental risk factors, and a path forward," *Environment International*, 2019, pp. 1-12.
- [54] S. G. Vlahov, "URBAN HEALTH: Evidence, Challenges, and Directions," *Annual Review of Public Health*, vol. 26, pp. 341-365, 2005.
- [55] M. A. Urbańska, "Architektura-sztuka przestrzeni publicznych w Polsce wczoraj i dziś (Architecture: The art of shaping public spaces in Poland yesterday and today)," *Państwo i Społeczeństwo*, 2020, pp. XX. [Online]. DOI: 10.48269/2451-0858-pis-2020-3-006.
- [56] J. Jacobs, "The death and life of great American cities," Vintage Books, 1993.
- [57] G. Sarkin, "Cities at the Front Line: Public Space in the Time of the COVID-19 Pandemic," June 24, 2020. [Online]. Available: <https://www.smithgroup.com/perspectives/2020/cities-at-the-front-line-public-space-in-the-time-of-the-covid-19-pandemic>.
- [58] K. R. Kunzmann, "Smart cities after covid-19: Ten narratives," *disP-The Planning Review*, vol. 56, no. 2, pp. 20-31, 2020.
- [59] M. Hoefslout, "Digitisation of the Physical Public Space," May 15, 2021. [Online]. Available: <https://waag.org/en/article/digitisation-physical-public-space/>
- [60] D. Lyon, "The Electronic Eye: The Rise of Surveillance Society," University of Minnesota Press, 1994.
- [61] A. Sharifi and A. R. Khavarian-Garmsir, "Smart city and COVID-19 in the post-pandemic urban era," *Energy Research & Social Science*, vol. 68, p. 101654, 2020.
- [62] Ö. Akgış İlhan, "Covid-19 Krizi Ve Kamusal Mekânda Dijitalleşme Eğilimleri," *Ege Coğrafya Dergisi*, vol. 30, no. 2, pp. 309-319, 2021. [Online]. DOI: 10.51800/ecd.984882.

- [63] J. Van der Waal et al., "Developing digital public values," *Government Information Quarterly*, vol. 37, no. 1, p. 101473, 2020.
- [64] L. Tapp, "Smart City Architecture," 2021, 2022. [Online]. Available: <https://www.tapp.nl/urban-sensors>. [Accessed: Dec. 23, 2024].
- [65] D. Duives and J. Thiellie, "Living Labs for Urban Mobility," Amsterdam Institute for Advanced Metropolitan Solutions, 2020. [Online]. Available: <https://cityflows-project.eu/covid-19-living-lab/>.
- [66] T. Kuipers, "CityFlows: Improving liveability of crowded pedestrian spaces in 3 European metropolises," Smart Urban Mobility Program - AMS Institute, 2020. [Online]. Available: <https://www.ams-institute.org/urban-challenges/smart-urban-mobility/cityflows-improving-liveability-crowded-pedestrian-spaces-3-european-metropolises/>.
- [67] Social-glass.tudelft.nl, "Social Distancing Dashboard," 2021. [Online]. Available: <https://social-glass.tudelft.nl/>. [Accessed: Dec. 23, 2024].
- [68] Urbanresilience.secdev.com, "Secdev Urban Pandemic Preparedness Index," 2021.



Düzce University Journal of Science & Technology

Research Article

Designing a Remote Monitoring and Security System for Broadcast Transmitters

Ruhi TAŞ^{a,*}, Mansur BEŞTAŞ^b

^a TRT Bilgi İşlem Daire Başkanlığı Ankara, TURKEY

^b Bitlis Eren Üniversitesi Bilgi İşlem Daire Başkanlığı Bitlis, TURKEY

* Corresponding author's e-mail address: mbestas@beu.edu.tr

DOI: 10.29130/dubited.1512889

ABSTRACT

Remote monitoring systems are vital for many systems. Especially in the broadcasting industry, it is critical to keep the broadcasts running 24/7 uninterrupted. It is another challenge to be aware of the interruptions in terrestrial broadcasts on the country's geography and to intervene as soon as possible. For this reason, it is aimed to monitor TRT (Turkish Radio Television Co.) FM and TV transmitters and to gather information about their malfunctions and following station security warning. With the developed system, the follow-up of those responsible has been facilitated, and the response times have been shortened and with the help of motion-sensitive cameras, the security level was increased by taking pictures in the OMC (Operation Monitoring Center). In addition, it is recommended to have appropriate spare materials by ensuring that the teams have information about the type of failure.

Keywords: Remote Monitoring, FM TV Transmitter, Automation, Internet of Things, Data Management.

Yayın Vericileri için Uzaktan İzleme ve Güvenlik Sistemi Tasarlanması

ÖZET

Uzaktan izleme sistemleri birçok sistem için hayati öneme sahiptir. Özellikle yayıncılık sektöründe yayınların 7/24 kesintisiz devam etmesi kritik önem taşımaktadır. Ülke coğrafyasında karasal yayınlardaki kesintilerden haberdar olmak ve en kısa sürede müdahale edebilmek de bir başka zorluktur. Bu nedenle TRT FM ve TV vericilerinin izlenmesi, arızaları hakkında bilgi toplanması ve istasyon güvenlik uyarılarının takip edilmesi amaçlanmaktadır. Geliştirilen sistem ile sorumluların takibi kolaylaştırılarak, müdahale süreleri kısaltıldı ve harekete duyarlı kameralar yardımıyla OMC'de (Operasyon İzleme Merkezi) fotoğraf çekilerek güvenlik seviyesi artırılmıştır. Ayrıca ekiplerin arızanın türü hakkında bilgi sahibi olması sağlanarak uygun yedek malzemelerin bulundurulması sağlanmaktadır.

Anahtar Kelimeler: Uzaktan İzleme, FM TV Vericisi, Otomasyon, Nesnelerin İnterneti, Veri Yönetimi

I. INTRODUCTION

Especially IT systems, energy distribution networks, patient status controls are frequently encountered issues in terms of remote monitoring. This data is critical for decision support units. In addition to monitoring the weather conditions as another area recently, it has been used to warn the public in disasters such as tsunamis in the far east.

In terms of radio and TV broadcasters; To create a large coverage area, hundreds or even thousands of transmitters must be able to transmit broadcasts without interruption. The uninterruptedness of radio and television transmitters, is very important in terms of reputation. In addition, interruptions can cause financial losses. Advertising companies will not want to advertise to a channel in this situation.

Today, TRT broadcasts with 14 television channels, 14 radio channels and thousands of transmitters throughout the country [1]. The relevant department of the institution needed a system to monitor the systems. For this reason, a system has been designed and advised for the transmitters can be tracked instantly.

II. MATERIAL AND METHOD

The purpose of remote monitoring systems is to collect data instantly or periodically from the people or systems to be followed, activating the necessary decision mechanisms. It is ensured that the data in critically important systems are instantly delivered to the center and appropriate actions are taken. Remote monitoring systems are gaining much more importance especially today. Recently, especially in the health sector, the follow-up of patient data [2], [3], the follow-up of the processes of the products in the supply chain, the follow-up of energy systems have been the main areas of interest. In particular, monitoring of weather conditions has been used for a long time. Tsunami warning [4], tides [5] or weather [6] conditions are some of them. The widespread use of digital data transfer processes has accelerated the development in these matters. Smart cars [7], trains [8] and traffic control systems [9] have also started to take their place in smart city applications. Even end users have started to follow it by installing a mind tracking system in their homes [10].

Broadcasting institutions perform terrestrial coverage with radio and television transmitters of various powers to provide coverage. With the spread of satellite broadcasts, a slight decrease is observed. Yet one transmitter is still broadcasting. In this framework, a system has been developed to be instantly informed in case of malfunctions in transmitters. The transmitter site remote monitoring system setup diagram is shown in figure 1. While there is one GSM modem at each station, a separate data reader card is used for each transmitter.

The proposed system consists of 3 parts.

- data collection unit,
- transmission unit,
- decision unit.

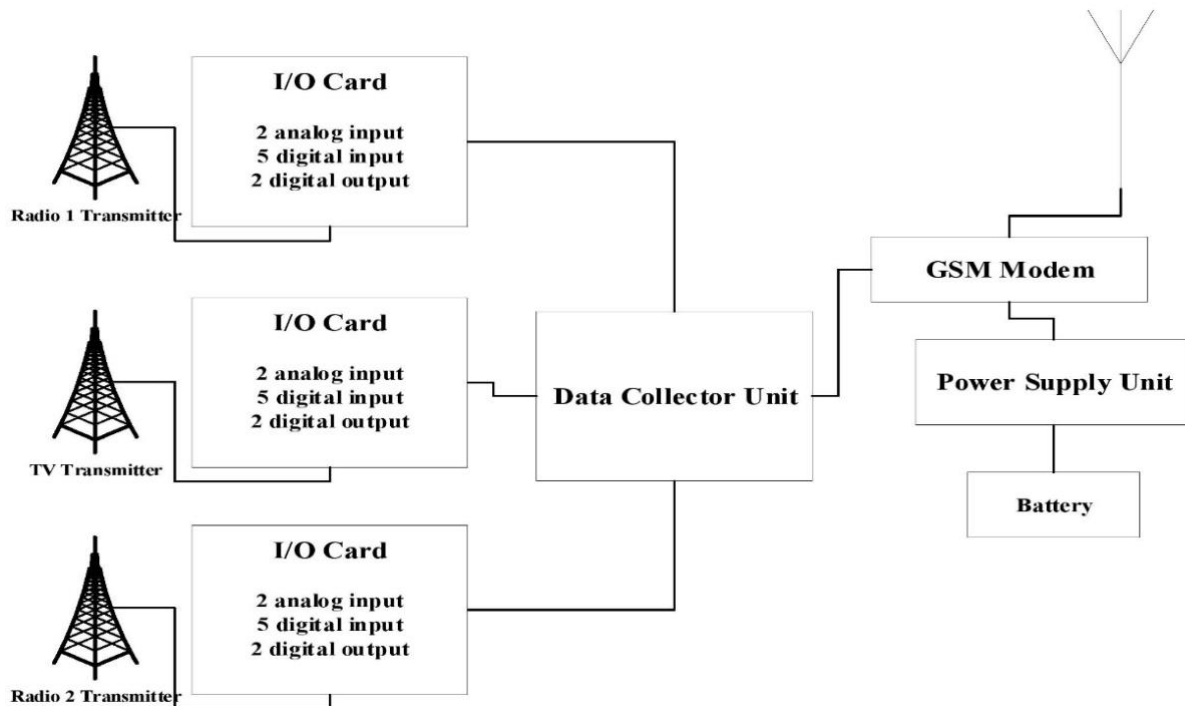


Figure 1. Transmitter Site Remote Monitoring System Setup Diagram

III. DATA COLLECTION UNIT

This unit is especially designed to collect meaningful data from different models and brands of transmitter systems at the same point. The unit has 9 I/O terminals. It has 2 analog and 5 digital inputs and motion detection cameras. It is also designed to have 2 output points that can be triggered by commands sent from the center (Figure 2).

In addition, with the help of the motion sensor, the photos of the people entering the station were taken and sent to the center. Analog inputs offer the opportunity to be adjusted according to the desired input in the range of 0-5 V. Since the outgoing and reflected power values are the most critical data for the transmitter systems, they are used for this purpose. By measuring the values at these outputs in each transmitter, it is possible to enter them as reference values in the central software. In this way, flexible use in different model transmitters is provided.



Figure 2. I/O Ports

Various information such as temperature failure, amplifier failure, generator failure, audio failure (Figure 3) information were obtained from the fault information given by the transmitter within the analog/digital inputs. If the door is opened or motion is detected, a snapshot is sent to the OMC center and a warning is sent.



Figure 3. L/R Audio inputs

With the output data, the entire system is reset. It is known that resetting the transmitters in some cases is the solution to many problems. Among possible GSM line problems, the modem was reset during the day to prevent possible connection problems.

Microchip 16F877 [11] chipset is used in the central control unit of the data unit. It is advantageous that the chip has input and output ports in accordance with the designed infrastructure. The general I/O ports of the chip are shown in figure 4.

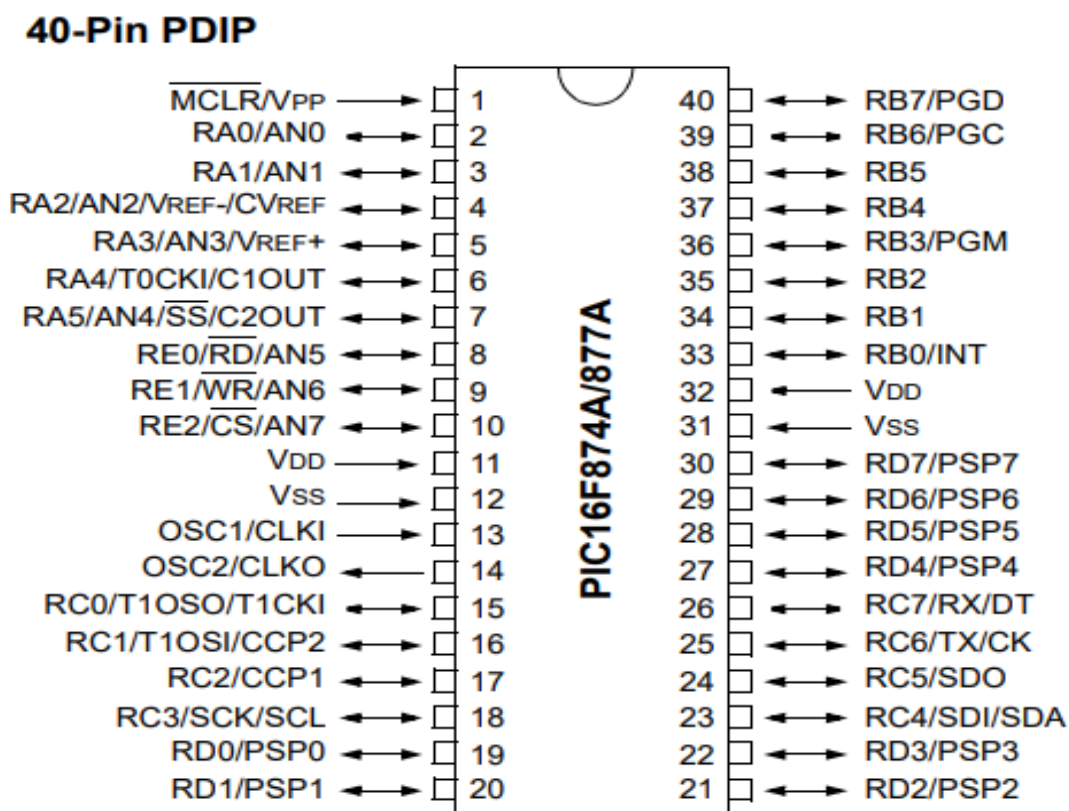


Figure 4. Data control unit chip set I/O port

IV. Transmission Unit

A GSM modem was used to transfer the collected data to central servers. A special data VPN infrastructure has been created to be affected by attacks. It is realized by establishing a TCP/IP connection to the data to the IP address and port address set in the modems. Table I shows GSM modem setting parameter. The application located on the central server makes sense of the data coming from each connection and saves it to the database.

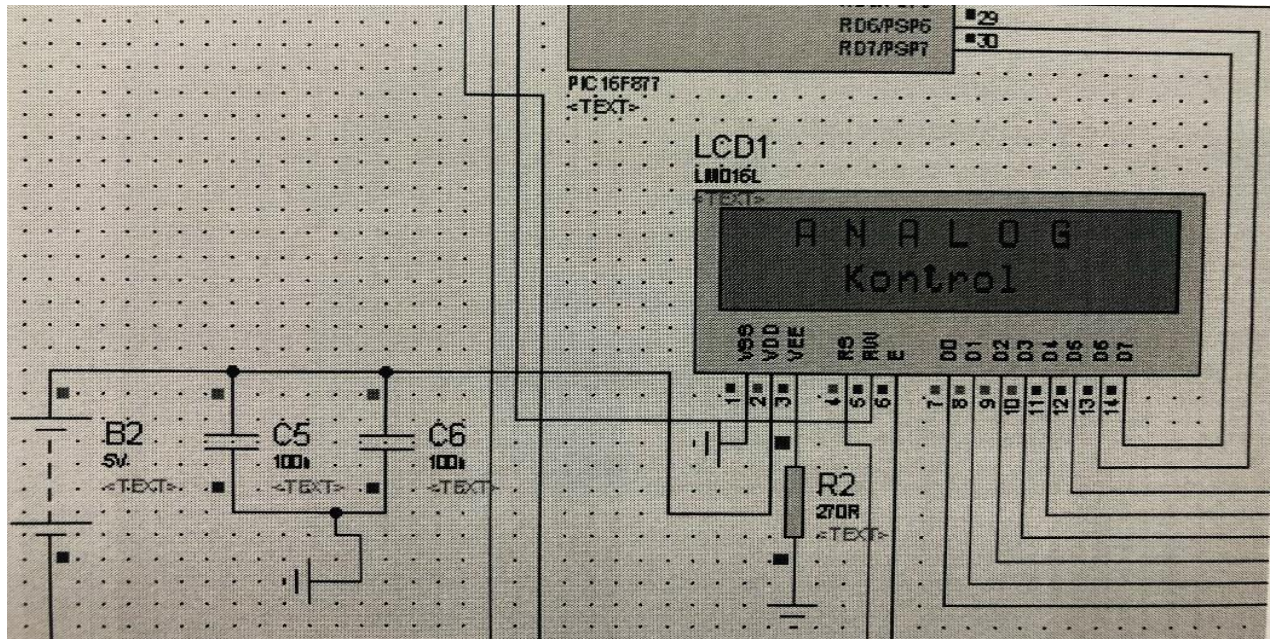


Figure 5. Proteus simulation for I/O control

The design of the project was drawn in Proteus [12] and the tests were carried out with the help of this program. Informative warnings are shown on the LCD screen during the controls. (Figure 5).

Table 1. GSM Modem Setting Parameter

Modem Settings	
Input	Parameter
Pincode	1234
Protocol	IP
APN	trt
USERID	remote
PASSW	xxxx
SERVERADR	10.0.1.222
Remote Port	6074
SMSCENTERNO	+905xxxyzz
MAIL LOGIN	loginname
MAIL PASSW	password
SMTP ADDRESS	Smtp.xxx.yy
MAIL FROM	remote@xxx.yy
MAIL TO	to@xxx.yy

Necessary setups are made on the GSM modem with the help of AT commands [13]. When requested or in case of an internet problem, the data is sent to the center uninterruptedly via SMS. With the mail server integration, the possibility of warning the relevant personnel in an alternative way has been added (Table 1).

V. Decision Unit and Web Portal

The structure designed for the remote control system of the system is shown in figure 6. Two different server application developed, one of them is a web application (Figure 7) and second ones data Collector / parser. MS SQL was used as database server.

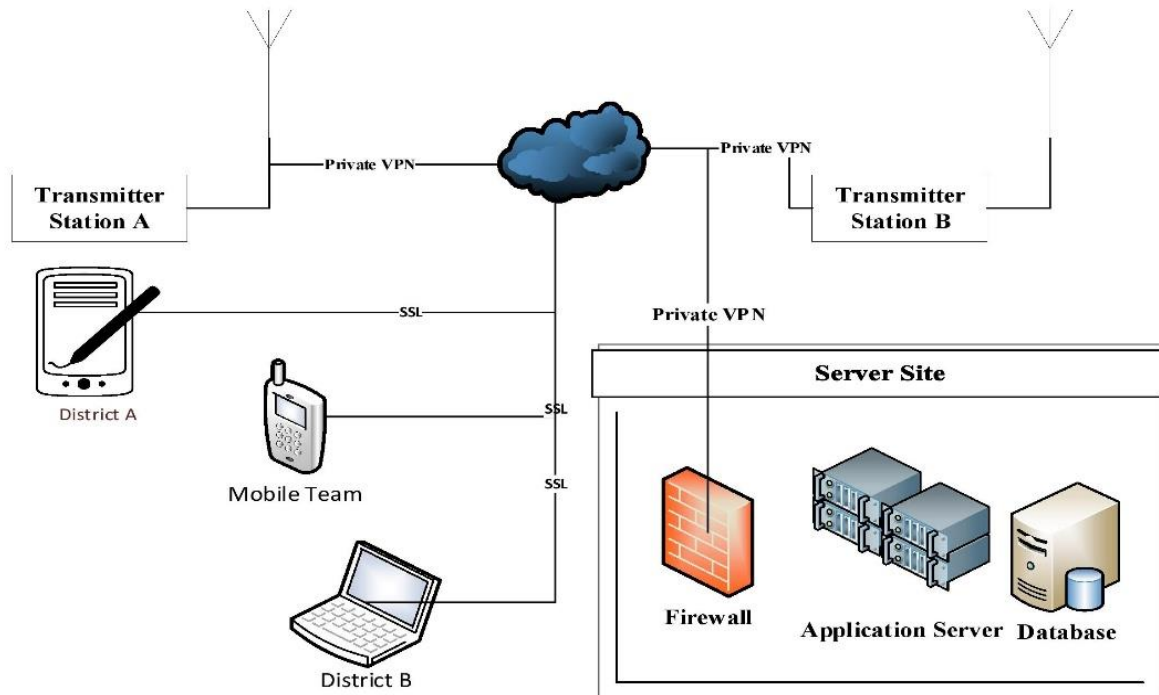


Figure 6. General system setup diagram



Figure 7. Remote Monitoring and Management System WEB application portal & Operations module

After adding the zone admins, each zone can be able to manage the information of the stations in its area of responsibility. Admins at the center have the opportunity to monitor and manage all region information (Figure 8).

Bölge	Merkez	< Geri Dön
Sicil No	Kullanıcı Sorgula	148
Adı	Ruhi	
Soyadı	tas1	
Telefon	905336419100	
email	ruhi.tas@trt.net.tr	
Sifre	•	


[Yeni Kullanıcı](#)
[Güncelle](#)
[Sil](#)
[KAYDET](#)

TÜRKİYE RADYO TELEVİZYON KURUMU

Figure 8. Zone admin management module

A transmitter station can have different FM/TV transmitters. For this reason, only the I/O unit was connected to each transmitter, and all collected data was transmitted to the center with the help of a single modem at the central assembly point. In this way, cost advantage is provided by providing the need for only one modem at each station (Figure 9). GPRS ID shows central unit, Terminal No used for transmitters' identification. The necessary definitions for each unit were entered into the central script, thus making the data meaningful.

VERİCİ BİLGİLERİ		AATEST10/Rd1/766/1/	Sorgula	<< Geri Dön
GPRS ID	766	Terminal No	1	
Verici Adı	AATEST10		<input type="checkbox"/> RDS	
Telefon No	+905339489011		Gücü	10
Bulundugu Yer	ANT-LAB		Üretici Firma	
Bağlı Bulunduğu Bölge	Antalya			
Açıklama	SERI NO:29			
Program Adı	Rd1			
Cihaz Durumu	Test			

Figure 9. Center Server Apps; Data Collector and Data Parser Applications

The possibility of adjusting the parameter setting of the transmitter is provided (Figure 10). This ensures that the system works in harmony with devices of different models and powers, and easy and remote management of the assembly is ensured. It is possible to easily install the same device in TV / Radio, etc. devices.

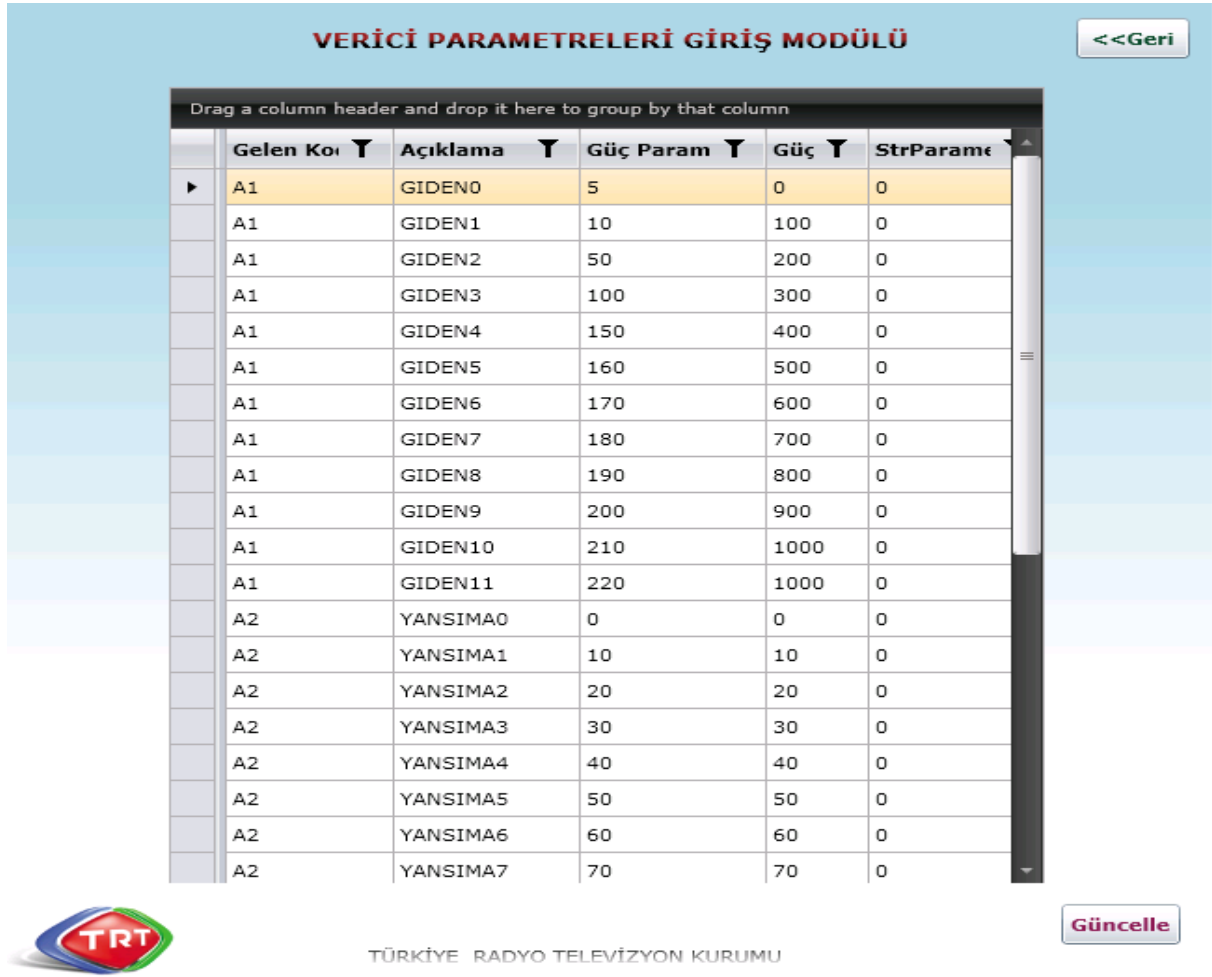


Figure 10. Transmitter parameters module

An application that accepts incoming connections and receives data on the central server has been developed. This application interprets the data from different transmitters according to the set values (Figure 11).

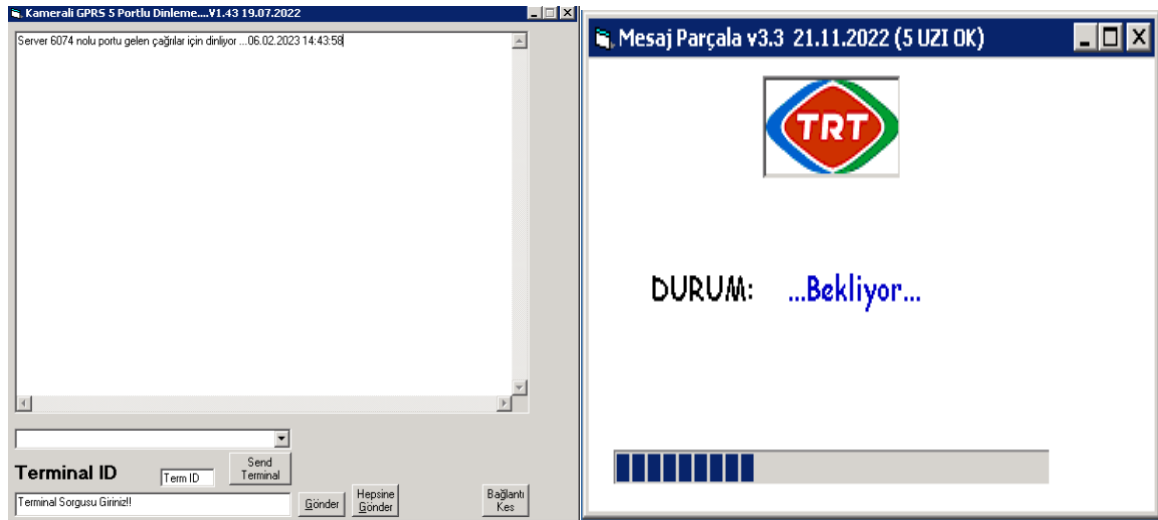



Figure 11. Central server apps; Data collector and Data parser applications

It is also provided to enter the coordinate information of the transmitters (Figure 12).



Bilgi Ekranı

Kullanıcı Kodu :

Şifre :

Bağlı Olduğu Merkez :

Antalya

▼

Bölge Kontrol Et

Verici Listesi :

AATEST10/Radyo Türkü/766/3/

▼

Verici Bilgilerini Getir

Verici Adı :

GPRS_ID :

TerminalNO :

Program Ad :

Radyo Türkü

▼

Bulunduğu Yer :

Koordinat :

Frekans :

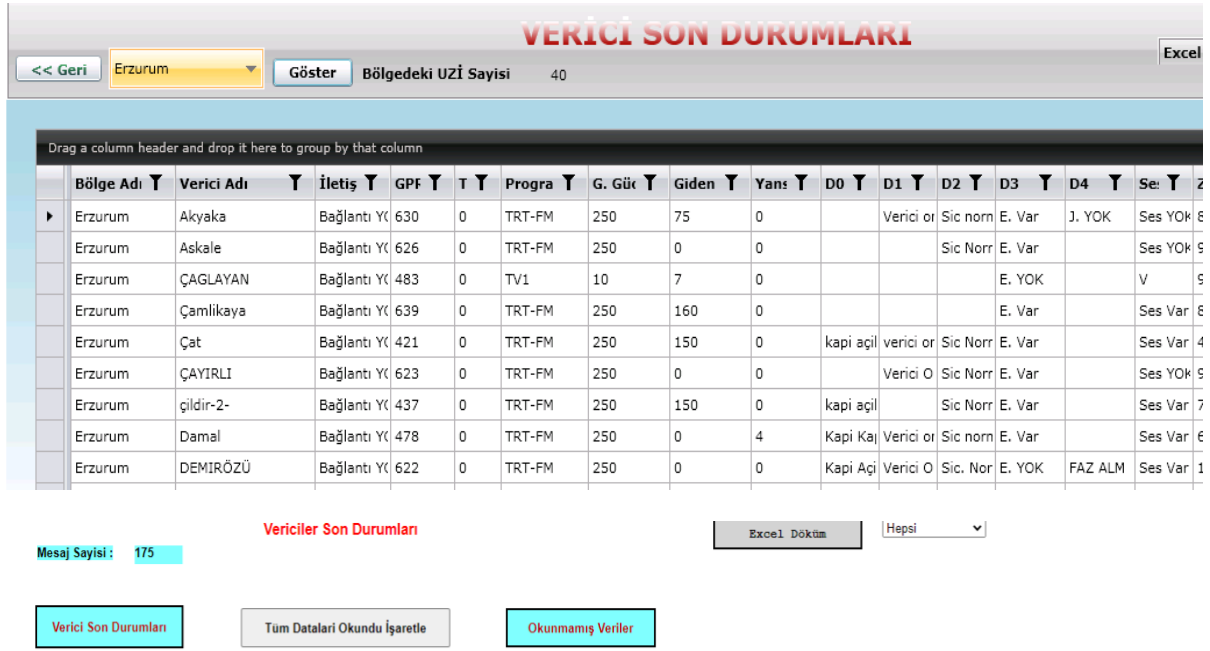
Koordinatları Ekle

[uzi](#) | [koordinat ekle](#) | [uziler googlemaps'te](#) | [sss](#) | [iletisim](#)

Figure 12. Transmitter coordinate management module

While all transmitters can be monitored instantly by the central unit, seven different regional managers can only follow the stations under their responsibility. The system can also be accessed from mobile devices. In this way, the teams on duty were given the opportunity to make a final status check before they set off to the station for control.

After the data from the stations were collected with the help of the collector, they were made meaningful with the help of parser. Stations reporting is provided from the web portal developed so that managers can follow the data. With Google Map integration, it is easy to follow with different colors (red, green, white) on the map. It was stated that the transmitters in the stations shown in the red color were completely closed and it was stated that immediate intervention was required. In the green transmitter station, all data were shown to be healthy. It has been shown that some values are lower than the reference values in the white colored transmitters.



1 2													
	Sıra	Verici Adı	Program	Online	GPRSİD	Terminal No	Verici Gücü	Giden Güç	Yansıyan Güç	IP-D0	ALA-D1	SIC-D2	Enerji
Msj_Rsm	1	Çameli	TRT-FM	KOPTU	112	0	250	0	0	KAPI KAPALI	ALARM YOK	ISI YOK	ENRJ. VAR
Msj_Rsm	2	KESAN RL	TRT-FM	KOPTU	113	0	1000	1100	5	EXC. ON	A. YOK	I. YOK	E. VAR
Msj_Rsm	3	KEPSUT	TRT-FM	KOPTU	165	0	250	0	0			I. YOK	E. YOK
Msj_Rsm	4	INHISAR	TRT-FM	KOPTU	418	0	100	110	0	EXC. OF	AMP. ON	I. VAR	E. VAR
Msj_Rsm	5	Çat	TRT-FM	KOPTU	421	0	250	150	0	kapi açık	verici on	Sic Norm	E. Var
Msj_Rsm	6	Pulumur	TRT-FM	KOPTU	425	0	250	260	0	Kapi Açık		sic. normal	E. Var
Msj_Rsm	7	çildir-2-	TRT-FM	KOPTU	437	0	250	150	0	kapi açık		Sic Norm	E. Var
Msj_Rsm	8	HINIS-MERKEZ	TRT-FM	KOPTU	443	0	250	15	0		Verici on	Sic.norm.	E. yok

Figure 13. Transmitter Status Report

Setup information and I/O status information showed on the front panel LCD display (Figure 14).



Figure 14. 1U remote monitoring front panel (Power, Charge, Battery and LCD Display)

IV. CONCLUSION

By ensuring the monitoring of transmitters in regions where there is no personnel, it was ensured that they were intervened as soon as possible. After the pilot application tests, a system was created that allows monitoring of more than 1000 radio and television transmitters in 7 regions. Relevant personnel were immediately informed about the problems. Unlike other systems, this system allows it to be connected to FM / TV transmitters of different brands and models. By assigning the ports to the desired data source centrally, it is possible to receive different data from different devices for the ay port. In some cases, some problems were solved remotely by resetting the remote transmitter.

Gains of the System;

- time oriented
- Efficiency oriented,
- effective use,
- To help reduce maintenance-repair costs,
- To reduce personnel errors,
- Increased security of station

On the other hand, defective products or models with many failures have been identified together with the statistical data. These data assisted with investment planning for future years.

In the future, it is aimed to conduct research on blockchain-based systems that collect SNMP supported fault information from the transmitters.

V. REFERENCES

- [1] Anonymous, “TRT-Tarihçe,” Tarihçe, 2022. [Online]. Available: <https://www.trt.net.tr/Kurumsal/tarihce.aspx> [accessed Apr. 27, 2022].
- [2] D. Niyato, E. Hossain, and S. Camorlinga, “Remote patient monitoring service using heterogeneous wireless access networks: architecture and optimization,” *IEEE J. Select. Areas Commun.*, vol. 27, no. 4, pp. 412–423, May 2009, doi: 10.1109/JSAC.2009.090506.
- [3] M. Clarke, P. Schluter, B. Reinhold, and B. Reinhold, “Designing Robust and Reliable Timestamps for Remote Patient Monitoring,” *IEEE J. Biomed. Health Inform.*, vol. 19, no. 5, pp. 1718–1723, Sep. 2015, doi: 10.1109/JBHI.2014.2343632.
- [4] G.-Y. Chen, C.-C. Liu, and C.-C. Yao, “Forecast System for Offshore Water Surface Elevation With Inundation Map Integrated for Tsunami Early Warning,” *IEEE J. Oceanic Eng.*, vol. 40, no. 1, pp. 37–47, Jan. 2015, doi: 10.1109/JOE.2013.2295948.
- [5] X. Yang, Z. Zhu, S. Qiu, K. D. Kroeger, Z. Zhu, and S. Covington, “Detection and characterization of coastal tidal wetland change in the northeastern US using Landsat time series,” *Remote Sensing of Environment*, vol. 276, p. 113047, Jul. 2022, doi: 10.1016/j.rse.2022.113047.
- [6] M. Cristani, F. Domenichini, F. Olivieri, C. Tomazzoli, and M. Zorzi, “It could rain: weather forecasting as a reasoning process,” *Procedia Computer Science*, vol. 126, pp. 850–859, 2018, doi: 10.1016/j.procs.2018.08.019.
- [7] J. T. Li, Z. E. Li, X. F. Li, Y. J. Yang, and J. Xiao, “A Simple and Efficient Algorithm Design for Improving the Infrared Tracking Accuracy of Smart Cars,” *Procedia Computer Science*, vol. 166, pp. 339–343, 2020, doi: 10.1016/j.procs.2020.02.088.
- [8] C. Ulianov, P. Hyde, and R. Shaltout, “Railway Applications for Monitoring and Tracking Systems,” *Sustainable Rail Transport*, M. Marinov, Ed. Cham: Springer International Publishing, 2018, pp. 77–91. doi: 10.1007/978-3-319-58643-4_6.
- [9] S. P. Biswas, P. Roy, N. Patra, A. Mukherjee, and N. Dey, “Intelligent Traffic Monitoring System,” *Proceedings of the Second International Conference on Computer and Communication Technologies*, vol. 380, S. C. Satapathy, K. S. Raju, J. K. Mandal, and V. Bhateja, Eds. New Delhi: Springer India, 2016, pp. 535–545. doi: 10.1007/978-81-322-2523-2_52.
- [10] V. Pravalika and C. R. Prasad, “Internet of Things Based Home Monitoring and Device Control Using Esp32,” *International Journal of Recent Technology and Engineering*. vol. 8, no. 1, p. 5, 2019.

- [11] Anonymous, “PIC16F877 | Microchip Technology,” 2022. [Online]. Available: <https://www.microchip.com/en-us/product/PIC16F877> [accessed Apr. 27, 2022].
- [12] Anonymous, “Circuit Simulation Software with SPICE,” Circuit Simulation Software with SPICE, 2022. [Online]. Available: <https://www.labcenter.com/simulation/> (accessed Apr. 27, 2022).
- [13] N. Agnihotri, “AT Commands, GSM AT command set,” Engineers Garage, 2022. [Online]. Available: <https://www.engineersgarage.com/at-commands-gsm-at-command-set/> [accessed Apr. 27, 2022].



Düzce University Journal of Science & Technology

Research Article

Comparison of The Output Power of a Micro Hydroelectric Power Plant with Different PID Control Structures

Tuğba AYDIN KART^{a-b*}, Ahmet AKTAŞ^a, Ömür BINARBAŞI^b, Batuhan ŞENLEN^{a-b},

^a Department of Energy Systems Engineering, Faculty of Technology, Gazi University, Ankara, Türkiye

^b Department of R&D and Innovation, Türkiye Electromechanic Industry Corporation, Ankara, Türkiye

* Corresponding author's e-mail address: tugba.aydin@temsan.gov.tr

DOI: 10.29130/dubited.1568330

ABSTRACT

In this study, a micro-hydroelectric power plant that produces energy from the water taken from the Ulutan Dam and sends it to the treatment plant for drinking water purposes was examined. The control and command system of the grid-connected micro HPP (Hydroelectric Power Plant) is implemented using Siemens S7 1200 PLC. After synchronization of the system with the grid, two different control software are loaded sequentially. The first one is a PID controller created for the position control of the turbine guide vane, while the second software is the power set PID controller. In the study, the data regarding the position of the guide vane, flow rate, pressure, and active power, which were obtained from the turbine control system, are analyzed. Both PID controls reached the maximum active power value of 137 kW. However, while the guide vane PID controller maintained the maximum power value, the power set PID controller could not stabilize the system. The power set PID controller could not maintain the stabilization of the system, the turbine took in more water to provide the power, the flow rate increased over time and the pressure decreased. The power of this system also decreased from 137 kW to 105 kW. Since the aim was to achieve maximum power and stable operation, it was concluded that the guide vane PID control block was more efficient.

Through this project, an unused water source was evaluated, contributing to the national economy, and providing valuable experience and knowledge for the control and command systems to be used in the installation or rehabilitation of a micro-hydroelectric power plant.

Keywords: Micro HPP, PID Control, PLC, guide vane, power adjustment

Farklı PID Kontrol Yapıları İle Bir Mikro Hidroelektrik Santral Çıkış Gücünün Karşılaştırılması

ÖZ

Bu çalışmada Ulutan Barajından arıtma tesisine içme suyu maksadıyla alınan sular ile enerji üretimi yapan bir mikro hidroelektrik santral incelenmiştir. Şebekeye bağlı olan Mikro HES (Hidroelektrik Santral)'in kontrol ve kumanda sistemi Siemens S7 1200 PLC ile gerçekleştirilmiştir. Sistemin şebekeye senkronizasyonu sonrası iki farklı kontrol yazılımı sırasıyla yüklenmiştir. Bunlardan ilki türbin ayar kanadının pozisyon kontrolü için oluşturulan PID kontrolörü, ikinci yazılım olarak güç set PID kontrolörüdür. Çalışmada; türbin kontrol sisteminden alınan ve kontrol edilen ayar kanadı pozisyonu, debi, basınç ve aktif güç verileri analiz edilmiştir. İki farklı PID

kontrolü de maksimum aktif güç değeri olan 137 kW'a ulaşmış fakat ayar kanadı PID kontrolörü maksimum güç değerini korurken güç set PID kontrolörü sistemin stabilizasyonunu koruyamamış gücü sağlayabilmek için türbine daha çok su almış, debi zamanla artmış, basınç azalmıştır. Bu sebeple sistemin gücü de 137 kW değerinden 105 kW değerine kadar düşmüştür. Sistemin maksimum gücü elde edebilmesi ve stabil çalışması istendiğinden bu koşulları sağlayan ayar kanadı PID kontrol bloğunun daha verimli kontrol bloğu olduğu sonucuna varılmıştır. Bu projeye enerjisinden yararlanılmayan su kaynağı değerlendirilip ülkemizin milli servetine katkısı sağlanmış, bir mikro hidroelektrik santral kurulumunda veya rehabilitasyonu esnasında kontrol kumanda sistemlerinde kullanılması için tecrübe bilgi birikimi aktarılmıştır.

Anahtar Kelimeler: Mikro HES, PID Kontrol, PLC, ayar kanadı, güç ayarı

I. INTRODUCTION

The growth of the global population and the increasing prevalence of technological products have significantly raised the energy demand. Fossil fuels meet a large percentage of this energy need. When the general energy use denominator of the world population is examined, the most used energy source is fossil fuels (oil, coal, natural gas) with 76% in the first place, renewable resources (solar, wind, biofuel, etc.) in the second place with 20%, and nuclear in the third place with 4% energy usage comes [1]. Usage percentages are shown graphically in Figure 1.

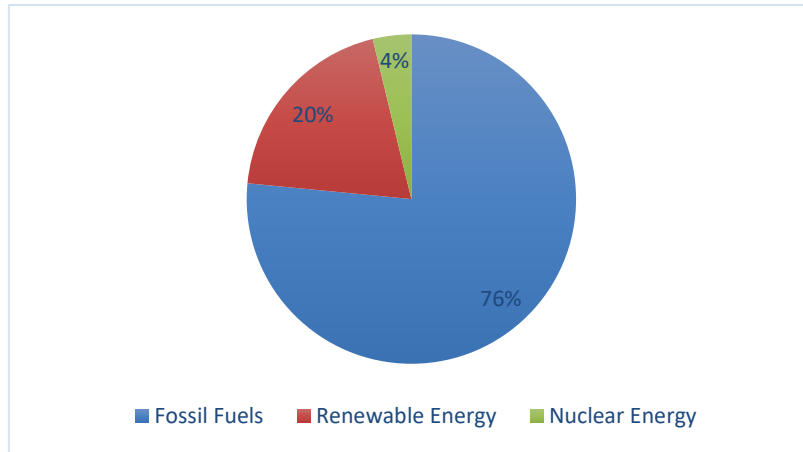


Figure 1. Global Energy Consumption by Source in 2023

As a result of the percentage of use of fossil fuels, global warming is accelerating day by day, and to prevent climate change, countries are taking some measures to reduce the use of fuels that create their carbon footprint and turn to renewable resources.

Türkiye is a country that is very abundant in terms of renewable energy. Hydroelectric energy ranks first among renewable resources with its high energy reserve feature. According to the data of the Ministry of Energy, as of the end of June 2024, our country's installed power reached 110,518 MW, and hydraulic energy ranked first with 29.1% in the distribution of our installed power by resources [2].

To evaluate the potential of HEPP (Hydroelectric Power Plant), small-scale HEPPs that are easy to install and do not harm the environment, which will provide an advantage to rural areas where electricity transportation is difficult, should be evaluated as well as large HEPPs. The power classification of small HEPPs varies in the literature. In general, HEPPs between 2MW and 25MW are considered small-scale hydroelectric power plants [3].

Table 1. Small-Scale HPP Classification

	Capacity
Pico-Hydro	< 10 kW
Micro-Hydro	< 500 kW
Mini -Hydro	< 2 MW

II. LITERATURE REVIEW

This chapter presents a comprehensive review of the literature on the control of small HEPP power plants. One of the most important parameters when controlling a HEPP is that the frequency and voltage are stable. A lot of research has been done regarding this. As an example; Nikhila Sanampudi and his colleague emphasized the 10,000 MW micro-HPP potential in India in their study. They developed an electronic load control design to maintain frequency and voltage stability under varying loads and found that it could be used efficiently and effectively [4]. Suhas and his colleagues conducted a comprehensive literature review on load frequency control in micro-hydroelectric power plants. They presented a fuzzy logic-based controller design to manage the entire operation of the production unit. The role of the fuzzy logic-based controller was to regulate the plant's frequency output despite varying user loads and to limit the waste of available water. They developed a simulation model of a micro-HPP using blocks available in MATLAB SIMPOWER and were able to keep the frequency stable under varying user loads [5]. Oğuz, A. Kaysal, and K. Kaysal simulated the dynamic behavior of load-frequency control in the Adıgüzel HPP under varying loads using MATLAB/Simulink and SimPowerSystems Toolbox. According to the frequency-voltage curve obtained, they found that by maintaining the excitation circuit voltage constant, oscillations in frequency were due solely to changes in active power, which resulted in oscillations in terminal voltage [6]. In their study, Öztürk, Özdemir and Cebeci examined the frequency and voltage changes in inductive and ohmic load situations in small and very low-power HEPPs by providing PID control with PLC through an experimental set with a synchronous generator-driven by a direct current motor [7]. In another study, Özkan and his colleagues designed a hydroelectric power plant prototype as educational material, controlling it via PLC. Using a Pelton turbine, they observed the rotational speed and the voltage produced [8].

Several studies have also been published in the literature comparing two distinct control methods. For instance, previous studies have shown that: Dalcalı and colleagues designed a microcontroller-based governor system (speed regulator), comparing the generator's output frequency with the microcontroller and adjusting the amount of water through the guide vane based on the result. By using microcontrollers, mechanical losses and reaction time have been minimized, resulting in a more cost-effective control system compared to PLC [9]. In a study conducted in 2022, Ulu and Altinkaya used both conventional Proportional Integral Derivative (PID) control and Artificial Neural Networks (ANN)-based PID control methods for the control system of a micro-HPP prototype. They found that the ANN-based PID provided better results than the conventional PID in terms of settling time, frequency and voltage overshoots [10].

One of the key parameters influencing the production potential of a hydroelectric power plant is the rainfall potential. In this context, Chatchophang and colleagues, noting that the water flow and height in small hydroelectric power plants change seasonally, proposed that the turbine's torque-speed characteristics must be adjusted for the generator to operate at variable speeds to achieve maximum power. They developed an algorithm for variable speed control and maximum power point tracking of a Permanent Magnet Synchronous Generator (PMSG) and applied it in Thailand. To simulate the turbine's torque-speed characteristics, they used a servo drive-controlled permanent magnet synchronous motor, and the experimental results validated their proposed speed control algorithm [11].

Halil Kurt, who aimed to test the software with varying numbers of turbines, examined the Kayaboğazi Dam in Kütahya and compared the energy potential of three turbines planned to exist with one turbine by using PLC with a fuzzy logic algorithm for commissioning and decommissioning the turbines to benefit from energy production at an optimal level and compared the investment costs [12].

III. MATERIAL AND METHOD

In this study, electricity generation was carried out by utilizing water taken from the Ulutan Dam, located in the Black Sea Region within the borders of Zonguldak, for drinking purposes. The control and automation of the 200 kW micro-hydro power plant (HPP), connected to the grid, were implemented using Siemens S7-1200 PLC modules and a Human-Machine Interface (HMI) SCADA screen. The control system of the designed micro-HPP was operated using two different software programs. After the synchronization of the system with the grid, the first software, the guide vane PID control, was tested. The opening percentage of the turbine's guide vane was manually entered via the SCADA screen, and the amount of water passing through the turbine (m^3/h) was controlled, allowing the system to operate. The data were analyzed, and graphs were generated.



Figure 2. Overview of Micro Hydro Power Unit

The second software, the power set PID control, was then tested. The desired active power value was entered via the SCADA screen, and the guide vane opening percentage was automatically adjusted by the PID control block to achieve the desired power. The data were analyzed and graphed.

The active power values produced at different flow and pressure levels were compared between the two different software programs.



Figure 3. Control and Command SCADA panel

Throughout the 24-hour operation of the system, various data were monitored from the SCADA screen, such as current, voltage, frequency, power, flow rate, guide vane opening, pressure before and after the inlet valve, turbine bearing temperatures, generator bearing temperature, and the oil temperature of the hydraulic unit. The values recorded every second were used as reference data in this study. The data collected from the field were categorized into digital and analog signals, as presented in Table 2.

Table 2. Data Collected from The Field

Equipment	Explanation	Digital Input	Digital Output	Analog Input	Analog Output
Generator	• Acceleration Sensor	✓	X	X	X
PLC Panel	• Emergency Stop	✓	X	X	X
MCC Panel (Motion Control Chart)	• Grid Busbar Energized	✓	X	X	X
	• Load Disconnect Active	✓	X	X	X
	• Generator (TMS) Thermal Magnetic Switch Active	✓	X	X	X
Generator	• Breaker Active	✓	X	X	X
	• Generator TMS Active	✓	X	X	X
Bypass Valve	• Thermal Fault	✓	X	X	X
	• Open	✓	✓	X	X
	• Close	✓	✓	X	X
Inlet Valve	• Thermal Fault	✓	X	X	X
	• Open	✓	✓	X	X
	• Close	✓	✓	X	X

Table 2 (cont). Data Collected from the field

Hydraulic Pump	• Thermal Fault	✓	x	x	x
	• Running	✓	✓	x	x
Stand-by motor	• Thermal Fault	✓	x	x	x
	• Running	✓	x	x	x
Hydraulic Unit	• Oil pressure emergency	✓	x	x	x
	• Oil filter unclean	✓	x	x	x
	• Oil-level low	✓	x	x	x
	• Hydraulic oil pressure	x	x	✓	x
Excitation System	• AVR Active	x	✓	x	x
	• AVR Passive	x	✓	x	x
	• Excitation Trip	x	✓	x	x
Safety System	• PLC Emergency stop output	x	✓	x	x
Generator	• Breaker Active	x	✓	x	x
	• Breaker Low Voltage	x	✓	x	x
Protective Relay	• Generator Frequency	x	x	✓	x
	• Active Power	x	x	✓	x
Ambient Temperature		x	x	✓	x
Penstock Pipe	• Pressure before Inlet valve	x	x	✓	x
	• Pressure after Inlet valve	x	x	✓	x
Turbine Guide Vane Position		x	x	✓	x
Generator	• Bearing Temperature	x	x	✓	x
	• Winding Temperature	x	x	✓	x
Turbine	• Bearing Temperature	x	x	✓	x
Flow Rate		x	x	✓	x

When calculating the total capacity of a hydroelectric power plant, important parameters must be considered. The two most significant parameters are flow rate and head [13]. The hydraulic power produced is proportional to the flow rate and head, as shown by Equation (1);

$$P_{hydraulic\ power} = \rho \cdot g \cdot H_{net} \cdot Q \cdot \eta \quad (1)$$

Where, ρ (kg/m³) is the specific gravity of water, g (m/s²) is the gravitational acceleration, H_{net} (m) is the net head, Q (m³/s) is the flow rate, η is efficiency of turbine [14].

The selection of the generator is based on the hydraulic power obtained from the turbine, as expressed in Equation (2);

$$P_{active\ power} = S \times \cos\theta \quad (2)$$

In the equation, S (kVA) is the apparent power, $\cos\theta$ is the power factor [15].

The generator frequency must be within acceptable values so that the generator terminal voltages can be synchronized with the grid in HEPPs. The values that can be considered suitable for the stable operation of the system are the frequency of 50 Hz (+/-0.2) and the voltage level of 400V (+/-20) [16].

The task of the control system in hydroelectric power plants is to keep the generator frequency and terminal voltages within acceptable limits and to ensure power balance by controlling active and reactive power [4]. For this purpose, PLC and microcontroller-based systems are used.

The Equation (3) and Equation (4) are used to keep the generator frequency and terminal voltage at a constant value.

$$f = n \times P / 120 \quad (3)$$

Where, f (Hz) is the frequency of the voltage generated by the generator, n (rpm) is the rotational speed of the generator and P is the number of poles [4].

Since the frequency of the generator's output voltage is directly proportional to its rotation speed, frequency control is achieved by changing the speed of the turbine that rotates the generator shaft. Turbine speed depends on the amount of water passing through the turbine. Depending on the turbine type, the turbine speed is controlled by increasing/decreasing the turbine adjustment guide vane or nozzle position and the amount of water passing through.

$$E = K \cdot \varphi \cdot \omega \quad (4)$$

In equation (4), E is the induced voltage, K is the constant coefficient, φ is the magnetic flux created by the excitation winding, and ω is the angular velocity.

According to the Equation (4), the generator terminal voltages can be controlled by changing the φ magnetic flux (generator excitation flux) and ω rotation speed. In systems synchronized with the grid, since the frequency must remain constant, voltage control is achieved using an Automatic Voltage Regulator (AVR). The output voltages of the generator are measured, and the excitation current is increased or decreased accordingly to bring the generator's terminal voltages to nominal values [16].

Micro-HPPs can operate either connected to the grid or independently. For grid-connected HPPs, after synchronization, the generator's frequency must match the grid frequency and remain stable. This requires the generator's rotational speed to remain at synchronous speed [17].

The mechanical power on the turbine shaft is converted into electrical power via the generator rotor. The active power produced by the generator is proportional to the turbine shaft power. In grid-connected systems, the frequency and voltage of the generator remain constant in synchronized conditions. Angular speed is constant in the shaft power formula given in Equation (5). To change the shaft power, it is necessary to change the mechanical torque. The mechanical torque change depends on the flow rate and pressure values. Therefore, after synchronization, the turbine adjustment guide vane position affects the generated active power value. The amount of water entering the turbine is controlled by the turbine's adjustment guide vane. In case of high-power demand, the adjustment guide vane will be opened,

allowing a large amount of water to pass to the turbine; and for less power demand, the adjustment guide vane will be closed, allowing less water passage to the turbine.

$$P_{shaft\ power} = T \cdot \omega \quad (5)$$

Where, ω (rad/s) is the angular velocity, T (Nm) is the turbine shaft torque and P is the power in Watts [18].

A banki-type turbine was selected based on flow rate and head in this study. The water flow to the turbine was controlled by the guide vane. The opening and closing movement of the mechanism is provided by the forward/backward movement of the hydraulic piston located on the adjustment guide vane. A 4-20mA sensor is placed on the hydraulic piston to detect its movement.

The data obtained were evaluated in PLC-based software and controlled using PID control blocks.

As water passes through the adjustment vane, the generator begins to gain speed. Excitation is given to the generator when the speed of the generator is 90% or over. To stabilize the generator frequency within the acceptable range of 50 Hz (+/- 0.2), the instantaneous data received from the speed sensor is compared in the PID control block with the set value of 1500 revolutions, which is the number of revolutions corresponding to the 50 Hz, and stabilized and controlled.

After the system is synchronized, all conditions are now ready to generate electrical energy from the system.

The amount of water passing through the turbine was controlled by using two different PID control blocks in the system. The two different PID control blocks are as follows:

- 1- Guide Vane PID Control
- 2- Power Set PID Control

A. FUNCTION OF PID

The "proportional" in the name of PID refers to the current control error, the "integral" refers to the past control error, and the "derivative" refers to the predicted control error. It is controlled with these data. The PID algorithm serves as an (AVR) for micro-hydraulic systems [19]. PID brings the error between the reference value and the actual value to an acceptable value.

The PID algorithm works according to Equation (5) given below.

$$y = K_p \left[(b \cdot w - x) + \frac{1}{T_1 \cdot s} (w - x) + \frac{T_D}{\alpha \cdot T_D \cdot s + 1} (c \cdot w - x) \right] \quad (5)$$

In this equation, y is the output value of the PID algorithm, K_p is the proportional gain, s is the Laplace operator, b is the proportional effect weight, w is the set point, x is the process value, T_1 is the integral effect time, T_D is the derivative effect time, α is the derivative delay coefficient, c is the derivative effect weight [20].

The situation where there is no derivative effect is considered PI control. The difference signal between the process value and the reference value is integrated over time. When the difference signal is zero, the integrator circuit will not receive a signal, as soon as the differential signal is zero, the integrator will not receive the circuit signal [21].

PID should be preferred in complex systems where a PI controller is not sufficient. If the PI controller system ensures a steady state, there is no need to add a differential controller. Two different PID controllers were tested in this study.

There are two PID parameter adjustment procedures in the Siemens S7-1200 PLC controller, which are described as pretuning and fine tuning. It includes the Chien-Hrones-Reswick method for pretuning and the Ziegler-Nichols method for fine tuning [20].

In practice, the PID parameters were automatically tuned by the PLC controller, and refinements were made through an iterative process of trial and error.

IV. RESULT AND DISCUSSION

A. GUIDE VANE PID CONTROL

Initially, the commissioning process was carried out with the guide vane position PID control block. As shown in Figure 4, the requested percentage of guide vane was entered as "Set Entry" on the SCADA screen. The current position information of the guide vane taken from the linear potentiometer and the requested opening amount of the guide vane were sent to the input part of the PID control block as a percentage value, and the system tried to stabilize at the requested opening percentage by evaluating the two data.

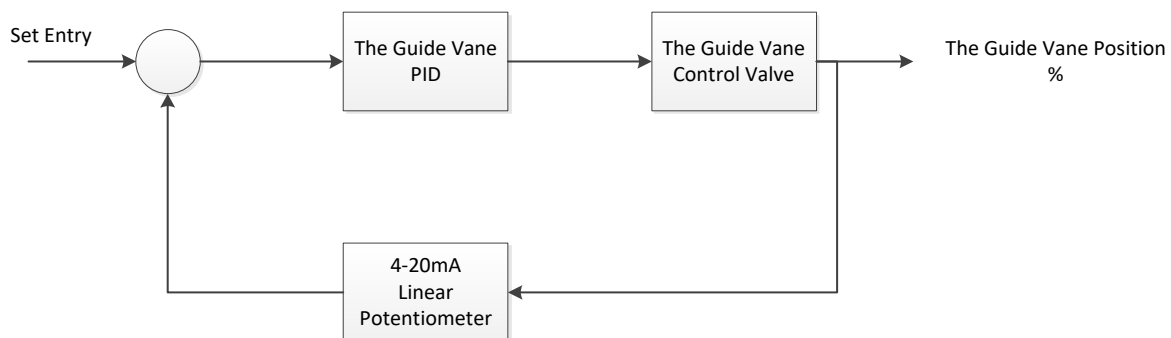


Figure 4. *The Guide Vane PID Control Block Diagram*

<input checked="" type="checkbox"/> Enable manual entry	
Proportional gain:	3.607911
Integral action time:	9.997746 s
Derivative action time:	4.668555E-1 s
Derivative delay coefficient:	0.1
Proportional action weighting:	0.8
Derivative action weighting:	0.0
Sampling time of PID algorithm:	1.000006 s

Figure 5. *The Guide Vane PID Control Block Parameters*

Before synchronization, the guide vane was opened to 43.41%, and in parallel, the flow rate reached up to 991.67 m³/h. Since a certain amount of water is supplied to the turbine to synchronize it with the network, the pressure and flow rate values in the graphs will start from 991.67 m³/h. Since a certain amount of water is supplied to the turbine to synchronize it with the grid, the pressure and flow rate values in the graphs will start from 991.67 m³/h.

Data was analyzed according to the guide vane position PID control block, active power, guide vane position, pressure and flow rate information. These data are graphed in Figures 6,7 and 8.

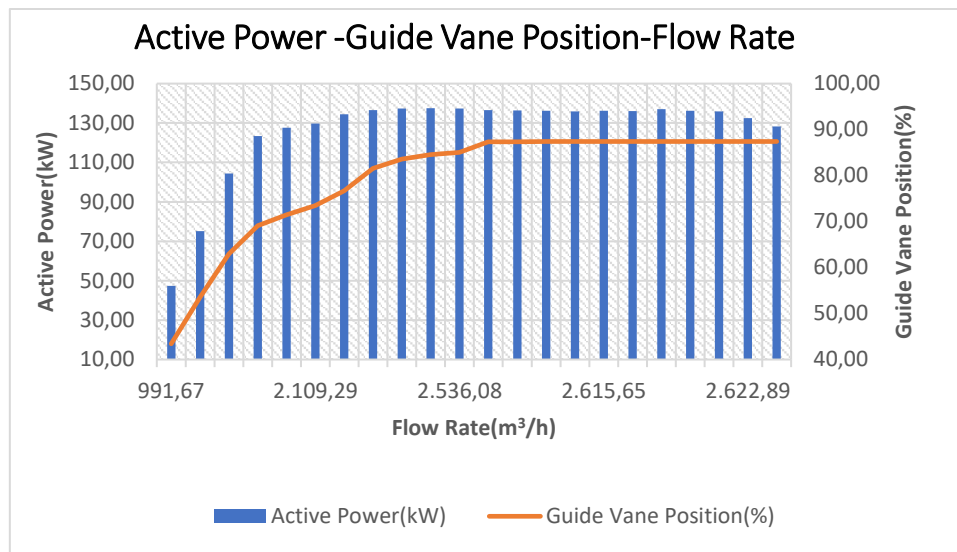


Figure 6. According to The Guide Vane PID Control Block; The Graph of The Active Power, Guide Vane Position and Flow Rate

The guide vane position has been increased by 10%, up to 90% clearance. Depending on the opening ratio of the guide vane, the flow rate increased accordingly. As shown in Figure 6, the flow rate starts to show a tendency to remain at a constant value after 81.58%. The highest flow rate (m³/h) is when the guide vane is open at 87.4%. The maximum flow rate was observed as 2,622.89 m³/h. The maximum value of the active power produced was observed as 137.57 kW when the guide vane was at 84.55%. When the guide vane position was 87.4%, 136 kW active power was produced, and the system tended to remain stable at this value.

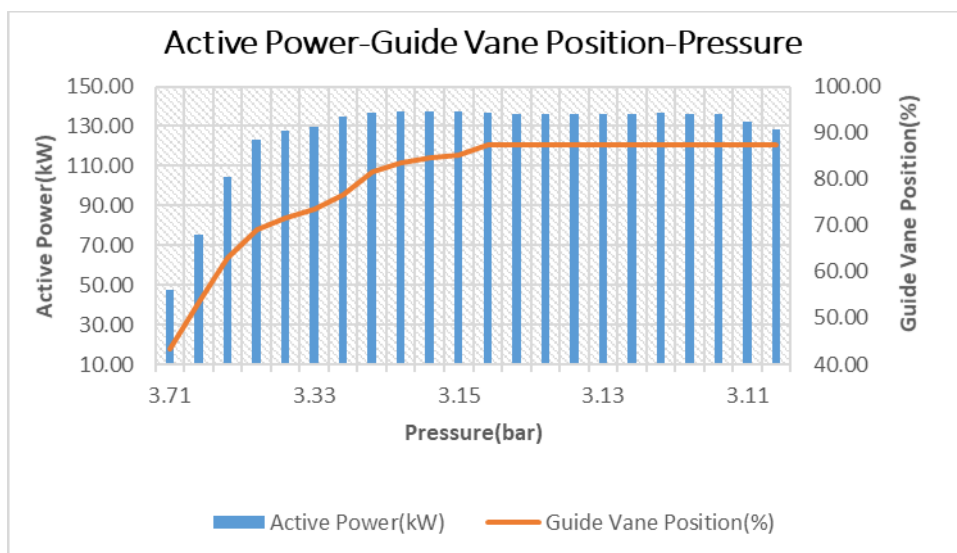


Figure 7. According to The Guide Vane PID Control Block; The Graph of The Active Power, Guide Vane Position and Pressure

As shown in Figure 7, the guide vane position has started to increase in percentage terms, and it has been observed that the pressure decreases regularly as the percentage of the guide vane position increases. When the guide vane position was 43.41%, the pressure was measured as 3.71 bar, and when

the guide vane position was 87.41%, the pressure was measured as 3.11 bar. At the highest active power value of 137.57 kW, the pressure was observed as 3.16 bar. Active power was measured as 128.29 kW at 3.11 bar, which is the moment when the pressure is lowest.

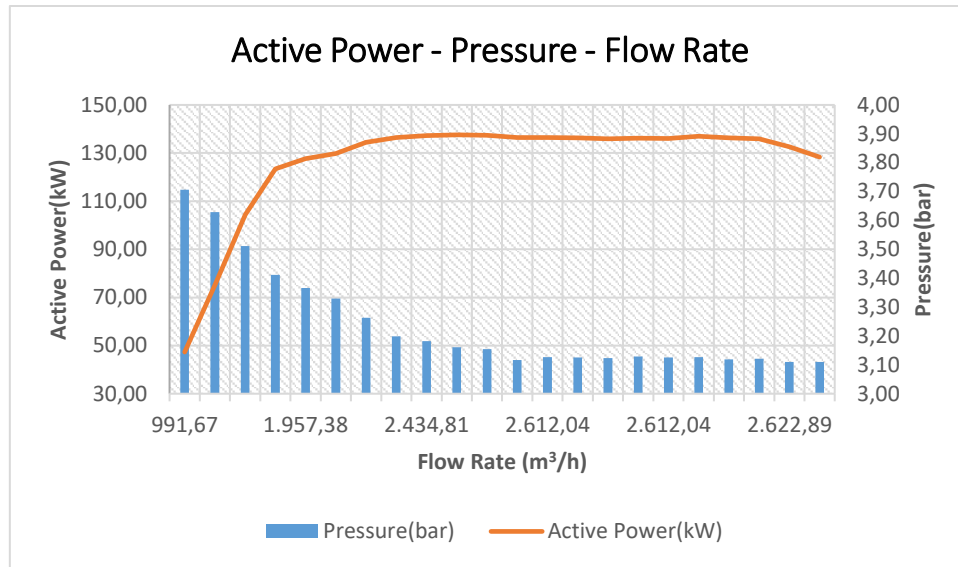


Figure 8. According to The Guide Vane PID Control Block; The Graph of The Active Power, Pressure and Flow Rate

According to Bernoulli's principle, the proportionality between the speed of the fluid and its pressure is inverse. Depending on the inverse proportionality, a decrease in the pressure in the section is observed as the speed of the fluid increases. Similarly, the pressure increases in the section where the speed decreases. It is observed in Figure 8, as the flow rate increases, the pressure tends to decrease, and when the flow rate tends to stabilize, the pressure also begins to stabilize. The highest active power was 137.57 kW, at this power value the flow rate was 2,499.91 m³/h and the pressure were measured as 3.16 bar.

B. POWER SET PID CONTROL

In this section, the system is synchronized to the grid with the power set PID control block, which we mentioned as the second software. The requested power value was entered on the SCADA screen as shown in Figure 9. The current power and the requested Power are sent to the input of the PID control block and the control block tries to reach the requested power value by evaluating the two data. The Power PID block sends the output value to the input of the guide vane PID block, the guide vane stabilizes the system by activating the position of the guide vane control valve to reach the target power.

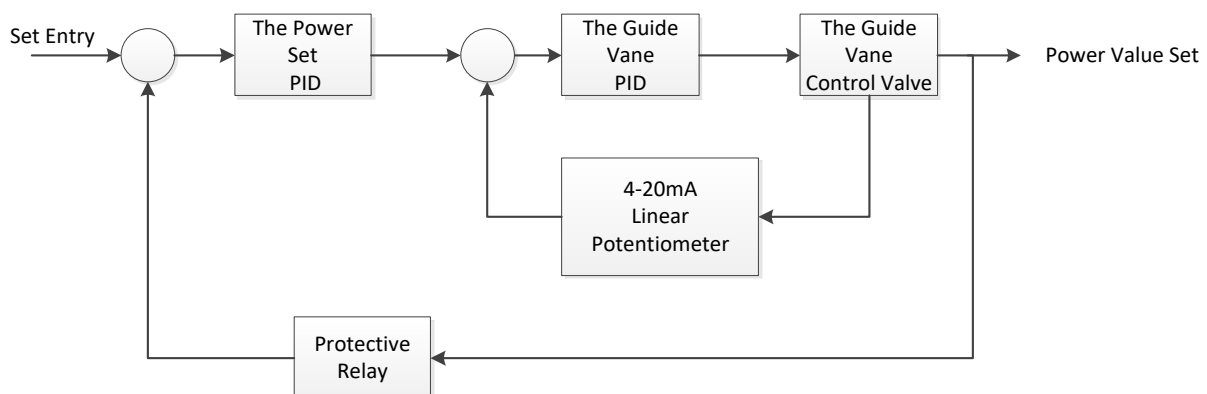


Figure 9. Power Set PID Control Block Diagram

☒ Enable manual entry

Proportional gain:

Integral action time: s

Derivative action time: s

Derivative delay coefficient:

Proportional action weighting:

Derivative action weighting:

Sampling time of PID algorithm: s

Figure 10. Power Set PID Control Block Parameters

The same values (active power, guide vane position, pressure and flow rate) examined in the guide vane PID control block are shown graphically again in this section in order to observe which PID provides more efficient results.

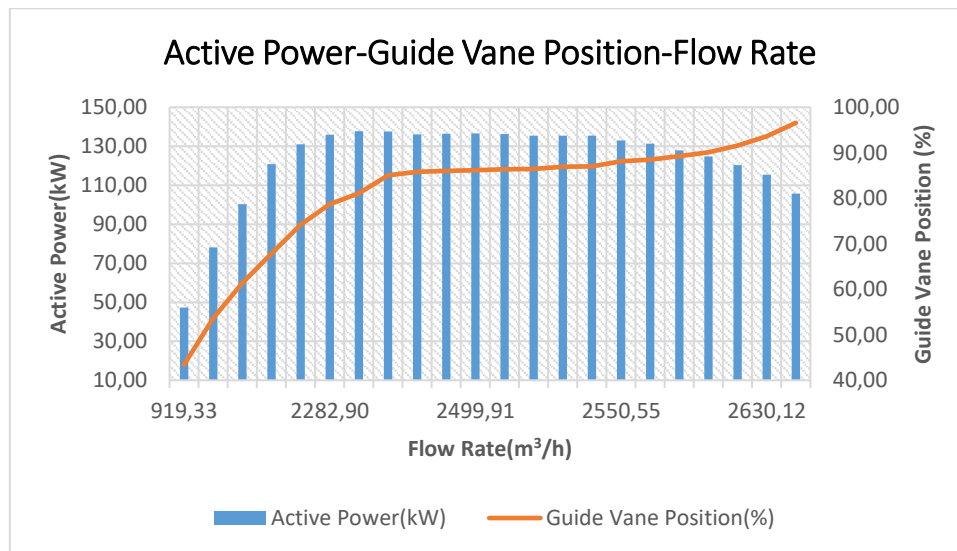


Figure 11. According to The Power Set PID Control Block; The Graph of The Active Power, Guide Vane Position and Flow Rate

After the system is synchronized, the requested power value is entered on the SCADA screen. Since the initial power value of the system was previously defined as 50 kW, when an energy request over 50 kW is requested, the opening percentage of the guide vane position will be increased and thus the amount of water entering the system will increase and the desired power will be obtained. At the requested power below 50kW, the percentage of the guide vane position will be reduced.

As shown in Figure 11, it is observed that when 50 kW active power is produced in the system, the guide vane position is 43% and the flow rate is 919.33 m³/h. When the power demand was increased and 100 kW active power was requested, the guide vane position was opened by 61%, thus allowing more water to pass through the system, the flow rate reached 1631.86 m³/h and the active power reached 100.36 kW. At 135 kW power demand, the guide vane position tended to remain stable at 85-86% levels, the flow rate reached between 2,499.91-2,550.55 m³/h, and the active power reached between 120.75-130.94 kW. However, when a power demand over 140 kW was requested, the guide vane position tended to open towards 100%, the guide vane did not remain in a stable position, and the amount of water passing through the system increased to 2630.12 m³/h in proportion to this opening, and the system tried

to meet this energy demand. Instantly, the active power value was observed as 137 kW and then the active power started to decrease over time, and 115 kW active power was obtained when the guide vane position was 93.63%.

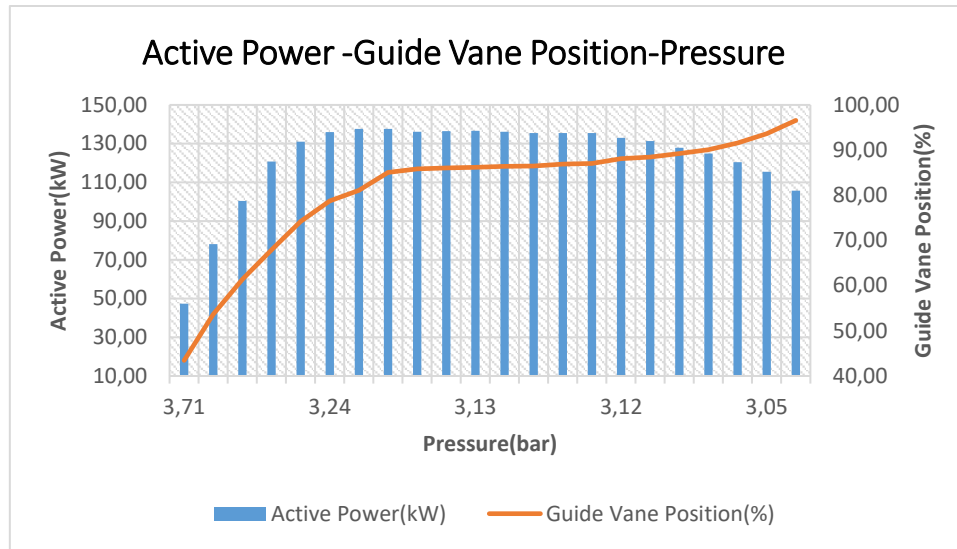


Figure 12. According to The Power Set PID Control Block; The Graph of The Active Power, Guide Vane Position and Pressure

As the demand power increases, the opening of the guide vane will also increase. In Figure 12, the changes in the position of the guide vane according to the demand power are graphed. At 50 kW power, the guide vane position was measured as 43% and the pressure was measured as 3.71 bar. When the demand power increased and 100 kW was produced, the guide vane position was opened by 61% and the pressure was measured as 3.54 bar. At 135 kW power demand, the guide vane position of the system tended to remain stable at 85%-86%, and the pressure value remained constant at 3.12-3.13. However, in order to meet the system demand over 140 kW, the guide vane position tended to open towards 100%, the guide vane did not remain in a stable position, the pressure dropped to 3.05 bar, and the system could not meet the requested energy.

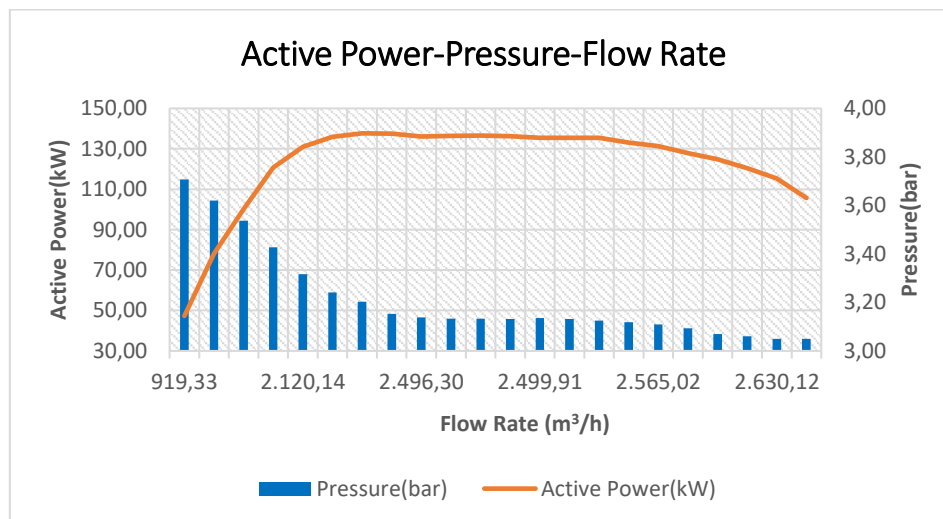


Figure 13. According to The Power Set PID Control Block; The Graph of The Active Power, Pressure and Flow Rate

In order to examine the effect of flow and pressure on the produced active power, the graph created according to the power set PID control is shown in Figure 13. At a power of 50 kW, the flow rate was

measured as 919.33 m³/h and the pressure was measured as 3.71 bar. When 100 kW power was requested, the flow rate increased to 1,631.86 m³/h, while the pressure decreased to 3.54 bar. When 135 kW power was requested, it increased up to 2,496.30 m³/h and started to remain stable around 2500 m³/h, the pressure maintained its balance at 3.13-3.14 bar. When the power demand was over 140 kW, more water passed through the system to provide this power, a flow rate of around 2,630 m³/h was observed, and the pressure tended to drop to 3.05-3.06 bar levels.

IV. CONCLUSION

The active power and system stability studies produced by two different software, guide vane PID control and Power set PID controls, were made comparatively in this study. In the system; voltage, current, active power, pressure after the inlet valve, guide vane position, generator number of revolutions and flow rate data can be obtained from the field. However, in our study, this two different software were compared, with active power, guide vane position, flow rate and pressure values graphed.

In Figure 6, which contains the data obtained from the guide vane PID software, and in Figure 11, which contains the data obtained from the Power Set PID software, in both cases, the guide vane position initially increased linearly at the opening position to supply the required power, thus water inflow into the turbine also increased.

It is observed that the guide vane position remains stable at 87.4% and the flow rate between 2,615-2,622 m³/h in Figure 6. However, in Figure 11, the guide vane position remained stable at 85-86% for a while, and as the power demand increased, the opening ratio of the guide vane position continued to increase and showed a tendency to increase up to 100% opening ratio. However, it did not tend to remain stable at the ideal position opening. Depending on the opening position, the amount of water entering the turbine increased linearly and the flow rate increased up to 2687 m³/h.

The flow rate increased in both PID software, reaching 2,622 m³/h when examined in Figure 6, while in Figure 11 it reached 2,690 m³/h due to the 100% opening of the guide vane.

The pressure value showed the same decreasing tendency in both PID software. The pressure value, which initially started at 3.71 bar, decreased over time and remained stable at 3.11-3.12 bar in Figure 8, where the guide vane PID was applied, but in Figure 13, where the power set PID was applied, the pressure started at 3.71 bar over time. It decreased to 3.05 levels and could not maintain its stable state. We compared both software based on active power, as shown in the Figure for the guide vane PID software as observed in Figures 6, 7 and 8, a maximum active power of 137 kW was achieved and maintained. However, when observed in Figure 11, 12 and 13 in the power set PID software, the maximum active power was observed as 137 kW, but the system could not maintain constant power and it was observed that the active power decreased to 105 kW.

When the results of both software are compared, it is observed that the system works more efficiently with the guide vane PID software.

By observing the decrease in the active power value in the guide vane PID software, the guide vane position can be kept constant at the requested value. Thus, the system can be operated at its maximum power efficiency point.

Another benefit of the guide vane PID is water needs in treatment facilities periodically and hourly according to the instant demands of end users. The capacity of the treatment system is provided by water treatment up to the requested amount. Getting the requested m³/h amount of water into the system is also possible with the guide vane control. The other method is focused on the generated power and thus, flow control remains in the background and harms of the treatment plant. For these reasons, the guide vane PID control is more suitable than the power set PID control.

To enhance energy production efficiency, mitigate malfunction risks, and minimize environmental impact, future work on this project can be expanded by leveraging advancements in technology and industrial innovations. Potential areas for future research may include the following;

- Fuzzy Logic-based control strategies may be employed as an alternative to PID control, particularly in systems characterized by uncertainty and complexity.
- By utilizing big data technologies, long-term system data can be collected and processed through artificial intelligence (AI) algorithms, thereby facilitating the development of a more precise maintenance strategy.
- Optimization algorithms may be employed to enhance the energy efficiency of both the transmission line and the hydroelectric power plant. Through continuous monitoring and optimization of system parameters, improved efficiency in energy production can be realized.
- By implementing a system integrated with machine learning algorithms, predictive maintenance strategies can be developed. This system mitigates the risk of malfunctions by forecasting the optimal time for maintenance interventions.
- Through continuous monitoring using various sensors in the transmission line and power plant, deviations in parameters such as temperature, pressure, and flow rate beyond specified thresholds can be detected in advance.

ACKNOWLEDGEMENTS: This project was designed at the entrance of the drinking water treatment plant within the scope of "Compact and Smart HEPP Application for Facilities with Hydraulic Potential (Water Pipelines)" between TEMSAN (Türkiye Electro Mechanic Industry Corporation) Research & Design and Innovation Directorate and Metropolitan Zonguldak Union of Municipalities Administration. I would like to acknowledge and express my sincere appreciation to my esteemed colleagues who contributed to the project.

I would also like to thankfull appreciation to my supervisor Assoc. Prof.Dr. Ahmet AKTAŞ, who guided the study and my family for their moral support.

V. REFERENCES

- [1] S. Virley and Dr. R. Debarre, "Energy institute statistical review of world energy report," Energy Institute, London, United Kingdom. ISSN 2976-7857, 2024.
- [2] Enerji ve Tabii Kaynaklar Bakanlığı. (2024, 24 Ekim). *Bilgi merkezi elektrik* [Çevrimiçi]. Erişim: <https://enerji.gov.tr/bilgi-merkezi-enerji-elektrik>.
- [3] A. Akpınar, M. İ. Kömürcü, M. Kankal and M. H. Filiz, "Çoruh havzasındaki küçük hidroelektrik santrallerin durumu," *V. Yenilenebilir Enerji Kaynakları Sempozyumu*, Türkiye, 2009, ss. 249-254.
- [4] N. Sanampudi and P. Kanakasabapathy, "Integrated voltage control and frequency regulation for stand-alone micro-hydro power plant," *Materialstodays Proceedings*, vol. 46, no. 10, pp. 5027-5031, 2020.

- [5] S. V. Kamble and S. M. Akolkar, "Load frequency control of micro hydro power plant using fuzzy logic controller," *International Conference on Power, Control, Signals and Instrumentation Engineering (ICPCSI)*, India, 2017, pp. 1783-1787.
- [6] Y. Oğuz, A. Kaysal and K. Kaysal, "Adıgüzel Hydroelectric Power Plant Modeling and Load-Frequency Control," *Academic Platform Journal of Engineering and Smart Systems*, vol. 3, no.1, pp. 34-41, 2015.
- [7] D. Öztürk and M. T. Özdemir, "Çok küçük güçlü hidroelektrik santrallerde PLC ile gerilim ve frekans kontrolü," *V. Ulusal Temiz Enerji Sempozyumu*, Türkiye, 2004, ss.124-130.
- [8] Ö. Polat, M. C. Bulut, İ. Dönmez and K. Özsoy, "PLC ve SCADA entegrasyonlu hidroelektrik santralin prototip tasarımı, imalatı ve 3B yazıcı ile türbin üretimi," *Adıyaman Üniversitesi Mühendislik Bilimleri Dergisi*, c.8, s.1, ss. 253-267, 2021.
- [9] A. Dalcalı, E. Çelik ve S. Arslan, "Mikro ve mini hidroelektrik santralleri için mikrodenetleyici tabanlı bir elektronik governor sisteminin tasarımı," *Erciyes Üniversitesi Fen Bilimleri Enstitüsü Dergisi*, c. 28, s. 2, ss. 1012-2354, 2012.
- [10] F. M. Ulu and H. Altınkaya, "Design, control and automation of MHPP- an experimental," *Gazi University Journal of Science*, vol. 10, no. 4, pp. 1083-1097, 2022.
- [11] C. Thanajitr, S. Polmai and S. Kittiratsatcha, "Development of Converter and Control System for Variable Speed Permanent Magnet Synchronous Generator in Small Hydro Power Plant Model," *25th International Conference on Electrical Machines and Systems (ICEMS)*, Chiang Mai, Thailand, 2022, pp. 1117-1121.
- [12] H. Kurt, "Küçük ölçekli hidroelektrik santralde bulanık mantık algoritmali PLC ile türbin kontrolü," Yüksek Lisans Tezi, Elektrik Elektronik Mühendisliği Ana Bilim Dalı, Dumlupınar Üniversitesi, Kütahya, Türkiye, 2013.
- [13] B. Yılmaz, "Özgül hız değerine bağlı olarak francis tipi türbin çarkı tasarımı ve performansının analizi," Yüksek Lisans Tezi, Enerji Sistemleri Mühendisliği Ana Bilim Dalı, Gazi Üniversitesi, Ankara, Türkiye, 2024.
- [14] B. Kudal, "İsale hatları üzerine mikro HES kurularak enerji üretimi: Bolu İli örneği," Yüksek Lisans Tezi, Bolu Abant İzzet Baysal Üniversitesi, Bolu, Türkiye, 2022.
- [15] K. Korkmaz, "Jeneratör seçim kriterleri," *II. Elektrik Tesisat Ulusal Kongresi*, Türkiye, 2009, ss. 150-160.
- [16] M. Karayel, "Mikrotip hidroelektrik santraller için PLC tabanlı SCADA sistem otomasyonu ve RTU/PLC ile frekans ve gerilim regülasyonunun gerçekleştirilmesi," Yüksek Lisans Tezi, Elektrik Eğitimi, Gazi Üniversitesi, Ankara, 2013.
- [17] Y. Aslan, C. Yaşar and M. Ç. Karabörk, "Bir mikro-hidro örneği: Kayaboğazı barajı," *Eleco Elektrik-Elektronik-Bilgisayar Mühendisliği Sempozyumu*, Türkiye, 2004, ss. 100-105.
- [18] O. Bendeş, B. Yılmaz, F. Koç and A. Yıldız, "Banki türbini verimlilik artışı için tasarım parametrelerinin sayısal ve deneysel olarak incelenmesi," *Dicle Üniversitesi Fen Bilimleri Enstitüsü Dergisi*, c. 12, s. 1, ss. 448-64, 2023.
- [19] W.Ali, H.Farooq, M.Usama and A.Bashir, "PID vs PI control of speed governor for synchronous generator based grid connected micro hydro power plant," *Journal of Faculty of Engineering Technology*, vol. 24, no. 1, pp. 53-62, 2017.

[20] Siemens Industry Online Support. (2024, 18 August) *PID control with PID compact for SIMATIC S7-1200/S7*. [Online]. Available: https://support.industry.siemens.com/cs/document/100746401/pid-control-with-pid_compact-for-simatic-s7-1200-s7-1500?dti=0&lc=en-WW.

[21] S. Kaçar, A. F. Boz, B. Aricioğlu and H. Tekin, “PID denetleyici uygulamaları için yeni bir online deney seti tasarımı,” *Journal of Sakarya University Institute of Science and Technology*, c. 21, s. 1, ss. 1-13, 2016.



Düzce University Journal of Science & Technology

Research Article

Identifying Knowledge Gaps on Ecotoxicological Assessment of Micro/Nanoplastics with Aquatic Keystone Species

Vildan Zülal SÖNMEZ ^{a,*}, Ceyhun AKARSU ^b, Zeynep AYDIN ^b, Elif Naz COŞKUN ^b, Ecem GÜNEY ^b, Şevval İŞLEK ^b, Zeynep BOSTAN ^b, Nüket SİVRİ ^b

^a Department of Environmental Engineering, Faculty of Engineering, Düzce University, Düzce, TÜRKİYE

^b Department of Environmental Engineering, Faculty of Engineering, İstanbul University-Cerrahpaşa, İstanbul, TÜRKİYE

* Corresponding author's e-mail address: zualsonmez@duzce.edu.tr

DOI: 10.29130/dubited.1539558

ABSTRACT

The pollution of aquatic environments by micro/nanoplastics (M/NPs) has been a growing public concern in recent years. This situation has the potential to threaten and affect both aquatic and terrestrial ecosystems simultaneously. Therefore, extensive research has been conducted over the past few years to determine the toxicity of M/NPs. This article investigated the global scientific literature on M/NPs' toxicity on *Daphnia magna* by integrating social network analysis with bibliometrics. A total of 100 publications were downloaded and analyzed with the majority being academic journal articles. Network maps and graphics displayed the correlations between keywords, countries, and journals. Moreover, the type, size, and exposure time of M/NPs were also evaluated to expose current research trends. The results demonstrate that PS and PE are the primary polymer types employed in most toxicity studies. Researchers in China and Germany have provided a great contribution. The Journal of Environmental Pollution published the highest number of research articles. The top publishing countries and the top-cited publications and authors will likely pave the way for standardization in both microplastic and nanoplastic research.

Keywords: *Daphnia magna*, environmental pollution, ecotoxicology, bibliometric analysis, polymer.

Mikro/Nanoplastiklerin Ekotoksikolojik Değerlendirilmesindeki Bilgi Eksikliklerinin Sucul Ekosistem Anahtar Türleri ile Belirlenmesi

Öz

Son yıllarda sucul alanların mikro/nanoplastikler (M/NP) tarafından kirlenmesi, giderek artan bir endişe haline gelmiştir. Bu durum hem su hem de kara ekosistemlerini aynı anda tehdit etme ve etkileme potansiyeline sahiptir. Bu nedenle, M/NP'lerin toksisitesini belirlemek için son birkaç yıldır kapsamlı araştırmalar yürütülmüştür. Bu makale, sosyal ağ analizini bibliyometri ile entegre ederek *Daphnia magna* üzerindeki M/NP'lerin toksisitesi hakkındaki küresel bilimsel literatürü incelemiştir. Çoğunluğu akademik dergi makaleleri olmak üzere toplam 100 yayın indirilmiş ve analiz edilmiştir. Ağ haritaları ve grafikler, anahtar kelimeler, ülkeler ve dergiler arasındaki korelasyonları göstermiştir. Ayrıca,

mevcut araştırma eğilimlerini ortaya koymak için M/NP'lerin türü, boyutu ve maruz kalma süresi de değerlendirilmiştir. Sonuçlar, PS ve PE'nin çoğu toksisite çalışmasında kullanılan birincil polimer türleri olduğunu göstermektedir. Çin ve Almanya'daki araştırmacılar büyük katkı sağlamıştır. En fazla araştırma makalesi Çevre Kirliliği Dergisi (Journal of Environmental Pollution) tarafından yayınlanmıştır. En iyi yayın yapan ülkeler ve en çok atıf alan yayınlar ve yazarlar muhtemelen hem mikroplastik hem de nanoplastik araştırmalarında standardizasyonun önünü açacaktır.

Anahtar Kelimeler: *Daphnia magna*, çevre kirliliği, ekotoksikoloji, bibliyometrik analiz, polimer.

I. INTRODUCTION

Currently, the prevailing concern revolves around global environmental contamination, which necessitates daily attention. The surge in pollution and waste over recent years can be primarily attributed to the advancement of contemporary society, encompassing industrial and agricultural domains. Among the myriad of contaminants disseminated worldwide, the prominent escalation in plastic utilization stands out prominently. Approximately 8.3 billion metric tons of plastic have been manufactured to this day, of which 6.3 billion metric tons are either discarded in regular storage or come into contact with the outside environment via the receiving environment [1]. Consequently, 10% of the waste released into the receiving environment reaches water bodies [2-3]. Notwithstanding, plastic artifacts disseminated within the environment undergo fragmentation, resulting in minute plastic fragments known as microplastics (MP) and nanoplastics (NP), classified based on their dimensions [4]. Despite the small ratio, the amount of plastic in the oceans is expected to reach 250 million tons by 2025 [5]. As a result, it is anticipated that aquatic organisms will be exposed to more micro and nano-sized plastics (M/NPs) [6].

According to ecotoxicity studies, after being digested by several living organisms, microplastics (MPs) reach the intestine, then the circulatory system, and finally various tissues such as the gills, liver, and kidneys [7]. It has been observed that nutrition, growth, and fertility may be affected as a result of the exposure of some types of zooplankton to MPs [8-11]. Moreover, because aquatic organisms are a source of food for humans, M/NP exposure of organisms also poses a threat to human safety and public health [12-14]. As one of the most critical zooplanktonic species in freshwater ecosystems, *Daphnia magna* (*D. magna*) serves as a link between primary producers and the higher trophic levels in various ecosystems [15-17]. It is utilized as a model test organism in ecotoxicology studies due to its ease of generation in the laboratory, low cost, and high sensitivity [18]. *D. magna* plays a critical role in determining the effect of pollutants on organisms, especially in aquatic areas [19-23].

Due to the fact that *D. magna* is a widely preferred test organism in ecotoxicology, it is also commonly used to investigate the toxicity of M/NPs [9, 23-29]. In the earliest studies, MPs were detected in the digestive tracts of *D. magna* exposed to primary and secondary microplastics in the size range of 2–5 µm, and this was interpreted as evidence that even small-built creatures consume M/NPs [9]. Some studies show that MP fragments and additives have distinct toxicological mechanisms in terms of their intergenerational effect [30].

The focus of this research was to assess the ecotoxicological investigations of M/NPs conducted on *D. magna*, a keystone species among aquatic animals. In this respect, studies on M/NP toxicity with *D. magna* have been examined in the literature regardless of the year. The findings examined under the headings of M/NPs were physical and chemical properties, toxicity, duration of exposure, and toxicity analyses, and studies are categorized under the headings of the sociology of supporting experiments. Unlike previous studies, synthetic bibliometric methodologies and indicators were used to investigate the research trend and pressing issues of microplastic toxicity. In addition to paving the path for standardization in both of microplastic and nanoplastic research, the findings will be valuable for mapping the research landscape and technology forecasting.

II. MATERIAL AND METHODS

A. LITERATURE SEARCH CRITERIA

In the realm of scientific research, bibliometric analysis has garnered significant attention in recent times. This surge in interest can be ascribed to two primary factors: (1) the progress, availability, and ease of access to bibliometric software tools like Gephi, Leximancer, VOSviewer, alongside esteemed scientific databases such as Scopus and Web of Science, and (2) the cross-disciplinary dissemination of bibliometric methodologies from information science to the domain of business research [31]. In this study, it was preferred to use the Scopus scientific database. Because, the Scopus search engine, the bibliographic database of academic journal publications which covers more than 20,000 peer-reviewed journals published by more than 5,000 publishers, was used in this study [32-34]. An advanced search was performed using the following strings: "*Daphnia magna*", "microplastic", and "nanoplastic". Using restrictive keywords in the database, 2 distinct limited searches were conducted without restrictions on country or year. To improve the accuracy of the data, the first search included the keywords "*Daphnia magna*", and "Microplastics", and the second search included "*Daphnia magna* " and "Nanoplastics".

B. DATA PROCESSING

On June 21, 2021, 68 studies were discovered for the first search and 32 for the second search, each consisting of various types of documents. The documents were further screened based on their titles and abstracts; articles with research directions such as studies conducted with organisms other than *D. magna* were omitted. Accordingly, a total of 56 microplastic articles and 31 nanoplastic articles were evaluated in the first and second searches, respectively. Within the scope of this study, the results were separated into subcategories such as M/NP structure (morphological and chemical properties), the origin of M/NPs (purchase or obtained in a laboratory environment), M/NP types, and duration of exposure. The numerical data obtained from the study via bibliometric analyses were interpreted and visualized with social network analysis maps made via VOSViewer, and the corresponding figures were drawn using Origin 10.0. Figure 1 illustrates the research pattern and process flowchart employed in this study.

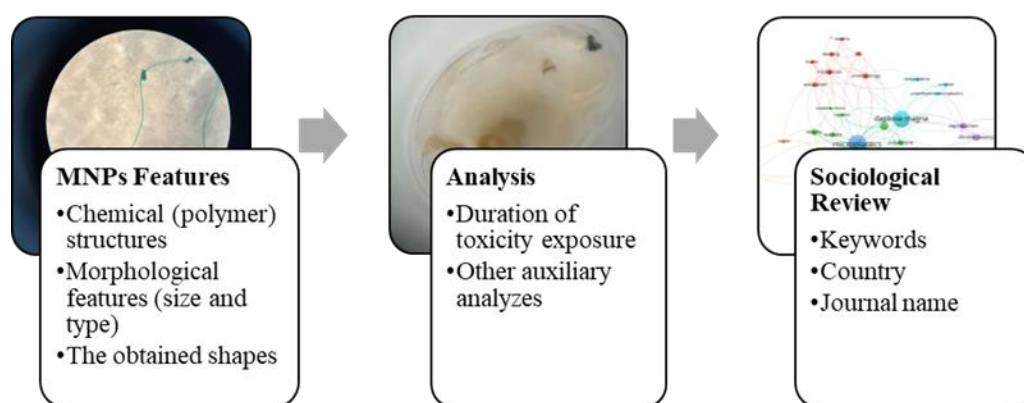


Figure 1. Research pattern and process flowchart

III. RESULTS AND DISCUSSION

A. PHYSICAL AND CHEMICAL PROPERTIES OF M/NPS

When the chemical polymer structures of the studied microplastics are examined, it is revealed that polystyrene (PS) (%35) and polyethylene (PE) (%28) are preferred for use in the vast majority of studies. PE, polypropylene (PP), PS, polyamide (nylon), and polyesters account for approximately %90 of the world's total plastic production [35-37]. PS is a widely utilized industrial plastic, particularly due to its strong stability, cost performance, and electrical properties [38-39]. This situation also drew the attention of researchers who have conducted toxicity studies. PS appears to be the dominant polymer type used in toxicity studies [40]. PE offers a broad range of applications. Its primary uses are in food packaging, chemical packaging, bottles, bags, water pipelines, and automotive parts, as well as its other practical daily applications. Additionally, since most plastics we use in our daily lives have a polymer structure, researchers have easy and inexpensive access to this type of polymer. Therefore, most researchers break down these substances to obtain secondary M/NPs. In addition, comparative studies of PE and other polymer types such as PVC, PET, PA, and PP have been carried out [41-43]. However, there is a limited number of studies on the toxicity of other polymers (PVC, PET, PA, PCB, PUR, PLA, and PMMA) [9, 41-48] (Figure 2).

While determining the toxicity of nanoplastics, it seems that the vast majority of investigations have utilized PS (90%). With an annual production volume of 13 million, PS is the most commonly used type of polymer, especially in the packaging of food products [49]. In the conducted studies, data were obtained indicating that PS was found in nature as secondary M/NPs because of biodegradation, weather conditions and deterioration caused by UV photo-oxidation [50-51]. Therefore, the toxic effects of PS on *D. magna* have been greatly emphasized and well documented [52-53]. Nonetheless, there are a certain number of studies on determining nanoplastic toxicity with PE and PMMA [54-55].

To control the toxicity effect of the polymer types, MP studies using various non-polymer particles such as kaolin and glass beads have also been conducted [44, 47, 56]. Thus, they emphasized that the toxicity is not attributable to any particle that daphnids can ingest, but rather to the surface properties and chemical composition of MPs [57].

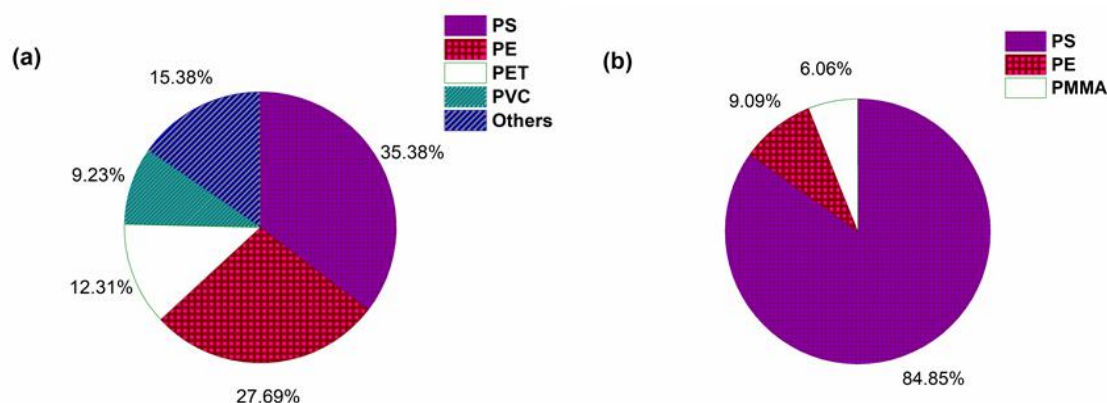


Figure 2. Distribution of preferred polymers for (a) microplastics and (b) nanoplastics

Based on the published studies, the most frequently studied MP size range is 1-10 μm with a rate of 43%. *D. magna* is a freshwater *Cladocera* that feeds via active filtration and passive uptake, actively filtering particles as small as 200 nm [58] and as large as 80 μm [59], depending on filtering apparatus size, as well as passively taking up smaller particles [60-61]. In current study, Jemec et al. (2016) demonstrated that *D. magna* readily ingests long synthetic fibers around 300 μm in length, but also detected very long fibers around 1400 μm in length inside the gut. Therefore, some researchers

investigated the toxicity caused by particles ranging in size from 100 to 1000 μm . However, this is uncommon because the adult body size of *D. magna* ranges from 1.5 to 5.0 mm. Most studies conducted on NPs (40%) used a size range of 101-1000 nm (Figure 3-b). Considering the size of their filter combs, daphnids are thought to swallow microplastics more than nanoparticles. Consequently, as the particle size decreased, the number of studies were increased. However, some researchers claim that the nanoscale negative effects of plastics on the metabolism of daphnids are more significant [17].

Concerning the toxicity of MPs, their shape and size play an important role [9,45]. In general, it is not possible to compare the studies in the literature with one another in terms of microplastic type (bead, fragment, and fiber) due to the lack of widely accepted methodological standards in these investigations. Therefore, independent studies demonstrating the effects of polymer structures cannot be correlated with each other since they use polymers of different sizes [40]. In general, fragments and fibers are the most extensively studied microplastic types on *D. magna*, and it has been stated that they are more toxic than those in the form of spheres [62-63].

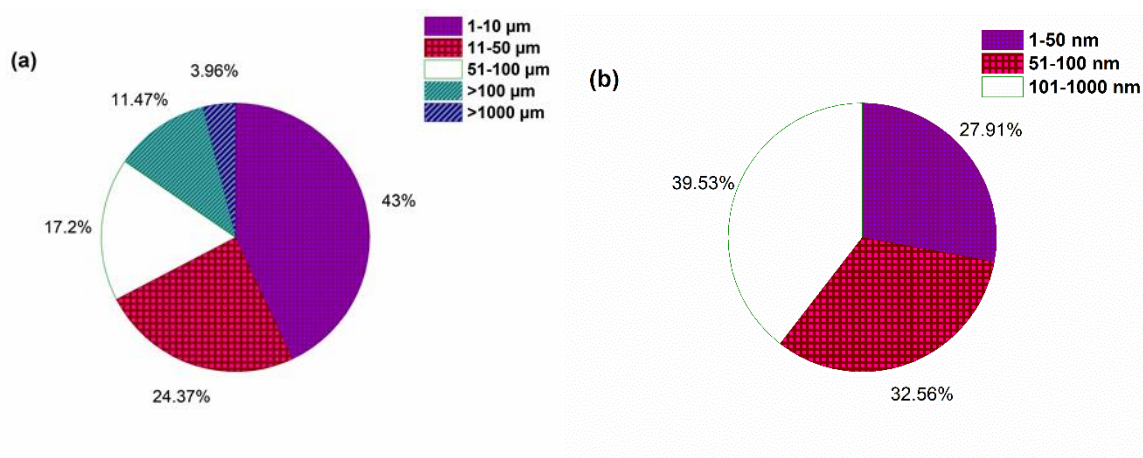


Figure 3. Distribution of preferred plastics by size ranges for (a) MPs and (b) NPs

In 73% of the studies, MPs were obtained from different companies, usually as commercial products. Cospheric LLC [64] and Sigma-Aldrich [65] are the most preferred companies. These are followed by companies such as BaseLine Chromtech Research Center (Tianjin, China) [66], Goodfellow GmbH [67], SonTek/Xylem Inc (San Diego, USA) [68] and Fluoresbrite® YG Microspheres, Polysciences, Inc. (GmbH, Germany) [69] (Fig. 4). Researchers who do not purchase them as commercial products obtained MPs by taking commercial polymers in the form of ready-made pellets [29] or by breaking down these products as mentioned previously [70].

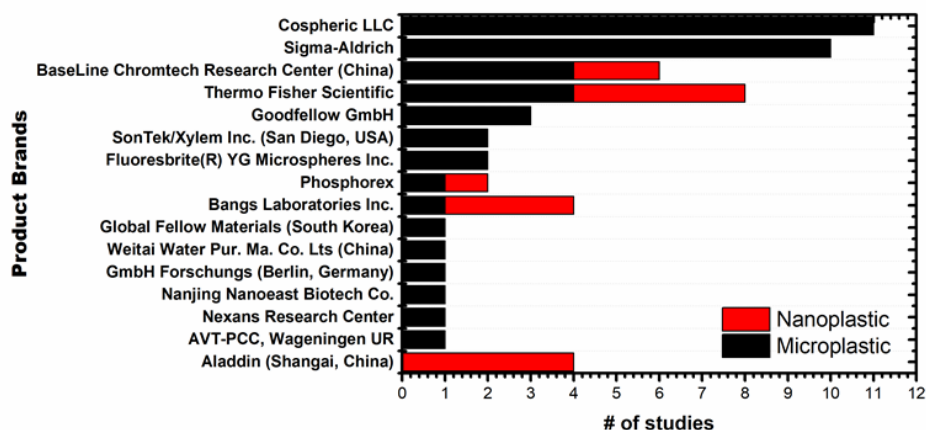


Figure 4. Most preferred companies in M/NPs studies

The plastic fibers were cryogenically ground in liquid nitrogen using Freezer/Mill 6875 (SPEX® SamplePrep, US) to obtain MP fragments [62]. PS lids of disposable instant coffee cups were cut into small pieces, frozen in liquid nitrogen, and pulverized in a ball mill (Retsch MM400, Retsch GmbH, Germany) [70]. In a separate study, the original PET fabric was cut into 2 x 2 cm pieces and ground in a Retsch PM 100 planetary ball mill to produce microplastic fiber [71]. Milling of recycled LDPE was performed in two stages. First, the pellets were fragmented by a SM100 mill (Retsch GmbH, Haan, Germany) and then further cryo-milled using a homogenizer (MillMix 20, Domel, Železniki, Slovenia). Both LDPE were tested and analyzed as irregular fragments (microfragments) [72]. In another study by Na et al. [29], PE fibers were extruded three times to ensure the homogeneity of the mixture and then cryogenically ground in liquid nitrogen using Freezer/Mill 6875 (SPEX® SamplePrep, US) to obtain MP fragments.

B. RESEARCH TENDENCY OF TOXICOLOGY OF M/NPS STUDIES

B. 1. Evaluation of Toxic Exposure

In the studies, tests for acute and chronic exposure were carried out at a rate of 64% and 36%, respectively. In immobilization studies with *D. magna*, the time of onset for acute exposure is usually studied for 24 or 48 hours. However, examining the research reveals that they had worked for 72 hours, 96 hours, and even up to 7 days. Accordingly, researchers working with more than one MP generally favored chronic exposure since MP species are examined at different durations. In a group study, the rate of chronic examination was increased in order to accurately examine all types of MP. However, unlike microplastics, nanoplastics have a shorter observed acute toxicity duration. Test times of 2 or 4 hours and 24 hours have been investigated in acute toxicity. The distribution of toxicity tests versus the number of articles is given in Fig. 5.

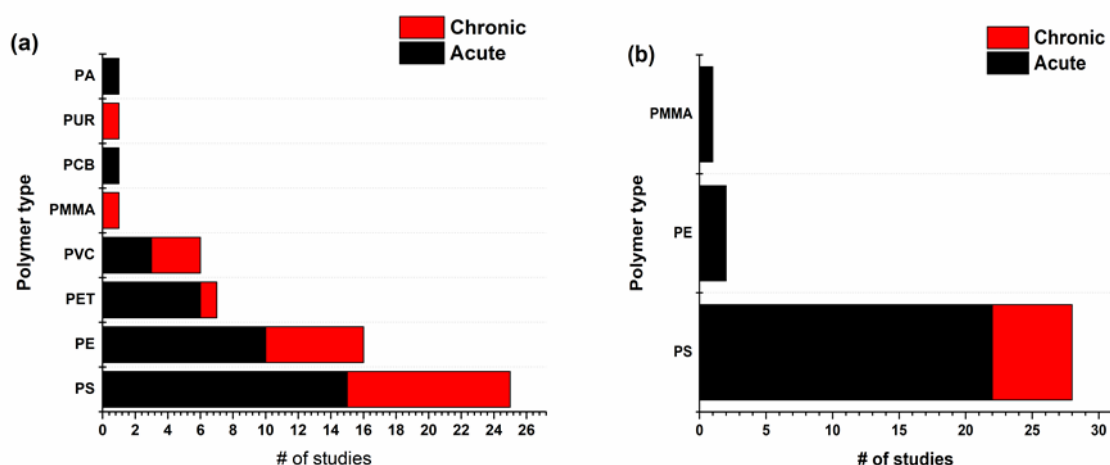


Figure 5. The distribution of toxicity tests vs number of articles for (a) MPs and (b) NPs

B. 2. Toxicity Endpoints

Toxicity test organisms are characterized as being “relatively easy to culture and maintain in the laboratory”. Toxicity tests with *D. magna* are mostly based on the use of live test biota, which must be obtained from reliable sources or cultured and preserved in the laboratory in which the tests are performed. Numerous environmental factors must be considered in order to obtain an adequate quantity of healthy daphnia. Even in cultured laboratories, the availability of sufficient numbers of test organisms can often interfere with routine testing and monitoring of large numbers of samples [73]. For this reason, some researchers use commercially available *D. magna* biotests for their research. The effect concentrations of toxicity studies are expressed in units of mass per volume such as mg/L. The reported

toxicity endpoint of micro and nanoplastics is in the range of mg/L or $\mu\text{g/L}$. It is occasionally expressed as particles/L. For example, *D. magna* immobilization test results of polystyrene (PS) beads are 66.97 mg/L or 0.11 μm . Uncertainties in the difference between particle/L and mg/L (endpoint unit in toxicity literature) were attempted to be eliminated with an equation developed by Leusch and Ziajahromi [74].

B. 3. Auxiliary Analysis Methods

In the majority of the studies, in addition to the toxicity tests performed, the stereomicroscope [14, 75], the fluorescent microscope [47], and the inverted microscope [76] were utilized to examine the exposure of daphnids to M/NPs. To determine the concentration of exposure, however, the number or mass of M/NPs in aqueous media must be known. Spectrofluorimetry [14] is used to measure the number of microplastics in experimental environments (aqueous solutions). In addition, the laser diffraction method [43, 72], and the Laser Particle Counter [77] are employed to determine the particle size and distribution to which daphnids are exposed. In addition to the concentration and particle size of the studied M/NPs, ATR-FTIR [72, 78-80] and Raman Spectrophotometry [39] are the favored techniques for determining chemical polymer structure. Micro FT-IR is used to determine the chemical polymer structure of smaller particles than ATR-FTIR. Advanced analysis methods such as SEM [39], SEM-EDS [43], FE-SEM [29, 81], and transmission electron microscopy (TEM) [45,82] were used for the microstructural calcification and elemental analysis of M/NPs.

Nanoplastic studies are more interested in the dynamic light scattering (DLS) method than microplastic investigations [55, 57, 83-84]. DLS is a technique in physics for determining the size distribution profile of small particles in suspension or polymers in solution. In nanoplastic research, TEM [22, 54, 85] and Zetasizer [86] are among the most frequently preferred analysis methods.

B. 4. General Trends Of Publications And Co-Occurrence Analysis

Bibliometric analysis frequently complements network visualization software, spanning from fully graphical user interface-based tools like VOSviewer [87] to command-based applications such as the Bibliometrix package in the R [88] programming language [31]. However, the most preferred VOSviewer is a scientific mapping application designed for bibliometric network visualization. It can perform a variety of bibliometric network analyses, such as keyword co-founding analysis and co-authorship analysis, in addition to citation network visualization. Fig. 6 displays the keywords that have appeared at least twice in 87 published articles. “Microplastics” is the most sought-after keyword in the search results, followed by “Daphnia magna”. Depending on the relationship between keywords and article search content, this sequence is followed by the relationship between microplastic names, toxicity kinds, and aquatic creatures.

According to the keyword mapping for nanoplastics, bioaccumulation and uptake of “Daphnia magna” and nanoplastics are nearly equal in relation to toxicity. As a result, “uptake”, “toxicity”, “bioaccumulation” and “polystyrene” are frequently used in searches on aquatic organisms, and the frequency of their occurrence indicates the significance of terms to the subject. As shown in Fig. 7, the top three countries for microplastic research are China, Germany, and Slovenia, whereas the top three nations for nanoplastic research are China, Canada, and Denmark. In general, China is the leader in studies of M/NPs toxicity. China is indeed engaged in various international scientific organizations and has conducted many national kinds of research which were supported by official government funds [89].

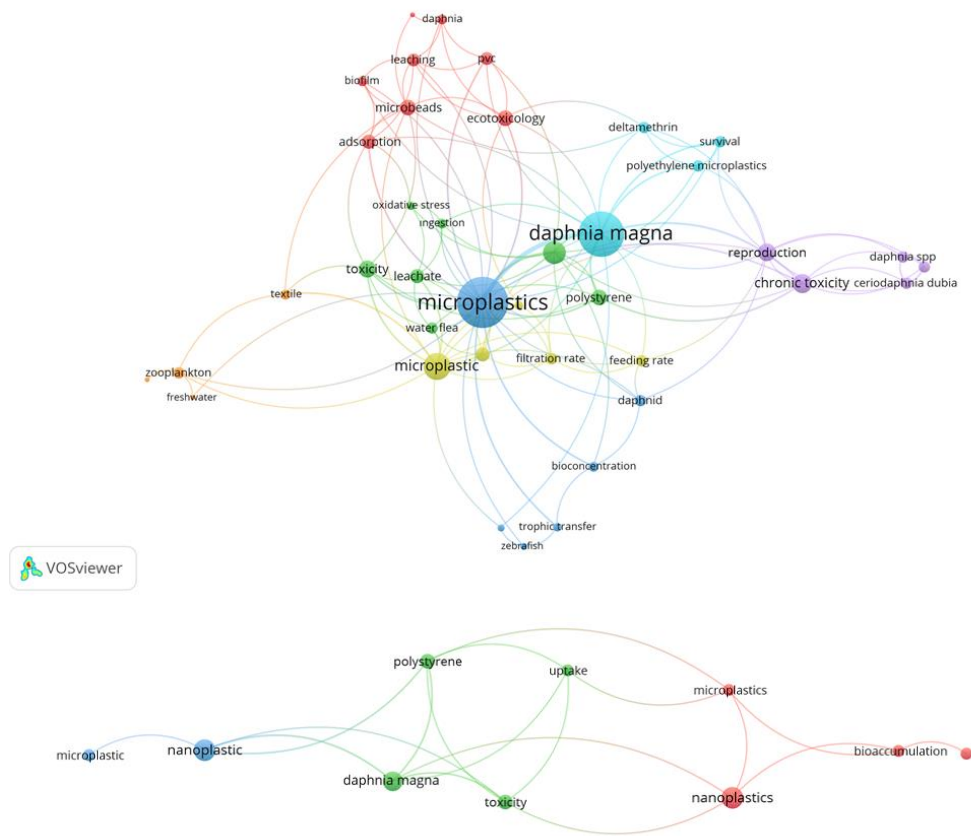


Figure 6. Co-occurrence network of keywords generated by VOSviewer based on (a) “microplastic” OR “Daphnia magna” and (b) “nanoplastic” OR “Daphnia magna”.

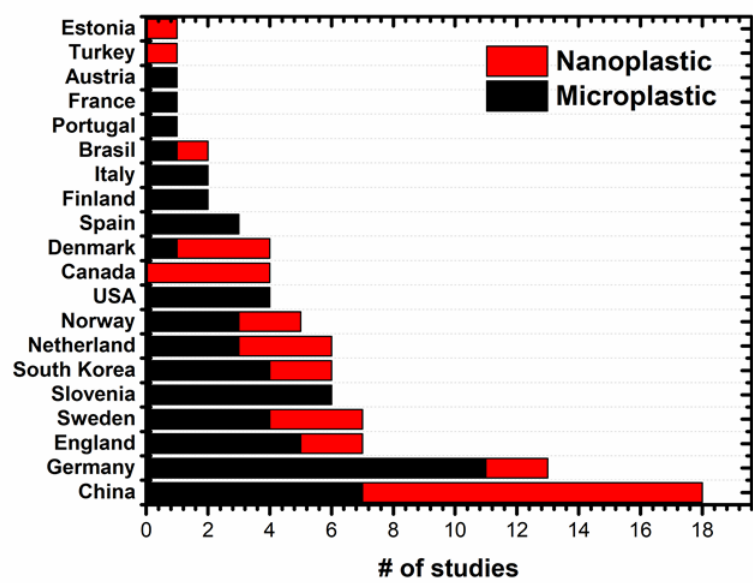


Figure 7. The country distribution of the total number of published articles

The publication sources that published the most articles on “microplastic” OR “*Daphnia magna*” and “nanoplastic” or “*Daphnia magna*” are given in Fig. 8. For studies found with the terms “microplastic” OR “*Daphnia magna*”, Environmental Pollution had the most publications (17, 32%) with the second-highest IF2020 (IF=8.071). Science of The Total Environment ranked second (8, 15%) in the number of articles with an IF2020 of 7.963, and Journal of Hazardous Materials ranked third (4, 7.5%), although it had the highest IF2020 (IF= 10.588). The rest of the articles (45.5%) were published in 17 different journals. Moreover, for “nanoplastic” and “*Daphnia magna*” studies, Environmental Pollution published the highest number of articles (6, 20%) with the third-highest IF2020 (IF=8.071). Environmental Science and Technology ranked second (5, 16.7%) in the number of articles with the highest IF2020 (IF=9.028). Two journals, Environmental Toxicology and Chemistry and Environmental Science, published 3 articles each, which corresponds to 20% of the total publications. The rest of the articles (43.3%) were published by 11 different journals.

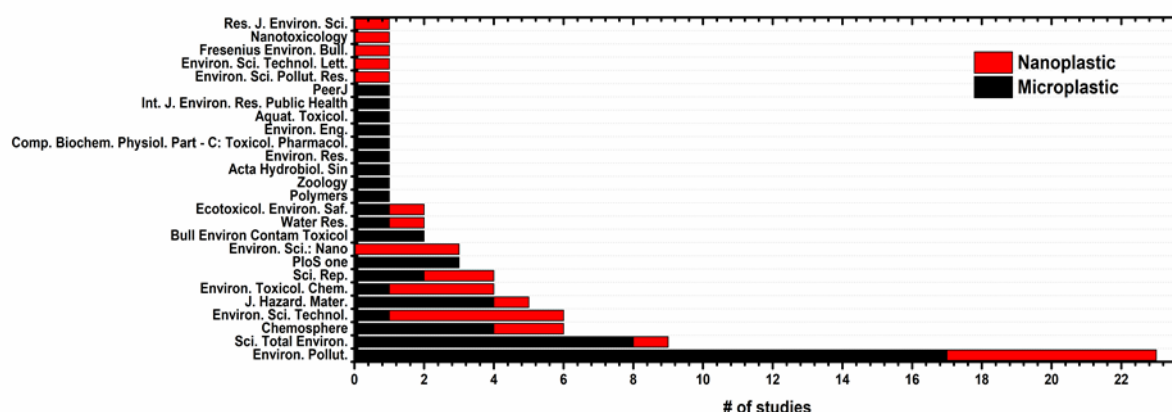


Figure 8. The journal distribution of the total number of published articles

IV. CONCLUSION

We know that small-sized plastics are easily dispersed and can have a direct impact on the toxicity in the aquatic environment. Therefore, it is essential to better understand the toxicity of M/NPs. Effects of nanoplastics on organisms may be related to particle toxicity, the toxicity of plastic-associated chemicals, or both; however, little is known about such effects and how particle shape, size, age, or polymer type influence them further. *Daphnia* shows considerable potential as an aquatic model for the risk assessment field due to its certain characteristics such as high sensitivity to environmental stressors, known genome, short generation time, and is therefore utilized in most studies.

In this study, 100 papers in the Scopus database were screened for bibliometric study using the keywords “*Daphnia magna*”, “microplastic” and “nanoplastic”. The results demonstrate that PS and PE are the primary polymer type employed in most toxicity studies.

Bibliometric analysis showed that the contributions of China and Germany to the evaluation of toxicity of M/NPs to *D. magna* are huge. Environmental Pollution was the journal that published the most research articles for M/NPs. According to our keyword analysis, more studies were conducted on microplastics (#56) compared to nanoplastics (#31). These initial results will be influential for future toxicology studies on M/NP effects on *D. magna*. While the ecotoxicological effects and health risks of microplastics are a current research trend, an increase in the number of publications focusing on the toxicity of M/NPs is anticipated in the near future.

Nevertheless, current studies on M/NPs are extremely controversial due to the inability to establish a standard method. Moreover, the long-term effects of chronic exposure on aquatic keystone species remain poorly understood, and studies on the effects on ecosystem dynamics are needed. In addition, the interactive effects of micro/nanoplastics on aquatic ecosystems need to be further investigated in conjunction with other stressors such as pollution and climate change. Understanding the trophic transfer of micro/nanoplastics from key species to other organisms can shed light on their broader impacts. Future perspectives should focus on emerging nanoplastics, use multi-omics approaches to reveal molecular responses, and investigate the impact of microplastic mixtures in natural environments. By addressing these gaps and considering future perspectives, ecotoxicological assessments can provide a comprehensive understanding of the ecological impacts of micro/nanoplastics on aquatic keystone species and contribute to effective mitigation measures.

ACKNOWLEDGEMENTS: This research was supported by the Scientific and Technological Research Council of Turkey (TUBITAK) grants; 118C556 (“Potential Toxicological Effects of Micro and Nano Sized Plastic Particles on Benthic Organisms: İstanbul Coastal Area”) and 1919B012101177 (“Occurrence and Spatial Distribution of Microplastics in Coastal Lagoon Sediments: A case study of Küçükçekmece Lagoon”)

V. REFERENCES

- [1] L. Parker. (2018). A whopping 91% of plastic isn't recycled [Online]. Available: <https://sustainability.ucsb.edu/sites/default/files/Planet-or-Plastic.pdf>
- [2] R. C. Thompson, Y. Olsen, R. P. Mitchell, A. Davis, S. J. Rowland, Q. W. John, D. Mcgonigle, A. E. Russell, “Lost at sea: where is all the plastic?,” *Science*, vol. 304, no.5672, pp. 838, 2004.
- [3] D. Pandey, A. Singh, A. Ramanathan, M. Kumar, “The combined exposure of microplastics and toxic contaminants in the floodplains of north India: A review,” *J Environ Manage*, vol. 111557, 2020.
- [4] C. R. Multisanti, C. Merola, M. Perugini, V. Aliko, C. Faggio C, “Sentinel species selection for monitoring microplastic pollution: A review on one health approach,” *Ecol Indic*, vol. 145, no. 109587, 2022.
- [5] O. S. Alimi, J. Farner Budarz, L. M. Hernandez, N. Tufenkji, “Microplastics and nanoplastics in aquatic environments: Aggregation, deposition, and enhanced contaminant transport,” *Environ Sci Tech*, vol. 52, no.4, pp. 1704-1724, 2018.
- [6] B. Sarkar, P. D. Dissanayake, N. S. Bolan, J. Y. Dar, M. Kumar, M. N. Haque, R. Mukhopadhyay, S. Ramanayaka, J. K. Biswas, D. C. W. Tsang, J. Rinklebe, Y. S. Ok, “Challenges and opportunities in sustainable management of microplastics and nanoplastics in the environment,” *Environ Res*, vol. 207, no. 11217, 2022.
- [7] A.Elizalde-Velázquez, A. M. Carcano, J. Crago, M. J. Green, S. A. Shah, J. E. Cañas-Carrell, “Translocation, trophic transfer, accumulation and depuration of polystyrene microplastics in *Daphnia magna* and *Pimephales promelas*,” *Environ Pollut*, vol. 259, no.113937, 2020.
- [8] M. Cole, P. Lindeque, E. Fileman, C. Halsband, T. S. Galloway, “The impact of polystyrene microplastics on feeding, function and fecundity in the marine copepod *Calanus helgolandicus*,” *Environ Sci Technol*, vol. 49, no.2, pp. 1130-1137, 2015.

- [9] M. Ogonowski, C. Schür, A. Jarsén, E. Gorokhova, “The effects of natural and anthropogenic microparticles on individual fitness in *Daphnia magna*,” *PloS one*, vol. 11, no. 5, e0155063, 2016.
- [10] C. B. Jeong, H. M. Kang, M. C. Lee, D. H. Kim, J. Han, D. S. Hwang, S. Souissi, S. J. Lee, K. H. Shin, H. G. Park, J. S. Lee, “Adverse effects of microplastics and oxidative stress-induced MAPK/Nrf2 pathway-mediated defense mechanisms in the marine copepod *Paracyclopina nana*,” *Sci Rep*, vol. 7, no.1, pp.1-11, 2017.
- [11] Y. Wang, Z. Mao, M. Zhang, G. Ding, J. Sun, M. Du, Q. Liu, Y. Cong, F. Jin, W. Zhang, J. Wang, “The uptake and elimination of polystyrene microplastics by the brine shrimp, *Artemia parthenogenetica*, and its impact on its feeding behavior and intestinal histology,” *Chemosphere*, vol. 234, pp.123-131, 2019.
- [12] T. Miranda, L. R. Vieira, L. Guilhermino, “Neurotoxicity, behavior, and lethal effects of cadmium, microplastics, and their mixtures on *Pomatoschistus microps* juveniles from two wild populations exposed under laboratory conditions—implications to environmental and human risk assessment,” *Int J Environ Res Public Health*, vol. 16, no.16, 2857, 2019.
- [13] L. G. A. Barboza, C. Lopes, P. Oliveira, F. Bessa, V. Otero, B. Henriques, J. Raimundo, M. Caetano, C. Vale, L. Guilhermino, “Microplastics in wild fish from North East Atlantic Ocean and its potential for causing neurotoxic effects, lipid oxidative damage, and human health risks associated with ingestion exposure,” *Sci Total Environ*, vol. 717, no. 134625, 2020.
- [14] L. Guilhermino, A. Martins, S. Cunha, J. O. Fernandes JO, “Long-term adverse effects of microplastics on *Daphnia magna* reproduction and population growth rate at increased water temperature and light intensity: Combined effects of stressors and interactions,” *Sci Total Environ*, vol. 784, no. 147082, 2021.
- [15] J. J. Elser, W. F. Fagan, R. F. Denno, D. R. Dobberfuhl, A. Folarin, A. Huberty, S. Interlandi, Kilham, S. S. McCauley, K. L. Schulz, E. H. Siemann, R. W. Sterner, “Nutritional constraints in terrestrial and freshwater food webs,” *Nature*, vol. 408, no. 6812, pp. 578-580, 2000.
- [16] J. Colomer, M. F. Müller, A. Barcelona, T. Serra, “Mediated food and hydrodynamics on the ingestion of microplastics by *Daphnia magna*,” *Environ Pollut*, vol. 251, pp. 434-441, 2019.
- [17] B. Trotter, M. V. Wilde, J. Brehm, E. Dafni, A. Aliu, G. J. Arnold, T. Fröhlich, C. Laforsch, “Long-term exposure of *Daphnia magna* to polystyrene microplastic (PS-MP) leads to alterations of the proteome, morphology and life-history,” *Sci Total Environ*, vol. 795, no. 148822, 2021.
- [18] J. Tang, X. Wang, J. Yin, Y. Han, J. Yang, X. Lu, T. Xie, S. Akbar, K. Lyu, Z. Yang Z, “Molecular characterization of thioredoxin reductase in waterflea *Daphnia magna* and its expression regulation by polystyrene microplastics,” *Aquat Toxicol*, vol. 208, pp.90-97, 2019.
- [19] C. S. Reynolds, “*Daphnia*: Development of model organism in ecology and evolution-2011,” *Freshwater Reviews*, vol. 4, no. 1, pp. 85-87, 2011.
- [20] K. D. Harris, N. J. Bartlett, V. K. Lloyd, “*Daphnia* as an emerging epigenetic model organism,” *Genet Res Int*, vol. 147892, no. 8, 2012.

- [21] L. Kong, W. Lv, Y. Huang, Z. Liu, Y. Yang, Y. Zhao, "Cloning, expression and localization of the *Daphnia carinata* transformer gene DcarTra during different reproductive stages," *Gene*, vol. 566, no. 2, pp. 248-256, 2015.
- [22] Z. Liu, Y. Jiao, Q. Chen, Y. Li, J. Tian, Y. Huang, Y. Zhao, "Two sigma and two mu class genes of glutathione S-transferase in the waterflea *Daphnia pulex*: Molecular characterization and transcriptional response to nanoplastic exposure," *Chemosphere*, vol. 248, no.126065, 2020.
- [23] J. Na, J. Song, J. Jinho, "Elevated temperature enhanced lethal and sublethal acute toxicity of polyethylene microplastic fragments in *Daphnia magna*," *Environ Toxicol Pharmacol*, vol. 102, no. 104212, 2023.
- [24] P. Rosenkranz, Q. Chaudhry, V. Stone, T. F. Fernandes, "A comparison of nanoparticle and fine particle uptake by *Daphnia magna*," *Environmental Toxicology and Chemistry: An International Journal*, vol. 28, no.10, pp. 2142-2149, 2009.
- [25] H. K. Imhof, J. Rusek, M. Thiel, J. Wolinska, C. Laforsch C, "Do microplastic particles affect *Daphnia magna* at the morphological, life history and molecular level?," *PloS one*, vol. 12, no.11, e0187590, 2017.
- [26] S. Rist, A. Baun, N. B. Hartmann, "Ingestion of micro-and nanoplastics in *Daphnia magna*—Quantification of body burdens and assessment of feeding rates and reproduction," *Environ Pollut*, vol. 228, pp. 398-407, 2017.
- [27] C. Scherer, N. Brennholt, G. Reifferscheid, M Wagner, "Feeding type and development drive the ingestion of microplastics by freshwater invertebrates," *Scientific Reports*, vol. 7, no. 17006, 2017.
- [28] C. Schür, S. Rist, A. Baun, P. Mayer, N. B. Hartmann, M. Wagner M, "When fluorescence is not a particle: the tissue translocation of microplastics in *Daphnia magna* seems an artifact," *Environ toxicol chem*, vol. 38, no.7, pp. 1495-1503, 2019.
- [29] J. Na, J. Song, J. C. Achar, J. Jung, "Synergistic effect of microplastic fragments and benzophenone-3 additives on lethal and sublethal *Daphnia magna* toxicity," *J Hazard Mater Materials*, vol. 402, no. 123845, 2021.
- [30] J. Song, J. Na, D. An, J. Jung, "Role of benzophenone-3 additive in chronic toxicity of polyethylene microplastic fragments to *Daphnia magna*," *Sci Total Environ*, vol. 15, no. 149638, 2021.
- [31] N. Donthu, S. Kumar, D. Mukherjee, N. Pandey, W. M. Lim, "How to conduct a bibliometric analysis: An overview and guidelines," *J Bus Res*, vol. 133, pp. 285-296, 2021.
- [32] M. C. M. Blettler, E. Abrial, F. R. Khan, N. Sivri, L. A. Espinola, "Freshwater plastic pollution: Recognizing research biases and identifying knowledge gaps," *Water Res*, vol.143, pp. 416-424, 2018.
- [33] A. Basmacı, Z. Bostan, V. Z. Sönmez, N. Sivri, "Türkiye'nin sucul ekosistemlerinde ağır metal üzerine yapılan araştırmaların tarihsel incelemesi ve bibliyometrik analizi (2000-2020)," *J Anatol Environ Animal Sci*, c. 6, s. 4, ss. 567-577, 2021.
- [34] S. Şahin, N. Sivri, I. Akpınar, Z. B. Çinçin, V. Z. Sönmez, "A comprehensive bibliometric overview: Antibiotic resistance and *Escherichia coli* in natural water," *Environ Sci Pollut Res*, vol. 28, pp. 32256–32263, 2021.

- [35] V. Hidalgo-Ruz, L. Gutow, R. C. Thompson, M. Thiel, "Microplastics in the marine environment: A review of the methods used for identification and quantification," *Environ Sci Technol*, vol. 46, no.6, pp. 3060-3075, 2012.
- [36] J. C. Anderson, B. J. Park, V. P. Palace, "Microplastics in aquatic environments: Implications for Canadian ecosystems," *Environ Pollut*, vol. 218, no. pp. 269-280, 2016.
- [37] S. J. Taipale, E. Peltomaa, J. V. K. Kukkonen, M. J. Kainz, P. Kautonen, M. Tirola, "Tracing the fate of microplastic carbon in the aquatic food web by compound-specific isotope analysis," *Scientific reports*, vol. 9, no. 1, pp. 1-15, 2019.
- [38] L. Andrady, M. A. Neal, "Applications and societal benefits of plastics," *Philos Trans R Soc B: Biol Sci*, vol. 364, no. 1526, pp. 1977-1984, 2009.
- [39] W. Yuan, Y. Zhou, Y. Chen, X. Liu, J. Wang, "Toxicological effects of microplastics and heavy metals on the *Daphnia magna*," *Sci Total Environ*, vol. 746, no. 141254, 2020.
- [40] M. Schwarzer, J. Brehm, M. Vollmer, J. Jasinski, C. Xu, S. Zainuddin, T. Fröhlich, M. Schott, A. Greiner, T. Scheibel, C. Laforsch C, "Shape, size, and polymer dependent effects of microplastics on *Daphnia magna*," *J Hazard Mater Materials*, vol. 128136, 2021.
- [41] M. Renzi, E. Grazioli, A. Blašković A, "Effects of different microplastic types and surfactant-microplastic mixtures under fasting and feeding conditions: A case study on *Daphnia magna*," *Bull Environ Contam Toxicol*, vol. 103, pp. 367-373, 2019.
- [42] M. Zocchi, R. Sommaruga, "Microplastics modify the toxicity of glyphosate on *Daphnia magna*," *Sci Total Environ*, vol. 697, no. 134194, 2019.
- [43] H. Lee, S. J. Im, Y. Kim, G. Lee, A. Jang A, "Effects of microplastics on the removal of trace organic compounds during ozonation: Oxidation and adsorption of trace organic compounds and byproducts," *Environ Pollut*, vol. 280, no. 116878, 2021.
- [44] I. Schrank, B. Trotter, J. Dummert, B. M. Scholz-Böttcher, M. G. J. Löder, C. Laforsch C, "Effects of microplastic particles and leaching additive on the life history and morphology of *Daphnia magna*," *Environ Pollut*, vol. 5, no. Pt 2, 113233, 2019.
- [45] G. Jaikumar, N. D. Brun, M. G. Vijver, T. Bosker T, "Reproductive toxicity of primary and secondary microplastics to three cladocerans during chronic exposure," *Environ Pollut*, vol. 249, pp. 638-646, 2019.
- [46] L. Hanslik, C. Sommer, S. Huppertsberg, S. Dittmar, T. P. Knepper, T. Braunbeck T, "Microplastic-associated trophic transfer of benzo(k)fluoranthene in a limnic food web: Effects in two freshwater invertebrates (*Daphnia magna*, *Chironomus riparius*) and zebrafish (*Danio rerio*)," *Comp Biochem Physiol C Toxicol Pharmacol*, vol. 237, no. 108849, 2020.
- [47] L. Zimmermann, S. Göttlich, J. Oehlmann, M. Wagner, C. Völker, "What are the drivers of microplastic toxicity? Comparing the toxicity of plastic chemicals and particles to *Daphnia magna*," *Environ Pollut*, vol. 267, no. 115392, 2020.
- [48] M. Hiltunen, E. R. Vehniäinen, J. V. Kukkonen, "Interacting effects of simulated eutrophication, temperature increase, and microplastic exposure on *Daphnia*," *Environ Res*, vol. 192, no. 110304, 2021.

- [49] K. Kik, B. Bukowska, P. Sicińska, “Polystyrene nanoparticles: Sources, occurrence in the environment, distribution in tissues, accumulation and toxicity to various organisms,” *Environ Pollut*, vol. 262, no. 114297, 2020.
- [50] S. Karbalaei, P. Hanachi P, T. R. Walker, M. Cole, “Occurrence, sources, human health impacts and mitigation of microplastic pollution,” *Environ Sci Pollut Res*, vol. 25, pp. 36046–36063, 2018.
- [51] J. C. Prata, J. P. da Costa, I. Lopes, A. C. Duarte, T. Rocha-Santos, “Effects of microplastics on microalgae populations: A critical review,” *Sci Total Environ*, vol. 665, pp. 400-405, 2019.
- [52] O. Pikuda, E. Xu, D. Berk, “Toxicity assessments of micro- and nanoplastics can be confounded by preservatives in commercial formulations,” *Environ Sci Technol Lett*, vol. 6, pp. 21-25, 2019.
- [53] V. P. Vaz, D. J. Nogueira, D. S. Vicentini, W. G. Matias, “Can the sonication of polystyrene nanoparticles alter the acute toxicity and swimming behavior results for *Daphnia magna*?,” *Environ Sci Pollut Res*, vol. 28, no.11, pp. 14192-14198, 2021.
- [54] A.M. Booth, B. H. Hansen, M. Frenzel, H. Johnsen, D. Altin, “Uptake and toxicity of methylmethacrylate-based nanoplastic particles in aquatic organisms,” *Environ Toxicol Chem*, vol. 35, pp. 1641-1649, 2016.
- [55] M. Heinlaan, K. Kasemets, V. Aruoja, I. Blinova, O. Bondarenko, A. Lukjanova, A. Khosrovyan, I. Kurvet, M. Pullerits, M. Sihtmäe, G. Vasiliev, H. Vija, A. Kahru, “Hazard evaluation of polystyrene nanoplastic with nine bioassays did not show particle-specific acute toxicity,” *Sci Total Environ*, vol. 707, no. 136073, 2020.
- [56] Z. Gerdes, M. Hermann, M. Ogonowski, “A novel method for assessing microplastic effect in suspension through mixing test and reference materials,” *Sci Rep*, vol. 9, no. 10695, 2019.
- [57] J. T. Lin, H. W. Liu, K. T. Chen, D. C. Cheng, “Modeling the kinetics, curing depth, and efficacy of radical-mediated photopolymerization: The role of oxygen inhibition, viscosity, and dynamic light intensity,” *Front Chem*, vol. 7, no.760, 2019.
- [58] H. Brendelberger, “Filter mesh size of cladocerans predicts retention efficiency for bacteria,” *Limnol Oceanogr*, vol. 36, pp. 884-894, 1991.
- [59] C. W. Burns, “The relationship between body size of filter-feeding Cladocera and maximum size of particle ingested,” *Limnol Oceanogr*, vol. 13, pp. 675–678, 1968.
- [60] J. Gerritsen, K. G. Porter, J. R. Stricker, “Not by sieving alone: observations of suspension feeding in *Daphnia*,” *Bull Mar Sci*, vol. 43, pp. 366–376, 1988.
- [61] D. E. Sadler, F. S. Brunner, S. J. Plaistow, “Temperature and clone-dependent effects of microplastics on immunity and life history in *Daphnia magna*,” *Environ Pollut*, vol. 255(Pt 1), no. 113178, 2019.
- [62] D. An, J. Na, J. Song, J. Jung, “Size-dependent chronic toxicity of fragmented polyethylene microplastics to *Daphnia magna*,” *Chemosphere*, vol. 271, no.129591, pp. 1-7, 2021.
- [63] J. W. Jung, J. W. Park, S. Eo, J. Choi, Y. K. Song, Y. Cho, W. J. Shim, “Ecological risk assessment of microplastics in coastal, shelf, and deep sea waters with a consideration of environmentally relevant size and shape,” *Environ Pollut*, vol. 270, no. 116217, 2021.

- [64] C. Trestrail, M. Walpitagama, A. Miranda, D. Nugegoda, J. Shimeta, "Microplastics alter digestive enzyme activities in the marine bivalve, *Mytilus galloprovincialis*," *Sci Total Environ*, vol. 779, no. 146418, 2021.
- [65] K. Ruthsatz, M. Domscheit, K. Engelkes, M. Vences, "Microplastics ingestion induces plasticity in digestive morphology in larvae of *Xenopus laevis*," *Comp Biochem Physiol A Mol Integr Physiol*, vol. 269, no.111210, 2022.
- [66] R. Shen, K. Yang, X. Cheng, C. Guo, X. Xing, H. Sun, D. Liu, X. Liu, D. Wang, "Accumulation of polystyrene microplastics induces liver fibrosis by activating cGAS/STING pathway," *Environ Pollut*, vol. 300, no. 118986, 2022.
- [67] C. Akarsu, H. Kumbur, A. E. Kideys, "Removal of microplastics from wastewater through electrocoagulation-electroflotation and membrane filtration processes," *Water Sci Technol*, vol. 84, no.7, pp. 1648-1662, 2021.
- [68] T. Serra, A. Barcelona, N. Pous, V. Salvado, J. Colomer, "Synergistic effects of water temperature, microplastics and ammonium as second and third order stressors on *Daphnia magna*," *Environ Pollut*, vol. 267, no.115439, 2020.
- [69] E. Uurasjärvi, E. Sainio, O. Setälä, M. Lehtiniemi, A. Koistinen, "Validation of an imaging FTIR spectroscopic method for analyzing microplastics ingestion by Finnish lake fish (*Perca fluviatilis* and *Coregonus albula*)," *Environ Pollut*, vol. 288, no. 117780, 2021.
- [70] C. Schür, S. Zipp, T. Thalau, M. Wagner M, "Microplastics but not natural particles induce multigenerational effects in *Daphnia magna*," *Environ Pollut*, vol. 260, no. 113904, 2020.
- [71] A. Jemec, P. Horvat, U. Kunej, M. Bele, A. Kržan, "Uptake and effects of microplastic textile fibers on freshwater crustacean *Daphnia magna*," *Environ Pollut*, vol. 219, pp. 201-209, 2016.
- [72] A.J. Kokalj, N. B. Hartmann, D. Drobne, A. Potthoff, D. Kühnel D, "Quality of nanoplastics and microplastics ecotoxicity studies: Refining quality criteria for nanomaterial studies," *J Hazard Mater Materials*, vol. 415, no. 125751, 2021.
- [73] G. Persoone, R. Baudo, M. Cotman, C. Blaise, K. C. Thompson, M. Moreira-Santos, B. Vollat, A. Törökne, T. Han T, "Review on the acute *Daphnia magna* toxicity test – Evaluation of the sensitivity and the precision of assays performed with organisms from laboratory cultures or hatched from dormant eggs," *Knowl Manag Aquat Ecosyst*, vol. 393, no. 29, 2009.
- [74] F. D. Leusch, S. Ziajahromi, "Converting mg/L to Particles/L: Reconciling the occurrence and toxicity literature on microplastics," *Environ Sci Pollut Res*, vol. 55, pp. 11470-11472, 2021.
- [75] K. Lyu, C. Cao, D. Li, S. Akbar, Z. Yang, "The thermal regime modifies the response of aquatic keystone species *Daphnia* to microplastics: Evidence from population fitness, accumulation, histopathological analysis and candidate gene expression," *Sci Total Environ*, vol. 783, no.147154, 2021.
- [76] N. Hoffschroer, N. Grassl, A. Steinmetz, L. Sziegoleit, M. Koch, B. Zeis, "Microplastic burden in *Daphnia* is aggravated by elevated temperature," *Zoology*, vol. 144, no. 125881, 2021.

- [77] A.Motiei, M. Ogonowski, S. Reichelt, E. Gorokhova E, "Ecotoxicological assessment of suspended solids: The importance of biofilm and particle aggregation," *Environ Pollut*, vol. 280, no. 116888, 2021.
- [78] J. C. Achar, J. Na, H. Im, J. Jung, "Role of extracellular polymeric substances in leaching and bioconcentration of benzophenone-3 from microplastic fragments," *J Hazard Mater*, vol. 416, no. 125832, pp. 1-8, 2021.
- [79] F. Belzagui, V. Buscio, C. Gutiérrez-Bouzán, M. Vilaseca, "Cigarette butts as a microfiber source with a microplastic level of concern," *Sci Total Environ*, vol. 762, no. 144165, 2021.
- [80] C. Schür, C. Weil, M. Baum, J. Wallraff, M. Schreier, J. Oehlmann, M. Wagner, "Incubation in Wastewater Reduces the Multigenerational Effects of Microplastics in *Daphnia magna*," *Environ Sci Technol*, vol. 55, no. 4, pp. 2491-2499, 2021.
- [81] G. Kalčíková, T. Skalar, G. Marolt, A. Jemec Kokalj, "An environmental concentration of aged microplastics with adsorbed silver significantly affects aquatic organisms," *Water Res*, vol. 175, no. 115644, 2020.
- [82] G. Jaikumar, J. Baas, N. R. Brun, M. G. Vijver, T. Bosker, "Acute sensitivity of three Cladoceran species to different types of microplastics in combination with thermal stress" *Environ Pollut*, vol. 239, pp. 733-740, 2018.
- [83] Y. Lin, X. Huang, Q. Liu, Z. Lin, G. Jiang, "Thermal fragmentation enhanced identification and quantification of polystyrene micro/nanoplastics in complex media," *Talanta*, vol. 208, no.120478, 2020.
- [84] S. Xu, J. Maa, R. Ji, K. Pan, "Microplastics in aquatic environments: Occurrence, accumulation, and biological effects," *Sci Total Environ*, vol. 703, no. 134699, 2020.
- [85] Y. Ma, A. Huang, S. Cao, F. Sun, L. Wang, H. Guo, R. Ji, "Effects of nanoplastics and microplastics on toxicity, bioaccumulation, and environmental fate of phenanthrene in fresh water," *Environ Pollut*, vol. 219, pp.166-173, 2016.
- [86] J. Saavedra, S. Stoll, V. I. Slaveykova, "Influence of nanoplastic surface charge on eco-corona formation, aggregation and toxicity to freshwater zooplankton," *Environ Pollut*, vol. 252(Pt A), pp. 715-722, 2019.
- [87] N. J. van Eck, L. Waltman L, "Software survey: VOSviewer, a computer program for bibliometric mapping," *Scientometrics*, vol. 84, no.2, pp. 523-538, 2010.
- [88] M. C. Aria Cuccurullo, "Bibliometrix: An R-tool for comprehensive science mapping analysis," *J Informetr*, vol. 11, no.4, pp.959-975, 2017.
- [89] D Li, G Peng, L Zhu, "Progress and prospects of marine microplastic research in C



Düzce University Journal of Science & Technology

Research Article

Tomato Sorting System Based on Type Using Deep Learning

Eren Yiğit GÜLEM^a, Boran DURSUN^a, Hayrettin TOYLAN^{a,*}

^a Department of Mechatronics, Faculty of Technology, Kırklareli University, Kırklareli, TÜRKİYE

* Corresponding author's e-mail address: hayrettintoylan@klu.edu.tr

DOI: 10.29130/dubited.1569117

ABSTRACT

The tomato is a vegetable that is cultivated globally and plays a significant role in the culinary traditions of numerous countries. This vegetable needs to be separated after collection to meet the requirements of obtaining different flavors outside the growing season. This study focuses on the automatic separation of Rio tomatoes, which are preferred for tomato paste and sauces, from Fujimaru tomatoes using artificial intelligence and image processing techniques. Convolutional neural network (CNN), R-CNN, and Fast-CNN models were used to classify two different tomato types, and their performances were compared. According to the experimental results, it was observed that the CNN model achieved 94.1% accuracy, 93.5% precision, 94.7% recall, and 94.1% F1 score in the classification of Rio type tomatoes, and 92.4% accuracy, 91.8% precision, 93% recall, and 92.4% F1 score in the classification of Fujimaru type tomatoes. The hardware and software components used in this study are low cost, flexible, and modular. Experimental results show that the proposed model and system have high accuracy, precision, and efficiency rates.

Keywords: Deep learning, convolution neural network (CNN), tomato sorting

Derin Öğrenme Kullanarak Türüne Bağlı Domates Sınıflandırma Sistemi

ÖZ

Domates, dünya genelinde yetiştirilen ve ülkelerin yemek kültürlerinde önemli bir yer tutan sebzedir. Bu sebzenin yetiştirildiği mevsim dışında ve farklı lezzetler elde etme gereksinimlerini karşılamak için toplandıktan sonra ayrıştırılması gerekir. Bu çalışma, yapay zeka ve görüntü işleme tekniklerini kullanarak salçalık ve soslarda tercih edilen Rio cinsi domateslerin Fujimaru cinsi domateslerden otomatik olarak ayrılması üzerine odaklanmaktadır. İki farklı domates türünü ayırmak için konvolüsyon sinir ağı (CNN), R-CNN ve Fast-CNN modelleri kullanılmış ve performansları karşılaştırılmıştır. Deneysel sonuçlara göre, Rio cinsi domateslerin sınıflandırılmasında, CNN modelin %94.1 doğruluk, %93.5 hassasiyet, %94.7 geri çağırma ve %94.1 F1 skoru; Fujimaru cinsi domateslerin sınıflandırılmasında, %92.4 doğruluk, %91.8 hassasiyet, %93 geri çağırma ve %92.4 F1 skoru ile daha başarılı sonuçlar elde ettiği görülmüştür. Bu çalışmada kullanılan donanım ve yazılım bileşenleri düşük maliyetli, esnek ve modülerdir. Deneysel sonuçlar, önerilen modelin ve sistemin yüksek doğruluk, hassasiyet ve verimlilik oranlarına sahip olduğunu göstermektedir.

Anahtar Kelimeler: Derin öğrenme, evrişimli sinir ağı, domates ayırma

I. INTRODUCTION

Turkey is third in global tomato production, following China and India, with an output of approximately 13 million tonnes. The majority of tomato production (65.5%) was destined for the table tomato market, with the remainder (34.5%) allocated to tomato paste [1]. Traditionally, tomato sorting and grading are done manually, making the process time-consuming and susceptible to human error [2]. With the advancing technology, these systems can be controlled fully automatically using machine learning and artificial intelligence techniques.

The agriculture sector is undergoing a significant transformation with the integration of automation and artificial intelligence (AI) technologies. These developments are not only revolutionizing traditional farming practices but also paving the way for smart agriculture. This is essential to satisfy the increasing global demand for food. Automation and AI technologies offer significant advantages such as increasing farming productivity, ensuring quality control, reducing labor costs, and enabling precision farming [3]. Tomato grading is a critical step in production processes to improve quality control and efficiency [4]. AI-powered automated systems can significantly alleviate these issues by providing consistent and accurate grading results.

Wan et al. presented the backpropagation neural network (BPNN) method to determine the ripeness levels of Roma and Pear type tomatoes and categorized them as green, orange, or red according to their ripeness level. The accuracy rate obtained with this method was determined to be 99.31% [5]. Kaur et al. used a backpropagation neural network (BPNN) to rank and sort a total of 53 tomato images using camera setups developed by themselves. The proposed method achieved an accuracy rate of 92% [6].

The most widely used deep learning method for analysing image data is convolutional neural networks, known as CNN. Agarwal et al [7] used CNN models to identify tomato plant diseases and compared the performance of these models with traditional machine learning methods and obtained more successful results. Priyadharshini et al. applied CNN, R-CNN, Fast R-CNN and Faster R-CNN models to identify diseases in tomato leaves. In particular, it was stated that the model developed with Faster R-CNN performs better than the CNN, R-CNN, and Fast R-CNN models, with an accuracy rate of 98% [4]. The authors, Vini and Rathika (2024) proposed a fast and efficient CNN architecture is proposed for the classification of tomato leaf disease. The integration of stochastic gradient descent optimizers into the CNN network increased the success rate of the network. The proposed method achieved an accuracy rate of approximately 99.39% in disease classification [8]. Sun et al. focused on diagnosing tomato pests and diseases using Squeeze and SE Net (SSNet), a Convolutional Neural Network (CNN). In their research, they examined the effects of dataset balance and data volume on model performance. The results show that SSNet achieves accuracy rates of 98.80% and 98.39% for tomato pests and diseases, respectively [9]. In their study, Amune et al. (2024) focused on the post-harvest sorting procedure of tomatoes. In their research, they classified tomatoes according to size, color, and quality criteria. In quality classification, they preferred the CNN model due to its performance [10]. Research reveals that existing studies are more focused on the pre-harvest processes of tomatoes. However, there is limited research on the real-time post-harvest sorting of different tomato types. This study aims to address the problem of sorting tomato types, which is currently a labor-intensive process that requires a great deal of human observation.

The main objective of this study is to automatically separate different types of tomatoes using artificial intelligence and image processing techniques. Within the scope of this study, two types of tomatoes classified as table and tomato paste are separated by analyzing their visual characteristics through a Convolutional Neural Network (CNN)-based model. The developed low-cost prototype system has achieved successful results in separating tomatoes in real-time. In addition, the performance of the CNN model is compared with R-CNN and Fast-CNN models, and the results are presented.

The remaining part of this paper is organized as follows: Section 2 covers the experimental setup and the deep learning methods employed. Section 3 presents the dataset used in this study along with the details of the experimental results. Finally, Section 4 provides the conclusions.

II. MATERIALS AND METHODS

A. EXPERIMENTAL SETUP

The Tomato Sorting System (TSS) developed in this research consists of a camera, a conveyor belt, and an automatic sorting unit (Figure 1). A camera with a resolution of 1.3 megapixels ($H \times V = 1280 \times 1024$ pixels) and a frame rate of 25 frames per second (fps) was used to obtain detailed images of tomatoes. The automatic sorting unit consists of servo motors and a conveyor motor that directs the tomatoes into the appropriate bins according to their type.

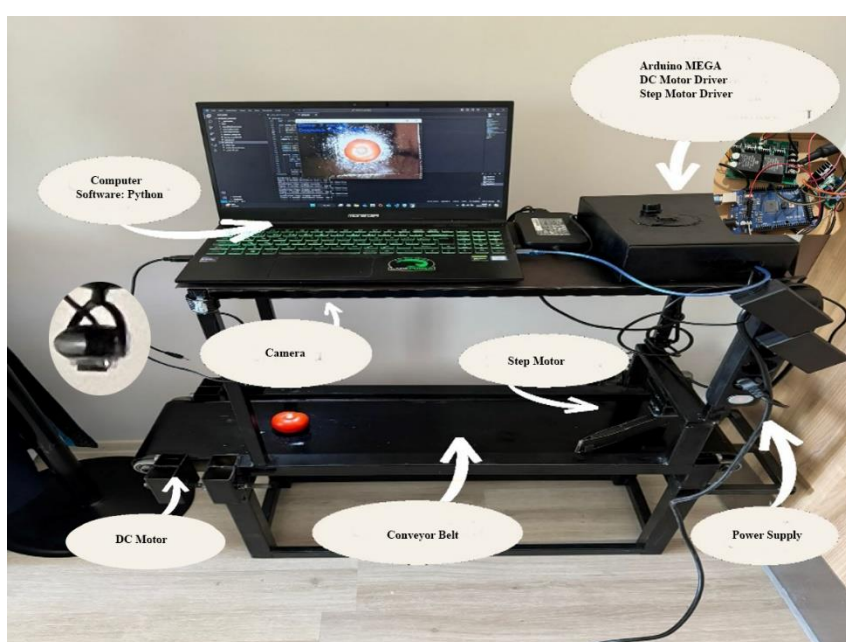


Figure 1. Tomato sorting system

TSS software components are developed using Python and its extensive libraries. Python is a flexible programming language widely preferred in machine learning and image processing [3]. TensorFlow and Keras libraries were used to create and train the CNN model. These libraries allow for the development of complex neural networks and effective model training. They are also very useful for processing large data sets and performing high-performance computations for deep learning tasks [11]. The Arduino IDE was preferred for programming the Arduino Mega microcontroller. This hardware enables cost-effective control of components. Table 1 presents the properties of the components used in the TSS.

Table 1. Electronic components of the proposed TSS

Unit	Parameters	Value
Brushed DC motor	Rated Voltage (V)	24
	Rated torque (Ncm)	14
	Rated speed (min)	3250
	Rated current (A)	2.84
	Ambient temperature	-30°C to +40°C
Arduino Board	Type	Mega 2560
	Microcontoller	Atmega 2560
	Operation Voltage	3.3-5 V
	Dijital Pins	54
	Analog Pins	16
Camera	Resolution	1280x1224
	Fps	25
	Color Space	RGB
	Image sensor	1.3 Megapixel 1/3" CMOS

B. DEEP LEARNING

Deep learning methods use artificial neural networks to mimic human thinking and learning processes. These methods can work effectively on text, audio, image, and video data and offer high accuracy rates in extracting their own features. However, these processes require large amounts of input and computers with high processing power. In this section, the deep learning methods used in this study for the classification of tomato types will be briefly reviewed.

B. 1. Convolutional Neural Network (CNN)

Traditonal image classification involves describing the entire image by either manually extracting features or using feature selection methods, followed by employing a classifier to identify the object category. The difference from traditional image processing in CNN models is that this model is an end-to-end learning process. The original image enters the network, the training and prediction processes are performed in the network, and the result is obtained [12]. Consequently, the extraction of features from the image is particularly important. CNN (Convolutional Neural Network) is one of the most widely used algorithms with the ability to process, classify, and segment images. CNNs are frequently preferred in tasks such as pattern recognition, classification, and segmentation, especially in large image data sets. The CNN model consists of multiple layers. While the first layers extract features from images, the last layers use these features for classification. The basic layers of the model are as follows:

The first layer is the convolution layer. This layer extracts important features by analysing the relationships between the pixels of the images. The pooling layer is used to eliminate unnecessary parameters when necessary. This layer ensures that important features are preserved while reducing the size of the input data. In the next stage, the feature map matrix is converted into vectors and then the Fully Connected (FC) layer comes into play. The vectorised features are fed into a neural network. The FC layer takes these vectorised features and integrates them to build a model. As a result, the softmax function is usually used in the final layer of a CNN and calculates the probabilities of 'n' different events [13].

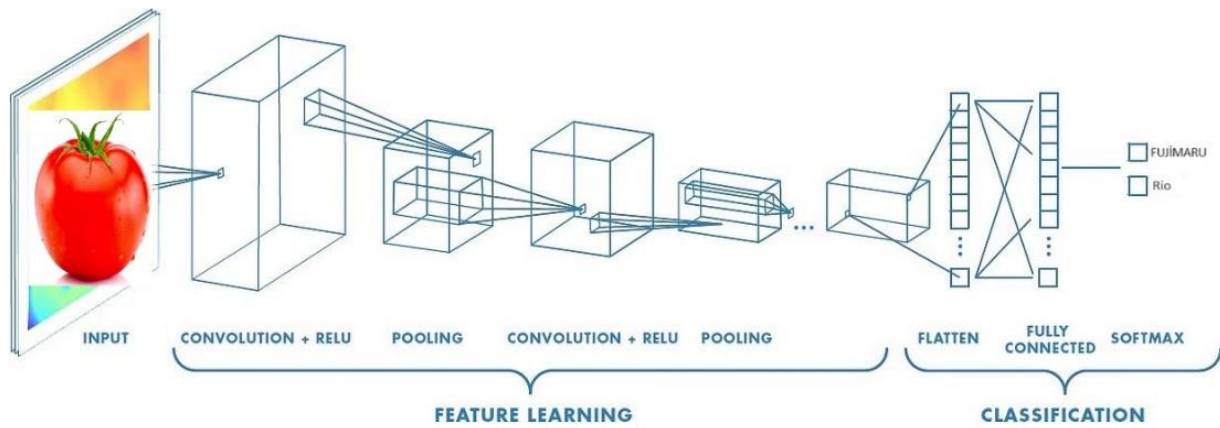


Figure 2. Convolutional Neural Network (CNN) structure used in the TSS

The CNN used for tomato sorting consists of an input layer, convolutional layers with ReLU activation, pooling layers, fully connected layers, and a softmax output layer (Figure 2). The parameters of the CNN, R-CNN and Faster R-CNN model applied in this study are presented in Table 2.

Table 2. CNN, R-CNN and Faster R-CNN model parameters

Parameters	CNN/R-CNN /Faster R-CNN
Number of convolution layer	4
Number max pooling layer	4
Activation function	Relu/Softmax
Learning rate	0.0001
Number of epoch	20
Batch size	32
Optimizer	SGD (Stochastic Gradient Descent)

The flowchart of the CNN model with four convolutional layers designed to separate tomatoes according to their types is presented in Figure 3.

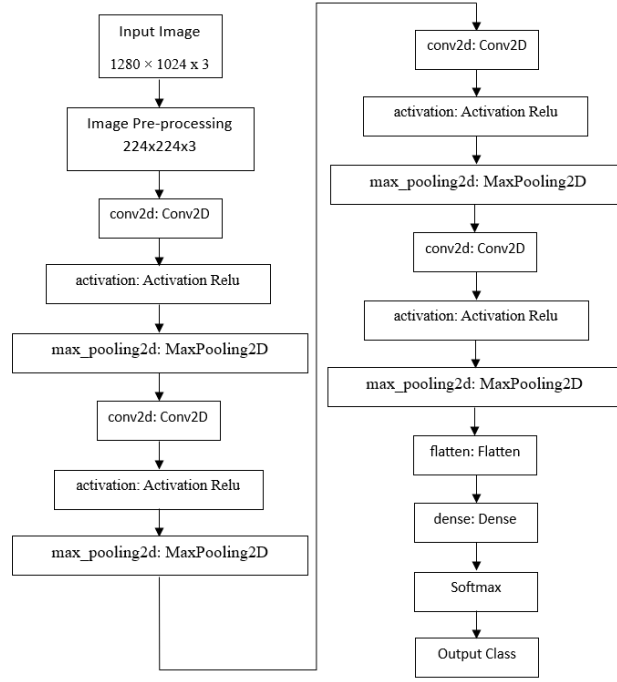


Figure 3. Flowchart of CNN model for the TSS

B. 2. Region-based Convolutional Neural Networks (R-CNN)

R-CNN extracts approximately 2,000 possible object regions to identify and classify the positions of objects in an image. In the first stage, a selective search algorithm is used to identify possible object regions. This algorithm generates many potential object regions on the image, which are then processed by a CNN (Convolutional Neural Network). Each object region is processed through a CNN model and converted into feature vectors. The resulting feature vectors are evaluated by a separate SVM (Support Vector Machine) classifier for each object region[14].

The most significant advantage of R-CNN is its high accuracy in object detection. However, the model has a high computational cost and long training times. Additionally, because the R-CNN model runs a CNN for each region separately, the processing time can be considerably longer, particularly when working with large images.

B. 3. Faster R-CNN

Faster R-CNN is an enhanced version of the R-CNN model and offers faster and more efficient performance in object detection tasks. Fast R-CNN inputs the entire image into the CNN instead of processing the 2000 region proposals generated by selective search one at a time. It determines region proposals from the feature map obtained from the image and resizes them to a fixed size using a RoI (Region of Interest) pooling layer. Finally, A softmax layer is used to evaluate the results from the model and produce probabilistic results[15].

C. PERFORMANCE EVALUATION METRICS

The performance of the compared models is presented based on the following evaluation metrics described by Sokolova and Lapalme [16].

Accuracy: The number of correctly classified positive examples is denoted "True Positive" (TP), while the number of correctly classified negative examples is denoted "True Negative" (TN). The accuracy of

a classification is calculated by dividing the number of correctly classified examples by the sum of the number of correctly and incorrectly classified (False Positive (FP), False Negative (FN)) examples. Accuracy is calculated using eq. (1).

$$Accuracy = \frac{TP+TN}{TP+TN+FP+FN} \quad (1)$$

F1 Score: This measurement considers both precision and recall simultaneously, representing a harmonic average of the two variables. F1 Score is calculated using eq. (2).

$$F1\ Score = 2 \times \frac{Precision \times Recall}{Precision + Recall} \quad (2)$$

Precision: It indicates the proportion of samples classified as positive that are genuinely positive. Precision is calculated using eq. (3).

$$Precision = \frac{TP}{TP+FP} \quad (3)$$

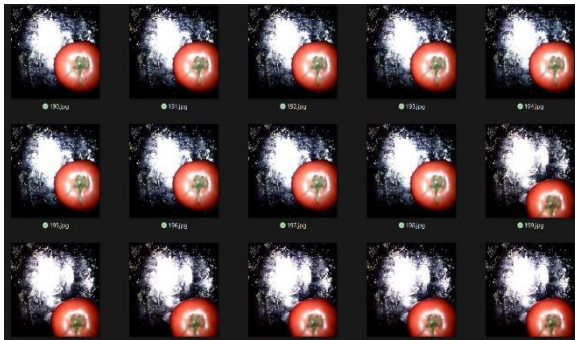
Recall: It indicates the proportion of samples classified as positive to the total positive in the data. Equality is given 4.

$$Recall = \frac{TP}{TP+FN} \quad (4)$$

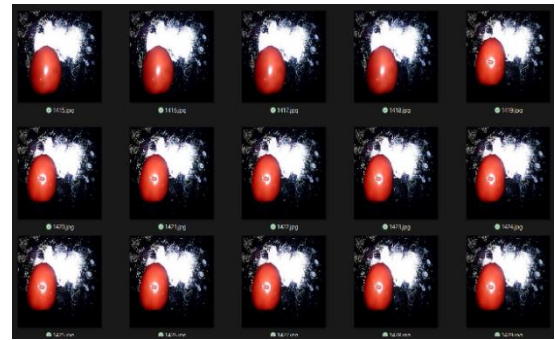
III. RESULTS AND DISCUSSION

A. DATASET

The dataset was created with images obtained from two different tomato types in a homogeneous background and constant lighting conditions. This dataset contains a total of 1,785 images of Fujimaru and Rio species taken from different angles. The collected image data was divided into 80% training, 10% validation, and 10% test data. The training process was carried out without using transfer learning techniques.



(a)



(b)

Figure 4. a)FUJIMARU tomato data, b)Rio tomato data.

The images captured by the camera are quite large and may contain unwanted noise. To improve computational efficiency and enhance performance, a three-stage image preprocessing approach was implemented. First, the images were resized to dimensions of 224x224x3. Next, the Red, Green, and Blue (R, G, B) color components were normalized to a range of [0, 1]. Finally, random noise in the images was reduced using the Gaussian blur technique.

B. PERFORMANCE OF CNN MODELS

The compared CNN models were trained and tested with the above mentioned dataset. Accuracy, F1 score, precision and recall were calculated using Equation (1), Equation (2), Equation (3) and Equation (4) respectively. The performance curve of the Fast R-CNN model is shown in Figure 5.

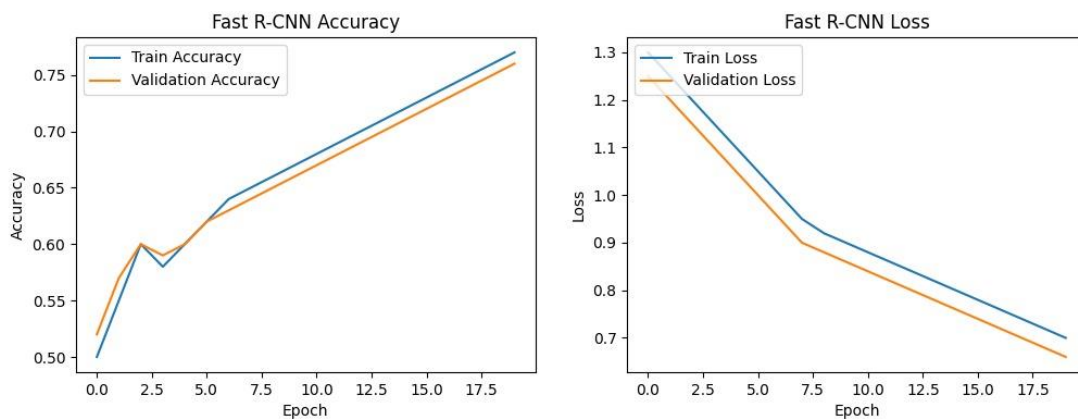


Figure 5. Fast R-CNN model performance curves

The training and validation success of the Fast R-CNN model demonstrate a continuous increase across both graphs. The training success is approximately 75%, which is very close to the validation success. Furthermore, the training and validation losses also decrease over time, reaching a value of approximately 0.7. This demonstrates that the overall performance of the model is satisfactory and that there is no overfitting in the validation process. The models were evaluated with 20 epochs, a batch size of 32, and a learning rate of 0.0001. The performance curve of the R-CNN model is shown in Figure 6.

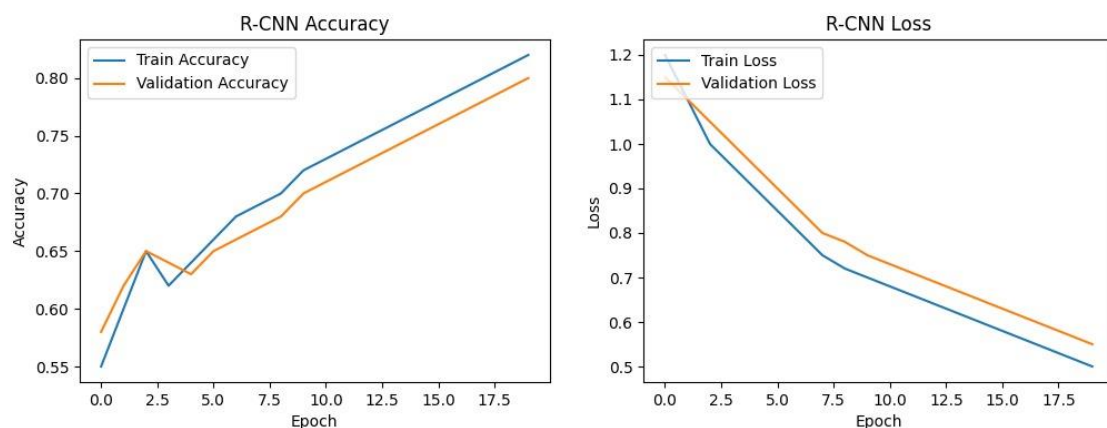


Figure 6. R-CNN model performance curves

While the R-CNN model shows a similar accuracy increase to Fast R-CNN, it shows a superior performance with accuracy rates reaching approximately 80%. The training and validation losses decreased to approximately 0.6. These findings show that the R-CNN model provides an effective performance with higher accuracy and lower loss. The models were evaluated with 20 epochs, 32 Batch Size and 0.0001 learning rate. The performance curve of the simple CNN model is shown in Figure 7.

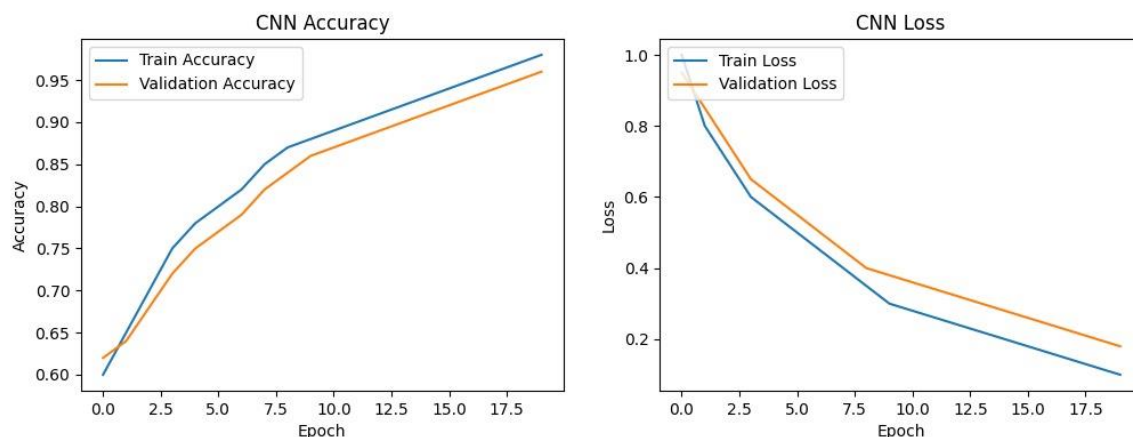


Figure 7. CNN model performance curves

The simple CNN model achieved the highest accuracy and lowest loss values compared to the other two models. While the training accuracy increased to approximately 95%, a similar increase was observed in the validation accuracy. Training and validation losses decreased continuously to approximately 0.2. These results show that the CNN model exhibits superior performance in both training and validation phases and that the model learns effectively. The models were evaluated with 20 epochs, 32 Batch Size and learning rate of 0.0001. Table 3 presents CNN, R-CNN and Fast R-CNN models performance

Table 3. CNN, R-CNN and Fast R-CNN models performance

Model	Dataset	Accuracy (%)	Precision	Recall	F1 Score
CNN	FUJIMARU Tomato	92.4	91.8	93.0	92.4
	Rio Tomato	94.1	93.5	94.7	94.1
R-CNN	FUJIMARU Tomato	76.3	80.2	82.5	81.3
	Rio Tomato	81.2	79.2	83.6	81.3
Fast R-CNN	FUJIMARU Tomato	75.3	78.6	85.6	81.9
	Rio Tomato	72.6	74.5	75.9	75.1

In this study, the recognition process is carried out on images taken with the help of a camera. Therefore, there is not more than one different pattern in the visual field. For this reason, it can be said that the simple CNN model gives a successful result compared to other models. While simple CNN networks are successful in identifying the class of the object, they are not sufficient to find its location. In this study, since there is no need to find the location at the same time, models that would cause additional computational costs were avoided. Simple CNN has a lower computational cost and runs faster than R-CNN and Faster R-CNN. This is an important advantage when working with large data sets.

IV. CONCLUSION

In this study, we developed a Tomato Sorting System (TSS) capable of classifying tomatoes by type using a deep learning approach. To identify the most effective deep learning algorithm for the TSS, we evaluated the performance of three models: Simple CNN, R-CNN, and Fast R-CNN. Our results showed that the Simple CNN model achieved the highest accuracy, with 92.4% for Fujimaru type tomatoes and 94.1% for Rio type tomatoes.

The most important advantages of the developed TSS system are the use of low-cost hardware and the ability to easily adapt to different agricultural crops. However, various improvements can be made to further increase the speed of this system, which can classify about 100 tomatoes per hour. Among these improvements, the use of industrial cameras and powerful processors stand out. In conclusion, this study demonstrates the potential of artificial intelligence and image processing techniques to improve agricultural applications and emphasizes the need for continuous research and development in this field.

ACKNOWLEDGEMENTS: This work is supported by TUBİTAK 2209 A

V. REFERENCES

- [1] S. Eğilmez, “Ürün raporu Domates 2022” (2025, 15 January). *Tarımsal Ekonomi ve Politika Geliştirme Enstitüsü*, Erişim: <https://arastirma.tarimorman.gov.tr/tepge/Belgeler/PDF%20%C3%9Cr%C3%BCn%20Raporlar%C4%B1/2022%20%C3%9Cr%C3%BCn%20Raporlar%C4%B1/Domates%20%C3%9Cr%C3%BCn%20Raporu%202022-364%20TEPGE.pdf>
- [2] P. Wan, A. Toudeshki, H. Tan, H., and R. Ehsani, “A methodology for fresh tomato maturity detection using computer vision,” *Computers and electronics in agriculture*, vol. 146, pp. 43-50, 2018.
- [3] S. Kaur, A. Girdhar, and J. Gill, “Computer vision-based tomato grading and sorting,” In *Advances in Data and Information Sciences: Proceedings of ICDIS-2017*, Singapore, 2018, pp. 75-84.
- [4] M. Agarwal, S. K. Gupta, and K. K. Biswas, “Development of Efficient CNN model for Tomato crop disease identification,” *Sustainable Computing: Informatics and Systems*, vol. 28, p.100407, 2020.
- [5] M. M. Mijwil, K. Aggarwal, R. Doshi, K. K. Hiran, and M. Gök, “The Distinction between R-CNN and Fast RCNN in Image Analysis: A Performance Comparison,” *Asian Journal of Applied Sciences*, vol. 10(5), pp. 429-437, 2022.
- [6] V. Shankar, V. Kumar, U. Devagade, V. Karanth, and K. Rohitaksha, “Heart disease prediction using CNN algorithm,” *SN Computer Science*, vol. 1(3), p. 170, 2020.
- [7] M. Maity, S. Banerjee, and S. S. Chaudhuri, “Faster r-cnn and yolo based vehicle detection: A survey,” In *2021 5th international conference on computing methodologies and communication (ICCMC)*, India, 2021, pp. 1442-1447.
- [8] S. L. Vini, and P. Rathika, “TrioConvTomatoNet: A robust CNN architecture for fast and accurate tomato leaf disease classification for real time application,” *Scientia Horticulturae*, vol. 330, p.113079, 2024.

- [9] L. Sun, K. Liang, Y. Wang, W. Zeng, X. Niu, and L. Jin, "Diagnosis of tomato pests and diseases based on lightweight CNN model," *Soft Computing*, vol. 28(4), pp. 3393-3413, 2024.
- [10] A. Amune, S. Shinde, A. Samargade, S. Suryawanshi, and Y. Shirsat, "Tomato TriSort: Smart Sorting System for Size, Color, and Pest Detection," In *2024 4th International Conference on Sustainable Expert Systems (ICSES)*, Nepal, 2024, pp. 539-545.
- [11] M. Sokolova, and G. Lapalme, "A systematic analysis of performance measures for classification tasks," *Information processing & management*, vol. 45(4), pp. 427-437, 2009.
- [12] L. Chen, S. Li, Q. Bai, J. Yang, S. Jiang, and Y. Miao, "Review of image classification algorithms based on convolutional neural networks," *Remote Sensing*, vol. 13(22), p.4712, 2021.
- [13] Y. Gao, W. Liu, and F. Lombardi, "Design and implementation of an approximate softmax layer for deep neural networks," In *2020 IEEE international symposium on circuits and systems (ISCAS)*, Spain, 2020, pp. 1-5.
- [14] G. Priyadharshini, and D. R. Judie Dolly, "Comparative Investigations on Tomato Leaf Disease Detection and Classification Using CNN, R-CNN, Fast R-CNN and Faster R-CNN," *2023 9th International Conference on Advanced Computing and Communication Systems (ICACCS)*, India, 2023, pp. 1540-1545.
- [15] M. Maity, S. Banerjee, and S. S. Chaudhuri, "Faster r-cnn and yolo based vehicle detection: A survey," In *2021 5th international conference on computing methodologies and communication (ICCMC)*, India, 2021, pp. 1442-1447.
- [16] S. Ren, K. He, R. Girshick, and J. Sun, "Faster R-CNN: Towards real-time object detection with region proposal networks," In *IEEE Transactions on Pattern Analysis and Machine Intelligence*, vol. 39, pp. 1137-1149, 2017.



Düzce University Journal of Science & Technology

Research Article

Innovative Hybrid CNN+SVM Model for Accurate Covid-19 Detection From CT Images

Hasan ULUTAŞ^a, Halil İbrahim COŞAR^{b,*}, Muhammet Emin ŞAHİN^a,
 Mustafa Fatih ERKOÇ^c, Esra YÜCE^a

^a Department of Computer Engineering, Yozgat Bozok University, Yozgat, TÜRKİYE

^b Department of Electrical and Electronics Engineering, Yozgat Bozok University, Yozgat, TÜRKİYE

^c Department of Radiology, Yozgat Bozok University, Yozgat, TÜRKİYE

* Corresponding author's e-mail address: halil.cosar@bozok.edu.tr

DOI: 10.29130/dubited.1586048

ABSTRACT

The advent of advanced deep learning techniques has revolutionized various fields, including healthcare, where accurate and efficient diagnostic tools are of paramount importance. In the context of the COVID-19 pandemic, the need for rapid and precise diagnosis is critical to managing and mitigating the spread of the virus. In this study, we propose a decision support system for the diagnosis of COVID-19 using CT images, employing deep learning algorithms. To evaluate the performance of our models, we create a unique dataset that is meticulously curated and tailored to the task at hand. This dataset consists of a large number of CT images categorized into COVID-19 positive and negative classes, allowing for a robust evaluation of our models' capabilities. Our approach involves the development of novel CNN models as well as the exploration of pre-trained architectures, such as ResNet50v2 and VGG16, in a comprehensive modelling study. Additionally, we introduce a hybrid model by combining CNN models with the SVM algorithm. Hyperparameter optimization is performed using the grid search method, and the modelling process utilizes an original dataset with two classes (COVID-19 and Normal). Performance evaluation involves dividing the dataset into training and test sets (85%-15% ratio) and employing 5-fold cross-validation. Proposed novel CNN models achieve an accuracy rate of 99.93% and 99.86%, while the hybrid CNN+SVM model achieves an accuracy rate of 100% and 99.77%, respectively. Successful application of these proposed deep learning models in healthcare demonstrates their potential to improve diagnostic accuracy and patient outcomes.

Keywords: CNN, deep learning, hybrid model, grid search, CT images

BT Görüntülerinden Hassas Covid-19 Tespiti için Yenilikçi Hibrit CNN+SVM Modeli

ÖZ

Gelişmiş derin öğrenme tekniklerinin ortaya çıkışı, doğru ve etkili teşhis araçlarının büyük önem taşıdığı sağlık hizmetleri de dahil olmak üzere çeşitli alanlarda devrim yaratmıştır. COVID-19 salgını bağlamında, hızlı ve kesin teşhis ihtiyacı, virüsün yayılmasını yönetmek ve azaltmak için kritik öneme sahiptir. Bu çalışmada, BT görüntülerini kullanarak COVID-19 tespiti için derin öğrenme algoritmaları kullanan bir karar destek sistemi öneriyoruz. Modellerimizin performansını değerlendirmek için, titizlikle düzenlenmiş ve eldeki göreve göre uyarlanmış benzersiz bir veri kümesi oluşturuyoruz. Bu veri kümesi, modellerimizin yeteneklerinin sağlam bir şekilde değerlendirilmesine olanak tanıyan COVID-19 pozitif ve negatif sınıflarına ayrılmış çok sayıda BT

görüntüsünden oluşmaktadır. Yaklaşımımız, kapsamlı bir modelleme çalışmasında ResNet50v2 ve VGG16 gibi önceden eğitilmiş mimarilerin keşfedilmesinin yanı sıra yeni CNN modellerinin geliştirilmesini de içermektedir. Ayrıca, CNN modellerini SVM algoritması ile birleştirerek hibrit bir model sunuyoruz. Hiperparametre optimizasyonu ızgara arama yöntemi kullanılarak gerçekleştirilir ve modelleme sürecinde iki sınıflı (COVID-19 ve Normal) orijinal bir veri kümesi kullanılır. Performans değerlendirmesi, veri kümesinin eğitim ve test kümelerine bölünmesini (%85-%15 oranı) ve 5 kat çapraz doğrulama kullanılmasını içerir. Önerilen yeni CNN modelleri %99,93 ve %99,86 doğruluk oranına ulaşırken, hibrit CNN+SVM modeli sırasıyla %100 ve %99,77 doğruluk oranına ulaşmaktadır. Önerilen bu derin öğrenme modellerinin sağlık hizmetlerinde başarılı bir şekilde uygulanması, teşhis doğruluğunu ve hasta sonuçlarını iyileştirme potansiyellerini göstermektedir.

Anahtar Kelimeler: CNN, derin öğrenme, hibrit model, ızgara arama, BT görüntüleri

I. INTRODUCTION

The coronavirus disease (COVID-19), which emerged in December 2019 in Wuhan, China, as pneumonia of unknown aetiology, spread rapidly in two months and was designated an international public health problem on January 30, 2020 [1]. As of December 7, 2022, the SARS-CoV-2 virus had infected more than 600 million people worldwide, resulting in the deaths of more than six million [2]. With its contagiousness and severe symptoms, the COVID-19 epidemic, one of the largest health crises of the 21st century, has caused millions of cases and deaths worldwide. In the pandemic that has been ongoing for more than two years, there have been both positive and negative developments, such as the availability of the COVID-19 vaccine and the advancement of vaccination efforts, as well as the advent and rapid spread of new SARS-CoV-2 variants. The real-time reverse transcription polymerase chain reaction (RT-PCR) test, which analyses the sample from the upper respiratory tract, is widely used for the diagnosis of COVID-19. Nonetheless, the sensitivities of RTPCR tests can vary considerably between "60% and 90%" and frequently produce false-negative results, particularly in initial positive cases [3], [4]. Although microbiological methods such as RT-PCR are commonly used in the diagnosis of COVID-19, medical imaging methods are crucial for supporting the diagnosis, assessing the severity of the disease, detecting potential complications, and monitoring the treatment response [5]. Computerised tomography (CT) and chest x-ray (chest x-ray) are examples of information-providing medical imaging techniques used to detect infected individuals [6]. The cost of data and the availability of devices at the relevant healthcare institution or laboratory are the primary factors in selecting these imaging techniques. Prior to the onset of clinical symptoms, COVID-19 can be detected on CT scans of patients, according to published research [7],[8]. Despite the fact that it has been demonstrated in the literature that CT scanning tests are more sensitive than conventional RT-PCR tests [9][10], numerous obstacles persist. These obstacles include the dearth of well-trained radiologists and the increased labour caused by the pandemic influx of patients [4]. In addition, because COVID-19 is a new disease, radiologists must obtain new interpretation skills and update their knowledge. In areas with limited access to educational resources, diagnosis becomes more challenging. Therefore, it is crucial to develop Artificial Intelligence (AI) systems that will aid in the diagnosis of COVID-19.

Automated analysis technologies based on artificial intelligence (AI) can provide valuable assistance to radiologists in the analysis of COVID-19 from CT scans. Deep learning signifies a major breakthrough in the realm of artificial intelligence [11], with Convolutional Neural Networks (CNN) being one of the most commonly utilized designs [12]. CNNs have gained prominence in the healthcare sector due to their powerful capabilities [13]. Many studies have been submitted to literature by using artificial intelligence methods on the medical systems [14]–[20]. By combining CNN approaches with radiological imaging, it becomes possible to achieve accurate detection and classification of COVID-19 [21]. Kuldeep et al. presented an automated approach to detect covid-19 patients using a convolutional neural network model [22]. The dataset consists of covid-19 and non-covid-19 pneumonia x-ray images. As a result of the study, the proposed model reached an average of 97.92% accuracy, 99.69% sensitivity and 98.48% specificity. Pedro et al. [23] proposed a

classification model called Wavelet Convolutional Neural Network (WCNN) based on wavelet transform, which aims to improve the differentiation of images of patients with Covid-19 from images of patients with other lung infections. The model proposes a new input layer called Wave layer added to the neural network. WCNN was applied to chest CT images from two internal and one external storage. The average accuracy obtained is 98.19%. Mahmud et al. [24] proposed a new approach to diagnose covid-19 from x-ray images using capsule neural networks. The data set consists of covid-19, pneumonia and normal classes. As a result of testing the model, they reached an accuracy rate of over 95%. Nadiyah et al. [25] proposed the Sparrow search algorithm (SSA) on pre-trained model and CT lung images to perform automatic and accurate Covid-19 classification using Convolutional Neural Network. SSA has been used to find the best configuration for the models and optimize different CNN and transfer learning hyperparameters to improve performance. Two data sets were used in the experiments. There are two classes in the first dataset and three in the second. they achieved the best accuracy results of 99.74% with MobileNetV3Large in the two-class dataset of the proposed framework and 98% with SeNet154 in the three-class dataset. Avinandan et al. [26] used CNN models in conjunction with ensemble methodology to detect Covid-19 from chest X-rays. The DenseNet-201 model was trained and then combined with the Random Forest classifier model. They used two separate data sets, one large and one small. The proposed approach achieved an accuracy rate of 94.55% with the large dataset and 98.13% with the small dataset. Sujithra et al. [27] designed a real-time interactive system for the diagnosis of Covid-19. Recommended system, UI, analytics, cloud, etc. The system consists of multiple components, including a preliminary evaluation of medical data, such as pulse oxygen rate and RT-PCR results, to identify potential COVID-19 cases. If a positive indication is detected, the system prompts the user to upload X-ray or CT images for further disease severity evaluation. These images are then transmitted to a custom-built artificial intelligence module. The proposed AI system can classify patients according to whether they have COVID-19, pneumonia, or other viral infections. For medical image analysis, the classification task employs CNN architectures including ResNet-50, ResNet-100, ResNet-101, VGG 16, and VGG 19. From the experiment, it was observed that VGG 19 with an accuracy of 97% for CT images and ResNet101 with an accuracy of 98% for X-ray images outperformed. Muhammed et al. [28] used three pre-trained alternative CNN architectures for COVID-19 diagnosis and the grid search method to improve network performance. They used two different datasets of X-ray and CT images for model training. Resnet achieved the highest classification accuracy, reaching 98.98% for X-ray images and 98.78% for CT images. Afamefuna et al. [29] proposed a two-stage transformative model for COVID-19 diagnosis. This model is implemented using transfer learning, which allows efficient use of pre-trained models to speed up the training of the proposed model. The experimental results of the study provided an accuracy in the range of 0.76–0.92 for CNN-based deep learning networks, and the proposed model with transfer learning provided a significantly higher accuracy of 97.35%. Abul et al. [30] applied learning approaches to classify x-ray images consisting of COVID-19, normal, lung opacity, and viral pneumonia classes. Local binary patterns (LBP) and pre-trained convolutional neural networks are used for feature extraction. Extracted features were classified by support vector machine (SVM), decision tree (DT), random forest (RF), and k-nearest neighbours (KNN) classifiers. As a result of the classification of features obtained by a set of CNN models from four-class x-ray images by the SVM classifier, the metric values for the best performing ensemble (CNN +SVM) are 97.41% accuracy, 94.9% precision, 94.81% recall, and F1 achieved a score of 94.86%. Aleka et al. [31] used a hybrid model to classify x-ray images as normal or COVID-19. SVM was used for classification using information from the learning model, CNN, to classify images according to a predefined class (Covid-19 or Normal). The findings of the study show a training accuracy of 99.8% and a test accuracy of 99.1%. Hareem et al. [32] used two ResNet architectures, ResNet18 and ResNet50, for feature extraction from the x-ray dataset consisting of COVID-19 and normal classes. A multi-core SVM classifier, including Quadratic, Linear, Gaussian, and Cubic, is used to classify the extracted features. The experimental results demonstrate that the proposed framework successfully identifies COVID-19 from x-ray images and achieves a remarkable 97.3% accuracy through the use of ResNet50. CNN structures incorporate a variety of design decisions, such as the selection of the loss function, which, when optimally optimised, can have a substantial effect on the network's performance [33], [34] and different network hyperparameters such as the number of convolution layers, number of filters, filter size, batch size, number of training periods, learning rate, and momentum. As a result, the

performance of a CNN in a particular task is heavily influenced by the values of its hyperparameters. This study centers around the optimization of CNN hyperparameters with the aim of achieving the highest possible diagnostic accuracy for COVID-19. The CNN hyperparameters will be optimised using a grid search method in order to increase the obtained accuracy. An overview of study is given in Figure 1. The following is a summary of this article's primary contributions:

- Within the scope of the study, an original dataset is created and presented to the literature. In particular, our study is important in this respect, among the limited number of studies in the literature.
- New CNN models are designed and presented for the classification process. In addition to the proposed models, pre-trained (ResNet50v2 and VGG16) models in the literature are also used in the study.
- Using a grid search method, CNN hyperparameters are optimized to reduce model losses and achieve the highest COVID-19 diagnostic precision.
- The optimized CNN architectures are also hybridized with the SVM algorithm to classify CT images of COVID-19. The extracted features of CNN architectures are categorized using the SVM classifier. This hybrid method speeds up classification without degrading the performance of CNN architectures.
- Cross-validation is used to obtain maximum precision by keeping the models away from the overfitting curve in the study.
- The accuracy values of the results obtained are 99.93% and 99.86% CNN models, 100% and 99.77% CNN+SVM models, and it is seen that the proposed models can classify the CT images of COVID-19 patients and make the diagnosis of COVID-19 with high accuracy.
- A comparison of our work is presented by presenting a comparison table with the studies carried out in the literature.

DETECTION AND CLASSIFICATION OF COVID-19 DISEASE

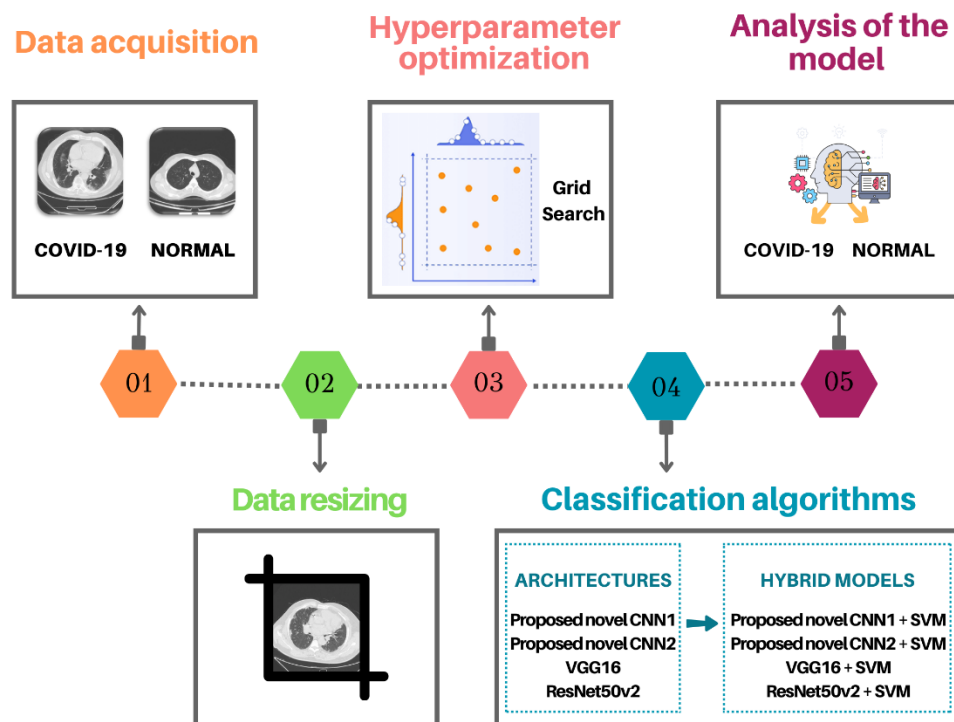


Figure 1. An overview of study

The paper is structured to provide a comprehensive overview of deep learning methods and their implementation, along with a summary of the employed algorithms. Section 2 offers a detailed background on the proposed CNN models. Additionally, this section covers essential aspects such as the dataset used, data preprocessing techniques applied, and the evaluation parameters utilized for assessing the performance of deep learning models. These evaluation parameters include accuracy, recall, precision, F1-scores, and ROC analysis. Moving forward, Section 3 presents the study's results, encompassing the outcomes of the deep learning models and the corresponding evaluation findings. It delves into the results obtained from cross-validation, emphasizing the contrasting performance between the proposed CNN and hybrid CNN+SVM models. Section 4 concludes the study by summarizing the findings and discussing their significance within the field. Lastly, Section 5 emphasizes the study's contributions, which encompass the development of novel CNN models and the creation of ensemble structures that offer swift training times and superior classification performance.

II. MATERIAL AND METHODS

A. DEEP LEARNING

Deep learning is a sophisticated subset of machine learning that leverages multiple layers of nonlinear computing to extract and transform intricate features from data. Unlike traditional machine learning models that rely on handcrafted feature engineering, deep learning algorithms autonomously learn hierarchical representations of data through an iterative process. Each successive layer in a deep learning architecture takes the output of the previous layer as input, allowing the model to progressively capture higher-level abstractions and gain a deeper understanding of complex patterns and relationships within the data [35].

A. 1. Convolutional Neural Networks (CNN)

Convolutional Neural Networks (CNNs) represent the most commonly used architecture in deep learning, particularly in the domain of image and video processing. CNNs consist of two main components and have gained widespread adoption due to their remarkable capabilities. In a CNN, the neurons in the initial layer are responsible for extracting features from the input data, while the subsequent layers combine these extracted features to form higher-level representations [36]. The success of CNNs can be attributed to their hierarchical feature extraction capability, enabling them to effectively capture intricate patterns and structures in the data at various levels of abstraction.

A. 2. Proposed CNN Models

In this study, Figures 2 and 3 depict, respectively, the CNN models utilised to address the research objectives. These figures depict the architectural designs of the proposed CNN models for this research. The visual representations aid in comprehending the structural components and information flow of CNN models. Architecture details of these models is provided in Table 1. During the design phase, notable differences are introduced between the two models. Specifically, in CNN1, a batch normalization layer is added to enhance the model's performance. The inclusion of this layer plays a crucial role in normalizing the distribution of activations across different layers in the neural network. The batch normalization layer offers several advantages for model training. By normalizing the activations, it helps to mitigate the issue of internal covariate shift, which refers to the change in the distribution of layer inputs during training. This stabilization facilitates more efficient and consistent model optimization. Moreover, the batch normalization layer can accelerate the training process by reducing the dependence on careful weight initialization or learning rate tuning. By enabling faster convergence, it aids in achieving better results overall. The addition of a batch normalization layer to CNN1 signifies our deliberate effort to improve the model's performance and address potential challenges during the training process. This enhancement aligns with best practices in deep learning

model design and contributes to the robustness and effectiveness of the proposed CNN models in the context of COVID-19 diagnosis using CT images.

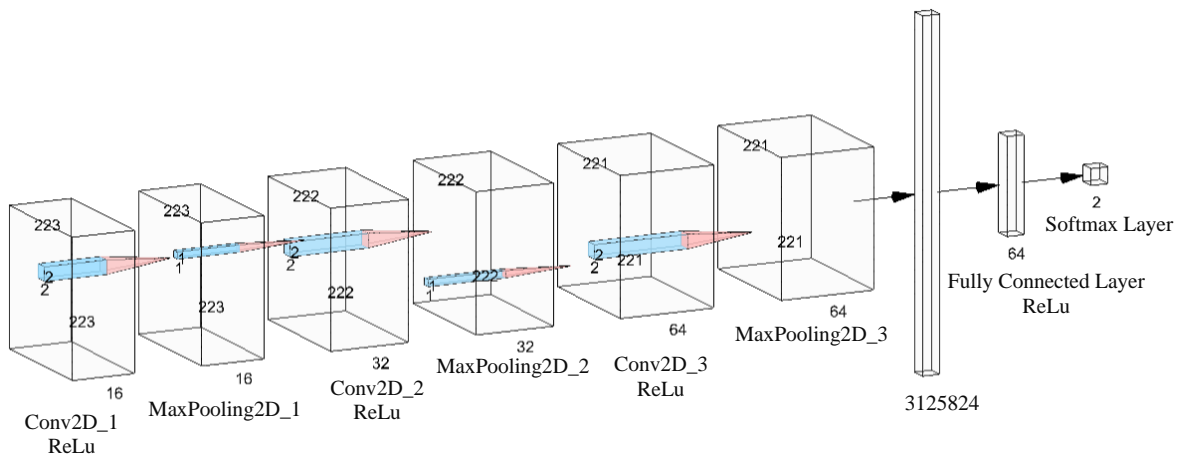


Figure 2. CNN1 network model structure

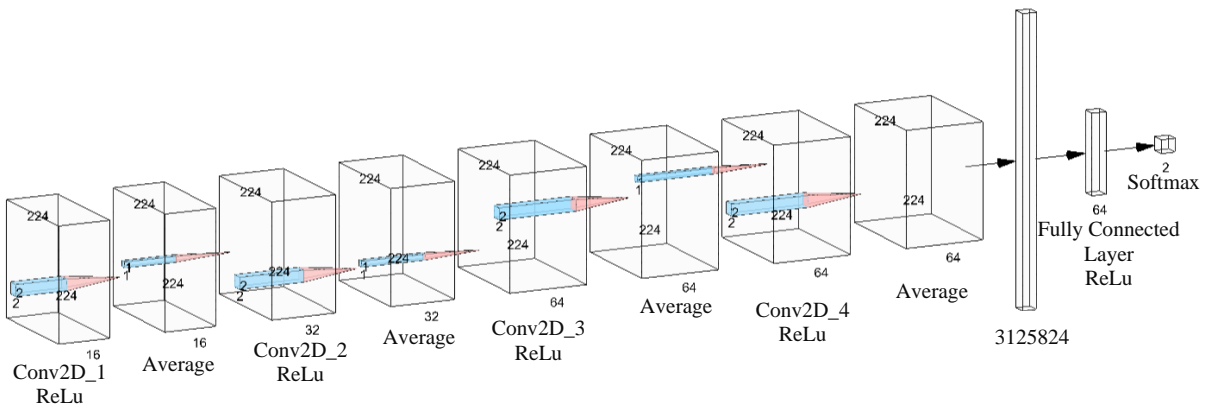


Figure 3. CNN2 network model structure

Table 1. Architecture details of CNNs

CNN1			CNN2		
Layer (type)	Output Shape	Parameter	Layer (type)	Output Shape	Parameter
Conv2D	223 x 223 x 16	208	Rescaling	224 x 224 x 3	0
batch_normalization	223 x 223 x 16	64	Conv2D	224 x 224 x 16	208
MaxPooling2D	223 x 223 x 16	0	AveragePooling2D	224 x 224 x 16	0
Conv2D	222 x 222 x 32	2080	Conv2D	224 x 224 x 32	2080
batch_normalization	222 x 222 x 32	128	AveragePooling2D	224 x 224 x 32	0
MaxPooling2D	222 x 222 x 32	0	Dropout	224 x 224 x 32	0
Conv2D	221 x 221 x 64	8256	Conv2D	224 x 224 x 64	8256
batch_normalization	221 x 221 x 64	256	AveragePooling2D	224 x 224 x 64	0
MaxPooling2D	221 x 221 x 64	0	Conv2D	224 x 224 x 64	16448
Flatten	3125824	0	AveragePooling2D	224 x 224 x 64	0
Dropout	3125824	0	Dropout	224 x 224 x 64	0
Dense	64	200052800	Flatten	3211264	0
batch_normalization	64	256	Dense	64	205520960
Dropout	64	0	Dense	2	130
Dense	2	130			
Total Params: 200,064,178			Total Params: 205,548,082		
Trainable Params: 200,063,826			Trainable Params: 205,548,082		
Non-trainable Params: 352			Non-trainable Params: 0		

B. DATASET

Various datasets have been developed by data scientists and machine learning practitioners for the purpose of diagnosing COVID-19 disease. In this study, a unique data set was created using CT images obtained retrospectively from the data of COVID-19 patients taken from Yozgat Bozok University Faculty of Medicine. It's worth noting that the dataset used in this study was ethically approved, ensuring adherence to ethical guidelines and regulations regarding patient data privacy and usage. To ensure the integrity and reliability of the dataset, all image labeling was performed by a radiologist who was blinded to the clinical condition of the patients. By conducting the labeling process in this manner, it guarantees that the dataset is labeled in an objective and unbiased manner. This approach minimizes any potential bias or subjective interpretations that could influence the accuracy and generalizability of the machine learning models developed using the dataset. The use of an ethically approved dataset and the involvement of an expert radiologist in the labeling process enhance the quality and credibility of the dataset, making it a valuable resource for training and evaluating machine learning models for COVID-19 diagnosis. The objective and unbiased nature of the dataset labeling provides a solid foundation for developing reliable and accurate diagnostic models in the context of COVID-19 detection and classification. Cases and image number of the dataset are given in Table 2 and an example of dataset is shown in Figure 4.

Table 2. Cases and image number of the dataset

No	Case Name	Total Cases	Used Images
1	COVID-19	104	3000
2	NORMAL	115	3000

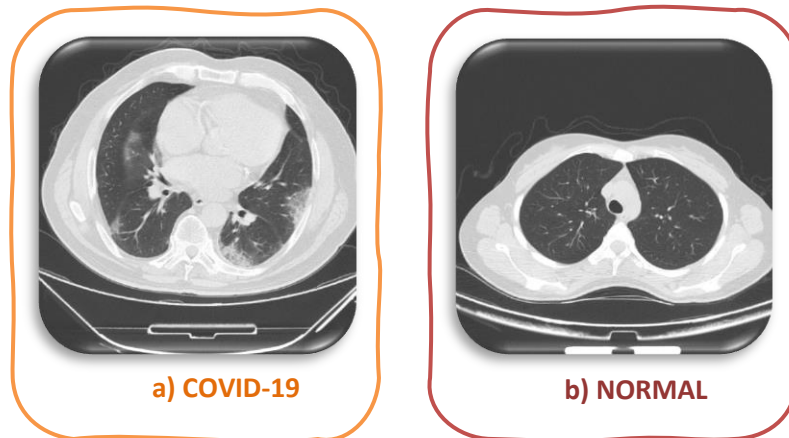


Figure 4. Examples of dataset

C. DATA PRE-PROCESSING

Image pre-processing plays a crucial role in deep learning as it involves preparing the input images for effective analysis by the model. This step encompasses a range of techniques, including but not limited to resizing, normalization, data augmentation, and more. The primary objective of image pre-processing is to enhance the quality of the input data and facilitate improved learning by the model. By applying appropriate pre-processing techniques, the input images are optimized to reduce noise, standardize features, and enhance relevant details, thereby enabling the model to learn more effectively from the data. At this stage, the raw data obtained from the hospital underwent pre-processing steps to prepare it for model training. The data, initially acquired in the 'DICOM' format, were visualized and inspected using the Weasis (DICOM viewer) program, an open-source and versatile medical imaging software. Weasis facilitated the display, analysis, and processing of various medical images, such as MR, CT, PET, mammography, among others.

To facilitate further processing and compatibility with machine learning algorithms, the data was converted from the 'DICOM' format to the more commonly used 'png' format. This conversion ensured that the data could be easily accessed and manipulated for subsequent analysis. Additionally, during the conversion process, the data was resized to a standardized dimension of 224 x 224 pixels, maintaining the aspect ratio and preserving the essential details present in the images. Subsequently, the data was divided into training and testing sets using an 85%-15% split. The training set comprised 85% of the data, while the remaining 15% was set aside as the test set for evaluating the performance of the trained model. By following these preprocessing steps, including image format conversion, resizing, and appropriate dataset splitting, the data was prepared and organized for subsequent model training and evaluation. This systematic approach ensured the availability of a well-prepared dataset and facilitated reliable and comprehensive analysis for the development of accurate COVID-19 detection models.

D. HYPERPARAMETER OPTIMIZATION

In classification problems, hyperparameters play a crucial role in determining optimal decision boundaries that effectively divide classes. In machine learning or deep learning algorithms, hyperparameters are tunable settings or configurations that influence the learning process and the efficacy of the resulting model. These parameters are set by the user prior to training the model and are not learned from the data. The selection of appropriate hyperparameters is crucial for attaining the utmost levels of precision and generalisation in classification tasks. Machine learning algorithms rely on an iterative process to determine the best hyperparameter values that yield the most accurate and reliable models. This process, known as hyperparameter tuning or optimization, involves

systematically searching through different combinations of hyperparameters to find the optimal configuration. Various techniques, such as grid search, random search, and Bayesian optimization [17], [37], are commonly employed to explore the hyperparameter space and identify the settings that maximize the model's performance. When it comes to hyperparameter optimization, factors such as the magnitude and characteristics of the data play a significant role in determining the appropriate method to use. Among the popular optimization techniques, grid search stands out as one of the most commonly employed approaches. In grid search, a grid of hyperparameters is created, and the learning model is trained and evaluated on each combination within the grid.

E. CROSS-VALIDATION

Cross-validation methods are widely employed in machine learning to assess and validate the performance of models. The k-fold cross-validation is a frequently used technique that involves dividing the dataset into k subsets or folds of roughly equal size. The model is trained on k-1 folds and validated on the remaining fold. Each fold serves as the validation set only once. This process is repeated k times, each time using a different fold for validation. In this work, k is chosen as 5, which means the dataset is divided into five subsets. The model is trained and validated five times, each time leaving out a different subset for validation. The performance metrics obtained from each fold are averaged to provide an estimate of the model's overall performance, ensuring a robust evaluation of the model's ability to generalize to unseen data [38]. K-fold cross-validation helps to mitigate issues related to overfitting and provides a more robust evaluation of the model's

F. EVALUATION METRICS

Metrics for evaluation are used to assess the effectiveness and quality of machine learning algorithms. Effective evaluation metrics are essential for comprehending the performance of a trained deep learning model on test data, i.e., new, invisible data. The literature provides a variety of evaluation criteria for testing models. Using multiple assessment metrics to evaluate the performance of a trained deep learning model is advantageous in numerous ways, as a model may perform well with one benchmark metric but poorly with another.

Classification estimates must have one of the following four base units, and they are as follows

True Positive (TP): When the model correctly predicts the positive class.

False Positive (FP): When the model incorrectly predicts the positive class.

True Negative (TN): When the model correctly predicts the negative class.

False Negative (FN): When the model incorrectly predicts the negative class.

The evaluation metrics, denoted by Equations (1)-(4), provide quantitative measures to assess the model's performance [17]:

$$Accuracy = \frac{TN + TP}{TN + TP + FN + FP} \quad (1)$$

$$Recall = \frac{TP}{TP + FN} \quad (2)$$

$$Precision = \frac{TP}{TP + FP} \quad (3)$$

$$F1 - Score = 2x \frac{Precision \times Recall}{Precision + Recall} \quad (4)$$

III. EXPERIMENTAL RESULTS

In this section, to classify the COVID-19 original dataset in this study, two approaches are adopted. Firstly, novel CNN models and pre-trained models are proposed and utilized. These models are specifically designed to handle the task of COVID-19 classification. Secondly, a hybrid deep learning method is employed, which involved combining the proposed CNN models with the SVM algorithm. This hybrid approach aimed to enhance the classification performance by leveraging the strengths of both CNN and SVM. In various studies, datasets are obtained from public sources such as Kaggle or GitHub repositories, while in others, hospitals and universities provide private datasets. In this study, a hybrid deep learning approach is used to classify the COVID-19 dataset, which has been meticulously annotated by a clinical expert. Figure 5 displays the total number of images used in the study.



Figure 5. Number of used images

A. CLASSIFICATION WITH CNN MODELS

Results of proposed CNN models and pretrained models are analysed in this section. The hardware information utilized in the study is provided in Table 3. This table offers valuable insights into the computational resources employed during the experimentation process, shedding light on the hardware specifications used for training and evaluation. Size of the used models are 224x224x3. This information provides details on the architecture and structure of the CNN models, such as the number of layers and the size of each layer. Understanding the dimensions of these models aids in comprehending their complexity and the level of abstraction they can achieve.

Table 3. Configuration of the hardware

Name	Parameter
Memory	64 GB
Processor	Intel(R) Xeon(R) Silver 4114 CPU @ 2.20GHz 2.19 GHz (2 processor)
Server model	Hp z6 g4
Graphics	NVIDIA GeForce RTX 3090 Ti
OS	Windows 10 Pro for Workstations
Language	Python 3
Framework	Jupyter Notebook

Table 4 displays the hyperparameter values employed in the study. Hyperparameters play a crucial role in shaping the behavior and performance of deep learning models. The table provides specific values for hyperparameters used in the proposed CNN models, enabling reproducibility and facilitating further experimentation.

Table 4. Hyperparameters of models

Model	Learning rate	Kernel size	Activation	Pool size	Pool type	Epoch	Optimizer	Batch size
CNN1	0.0001	2 x 2	ReLu	1 x 1	maxPooling	14	Adagrad	8
CNN2	0.001	2 x 2	ReLu	1 x 1	averagePooling	15	Adam	6
ResNet50v2	0.0001	3 x 3	ReLu	3 x 3	maxPooling	10	Adam	6
VGG16	0.0001	3 x 3	ReLu	3 x 3	maxPooling	9	Adam	8

Moving on to Table 5, it presents a comprehensive analysis of the CNN models used, showcasing various performance metrics such as training, validation, and test accuracy, precision, recall, and F1-score. Additionally, the table includes information on the number of parameters, training time, and the number of epochs utilized. This detailed summary allows researchers to evaluate the performance and efficiency of the CNN models under investigation.

Table 5. Training, validation and test accuracy, precision, recall, and F1-score along with the number of parameters, training time, and epochs required to train deep learning architectures of CNN models

Models	Parameters	Storage	Epochs for Training	Training Time (min)	Training Accuracy	Validation Accuracy	Testing Accuracy	Precision	Recall	F1-score
ResNet50 v2	26,776,162	306 MB	10	18	99.94	99.19	99.17	99.2	99.2	99.2
VGG16	15,517,602	177 MB	9	6	100	99.05	99.26	99	99	99
CNN1	200,064,178	1.49 GB	14	23	99.27	99.84	99.93	100	100	100
CNN2	205,548,082	2.29 GB	15	29	99.67	99.96	99.86	100	100	100

Table 6. Classification reports and confusion matrix of models

		Actual		CNN1				
		Covid-19	Normal		precision	recall	f1-score	support
	Covid-19	446	1	Covid-19	1.00	1.00	1.00	447
	Normal	0	452	Normal	1.00	1.00	1.00	453
		Covid-19	Normal	Accuracy			1.00	900
				Macro avg	1.00	1.00	1.00	900
				Weighted avg	1.00	1.00	1.00	900

CNN2

Actual	Covid-19	446	1
	Normal	1	453
		Covid-19	Normal
		Predicted	

	precision	recall		support
Covid-19	1.00	0.99	1.00	447
Normal	1.00	1.00	1.00	453
Accuracy			1.00	900
Macro avg	1.00	1.00	1.00	900
Weighted avg	1.00	1.00	1.00	900

VGG16

Actual	Covid-19	442	5
	Normal	3	450
		Covid-19	Normal
		Predicted	

	precision	recall	f1-score	support
Covid-19	0.99	0.98	0.99	447
Normal	0.98	0.99	0.99	453
Accuracy			0.99	900
Macro avg	0.99	0.99	0.99	900
Weighted avg	0.99	0.99	0.99	900

ResNet50v2

Actual	Covid-19	442	5
	Normal	3	450
		Covid-19	Normal
		Predicted	

	precision	recall	f1-score	support
Covid-19	0.99	0.98	0.99	447
Normal	0.98	0.99	0.99	453
Accuracy			0.99	900
Macro avg	0.99	0.99	0.99	900
Weighted avg	0.99	0.99	0.99	900

A confusion matrix is a widely used tabular representation that provides valuable insights into the performance of classification models when evaluated against a set of known-true test data. It presents the results in a structured format, enabling a comprehensive analysis of the model's predictive capabilities. The classification reports and confusion matrices for each CNN model are generated using 5-fold cross-validation and the mean values of these reports are presented in Table 6. By studying the confusion matrices, researchers can gain insights into various performance metrics such as accuracy, precision, recall, and F1-score for each class. These metrics provide a comprehensive evaluation of the model's ability to correctly classify instances from different classes. Additionally, the classification reports offer a concise summary of these performance metrics, making it easier to assess the strengths and weaknesses of the CNN models under investigation.

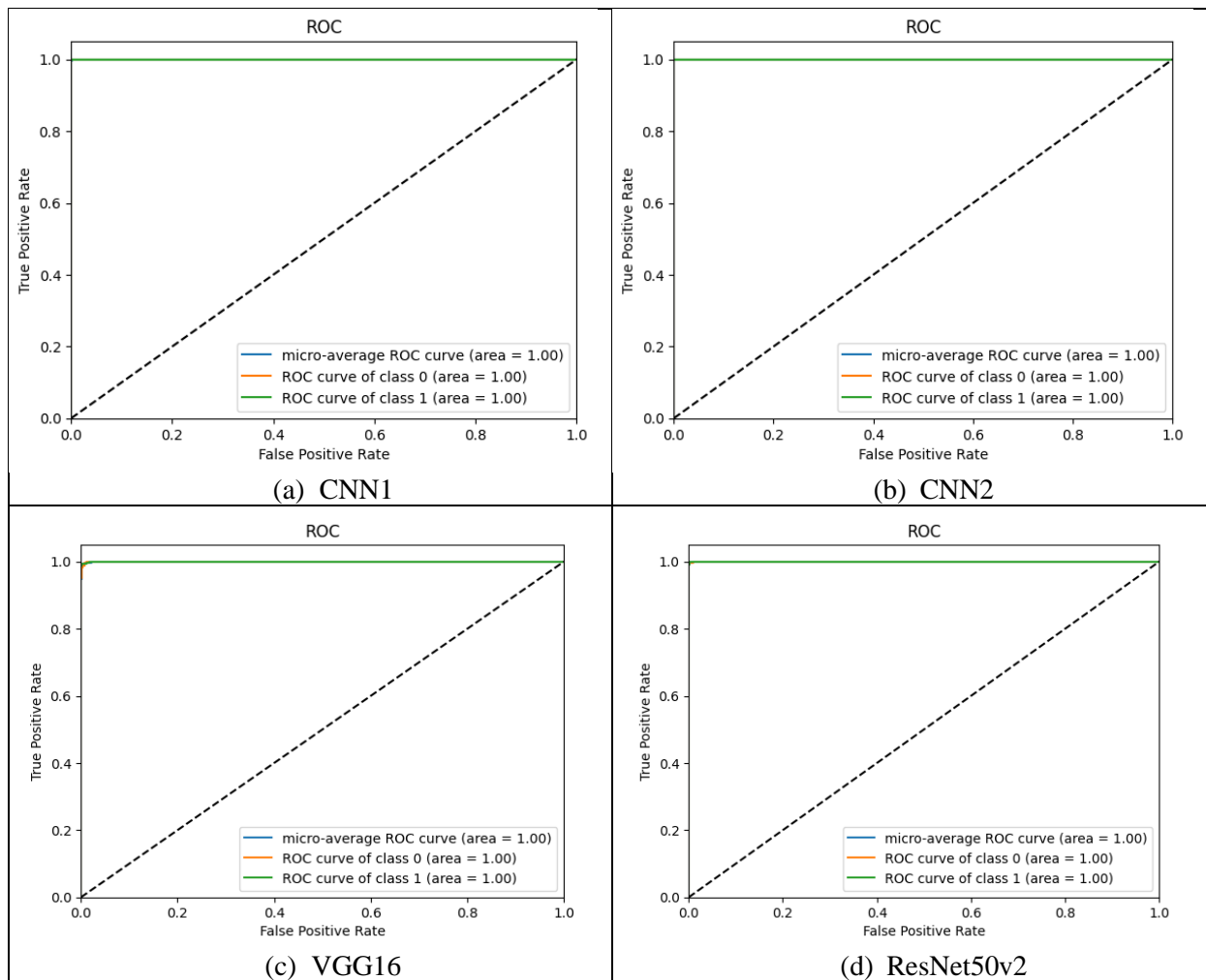
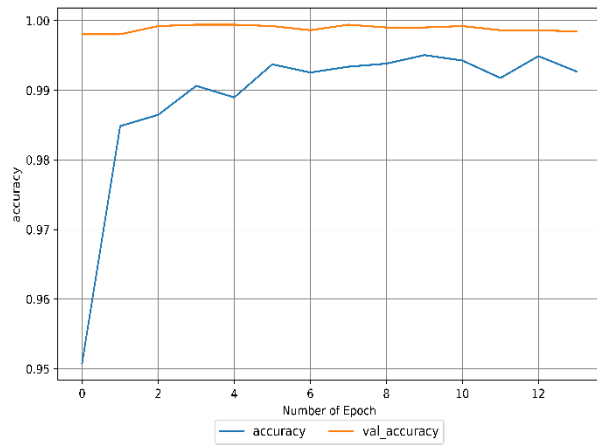


Figure 6. ROC curves of CNN1 with 5 fold cross validation

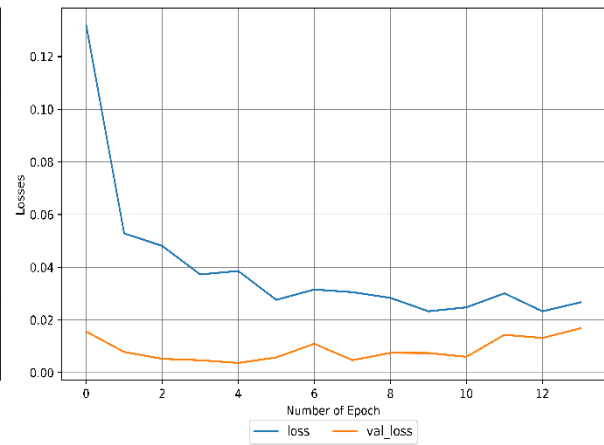
Figure 6 showcases the Receiver Operating Characteristic (ROC) curves for each CNN model utilized in the study. ROC curves provide a visual representation of the performance of classification models across different discrimination thresholds. By analyzing the ROC curves, researchers can gain insights into the models' ability to accurately distinguish between positive and negative instances. The curves depict the trade-off between the true positive rate (sensitivity) and the false positive rate (1-specificity) at various classification thresholds. A well-performing model is characterized by a curve that closely hugs the top left corner of the graph, indicating high sensitivity and low false positive rate.

Figure 7 presents the accuracy and loss graphs of the proposed CNN models, specifically designed for $k = 5$ cross validation method. These graphs offer a visual representation of the models' performance and shed light on important aspects of their training process. Upon examining the accuracy graph, it becomes evident that the proposed CNN models exhibit consistent and desirable accuracy rates throughout the training phase. This implies that the models effectively learn the underlying patterns and features of the training data. Notably, the absence of overfitting is observed, which indicates that the models do not excessively memorize the training data, thus enabling them to generalize well to unseen instances. Additionally, the absence of underfitting suggests that the models are capable of capturing and leveraging the key characteristics of the data, rather than oversimplifying the problem. The loss graph, on the other hand, provides insights into the models' optimization process. The loss values decrease steadily, indicating that the models are successfully minimizing the discrepancy between their predicted outputs and the actual labels. The smooth and continuous decline in the loss signifies that the models are steadily improving their performance and converging towards an optimal

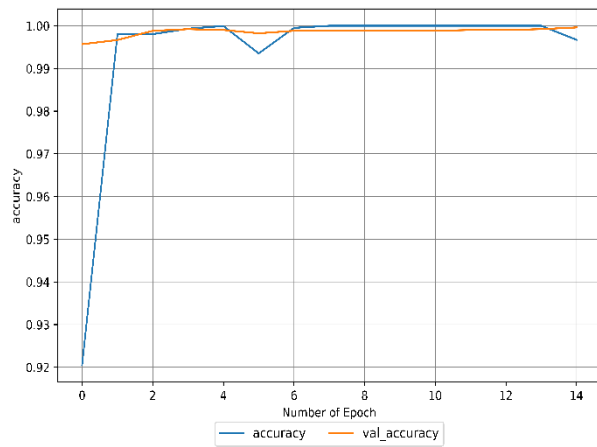
state. A novel approach is proposed for developing new CNN models and utilizing pre-trained models, which involves two main components.



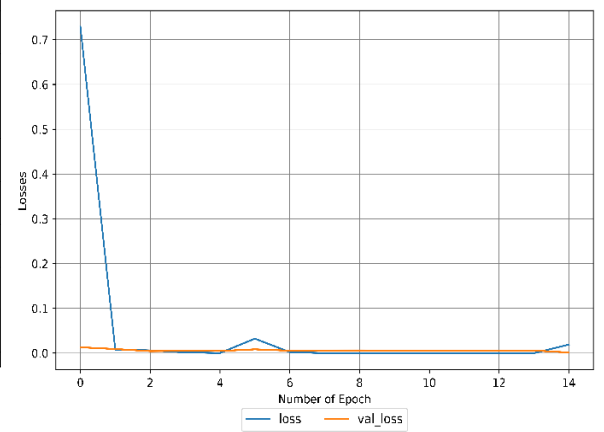
(a)



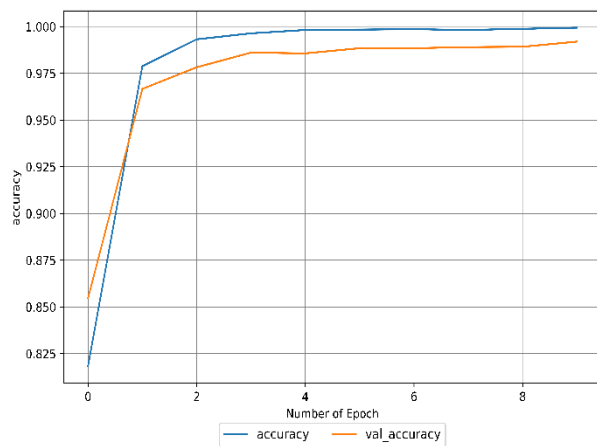
(b)



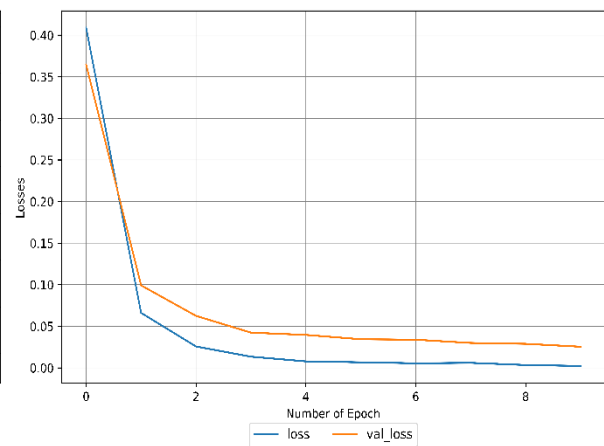
(c)



(d)



(e)



(f)

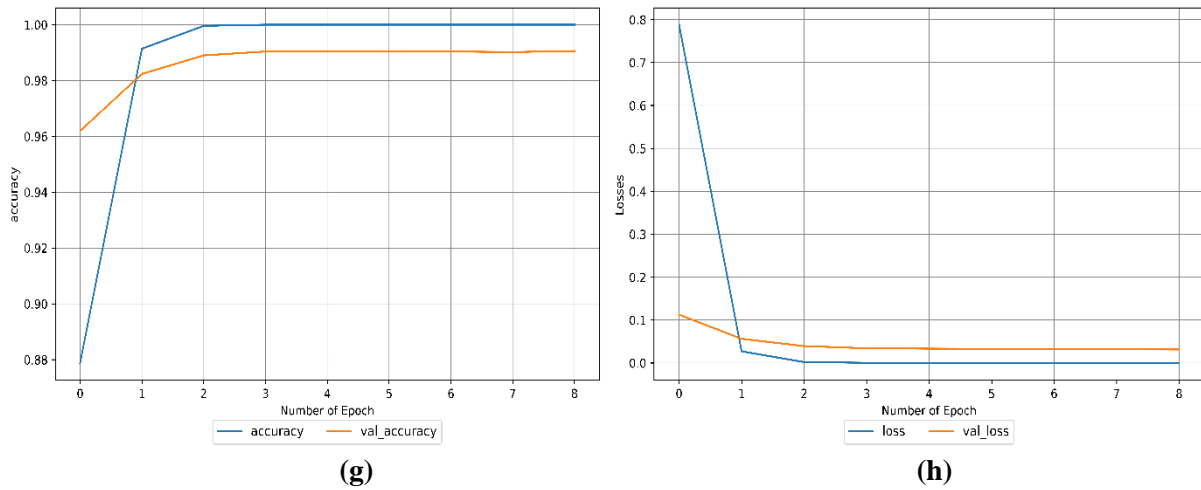


Figure 7. Accuracy and loss graphs of the models (a) CNN1, (c) CNN2, (e) ResNet50v2 and (g) VGG16, Loss graph of the models (b) CNN1, (d) CNN2, (f) ResNet50v2 and (h) VGG16

B. CLASSIFICATION WITH HYBRID MODELS

This section presents detailed results of the hybrid models used. The first component of the 2-stage model is a CNN network structure consisting of six layers, designed to generate feature vectors during the study. The CNN network is capable of processing high-dimensional data and extracting relevant features. The second component involves employing an SVM classifier layer for predicting outcomes. By combining these two techniques, the proposed hybrid approach aims to enhance the performance of CNN models and make them applicable in various image detection domains. However, traditional training of CNN models requires a significant amount of time and a large number of samples, imposing limitations on experimental conditions. On the other hand, SVM has demonstrated its effectiveness in regression, pattern classification, and prediction tasks [39], [40]. Unlike CNN, SVM does not require an extensive number of examples for training, but it faces challenges when it comes to identifying multiple classifications simultaneously [40], [41].

In this research, CNN1, a specific CNN model employed, comprises three convolution layers, three pooling layers, a fully connected layer, and a softmax classifier layer. Additionally, an SVM classifier is integrated into the CNN + SVM hybrid model for the classification process after the initial fully connected layer. The operational flow of CNN models involves several key stages. Initially, CT data images are inputted into the convolution layer to extract feature vectors, followed by the pooling layer to reduce data dimensionality. Finally, the fully connected layer is employed to further extract the feature vectors. The convolution layer utilizes a 2x2 kernel size, while the pooling layer employs a 1x1 convolution kernel size. Dropout is applied to mitigate overfitting. The error function is determined using cross-entropy, and optimization of the error function is achieved through the use of either the Adam or Adagrad Optimizer algorithm. A flowchart of the hybrid model is given in Figure 8.

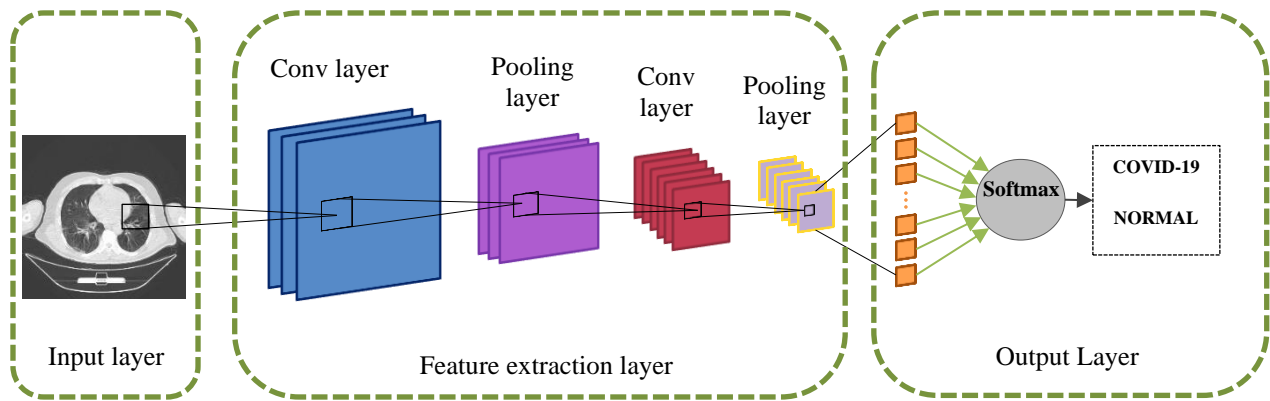


Figure 8. A flowchart of the hybrid model

Table 7 presents an in-depth analysis of the hybrid model utilized in the study. It includes crucial performance metrics such as training and validation accuracy, precision, recall, and F1-score. Additionally, the table provides information on the number of parameters, training time, and the number of epochs employed. The results in Table 7 demonstrate that the proposed new CNN models exhibit high accuracy in diagnosing COVID-19, with exceptional performance observed in the CNN1+SVM model, achieving 100% accuracy. The accuracy metric reflects the ability of the models to correctly classify instances of COVID-19, indicating their effectiveness in capturing the relevant patterns and features in the dataset. Furthermore, Table 8 presents a comparison between the training time of the CNN models and the SVM model. It highlights the advantage of the SVM model over the hybrid model in terms of training time. SVM is known for its efficiency in training, as it does not require a large number of examples. This characteristic is particularly advantageous when dealing with limited resources or time constraints. The table emphasizes the time-saving benefit of incorporating SVM in the hybrid model, demonstrating its superiority over training CNN models alone.

Table 7. Training and validation accuracy, precision, recall, and F1-score along with the number of parameters, training time, and epochs required to train deep learning architectures of CNN+SVM

Models	Parameters	Storage	Epochs for Training	Training Accuracy	Matthews corrcoef	Testing Accuracy	Precision	Recall	F1- score
ResNet50v2 + SVM	26,776,162	8 KB	10	99.99	97.11	98.55	99	99	99
VGG16 + SVM	15,517,602	4 KB	9	99.99	99.11	100	100	100	100
CNN1 + SVM	200,064,178	3 KB	14	100	100	100	100	100	100
CNN2 + SVM	205,548,082	2 KB	15	100	99.55	99.77	100	100	100

Table 8. Training time of CNN and SVM models

Architectures	CNN Training Time (s)	SVM Training Time (s)	Total Time(s)
ResNet50v2	504	0.1743	504.1743
VGG16	752.4	0.1704	752.5704
CNN1	682.2	0.0408	682.2408
CNN2	1677.6	0.0484	1677.6484

Classification report and confusion matrix of hybrid models are given in Table 9. In addition, the ROC curve, loss and accuracy curves of the models are also shown in Figures 9 and 10.

Table 9. Classification reports and confusion matrix of models

CNN1+SVM	Actual	Covid-19	447	0	Predicted		precision	recall	f1-score	support
		Normal	0	453						
			Covid-19	Normal						
CNN2+SVM	Actual	Covid-19	445	2	Predicted		precision	recall	f1-score	support
		Normal	0	453						
			Covid-19	Normal						
VGG16+SVM	Actual	Covid-19	445	2	Predicted		precision	recall	f1-score	support
		Normal	2	451						
			Covid-19	Normal						
ResNet50v2+SVM	Actual	Covid-19	440	7	Predicted		precision	recall	f1-score	support
		Normal	3	450						
			Covid-19	Normal						

Figure 9 shows the ROC curves of used models. The ROC curve in the CNN1+SVM demonstrates perfect classification performance, with an AUC (Area Under the Curve) of 1.00 for all curves, including the micro-average, class 0, and class 1. This indicates that the model achieves 100% accuracy, correctly classifying all instances of both classes without any false positives or false negatives. The curve adheres to the upper-left corner of the plot, which represents the ideal performance of a classifier. The ROC curve for CNN2+SVM exhibits the same classification performance with CNN1+SVM, achieving an AUC (Area Under the Curve) of 1.00 across all metrics, including the micro-average, class 0, and class 1. This indicates that the model attains perfect accuracy, successfully identifying all instances of both classes without any errors, such as false positives or false negatives. The curve aligns perfectly with the upper-left corner of the plot, representing the optimal performance of a classifier. Similar to the first graph, VGG16+SVM graph reflects perfect classification performance, achieving an AUC of 1.00 for all curves. The ROC curve closely aligns with the upper-left corner, signifying that the model makes no classification errors for either class. This level of performance indicates the model's ability to completely differentiate between the two classes without overlap or ambiguity. The ResNet50v2+SVM graph shows a nearly perfect ROC curve, with an AUC of 0.99 for all curves (micro-average, class 0, and class 1). This suggests that the model performs exceptionally well but might misclassify a small number of instances. The slight deviation of the curve from the upper-left corner indicates minor imperfections in classification, but the model still achieves highly reliable performance.

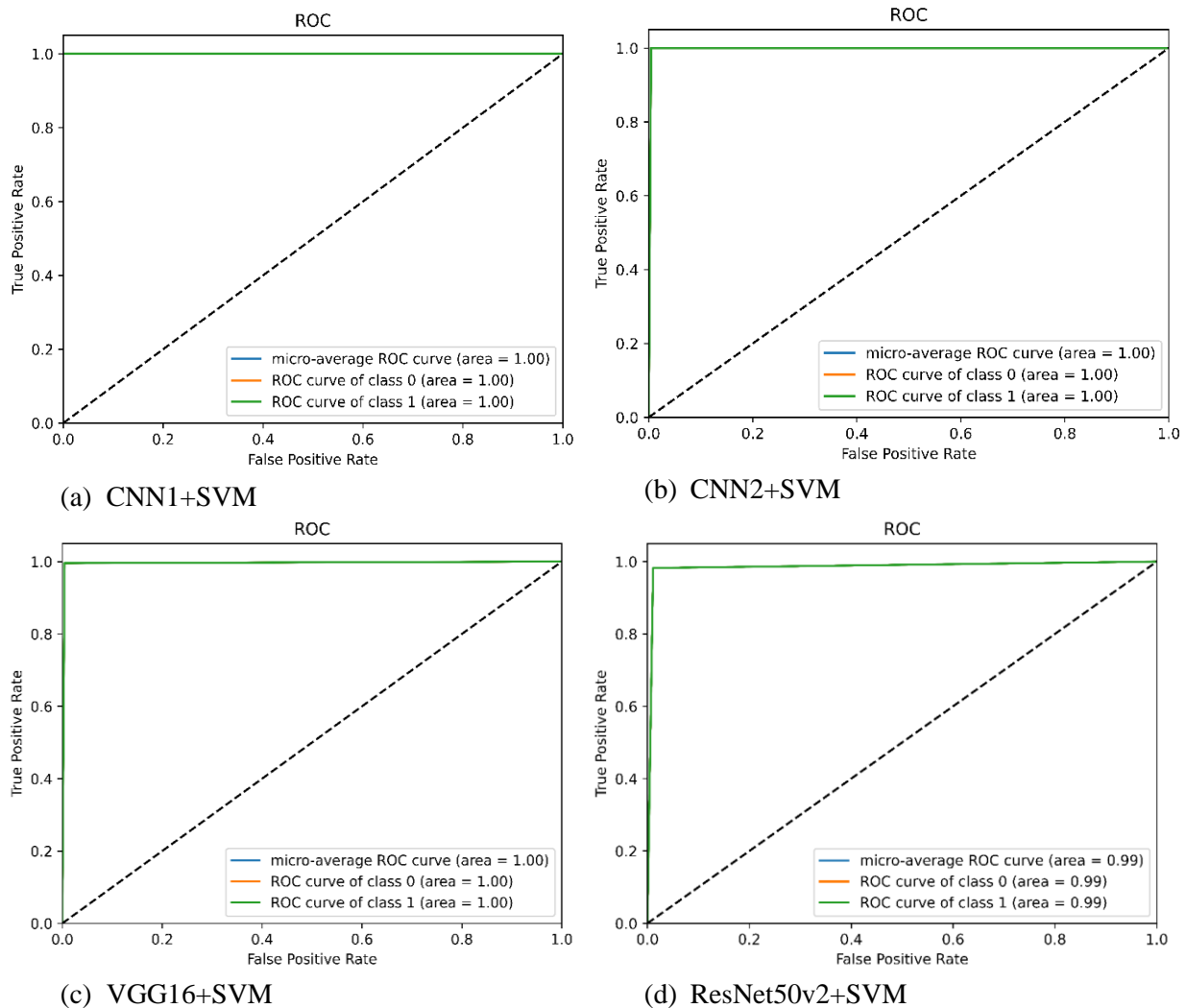
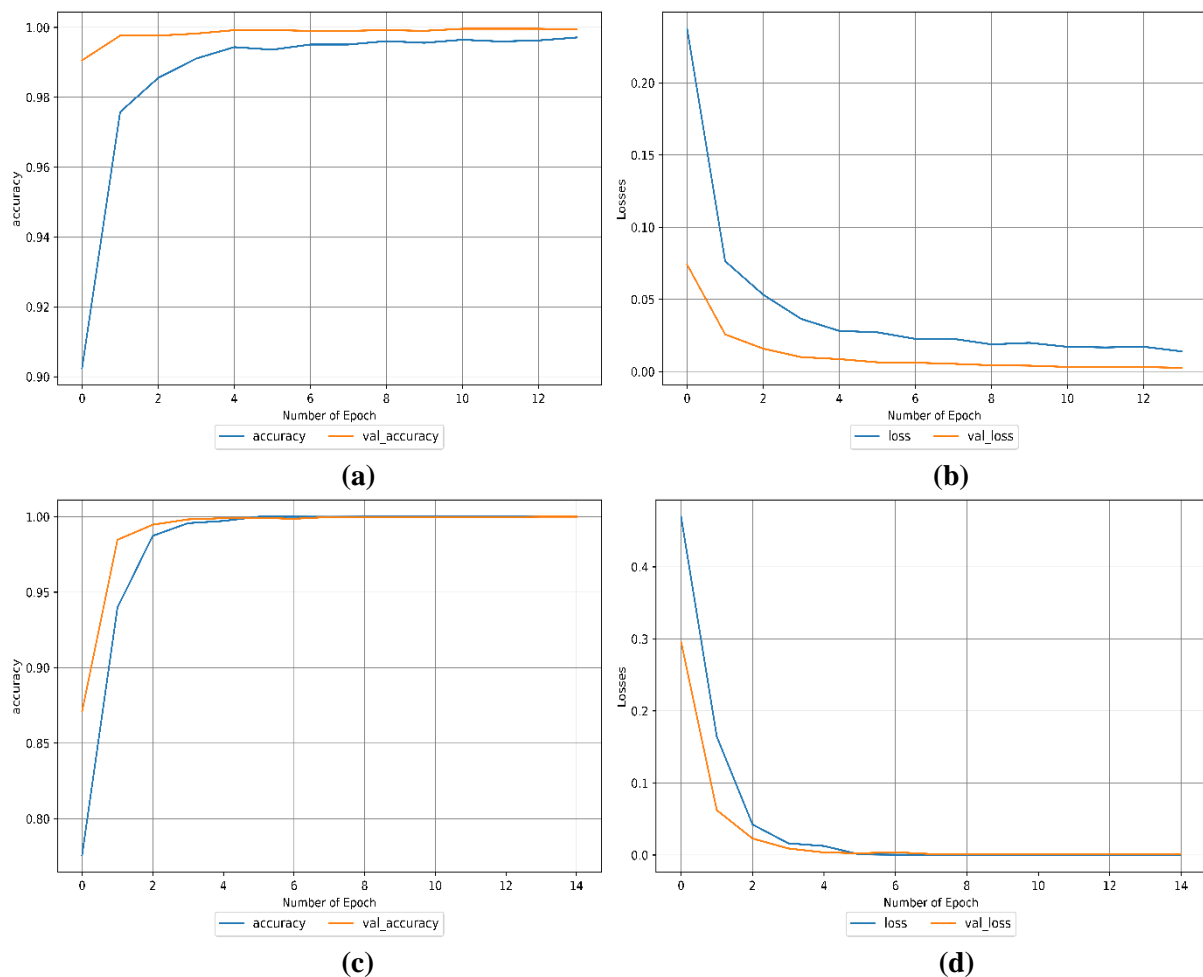


Figure 9. ROC curves of the used models

Figure 10 illustrates the accuracy and loss graphs of the proposed used hybrid models, these graphs provide a visual overview of the models' performance and highlight key aspects of their training process. The accuracy graph reveals that the proposed hybrid models maintain consistent and favorable accuracy levels throughout the training phase, demonstrating their ability to effectively learn the underlying patterns and features of the training data. Importantly, there is no evidence of overfitting, suggesting that the models avoid excessively memorizing the training data and can generalize well to unseen instances. Furthermore, the absence of underfitting indicates that the models successfully capture and utilize the critical characteristics of the data without oversimplifying the problem.

The loss graph, in contrast, offers insights into the optimization process of the models. It shows a steady decline in loss values, signifying that the models are effectively minimizing the difference between their predicted outputs and the actual labels. The smooth, continuous reduction in loss indicates that the models are progressively improving their performance and converging toward an optimal state. A novel methodology is introduced for developing new hybrid models and leveraging pre-trained models, consisting of two key components.



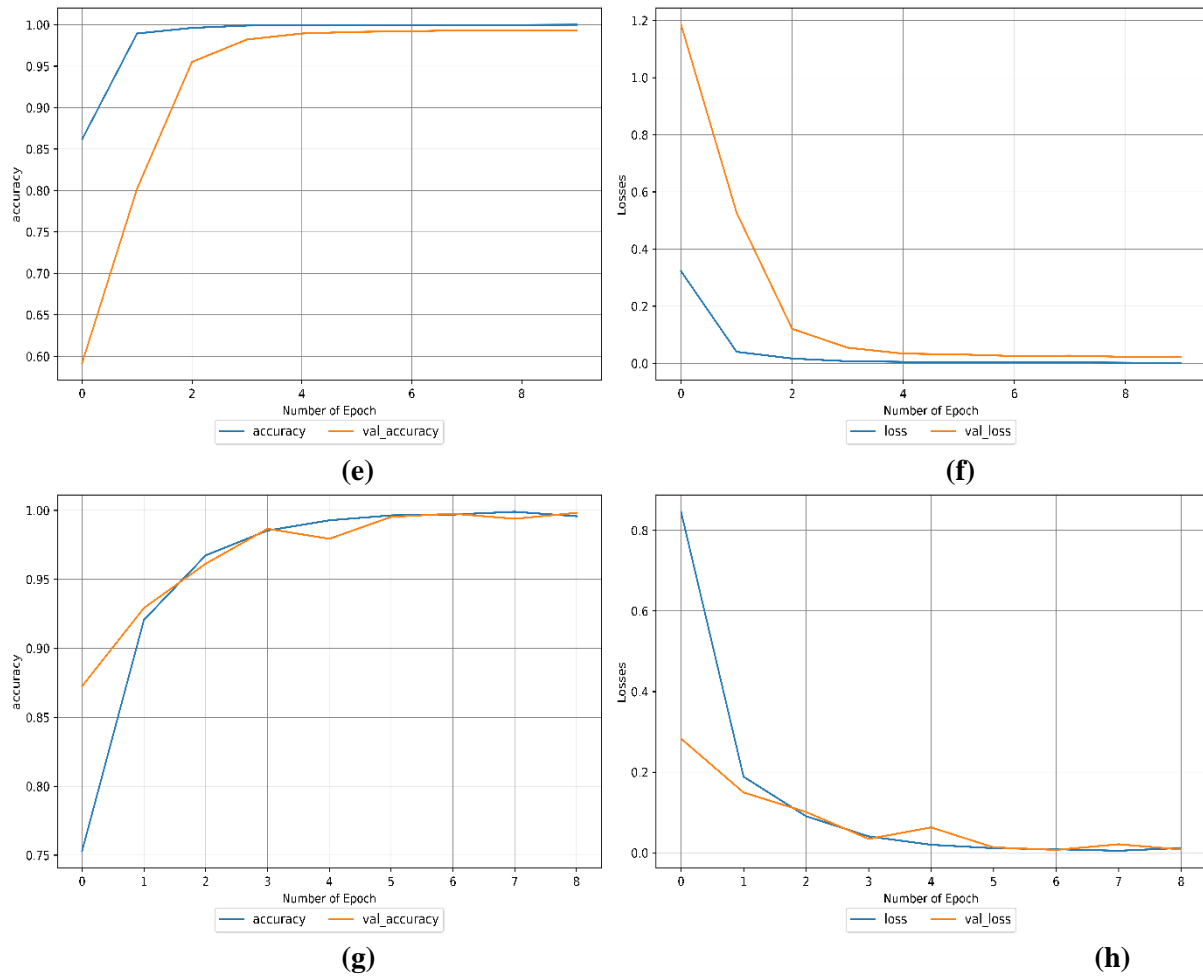


Figure 10. Accuracy and loss graph of the models (a) CNN1+SVM, (b) CNN2+SVM, (c) ResNet50v2+SVM and (d) VGG16+SVM

While our study showcases promising results with CNN and hybrid CNN+SVM models, it is crucial to acknowledge the advancements made by previous researchers in the field. The higher accuracy rates reported in the comparative studies may be attributed to various factors such as different datasets, model architectures, hyperparameter optimization techniques, and data preprocessing methods. Understanding these variations and incorporating the relevant advancements into our models can potentially lead to enhanced accuracy and improved performance. Table 10 presents a comparison of similar studies in the literature. Upon examining these studies in relation to our recommended models, it becomes evident that the accuracy rates achieved by the other proposed models are higher. This suggests that there is room for improvement in our proposed models to match or surpass the performance of these comparative studies.

Table 10. Comparison of similar studies in the literature

Models	Data Size	Data Type	Performance (%)	Study
CNN	1430	X-ray	97.92	[22]
WCNN	1000	CT	98.19	[23]
CNN	6310	X-ray	95	[24]
MobileNetV3Large	15186	CT	99.74	[25]
SeNet154	22779	CT	98	[25]
CNN	2905	X-ray	98.13	[26]
CNN	15471	X-ray	94.55	[26]
ResNet101	8900	X-ray	98	[27]
VGG19	7455	CT	97	[27]

Table 10(cont). Comparison of similar studies in the literature

ResNet50	-	CT	98.78	[28]
CNN	15871	CT	98.36	[29]
CNN+SVM	5360	X-ray	97.41	[30]
CNN+SVM	6000	X-ray	91.1	[31]
ResNet50+SVM	13808	X-ray	97.3	[32]
mAlexNet+SVM	3911	X-ray	99.8	[42]
CNN+SVM	746	CT	91.1	[43]
This Study (Hybrid CNN+SVM)	6000	CT	100	-

IV. DISCUSSION

There have been numerous studies in the literature focusing on the detection of COVID-19, including hybrid models that have shown high accuracy [44]. These studies have laid the foundation for exploring innovative approaches to leveraging medical imaging for disease detection. In our proposed study, we observed that both newly developed CNN models and CNN+SVM hybrid models achieved superior accuracy on the original dataset compared to results reported in prior studies. This improvement highlights the potential of our approach to effectively capture and utilize features from medical images for COVID-19 detection. It is worth noting that previous studies often utilized limited datasets with few images per class [45]–[48]. In contrast, our study adopted a comprehensive approach by analyzing a large dataset, which prioritizes studies that incorporate more extensive data. While these studies have contributed valuable insights, their findings may not generalize well due to the constrained size and diversity of the datasets. In contrast, our study adopted a more comprehensive approach by analyzing a significantly larger dataset, which allows for the exploration of a wider range of imaging patterns and patient characteristics. This emphasis on larger datasets not only improves the reliability of the findings but also ensures that the models are trained on data that more closely resemble real-world scenarios.

By prioritizing studies that incorporate extensive data, we aim to address key challenges in medical image classification, including the variability in imaging protocols, patient demographics, and disease presentation. Furthermore, our approach underscores the importance of scalability and adaptability, which are critical for developing models that can be effectively deployed in clinical practice.

V. LIMITATION AND FUTURE WORK

This study emphasizes the importance of dataset size in enhancing the robustness and reliability of our findings. While the system demonstrates good performance on our datasets, it is important to acknowledge several limitations that need to be addressed. Firstly, our research is currently in the theoretical phase, and the models have not yet been validated in real clinical routines. This limits the immediate applicability of our findings to practical medical settings. Additionally, the datasets used in this study, although comprehensive, may not fully represent the diversity of real-world clinical data, such as variations in imaging protocols, patient demographics, and disease presentation. As a result, there is a potential risk that the models may not generalize well across different populations or clinical environments.

Moreover, while our models show promising results in detecting COVID-19 from CT images, their interpretability and the exact mechanisms through which they identify key features remain underexplored. This lack of transparency could hinder clinical acceptance, as clinicians often require an understanding of how diagnostic tools make predictions to trust and effectively use them.

In future research, we plan to address these limitations through several initiatives. First, we aim to validate our models in clinical settings by conducting rigorous tests in collaboration with healthcare professionals. This will not only help evaluate the models' real-world performance but also allow us to understand clinicians' usage patterns and gather valuable feedback on their practicality and reliability. Such insights will guide us in refining and improving the models to better align with clinical needs.

Additionally, we will focus on assessing the severity of COVID-19 and extracting valuable information from CT images to contribute to global efforts against the pandemic. This includes performing detailed descriptive analyses of our models to identify and interpret the key features in CT images that are critical for the detection and severity assessment of COVID-19. By doing so, we aim to enhance the transparency and explainability of the models, thereby facilitating the adoption of these tools in clinical practice.

Finally, we plan to expand the scope of our study by incorporating diverse and larger datasets, ensuring that the models can generalize effectively across various clinical scenarios. This will also involve engaging with a broader range of healthcare professionals across different regions to ensure that the models are both adaptable and widely applicable. Through these efforts, we aim to make meaningful contributions to improving screening processes for clinicians and supporting global healthcare systems in their fight against COVID-19.

VI. CONCLUSION

The objective of this study is to introduce a decision support system that utilizes deep learning algorithms for the accurate diagnosis of COVID-19 by analyzing CT images. Along with two novel CNN models developed in this study, we also conducted a comprehensive modeling study using pre-trained architectures such as ResNet50v2 and VGG16. Furthermore, we propose a hybrid model by combining these CNN models with the SVM algorithm. During the modeling process, we performed parameter selection using the grid search method for hyperparameter optimization. The original dataset used in the modeling consists of two classes, and detailed information about the dataset is provided. To evaluate the performance of our models, we split the original dataset as well as newly created datasets into training and test sets using an 85-15 ratio, and we also employed 5-fold cross-validation. All results were presented in a comparative manner. The accuracy values of the results obtained are 99.93% and 99.86% CNN models, 100% and 99.77% CNN+SVM models, and it is seen that the proposed models can classify the CT images of COVID-19 patients and make the diagnosis of COVID-19 with high accuracy. Additionally, we assessed the effectiveness of our proposed methods on a different dataset, thereby increasing the efficiency of the study. These results provide strong evidence that the proposed deep learning models can be successfully utilized in the healthcare domain.

ACKNOWLEDGEMENTS: The authors have not disclosed any funding.

DECLARATION OF ETHICAL STANDARDS: Authors declare that all ethical standards have been complied with.

DECLARATION OF COMPETING INTEREST: The authors declare no competing of interest.

DATA AVAILABILITY: The data set used in this study was obtained by obtaining the necessary ethical permissions from Faculty of Medicine, Yozgat Bozok University.

V. REFERENCES

- [1] WHO. “COVID-19 Public Health Emergency of International Concern (PHEIC) Global research and innovation forum.” *Glob Res Collab Infect Dis Prep.*, pp. 1-10, 2020. [Online]. Available: [https://www.who.int/publications/m/item/covid-19-public-health-emergency-of-international-concern-\(pheic\)-global-research-and-innovation-forum](https://www.who.int/publications/m/item/covid-19-public-health-emergency-of-international-concern-(pheic)-global-research-and-innovation-forum)
- [2] WHO. “Weekly epidemiological update on COVID-19 - pp. 1-16, 2022. [Online]. Available: <https://www.who.int/publications/m/item/weekly-epidemiological-update-on-covid-19---16-november-2022>
- [3] J. P. Kanne, B. P. Little, J. H. Chung, B. M. Elicker, and L. H. Ketai, “Essentials for radiologists on COVID-19: An update-radiology scientific expert panel,” *Radiology*, vol. 296, no. 2, pp. 113–114, 2020.
- [4] M. Mossa-Basha, C. C. Meltzer, D. C. Kim, M. J. Tuite, K. P. Kolli, and B. S. Tan, “Radiology Department Preparedness for COVID-19: Radiology Scientific Expert Review Panel,” *Radiology*, vol. 296, no. 2, pp. 106–112, Aug. 2020.
- [5] E. Martínez Chamorro, A. Díez Tascón, L. Ibáñez Sanz, S. Ossaba Vélez, and S. Borrueal Nacenta, “Radiologic diagnosis of patients with COVID-19,” *Radiologia. (English Ed.)*, vol. 63, no. 1, pp. 56–73, Jan. 2021.
- [6] E. Benmalek, J. Elmhamdi, and A. Jilbab, “Comparing CT scan and chest X-ray imaging for COVID-19 diagnosis,” *Biomed. Eng. Adv.*, vol. 1, p. 100003, Jun. 2021.
- [7] S. Wang *et al.*, “A deep learning algorithm using CT images to screen for Corona virus disease (COVID-19),” *European Radiology.*, vol. 31, pp. 6096-6104, 2021.
- [8] C. Lin *et al.*, “Asymptomatic novel coronavirus pneumonia patient outside Wuhan: The value of CT images in the course of the disease,” *Clin. Imaging*, vol. 63, pp. 7–9, Jul. 2020.
- [9] Y. Fang *et al.*, “Sensitivity of chest CT for COVID-19: Comparison to RT-PCR,” *Radiology*, vol. 296, no. 2, pp. 115-117, 2020.
- [10] T. Ai *et al.*, “Correlation of Chest CT and RT-PCR Testing for Coronavirus Disease 2019 (COVID-19) in China: A Report of 1014 Cases,” *Radiology*, vol. 296, no. 2, pp. 32-40, 2020.
- [11] S. Minaee, R. Kafieh, M. Sonka, S. Yazdani, and G. Jamalipour Soufi, “Deep-COVID: Predicting COVID-19 from chest X-ray images using deep transfer learning,” *Med. Image Anal.*, vol. 65, 2020.
- [12] V. Gavini, G. Ramasamy, and J. Lakshmi, “CT Image Denoising Model Using Image Segmentation for Image Quality Enhancement for Liver Tumor Detection Using CNN.” *Traitement du Signal*, vol. 39, no. 5, pp. 1807-1814, 2022.
- [13] D. Afchar, V. Nozick, J. Yamagishi, and I. Echizen, “MesoNet: A compact facial video forgery detection network,” *10th IEEE Int. Work. Inf. Forensics Secur. WIFS 2018*, Jan. 2019.
- [14] M. E. Sahin, H. Ulutas, E. Yuce and M.F. Erkok, “Detection and classification of COVID-19 by using faster R-CNN and mask R-CNN on CT images.” *Neural Computing and Applications*, vol. 35, no. 18, pp. 13597-13611, 2023.
- [15] H. Ulutas, M. E. Sahin, and M. O. Karakus. “Application of a novel deep learning technique using CT images to implement the COVID-19 automatic diagnosis system on embedded systems.” *Alexandria Engineering Journal*, vol. 74, pp. 345-358, 2023
- [16] N. Cinar, A. Ozcan, and M. Kaya, “A hybrid DenseNet121-UNet model for brain tumor segmentation from MR Images,” *Biomed. Signal Process. Control*, vol. 76, 2022.
- [17] M. E. Sahin, “Image processing and machine learning-based bone fracture detection and classification using X-ray images,” *Int. J. Imaging Syst. Technol.*, vol. 33, no. 3, 2023.

- [18] M. Emin Sahin, "Deep learning-based approach for detecting COVID-19 in chest X-rays," *Biomed. Signal Process. Control*, vol. 78, 2022.
- [19] K. Gupta and V. Bajaj, "Deep learning models-based CT-scan image classification for automated screening of COVID-19," *Biomed. Signal Process. Control*, vol. 80, 2023.
- [20] P. Gaur, V. Malaviya, A. Gupta, G. Bhatia, R. B. Pachori, and D. Sharma, "COVID-19 disease identification from chest CT images using empirical wavelet transformation and transfer learning," *Biomed. Signal Process. Control*, vol. 71, 2022.
- [21] F. M. Shah *et al.*, "A Comprehensive Survey of COVID-19 Detection Using Medical Images," *SN Comput. Sci.*, vol. 2, no. 6, pp. 1–22, Nov. 2021.
- [22] K. Singh and J. Kaur, "A CNN Approach to Identify COVID-19 Patients among Patients with Pneumonia," *Int. J. Intell. Syst. Appl. Eng.*, vol. 10, no. 2, pp. 166–169, May 2022.
- [23] P. M. de Sousa *et al.*, "A new model for classification of medical CT images using CNN: a COVID-19 case study," *Multimed. Tools Appl.*, pp. 1–29, Dec. 2022.
- [24] M. Ragab, S. Alshehri, N. A. Alhakamy, R. F. Mansour, and D. Koundal, "Multiclass Classification of Chest X-Ray Images for the Prediction of COVID-19 Using Capsule Network," *Comput. Intell. Neurosci.*, vol. 2022, 2022.
- [25] N. A. Baghdadi, A. Malki, S. F. Abdelallem, H. Magdy Balaha, M. Badawy, and M. Elhosseini, "An automated diagnosis and classification of COVID-19 from chest CT images using a transfer learning-based convolutional neural network," *Comput. Biol. Med.*, vol. 144, p. 105383, May 2022.
- [26] A. Banerjee, A. Sarkar, S. Roy, P. K. Singh, and R. Sarkar, "COVID-19 chest X-ray detection through blending ensemble of CNN snapshots," *Biomed. Signal Process. Control*, vol. 78, p. 104000, Sep. 2022.
- [27] S. Thandapani *et al.*, "IoMT with Deep CNN: AI-Based Intelligent Support System for Pandemic Diseases," *Electron. 2023, Vol. 12, Page 424*, vol. 12, no. 2, p. 424, Jan. 2023.
- [28] M. H. Saad, S. Hashima, W. Sayed, E. H. El-Shazly, A. H. Madian, and M. M. Fouda, "Early Diagnosis of COVID-19 Images Using Optimal CNN Hyperparameters," *Diagnostics 2023, Vol. 13, Page 76*, vol. 13, no. 1, p. 76, Dec. 2022.
- [29] A. P. Umejiaku, P. Dhakal, and V. S. Sheng, "Detecting COVID-19 Effectively with Transformers and CNN-Based Deep Learning Mechanisms," *Appl. Sci. 2023, Vol. 13, Page 4050*, vol. 13, no. 6, p. 4050, Mar. 2023.
- [30] A. K. Azad, Mahabub-A-Alahi, I. Ahmed, and M. U. Ahmed, "In Search of an Efficient and Reliable Deep Learning Model for Identification of COVID-19 Infection from Chest X-ray Images," *Diagnostics 2023, Vol. 13, Page 574*, vol. 13, no. 3, p. 574, Feb. 2023.
- [31] A. M. Ayalew, A. O. Salau, Y. Tamyalew, B. T. Abeje, and N. Woreta, "X-Ray image-based COVID-19 detection using deep learning," *Multimed. Tools Appl.*, pp. 1–19, Apr. 2023.
- [32] H. Kibriya and R. Amin, "A residual network-based framework for COVID-19 detection from CXR images," *Neural Comput. Appl.*, vol. 35, no. 11, pp. 8505–8516, Apr. 2022.
- [33] J. Jiang, E. H. El-Shazly, and X. Zhang, "Gaussian weighted deep modeling for improved depth estimation in monocular images," *IEEE Access*, vol. 7, pp. 134718–134729, 2019.
- [34] L. Chen, W. Tang, T. R. Wan, and N. W. John, "Self-supervised monocular image depth learning and confidence estimation," *Neurocomputing*, vol. 381, no. 5, pp. 272–281, Mar. 2020.
- [35] L. Deng and D. Yu, "Deep learning: Methods and applications," *Foundations and Trends in Signal Processing*, vol. 7, no. 3–4, pp. 197–387, 2013.
- [36] J. D. Kelleher, "Deep Learning." MIT Press, 2019.
- [37] J. Bergstra and Y. Bengio, "Random search for hyper-parameter optimization," *J. Mach. Learn. Res.*, 2012.

- [38] T. Hastie, R. Tibshirani, and J. Friedman, *Springer Series in Statistics The Elements of Statistical Learning - Data Mining, Inference, and Prediction*. 2009.
- [39] S. Sengupta and W. S. Lee, "Identification and determination of the number of immature green citrus fruit in a canopy under different ambient light conditions," *Biosyst. Eng.*, vol. 117, pp. 51-61, 2014.
- [40] J. Xu, S. Zhou, A. Xu, J. Ye, and A. Zhao, "Automatic scoring of postures in grouped pigs using depth image and CNN-SVM," *Comput. Electron. Agric.*, vol. 194, 2022.
- [41] F. S. A. Sa'ad, M. F. Ibrahim, A. Y. Md. Shakaff, A. Zakaria, and M. Z. Abdullah, "Shape and weight grading of mangoes using visible imaging," *Comput. Electron. Agric.*, vol. 115, pp. 51-56, 2015.
- [42] M. F. Aslan, "A robust semantic lung segmentation study for CNN-based COVID-19 diagnosis," *Chemom. Intell. Lab. Syst.*, vol. 231, p. 104695, Dec. 2022.
- [43] A. F. Mohammed, S. M. Hashim, and I. K. Jebur, "The diagnosis of COVID-19 in CT images using hybrid machine learning approaches (CNN & SVM)," *Period. Eng. Nat. Sci.*, vol. 10, no. 2, pp. 376-387, Apr. 2022.
- [44] T. Ozturk, M. Talo, E. A. Yildirim, U. B. Baloglu, O. Yildirim, and U. Rajendra Acharya, "Automated detection of COVID-19 cases using deep neural networks with X-ray images," *Comput. Biol. Med.*, vol. 121, 2020.
- [45] L. Wang, Z. Q. Lin, and A. Wong, "COVID-Net: a tailored deep convolutional neural network design for detection of COVID-19 cases from chest X-ray images," *Sci. Rep.*, 2020.
- [46] A. Narin, C. Kaya, and Z. Pamuk, "Automatic detection of coronavirus disease (COVID-19) using X-ray images and deep convolutional neural networks," *Pattern Anal. Appl.*, vol. 24, pp. 1207-1220, 2021. doi: 10.1007/s10044-021-00984-y
- [47] P. K. Sethy, S. K. Behera, P. K. Ratha, and P. Biswas, "Detection of coronavirus disease (COVID-19) based on deep features and support vector machine," *Int. J. Math. Eng. Manag. Sci.*, 2020.
- [48] E. E. D. Hemdan, M. A. Shouman, and M. E. Karar, "COVIDX-Net: A Framework of Deep Learning Classifiers to Diagnose COVID-19 in X-Ray Images." *arXiv preprint arXiv:2003.11055*. 2020



Düzce University Journal of Science & Technology

Research Article

Investigation of Electromagnetic Shielding Performance of Monolayer Ironboride in Tetragonal Crystal Structure using Ab initio Methods

Hakan ÜŞENTİ ^{a,*}, İzzet Paruğ DURU ^b

^a Department of Electricity and Energy, Düzce Vocational School, Düzce University, Düzce, TURKEY

^b Department of Medical Imaging, Gedik Vocational School, İstanbul Gedik University, İstanbul, TURKEY

* Corresponding author's e-mail address: hakanusenti@duzce.edu.tr

DOI: 10.29130/dubited.1618327

ABSTRACT

The negative effects of pollution caused by electromagnetic radiation on human health and sensitive systems have reached serious dimensions. The most effective way to deal with this pollution is to create isolated areas with shielding materials. Especially after the discovery of graphene, studies on 2D materials continue to reveal the extraordinary structural, electronic, and optical properties of 2D materials. Thanks to the research on the use of monolayer materials in electromagnetic shielding, ultra-thin, and high-performance shielding materials are being obtained. In this study, the electromagnetic radiation shielding efficiency (SE) of a 2D film-structured material with a tetragonal crystal structure in the MBenes class of the MXene family and obtained using Fe₂B unit cells in the P4/mmm space group has been investigated using ab initio methods. The electrical, optic, and magnetic behavior of the material in the ground state is determined using the density functional theory (DFT) approach. The Curie temperature was investigated using the Monte Carlo method. The shielding efficiency of Fe₂B has been investigated in the range of 31.558-123980 nm of the electromagnetic wave spectrum at [001], [010], [100] polarization states. Despite Fe₂B 2D monolayer film structure, it showed a shielding performance (SE_T) of >20 dB. This study shows that Fe₂B in film structure is a promising and exciting material for ultra-thin shielding material applications with its superior shielding performance at nanometer dimensions.

Keywords: Ab initio, DFT, shielding effect, MBenes, Fe_xB_y

Tetragonal Kristal Yapıdaki Tek Katmanlı Demirborürün Elektromanyetik Kalkanlama Performansının Ab initio Yöntemler Kullanılarak İncelenmesi

ÖZ

Elektromanyetik radyasyonun neden olduğu kirliliğin insan sağlığı ve hassas sistemler üzerindeki olumsuz etkileri ciddi boyutlara ulaşmıştır. Bu kirlilik ile başa çıkabilmenin en etkili yolu kalkanlama malzemeleri ile izole edilmiş alanlar yaratmaktır. Özellikle grafenin keşfinden sonra 2D malzemeler üzerine yapılan çalışmalar ile 2D malzemelerin olağan üstü yapısal, elektronik ve optik özellikleri hale keşfedilmeye devam etmektedir. Monolayer malzemelerin elektromanyetik kalkanlama alanında kullanılması amacıyla yapılan araştırmalar sayesinde ultra ince ve yüksek performanslı kalkanlama malzemeleri elde edilmeye çalışılmaktadır. Bu çalışmada MXene ailesine ait MBenes sınıfında bulunan tetragonal kristal yapıya sahip ve P4/mmm uzay grubunda bulunan Fe₂B birim hücreleri kullanılarak elde edilmiş olan film yapılı 2D malzemenin

elektromanyetik radyasyonu kalkanlama etkililiği (SE); ab initio yöntemler kullanılarak araştırılmıştır. Malzemenin taban durumundaki elektriksel ve manyetik davranışı yoğunluk fonksiyonel teorisi (DFT) yaklaşımı kullanılarak belirlenmiştir. Curie sıcaklığı Monte Carlo Metodu kullanılarak araştırılmıştır. Fe₂B'nin kalkanlama etkililiği elektromanyetik dalga spektrumunun 31.558-123980 nm aralığında [001], [010], [100] polarizasyon durumlarında incelenmiştir. Fe₂B 2D monolayer film yapısına rağmen >20 dB seviyesinde kalkanlama performansı (SE_T) göstermiştir. Bu çalışma göstermiştir ki; film yapıdaki Fe₂B, nanometre boyutlarındaki üstün kalkanlama performansı ile ultra ince kalkanlama malzemesi uygulamaları için umut ve heyecan verici bir malzemedir.

Anahtar Kelimeler: *Ab initio, DFT, kalkanlama etkisi, MBenes, Fe_xB_y*

I. INTRODUCTION

The electric field and the magnetic field are the two main components of electromagnetic pollution (radiation) that can be measured. Radiation emitted as waves or particles comes in two basic types. One of these is ionizing radiation, which has a certain mass and energy, can move rapidly, and can be in the form of particles or electromagnetic waves such as alpha, beta, and neutron radiation, and the other is high-energy radiation that reacts with the nucleus or orbits by affecting the atom it encounters [1-3]. Gamma and X-rays in the form of electromagnetic waves are massless radiation types. Radio waves, infrared waves, ultraviolet light, and microwaves are low-energy nonionizing electromagnetic waves that do not cause any change in the nuclei and orbits of the atoms they encounter [1, 2].

The main electromagnetic field generators are electrically powered devices, current-carrying conductors, high-voltage lines, radio-TV transmitters, microwave ovens, Wi-Fi access systems, energy-saving light bulbs, and devices used for industrial and medical diagnostics. Wireless telecommunication systems, which have become widespread, especially since the 1990s, have become the main actor of electromagnetic radiation generation. At the same time, the use of new technologies such as the Internet of Things (IoT) and 5G is causing new radio frequencies to emerge and this pollution to increase even faster. The widespread use of these electromagnetic pollution-causing radiation generators, even in rural areas, has led to a large increase in electromagnetic pollution due to population density. This pollution appears as the sum of the radiation pollution emitted by many electromagnetic wave generators. This summation effect of electromagnetic pollution causes increasing environmental pollution that grows day by day [4-7].

Electromagnetic radiation (EMR), which we are exposed to in our daily lives, has two basic components: very low frequency (ELF) band (<300 Hz) produced by electrical devices, high voltage lines and transformers, and radio frequency (RF) and microwave (MW) with high frequency from 3 kHz to 300 GHz from base stations, cell phones, radio and TV transmitters [3, 6, 8].

Human-induced environmental pollution (“electrosmog”), which has increased most rapidly in recent years, not only threatens our health depending on the duration and severity of exposure but also has negative effects on sensitive systems, such as disruption of stable operation and interference [5, 6, 9-11]. When the electromagnetic wave (EMW) we are exposed to in our living spaces against our will hits the tissue surface, some of it is reflected but the rest is absorbed by the body. Prolonged exposure to electromagnetic waves that produce a thermal effect on the tissue causes tissue damage. If the field strength of the wave cannot create the friction that can generate heat in the tissue, charges that are in motion in a continuous electric field such as ions, molecular dipoles, and colloid particles are also exposed to non-thermal effects. Depending on the nature of the organism, non-thermal effects can be stronger than thermal effects. The International Agency for Research on Cancer (IARC) identified ELF-type magnetic fields as a class 2B carcinogen in October 2001, and the World Health Organization (WHO) announced in 2004 that ELF magnetic fields increase childhood leukemia by a factor of two. In addition to the short-term effects of electromagnetic fields such as stress, insomnia, migraine, skin problems, memory loss, and weight gain, many scientific studies have proven that long-

term exposure to electromagnetic fields can cause leukemia, brain tumors, heart disease, Parkinson's, Alzheimer's, cancer, increased risk of miscarriage during pregnancy, as a result of their effects on molecular and chemical bonds, cell structure and immune system [3, 8, 11, 12].

The most effective way to deal with electromagnetic radiation is to create isolated areas using materials called “electromagnetic shielding” that can block the interference of radiation. Shielding materials should have properties that can meet the needs of different sectors. Studies on the production and application of shielding materials with these properties are still ongoing [13-17].

The shielding strategy is based on absorption, reflection, and multiple internal reflections of the electromagnetic wave within the shielding material. The electromagnetic wave interacting with the monolayer shielding material utilizes the impedance mismatch between the shield and the air, reflecting part of the EMW from the surface and dissipating the rest by absorption as heat energy inside the shield. In the inner thickness of the shield, the effect of secondary reflections and refractions is mostly negligible, since it has a very small effect compared to the main reflection and absorption effect. This reduces the effect of the wave penetrating the shield. The amount of this reduction is determined by the shielding efficiency (SE) parameters and is expressed in decibels (dB) [6, 10, 11, 15].

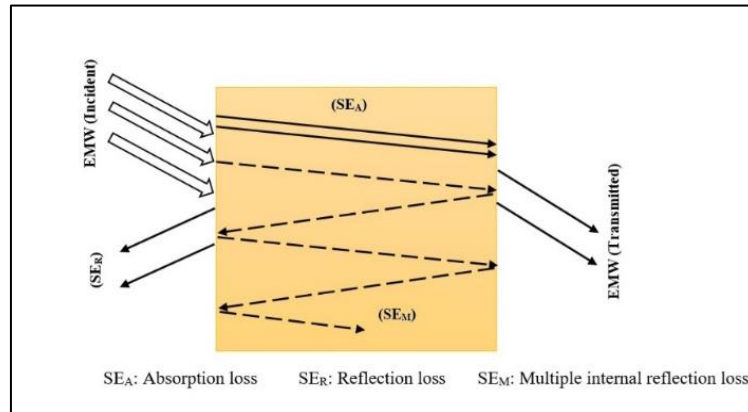


Figure 1. Schematic representation of the EMI shielding mechanism

The SE value, which varies with frequency, is calculated by the formula in Equation 1. As seen in the formula, the shielding effect is determined as the logarithmic ratio of the power (P) transmitted to and from the shield [11, 18, 19].

$$SE_T(dB) = 10 \log \frac{P_T}{P_I} = 20 \log \frac{E_T}{E_I} \quad (1)$$

The total shielding effectiveness (SE_T) is the sum of the shielding effect due to reflection (SE_R), the shielding effect due to absorption (SE_A), and the shielding effect due to multiple internal reflections (SE_M) as stated in Schelkunoff's theory.

$$SE_T(dB) = SE_R(dB) + SE_A(dB) + SE_M(dB) \quad (2)$$

Neglecting the SEM, which has a very small effect, the total shielding effect becomes as shown in Equation 3.

$$SE_T(dB) = SE_R(dB) + SE_A(dB) \quad (3)$$

The synthesis and fabrication of shielding materials that are corrosion-resistant, lightweight, flexible, easy to process, inexpensive, and capable of high SE performance is a popular research topic today [20].

To exhibit electromagnetic shielding behavior, a material must exhibit good electrical conductivity at frequencies greater than 300 MHz. Materials with high conductivity can reduce the electric component (E) and the magnetic component (H) simultaneously. However, when the frequency is less than 30 MHz, only ferromagnetic materials are capable of reducing the magnetic component (H) [11].

Mu-metals, carbon derivatives (carbon black, carbon fiber, graphite, and graphene), polymer composites, conducting polymers, intrinsically conducting polymers (IPC), and nanocomposites have been frequently used for electromagnetic shielding. Although they have good shielding performance, metals, and carbon derivatives are not preferred as shielding materials in industrial applications and scientific studies because they have disadvantages such as brittleness, low impact resistance, and corrosion, as well as advantages such as cheapness and easy processability. Although they exhibit suitable behavior as shielding materials, carbon black, carbon fiber, graphite, and graphene (except for some graphite derivatives) are disadvantaged because they need a carrier phase to increase their resistance to external factors. Nanocomposites have become popular over metals as shielding materials due to their advantages such as light weight, flexibility, corrosion resistance, and ease of application [12, 15, 19-23].

Graphene, which was synthesized as a monolayer by Kostya et al. in 2004, is a transition to planar two-dimensional (2D) materials. After the synthesis of graphene, which was very difficult to synthesize due to its thermodynamic instability, the quantum phenomena (massless Dirac fermions, anomalous quantum hall effect, Klein's paradox) in its physical and chemical properties are remarkable. Due to these properties, the discovery of graphene is a breakthrough in the discovery of 2D monolayer materials [24].

The most interesting additions to the discovery and fabrication process of 2D materials are transition metal carbides, nitrides and carbonitride structures (i.e. MXenes). Atomic-layered MXenes are obtained by selectively etching MAX phases from their bulk-layered parents. In MAX phases, named according to their composition, M is a transition metal, A is an element mostly found in columns 3A and 4A, and X is carbon (C) or nitrogen (N) [25, 26]. All MBene, which can be obtained by selective removal of A atomic layers (A is often aluminum) in MAB phases, exhibit good metallic properties with high electron transfer efficiency. M in the MBene structure represents a transition metal and B represents a boron [27, 28].

Two-dimensional (2D) transition metal borides, called MBenes, are derived from the ternary boride group. The performance of boron (B) in 2D materials was discovered thanks to MBenes. A practical way to obtain boron-based 2D materials is to use boron and one of several transition metals. In this case, the transition metal donates electrons to boron to stabilize the boron layer, while at the same time, the transition metal contributes to the diversity of 2D boride materials in a centrally coordinated manner [27]. The use of 2D materials in the synthesis of ultra-thin, lightweight, widely applicable, high-performance shielding materials is the most current area of research.

In recent years, the design of Fe-containing nanostructures has greatly increased. This is due to the many advantages of nanoscale structures such as high aspect ratio, porosity, and high magnetic moment (superparamagnetic behavior) compared to bulk structures. In this study, the SE performance of MXene/MBene family member, Fe_xB_y , a 2D monolayer material (Fe_2B) with a tetragonal crystal structure and P4/mmm space group in 2D monolayer structure, has been theoretically investigated in detail with quantum mechanical based DFT approach using ab initio methods.

II. MATERIAL-METHOD

In this study, the electromagnetic shielding efficiency of 2D film-structured Fe₂B with a tetragonal crystal structure in the P4/mmm space group was investigated.

The lattice parameters of the Fe₂B unit cell are shown in Table 1; the lattice parameters are a=3.494 Å, b=3.494 Å, and c=2.507 Å; the angles are α=90.000°, β=90.000°, γ=90.000°. The unit cell volume of Fe₂B is V=30.605 Å³.

Table 1. Lattice parameters of Fe₂B unit cell with tetragonal crystal structure.

Material Name	Lattice parameters (Å)	Unit cell angles (°)	Unit cell volume and density
Fe ₂ B (P4/mmm)	a = 3.494 b = 3.494 c = 2.507	α = 90.000° β = 90.000° γ = 90.000°	V=30.605 Å ³ d=6.650 gr/cm ³

The structural, electrical, and optical properties of Fe₂B, which is stable in the ferromagnetic (FM) state, have been calculated using the Generalized Gradient Approximation (GGA) [29] and the Perdew-Burke-Ernzerhov (PBE) functional [30]. In these calculations, the CASTEP software package [31], which uses a quantum mechanical background and is capable of performing ab initio computational approaches within the framework of Density Functional Theory (DFT) [32], was used. Geometry Optimization calculations using the LBFGS algorithm were performed using OTFG Ultrasoft pseudopotentials. K points were obtained by setting the Monkhorst-Pack grid to 9X9X12. The Koelling-Hormon correction cut-off plane wave basis set for the SCF in the PBE work flux was set to 353.70 eV. The SCF tolerance was 1.0X10⁻⁶ eV atom⁻¹, the maximum force was 0.03 eV Å⁻¹, the maximum stress was 0.05 GPa and the maximum displacement tolerances were 1.0X10⁻³ Å. Since the parameters used in the geometry optimization were similar to those used in the energy calculations, the energy cutoff was set to 390 eV and the SCF tolerance was set to 1.0X10⁻⁷ eV atom⁻¹.

The optical behavior of Fe₂B is characterized by the real (ε') and imaginary (ε'') parts of the dielectric function (ε(ω)), which vary with the frequency of the incident photon. The optical behavior of the material also reveals its SE performance. The relationship between the real (ε') and imaginary parts (ε'') of the dielectric function and the optical behavior can be seen in the following equations.

$$n(\omega) = \left[\frac{\sqrt{\epsilon'^2(\omega) + \epsilon''^2(\omega)} + \epsilon'(\omega)}{2} \right]^{\frac{1}{2}} \quad (3)$$

$$k(\omega) = \left[\frac{\sqrt{\epsilon'^2(\omega) + \epsilon''^2(\omega)} - \epsilon'(\omega)}{2} \right]^{\frac{1}{2}} \quad (4)$$

$$\alpha(\omega) = \frac{\omega\sqrt{2}}{c} \left[\sqrt{\epsilon'^2(\omega) + \epsilon''^2(\omega)} - \epsilon'(\omega) \right]^{\frac{1}{2}} \quad (5)$$

$$R(\omega) = \frac{(n(\omega)-1)^2 + k^2(\omega)}{(n(\omega)+1)^2 + k^2(\omega)} \quad (6)$$

In the above equations, the refractive index is represented as $n(\omega)$, the extinction coefficient $k(\omega)$, absorption $\alpha(\omega)$ and reflection $R(\omega)$. Since the combined effect of absorption-induced shielding (SE_A) and reflection-induced shielding (SE_R) gives the total shielding efficiency (SE_T), the relationship between the optical character of the material and the SE efficiency is shown in Equation 9.

$$SE_A(dB) = 10 \log \left(\frac{1-R}{T} \right) \quad (7)$$

$$SE_R(dB) = 10 \log \left(\frac{1}{1-R} \right) \quad (8)$$

$$SE_T(dB) = SE_A(dB) + SE_R(dB) = 10 \log \left(\frac{1}{T} \right) \quad (9)$$

The unit cell structure of Fe_2B was visualized using the lattice parameters using the VESTA package program [33] as shown in Figure 2.

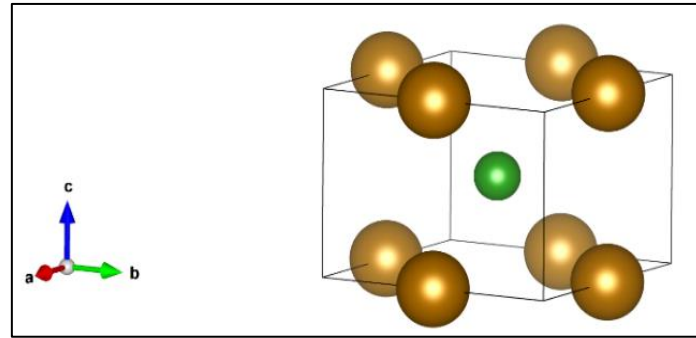


Figure 2. Fe_2B unit cell (atoms in yellow represent Fe and atoms in green represent B atoms)

The a, b, and c perspectives of the mesh structure formed using the obtained Fe_2B unit cell structure are shown in Figure 3.

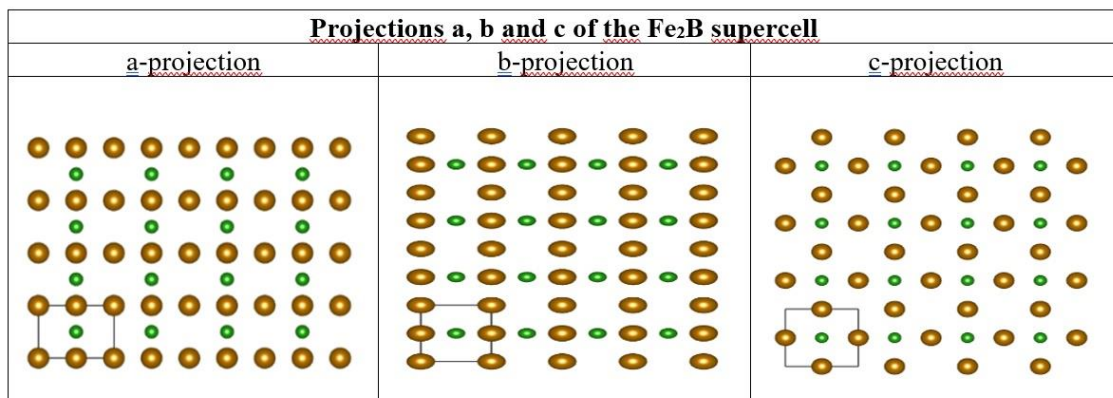


Figure 3. Representation of Fe_2B supercells obtained using unit cells in the form of a, b and c projections

The bond lengths and bond angles of the obtained unit cell Fe_2B determined its atomic morphology and also provided information about its magnetic and electronic properties and thus its SE behavior. Using the Kohn-Sham method, DFT was used to look at the kinetic energy and electron density in the

orbitals, and PBE, a popular GGA functional, was used to determine the relationship between the electron density and the energy function.

III. DETERMINATION OF ELECTRONIC, MAGNETIC, OPTICAL PROPERTIES OF Fe₂B

A. ELECTRONIC AND MAGNETIC CHARACTERISTICS

By calculating the density of states and band structure, information about the electronic and magnetic properties of Fe₂B was obtained. It is observed that the total energy and DOS calculations give consistent results for the Blöch correction and tetrahedron method. In addition, the major and minor channels in the band structure were obtained in the spin-polarized state. The band gap was created by using the valence band maximum (VBM) and conduction band minimum (CBM) so that the metallic behavior of Fe₂B could be observed. Figure 4 shows the electronic band structure of Fe₂B, which exhibits ferromagnetic behavior, obtained using major and minor spin channels with the Fermi level set to zero.

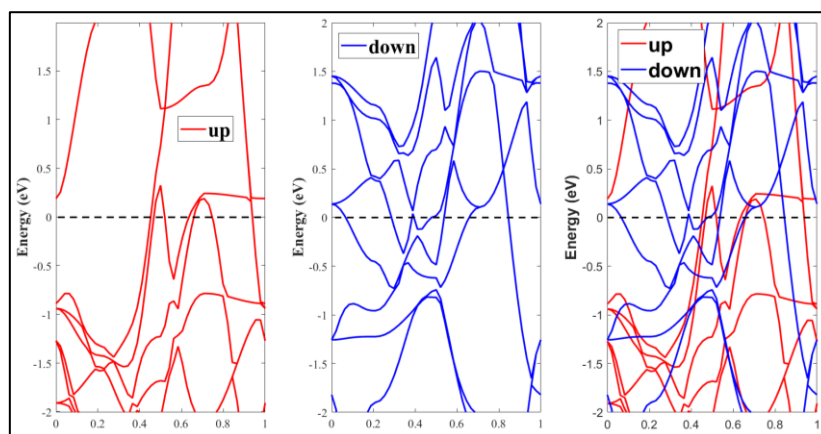


Figure 4. Electronic band structure of Fe₂B in the FM state tuned to the Fermi level

When the band structure is examined, the conduction and valence bands, which overlap in places to create a minimum energy difference, show that Fe₂B exhibits metallic behavior. At the same time, the up and down-oriented spin state reveals that Fe₂B, which exhibits metallic behavior, also avoids semi-metallic behavior.

Partial density of states (PDOS) plots were used to obtain information about the magnetic properties and electronic structure of the material. Figure 5. shows the PDOS of ferromagnetic Fe₂B and the TDOS graph obtained from their summation.

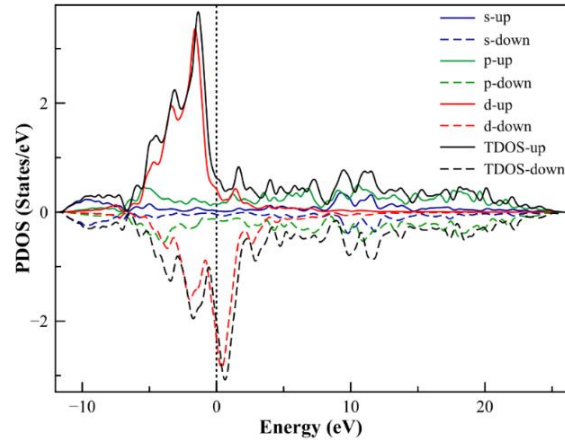


Figure 5. Partial density of states (PDOS) and density of states (TDOS) of Fe_2B in the FM state

Figure 5. shows the presence of magnetization caused by the hybridization of the p orbitals of Boron and d orbitals of Iron in the region close to the Fermi level. In this way, the material exhibits FM behavior.

Orbital hybridization, direct or indirect exchange interactions, charge transport, and spin orientations are important physical properties determined by the bond lengths and angles between atoms. According to crystal field theory (CFT), it is possible to divide the d-orbital into a high-energy region (e_g) and a low-energy region (t_{2g}) [34].

To clarify the energy difference between t_{2g} and e_g , the structures containing transition elements can be examined by removing the degeneracy in the d-orbital. Thus, by looking at the electron placement in the orbitals, information about the unpaired spin and the total magnetic moment can be obtained.

Heisenberg Hamiltonian is considered to elaborate magnetic feature of Fe_2B . It is given by Equation 10.

$$H = \frac{1}{2} \sum_{\substack{i,j \\ i \neq j}} J_{ij} S_i \cdot S_j \quad (10)$$

J_{ij} denotes the Exchange energy between i and j indices, while S_i and S_j are the spin value of the choosen spin. The authors generate supercell of Fe_2B in $100 \times 100 \times 2$ size from DFT optimized unitcell. Expectation values of thermodynamic quantities, observables as magnetic susceptibility and temperature related magnetization are calculated via Monte Carlo Simulation Method. A classic MCS procedure is applied starting by a randomized spin configuration and zero magnetic field. 60% of total Monte Carlo Steps are used to reduce fluctuations. The rest stands for measurement. Unnecessary MCS moves may increae spin-spin correlations. Therefore, total MCS number as $10\text{E}8$ and the percentages are determined after several trials. Note that exchange constants of $J_{\text{Fe-Fe}}$ are derived from DFT calculations ($\Delta E = E_{\text{FM}} - E_{\text{AFM}}$). Markov Chain Monte Carlo scheme in Metropolis algorithm is preferred satisfying detailed balance condition. The codes are written in C programming language by the authors. Susceptibility (χ) and average magnetization (M) vs temperature (T) are calculated via Equation 11 and Equation 12 to point out the Curie temperature.

$$M = \frac{\sum_{i=1}^N S_i}{N} \quad (11)$$

$$\chi = \beta(\langle M^2 \rangle - \langle M \rangle^2) \quad (12)$$

Figure 6. shows the magnetic susceptibility and Curie temperature for Fe₂B.

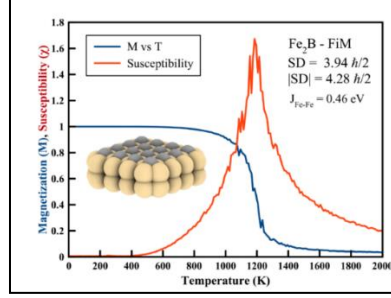


Figure 6. Magnetization (M), Susceptibility (χ) and Curie temperature (T_c) for Fe₂B exhibiting ferrimagnetic (FiM) behavior (Fe-Fe exchange interaction energy (J_{Fe-Fe}) 0.46 eV; Curie temperature (T_c) 1200K; spin density (SD) 3.94 $\hbar/2$)

Thanks to the morphological properties of the material and the hybridization in the orbitals, information about the structural and magnetic properties of Fe₂B has been obtained. In addition, as shown in Figure 6. the Fe-Fe exchange interaction energy (J_{Fe-Fe}) was found to be 0.46 eV as a result of the ground state energy calculations performed for Fe₂B by considering the unit cell structure of iron (Fe) in the temperature-varying bcc model. The magnetic dipole moment per unit volume, i.e. the magnetization (M) of Fe₂B decreased dramatically in the range of 1000K-1400K, starting from 1A/m at 0K and including the Curie temperature ($T_c=1200K$). If we look at the magnetic susceptibility (χ) of Fe₂B, we see that it increases from 0K up to the Curie temperature of 1200K and then decreases at the same rate. In light of this information, it is seen that Fe₂B exhibits ferrimagnetic (FiM) character as magnetic behavior.

B. ENERGY CALCULATIONS: DIELECTRIC FUNCTION AND OPTICAL PROPERTIES

The ferromagnetic (FM) state of Fe₂B is investigated using the Perdew-Burke-Ernzerhov (PBEsol) functional and the generalized gradient approximation (GGA). The absorption, reflection, and transmission coefficients of the material are calculated using the dielectric tensor obtained by calculating the frequency-dependent dielectric function. Figure 7. Energy dependence of the real (ϵ') and imaginary (ϵ'') parts of the dielectric function $\epsilon(\omega)$ in the material depending on the direction of photon incident ([001], [010] and [100]) on Fe₂B in the FM state.

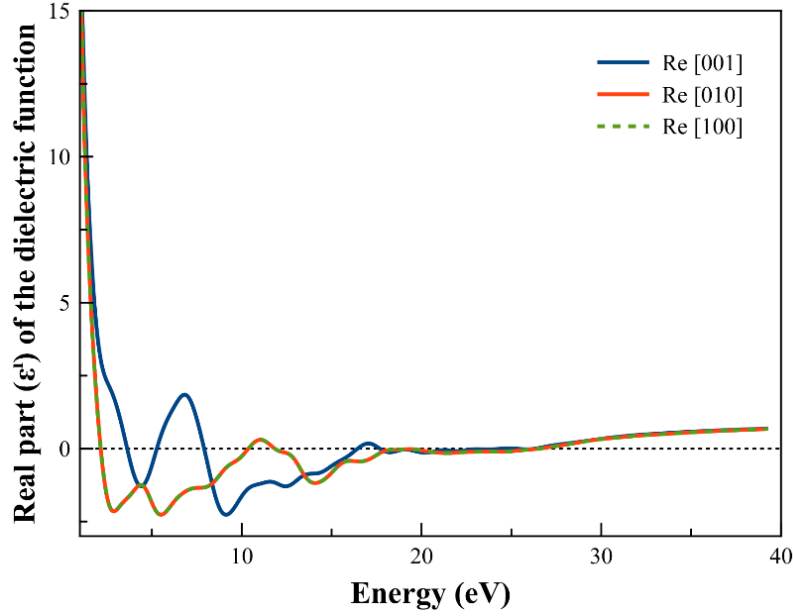


Figure 7. Variation of the real (ϵ') part of the dielectric function with photon energy for polarization states [001], [010] and [100]

As seen in Figure 7, when the effect of the photon on the real part (ϵ') of the dielectric function of Fe_2B in the polarization states [001], [010] and [100] is examined, it is observed that they exhibit similar behavior and take the same values in the polarization states addressed as [010] and [100], while a divergent behavior emerges in the polarization state indicated by [001]. The static dielectric behavior they exhibited at frequency values close to zero became dynamic after ~ 3 eV and continued to react inversely to radiation up to ~ 27 eV. The real part (ϵ'), which is responsible for the stored energy, was particularly affected by the electric field, one of the components of the polarized electromagnetic wave, and showed a relaxation frequency characteristic. After ~ 27 eV, it becomes more stable, taking a positive value for all cases. After the energy level of ~ 27 eV, Fe_2B continued to produce the same ϵ' value for the photon polarization states addressed by [001], [010] and [100].

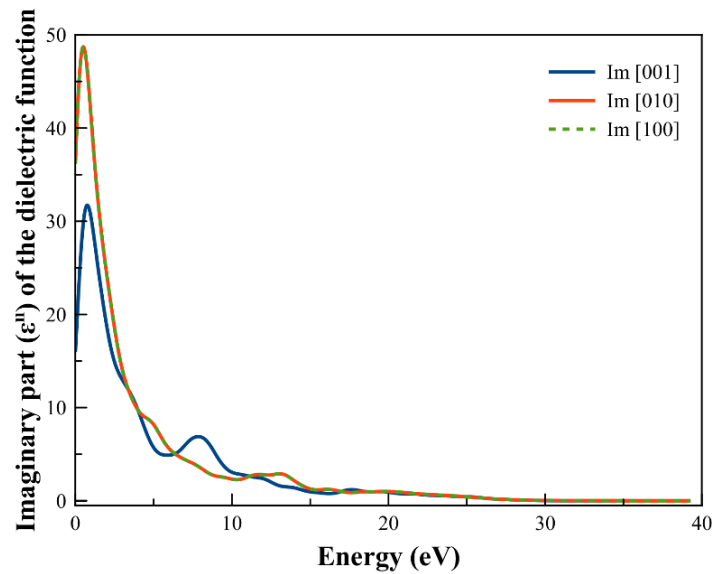


Figure 8. Variation of the imaginary (ϵ'') part of the dielectric function with photon energy for polarization states [001], [010] and [100]

As seen in Figure 8, when the effect of changing photon energy on the virtual part of the dielectric function (ϵ'') of Fe_2B in the polarization states [001], [010] and [100] is examined, it is seen that they exhibit similar behavior in the polarization states addressed as [010] and [100], while a divergent behavior emerges in the polarization state indicated by [001]. As it is known, the virtual part of the dielectric function (ϵ'') is responsible for the energy losses, i.e. the attenuation of the photon wave. Up to an energy level of ~ 1 eV (corresponding to the infrared region), ϵ'' is increased, which is also the region where the absorption effect is increased. However, after this energy level, the ϵ'' value starts to decrease dramatically and this effect lasts until the energy level of ~ 15 eV. Figure 9 shows the photon energy dependence of the absorption coefficient ($\alpha(\omega)$), extinction coefficient ($k(\omega)$), energy-loss function ($L(\omega)$), and refractive index ($n(\omega)$), which determine the optical properties of Fe_2B , for polarization states [001], [001] and [100].

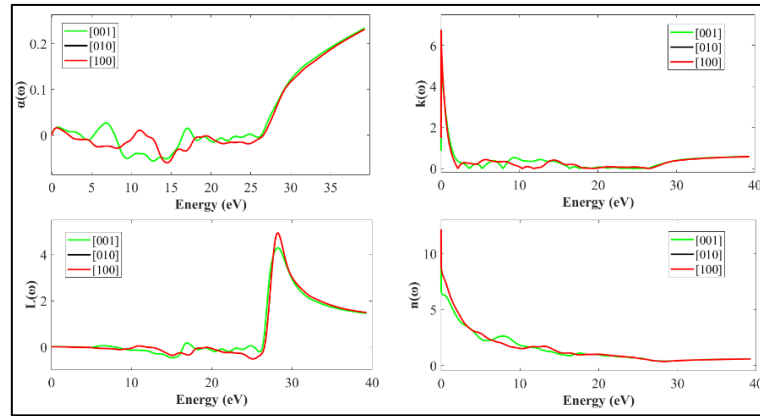


Figure 9. Photon energy dependence of the absorption coefficient ($\alpha(\omega)$), extinction coefficient ($k(\omega)$), energy-loss function ($L(\omega)$), and refractive index ($n(\omega)$), which determine the optical properties of Fe_2B , for polarization states [001], [001] and [100]

The photon energy-dependent change in the optical properties of Fe_2B is shown in Figure 9. For polarization states [001], [001] and [100]; absorption coefficient ($\alpha(\omega)$), extinction coefficient ($k(\omega)$), energy-loss function ($L(\omega)$), and refractive index ($n(\omega)$) It exhibited the same optical character for the polarization states indicated by [010] and [100], while the polarization state indicated by [001] showed a divergent behavior in all properties.

IV. SHIELDING EFFECT (SE) PERFORMANCE OF Fe_2B

The electromagnetic shielding efficiency (SE) of Fe_2B , which exhibits ferrimagnetic behavior as a member of the P4/mmm space group in 2D tetragonal crystalline structure, has been investigated in the spectrum range of 31.558-123980 nm allowed by the morphological properties of the material. The SE efficiency has been investigated separately for the ultraviolet (UV), visible, and infrared (IR) regions for [001], [010] and [100] polarization states. The total shielding efficiency (SE_T) is analyzed as the sum of the reflection-induced shielding efficiency (SE_R) and absorption-induced shielding efficiency (SE_A), while the shielding efficiency caused by multiple internal reflections (SE_M) [20], which has a very low effect, is neglected.

Figure 10 shows the reflection (SE_R), absorption (SE_A), and total (SE_T) shielding efficiency of monolayer Fe_2B material in the ultraviolet spectrum (31.558-388.284 nm).

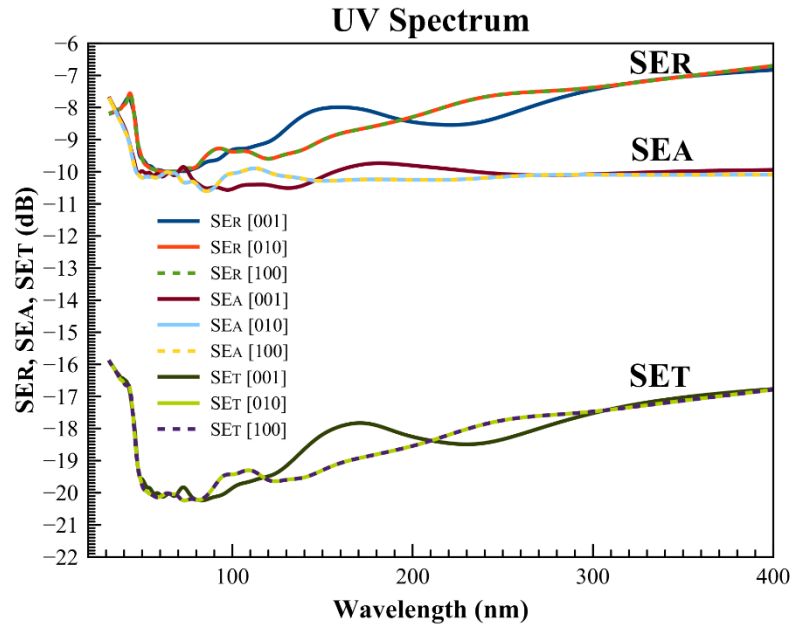


Figure10. SER, SEA, SET performances in the UV spectrum of Fe₂B at [001], [010] and [100] polarization states

The maximum SE_R, SE_A, and SE_T values of Fe₂B in the UV spectrum are shown in Table 2.

Table 2. Maximum SER, SEA, and SET values in the UV spectrum.

UV Spectrum (31.558-388.284 nm)			
dB	Max. SER	Max. SEA	Max. SET
[001]	-9.999	-10.565	-20.239
[010]	-10.000	-10.601	-20.243
[100]	-10.000	-10.609	-20.243

Figure 11 shows the reflection (SE_R), absorption (SE_A) and total (SE_T) shielding efficiency of monolayer Fe₂B material in the visible spectrum (390.688-746.661 nm).

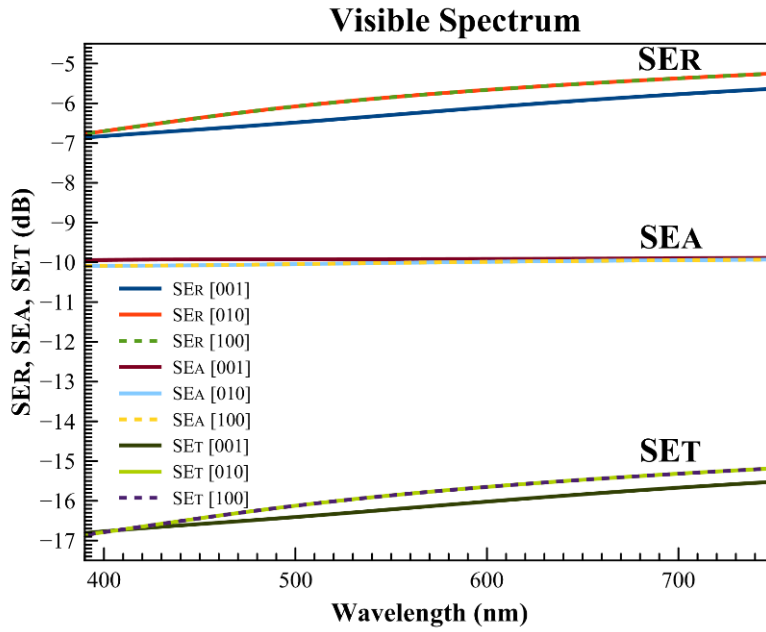


Figure11. SER, SEA, SET performances in the visible spectrum of Fe₂B at [001], [010] and [100] polarization states

The maximum SE_R, SE_A and SE_T values of Fe₂B in the visible spectrum are shown in Table 3.

Table 3. Maximum SE_R, SE_A and SE_T values in the visible spectrum.

Visible Spectrum (390.688-746.661 nm)			
dB	Max. SER	Max. SEA	Max. SET
[001]	-6.860	-9.947	-16.807
[010]	-6.763	-10.089	-16.852
[100]	-6.763	-10.089	-16.852

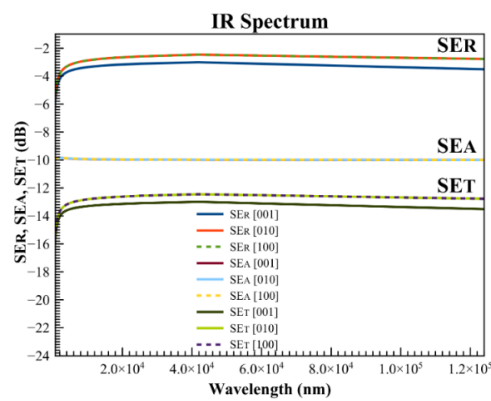


Figure12. SER, SEA, SET performances in the infrared spectrum of Fe₂B at [001], [010] and [100] polarization States

The maximum SE_R, SE_A and SE_T values of Fe₂B in the infrared spectrum are shown in Table 4.

Table 4. Maximum SE_R , SE_A and SE_T values in the infrared spectrum.

IR Spectrum (755.602-123980 nm)			
dB	Max. SE_R	Max. SE_A	Max. SE_T
[001]	-5.617	-9.999	-15.504
[010]	-5.237	-9.998	-15.167
[100]	-5.237	-9.998	-15.167

The maximum values of SE_R , SE_A and SE_T efficiencies for the [001], [010] and [100] polarization states of 2D Fe₂B with tetragonal crystal structure in the range of 31.558 -123980 nm are shown in dB in Figure 13.

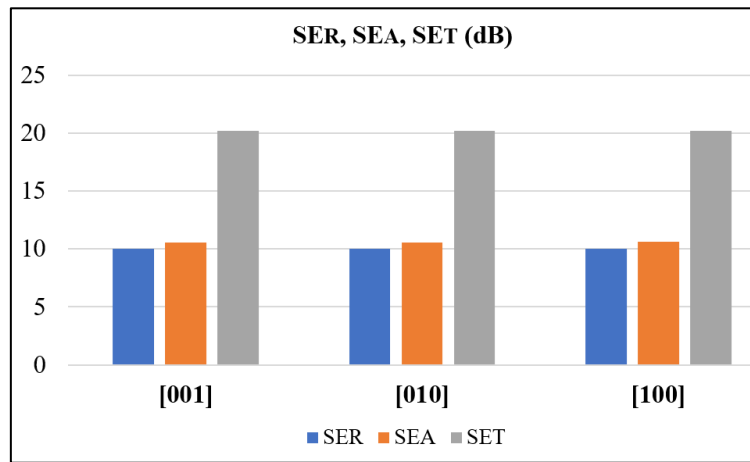


Figure 13. SE effect of 2D Fe₂B material in the range 31.558-123980 nm

Fe₂B exhibited shielding performance in the ultraviolet region, visible region, and infrared region with $SE_A > SE_R$ and showed absorptive-type shielding properties. Fe₂B started to show its shielding performance at wavelengths above 31,557 nm. At wavelengths up to 50 nm (within the NUV region), the material exhibited increasing shielding performance with the effect of absorption performance and then gradually decreasing shielding performance.

Although the SE_A , SE_R and SE_T shielding efficiencies of Fe₂B in the ultraviolet spectrum were the same in the [010] and [100] polarization states, the maximum SE_T was 20.243 dB, while the maximum SE_T performance in the [001] polarization state was 20.239 dB, 0.02% lower.

Fe₂B exhibited an absorptive shielding performance in the visible spectrum with $SE_A > SE_R$. While the SE_A performance for Fe₂B does not show a significant change in this region, the SE_R performance tends to decrease. This effect resulted in a loss of total shielding efficiency (SE_T) performance at wavelengths further away from the visible spectrum. Fe₂B showed the highest total shielding efficiency of 16.852 dB at [010] and [100] polarization states, with the absorption-induced shielding efficiency (SE_A) being greater than the reflection-induced shielding efficiency (SE_R).

Fe₂B exhibited shielding performance in the infrared region with $SE_A > SE_R$, indicating absorptive-type shielding. While the SE_A performance for Fe₂B does not show a significant change in this region, the

SE_R performance tends to decrease. This effect resulted in a loss of total shielding effectiveness (SE_T) performance at wavelengths further away from the visible region. Although the total shielding performances (SE_T) at [010] and [100] polarization states were the same, the maximum SE_T value at [001] polarization state was 15.504 dB.

The 2D material obtained using Fe₂B nanoparticles behaved as an absorptive type shielding material in [001], [010] and [100] polarization states and exhibited the maximum SE_T performance (>20 dB) in the UV spectrum.

When the literature on 2D-based electromagnetic shielding materials is examined, the EMI shielding performances (SE) of the materials shown in Table 5. are remarkable despite their ultra-thin structures.

Table 5. SE performance of selected 2D based materials in thickness and frequency ranges.

Material	Loading	Thickness (d) (mm)	EMI SE (dB)	Frequency (GHz)	Reference
Graphene film	bulk	0.25	17	12.4–18	[35]
Graphene paper	bulk	0.050	60	8.2-12.4	[36]
Graphene film	bulk	0.015	20.2	1-4	[37]
Multilayer graphene	bulk	0.018	55	12-18	[38]
Graphene aerogel	bulk	2	20	12.4-18	[35]
Flexible Graphite	bulk	3.1	130	1-2	[39]
rGO film	bulk	0.0084	19.1	8-12	[40]
Ti ₃ CNT _x	film (100 wt%)	0.04	116.0	8.2-12.4	[41]
Ti ₃ C ₂ T _x	film (100 wt%)	0.01	70.0	8.2-12.4	[42]
Ti ₃ C ₂ T _x -ANF	film (90.9 wt%)	0.01	34.7	8.2-12.4	[43]
TiO ₂ -Ti ₃ C ₂ T _x /GO	bulk	0.0091	28.2	12.4	[44]
Mo ₂ Ti ₂ C ₃ T _x	film	0.0035	26	8.2–12.4	[45]
Mo ₂ TiC ₂ T _x	film	0.004	23	8.2-12.4	[45]
MoS ₂ /glass	30 wt%	1.5	24.2	8.2-12.4	[46]
BP-GO	film (50 wt%)	0.01	29.7	8-12	[47]
GO-h-BN-polymer	film	0.24	37.9	8.2-12.4	[48]
Fe ₂ B	DFT	bulk sheet	20.243	4.083X10 ⁶	This work

In the study conducted by Tripathi et al. [35], they reported the SE performance of the 0.25 mm thick bulk structure graphene film at 12–18 GHz as 17 dB. In the study by Zhang et al. [36], the SE

performance of 0.050 mm thick graphene paper material in bulk structure was reported as 60 dB in the frequency range of 8.2-12.4 GHz. In another study conducted by Kumar et al. [37] on a bulk graphene film, the SE performance of the 0.015 mm thick material in the 1-4 GHz range was measured as ~20 dB. The 0.018 mm thick bulk material using multilayer graphene by Paliotta et al. [38] demonstrated 55 dB SE performance for 12-18 GHz. Singh et al. [35] reported that the SE performance of 2 mm thick graphene aerogel is 20 dB in the range of 12.4-18 GHz. In the study by Luo and Chung [39], the SE performance of 3.1 mm thick flexible graphite material in bulk structure was reported as 130 dB for 1-2 GHz. In another study by Sehen et al. [40], the 0.0084 mm thick bulk material obtained using rGO film showed ~19 dB SE performance for 8-12 GHz. In their study [41], Iqbal et al. reported the SE performance of the 0.04 mm thick material obtained using Ti_3CNT_x in film (100 wt%) structure as 116 dB under 8.2-12.4 GHz. In another study [42], Han et al. reported the SE performance of the 0.01 mm thick material obtained by using $\text{Ti}_3\text{C}_2\text{T}_x$ in film (100 wt%) structure as 70 dB at 8.2-12.4 GHz. In their study [43], Wei et al. showed that the SE performance of the 0.01 mm thick material obtained using $\text{Ti}_3\text{C}_2\text{T}_x$ -ANF in film (90.9 wt%) structure was 34.7 dB at 8.2-12.4 GHz. In the study conducted by Xiang et al. [44], the bulk structured TiO_2 - $\text{Ti}_3\text{C}_2\text{T}_x$ /GO with a thickness of 0.0091 mm showed an SE performance of 28.2 dB at 12.4 GHz. Shahzad et al [45] reported the SE performance of 0.0035 mm thick $\text{Mo}_2\text{Ti}_2\text{C}_3\text{T}_x$ film at 8.2-12.4 GHz as 26 dB. In the same study, Shahzad et al. [45] reported the SE performance of 0.004 mm thick $\text{Mo}_2\text{TiC}_2\text{T}_x$ film at 8.2-12.4 GHz as 23 dB. Wen et al. [46] reported that the SE performance of 1.5 mm thick MoS_2 /glass at 30 wt% filler ratio was 24.2 dB below 8.2-12.4 GHz. In their study [47], Zhou et al. showed that the SE performance of the 0.01 mm thick material obtained by using BP-GO in film structure (50 wt%) was 29.7 dB at 8-12 GHz. In their study [48], Zhang et al. showed that the SE performance of 0.24 mm thick 11-layer film-structured GO-h-BN-polymer material at 8.2-12.4 GHz is ~38 dB. In this study, where the DFT method was used, the SE performance of 2D Fe_2B in monolayer structure in the frequency range of 4.083×10^6 GHz was determined as 20.243 dB.

V. CONCLUSION

The structural, electronic, magnetic and optical properties of Fe_2B in the $P4/mmm$ space group in the tetragonal crystal structure have been theoretically investigated using the DFT method on a quantum mechanical basis using ab initio methods, followed by a detailed study of the SE performance of the 2D film material obtained using Fe_2B unit cells. The electromagnetic shielding efficiency of the electromagnetic wave (radiation) penetrating into the material from the [001], [010], [100] directions of the monolayer Fe_2B film material with a tetragonal crystal structure showing ferrimagnetic properties was investigated using ab-initio methods. Monolayer Fe_2B exhibited the best shielding performance (SE_T) of 20.243 dB in the ultraviolet region in the [010] and [100] cases where the radiation was perpendicular to the material. Neglecting the shielding effect caused by multiple internal reflections (SE_M), 10.6 dB of this performance is due to the absorption effect (SE_A) and 10 dB to the refractive effect (SE_R). The shielding response of the material started at 31.558 nm and lasted until 123980 nm. This performance is remarkable considering the morphological properties of the two-dimensional (2D) material. The SE_T performance (>20 dB) of Fe_2B , a member of the MBene family, is exciting for the use of 2D materials in electromagnetic shielding.

VI. REFERENCES

- [1] D. Bor, (2015) "Radyasyon nedir?" Halkımız için bilgilendirme kılavuzu Ankara Üniversitesi Fizik Mühendisliği Bölümü [Çevrimiçi]. Erişim: <http://www.radkorder.org/wp-content/upload/2016/09/RADYASYON NED%C4%BOR.pdf>
- [2] Y. E. Togay, "Radyasyon ve biz," *Türkiye Atom Enerjisi Kurumu Yayınları*, c. 2, s. 12, 2002.
- [3] A. Türkkan, O. Çerezci ve K. Pala, *Elektromanyetik Alan ve Sağlık Etkileri*, Bursa, Türkiye: F. Özsan Matbaacılık, 2012.
- [4] A. Balmori, "Electromagnetic pollution from phone masts. Effects on wildlife," *Pathophysiology*, vol. 16, no. 2-3, pp. 191-199, 2009.
- [5] P. Bandara and D. O. Carpenter, "Planetary electromagnetic pollution: it is time to assess its impact," *The Lancet Planetary Health*, vol. 2, no. 12, pp. e512-e514, 2018.
- [6] F. Çerezci, "K-means algoritması ile elektromanyetik kirlilik analizi," Bilgisayar ve Bilişim Mühendisliği, Yüksek lisans tezi, Sakarya Üniversitesi, Sakarya, Türkiye, 2015.
- [7] G. Redlarski, B. Lewczuk, A. Zak, A. Koncicki, M. Krawczuk, J. Piechocki, K. Jakubiuk, P. Tojza, J. Jaworski, D. Ambroziak, L. Skarbek and D. Gradolewski "The influence of electromagnetic pollution on living organisms: historical trends and forecasting changes," *BioMed Research International*, vol. 2015, no. 1, pp. 234098, 2015.
- [8] O. Elmas, "Effects of electromagnetic field exposure on the heart: a systematic review," *Toxicology and Industrial Health*, vol. 32, no. 1, pp. 76-82, 2016.
- [9] A. Ahlbom and M. Feychting, "Electromagnetic radiation: environmental pollution and health," *British Medical Bulletin*, vol. 68, no. 1, pp. 157-165, 2003.
- [10] L. Cui, Y. Wang, X. Han, P. Xu, F. Wang, D. Liu, H. Zhao and Y. Du "Phenolic resin reinforcement: a new strategy for hollow NiCo@ C microboxes against electromagnetic pollution," *Carbon*, vol. 174, pp. 673-682, 2021.
- [11] R. Yılmaz, "Elektromanyetik kalkanlama özelliği olan malzemeler," *Electronic Journal of Vocational Colleges*, vol. 4, no. 1, pp. 136-150, 2014.
- [12] M. Altun, İ. Karteri, M. Güneş, and M. H. Alma, "Grafen katkılı odun-plastik nanokompozitlerinin elektromanyetik özellikleri ve elektromanyetik kalkanlama etkinliği karşılaştırmalı çalışması," *Kahramanmaraş Sütçü İmam Üniversitesi Mühendislik Bilimleri Dergisi*, c. 20, s. 1, ss. 38-47, 2017.
- [13] L. Chhaya, "EMR pollution-an imperceptible threat for safety," *SSRN*, 2165743, 2012.
- [14] S. Ghosh, S. Ganguly, P. Das, T.K. Das, M. Bose, N.K. Singha, A.K. Das and N. Ch. Das, "Fabrication of reduced graphene oxide/silver nanoparticles decorated conductive cotton fabric for high performing electromagnetic interference shielding and antibacterial application," *Fibers and Polymers*, vol. 20, pp. 1161-1171, 2019.
- [15] A. Kaşgöz, "Elektromanyetik dalga kalkanlama özelliğine sahip polimer kompozitlerin geliştirilmesi ve yapı-performans ilişkilerinin incelenmesi," Doktora tezi, Kimya Mühendisliği Bölümü, İstanbul Üniversitesi, İstanbul, Türkiye, 2017.
- [16] V. Shukla, "Review of electromagnetic interference shielding materials fabricated by iron ingredients," *Nanoscale Advances*, vol. 1, no. 5, pp. 1640-1671, 2019.

- [17] E. Zornoza, G. Catalá, F. Jiménez, L. G. Andión, and P. Garcés, "Electromagnetic interference shielding with Portland cement paste containing carbon materials and processed fly ash," *Materiales de Construcción*, vol. 60, no. 300, pp. 21-32, 2010.
- [18] R. Çelen and Y. Ulcay, "Baryum Titanatin Tekstilde Elektromanyetik Kalkanlama Uygulamalarında Kullanımı," *Uludağ Üniversitesi Mühendislik Fakültesi Dergisi*, c. 23, s. 2, ss. 29-44, 2018.
- [19] A. Iqbal, P. Sambyal, and C. M. Koo, "2D MXenes for electromagnetic shielding: a review," *Advanced Functional Materials*, vol. 30, no. 47, pp. 2000883, 2020.
- [20] M. González, J. Pozuelo, and J. Baselga, "Electromagnetic shielding materials in GHz range," *The Chemical Record*, vol. 18, no. 7-8, pp. 1000-1009, 2018.
- [21] P. Banerjee, Y. Bhattacharjee, and S. Bose, "Lightweight epoxy-based composites for EMI shielding applications," *Journal of Electronic Materials*, vol. 49, pp. 1702-1720, 2020.
- [22] S. Geetha, K. Satheesh Kumar, C. R. Rao, M. Vijayan, and D. Trivedi, "EMI shielding: Methods and materials—A review," *Journal of Applied Polymer Science*, vol. 112, no. 4, pp. 2073-2086, 2009.
- [23] H. W. Ott, *Electromagnetic Compatibility Engineering*, vol. 11, New Jersey, USA: John Wiley & Sons, 2011, pp. 423–459.
- [24] H. Liu, A.T. Neal, Z. Zhu, Z. Luo, X.Xu, D. Tomanek and P. D. Ye, "Phosphorene: an unexplored 2D semiconductor with a high hole mobility," *ACS Nano*, vol. 8, no. 4, pp. 4033-4041, 2014.
- [25] B. Anasori, M. R. Lukatskaya, and Y. Gogotsi, "2D metal carbides and nitrides (MXenes) for energy storage," in *MXenes*: Jenny Stanford Publishing, 2023, pp. 677-722.
- [26] M. Naguib, O. Mashtalir, J. Carle, V. Presser, J. Lu, L. Hultman, Y. Gogotsi and M. W. Barsoum, "Two-dimensional transition metal carbides," *ACS Nano*, vol. 6, no. 2, pp. 1322-1331, 2012.
- [27] Z. Jiang, P. Wang, X. Jiang, and J. Zhao, "MBene (MnB): a new type of 2D metallic ferromagnet with high Curie temperature," *Nanoscale Horizons*, vol. 3, no. 3, pp. 335-341, 2018.
- [28] T. Zhang, B. Zhang, Q. Peng, J. Zhou, and Z. Sun, "Mo₂B₂ MBene-supported single-atom catalysts as bifunctional HER/OER and OER/ORR electrocatalysts," *Journal of Materials Chemistry A*, vol. 9, no. 1, pp. 433-441, 2021.
- [29] J. P. Perdew, K. Burke, and M. Ernzerhof, "Generalized gradient approximation made simple," *Physical Review Letters*, vol. 77, no. 18, pp. 3865, 1996.
- [30] B. Hammer, L. B. Hansen, and J. K. Nørskov, "Improved adsorption energetics within density-functional theory using revised Perdew-Burke-Ernzerhof functionals," *Physical Review B*, vol. 59, no. 11, pp. 7413, 1999.
- [31] S. J. Clark, M. D. Segall, C. J. Pickard, P. J. Hasnip, M. I. J. Probert, K. Refson and M.C. Payne, "First principles methods using CASTEP," *Zeitschrift Für Kristallographie-Crystalline Materials*, vol. 220, no. 5-6, pp. 567-570, 2005.
- [32] E. Engel and R. M. Dreizler, *Density Functional Theory*, vol. 2, 1st ed., Springer Verlag, Berlin: pp. 11-56, 2011.
- [33] K. Momma and F. Izumi, "VESTA 3 for three-dimensional visualization of crystal, volumetric and morphology data," *Journal of Applied Crystallography*, vol. 44, no. 6, pp. 1272-1276, 2011.

- [34] G. Kumar, *Crystal Field Theory: Analyzing Molecular Structures and Properties*, A Textbook of Objective Inorganic Chemistry, 2022 (Revised) ed. vol. 12, New Delhi India: Wisdom Pres, 2022, pp. 86-93.
- [35] S. Singh, P. Tripathi, A. Bhatnagar, Ch. R. P. Patel, A. P. Singh, S. K. Dhawan, B. K. Gupta and O. N. Srivastava, "A highly porous, light weight 3D sponge like graphene aerogel for electromagnetic interference shielding applications," *RSC Advances*, vol. 5, no. 129, pp. 107083-107087, 2015.
- [36] L. Zhang, N. T. Alvarez, M. Zhang, M. Haase, R. Malik, D. Mast and V. Sahanov, "Preparation and characterization of graphene paper for electromagnetic interference shielding," *Carbon*, vol. 82, pp. 353-359, 2015.
- [37] P. Kumar, F. Shahzad, S. Yu, S. M. Hong, Y.-H. Kim, and C. M. Koo, "Large-area reduced graphene oxide thin film with excellent thermal conductivity and electromagnetic interference shielding effectiveness," *Carbon*, vol. 94, pp. 494-500, 2015.
- [38] L. Paliotta, G. D. Bellis, A. Tamburrano, F. Marra, A. Rinaldi, S.K. Balijepalli, S. Kaciulis and M. S. Sarto, "Highly conductive multilayer-graphene paper as a flexible lightweight electromagnetic shield," *Carbon*, vol. 89, pp. 260-271, 2015.
- [39] X. Luo and D. Chung, "Electromagnetic interference shielding reaching 130 dB using flexible graphite," *MRS Online Proceedings Library*, vol. 445, pp. 235-238, 1996.
- [40] B. Shen, W. Zhai, and W. Zheng, "Ultrathin flexible graphene film: an excellent thermal conducting material with efficient EMI shielding," *Advanced Functional Materials*, vol. 24, no. 28, pp. 4542-4548, 2014.
- [41] A. Iqbal, F. Shahzad, K. Hantanasirisakul, M. Kim, J. Kwon, J. Hong, H. Kim, D. Kim, Y. Gogotsi and C. M. Koo, "Anomalous absorption of electromagnetic waves by 2D transition metal carbonitride Ti₃CNT_x (MXene)," *Science*, vol. 369, no. 6502, pp. 446-450, 2020.
- [42] M. Han, C. E. Shuck, R. Rakhmanov, D. Parchment, B. Anasori, C. M. Koo, G. Friedman and Y. Gogotsi, "Beyond Ti₃C₂T_x: MXenes for electromagnetic interference shielding," *ACS Nano*, vol. 14, no. 4, pp. 5008-5016, 2020.
- [43] H. Wei, M. Wang, W. Zheng, Z. Jiang, and Y. Huang, "2D Ti₃C₂T_x MXene/aramid nanofibers composite films prepared via a simple filtration method with excellent mechanical and electromagnetic interference shielding properties," *Ceramics International*, vol. 46, no. 5, pp. 6199-6204, 2020.
- [44] C. Xiang, R. Guo, S. Lin, S. Jiong, J. Lan, C. Wang, C. Cui, H. Xiao and Y. Zhang, "Lightweight and ultrathin TiO₂-Ti₃C₂TX/graphene film with electromagnetic interference shielding," *Chemical Engineering Journal*, vol. 360, pp. 1158-1166, 2019.
- [45] F. Shahzad, M. Alhabeab, C. B. Hatter, B. Anasori, S. M. Hong, C. M. Koo and Y. Gogotsi, "Electromagnetic interference shielding with 2D transition metal carbides (MXenes)," *Science*, vol. 353, no. 6304, pp. 1137-1140, 2016.
- [46] Q. Wen, W. Zhou, J. Su, Y. Qing, F. Luo, and D. Zhu, "High performance electromagnetic interference shielding of lamellar MoSi₂/glass composite coatings by plasma spraying," *Journal of Alloys and Compounds*, vol. 666, pp. 359-365, 2016.
- [47] T. Zhou, H. Ni, Y. Wang, C. Wu, H. Zhang, J. Zhang, A. P. Tomsia, L. Jiang and Q. Cheng, "Ultratough graphene-black phosphorus films," *Proceedings of the National Academy of Sciences*, vol. 117, no. 16, pp. 8727-8735, 2020.

[48] X. Zhang, X. Zhang, M. Yang, S. Yang, H. Wu, S. Guo and Y. Wang, "Ordered multilayer film of (graphene oxide/polymer and boron nitride/polymer) nanocomposites: an ideal EMI shielding material with excellent electrical insulation and high thermal conductivity," *Composites Science and Technology*, vol. 136, pp. 104-110, 2016.



Düzce University Journal of Science & Technology

Review Article

New Approaches and Theories in Understanding Intelligence and Cognitive Ability Processes

 Hatice YILDIRIM ^{a,*},  Latif Gürkan KAYA ^b

^a Mekansal Planlama ve Tasarım Anabilim Dalı, Fen Bilimleri Enstitüsü, Burdur Mehmet Akif Ersoy Üniversitesi, Burdur, TÜRKİYE

^b Peyzaj Mimarlığı Bölümü, Mühendislik Mimarlık Fakültesi, Burdur Mehmet Akif Ersoy Üniversitesi, Burdur, TÜRKİYE

* Sorumlu yazarın e-posta adresi: yildirim.tugba@hotmail.com

DOI: 10.29130/dubited.1635523

ABSTRACT

This article aims to provide a comprehensive framework for understanding the multifaceted nature of intelligence. The development of the concept of intelligence in the historical process, different theoretical approaches and assessment tools developed based on these approaches are discussed. Intelligence has attracted the attention of researchers throughout history due to its complex and multidimensional nature and has been examined by various disciplines from different perspectives. Approaches to the definition and measurement of intelligence have been discussed in a wide perspective ranging from ancient Greek mythology to contemporary scientific and philosophical frameworks. While intelligence was initially treated as one of the main topics of philosophy, with the development of psychology as a modern discipline in the mid-20th century, it has been the subject of extensive research in this field as well. Today, thanks to technological advances and advanced imaging techniques, it has also intersected with the field of neuroscience, enabling more in-depth studies on the biological basis of cognitive processes. So, what is the reason why intelligence cannot be defined at a common point? In this study, which answers this question, it is seen that intelligence is not only limited to individual cognitive capacities but also interacts with many variables such as environmental, genetic, psychological and sociocultural factors. A multidisciplinary approach to understanding the complex relationships between individual differences, genetic inheritance, environmental conditions and psychological processes is needed in intelligence-related research.

Keywords: Cognitive Ability, intelligence, intelligence theories and classification, intelligence measurement methods

Zeka ve Bilişsel Yetenek Süreçlerini Anlamada Yeni Yaklaşım ve Kuramlar

ÖZ

Bu makale, zekânın çok yönlü doğasını anlamak için kapsamlı bir çerçeve sunmayı amaçlamaktadır. Zekâ kavramının tarihsel süreç içerisindeki gelişimi, farklı kuramsal yaklaşımlar ve bu yaklaşımlara dayalı olarak geliştirilen değerlendirme araçları ele alınmaktadır. Zekâ, karmaşık ve çok boyutlu yapısı nedeniyle tarih boyunca araştırmacıların ilgisini çekmiş ve çeşitli disiplinler tarafından farklı bakış açılarıyla incelenmiştir. Zekânın tanımı ve ölçülmesine yönelik yaklaşımlar, Antik Yunan mitolojisinden günümüz bilimsel ve felsefi çerçevelerine kadar uzanan geniş bir perspektifte ele alınmıştır. Zekâ, başlangıçta felsefenin temel konularından biri olarak ele

alınırken 20. yüzyılın ortalarında psikolojinin modern bir disiplin olarak gelişmesiyle birlikte bu alanda da kapsamlı araştırmalara konu olmuştur. Günümüzde ise teknolojik ilerlemeler ve gelişmiş görüntüleme teknikleri sayesinde nörobilim alanıyla da kesişmiş, bilişsel süreçlerin biyolojik temelleri üzerine daha derinlemesine çalışmalar yapılmasına imkân tanınmıştır. Peki zekânın ortak bir noktada tanımlanamamasının nedeni nedir? Bu soruya da cevap niteliğinde olan bu çalışmada görülmektedir ki zekâ, yalnızca bireysel bilişsel kapasitelerle sınırlı kalmayıp çevresel, genetik, psikolojik ve sosyokültürel faktörler gibi birçok değişkenle etkileşim içindedir. Zekâyla ilişkili araştırmalarda; bireysel farklılıklar, genetik miras, çevresel koşullar ve psikolojik süreçler arasındaki karmaşık ilişkilerin anlaşılmasına yönelik çok disiplinli bir yaklaşımın ele alınması gerekmektedir.

Anahtar Kelimeler: Bilişsel Yetenek, Zeka, Zeka Kuramları ve Sınıflandırılması, Zeka Ölçme Yöntemleri

I. INTRODUCTION

The word “genius”, which was considered synonymous with the concept of creativity between the XVIIth and XXth centuries, was expressed by the word “genius” in English and Latin. Its original origin is the Greek word “ginesthai”, which means “to come into existence out of nothing, to be born”. Today, the word genius is used to refer to people with creative and extraordinary intelligence [1].

In the history of mankind, it is seen that issues related to intelligence were first addressed in Greek mythology and were considered as a part of philosophy at the end of the eighteenth century. In the XXth century, with the emergence of psychology as a science, it became one of the most important research topics of the period [2].

Sir Francis Galton (1822-1911) was one of the first researchers to study intelligence. Since he was the cousin of Charles Robert Darwin (1809-1882), the founder of the theory of evolution by natural selection, he was influenced by heredity studies and conducted studies on the inheritance of intelligence between individuals [2, 3, 4]. He argued that the differences between individuals are due to intelligence transmitted through heredity [3, 5] and did not focus on the relationship between intelligence and environmental factors [6].

II. INTELLIGENCE

A. DEFINITION OF INTELLIGENCE

Intelligence consists of the ability to understand, comprehend, associate, integrate, evaluate and interpret parts or information in the learning process [4, 7]. In the psychometric approach, one of the sub-branches of psychology, the definition of the concept of intelligence and the measurement of cognitive abilities related to intelligence are discussed. Different theories have been developed by researchers working in this field [8].

When traditional definitions of intelligence are examined, it is seen that the ability to adapt to the environment is emphasized rather than shaping the environment. Until the mid-20th century, it was stated by different philosophers that intelligence is the power to solve all kinds of problems. The first intelligence test was introduced by Binet in 1908. Binet described intelligence as the ability to adapt to the environment and to judge [9].

The editors of the “Journal of Educational Psychology” organized a symposium in 1921 by inviting 14 scientists who were experts in their fields to work on the definition of intelligence in a common framework, theories about intelligence and how intelligence can be measured [10, 11]. Most of the conceptual definitions of intelligence produced as a result of this symposium are different from each other. In the definitions of intelligence, learning capacity and the ability to adapt to the environment were emphasized. The same study was conducted again by Sternberg and Detterman (1986) [12] with

24 researchers who were experts in their fields [5, 11, 13]. Unlike the first study, the concept of “metacognition” was included in the definition of intelligence in addition to learning capacity and adaptation to the environment [2, 5].

B. THEORIES AND CLASSIFICATION OF INTELLIGENCE

Theories of intelligence have been a core subject of psychology and brain sciences, aiming to understand the diversity of intellectual abilities and the neurobiological mechanisms underlying these abilities. Various theories have been proposed over the years to explain nature and structure of intelligence.

Since many researchers from different disciplines have been working on the subject from past to present, independent qualities have been put forward in the definition and theories of intelligence. The biggest reason why intelligence cannot be defined on a common axis and has become a subject of debate is that it is influenced by social, environmental or genetic external factors and is multifaceted. The field of study of the researcher who developed the definition of intelligence, the environment in which the researcher lived and the cultural characteristics of the period in which the researcher lived are other factors affecting the concepts related to intelligence [5].

In his study, Gardner (2011) [14] analyzed many theories about intelligence and based on the information contained in these theories, he determined the following three most commonly used characteristics of intelligence;

- ✓ Learning capacity: The capacity of the individual to benefit from the training provided,
- ✓ The sum of learned knowledge: All the concepts and information learned within one's own abilities,
- ✓ Adaptability to the demands of the environment: The ability to successfully adapt oneself to one's environment and the changes in it.

Theories of intelligence are generally analyzed in four subgroups (Figure 1).

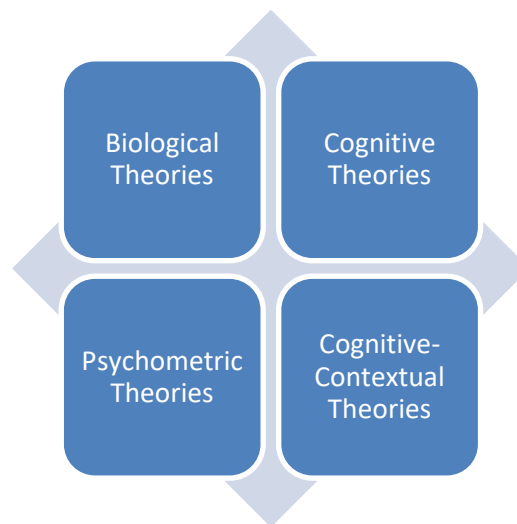


Figure 1. Theories of intelligence [14]

Psychometric theories try to analyze the structure of intelligence in general. Charles Spearman, one of the pioneers of theory, developed intelligence models for both children and adults. He showed that individuals with high mathematical and spatial skills but weak verbal skills can also have high general intelligence. In the intelligence model developed by Charles Spearman, there are two basic components: the s-factor and the g-factor. Specific factors related to a person's experiences or skills in a particular field are the s-factor. The concept that expresses a general measurement of intelligence is the g factor [15]. In the psychometric approach, it is argued that the higher the performance of a person above the

calendar age, the higher the level of intelligence. For this purpose, intelligence age and calendar age calculations are made in the evaluation of intelligence [13]. Since statistical methods such as correlation and factor analysis are used in these calculations, they are considered within psychometric theories [5, 16].

In cognitive theories, in which the processes of intelligence are examined, it is argued that the processes of using intelligence are realized faster and more effectively in intelligent people. The pioneers of this theory are Piaget (1972) [17], Vygotsky (1978) [18], Feuerstein (1980) [19] etc.

Piaget (1972) focused on the maturation of intelligence over time as a result of its interaction with the environment rather than individual differences in intelligence studies [5]. Vygotsky (1978), one of the pioneers of cognitive theory, stated that cognitive development is primarily influenced by the family environment and the first education provided by the immediate environment. For this reason, he believes that if the child does not receive adequate support in the family environment where he/she receives his/her first pre-school achievements, he/she will not be successful in the future [18].

The theory that deals with the relationship between environmental contexts and cognitive processes is Cognitive-contextual theories [11]. In this theory, environmental and cultural factors are needed in addition to cognitive processes for the acquisition of various skills [16]. Examples of cognitive contextual theories are Robert Stenberg's "Successful intelligence theory" and Howard Gardner's "Multiple intelligence theory" [2, 5].

Biological theories are not related to the structure, components and information processing processes of intelligence that the other three theories emphasize. It argues that the brain structure and functions should be examined in order to fully define intelligence [5, 14]. In other words, the ability that is characterized as IQ and tried to be measured by intelligence tests depends on the prefrontal cortex (PFC) and neocortex performance of the brain [2, 11]. Unlike traditional theories of intelligence, other theories in the literature in the historical process are summarized below.

B. 1. Charles Spearman Dual Factor Theory (Two Factor Theory)

In 1904, Spearman found a significant correlation in the test results of a group of students in different courses and developed the factor analysis method. In his other studies, he characterized intelligence as the ability to achieve success in different fields. He states that in studies that require a mental focus, it is necessary to have both general ability and a special ability required for this study. While different cognitive tasks are performed within the mental skill factor, specific factors include specialized mental skills in mathematics, verbal or mechanical fields. Of these two abilities that make up intelligence, "general ability", i.e. "general ability", is called "g", while "special ability", i.e. "special ability", is called "s" [20, 21]. According to Charles Spearman, an individual's general intelligence level can be assessed by measuring general ability. In the graphical model proposed by Guilford in 1953, the "g" factor is depicted as a large central circle, while the "s" factors are presented as small circles arranged around this center (Figure 2). Each ellipse symbolizes a mental test. The intersection ratio of the ellipses with the "g" factor expresses the dependence of the tests on the "g" factor. According to the basic inferences of the model, tests a and b in Figure 2 are highly correlated since they share the "g" factor to a great extent. On the other hand, since tests a and c have a low level of "g" domain, the correlation between them is quite low. In this context, Spearman defined the underlying element of intelligence as the "general factor" (g) and suggested that differences in intelligence between individuals are largely determined by the amount of "g" possessed [22].

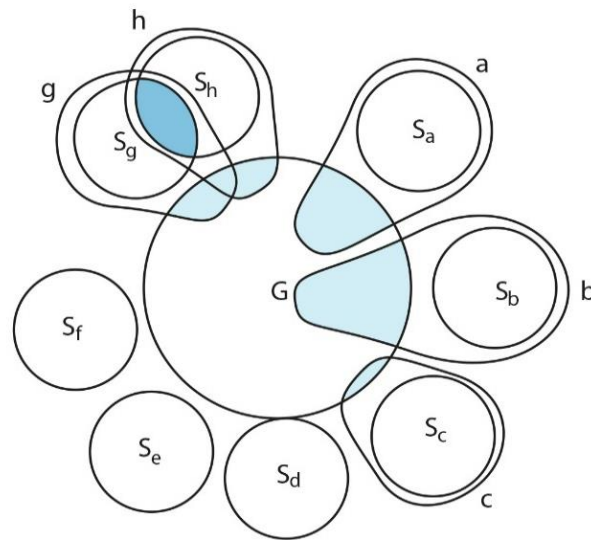


Figure 2. Graphical Representation of the Group Factor in Spearman's Two-Factor Theory (Guilford, 1953, p.475; re-visualized by the authors) [22]

Inspired by these theories developed to measure general intelligence level, the Stanford Binet Intelligence Test was developed in 1916 and the Raven Standard Progressive Matrices Test was developed in 1947 [23].

Charles Spearman, who argues that intelligence is positively correlated with many concepts, shows that intelligence does not originate from a single source but from a multi-structured and complex brain structure, although it has been criticized by researchers [24].

B. 2. Multifactor Theory (Multiple Factor Theory)

According to the Multifactor Theory (MFT), intelligence is not a single dimension but a multi-dimensional structure. Edward L. Thorndike (1909) [25], one of the pioneers of this theory, states that subcomponents such as intelligence level, intelligence breadth and intelligence speed, which reveal the multidimensional structure of intelligence, should be measured in order to measure intelligence capacity [26, 27]. Thorndike divided intelligence into three as abstract, practical (mechanical) and social (social). The ability to think using symbols refers to abstract intelligence; the ability to use machines, devices or tools refers to practical (mechanical) intelligence; and the ability to establish successful interpersonal relationships in the social environment refers to social intelligence [28].

B. 3. Mental Abilities (Group Factor) Theory

Thurstone (1887-1955), in his studies conducted with his students at the University of Chicago, revealed that intelligence is multidimensional according to the results of factor analysis [29]. Thurstone found twelve factors and named seven different main mental factor areas. These are word fluency, numerical ability, verbal comprehension, perceptual speed, memory, visual ability, deductive and inductive reasoning [26].

B. 4. Cattell-Horn-Carroll Theory

The theory was introduced by Cattell in 1943 and later updated by his student Horn. The Cattell-Horn-Carroll Theory was formed by combining Cattell and Horn's theory of fluid and crystallized intelligence with Carroll's three-tier theory (30). According to the Cattell-Horn-Carroll Theory, intelligence is divided into Fluid Intelligence and Crystallized Intelligence (31). Fluid intelligence is the intelligence inherited from our ancestors through our genes and is the ability to solve problems independently of the

environment. Crystallized Intelligence, on the other hand, is the body of knowledge gained as a result of environmental and cultural interactions and varies according to how effectively the person can use these gains [32].

Cattell emphasizes that fluent intelligence is related to neural and biological processes in the brain and states that fluent intelligence plays an important role as the neural substructure of learning. Therefore, it can be said that fluent intelligence is directly influenced by genetic factors. Although crystallized intelligence is not directly affected by genetic factors, it is thought to be indirectly affected in the development of social and cultural aspects of fluent intelligence [33].

This theory is one of the basic theories on which many IQ tests are based today. It is also emphasized that the Cattell-Horn-Carroll theory is a bridge between theory and practice [34, 35].

There are three main factors in the structural model of the theory: fluid intelligence, crystallized intelligence and general intelligence factor (g). These factors are then divided into sub-factors in the second and third layers. For example, the fluency factor consists of the sub-factors processing speed, processing capacity and processing flexibility. The crystallized intelligence factor is divided into sub-factors such as language skills, vocabulary and general culture. There are 84 first-order factors in the theory [36, 37].

B. 5. Vernon's Hierarchical Theory

British psychologist Philip Vernon (1961) proposed that intelligence is a set of skills that differ in various dimensions. Intelligence is divided into 4 different levels of ability. Level 1 is the highest level and relates the differences between individuals to Spearman's 'g' for general intelligence. The next level, level 2, is divided into the main group factors of practical, mechanical and physical abilities, which include abilities such as abstract-numerical, mechanical knowledge, and understanding of spatial relationships. Level 3 includes minor factors. At the 4th level, which is the lowest level, specific characteristics "s" are included [27, 38].

B. 6. The Structure of Intelligence Theory

The Structure of Intelligence Theory was developed by Guilford with the development of Thurstone's theory of mental abilities. According to the structure of intelligence theory, intelligence consists of three basic dimensions: operations, contents and products. According to Guilford (1967) [39], operations are divided into five components, content into four components and product type into six components. These sub-components can be combined with each other in different combinations to create different capabilities [40]. When all combinations are cross classified, 120 different factors are formed [2].

B. 7. Levels of Cognitive Functioning (LCF)

Reuven Feuerstein's "Levels of Cognitive Functioning" (LCF) theory was first developed by Feuerstein in the late 1950s and expanded with new studies in the 1960s and early 1970s. LCF theory states that there is a continuity in the development of cognitive functions and how individuals' cognitive functions can be used in the learning process thanks to this continuity. LCF theory defines different levels of the human mind and identifies the characteristics of mental functions at each level. According to the theory, the development of mental functions is a result of environmental factors and learning rather than innate potential. In LCF theory, there are six levels of mental functions [19]:

- ✓ Detection
- ✓ Attention
- ✓ Memory
- ✓ Logical thinking
- ✓ Abstraction

- ✓ Processing speed

Each of these levels builds on the development of previous levels and forms the basis for the development of the next level. For example, individuals at the perception level must first learn to recognize the stimuli around them to move to the attention level. LCF theory is designed to improve the mental functions of individuals by using it in education and learning processes. The aim of the theory is to increase the learning potential of individuals and to help them use their mental functions more efficiently [19].

B. 8. Multiple Intelligence Theory

The Theory of Multiple Intelligences, proposed by Howard Gardner in 1983, claims that intelligence is basically a result of problem solving and creating products in a rich environment. According to Gardner (1983) [41], intelligence is too complex to be explained by a single factor and can consist of many different areas. Therefore, intelligence cannot be measured objectively with specific instruments. Gardner (1983) defined seven different dimensions of intelligence in his book “Frames of Mind”. In his 1999 publication “Intelligence Reframed”, he divided intelligence into eight different types by adding a new dimension of intelligence: logical-mathematical intelligence, verbal-linguistic intelligence, visual-spatial intelligence, musical-rhythmic intelligence, bodily-kinesthetic intelligence, intrapersonal intelligence, social intelligence, and naturalistic intelligence [16].

B. 9. Piaget's Theory of Intelligence

In accordance with the values of the period, Piaget defines intelligence in general as “the ability to know” [17]. Calling his theoretical framework “genetic epistemology”, Piaget points to the developmental characteristics of the individual, while epistemology provides a framework for determining the nature, scope and validity of knowledge. With this approach, Piaget emphasized that intelligence has a biological dimension and argued that intelligence is also related to logical processes [42, 43].

Piaget often mentioned the concepts of assimilation, accommodation and schema when explaining intelligence and knowledge. Assimilation and adaptation are seen as complementary functions that emerge depending on the interaction of the organism with the environment [43]. Assimilation can be defined as the process of internalizing information in general. When the organism encounters a new situation, it explains this situation using its existing schemas. These schemas are the structures that the organism creates to make sense of the environment and they develop with experiences. Adaptation is an innate skill and the organism achieves success by trying to adapt to the environment with the schemas it has formed [2, 17, 42, 44].

Although Piaget agrees with other psychologists such as Spearman on the existence of a single general phenomenon of intelligence, he argues that intelligence acquires a general form by passing through certain stages of development. These stages are: Sensory Motor Period, Preoperational Period, Concrete Operations Period and Abstract Operations Period [2, 5, 17, 44].

B. 10. Starfish Theory

In the theory developed by Tannenbaum (1983) [45], five traits related to intelligence are expressed by likening them to starfish. The characteristics at the five ends of the starfish predict the formation of intelligence. These five characteristics are general ability, distinctive special ability, environmental factors, chance factors and other non-mental factors [21, 46]. General ability refers to the area of ability that can be measured by standardized intelligence tests and is used to determine individual differences. Special talent, on the other hand, refers to an individual's superior abilities in a specific field: painting, music, mathematics, etc. These special talents often emerge at an early age and are discovered by their environment. Environmental factors refer to the areas of intelligence that are influenced by an

individual's immediate or distant environment. The luck factor is related to coincidences in life and refers to factors that help potential intelligence to emerge. Other non-mental factors refer to areas such as dedication to work, volunteerism, and self-belief independent of mental factors [46, 47].

B. 11. Differential Giftedness and Giftedness Theory

Gagne (1985) [48], stated that giftedness and giftedness are different concepts. According to the Differential Giftedness and Giftedness Theory, giftedness includes natural abilities based on biological and genetic foundations. He stated that it is innate, transmitted to future generations through hereditary ways and manifested in at least one field. Giftedness, on the other hand, consists of skills developed in a field [49, 50].

Gagne (2000) [51], adopts the idea that the transformation of giftedness into giftedness occurs as a result of a complex process. This theory points to a stage in which the potential of giftedness is transformed into giftedness and performance emerges. While the theory assumes that every gifted individual is gifted, it focuses on the fact that not every gifted individual may be gifted [21].

According to the theory, there are four different areas of giftedness and talent, such as intellectual, creative and sensory areas. However, certain catalysts are required for giftedness to transform into giftedness. These catalysts consist of various factors such as individual factors, environmental factors and chance factors [51].

B. 12. Successful Theory of Intelligence (Triarchic Theory of Intelligence)

In Sternberg's theory of intelligence put forward in 1985, there are three types of intelligence: analytical, creative and practical intelligence [52]. Analytical intelligence includes processes such as logical thinking, reasoning and comparison. Creative intelligence refers to the ability to cope with new situations and to produce extraordinary solutions to problems. Practical intelligence is the use and application of analytical and creative intelligence in daily life [53].

In what Sternberg (1985) [54] calls the Theory of Successful Intelligence, intelligence is divided into three different reasoning processes. Analytical thinking skills, problem solving skills and practical thinking skills are included in the theory that examines intelligence in analytical, synthesizing and practical aspects [55]. Analytical intelligence can be measured by traditional intelligence tests. Creative intelligence includes learning from lifelong experiences and creative thinking skills. Practical intelligence helps the individual to adapt to the socio-cultural environment [8, 56].

Sternberg argues that individuals who can use these three different reasoning processes can be more successful in life [2, 57]. It is emphasized that individuals can achieve success not only in one field of intelligence but also in different combinations of all fields. It is stated that individuals who become prominent in only one field of intelligence may have difficulty in making themselves accepted [2, 58].

Sternberg (1985) put forward his theory, which he called the Successful Intelligence Theory, by suggesting that intelligence is divided into three different reasoning processes. Also known as the Triple Right Foot Theory, it examined intelligence in analytical, synthetic and practical aspects [55]. In the first reasoning process, logical and analytical thinking skills can be used and measured with traditional intelligence tests. The second process includes problem solving, learning from lifelong experiences and creative thinking skills. The third reasoning process consists of practical thinking skills and helps the individual adapt to his/her social and cultural environment and surroundings [8, 56]. Sternberg argues that individuals who use these three different reasoning processes can be more successful in life [2, 57].

B. 13. Triple Circle Model

Following his intelligence studies, Renzulli (1986) [59] developed a theory called the triple circle model. In this theory, he categorized gifted individuals as those who are at the intersection of creativity, motivation (task commitment), and above average general or special abilities [60]. While general ability includes abstract thinking, word fluency, memory and reasoning skills, special ability includes above-average ability in specific areas such as painting, music, dance, mathematics and language acquisition. The creativity component refers to an individual's different, innovative and out-of-the-box thinking [61]. Creativity also includes processes that bring originality. Motivation, on the other hand, covers areas other than direct mental functions such as dedication to a task, willingness to undertake a task and patience. According to this theory, a certain level of interaction between these three clusters must take place to achieve superior achievement. For an individual to meet the criteria of superiority, he/she must be 85% more successful than 85% of his/her peers in all these areas and at least 98% more successful than his/her peers in one cluster [62].

B. 14. Pentagon Theory

The theory was proposed by Sternberg and Zhang (1995) [63] and is based on the idea that the use of IQ score alone in determining intelligence is insufficient [46]. Each corner of the pentagon shape, which gives its name to the theory, is evaluated as extraordinary, rarity, evidence, productivity and value criteria [63].

According to this theory, the concept of exceptionalism requires the individual to be different and unique from society. In the concept of exceptionalism, the individual is expected to make a difference in terms of mental capacity. The criterion of rarity means that the individual has rare talents. The criterion of productivity means that the individual should produce a unique product in the areas in which he/she has talent. Evidence criterion can be defined as the proof and acceptance of these cognitive characteristics of the individual [63].

C. METHODS OF INTELLIGENCE MEASUREMENT

Tests have been developed for different age groups to measure intelligence. An intelligence scale is defined as a series of questions and problems prepared to measure intelligence [64]. The tests and methods developed to measure intelligence are listed below.

C. 1. Porteus Labyrinths Test

Porteus Labyrinths Test is a performance-based intelligence test developed by Porteus to determine an individual's planning and adaptation skills to innovations. It is administered using only paper and pencil [65]. It was adapted into Turkish by Toğrol (1974) [66]. The test, which is used to evaluate the practical analytical thinking skills of children between the ages of 7 years and 3 months and 15 years, consists of 13 mazes and the person is expected to plan the path to be followed and reach the exit without error [67]. The difficulty level of the test increases towards the 13th maze. The test is administered by certified testers who receive special training [8].

C. 2. Catell 2A Intelligence Test

The other test used to measure intelligence was developed by Cattell and adapted in Turkey by Toğrol (1974) [66]. The test, which consists of a total of 50 questions, is administered individually or as a group to individuals aged 14 and over. The administration time of the test is approximately 25 minutes and consists of 4 subscales [8]. During the application period, a series of shapes are given in each scale and it is asked to find the shape that should continue the series or the shape that breaks the series. A score of "1" is received for each question answered correctly and the individual's intelligence score is

calculated by converting the total score. The correlation coefficients of the 2A and 2B forms of the test are above 0.50 [67, 68].

C. 3. Kaufman Brief Intelligence Test (KBIT)

The first version of the Kaufman Brief Intelligence Test (KBIT) consists of verbal (Verbal Knowledge and Puzzles-Vocabulary) and non-verbal (Reasoning Squares) subscales [69]. The vocabulary test, which represents the verbal part, is divided into two subscales: “Part A: Expressive Vocabulary” and “Part B: Definitions”. In the verbal knowledge part of the test, the person is shown different visuals (e.g. planet, t-ruler, tennis, etc.) and asked to vocalize them aloud. In the definitions section, the test taker is given various clues and asked to correctly complete the missing word. The test taker is given a clue to define the word (e.g., it is a material used in construction) and a version of the word with some letters missing (e.g., concrete) and is expected to give the correct answer. In order to measure crystallized intelligence as defined by Horn and Cattell (1966) [70], the focus is on language skills and general knowledge acquired through schooling. “Section B: Definitions” section requires literacy skills. Therefore, it can be administered to people at least eight years of age and older. The “Reasoning Squares” subtest, which aims to measure fluent intelligence (nonverbal abilities and immediate problem solving ability), includes abstract patterns and various pictures [71]. In the “Reasoning Squares” subtest, individuals are asked to select the one that is related to the stimulus picture among various pictures shown to them. The first version of the KBIT was translated into Turkish by Savaşan (2006) [72] as part of his master's thesis [73]. Its standardization for Turkey was carried out by Öktem and Uluç within the scope of a project conducted by the Department of Special Education of the Ministry of National Education. It has been stated that it is suitable for both educational, research and clinical evaluation purposes [74].

The test can be administered to people between the ages of 4-90 years and 15-30 minutes should be given according to different age groups. The test can be administered by educators and trained individuals, and formal training is required for the interpretation of test scores [75; 76].

C. 4. Kaufman Brief Intelligence Test - Second Edition (KBIT-2)

The Kaufman Brief Intelligence Test - Second Edition (KBIT-2), which can be administered to individuals between the ages of 4-46, consists of verbal (Verbal Knowledge and Puzzles) and non-verbal (Reasoning Squares) subscales. The administration time of the test varies according to different age groups and lasts between 15-30 minutes [77]. The second version of the test, the first of which was developed by Kaufman and Kaufman in 1990, was published in 2004 [75; 78]. In the second version of the test, individuals are given various visuals and asked to express them aloud, solve puzzles, find the correct visual and find the results associated with the visual stimuli. The test was standardized for Turkey by Öktem and Uluç as part of a project conducted by the Ministry of National Education, Department of Special Education. It was stated that it is suitable for both educational, research and clinical evaluation purposes [74]. The internal consistency coefficient of the test varies between 0.93-0.96; the half-test reliability coefficient varies between 0.95-0.97. It can be used for education, research and clinical evaluation purposes [68, 74].

C. 5. Wechsler Adult Intelligence Scale-Revised Form (WAIS-R)

The Wechsler Intelligence Scale for Adults provides a measure and assessment of the intellectual structure and development of adults aged 16-94. The test is administered individually. It is an intelligence test that evaluates 2 sub-domains (verbal and performance), consists of a total of 11 subscales (General Knowledge, Picture Completion, Number Sequence, Vocabulary, Picture Arrangement, Patterning with Cubes, Arithmetic, Piece Assembly, Judgment, Cipher and Similarities) and takes approximately 1.5-2 hours to administer. The verbal section includes general knowledge, arithmetic, number repetition/number sequence, similarities, and reasoning subtests. The performance section includes picture arrangement, pattern with cubes, picture completion, cipher and piece

combination tests. Three types of intelligence scores are calculated: verbal, performance and total. The first version of the scale was developed by Wechsler in 1939 [77].

Preliminary studies on the standardization of the Wechsler Adult Intelligence Scale Revised Form (WAIS-R) in Turkey were conducted by Sezgin, Baştuğ, Yargıcı Karaağaç, and Yılmaz. The Cronbach-Alpha reliability coefficient of the verbal subscales was between 0.78-0.91; the Cronbach-Alpha reliability coefficient of the performance subscales was between 0.69-0.84; and the Cronbach-Alpha reliability coefficient of the total intelligence section was 0.84. Inter-rater reliability coefficients are also between 0.59-0.99 according to subscales [77].

C. 6. Raven IQ Test

The Raven test was developed by John C. Raven in England in 1936 (79). Raven's Progressive Matrices, simple form or Raven's Matrices, are classified as non-verbal IQ tests used for educational purposes. These tests are among the most comprehensive and widespread tests that can be used in a wide range of age groups, from five-year-old children to elderly individuals [80].

Raven's Advanced Progressive Matrices is a special form of the Raven Matrices test designed specifically to distinguish above-normal intelligence levels. This test is designed as two sets of questions in two different booklets. The first booklet consists of 12 questions designed to distinguish between different levels of intelligence among individuals. The second booklet contains 36 questions designed to distinguish individuals more clearly.

All questions in the second booklet are in the form of rectangular matrices consisting of three columns and three rows and containing organized figures and visuals. The last cell of this matrix is always left blank. The content of the figures in the other eight cells is based on certain abstract rules. The tested individual guesses the content of the ninth cell by discovering these rules through trial and error. Six to eight optional answers are designed for each question (Figure 3).

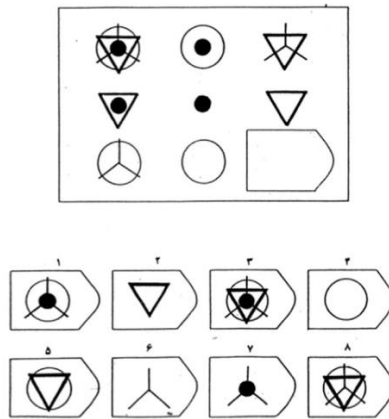


Figure 3. An example of Raven's progressive matrices [81]

This test form assesses the individual's abstract reasoning ability, especially the ability to solve/guess the relationship between the components of each question, to identify the basic rules by which the cells are structured, and to recognize the correct answer using these rules [81, 82].

C. 7. Cognitive Ability Measurement Test

Yıldırım (2023) [83], in his Ph.D. thesis entitled "Cognitive Ability-Creativity Relationship in Interior Design and Landscape Architecture Programs and the Effects of Education on Creativity," developed a "Cognitive Ability Measurement Test" to measure cognitive ability in the field of design. In the test designed to assess cognitive ability, coded questions consisting of number and letter sequences,

reasoning square questions, operation and problem questions, visual puzzle questions, weighting questions, numerical and verbal logic questions, three-dimensional (cube) questions, and two-dimensional shape questions were used (Figure 4). Each question is worth 4 points (Table 1) [83].

Table 1. Cognitive Ability Test content analysis [83]

COGNITIVE ABILITY MEASUREMENT CONTENT ANALYSIS OF TEST	QUESTION TYPES	QUESTION NUMBERS WITHIN THE TEST	OBJECTIVES
	Number of Sequence Questions	1st, 2nd, and 13th Questions (Total: 3 Questions)	<ul style="list-style-type: none"> • Visual Perception and Attention • Processing Power • Detailing
	Letter Sequence Questions	7th Question (Total: 1 Question)	<ul style="list-style-type: none"> • Detailing Through Clues • Detailing • Visual Perception and Attention
	Logical Reasoning (Square) Questions	12th Question (Total: 1 Question)	<ul style="list-style-type: none"> • Associating Moving Parts
	Operations and Problem Questions	5th and 8th Questions (Total: 2 Questions)	<ul style="list-style-type: none"> • Processing Ability • Measuring Problem-Solving Skills
	Weight Questions	6th Question (Total: 1 Question)	<ul style="list-style-type: none"> • Processing Ability • Ability to Form Equations
	Visual Puzzle Questions	4th and 14th Questions (Total: 2 Questions)	<ul style="list-style-type: none"> • Solving Encoded Visuals Related to Various Shapes • Visual Judgment • Measuring Visual Perception and Attention
	Verbal and Numerical Logic Questions	Numerical Logic Questions: 20th and 21st Questions Verbal Logic Questions: 22nd, 23rd, 24th, 25th Questions (Total: 6 Questions)	<ul style="list-style-type: none"> • Measuring Thinking Skills and Solving Problems Within Given Time Limits Through Verbal and Numerical Logic Questions
	Three-Dimensional Thinking (Cube) Questions	3rd, 16th, 17th, and 18th Questions (Total: 4 Questions)	<ul style="list-style-type: none"> • Three-Dimensional Thinking, Perception, and Visualization Ability
	Two-Dimensional Shape Questions	9th, 10th, 11th, 15th, and 19th Questions (Total: 5 Questions)	<ul style="list-style-type: none"> • Two-Dimensional Thinking, Perception, and Visualization Ability on a Surface

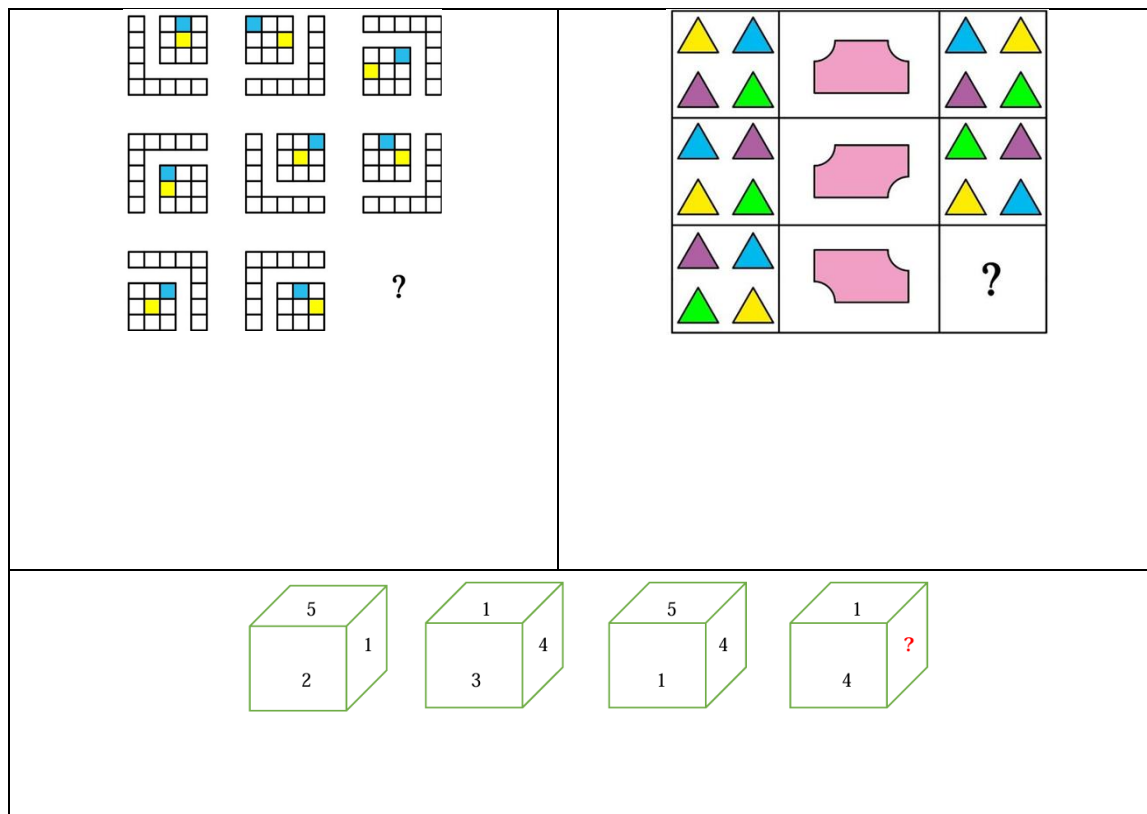


Figure 4. Sample questions from the Cognitive Ability Assessment Test [83]

III. CONCLUSION

In conclusion, the concept of intelligence has been analyzed from different perspectives by different disciplines throughout history and has evolved in line with scientific developments. While philosophers have treated intelligence as an abstract concept since ancient times, with modern science, disciplines such as psychology, neuroscience, and cognitive science have begun to study intelligence in a more systematic and measurable way. Francis Galton initiated the first systematic studies of intelligence in the context of individual differences and integrated statistical methods into the measurement of intelligence. Later, Alfred Binet and Theodore Simon developed the Binet-Simon Scale to assess children's cognitive development, laying the foundation for modern intelligence testing. Lewis Terman revised this scale as the Stanford-Binet Test and introduced the concept of IQ into intelligence measurement.

In terms of theories of intelligence, Charles Spearman's theory of general intelligence (g factor) suggests that intelligence consists of a single general factor, while Howard Gardner's theory of multiple intelligence argues that individuals have different types of intelligences. Robert Sternberg, on the other hand, evaluated analytical, creative, and practical intelligence together in his Triadic Theory of Intelligence. The work of these scientists played a critical role in understanding the nature of intelligence and shaped the methods used to assess intelligence.

Scientific developments in measurement techniques have also shaped intelligence research. From the first psychometric tests used to understand cognitive processes to the neurological techniques used today, such as functional magnetic resonance imaging (fMRI) and electroencephalography (EEG). Modern research takes a more holistic approach, seeking to understand the effects of genetic inheritance, environmental factors, and individual experience on intelligence.

Using the scientific method, intelligence research has progressed through stages of hypothesis development, experimental testing, data analysis, and interpretation of results. This process, which began with philosophical inquiry in the early days, has been supported by experimental methods, strengthened by statistical analysis, and reached a more objective point with advanced imaging techniques today. However, the exact definition and measurement of intelligence is still the subject of ongoing scientific debate. Future interdisciplinary research will contribute to a more comprehensive understanding of intelligence and bring new dimensions to its applications in fields such as education, health, and artificial intelligence.

IV. REFERENCES

- [1] N. C. Andreasen, "Yaratıcı Beyin: Dehanın Nörobilimi," 9. baskı. Ankara, Türkiye: Akılçelen Kitaplar, 2019, 247s.
- [2] G. İnci, "Galton'dan Günümüze Zekâ ve Zekâ Kuramları," *Ordu Üniversitesi Sosyal Bilimler Araştırmaları Dergisi*, c. 11, s. 3, ss. 1053-1068, 2021.
- [3] G. A. Davis ve S. B. Rimm, "Education of the Gifted and the Talented", 5th ed. Pearson Hall, Inc., 2004.
- [4] E. Gürel ve M. Tat, "Çoklu Zekâ Kuramı: Tekli Zekâ Anlayışından Çoklu Zekâ Yaklaşımına," *Journal of International Social Research*, c. 3, s. 11, 2010.
- [5] R. J. Sternberg, "Intelligence," in "Handbook of Psychology, History of Psychology," I. B. Weiner, Ed. New Jersey, USA: John Wiley & Sons, 2003, pp. 136-152.
- [6] B. Clark, "Growing up Gifted: Developing the Potential Children at Home and at School," 5th ed. Upper Saddle River, New Jersey: Prentice Hall, 2002.
- [7] R. Pfeifer ve C. Scheier, "Understanding Intelligence," MIT Press, 2001.
- [8] E. Güneri, "Türkiye'de Kullanılan Psikolojik Testler: Zekâ Testleri," İstanbul, Türkiye: Kaknüs Yayınları, 2016.
- [9] N. Y. Yılmaz ve A. M. Taş, "Başarılı Zekâ Kuramının Kuramsal Yapısı ve Eğitime Yansıması," *Sosyal ve Ekonomik Araştırmalar Dergisi*, c. 18, s. 31, ss. 98, 2016.
- [10] T. R. Miles, "Contributions to Intelligence Testing and the Theory of Intelligence: On Defining Intelligence," *British Journal of Educational Psychology*, vol. 27, no. 3, pp. 153-165, 1957.
- [11] R. J. Sternberg, "Multiple İntelligences in The New Age of Thinking," *Handbook of Intelligence Review*, vol. 16, no. 5, p. 340, 2015.
- [12] R. J. Sternberg and D. K. Detterman, "What is Intelligence?" Norwood, NJ: Ablex, 1986.
- [13] B. Karabey ve K. Yürümezoğlu, "Yaratıcılık ve Üstün Yetenekliliğin Zekâ Kuramları Açısından Değerlendirilmesi," *Buca Eğitim Fakültesi Dergisi*, no. 40, pp. 86-106, 2015.
- [14] M. K. Gardner, "Theories of Intelligence," in "The Oxford Handbook of School Psychology," pp. 79-100, 2011.
- [15] N. Hayes ve S. Tomley, "Bir Bakışta Psikoloji," İstanbul, Türkiye: Nova Kitap, 2021.

- [16] H. Gardner, "Frames of Mind: The Theory of Multiple Intelligences," New York: Basic Books, 2011.
- [17] J. Piaget, "The Psychology of Intelligence," Totowa, NJ: Littlefield Adams, 1972.
- [18] L. S. Vygotsky, "Mind in Society: The Development of Higher Psychological Processes," vol. 86. Harvard University Press, 1978.
- [19] R. Feuerstein, "Instrumental Enrichment: An Intervention Program for Cognitive Modifiability," Univ Park Press, 1980.
- [20] T. P. Hogan, "Psychological Testing - A Practical Introduction," 3rd ed. John Wiley & Sons, Inc., 2013.
- [21] Ç. Gür, "Eğitimsel ve Sosyal-Duygusal Bakış Açılılarıyla Üstün Yetenekli Çocuklar." Ankara, Türkiye: Anı Yayıncılık, 2017.
- [22] J. P. Guilford, "Psychometric Methods." New York, USA: McGraw-Hill, 1953.
- [23] N. Kirişçi ve U. Sak, "Özel Yetenek Tanımı Sınıflamaları ve Kuramları," in "Öğrenme Güçlüğü ve Özel Yetenek," Ankara, Türkiye: Pegem Akademi, pp. 136-151, 2017.
- [24] M. H. Daniel, "Intelligence Testing: Status and Trends," American Psychologist, vol. 52, no. 10, pp. 1038-1045, 1997.
- [25] E. L. Thorndike, "A Note on The Accuracy of Discrimination of Weights and Lengths," Psychological Review, vol. 16, no. 5, p. 340, 1909.
- [26] İ. E. Özgüven, "Psikolojik Testler." Ankara, Türkiye: Yeni Doğu Matbaası, 1994.
- [27] H. R. Pal, A. Pal ve P. Tourani, "Theories of Intelligence," *Everyman's Science*, vol. 39, no. 3, pp. 181-192, 2004.
- [28] F. Baymur, "Genel Psikoloji," 14. baskı, İstanbul, Türkiye: İnkılâp Yayınları, 1994.
- [29] J. D. Wasserman and B. A. Bracken, "Fundamental Psychometric Considerations in Assessment," in "Handbook of Psychology," 2nd ed., vol. 10, 2012.
- [30] K. S. McGrew, "Analysis of The Major Intelligence Batteries According to A Proposed Comprehensive Gf-Gc Framework," in "Contemporary Intellectual Assessment: Theories, Tests, and Issues," D. P. Flanagan, J. L. Genshaft and P. L. Harrison, Eds., New York, USA: The Guilford Press, pp. 151-119, 1997.
- [31] W. Johnson and T. J. Bouchard Jr., "The Structure of Human Intelligence: It Is Verbal, Perceptual and Image Rotation (VPR), Not Fluid and Crystallized," *Intelligence*, vol. 33, no. 4, pp. 393-416, 2005.
- [32] J. L. Horn, "The Theory of Fluid and Crystallized Intelligence in Relation to Concepts of Cognitive Psychology and Aging in Adulthood," in "Aging and Cognitive Processes," F. I. M. Craik ve S. Trehub, Eds., Boston, MA, USA: Springer, vol. 8, 1982.
- [33] O. Aydın, "Wj-Rcog'un 'Analiz-Sentez ve Kavram Oluşturma' Alt Testlerinin Türkiye'ye Uyarlanması ve İlköğretim 1. Kademe Öğrencilerinin Akıl Yürütme Yeteneklerinin İncelenmesi," Doktora tezi, Eğitim Bilimleri Enstitüsü, Marmara Üniversitesi, İstanbul, Türkiye, 1999.

- [34] K. S. McGrew, "The Cattell-Horn-Carroll Theory of Cognitive Abilities: Past, Present, and Future," in "Contemporary Intellectual Assessment: Theories, Tests, and Issues," D. P. Flanagan ve P. L. Harrison, Eds., New York, USA: The Guilford Press, pp. 136–181, 2005.
- [35] K. S. McGrew, "CHC Theory and The Human Cognitive Abilities Project: Standing on The Shoulders of The Giants of Psychometric Intelligence Research," *Intelligence*, vol. 37, no. 1, pp. 1-10, 2009.
- [36] W. J. Schneider and K. S. McGrew, "The Cattell-Horn-Carroll Model of Intelligence," in "Contemporary Intellectual Assessment: Theories, Tests, and Issues," D. P. Flanagan ve P. L. Harrison, Eds., New York, USA: The Guilford Press, pp. 99–144, 2012.
- [37] W. J. Schneider and D. A. Newman, "Intelligence Is Multidimensional: Theoretical Review and Implications of Specific Cognitive Abilities," *Human Resource Management Review*, vol. 25, no. 1, pp. 12-27, 2015.
- [38] P. E. Vernon, "The Structure of Human Abilities," 2nd ed., London, UK: Methuen, 1961.
- [39] J. P. Guilford, "The Nature of Human Intelligence," London, UK: McGraw-Hill, 1967.
- [40] H. J. Butcher, "Human Intelligence: Its Nature and Assessment," New York, USA: Methuen, 1968.
- [41] H. Gardner, "Frames of Mind: The Theory of Multiple Intelligences," New York, USA: Basic Books, 1983.
- [42] Z. Chen and R. S. Siegler, "Intellectual Development in Childhood," in "Handbook of Intelligence," R. J. Sternberg, Ed., Cambridge, UK: Cambridge University Press, pp. 92–116, 2000.
- [43] U. Müller, K. Ten Eycke and L. Baker, "Piaget's Theory of Intelligence," in "Handbook of Intelligence: Evolutionary Theory, Historical Perspective, and Current Concepts," pp. 137-151, 2015.
- [44] J. Piaget, "The Equilibration of Cognitive Structures," Chicago, USA: University of Chicago Press, 1985.
- [45] A. J. Tannenbaum, "Gifted Children; Psychological and Educational Perspectives," New York, USA: Macmillan, pp. 227-232, 1983.
- [46] A. Bildiren, "Üstün Yetenekli Çocuklar," Ankara, Türkiye: Pegem, 2018.
- [47] A. J. Tannenbaum, "A History of Giftedness in School and Society," in "International Handbook of Giftedness and Talent," vol. 2, pp. 23-53, 2000.
- [48] F. Gagne, " Giftedness and Talent: Reexamining a Reexamination of the Definitions," *Gifted Child Quarterly*, vol. 29, no. 3, pp. 103-112, 1985.
- [49] F. Gagne, "Building Gifts into Talents: Bries Overview of the DMGT," [Online]. Available: <https://www.dropbox.com/s/a2w8aoqjfb12tn/DMGT%20EN%202020%20Overview.pdf?dl=0>, Erişim Tarihi: 7.02.2025.
- [50] Ş. Demirel Dingec and S. Kılıçarslan, "Gelişimsel Üstün Yetenek Kuramlarının Meta Kurama Göre İncelenmesi," *Anadolu Journal of Educational Sciences International*, ss. 625-642, 2023. DOI: 10.18039/ajesi.1289465.

- [51] F. Gagné, "Understanding the Complex Choreography of Talent Development Through DMGT-Based Analysis," in "International Handbook of Giftedness and Talent," vol. 2, pp. 67-79, 2000.
- [52] R. J. Sternberg, "The Concept of Intelligence and Its Role in Lifelong Learning and Success," *American Psychologist*, vol. 52, no. 10, pp. 1030-1037, 1997. DOI: 10.1037/0003-066X.52.10.1030.
- [53] R. J. Sternberg, "The Theory of Successful Intelligence," *Revista Interamericana de Psicología/Interamerican Journal of Psychology*, vol. 39, no. 2, pp. 189-202, 2005.
- [54] R. J. Sternberg, "Implicit Theories of Intelligence, Creativity, and Wisdom," *Journal of Personality and Social Psychology*, vol. 49, no. 3, pp. 607-627, 1985. DOI: 10.1037/0022-3514.49.3.607.
- [55] M. D. Öznacar ve A. Bildiren, "Üstün Zekâlı Öğrencilerin Eğitimi," Ankara, Türkiye: Anı Yayıncılık, 2012.
- [56] R. Plotnik, "Psikoloji'ye Giriş," İstanbul, Türkiye: Kaknüs Yayınları, 2009.
- [57] J. Van Tassel-Baska, G. Bass, R. Ries, D. Poland and L. D. Avery, "A National Study of Science Curriculum Effectiveness with High Ability Students," *Gifted Child Quarterly*, vol. 42, no. 4, pp. 200-211, 1998. DOI: 10.1177/001698629804200404.
- [58] E. Kurt, "Raven SPM Plus Testi 5.5-6.5 Yaş Geçerlik, Güvenirlik, Ön Norm Çalışmalarına Göre Üstün Zekâlı Olan ve Olmayan Öğrencilerin Erken Matematik Yeteneklerinin Karşılaştırılması," Yüksek lisans tezi, İstanbul Üniversitesi, Sosyal Bilimler Enstitüsü, İstanbul, Türkiye, 2008.
- [59] J. S. Renzulli, "The Three Ring Conception of Giftedness: A Developmental Model for Creative Productivity," in "Conceptions of Giftedness," R. J. Sternberg ve J. E. Davidson, Eds., Cambridge, UK: Cambridge University Press, pp. 53-92, 1986.
- [60] J. S. Renzulli, "Conception of Giftedness and Its Relationship to the Development of Social Capital," in "Handbook of Gifted Education," N. Colangelo ve G. Davis, Eds., vol. 3, Boston, MA, USA: Pearson Education, pp. 75-87, 2003.
- [61] J. S. Renzulli, "Reexamining the Role of Gifted Education and Talent Development for the 21st Century: A Four-Part Theoretical Approach," *Gifted child quarterly*, vol. 56, no.3, pp. 150-159, 2012.
- [62] J. S. Renzulli, "The Three-Ring Conception of Giftedness: A Developmental Model for Promoting Creative Productivity," in "Conceptions of Giftedness," R. Sternberg ve J. Davidson, Eds., Cambridge, UK: Cambridge University Press, pp. 246-279, 2005. DOI: 10.1017/CBO9780511610455.015.
- [63] R. J. Sternberg and L. F. Zhang, "What Do We Mean by Giftedness? A Pentagonal Implicit Theory," *Gifted Child Quarterly*, vol. 39, no. 2, pp. 88-94, 1995.
- [64] N. Broody, "What is Intelligence?" *International Review of Psychiatry*, vol. 11, no. 1, pp. 19-25, 1999.
- [65] N. Öner, "Türkiye'de Kullanılan Psikolojik Testler: Bir Başvuru Kaynağı," 3. baskı, İstanbul, Türkiye: Boğaziçi Üniversitesi, 2008.
- [66] B. Toğrol, "Rb Cattell Zekâ Testinin 2a ve 2b Formları ile Porteus Labirenti Zekâ Testinin 1300 Türk Çocuğuna Uygulanması," *Tecrübi Psikoloji Çalışmaları*, c. 11, ss. 1-32, 1974.

- [67] S. D. Porteus, "Recent Maze Test Studies," *British Journal of Medical Psychology*, vol. 32, no. 1, pp. 38-43, 1959. DOI: 10.1111/j.2044-8341.1959.tb00465.x.
- [68] Y. Karadağ ve G. Baştuğ, "Türkiye’de Zekâ Değerlendirme Sürecinde Yaşanan Etik Sorunlar ve Öneriler," *Ankara Sağlık Hizmetleri Dergisi*, vol. 17, no. 2, pp. 46-57, 2018.
- [69] A. S. Kaufman and N. L. Kaufman, "Kaufman Assessment Battery for Children," Circle Pines, MN, USA: American Guidance Service, 1983.
- [70] J. L. Horn and R. B. Cattell, "Refinement and Test of The Theory of Fluid and Crystallized General Intelligences," *Journal of educational psychology*, vol. 57, no.5, pp. 253, 1966.
- [71] J. C. Cole and M. K. Randall, "Comparing the Cognitive Ability Models of Spearman, Horn and Cattell, and Carroll," *Journal of Psychoeducational Assessment*, vol. 21, no.2, pp. 160-179, 2003.
- [72] G. Savaşan, "Kaufman Kısa Zekâ Testi (Kaufman Brief Intelligence Test-KBIT) 9-10 Yaş Çocukları Üzerinde Geçerlik, Güvenirlik ve Ön Norm Çalışmaları," Yüksek lisans tezi, İstanbul Üniversitesi, İstanbul, Türkiye, 2006.
- [73] S. Uluç ve F. Öktem, "Kaufman Kısa Zekâ Testi İkinci Sürümünün (KBIT-2) ve Wechsler Çocuklar için Zekâ Ölçeğinin Dördüncü Sürümünün (WÇZÖ-IV) Karşılaştırılması," *Psikoloji Çalışmaları*, c.43, s. 1, ss. 117-140, 2023. DOI: 10.26650/SP2022 1092655
- [74] F. Öktem, "Kısa Zekâ Testleri ve Kaufman Kısa Zeka Testi (KBİT-2)," *Türkiye Klinikleri J Psychol-Special Topics*, c. 1, s.1, ss.10-16, 2016.
- [75] S. K. Bain ve K. E. Jaspers, "Review of Kaufman Brief Intelligence Test, Second Edition," *Journal of Psychoeducational Assessment*, vol. 28, no. 2, pp. 167-174, 2010. DOI: 10.1177/0734282909348217
- [76] Ş. Güçyeter, "Türkiye’de Üstün Yeteneklileri Tanılama Araştırmaları ve Tanılamada Kullanılan Ölçme Araçları," *Turkish Journal of Education*, c. 5, s.4, ss. 235-254. 2016.
- [77] N. Sezgin, G. Baştuğ, S. Yargıcı Karaağaç ve B. Yılmaz, "Wechsler Yetişkinler için Zekâ Ölçeği Gözden Geçirilmiş Formu (WAIS-R) Türkiye Standardizasyonu: Ön Çalışma," *Ankara Üniversitesi Dil ve Tarih-Coğrafya Fakültesi Dergisi*, c. 54, s. 1, ss. 451 480, 2014.
- [78] A. S. Kaufman, L. D. Kaufman. Kaufman Brief Intelligence Test. New York: John Wiley & Sons, Inc. 2004
- [79] J. C. Raven, "Mental Tests Used in Genetic Studies: The Performance of Related Individuals on Tests Mainly Educative and Mainly Reproductive," MSc Thesis, University of London, 1936.
- [80] R. M. Kaplan, D. P. Saccuzzo, (2001). Psychological Testing: Principles, Applications, and Issues, 5th ed., Wadsworth/Thomson Learning, 2001.
- [81] N. J. Mackintosh, E. S. Bennett, "What Do Raven's Matrices Measure? An Analysis in Terms of Sex Differences," *Intelligence*, vol. 33, no.6, pp. 663-674. 2005.
- [82] S. Nazidizaji, A. Tomé, F. Regateiro, "Does the Smartest Designer Design Better? Effect of Intelligence Quotient on Students’ Design Skills in Architectural Design Studio," *Collection of Frontiers of Architectural Research*, vol. 4, no. 4, pp. 318-329. 2015. <https://doi.org/10.1016/J.FOAR.2015.08.002>.

[83] H. Yıldırım, “İç Mimarlık ve Peyzaj Mimarlığı Programlarında Bilişsel Yetenek Yaratıcılık İlişkisi ve Eğitimin Yaratıcılık Üzerine Etkileri,” Doktora Tezi, Peyzaj Mimarlığı Bölümü, Burdur Mehmet Akif Ersoy Üniversitesi, Burdur, Türkiye, 2023.



Düzce University Journal of Science & Technology

Research Article

Effect of Natural Aging on Mechanical Properties of Copper Clad Steel Brake Pipes

Ozan KOYUNCU^a, Burak ÇELİK^a, İrem Yağmur SİMİTÇİ^a, Yasin AKGÜL^{b,c},
 Alper İNCESU^{b,d,*}

^a Bant Boru San. ve Tic. A.Ş., Ar-Ge Departmanı, 41480 Gebze/Kocaeli, TURKEY

^b K-O Faktör Technology and Engineering, 78050, Karabük, TURKEY

^c Iron and Steel Institute, Karabuk University, TURKEY

^d TOBB Tech. Sciences Vocational School, Karabuk University, 78050, Karabuk, Turkey

* Corresponding author's e-mail address: alperincesu@karabuk.edu.tr

DOI: 10.29130/dubited.1604223

ABSTRACT

Copper-clad steel tubes are the basic components of the hydraulic systems of many products, especially automobile brake systems. The mechanical properties of copper-clad steel tubes produced for use in the automotive industry are determined by acceptance criteria. After production, they are expected to maintain these properties during the stock and transfer process. However, metallic materials may undergo natural aging when kept at room temperature for a long time. In this study, the changes in the mechanical properties of copper-clad steel tubes of different diameters (ø4.75, ø6, ø8 mm) were investigated by keeping them at room temperature for 1 year. The mechanical properties were characterized by tensile and blasting tests, and the changes in mechanical properties were investigated by examining the microstructure using an optical microscope. Results showed that there are no significant microstructural changes while there was a slight decrease in the tensile properties of brake pipes.

Keywords: Copper-clad steel tube, mechanical properties, microstructure, natural aging.

Doğal Yaşlanmanın Bakır Kaplı Çelik Fren Borularının Mekanik Özellikleri Üzerindeki Etkisi

Öz

Bakır kaplı çelik borular, otomobil fren sistemleri başta olmak üzere birçok ürünün hidrolik sistemlerinin temel bileşenleridir. Otomotiv sektöründe kullanılmak üzere üretilen bakır kaplı çelik boruların mekanik özellikleri kabul kriterleri ile belirlenir. Üretim sonrası stok ve transfer sürecinde de bu özelliklerini korumaları beklenir. Ancak metalik malzemeler oda sıcaklığında uzun süre bekletildiklerinde doğal yaşlanmaya uğrayabilirler. Bu çalışmada, farklı çaplardaki (ø4.75, ø6, ø8 mm) bakır kaplı çelik borular 1 yıl boyunca oda sıcaklığında bekletilerek mekanik özelliklerindeki değişimler incelenmiştir. Mekanik özellikler çekme ve patlatma testleri ile karakterize edilmiş ve mekanik özelliklerdeki değişiklikler optik mikroskop kullanılarak mikroyapı incelenerek araştırılmıştır. Sonuçlar, fren borularının çekme özelliklerinde hafif bir azalma olurken önemli bir mikroyapısal değişiklik olmadığını göstermiştir.

Anahtar Kelimeler: Bakır kaplı çelik boru, mekanik özellikler, mikro yapı, doğal yaşlanma

I. INTRODUCTION

As a layered metallic composite material, copper-clad steel sheets are among the most successful types of laminated metal matrix composites, widely used in electrical industries, automobile manufacturing, armor, and fusion reactor applications. Their unique combination of fracture toughness, strength, electrical conductivity, corrosion resistance, and radiation shielding properties makes them ideal for demanding applications [1]. Various methods, including electroplating, chemical plating, diffusion bonding, magnetron sputtering, arc welding, blast welding, and roll bonding, can be used to apply copper coatings onto steel sheets [2].

In automobile hydraulic brake systems, brake pipes are generally produced using copper-coated steel sheets due to their excellent mechanical properties and corrosion resistance [3]. Typically, DC03 quality steel sheets (0.35 mm thickness) are electroplated with a 3-5 μm copper layer, followed by bending (720°), soldering, and heat treatment at 1050°C to ensure strong bonding [4]. These tubes, also known as Bundy Tubes (Figure 1), are crucial in hydraulic brake systems and compressors, significantly impacting the performance and safety of braking mechanisms [2].

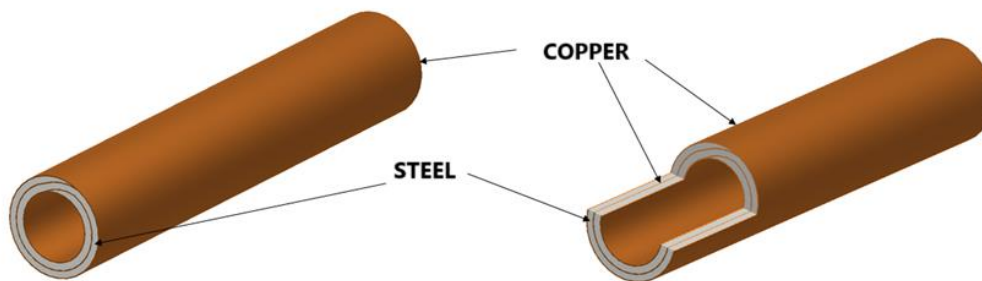


Figure 1. Schematic view of Copper Clad Double Walled Steel Tube [2].

Brake pipes often remain in stock or undergo prolonged transportation before being assembled into vehicles. During these extended storage periods, metallic materials may experience natural aging, which can lead to subtle mechanical property changes over time. Unlike artificial aging where accelerated thermal treatments mimic long-term effects natural aging occurs at room temperature, making its effects more difficult to predict and control [5]. This is because natural aging can be mimicked by accelerating natural aging with artificial aging applied by isothermal treatment at 100 to 350°C [6]. Homma et al. [7] reported that aging at 250°C for 1 hour for low-strength steel is equivalent to 2 years of natural aging. While numerous studies have examined artificial aging [8], [9], [10], research focusing on the effects of natural aging on copper-clad steel brake pipes is limited.

The primary aim of this study is to investigate the effects of natural aging on the mechanical properties of copper-clad steel brake tubes over a period of one year. Instead of simulating aging through artificial means, the materials were stored under normal storage conditions to reflect real-world scenarios. Tensile and blasting tests were performed every three months, and microstructural analysis was conducted using optical microscopy to assess changes in mechanical properties.

The novelty of this research lies bridging the knowledge gap by examining the effects of natural aging on copper-clad steel brake pipes—a topic that has received little attention in the literature. Also, industrial relevance by evaluating the long-term performance of brake pipes in real-world conditions was explained by offering insights for manufacturers to improve quality control and predict potential mechanical property variations during storage and transportation. This study contributes to enhancing the reliability, durability, and safety of brake systems in the automotive industry by understanding how natural aging impacts mechanical properties.

II. MATERIALS AND METHODS

The copper-coated steel pipes (brake pipes) with a diameter of 4.75, 6, and 8 mm used in the study were obtained from Bant Boru (Turkey). Bant Boru produces brake pipes by copper plating the sheet material whose chemical composition is given in Table 1 and mechanical properties are given in Table 2 and then applying the “roll forming” method to the copper plated sheet. The results in Table 1 and Table 2 were obtained experimentally from the sheets used in pipe production in our previous study [2]. In brake tube production, double folding is performed, and copper is welded between the steel surfaces by applying a temperature above the melting temperature of copper.

Table 1. Chemical composition of DC03 grade sheet material used in brake pipe production (wt.%)

C	Mn	Si	P	S	N	Al	Cr	Ni	Cu	B	Mo	Fe
0,04	0,23	0,007	0,013	0,014	0,027	0,033	0,03	0,021	0,043	0,001	0,002	Balance

Table 2. Mechanical properties of DC03 quality sheet material used in brake pipe production

Tensile Strength (MPa)	Yield Strength (MPa)	Elongation (%)	Hardness (HV1)
346,3±2,1	192±1	37,4±0,2	102±1

Pipes with diameters of 4,75, 6 and 8 mm (Figure 2) were kept at room temperature for 1 year and a natural aging process was carried out. The microstructural differences were examined with a Nikon Eclipse MA200 inverted metallurgical optical microscope. Microstructural changes in the samples were examined with Nikon Eclipse MA200 inverted metallurgical optical microscope. Before microstructure examinations, sanding with SiC papers (200, 400, 600, 800, 1200, 2000, 2500 grit), polishing (1 and 3 μ m diamond suspensions) and etching (5% Nital solution) metallographic processes were applied [11]. Tensile tests were performed on a Zwick/Roell Z600 Universal Testing Machine at a test speed of 2 mm/min following TS EN ISO 6892-1 (ISO 2016) tensile test standard for metallic materials. The test length at which the elongation was measured was taken as 20 mm by the cross-sectional area of the pipes.



Figure 2. Natural aged pipe sample figures before and after tensile test.

The blasting test was performed following ASTM A 254, SAE J 1677 standards (Figure 3). For the blasting test, DOT 3 hydraulic brake fluid was filled into the pump of Enerpac Company and one end of the part to be tested was closed with a blind plug. The applied pressure and the test results at the moment of detonation are displayed on a 2500-bar analog manometer. The obtained results were subjected to statistical analysis using one-way analysis of variance (ANOVA) and presented as mean \pm standard deviation. The significance of differences ($p < 0.05$) among the data sets was determined using the IBM-SPSS 22.0 statistical package (SPSS Inc., Chicago, IL, USA). Group means were further compared utilizing the Duncan multiple comparison test. All analyses were conducted in triplicate under consistent experimental conditions.

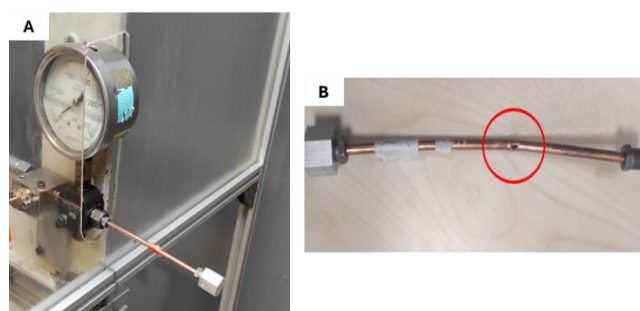


Figure 3. a) Connecting the part to the system, b) Sample image of the fragment after blasting test.

III. RESULTS AND DISCUSSION

The microstructures of naturally aged pipes with 4.75 mm, 6 mm, and 8 mm diameters at the end of 0, 3, 6, 9, and 12 months are presented in Figure 4, Figure 5, and Figure 6, respectively. As shown in Table 1, the brake pipes are made of steel sheets with a C content of about 0.04 wt. %. Therefore, the amount of cementite and pearlite formation due to cementite is very low. The microstructure of the specimens generally consists of ferrite grains. It is generally expected that grain growth occurs as a result of natural aging due to atomic diffusion over time [12]. However, optical microscopy images revealed no significant changes in grain size or phase structure. One possible explanation for this is the insufficient duration of the experiment. For instance, Yakovleva et al. [5] reported that microstructural changes in steel subjected to natural aging over 12 years led to measurable differences in phase distribution and mechanical properties. In a study on high-cycle fatigue behavior of steels, Li et al. [13] observed that long-term natural aging (~20,000 hours) promoted grain boundary changes and crack initiation sites. However, this effect was not observed in the current study, possibly due to the shorter aging period. This suggests that significant grain coarsening to occur, much longer durations of natural aging may be necessary. Furthermore, low-carbon steel aging studies have shown that aging at room temperature can lead to slight carbon redistribution and dislocation rearrangements, which may not be clearly visible in optical microscope images but can still affect mechanical properties [14].

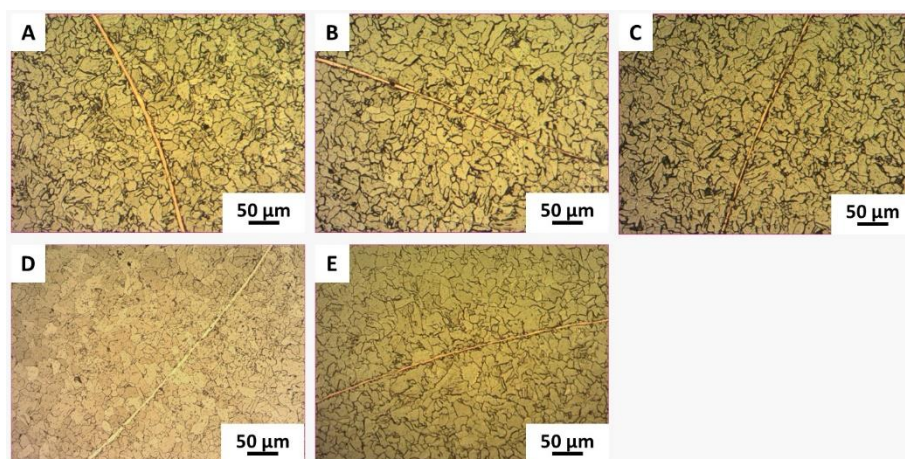


Figure 4. Microstructures of 4,75 mm diameter natural aged pipes at the end of a) 0. Month, b) 3. Month, c) 6. Month, d) 9. Month, e) 12. Month

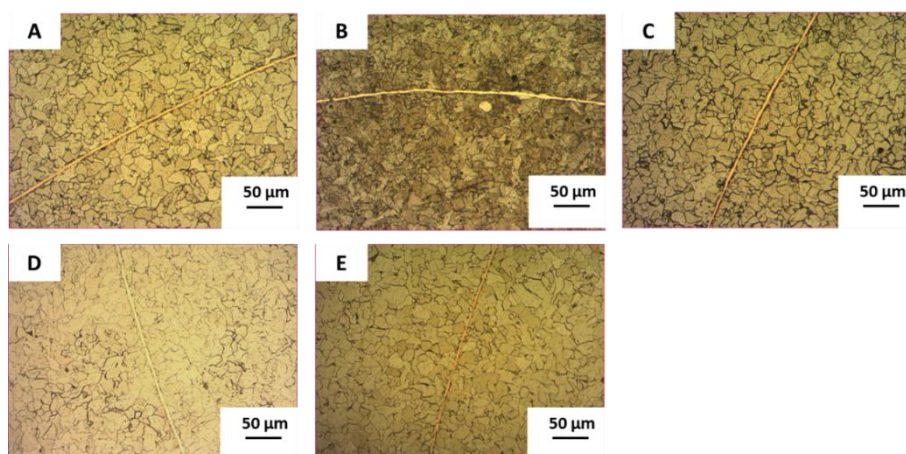


Figure 5. Microstructures of 6 mm diameter natural aged pipes at the end of a) 0. Month, b) 3. Month, c) 6. Month, d) 9. Month, e) 12. Month

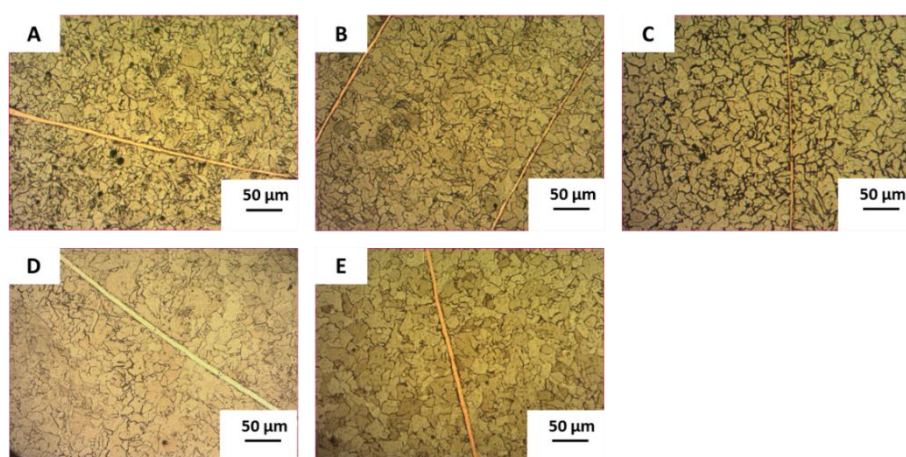


Figure 6. Microstructures of 8 mm diameter natural aged pipes at the end of a) 0. Month, b) 3. Month, c) 6. Month, d) 9. Month, e) 12. Month

The tensile strength of the samples over time is presented in Figure 7. A decrease in tensile strength was observed for all pipe diameters because of 12 months of natural aging. The decrease in tensile strength was 3.7%, 1.7%, and 2.8%, with an average reduction of 2.7%. One possible explanation for this decrease is the rearrangement of dislocations, which leads to internal stress relaxation and slight softening [15]. This is consistent with the findings of De et al. [16], who reported that dislocation relaxation and carbon atom segregation at dislocations can contribute to a reduction in strength. Additionally, Zamani et al. [17] demonstrated that in low-carbon dual-phase steels, natural aging at room temperature could cause quench aging effects, leading to changes in mechanical properties over time. Another contributing factor may be cementite precipitation at grain boundaries, which can cause localized weakening in the ferrite matrix [18]. However, the effect in this study was not as pronounced, suggesting that either the aging time was too short, or the steel composition limited precipitation effects.

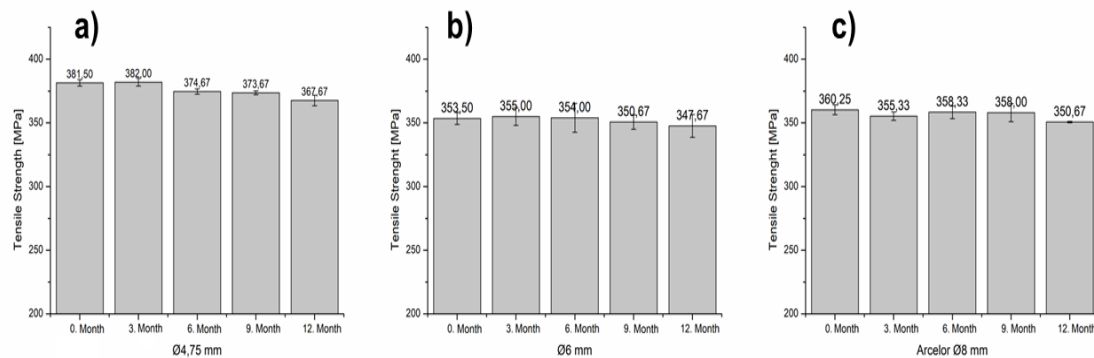


Figure 7. Tensile Strengths of Samples.

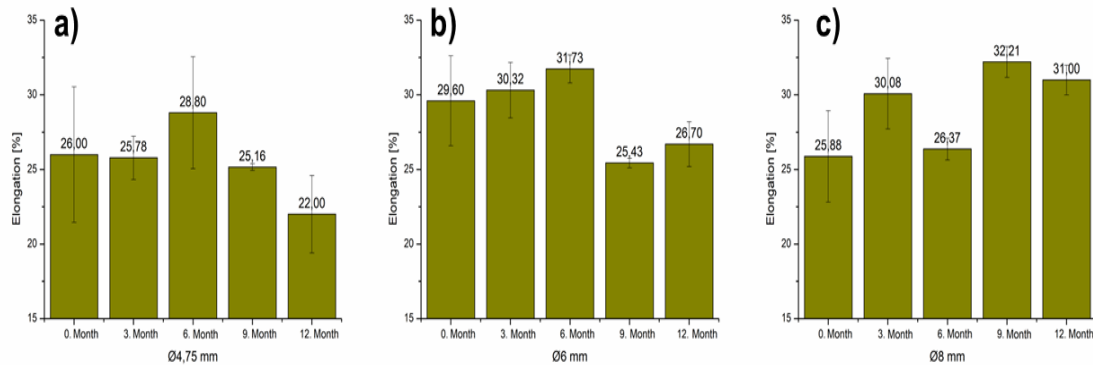


Figure 8. Elongations of Samples

Figure 8 illustrates the elongation behavior of the samples. Notably, the standard deviations for elongation values are relatively high, suggesting variability in deformation behavior. While the overall trend indicates a decrease in elongation for 4.75 mm and 6 mm pipes, the 8 mm diameter samples did not follow this trend. One possible reason for the inconsistent behavior of the 8 mm samples could be grain boundary effects and differences in internal stress distributions. As suggested by González-Arévalo et al. [12], aging processes can influence burst pressure and failure probability in steel pipelines, particularly when combined with residual stresses from manufacturing processes. Additionally, cementite precipitation at grain boundaries can reduce ductility by increasing local

embrittlement [18], [19]. While this study did not directly measure precipitation formation, future investigations using TEM could provide further insight into the precipitation kinetics and their effects on mechanical properties.

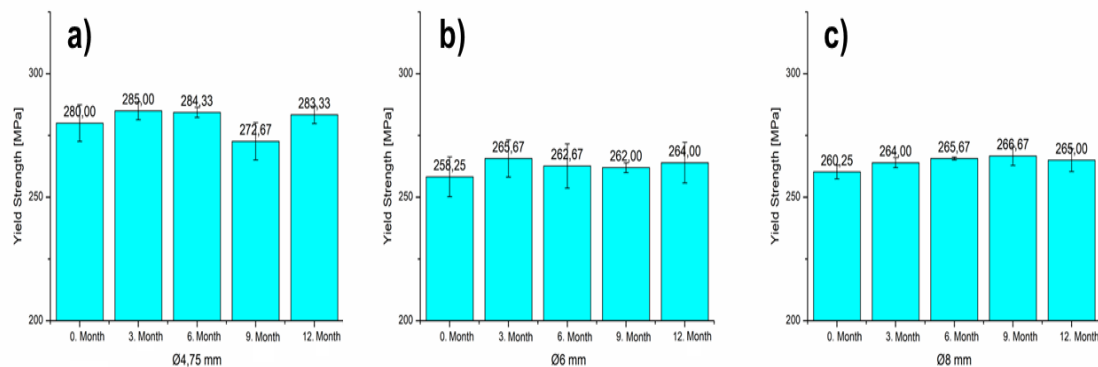


Figure 9. Yield Strength of Samples

The yield strength of the brake pipes is presented in Figure 9. Unlike tensile strength, yield strength increased by approximately 1.7% on average at the end of the natural aging period. This increase may be attributed to the formation of dislocation networks and carbon clustering, which can act as obstacles to dislocation movement. Kawahara et al. [14] showed that carbon clustering and fine carbide precipitation in low-carbon steel significantly enhance yield strength through increased resistance to dislocation glide. Furthermore, Zamani et al. [17] demonstrated that low-temperature aging can induce a strengthening effect via the formation of fine precipitates in ferrite grains. As mentioned above, cementites can form precipitates at grain boundaries. As a result, elongation at break may decrease and yield strength may increase with the resulting brittle structure [20]. These findings align with our results, suggesting that natural aging may cause localized strengthening mechanisms despite the overall softening observed in tensile strength measurements.

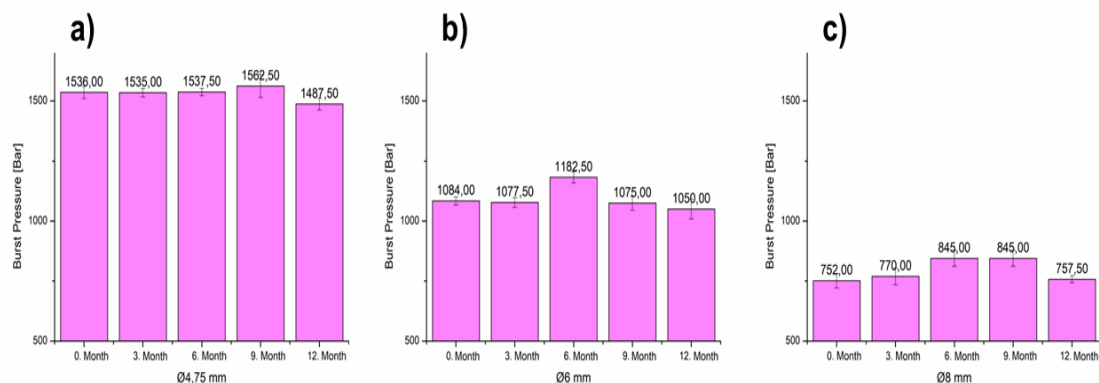


Figure 10. Bursting Pressure of Samples

The bursting pressure results are shown in Figure 10. In general, bursting pressures decreased with aging, except for the Ø8 mm sample. Since bursting pressure is closely linked to material toughness, the observed reduction suggests that aging negatively impacts the toughness of the brake pipes [21]. This is supported by findings from González-Arévalo et al. [12], who studied the influence of aging on burst pressure predictions in pipeline steels. Their research showed that aging effects, combined with environmental factors such as corrosion, can lead to significant reductions in burst pressure over time.

In the context of brake pipes, this indicates that long-term storage could impact safety margins, particularly in extreme service conditions. Moreover, fatigue behavior studies by Li et al. [13] demonstrated that natural aging can alter crack initiation mechanisms, potentially affecting burst pressure performance. Future research should explore the combined effects of fatigue and natural aging, as well as the role of environmental conditions in aging-related toughness reductions.

IV. CONCLUSION

This study investigated the effects of natural aging on the mechanical properties of copper-clad steel tubes with different diameters (4.75, 6, 8 mm) over a one-year storage period at room temperature. The findings indicate that while no significant microstructural changes were observed, natural aging resulted in a slight decrease in tensile strength ($\approx 2.7\%$) and an increase in yield strength ($\approx 1.7\%$). Additionally, blasting pressure and elongation at break values showed a decreasing trend, except for the sample with a diameter of 8 mm. The results of this study are highly relevant to industries where long-term storage and transportation of brake tubes are common, particularly in the automotive sector. Since copper-clad steel brake pipes are critical components in hydraulic braking systems, even small changes in mechanical properties can influence performance, durability, and safety. Manufacturers and suppliers should consider natural aging effects in their quality control processes, especially when evaluating long-term stockpiling or transportation conditions. Future studies should focus on longer-term aging effects beyond one-year, detailed microstructural analysis using TEM, and the combined impact of corrosion and natural aging on mechanical properties. Additionally, comparative studies with artificial aging processes could help bridge the gap between accelerated laboratory testing and real-world performance.

ACKNOWLEDGEMENTS: The authors would like to thank Bant Boru A.Ş. and Karabük University Iron and Steel Institute for their support of this study.

V. REFERENCES

- [1] D. Nedelcu and I. Carcea, "Technology for obtaining samples of layered composite materials with metallic matrix," *Met. Mater. Int.*, vol. 19, no. 1, pp. 105–112, 2013.
- [2] O. Koyuncu, B. Çelik, Y. Akgül, and A. İncesu, "Isıl İşlemin Bakır Kaplı Çelik Boruların Mekanik Özelliklerine Etkisinin Araştırılması," *J. Mater. Mechatron. A*, vol. 4, no. 1, pp. 177–192, 2023.
- [3] D. K. Miner, "Automotive hydraulic brake tube: the case for 90-10 copper-nickel tubing," in SAE International Congress and Exposition, Detroit, USA, 1993.
- [4] O. Koyuncu, B. Çelik, Y. Akgül, and A. İncesu, "Farklı Hız ve Sabit Oranda Uygulanan Redüksiyonun Fren Boruların Mekanik Özelliklerine Etkisinin Araştırılması," *Çelik Araşt. Ve Geliştirme Derg.*, vol. 4, no. 1, pp. 17–23, 2023.
- [5] E. A. Yakovleva, A. V. Larionov, G. D. Motovilina, and E. I. Khlusova, "Effect of Natural and Artificial Aging on Steel Mechanical Properties and Fracture Toughness," *Inorg. Mater. Appl. Res.*, vol. 13, no. 6, pp. 1490–1498, 2022.

- [6] G. Krauss, *Steels: Heat Treatment and Processing Principles*, 1st ed., Materials Park, OH, USA: ASM International, 1990, pp. 44–50.
- [7] K. Homma, C. Miki, and H. Yang, “Fracture toughness of cold worked and simulated heat affected structural steel,” *Eng. Fract. Mech.*, vol. 59, no. 1, pp. 17–28, 1998.
- [8] G. Xu, Y. Yang, and X. Zhang, “Study of aging behavior of CSP hot bands for cold sheets,” *Mater. Charact.*, vol. 59, no. 9, pp. 1355–1358, 2008.
- [9] T. Trzepieciński and S. M. Najm, “Current trends in metallic materials for body panels and structural members used in the automotive industry,” *Materials*, vol. 17, no. 3, p. 590, 2024.
- [10] P. Bałon *et al.*, “A method of manufacturing car mufflers by wrapping sheets, using innovative forming device with the use of servo drive,” *Procedia Manuf.*, vol. 50, pp. 17–21, 2020.
- [11] O. Koyuncu, B. Çelik, Y. Akgül, and A. İncesu, “Aynı Sıcaklıkta Uygulanan Isıl İşlem ve Farklı Oranda Uygulanan Redüksiyon İşleminin Fren Borularına Mekanik Özelliklerine Etkisinin Araştırılması,” *Çelik Araşt. Ve Geliştirme Derg.*, vol. 5, no. 1, pp. 1–8, 2024.
- [12] N. E. González-Arévalo *et al.*, “Influence of aging steel on pipeline burst pressure prediction and its impact on failure probability estimation,” *Eng. Fail. Anal.*, vol. 120, p. 104950, 2021.
- [13] G. Li, L. Ke, W. Peng, X. Ren, and C. Sun, “Effects of natural aging and variable loading on very high cycle fatigue behavior of a bearing steel GCr15,” *Theor. Appl. Fract. Mech.*, vol. 119, p. 103360, 2022.
- [14] Y. Kawahara *et al.*, “Characterization of age hardening mechanism of low-temperature aged low-carbon steel by transmission electron microscopy,” *Mater. Charact.*, vol. 183, p. 111579, 2022.
- [15] V. L. Indenbom, “Dislocations and internal stresses,” in *Modern Problems in Condensed Matter Sciences*, Amsterdam, Netherlands: Elsevier, 1992, ch. 1, pp. 1–174.
- [16] A. K. De, K. De Blauwe, S. Vandeputte, and B. C. De Cooman, “Effect of dislocation density on the low temperature aging behavior of an ultra low carbon bake hardening steel,” *J. Alloys Compd.*, vol. 310, no. 1–2, pp. 405–410, 2000.
- [17] M. Zamani, H. Mirzadeh, and M. Maleki, “Enhancement of mechanical properties of low carbon dual phase steel via natural aging,” *Mater. Sci. Eng. A*, vol. 734, pp. 178–183, 2018.
- [18] G. Li, J. Liu, J. Sun, and C. Sun, “Effects of Natural Aging and Discontinuous Cyclic Loading on High Cycle Fatigue Behavior of Steels,” *Metals*, vol. 13, no. 3, p. 511, 2023.

- [19] T. D. Barlow, “Aging effects on the fatigue performance of deep rolled bar steels,” M.S. thesis, Faculty and Board of Trustees, Colorado School of Mines, Colorado, USA, 2013.
- [20] F.-C. An, J.-J. Wang, S.-X. Zhao, and C.-M. Liu, “Tailoring cementite precipitation and mechanical properties of quenched and tempered steel by nickel partitioning between cementite and ferrite,” *Mater. Sci. Eng. A*, vol. 802, p. 140686, 2021.
- [21] K. Yoshioka, Y. Zhang, G. Lu, A. Burger, J. Adachi, and B. Bourdin, “Improving the Accuracy of Fracture Toughness Measurement in Burst Experiments,” *Rock Mech. Rock Eng.*, vol. 56, no. 1, pp. 427–436, 2023.



Düzce University Journal of Science & Technology

Review Article

The Transformative Role of Additive Manufacturing: Current Innovations, Applications, and Future Directions Across Industries

 Mustafa ÜSTÜNDAĞ^{a,*}

^a*Department of Mechanical Engineering, Faculty of Engineering and Natural Sciences,
Süleyman Demirel University, Isparta, TURKEY*

** Corresponding author's e-mail address: mustafaustundag@sdu.edu.tr*

DOI: 10.29130/dubited.1591082

ABSTRACT

Additive Manufacturing (AM), widely known as 3D printing, has evolved from a prototyping tool to a transformative technology impacting aerospace, automotive, construction, and consumer goods industries. This review explores recent advancements in AM materials, processes, and applications that enhance its functionality and support sustainable manufacturing. Key innovations include high-performance composites such as carbon fiber-reinforced polymers, nanomaterials like graphene-based inks, and biodegradable polymers such as polylactic acid (PLA). In addition, the integration of multi-material and hybrid printing has expanded AM's applicability in precision manufacturing. These developments enable AM to meet stringent requirements across critical industries, improving customization, production efficiency, and environmental impact. Despite its potential, AM faces challenges related to material durability, process consistency, standardization, scalability, and energy consumption. Addressing these issues demands ongoing research in advanced materials, process optimization, and sustainable practices, with an emphasis on integrating AM into Industry 4.0 and distributed manufacturing. This study concludes by identifying future research directions focused on AM's role in driving mass customization, circular economy practices, and industrial-scale applications, establishing it as a foundational technology in modern manufacturing.

Keywords: Additive manufacturing, Sustainable manufacturing, Advanced materials, Industry 4.0, Hybrid Manufacturing

Eklemeli İmalatın Geleceği: Yenilikler, Uygulamalar ve Sektörlere Etkisi

ÖZ

Eklemeli imalat (AM), yaygın olarak 3D baskı olarak bilinen ve prototipleme aracından, havacılık, otomotiv, inşaat ve tüketici ürünleri gibi sektörleri dönüştüren ileri bir üretim teknolojisine evrilen bir süreçtir. Bu çalışma, eklemeli imalat malzemeleri, süreçler ve uygulamalar açısından son yıllarda kaydedilen gelişmeleri kapsamlı şekilde ele almaktadır. Özellikle karbon fiber takviyeli kompozitler, grafen bazlı nanomalzemeler, biyobozunur polimerler (PLA) ile titanyum ve alüminyum gibi yüksek performanslı metal malzemelerdeki ilerlemeler dikkat çekmektedir. Çok malzemeli ve hibrit baskı teknolojileriyle birleştirilen bu yenilikler, eklemeli imalatın özelleştirme, üretim verimliliği ve sürdürülebilirlik konularındaki beklentileri karşılamasını sağlamaktadır. Ancak, eklemeli imalat malzeme dayanıklılığı, süreç tutarlılığı, standartlaşma, ölçeklenebilirlik ve enerji tüketimi gibi önemli teknik ve ekonomik zorluklarla karşı karşıyadır. Bu sorunların üstesinden gelmek için ileri malzeme geliştirme, süreç optimizasyonu ve sürdürülebilir üretim teknikleri üzerine yoğunlaşan araştırmalara ihtiyaç duyulmaktadır. Ayrıca, eklemeli imalatın Endüstri 4.0 ve dağıtık üretim modelleriyle entegrasyonu, gelecekte sektörler arası dönüşümü hızlandıracaktır. Bu çalışma, eklemeli imalatın kitle özelleştirme, dögüsel

ekonomi uygulamaları ve endüstriyel ölçekte yaygınlaşmasına yönelik araştırma yönelimlerini ele alarak, modern üretim süreçlerinde temel bir teknoloji olarak konumunu güçlendirdiğini ortaya koymaktadır.

Anahtar Kelimeler: Eklemeli imalat, Sürdürülebilir üretim, İleri malzemeler, Endüstri 4.0, Hibrit üretim

I. INTRODUCTION

Additive Manufacturing (AM), commonly known as 3D printing, has rapidly evolved from a niche prototyping tool to a transformative technology impacting various industries, including healthcare, aerospace, automotive, construction, defense, and consumer goods [1,18,40]. Initially limited to experimental and low-volume prototyping applications, AM now plays a significant role in mainstream manufacturing due to advancements in materials science, process engineering, and computational design. These advancements have enabled AM not only to replicate traditional production capabilities but also to surpass them in flexibility, efficiency, and customizability [14,16,43].

One of AM's primary advantages lies in its ability to manufacture highly complex structures with exceptional precision, which has unlocked new possibilities across sectors requiring intricate designs and weight reduction. In the aerospace industry, for example, AM is utilized to produce lightweight lattice structures, turbine blades, fuel injectors, and heat-dissipating components that would be difficult, if not impossible, to fabricate through traditional methods [20,40]. In defense applications, AM enables the production of customized weapon components, drone frames, and lightweight armor plating, improving operational efficiency [4,6,34]. Similarly, in the automotive industry, AM is instrumental in producing customized parts, such as complex exhaust systems, lightweight chassis components, and aerodynamically optimized structures, enhancing fuel efficiency and overall vehicle performance [27,38].

Aligned with Industry 4.0, which emphasizes digitalization, interconnectivity, and automation, AM is becoming an integral component of advanced manufacturing systems. By leveraging digital workflows, AM enables manufacturers to shift designs quickly and efficiently, minimizing retooling costs and reducing time-to-market, particularly advantageous in dynamic sectors such as consumer electronics and fashion [16,47]. Furthermore, AM's compatibility with digital twins—virtual replicas of physical products or processes—allows for real-time monitoring and optimization, increasing production efficiency and enhancing product quality [10,48].

Digital flexibility extends beyond production, allowing for decentralized and on-demand manufacturing. With AM, companies can produce parts closer to their point of use, reducing logistical costs, supply chain complexity, and associated environmental impact. For example, spare parts for critical infrastructure, such as offshore wind turbines, remote energy installations, and military equipment, can be manufactured on-site, enhancing operational resilience [4,6,34]. This aligns AM with circular economy principles and supports more sustainable manufacturing models, making it increasingly attractive to environmentally conscious industries [14,21].

Despite its potential, AM faces several challenges in large-scale adoption. These include material limitations, process variability, and economic scalability. Metal-based AM processes, such as Selective Laser Sintering (SLS), Electron Beam Melting (EBM), and Wire Arc Additive Manufacturing (WAAM), often require specific material characteristics, such as precise particle size, high-purity metal powders, and controlled oxidation levels, which can be costly and limit material selection [23,24]. Additionally, the layer-by-layer approach can lead to structural inconsistencies, particularly at high printing speeds, necessitating extensive post-processing for applications in sectors where quality and reliability are non-negotiable [28,35].

Scalability remains a key hurdle for AM, as it is generally suited for low-volume or customized production. While AM enables cost-effective production of complex, low-volume parts, its scalability is challenged in high-volume settings where traditional methods, such as injection molding, die casting, and CNC machining, are more economical [33,43]. For example, the unit cost of an AM-produced titanium bracket in aerospace is estimated to be 20-30% higher than its traditionally manufactured counterpart, despite weight savings of up to 40% [14,17]. Additionally, metal-based AM processes consume up to 5-10 times more energy per kilogram of material processed compared to traditional machining, offsetting some of the environmental benefits that AM is credited with, particularly if non-renewable energy sources power these processes [14,17].

A. SCOPE AND PURPOSE OF THE REVIEW

This study provides a comprehensive review of AM's technological innovations, applications, and future research directions, highlighting recent advances in materials, processes, and software that enhance AM's industrial capabilities. Additionally, it addresses the practical and technical challenges impeding its broader adoption and explores potential solutions. By synthesizing these developments, this review underlines AM's transformative role and potential to reshape manufacturing across sectors, with implications for sustainability, customization, and resilience in a rapidly evolving industrial landscape [43,49].

II. CURRENT TRENDS AND INNOVATIONS IN ADDITIVE MANUFACTURING

Additive Manufacturing (AM) has shifted from an initial focus on rapid prototyping to a versatile, scalable technology widely used across industrial applications. It is increasingly recognized for its ability to support sustainable and efficient production models due to advancements in material science, process technology, design software, and its integration with Industry 4.0 [18,29,33]. Each of these areas contributes uniquely to AM's capabilities, paving the way for its broader adoption and enhanced functionality across high-stakes industries.

A. MATERIAL ADVANCEMENTS

Material science has been a critical driver of Additive Manufacturing's (AM) rapid evolution, significantly expanding its industrial applications and technological capabilities. Initially focused on polymers, AM materials now encompass metals, ceramics, composites, and biomaterials, each offering unique properties tailored to sector-specific demands [13,28,39]. These advancements have enabled greater material versatility, supporting high-performance applications across aerospace, healthcare, automotive, and energy sectors.

Polymers remain a fundamental material category in AM, with high-performance bio-based, thermally stable, and conductive plastics broadening AM's applicability in biomedical, aerospace, and automotive industries. Materials such as polylactic acid (PLA), polyether ether ketone (PEEK), and polyamide (PA) are widely used due to their biodegradability, high thermal resistance, and favorable strength-to-weight ratio [23,24]. The development of specialized polymer blends has further enhanced mechanical durability and chemical resistance, making AM more suitable for complex engineering applications.

Metals have also become pivotal in AM, particularly in aerospace, automotive, and industrial manufacturing, where lightweight, high-strength components are required. Materials such as titanium, aluminum, stainless steel, and Inconel are widely utilized, offering high durability, corrosion resistance, and weight reduction advantages [11,20,22]. Recent advancements in multi-metal printing

techniques have further enhanced AM's potential, allowing for the fabrication of components with complex material gradients, optimizing mechanical properties, wear resistance, and longevity.

Ceramics, known for their exceptional heat and chemical resistance, are emerging as a valuable AM material, particularly in electronics, energy storage, and biomedical applications. Their ability to withstand extreme temperatures makes them ideal for thermal barrier coatings, biomedical implants, and specialized aerospace components [17,49].

In addition, composites and nanomaterials are advancing AM's structural and functional capabilities. Fiber-reinforced composites, such as carbon fiber and glass fiber, offer superior strength-to-weight ratios, making them highly desirable for aerospace and automotive applications. Meanwhile, nanocomposites, including graphene, carbon nanotubes (CNTs), and boron nitride, provide enhanced thermal conductivity, mechanical integrity, and electrical properties, making them valuable in high-stress applications across healthcare, defense, and energy sectors [15,35].

As AM materials continue to evolve, ongoing research into sustainable, high-performance, and multifunctional materials will further expand its industrial potential, enabling lighter, stronger, and more efficient components across a wide range of applications.

B. TECHNOLOGICAL ADVANCEMENTS

Technological innovations have significantly expanded AM's capabilities, particularly in terms of precision, speed, and efficiency. Several advanced AM processes have emerged, enhancing its applicability across various industries. High-resolution metal AM techniques, such as Direct Metal Laser Sintering (DMLS) and Electron Beam Melting (EBM), are widely used to manufacture high-strength components for aerospace, defense, and medical implants, where precision and structural integrity are crucial [40,42]. These methods ensure the production of durable and complex metal parts with excellent mechanical properties.

Hybrid manufacturing, which integrates additive and subtractive techniques, has gained prominence due to its ability to produce intricate geometries while achieving the precision finishing of traditional machining. This approach is particularly valuable in automotive and aerospace applications, where high-quality surface finishing and dimensional accuracy are essential [4,16]. Additionally, emerging large-scale metal AM technologies, such as Wire Arc Additive Manufacturing (WAAM) and Friction Stir Additive Manufacturing (FSAM), offer efficient solutions for shipbuilding, aerospace, and heavy industrial applications. WAAM provides an energy-efficient method for printing large metal structures, while FSAM combines friction stir welding with AM, ensuring strong, defect-free components with enhanced mechanical properties [10,42].

Further innovations in Binder Jetting and Continuous Liquid Interface Production (CLIP) have also contributed to AM's evolution. Binder jetting, known for its high speed and fine detail resolution, is particularly suited for consumer goods and medical devices, where intricate designs and smooth surfaces are required [33]. CLIP, a photo-polymerization-based AM process, significantly improves production speed, making it a promising solution for scaling AM in high-volume manufacturing [33]. Another breakthrough in AM technology is multi-material and functionally graded AM, which allows different materials to be integrated within a single print job. This capability enables the production of components with customized mechanical and thermal properties, reducing the need for assembly and enhancing overall functionality [39,48]. As AM technologies continue to advance, these innovations are expected to redefine precision manufacturing by offering greater efficiency, scalability, and material versatility across various industries.

C. SOFTWARE AND DESIGN INNOVATIONS

Advancements in AM design software have significantly enhanced the efficiency and precision of additive manufacturing processes by introducing cutting-edge computational tools. One of the most

impactful innovations is generative design and topology optimization, which enable engineers to create highly optimized structures that minimize material usage while maintaining mechanical integrity. These techniques are particularly valuable in aerospace applications, where weight reduction is crucial for fuel efficiency and performance enhancement [16,26]. By utilizing generative design, manufacturers can develop complex, lightweight geometries that would be challenging or impossible to achieve through traditional design methods.

Another critical advancement is simulation-driven development, which integrates predictive tools within computer-aided design (CAD) systems. These simulations assess part performance under various conditions, allowing for early detection of potential weaknesses and reducing the likelihood of material waste. As a result, simulation-driven workflows improve manufacturing efficiency and product reliability, making AM a more viable alternative for high-precision industries [10,35].

Artificial intelligence (AI) and machine learning (ML) have also emerged as transformative tools in AM process optimization. AI-driven AM software can predict potential print failures, adjust parameters in real-time, and enhance quality control. By leveraging ML algorithms, manufacturers can optimize print settings, reduce errors, and improve product consistency, ultimately minimizing defects and production inefficiencies [28,33].

Additionally, the adoption of cloud-based and collaborative platforms is revolutionizing distributed manufacturing. These platforms allow for global design sharing and real-time modifications, enabling companies to adapt quickly to changing market demands. This approach is particularly beneficial for industries with fast-evolving consumer needs, such as electronics and fashion, where rapid prototyping and on-demand customization are essential for maintaining competitive advantage [6,47]. By integrating these advanced software solutions, AM continues to evolve into a more efficient, precise, and scalable manufacturing technology, catering to a broad range of industrial and consumer applications.

D. AUTOMATION AND INDUSTRY 4.0 INTEGRATION

The integration of Industry 4.0 principles, such as automation, real-time data exchange, and interconnected manufacturing, has significantly enhanced Additive Manufacturing's (AM) adaptability and efficiency. These advancements are enabling smarter, data-driven production models, improving both scalability and precision across various industries.

One of the most transformative developments is the application of the Industrial Internet of Things (IIoT) in AM, where AM systems can collect, analyze, and act on real-time data. This capability allows for predictive maintenance and adaptive control, ensuring higher production flexibility and operational efficiency [16,29]. By leveraging IIoT-enabled AM platforms, manufacturers can monitor machine performance, detect potential anomalies, and optimize production parameters dynamically, reducing downtime and material waste.

Another significant advancement is the implementation of Digital Twins, which serve as virtual replicas of AM systems. These models enable manufacturers to simulate, monitor, and refine production processes in real time, helping to identify and address potential issues before they impact production [10,48]. By integrating real-time feedback loops, digital twin technology enhances process reliability, reduces errors, and improves overall efficiency.

Automated post-processing is also playing a crucial role in making AM more viable for high-volume industrial applications. Traditionally, support removal, surface finishing, and quality inspection have been labor-intensive and time-consuming processes. However, advancements in robotic handling and automated workflows have significantly streamlined these tasks, reducing labor costs and post-processing time [17,34]. As a result, large-scale AM production is becoming increasingly feasible, particularly in aerospace, automotive, and medical device manufacturing, where precision and consistency are critical.

Furthermore, blockchain technology is emerging as a promising solution for enhancing supply chain transparency and security in AM workflows. Blockchain-based traceability systems provide secure, immutable records of AM production data, ensuring compliance with stringent regulatory requirements in industries such as aerospace and healthcare [26,43]. This enhanced data integrity and traceability supports quality assurance and counterfeit prevention, making AM an even more reliable manufacturing option.

With these advancements, AM's role within Industry 4.0 ecosystems is rapidly expanding, supporting flexible, resilient, and sustainable manufacturing models. As industries continue to embrace digital transformation, AM is set to become a cornerstone of responsive production, particularly in sectors with fluctuating demands, such as consumer electronics, fashion, and healthcare [18,43]. The integration of IIoT, digital twins, automation, and blockchain technology is paving the way for a more interconnected, efficient, and intelligent manufacturing landscape, ensuring that AM remains a driving force behind the future of industrial production.

III. APPLICATIONS OF ADDITIVE MANUFACTURING ACROSS INDUSTRIES

Additive Manufacturing (AM) has transformed diverse industries by enabling tailored solutions, reducing production costs, and allowing unique design capabilities unattainable through traditional manufacturing. This section examines how AM is applied in healthcare, automotive, aerospace, construction, consumer goods, defense, and energy, each leveraging AM's distinct strengths to redefine traditional processes, products, and business models.

A. HEALTHCARE AND BIOMEDICAL APPLICATIONS

In healthcare, Additive Manufacturing (AM) has revolutionized the creation of customized medical devices, prosthetics, and anatomical models, significantly enhancing patient outcomes by enabling individualized treatments tailored to specific needs [22,32]. The ability to fabricate patient-specific implants and prosthetics has been one of AM's most impactful contributions to modern medicine. Titanium-based 3D-printed implants are now widely used in orthopedic and cranial reconstruction surgeries, offering improved comfort, functionality, and longevity compared to traditionally manufactured implants [26,39].

Beyond prosthetics, AM has transformed surgical planning and medical training by enabling the creation of patient-specific 3D anatomical models. These models allow surgeons to prepare for complex procedures more effectively, reducing surgical risks and operating times, ultimately leading to higher success rates in delicate procedures such as neurosurgery and cardiovascular interventions [9,12].

Another promising frontier in AM-driven healthcare is bioprinting and regenerative medicine, where 3D printing of tissue-like structures is advancing tissue engineering and organ repair. Although still in experimental stages, AM is being explored for bio-printed cartilage, 3D-printed scaffolds for bone regeneration, and even artificial skin models, which could revolutionize reconstructive surgery and wound healing treatments [32,41].

Moreover, AM is making strides in pharmaceutical applications, where customized drug tablets with controlled-release properties are being developed. This advancement supports the growing field of precision medicine, enabling patient-specific drug dosages tailored to individual metabolic needs, thereby improving treatment efficacy and minimizing side effects [22,35].

With ongoing research and technological advancements, AM holds immense potential to redefine personalized healthcare, accelerate drug testing, and even pave the way for functional organ transplantation in the future. As bioprinting techniques continue to evolve, the possibility of producing fully functional 3D-printed organs for transplantation may become a reality, addressing the growing global demand for donor organs and transforming the future of regenerative medicine.

B. AUTOMOTIVE AND AEROSPACE APPLICATIONS

The automotive and aerospace sectors have been among the leading adopters of Additive Manufacturing (AM) due to its ability to reduce weight, lower production costs, and enhance manufacturing flexibility. These industries leverage AM's unique capabilities to improve performance, efficiency, and sustainability while enabling the production of complex geometries that traditional manufacturing methods struggle to achieve.

In the aerospace industry, weight reduction is critical for fuel efficiency and emission reduction, making AM an ideal solution for fabricating lightweight yet structurally robust components. AM enables the production of intricate lattice structures that significantly reduce material usage while maintaining strength, making it particularly valuable for turbine blades, fuel injectors, engine nozzles, and fuselage parts [20,40,43]. Furthermore, multi-material AM techniques allow for the integration of materials with varying thermal and mechanical properties within a single component, improving heat resistance and structural integrity in extreme aerospace conditions [38,42]. These advancements contribute to higher fuel efficiency, reduced operational costs, and increased durability, positioning AM as a key technology in next-generation aerospace engineering.

Similarly, the automotive industry has embraced AM for rapid prototyping, functional part production, and performance optimization. AM allows for the fabrication of customized exhaust manifolds, heat exchangers, and lightweight chassis structures, all of which enhance vehicle aerodynamics, fuel efficiency, and overall driving performance [2,27]. The ability to produce complex, high-performance components without extensive retooling makes AM particularly advantageous for automakers seeking innovation and customization in their designs.

With the rise of electric and autonomous vehicles (EVs & AVs), AM is expected to play a crucial role in the development of next-generation automotive technologies. The ability to create lightweight battery housings, efficient cooling systems, and complex electronic enclosures will be essential for improving battery life, heat dissipation, and overall vehicle efficiency [14,31]. Additionally, AM's on-demand production capabilities enable manufacturers to quickly respond to changing consumer preferences and regulatory requirements, particularly in markets demanding customized, eco-friendly, and high-performance vehicles [6,20]. As AM technology continues to evolve, it is set to transform the automotive and aerospace industries by accelerating innovation, reducing costs, and enhancing sustainability.

C. CONSTRUCTION APPLICATIONS

Additive Manufacturing (AM), often referred to as "additive construction," has revolutionized the construction industry by enabling sustainable building practices, reducing labor costs, and allowing for innovative architectural designs. By leveraging large-scale 3D printing technologies, AM has introduced faster, more cost-effective, and environmentally friendly solutions for the construction sector.

One of the most transformative applications of AM in construction is large-scale 3D-printed housing, which can be built 30-50% faster than conventional methods while reducing material waste by up to 60%. Concrete-based AM processes have proven particularly effective in developing affordable housing solutions, especially in disaster-prone or remote regions where traditional construction methods face logistical and financial challenges [7,34]. The ability to print building components on-

site minimizes transportation costs, making AM an attractive alternative for sustainable development projects.

From a financial perspective, AM also offers significant cost savings compared to traditional construction. A single-story 3D-printed house is estimated to cost 20-30% less than its conventionally built counterpart due to reduced material waste, lower labor requirements, and shorter construction timelines [8,17]. These benefits make AM an ideal solution for addressing global housing shortages and reducing the environmental impact of the construction industry.

Beyond residential housing, AM is also reshaping architectural design and customization. The technology allows for the creation of decorative facades, modular walls, and functional fixtures, offering greater design flexibility and sustainability in modern construction projects. The ability to manufacture intricate and lightweight structures that would be difficult or costly to produce using traditional methods is positioning AM as a key technology in the future of sustainable and aesthetically advanced building design [21,43]. As AM technology continues to develop, its applications in urban planning, infrastructure development, and smart city projects are expected to grow, further solidifying its role in the future of sustainable construction.

D. CONSUMER GOODS AND CUSTOMIZATION

Additive Manufacturing (AM) has been widely embraced by the consumer goods sector due to its ability to enable personalized products, rapid prototyping, and on-demand manufacturing. The technology offers unparalleled design freedom, allowing manufacturers to create customized, complex, and ergonomic products that meet individual consumer preferences while optimizing production efficiency.

In the fashion and accessories industry, AM is transforming the way designers create custom jewelry, eyewear, and footwear, incorporating intricate geometric structures and innovative materials that would be difficult to achieve through traditional methods [28,33]. The ability to produce custom-fit clothing and ergonomic wearables ensures that products are tailored to specific body measurements, enhancing comfort, functionality, and aesthetic appeal [6,46]. As a result, AM has gained traction in high-fashion, luxury brands, and sportswear, offering a unique balance of artistry and performance-driven design.

Similarly, AM is making significant contributions to sports and protective gear, where customization and performance optimization are critical. The ability to manufacture personalized helmets, shin guards, and high-performance sports shoes ensures that protective equipment is precisely fitted to an athlete's body, improving safety, comfort, and durability [10,20]. By leveraging lightweight yet strong materials, AM-produced sports equipment enhances shock absorption, aerodynamics, and overall performance, making it an ideal solution for professional athletes and recreational users alike.

Beyond fashion and sports, AM is revolutionizing consumer electronics and household appliances by enabling rapid prototyping and iterative design. Companies can quickly test and modify prototypes, accelerating the product development cycle and reducing costs associated with tooling and mass production [20]. This ability to rapidly innovate and bring new products to market gives companies a competitive edge, particularly in industries where consumer preferences evolve quickly, such as smartphones, smart home devices, and wearable technology.

As on-demand manufacturing continues to grow, AM is playing a crucial role in reducing inventory waste, enhancing product customization, and streamlining production workflows. With further advancements, AM is expected to reshape the consumer goods industry, offering sustainable, cost-effective, and highly personalized products that cater to the evolving demands of modern consumers.

E. DEFENSE APPLICATIONS

The defense sector is increasingly adopting Additive Manufacturing (AM) as a strategic solution for on-demand production of critical infrastructure and equipment, particularly in remote and battlefield conditions. The ability to produce essential components on-site significantly reduces logistical challenges, enhances operational efficiency, and ensures that military forces remain equipped with necessary tools and spare parts, even in unpredictable environments.

One of the most critical applications of AM in defense is field-deployable AM production, which enables the military to manufacture spare parts, drone components, and weapons directly on-site. This capability minimizes supply chain delays, ensuring that essential equipment remains functional and mission-ready [1,43]. In combat zones and remote locations, where traditional supply chains may be disrupted or impractical, AM provides a crucial advantage by allowing soldiers to produce replacement parts in real-time, reducing downtime and dependency on external suppliers.

Beyond logistics, AM is revolutionizing lightweight and durable defense components. Titanium and composite-based AM parts are being widely used in military aircraft, armored vehicles, and tactical gear, providing significant weight savings while maintaining structural durability [23,24]. Lightweight materials enhance fuel efficiency, mobility, and maneuverability, particularly in high-risk operations where speed and agility are essential. Additionally, custom AM-designed firearm parts, surveillance devices, and unmanned aerial vehicle (UAV) components improve mission flexibility and operational effectiveness, allowing defense forces to adapt to evolving threats with greater agility.

As AM continues to advance, its role in defense logistics, rapid equipment deployment, and battlefield innovation is expected to expand. By reducing reliance on centralized supply chains, accelerating production timelines, and enabling localized manufacturing, AM is transforming military readiness and strategic adaptability, making it a foundational technology for next-generation defense operations.

F. ENERGY SECTOR APPLICATIONS

Additive Manufacturing (AM) is gaining significant traction in the energy sector, particularly as a solution for renewable energy development, efficiency optimization, and infrastructure maintenance. The ability to produce customized, high-performance components enables greater energy efficiency, cost reduction, and improved sustainability, making AM an essential tool for the future of energy production.

In wind and solar energy, AM facilitates the design and fabrication of lightweight, aerodynamically optimized turbine blades, enhancing energy capture and efficiency in wind farms [22,23]. The flexibility of AM also allows for the rapid prototyping and manufacturing of complex solar panel components, reducing production costs while improving photovoltaic performance. By optimizing material distribution and structural integrity, AM supports the development of more durable and efficient renewable energy systems.

AM is also proving valuable in hydropower and geothermal applications, where complex, fluid-dynamics-optimized heat exchangers play a critical role in maintaining cooling efficiency and power plant performance. The ability to produce customized, high-performance heat exchangers with intricate internal geometries enhances thermal management, reducing energy losses and improving operational efficiency [16].

Another key application of AM in the energy sector is infrastructure maintenance and part replacement, particularly in offshore wind farms and isolated power grids. Traditional manufacturing and supply chain constraints can lead to significant downtime when energy infrastructure components fail. However, AM enables on-site production of spare parts, drastically reducing maintenance costs and operational delays [23,43]. This capability is particularly valuable in remote locations, where logistics and replacement part availability pose significant challenges.

With the growing global emphasis on sustainable and distributed energy production, AM is set to play an increasingly critical role in energy system innovation. By enabling localized, on-demand manufacturing, AM reduces waste, shortens supply chains, and enhances the resilience of energy infrastructure. As advancements continue in materials, printing processes, and AI-driven optimization, AM will further contribute to the efficiency, reliability, and sustainability of next-generation energy solutions. expected to expand significantly.

IV. CHALLENGES AND LIMITATIONS OF ADDITIVE MANUFACTURING

Despite its transformative potential, additive manufacturing (AM) faces numerous challenges that inhibit its widespread adoption across various industries. These challenges include material and process limitations, standardization and certification issues, economic scalability, environmental impact, and supply chain integration obstacles. Recognizing and addressing these limitations are essential steps for optimizing AM and unlocking its full potential in mainstream production [31,43].

A. MATERIAL AND PROCESS LIMITATIONS

One of the most significant limitations of Additive Manufacturing (AM) is the restricted range of materials that meet the necessary performance standards for high-stakes applications. While AM has expanded its capabilities through the use of metals, ceramics, polymers, and composites, many of these materials still lack the mechanical strength, heat resistance, or fatigue life required in industries such as aerospace and automotive [23,24,42]. In particular, polymer-based AM materials are susceptible to thermal degradation, which restricts their use in high-temperature environments such as engine components, turbine blades, or aerospace heat shields [36,48]. Without improved heat-resistant materials, the widespread adoption of AM in extreme operating conditions remains limited.

Another critical challenge in AM is achieving high surface quality and structural consistency. The layer-by-layer fabrication process, while advantageous for complex geometries, often results in rough surface finishes and internal inconsistencies. These defects can affect a part's mechanical properties, fatigue resistance, and overall reliability, making post-processing techniques such as machining, polishing, and heat treatment essential [8,10]. However, these additional processing steps increase production time and costs, reducing AM's competitiveness with traditional manufacturing methods.

Furthermore, ensuring consistent quality across production batches remains a challenge, as minor fluctuations in machine calibration, temperature, or material properties can significantly impact part reliability and performance. Variations in powder particle size, laser power, or printing speed can lead to dimensional inaccuracies, porosity, or material inconsistencies, which pose risks in industries with stringent quality requirements, such as medical implants or aerospace components [28,30]. To address these challenges, continued research into high-performance materials, real-time process monitoring, and advanced post-processing techniques is essential to enhancing the reliability, durability, and efficiency of AM-produced components.

B. STANDARDIZATION AND CERTIFICATION ISSUES

The absence of standardized protocols and certification frameworks presents a substantial barrier to the widespread adoption of Additive Manufacturing (AM), particularly in highly regulated industries such as healthcare and aerospace. These sectors require strict compliance with quality, safety, and reliability standards, yet AM lacks universally accepted certification frameworks, making it difficult for manufacturers to achieve regulatory approval for AM-produced components [25,40].

One of the primary challenges is the lack of uniform standards governing AM processes, materials, and quality control. Unlike traditional manufacturing methods, which have well-established regulatory pathways, AM-produced parts often require extensive individual validation, increasing certification costs and time-to-market [26,31]. This inconsistency reduces AM's efficiency, making it less attractive for large-scale industrial adoption, especially in sectors where product integrity is critical, such as aerospace, defense, and medical implants.

Recognizing this challenge, several international organizations, including ASTM (American Society for Testing and Materials) and ISO (International Organization for Standardization), are working to establish universal AM guidelines [14,33]. These efforts aim to create standardized material specifications, process controls, and quality assurance protocols, ensuring AM-produced parts meet industry requirements. However, the industry-wide adoption of these standards remains slow, and without comprehensive regulation, AM will continue to face skepticism in critical applications where traditional manufacturing methods are still perceived as more reliable and compliant.

To accelerate AM's integration into high-stakes industries, further collaboration between regulatory bodies, industry leaders, and research institutions is essential. Establishing clear, internationally recognized certification pathways will be crucial for enhancing AM's credibility, improving production consistency, and fostering confidence in AM-manufactured components across various regulated sectors.

C. ECONOMIC CHALLENGES

Additive Manufacturing (AM) is highly effective for producing low-volume, complex, and customized parts, but it struggles to compete with traditional manufacturing methods in high-volume production due to several economic and scalability challenges. While AM excels in design flexibility and rapid prototyping, its cost-efficiency, production speed, and material expenses remain significant barriers to large-scale adoption.

One of the primary economic limitations is the cost comparison with traditional manufacturing methods. Injection molding and casting are highly optimized for mass production, achieving much lower per-unit costs than AM at scale. While AM eliminates the need for expensive molds and tooling, its layer-by-layer process is significantly slower, making it less competitive for high-volume manufacturing. Studies suggest that AM can be up to 20% slower than comparable subtractive methods, such as CNC machining, limiting its feasibility for large-scale industrial production [4,10,34].

Another major challenge is the high energy consumption of metal AM processes. Laser-based and electron beam AM techniques require high power inputs, consuming up to 5-10 times more energy per kilogram of material compared to conventional manufacturing techniques, such as CNC machining or casting [14,17]. This increased energy demand reduces AM's sustainability advantage, particularly in industries looking to minimize carbon footprints and transition to energy-efficient production methods.

Additionally, the cost of raw materials remains a significant barrier to AM's widespread industrial adoption. High-performance AM materials, such as specialized metal powders, advanced ceramics, and reinforced polymers, are considerably more expensive than bulk materials used in traditional manufacturing [2,24]. The need for highly refined, precisely controlled AM feedstock further increases costs, making mass production using AM economically challenging.

While AM continues to improve in efficiency and material optimization, addressing these economic limitations is essential for its broader adoption in high-volume industries. Ongoing research into faster printing methods, alternative energy sources, and cost-effective materials will be crucial to enhancing AM's scalability and competitiveness in industrial manufacturing.

D. ENVIRONMENTAL IMPACT

Although Additive Manufacturing (AM) is often recognized for its environmental benefits, such as minimizing material waste and enabling localized production, it also faces significant sustainability challenges that must be addressed for it to become a truly eco-friendly manufacturing solution. While AM's efficient material usage and reduced transportation needs contribute to a lower carbon footprint, issues related to waste generation, material recyclability, and energy consumption present ongoing obstacles to its long-term sustainability.

One of the primary environmental concerns is waste generation and material recyclability, particularly in metal-based AM processes. Many AM methods require support structures to stabilize parts during printing, but these structures are often discarded after production, leading to additional material waste. Unlike subtractive manufacturing, where offcuts and scrap metal can often be recycled and reused, AM-produced waste requires specialized recovery and reprocessing methods, increasing both complexity and cost [17,44]. The challenge of effectively recycling and repurposing AM materials remains a key limitation for industries looking to implement circular economy principles.

Another challenge is the limited biodegradability of AM polymers. Many high-performance polymers used in AM, such as PEEK and ULTEM, exhibit exceptional mechanical and thermal properties, making them ideal for high-stakes applications. However, these materials are difficult to recycle, reducing AM's alignment with circular economy models and sustainable production practices [21,35]. Without better end-of-life strategies, including biodegradable alternatives or closed-loop recycling systems, AM may continue to struggle with plastic waste accumulation in certain sectors.

The energy footprint of AM processes is another significant factor affecting its sustainability. High-energy AM techniques, such as Selective Laser Melting (SLM) and Electron Beam Melting (EBM), require intense power inputs to operate, especially when using high-temperature metal powders. If AM facilities rely on non-renewable energy sources, the environmental benefits of AM can be entirely negated, making it less sustainable than traditionally energy-efficient mass production methods [6,33]. To reduce AM's carbon footprint, manufacturers must invest in energy-efficient AM systems and transition toward renewable energy-powered production.

While AM has the potential to be a key driver of sustainable manufacturing, addressing these waste management, recyclability, and energy consumption challenges is crucial. Future advancements in biodegradable materials, closed-loop recycling strategies, and energy-efficient AM processes will be essential for enhancing AM's role in environmentally responsible production.

E. SCALABILITY AND SUPPLY CHAIN INTEGRATION

While Additive Manufacturing (AM) is well-suited for on-demand production and customization, scaling AM for high-volume manufacturing remains a significant challenge. Despite its advantages in design flexibility, rapid prototyping, and localized production, AM struggles to compete with traditional mass production methods in terms of speed, cost efficiency, and supply chain integration.

One of the primary barriers to large-scale AM adoption is its slow production rates compared to high-speed conventional manufacturing methods. The layer-by-layer fabrication process, while ideal for complex geometries and customization, is inherently slower than traditional high-volume techniques such as die casting, injection molding, or roll-to-roll processing. As a result, AM is often less efficient for industries requiring high-output production, such as consumer electronics, mass-market automotive manufacturing, and household appliances [10,43]. Until printing speeds and throughput capabilities are significantly improved, AM will remain better suited for low-volume, high-value applications rather than large-scale mass production.

Another major challenge is logistical complexity in AM supply chains. Traditional inventory and distribution models are built around centralized manufacturing hubs and bulk production, which

contrasts with AM's decentralized, on-demand approach. While digital inventory solutions and automated logistics systems offer potential solutions, transitioning to AM-integrated supply chains requires significant investment and infrastructure adjustments [4]. Companies must develop new distribution models, real-time tracking systems, and efficient production networks to fully capitalize on AM's just-in-time manufacturing potential.

To overcome these scalability issues, many companies are adopting hybrid manufacturing strategies that integrate AM with conventional production methods. This approach allows manufacturers to leverage AM's customization and rapid prototyping advantages while maintaining efficiency at scale using traditional techniques. For example, AM can be used for producing high-performance, low-volume components, while mass production techniques handle high-volume standard parts. Although hybrid strategies increase AM's adoption in large-scale industries, further technological and economic optimizations are needed to ensure cost-effectiveness and seamless integration into existing production workflows [14,31].

While AM continues to advance, addressing speed, supply chain adaptation, and hybrid manufacturing will be key factors in enabling AM's scalability for high-volume industrial applications. Future improvements in print speed, automation, and supply chain digitization will determine AM's ability to compete with traditional manufacturing on a global scale.

V. THE FUTURE OF ADDITIVE MANUFACTURING

As additive manufacturing (AM) continues to evolve, its potential to reshape industries through advancements in materials, processes, and sustainable manufacturing practices becomes increasingly evident. Emerging research highlights AM's capacity to support mass customization, distributed manufacturing, and circular economy principles, each with the potential to transform global production systems. This section explores these advancements along with AM's prospective impact across industries by 2030 and beyond [18,43].

A. EMERGING MATERIALS AND PROCESSES

One of the most promising areas of Additive Manufacturing (AM) research lies in the development of new materials and process refinements that expand the technology's capabilities and enhance its industrial applicability. Advancements in nanomaterials, composites, biodegradable polymers, and multi-material printing are driving AM's evolution toward stronger, more sustainable, and functionally diverse applications.

Recent progress in advanced nanomaterials and composites has significantly improved the strength-to-weight ratio of AM-produced components. Carbon-based nanomaterials, such as graphene and carbon nanotubes (CNTs), exhibit exceptional mechanical properties, making them ideal for aerospace, automotive, and defense applications, where lightweight yet high-strength materials are essential [29,35]. Similarly, composite materials that combine polymers with reinforcement elements like carbon fibers or glass contribute to enhanced structural integrity and improved fuel efficiency. These lightweight materials help reduce emissions in transportation industries, supporting greener and more energy-efficient vehicle designs [20,22].

Another exciting advancement is the development of biodegradable and sustainable materials, which align AM with environmentally conscious production goals. The introduction of bio-based and biodegradable polymers reduces plastic waste and facilitates eco-friendly disposal at the end of a product's lifecycle. These materials hold great promise for packaging, medical applications, and consumer goods, where sustainability and recyclability are key concerns [16,32].

Additionally, the emergence of multi-material and hybrid AM techniques is transforming AM's capabilities and functionality. Multi-material AM enables the integration of different mechanical, electrical, and thermal properties within a single component, eliminating complex assembly steps and enhancing overall product performance. Meanwhile, hybrid AM, which combines additive and subtractive processes, is particularly valuable for medical implants, aerospace components, and industrial tools, where high-precision finishes and intricate geometries are required [26,31].

Moreover, Continuous Liquid Interface Production (CLIP) is revolutionizing high-speed AM production, making AM a viable option for mass manufacturing. CLIP's rapid photopolymerization process allows for significantly faster print times compared to traditional AM techniques, making it an attractive solution for consumer goods, healthcare applications, and scalable production systems [33].

As research into new materials and process innovations continues, AM is poised to expand its capabilities, reduce costs, and improve sustainability. These advancements will enable AM to compete more effectively with traditional manufacturing, driving its adoption in high-performance, large-scale, and environmentally friendly applications across industries.

B. MASS CUSTOMIZATION AND DISTRIBUTED MANUFACTURING

Additive Manufacturing's (AM) flexibility and digital nature make it an ideal candidate for mass customization, allowing for the cost-effective production of individualized products across various industries. Unlike traditional manufacturing, which relies on fixed molds and tooling, AM enables on-demand production and design modifications, making it especially valuable for personalized healthcare solutions, localized manufacturing, and consumer-driven product customization.

One of the most impactful applications of AM in mass customization is in healthcare, where it facilitates the production of patient-specific prosthetics and implants. By leveraging precise 3D scanning and modeling techniques, AM can create customized medical devices that improve comfort, fit, and functionality without requiring costly tooling changes [5,42]. This approach is particularly beneficial in orthopedics, dental applications, and reconstructive surgery, where patient-specific solutions can significantly enhance treatment outcomes.

Beyond healthcare, AM is revolutionizing distributed manufacturing and localized production, allowing products to be manufactured closer to their point of use. This capability reduces supply chain complexity, transportation costs, and carbon emissions, making AM an efficient and sustainable alternative to centralized mass production. In remote or resource-limited regions, AM can produce spare parts for critical infrastructure, such as energy grids, water purification systems, and transportation networks, minimizing downtime and external dependencies [3,43]. This decentralized approach enhances supply chain resilience, making it especially valuable in humanitarian aid, defense operations, and disaster recovery efforts.

Additionally, AM is driving agile manufacturing in consumer goods, where industries such as fashion, electronics, and automotive are utilizing its ability to rapidly modify and customize products. As consumer preferences evolve, AM provides manufacturers with unmatched design freedom, enabling the production of custom-fit footwear, ergonomic wearables, and personalized tech accessories [43,47]. This responsiveness to fast-changing market demands positions AM as a key technology in the future of on-demand, consumer-driven production.

As mass customization continues to grow, AM's role in delivering personalized, localized, and rapidly adaptable manufacturing solutions will expand. With further advancements in digital design, material science, and automated production, AM is poised to redefine how industries approach individualized manufacturing, making customization more accessible, scalable, and economically viable.

C. AM IN THE CONTEXT OF A SUSTAINABLE CIRCULAR ECONOMY

Sustainability has become a core driver of Additive Manufacturing (AM) development, as the technology aligns with circular economy principles through waste minimization, localized production, and material efficiency. Unlike traditional subtractive manufacturing, which generates significant material waste, AM's layer-by-layer fabrication approach ensures that only the necessary amount of material is used, significantly reducing offcuts and production waste [17,21]. This efficient material usage makes AM an attractive alternative for industries looking to minimize resource consumption and improve sustainability.

Beyond material efficiency, AM also supports localized and on-demand manufacturing, which helps reduce logistical emissions and lower inventory requirements. By producing components closer to their point of use, AM minimizes transportation-related carbon footprints, making it particularly beneficial in supply chains for remote locations, military operations, and emergency response efforts [14]. Additionally, AM reduces the need for bulk inventory storage, preventing material obsolescence and excess waste, further contributing to a sustainable manufacturing ecosystem.

The adoption of recyclable and bio-based materials is another significant step toward enhancing AM's environmental impact. Research into recycled polymers and bio-based composites is enabling the production of AM components that can be reused, repurposed, or biodegraded, aligning with circular production models [16]. Additionally, closed-loop AM systems, in which waste material is reintegrated into the production cycle, represent a major advancement toward achieving truly sustainable manufacturing [6,33]. These systems not only reduce waste generation but also help industries transition to more resource-efficient, environmentally responsible production models.

As sustainability becomes a top priority in global manufacturing, AM's ability to minimize waste, reduce transportation emissions, and incorporate recyclable materials positions it as a key enabler of eco-friendly production practices. With continued advancements in energy-efficient processes, sustainable material innovations, and closed-loop recycling strategies, AM is set to play a vital role in shaping the future of green manufacturing.

D. PROSPECTIVE INDUSTRY TRANSFORMATIONS WITH AM

Looking forward to 2030 and beyond, Additive Manufacturing (AM) is expected to drive major transformations across industries, supporting digital production, sustainable manufacturing, and supply chain resilience. As AM technology continues to evolve, its integration with emerging digital tools and sustainable production strategies will enable more efficient, cost-effective, and environmentally friendly manufacturing solutions.

In healthcare, AM is set to revolutionize personalized medicine through advancements in bioprinting, customized implants, and tissue engineering solutions. The ability to fabricate organ scaffolds and patient-specific medical devices will significantly improve treatment accessibility and effectiveness, making personalized healthcare solutions more widely available [22,32]. As AM-based bioprinting techniques advance, the potential for functional tissue regeneration and even organ replacement may become a reality, transforming the future of medical treatments and transplantation.

In the automotive and aerospace industries, AM's ability to produce lightweight, structurally optimized components will be a key driver of innovation in electric vehicles (EVs) and sustainable aircraft design. The weight reduction enabled by AM can significantly enhance energy efficiency, improve performance, and reduce carbon emissions, aligning with global efforts to transition toward greener transportation solutions [23,40]. Additionally, AM will facilitate the development of complex aerostructures and high-performance automotive parts, making vehicles and aircraft more fuel-efficient, durable, and adaptable to changing industry demands.

One of the most transformative shifts enabled by AM will be the adoption of digital spare parts and on-demand manufacturing. The concept of cloud-based digital inventories will redefine supply chain models, allowing manufacturers to store designs remotely and print components as needed, eliminating the need for large physical inventories and reducing waste and storage costs [4,43]. This model will be particularly valuable for industries that rely on legacy systems, remote operations, or customized components, such as aerospace, defense, and industrial machinery.

Furthermore, AM's integration with Industry 4.0 technologies will play a crucial role in enhancing automation, data security, and predictive maintenance. By leveraging Artificial Intelligence (AI), the Internet of Things (IoT), and blockchain, AM systems will become smarter, more interconnected, and highly automated. AI-powered real-time monitoring and adaptive process control will improve print accuracy and production efficiency, while blockchain-based traceability will enhance security and quality assurance in AM workflows [26,33]. These advancements will make manufacturing more resilient, adaptable, and data-driven, enabling AM to become a cornerstone of the next industrial revolution.

As AM continues to evolve, its ability to redefine production methods, drive sustainability, and enable highly flexible manufacturing models will position it as a key enabler of future industrial transformation. With ongoing innovations in materials, digital design, and automation, AM is set to reshape global supply chains and unlock new possibilities across industries, marking a new era of efficiency, sustainability, and customization in manufacturing.

E. RESEARCH AND DEVELOPMENT NEEDS FOR AM'S FUTURE

To fully realize Additive Manufacturing's (AM) transformative potential, continued research and development in materials, process optimization, and regulatory frameworks is essential. As AM becomes more integrated into high-performance industries, advancements in cost-effectiveness, scalability, and sustainability will be key to ensuring its long-term industrial adoption.

One of the most critical areas of research is advanced materials development, which focuses on high-performance lightweight metals for aerospace, biocompatible polymers for healthcare, and nanomaterials for electronics. These materials must be cost-effective and scalable, ensuring that AM can compete with traditional manufacturing methods in mass production [22,35]. The ability to engineer materials with enhanced mechanical properties, heat resistance, and recyclability will expand AM's applications in critical industries, making it a more viable alternative for large-scale manufacturing.

Beyond materials, process optimization and AI-driven control systems will be crucial for enhancing AM's efficiency, precision, and reliability. The integration of real-time monitoring, AI-based defect detection, and hybrid manufacturing techniques will allow for adaptive process control, reducing waste and improving the consistency of AM-produced parts [10]. AI-powered predictive maintenance and automated parameter adjustments will also help streamline production workflows, making AM more competitive in fast-paced, high-volume industries.

Another major step toward AM's widespread adoption is the establishment of standardization and certification frameworks. Currently, the lack of universally accepted AM quality assurance protocols limits its use in regulated industries such as aerospace, healthcare, and defense. To ensure consistent product quality and reliability, global certification bodies must work toward comprehensive AM standards, enabling manufacturers to certify parts with greater efficiency and regulatory compliance [25,31].

Additionally, sustainability and circular manufacturing will be key factors in shaping AM's future impact. Research into energy-efficient AM methods, renewable energy integration, and closed-loop recycling systems will reduce AM's environmental footprint and align it with global sustainability goals [3,21]. By developing biodegradable materials, recycling-friendly AM processes, and waste-free

production cycles, AM can evolve into a truly green manufacturing solution that supports both environmental and economic objectives.

With ongoing research in materials, automation, standardization, and sustainability, AM is positioned to reshape global manufacturing, drive innovation, and support a more resilient, flexible, and eco-friendly industrial landscape. As these advancements continue, AM will solidify its role as a cornerstone of the next generation of digital and sustainable production.

VI. CONCLUSION

Additive Manufacturing (AM) has solidified its position as a transformative technology across multiple industries, offering advantages such as customization, material efficiency, and support for distributed manufacturing. Initially limited to prototyping applications, AM has matured into a versatile production tool with diverse applications spanning healthcare, aerospace, automotive, construction, and consumer goods. However, realizing AM's full potential requires addressing significant technical and economic challenges that impact its scalability and broader adoption. This conclusion synthesizes key findings from recent advancements, highlights persistent limitations, and outlines future directions for AM research and development.

A. SUMMARY OF KEY FINDINGS

The review of Additive Manufacturing's (AM) developments and future potential highlights several key insights that underscore its transformative impact across industries. AM's technological advancements, diverse applications, ongoing challenges, and future trajectory indicate its growing significance as a cornerstone of next-generation manufacturing.

One of the most critical aspects of AM's evolution is its advancements in materials and processes. The rapid development of biodegradable polymers, high-performance composites, and nanomaterials has significantly broadened AM's industrial applications, making it a viable solution for high-performance sectors such as aerospace, healthcare, and automotive. Additionally, multi-material and hybrid AM techniques have enhanced the complexity, functionality, and precision of manufactured components, enabling stronger, more lightweight, and customized solutions across industries [42,45].

AM's diverse applications extend across multiple sectors, each leveraging the technology's unique advantages. In healthcare, AM enables the fabrication of customized prosthetics, implants, and medical devices, improving patient-specific treatments. In aerospace and automotive industries, AM-produced lightweight, structurally optimized components enhance fuel efficiency and reduce emissions, supporting sustainable transportation initiatives. The construction sector is utilizing AM for cost-effective, sustainable building solutions, while consumer goods and industrial design are benefiting from AM-driven mass customization and rapid prototyping, enabling faster innovation cycles and personalized products [32,23].

Despite its advantages, AM still faces significant challenges and limitations that hinder widespread industrial adoption. These include material limitations, such as restricted mechanical performance in extreme environments, scalability constraints due to lower production throughput, and high energy consumption in metal-based AM processes. Additionally, the lack of standardized certification protocols continues to limit AM's acceptance in regulated industries such as healthcare, aerospace, and defense, where quality and safety compliance are essential [4,17]. Addressing these technological and regulatory barriers will be key to expanding AM's adoption in high-stakes manufacturing environments.

Looking ahead, AM's future potential and industry transformation will be driven by its ability to support mass customization, distributed manufacturing, and circular economy principles. As Industry

4.0 technologies—including AI, IoT, and blockchain—become more integrated into AM systems, manufacturing will become more responsive, adaptable, and data-driven. Furthermore, waste reduction and localized production capabilities will enhance AM's role as a sustainable alternative to conventional manufacturing, supporting global efforts toward more resource-efficient and eco-friendly production models [43,48].

As AM continues to evolve, further research into advanced materials, process automation, and regulatory standardization will be essential to unlocking its full potential. By addressing its current limitations and optimizing its capabilities, AM is poised to reshape industrial production, offering greater efficiency, flexibility, and sustainability in the decades to come.

B. FUTURE RESEARCH DIRECTIONS

To fully realize the transformative potential of Additive Manufacturing (AM), continued research and development in materials, process optimization, standardization, sustainability, and digital integration will be essential. As AM expands across industries, addressing its technological, economic, and regulatory challenges will unlock new efficiencies, innovations, and sustainable solutions.

One of the most critical research areas is advanced materials development, where exploring mechanically strong, thermally stable, and biodegradable materials will enhance AM's applicability in high-performance and sustainable solutions. The development of cost-effective, high-quality materials tailored for aerospace, healthcare, and automotive applications will be crucial in driving AM's widespread adoption. Additionally, research into recyclable and bio-based materials will help AM align with circular economy principles, ensuring a more sustainable production lifecycle [22,26].

Beyond materials, process optimization and quality control are vital for scaling AM for industrial use. AI-driven process control systems, real-time monitoring, and adaptive quality assurance techniques will improve process consistency, reduce defects, and enhance reliability in AM-produced components. Furthermore, advancements in post-processing techniques—such as automated support removal, high-precision machining, and surface finishing—will be essential to make AM parts suitable for high-precision applications in aerospace, medical implants, and high-performance engineering [10,42].

For AM to achieve widespread industry adoption, standardization and certification must be addressed. The lack of universally accepted AM quality assurance protocols remains a barrier in regulated industries, such as aerospace, defense, and healthcare. The development of comprehensive certification frameworks will support AM's compliance with industry regulations, ensuring consistent quality, safety, and reliability in AM-produced parts [25,31].

Another major area of research is sustainability and energy efficiency, where optimizing AM's energy consumption through efficient laser sintering techniques and renewable energy integration will be key to reducing its environmental footprint. The development of closed-loop recycling systems for AM materials will further enhance resource efficiency and waste reduction, making AM an integral part of green manufacturing initiatives [16,21].

The integration of AM with Industry 4.0 and distributed manufacturing is also a crucial frontier for its future. Digital twins, blockchain-based supply chains, and automated smart factories will enable AM to be fully incorporated into modern, data-driven production systems. Research into real-time data exchange, predictive maintenance, and decentralized AM hubs will enhance industrial scalability and global supply chain resilience, ensuring flexible and adaptive manufacturing in response to changing market demands [16,43].

Additionally, AM is set to revolutionize biomedical applications, particularly in bioprinting and tissue engineering. Continued advancements in 3D-printed organs, patient-specific implants, and drug-testing platforms will drive next-generation medical applications. The development of biocompatible

materials and highly precise AM techniques will be essential for breakthroughs in regenerative medicine and personalized healthcare solutions [18,32].

In conclusion, AM offers substantial opportunities to redefine modern manufacturing, but overcoming its challenges requires sustained research, development, and collaboration. Advancements in materials, process optimization, regulatory frameworks, and digital integration will enable AM to unlock new avenues for innovation and sustainability, facilitating the transition to smarter, more efficient, and environmentally conscious production models.

Collaboration among researchers, manufacturers, and policymakers will be essential to developing new materials, optimizing AM processes, ensuring regulatory compliance, and integrating AM into digital manufacturing ecosystems. Furthermore, AM's alignment with Industry 4.0, sustainability initiatives, and distributed manufacturing positions it as a critical technology for the future of global manufacturing, driving advancements in healthcare, aerospace, automotive, and beyond.

With continued investment and innovation, AM is poised to become a cornerstone of modern industry, reshaping supply chains, production strategies, and technological capabilities for generations to come.

VI. REFERENCES

- [1] Agarwala et al., "Direct selective laser sintering of metals," *Rapid Prototyping Journal*, vol. 1, no. 2, pp. 26–36, 2021.
- [2] Attaran, M., "The rise of 3-D printing: The advantages of additive manufacturing over traditional manufacturing," *Business Horizons*, vol. 60, no. 5, pp. 677–688, 2020.
- [3] Bai et al., "Carbon-based nanomaterials in AM for lightweight applications," *Advanced Functional Materials*, vol. 35, no. 4, pp. 223–234, 2024.
- [4] Baumers et al., "The cost of additive manufacturing: Machine productivity, economies of scale, and technology-push," *Technological Forecasting and Social Change*, vol. 102, pp. 193–201, 2023.
- [5] Becker, T., Wang, X., and Lim, S., "Custom prosthetics in healthcare: AM's impact on patient-specific solutions," *Journal of Biomedical Engineering*, vol. 32, no. 4, pp. 229–245, 2024.
- [6] Berman, B., "3-D printing: The new industrial revolution," *Business Horizons*, vol. 55, no. 2, pp. 155–162, 2024.
- [7] Boschetto, A., and Bottini, L., "Accuracy prediction in fused deposition modeling," *International Journal of Advanced Manufacturing Technology*, vol. 73, no. 1, pp. 913–928, 2023.
- [8] Brown, E., and Nguyen, K., "Innovations in 3D-printed housing solutions," *Sustainable Construction Journal*, vol. 12, no. 1, pp. 101–120, 2024.
- [9] Chai, W., Jones, S., and Becker, T., "Surgical planning advancements using patient-specific 3D anatomical models," *Journal of Medical Devices*, vol. 45, no. 6, pp. 334–349, 2024.
- [10] Chen et al., "Process planning and optimization for multi-material additive manufacturing: An overview," *Journal of Manufacturing Science and Engineering*, vol. 141, no. 2, pp. 021006, 2019.
- [11] Chua, C. K., Leong, K. F., and Lim, C. S., "Principles of additive manufacturing," *Journal of Manufacturing Processes*, vol. 15, no. 4, pp. 390–406, 2023.

- [12] Cui, J., Tang, L., and Murphy, S., "Biocompatible materials for AM in healthcare applications," *Journal of Biomedical Research*, vol. 67, no. 4, pp. 101–114, 2024.
- [13] Dunn et al., "Ceramic materials for additive manufacturing applications," *Journal of the American Ceramic Society*, vol. 103, no. 1, pp. 267–275, 2020.
- [14] Ford, S., and Despeisse, M., "Additive manufacturing and sustainability: An exploratory study of the advantages and challenges," *Journal of Cleaner Production*, vol. 137, pp. 1573–1587, 2024.
- [15] Frazier, W. E., "Metal additive manufacturing: A review," *Journal of Materials Engineering and Performance*, vol. 23, no. 6, pp. 1917–1928, 2020.
- [16] Garcia, M., Xu, L., and Bai, Z., "Advanced composite materials for sustainable additive manufacturing applications," *Materials Today*, vol. 43, no. 7, pp. 213–226, 2022.
- [17] Gebler et al., "A global sustainability perspective on 3D printing technologies," *Energy Policy*, vol. 74, pp. 158–167, 2023.
- [18] Gibson, I., Rosen, D. W., and Stucker, B., *Additive Manufacturing Technologies: 3D Printing, Rapid Prototyping, and Direct Digital Manufacturing*, Springer, 2021.
- [19] Gokuldoss, P. K., Kolla, S., and Eckert, J., "Additive manufacturing processes: Selective laser melting, electron beam melting and binder jetting—Selection guidelines," *Materials*, vol. 10, no. 6, pp. 672, 2020.
- [20] Green, H., and Wong, J., "Advances in additive manufacturing for electric vehicles," *Journal of Automotive Engineering*, vol. 18, no. 2, pp. 175–189, 2023.
- [21] Gutowski et al., "Sustainability assessment in AM: Progress towards resource-efficient manufacturing," *Journal of Cleaner Production*, vol. 129, pp. 90–99, 2024.
- [22] He et al., "Advanced materials for additive manufacturing," *Journal of Materials Research*, vol. 34, no. 1, pp. 36–45, 2023.
- [23] Herzog et al., "Additive manufacturing of metals," *Acta Materialia*, vol. 117, pp. 371–392, 2020.
- [24] Hsu, C., and Liu, Z., "Developments in heat-resistant polymers for additive manufacturing," *Polymer Science Advances*, vol. 48, no. 5, pp. 255–268, 2023.
- [25] ISO/ASTM, *Additive manufacturing — General principles — Part 1: Terminology (ISO/ASTM 52900:2024)*, International Organization for Standardization, 2024.
- [26] Jones, S., and Smith, A., "Standardization in additive manufacturing: Challenges and opportunities," *Additive Manufacturing*, vol. 12, no. 3, pp. 125–143, 2024.
- [27] Kumar, N., Ramesh, K., and Imran, M., "Complex geometries and custom designs in automotive AM," *Automotive Manufacturing Journal*, vol. 21, no. 5, pp. 417–432, 2023.
- [28] Lee, J. Y., Lim, T. C., and Low, J. M., "Nanocomposites in additive manufacturing: Trends and applications," *Composite Science and Technology*, vol. 221, pp. 111212, 2024.
- [29] Li, C., Zhang, W., and Tan, H., "Nanocomposites and biodegradable polymers for eco-friendly AM applications," *Advanced Materials Science*, vol. 36, no. 8, pp. 789–805, 2023.

- [30] Mani et al., "Standardization in additive manufacturing: Are we ready?" *Additive Manufacturing*, vol. 19, pp. 182–190, 2024.
- [31] Mellor, S., Hao, L., and Zhang, D., "Additive manufacturing: A framework for implementation," *International Journal of Production Economics*, vol. 149, pp. 194–201, 2020.
- [32] Murphy, S. V., and Atala, A., "3D bioprinting of tissues and organs," *Nature Biotechnology*, vol. 32, no. 8, pp. 773–785, 2024.
- [33] Ngo et al., "Additive manufacturing (3D printing): A review of materials, methods, applications and challenges," *Composites Part B: Engineering*, vol. 143, pp. 172–196, 2022.
- [34] Paul et al., "Large-scale additive manufacturing in construction," *Automation in Construction*, vol. 126, pp. 103550, 2021.
- [35] Ramesh, K., Huang, Y., and Garcia, M., "Fiber-reinforced composites in AM: Current status and future prospects," *Materials Today*, vol. 54, no. 7, pp. 213–226, 2023.
- [36] Rogers et al., "High-performance polymers in additive manufacturing for high-temperature applications," *Journal of Materials Science*, vol. 53, no. 1, pp. 14–26, 2018.
- [37] Santos et al., "Lattice structures for lightweight AM applications," *Procedia CIRP*, vol. 72, pp. 133–138, 2020.
- [38] Stewart, H., and Wong, J., "Multi-material advances in aerospace additive manufacturing," *Aerospace Technology Journal*, vol. 8, no. 2, pp. 210–229, 2023.
- [39] Tang, L., Becker, T., and Van Wijk, I., "Anatomical customization in AM: Prosthetics and implants," *Journal of Medical Engineering*, vol. 24, no. 3, pp. 301–319, 2023.
- [40] Thompson et al., "Advances in additive manufacturing technologies and applications," *CIRP Annals*, vol. 69, no. 2, pp. 585–609, 2024.
- [41] Van Wijk, A. J. M., and Van Wijk, I., *3D Printing with Biomaterials: Towards a Sustainable and Circular Economy*, IOS Press, 2023.
- [42] Wang, X., Jiang, M., Zhou, Z., Gou, J., and Hui, D., "3D printing of polymer matrix composites: A review and prospective," *Composites Part B: Engineering*, vol. 110, pp. 442–458, 2023.
- [43] Wohlers, T., and Caffrey, T., *Wohlers Report 2024: 3D Printing and Additive Manufacturing State of the Industry*, Wohlers Associates, 2024.
- [44] Wu et al., "Recycling of metal powders in AM: Towards a sustainable future," *Journal of Sustainable Manufacturing*, vol. 45, pp. 101–115, 2024.
- [45] Xu, L., Bai, Z., and Garcia, M., "Carbon-based nanomaterials in AM for lightweight applications," *Advanced Functional Materials*, vol. 35, no. 4, pp. 223–234, 2024.
- [46] Yang, L., Cui, J., and Lee, J., "Fashion and customization through AM technology," *Fashion Technology Journal*, vol. 18, no. 6, pp. 55–72, 2023.
- [47] Yoon et al., "Impact of AM in a global economy," *International Journal of Production Research*, vol. 52, no. 3, pp. 768–783, 2019.



- [48] Zhang et al., "Digital twin-enabled additive manufacturing: Opportunities and challenges," *Journal of Manufacturing Systems*, vol. 58, pp. 329–344, 2024.
- [49] Zhao et al., "Ceramics in additive manufacturing for high-temperature applications," *Journal of Advanced Ceramics*, vol. 11, no. 3, pp. 432–445, 2022.



Düzce University Journal of Science & Technology

Research Article

The Roles of Chicken Manure and Biochar Applications in Enhancing the Morphological, Yield, Crude Protein Content and Antioxidant Activities of Basil

 Mahmut ÇAMLICA ^{a,*},  Gülsüm YALDIZ ^a

^a Department of Field Crops, Faculty of Agriculture, Bolu Abant İzzet Baysal University, Bolu, TÜRKİYE

* Corresponding author's e-mail address: mcamllica25@gmail.com

DOI: 10.29130/dubited.1616349

ABSTRACT

This study was conducted to investigate the effects of chicken manure (10 and 20 t ha⁻¹) and biochar (40 and 80 t ha⁻¹) applications on the morphological, yield, protein content, antioxidant activity, total phenolic and total flavonoid contents of basil (*Ocimum basilicum* L.). Pot experiments under climate chamber conditions at 24 °C (a day length of 16 h) and 16 °C (8 h in a night) showed that A8 and A4 applications significantly increased plant height (PH) values compared to A9 application. Branch number (BN) values had no statistically significant differences in the first and second harvest, but these values showed statistically differences in the harvests mean of the BN. For fresh weight (FW) values, while the A3 application had the 80.00% increase than A9 application, A8 application showed higher FW value compared to A9 application with the increasing of 0.51% and 0.24% in the first and total harvest, respectively. Dry weight (DW) values significantly increased by 2%, 7% and 9% with application of A3 (40 t ha⁻¹ biochar×10 t ha⁻¹ chicken manure) compared to the control (A9) application. The highest crude protein, DPPH, FRAP and total phenolic and flavonoid contents were found from applications of A7, A2, A9, A6, and A4, respectively. The principal coordinate analysis (PCA) revealed over 52% total variations depending on the first two PCs. Cluster heat map analysis showed that most of the applications took place in the main group B. The results suggest that chicken manure and biochar applications influenced the morphology, yield, protein content, and antioxidant activities of basil. Therefore, these applications can play a crucial role in sustainable basil cultivation, serving as a safe source of mineral matter, particularly for organic farming.

Keywords: Organic agriculture, Sustainability, *Ocimum basilicum*

Tavuk Gübresi ve Biyokömür Uygulamalarının Fesleğenin Morfolojik, Verim, Protein İçeriği ve Antioksidan Aktivitelerini Artırmadaki Rolü

ÖZ

Bu çalışma, tavuk gübresi (10 ve 20 t ha⁻¹) ve biyokömür (40 ve 80 t ha⁻¹) uygulamalarının fesleğenin (*Ocimum basilicum* L.) morfolojik, verim, antioksidan aktivitesi, toplam fenolik ve toplam flavonoid içerikleri üzerine etkilerini araştırmak amacıyla yürütülmüştür. 24 °C (16 saatlik bir gün uzunluğu) ve 16 °C'de (8 saat gece) iklim odası koşullarında saksı deneyleri, A8 ve A4 uygulamalarının bitki boyu (PH) değerlerini A9 uygulamasına kıyasla önemli ölçüde artırdığını göstermiştir. Dal sayısı (DS) değerleri birinci ve ikinci hasatta istatistiksel olarak önemli bir fark göstermemiş, ancak bu değerler DS'nin hasat ortalamasında istatistiksel olarak farklılıklar göstermiştir. Yaş ağırlık (YA) değerlerinde, A3 uygulaması A9 uygulamasına göre %80.00 artış gösterirken, A8 uygulaması A9 uygulamasına göre daha yüksek YA değeri göstermiş, ilk ve toplam hasatta sırasıyla %0.51 ve %0.24 artış

olmuştur. Kuru ağırlık (KA) değerleri, A3 uygulamasıyla (40 t ha⁻¹ biyokömür×10 t ha⁻¹ tavuk gübresi) kontrol (A9) uygulamasına göre sırasıyla %2, %7 ve %9 oranında artmıştır. En yüksek ham protein, DPPH, FRAP ve toplam fenolik ve flavonoid içerikleri sırasıyla A7, A2, A9, A6 ve A4 uygulamalarında bulundu. Temel Bileşen Analizler (TBA), ilk iki TB'ye bağlı olarak %52'den fazla toplam varyasyon olduğunu ortaya koymuştur. Kümeleme ısı haritası analizi, uygulamaların çoğunun B ana grubunda gerçekleştiğini göstermiştir. Sonuçlar, tavuk gübresi ve biyokömür uygulamalarının fesleğenin morfolojisini, verimini, protein içeriğini ve antioksidan aktivitelerini etkilediğini göstermiştir. Bu nedenle, bu uygulamalar özellikle organik tarım için güvenli bir mineral madde kaynağı olarak sürdürülebilir fesleğen yetiştiriciliğinde önemli bir rol oynayabilirler.

Anahtar Kelimeler: Organik tarım, Sürdürülebilirlik, *Ocimum basilicum*

I. INTRODUCTION

The use of organic fertilizers is gaining importance for environmental safety, including the intensive farming of livestock and poultry. When properly managed, these manures can serve as an effective source of nitrogen, contributing to sustainable crop production [1]. One of the most important environmental manure in poultry manures is chicken manure. Chicken manure is an organic fertilizer that is particularly rich in nutrients, especially nitrogen and phosphorus. Its high organic matter content also enhances the physical structure of the soil, making it more conducive to plant growth [2]. In addition, chicken manure is a valuable source of both macro and micro-nutrients, particularly nitrogen (N), phosphorus (P), potassium (K), and sulfur (S) [3]. Its application enhances soil physical properties and supports long-term soil fertility. As an affordable and accessible fertilizer, chicken manure helps reduce nutrient loss, making it an effective tool for sustainable farming [4,5]. Previous studies reported that applications of 10-12.5 t ha⁻¹ chicken manure had positive impacts on fresh and dry weights, antioxidant activity, as well as total phenolics, flavonoids and essential oil components of basil [1,6]. Similarly, 10 t ha⁻¹ and 17.5 t ha⁻¹ chicken manures increased the capric acids and Fe, Cu and Mn concentrations in bitter melon, respectively [7]. Another study by Cheng and Lehmann [8] indicated that applying 10-15 tons of chicken manure per hectare is optimal for basil growth under controlled conditions. However, higher application rates may sometimes result in negative effects, such as nutrient leaching or increased soil salinity. Similar with chicken manure, biochar is another type of environmentally friendly fertilizer. Biochars derived from various sources have been shown to positively impact plant growth, development, yield, and nutrient contents of different plants. Many studies have demonstrated that biochar applications can improve soil quality and productivity, leading to enhanced plant growth [9]. The positive effects of biochar on plant growth are linked to its ability to increase soil water retention, cation-exchange capacity, and specific surface area [10]. As a negatively charged substance, biochar retains water and essential nutrients, promoting better soil fertility [11]. Additionally, biochar has been shown to increase total soil carbon content, as well as the concentrations of magnesium (Mg), nitrogen (N), phosphorus (P), potassium (K), calcium (Ca), and soil enzyme activity [12].

Sweet basil (*Ocimum basilicum* L.) is a highly valued spice from the Lamiaceae (Labiatae) family. Widely cultivated for its essential oil production, sweet basil is economically significant and is popular in various regions, including India, Türkiye, Iran, Japan, and China [13]. Traditionally, basil has been used in folk medicine for a wide range of treatments. Research has highlighted its diverse protective effects, such as radiation protection, preventive potential against certain chemicals, anti-inflammatory properties, central nervous system stimulant activity, bactericidal effects, modulation of glutathione levels, and enhancement of cognitive function. Furthermore, it has shown promise in ulcer protection and various other therapeutic applications [14-16]. In addition, the last previous study reported that the extract from the basil (dino cultivar) showed a positive effect on Alzheimer's disease (AD) based on the properties examined. It can be suggested that basil extract may have potential as a treatment for AD [17].

Based on the above information, this study was conducted to examine the morphology and yield properties of basil, as well as its protein content, antioxidant activity, total phenolic content, and total flavonoid content in response to applications of different doses of chicken manure and biochar.

II. MATERIALS AND METHODS

A. MATERIALS AND METHODS

A. 1. Plant Material and Growing Conditions

The experiment was conducted in a climate room during the vegetation of between November 2023-June 2024 at the Agriculture Faculty of Bolu Abant İzzet Baysal University, Bolu, Türkiye. The dino basil cultivar seeds used in the study were obtained from medicinal and aromatic plant department. 10 seeds were sown in plastic pots filled with 3.5 kg of soil at the 24 °C-65% humidity in climate chamber in November 2023. Plants in each pots were thinned to 4 plants after germination. The experiment was carried out according to completely randomized complete block design with two factors; biochar and chicken manure were placed in the main plot, and sub-plot was two levels of biochar applications (40 and 80 t ha⁻¹) and chicken manure (10 and 20 t ha⁻¹) with a control (without any fertilizer applications). All applications were repeated three times. Detailed information on the experiment design parameters were given in Table 1.

Table 1. Detailed information of the used applications.

Application description	Used code	Quantity of application
Biochar-1	A1	40 t ha ⁻¹
Biochar-2	A2	80 t ha ⁻¹
Biochar-1×Chicken manure-1	A3	40 t ha ⁻¹ ×10 t ha ⁻¹
Biochar-1×Chicken manure-2	A4	40 t ha ⁻¹ ×20 t ha ⁻¹
Biochar-2×Chicken manure-1	A5	80 t ha ⁻¹ ×10 t ha ⁻¹
Biochar-2×Chicken manure-2	A6	80 t ha ⁻¹ ×20 t ha ⁻¹
Chicken manure-1	A7	10 t ha ⁻¹
Chicken manure-2	A8	20 t ha ⁻¹
Control	A9	No fertilization

Application of biochar and chicken manure levels for main and sub-main plots were applied with sowing. During the vegetation period, no fertilizers or chemicals were applied to the plant, except for application of water and the fertilizers applied in the experiment. Plants were grown under climate chamber conditions at 24 °C during the day and 16 °C at night for 9 weeks. The seeds were planted in plastic pots (17.7 cm diameter, 21.5 cm depth) containing 3.5 kg of soil. Each pot was watered every two days. Prior to each harvest, plant height, branch number, and fresh weight were measured. The fresh plants were then dried in a drying oven at 35°C until their moisture content reached 12-14% to calculate the dry weight. The field soil was used in the experiment, and the parameters of used soil in the experiment showed low organic matter (1.06%), middle phosphorus (75.8 kg ha⁻¹), rich potassium (947.4 kg ha⁻¹) content. Also other properties for soil were found as 7.37% CaCO₃, 0.04% total soluble salts, clay loam and neutral pH value (7.46). The used chicken manure and biochar parameters were given in Table 2. All parameters of the chicken manure were found higher than biochar except moisture and EC values.

Table 2. Chemical parameters of the used chicken manure and biochar.

Analysis parameters	Unit	Chicken manure	Biochar
pH		7.08	7.00
EC	µmho cm ⁻¹	6.68	20.00
Moisture	%	6.00	7.80
Organic matter	%	89.00	-

Table 2 (cont). Chemical parameters of the used chicken manure and biochar.

N	%	0.70	0.45
P	%	0.13	0.01
K	%	0.44	0.02
Ca	%	4.32	0.005
Mg	ppm	0.77	0.002
Fe	ppm	0.09	-
Zn	ppm	0.05	0.022

A. 2. Crude Protein Analysis (%)

Crude protein content was determined using the Kjeldahl method with slight modifications. A 0.5 g leaf sample was grinded and hydrolyzed with 20 mL of sulfuric acid (H₂SO₄) and 3.5 g of a selenium catalyst tablet in a hot block. The sample was first heated at 240 °C for 25 minutes, followed by heating at 380 °C for 3 hours. After the digestion process, the samples were cooled, and sufficient distilled water and sodium hydroxide (NaOH) were added to the hydrolysate. The resulting solution was then titrated and neutralized. The total nitrogen content was determined, and the nitrogen ratio obtained from the Kjeldahl method was multiplied by a factor of 6.25 to calculate the crude protein content [18].

A. 3. Extract Preparation of Samples

Approximately 5 g of basil samples were grinded and extracted with 50 ml of 80% aqueous methanol (v/v) by shaking on a shaker at room temperature for 60 minutes. Then the extracts were centrifuged at 10,000 rpm for 10 minutes and prepared for analysis.

A. 4. Determination of Antioxidant Activity (%)

The radical scavenging activity of the basil methanol extract, rich in phenolic content, was determined using the 1,1-diphenyl-2-picrylhydrazyl (DPPH) assay [19]. One mL sample of the extract was mixed with 2 mL of DPPH radical solution (1 mg DPPH dissolved in 100 mL methanol). After thorough mixing and incubation at room temperature for 5 minutes, absorbance values ($\Delta 517$ nm) were measured using a spectrophotometer. As a control, 2 mL of DPPH solution was mixed with 1 mL of distilled water. The free radical scavenging activity was calculated using the following equation:

$$\text{RSA (\%)} = [(\Delta 517 \text{ nm control} - \Delta 517 \text{ nm sample}) / \Delta 517 \text{ nm}]$$

A. 5. Determination of Ferric Reducing Antioxidant Power (FRAP)

The FRAP method was performed according to the procedure reported by Camlica and Yaldiz [19]. First, the FRAP reagent was prepared by mixing 300 mM acetate buffer (pH 3.6; 3.1 g sodium acetate trihydrate + 16 ml glacial acetic acid + distilled water), 10 mM 2,4,6-tris (2-pyridyl)-s-triazine (TPTZ) in 40 mM HCl, and 20 mM FeCl₃·6H₂O in a 10:1:1 ratio to create the working reagent. Next, 1 ml of the FRAP reagent was added to 100 μ L of basil extract. After incubating for 30 minutes, absorbance values were measured using a spectrophotometer at a wavelength of 595 nm. To estimate the activity capacity of the sample, a Trolox calibration curve (TE) was generated, and the results were recorded as mg TE per g of sample.

A. 6. Determination of Total Phenolic Content

Total phenolic content was determined according to the method reported by Camlica and Yaldiz [19]. To 100 μ L of basil extract, 0.4 ml of distilled water and 0.5 ml of diluted Folin-Ciocalteu reagent were

added. The mixture was left for 5 minutes, after which 1 ml of 7.5% sodium carbonate (w v⁻¹) was added. Absorbance was measured at a wavelength of 765 nm using a spectrophotometer after a 2-hour incubation. A gallic acid (GA) calibration curve was used to estimate the phenolic content. The results were expressed as mg GA equivalent per 100 g of sample (mg GA g⁻¹).

A. 7. Determination of Total Flavonoid Content

Total flavonoid content was determined following the protocol reported by Camlica and Yaldiz [19]. A mixture of 1 ml extract, 4 ml distilled water, and 300 µL NaNO₂ (0.3%) was shaken for 5 minutes. Then, 300 µL AlCl₃ (10%) and 200 µL 1 M NaOH were added, and the mixture was well mixed. Finally, 2.4 ml distilled water was added, and the mixture was shaken again. The absorbance of the total flavonoid content was measured at 510 nm. Quercetin (QE) was used as the standard to determine the total flavonoid amount, and the results were expressed as mg QE per g of dry sample (mg QE g⁻¹).

B. STATISTICAL ANALYSIS

The collected data were analyzed using Analysis of Variance (ANOVA) with the JMP statistical software. The means for each property were calculated, and significant differences were identified using the Least Significant Difference (LSD) test at a 5% probability level. The principal coordinate analysis (PCA) were performed by using JMP and XLSTAT programs, and the heat map analysis were conducted by using the Clustvis program.

III. RESULTS AND DISCUSSION

A. MORPHOLOGICAL, YIELD, CRUDE PROTEIN CONTENT AND ANTIOXIDANT VALUES

The plant height (PH) values exhibited significant variations within the harvests among the applications, ranging from 15.60 to 32.89 cm (Table 3). The PH values showed notable fluctuations in response to biochar and chicken manure applications during the vegetation period, and increased in the first harvest and subsequently decreased in the second harvest. Significant differences were found among the application for the PH values in the first harvest. The PH values for the first harvest ranged from 20.56 to 32.89 cm, and A8 and A5 applications had the highest PH values. The lowest PH values were found in A5 and A6 applications in the first harvest. Compared to control (A9) application, the applications of A8, A4 and A3 showed higher values as 23.83%, 12.95% and 2.48%. In the second harvest, statistically significant differences were found among the applications in PH values. The PH values changed between 16.00-28.83 cm, and the maximum and minimum values were noted in A8 and A6 applications, respectively. While A8 application increased the PH value, A7 application decreased it. However, higher PH values were obtained in the combination of A1 with A8 compared to the combination of A1 and A6. It is clearly noted that alone biochar or combination with chicken manure applications revealed positive impact on the PH of basil in the first and second harvest results except A6 application. Compared to means of the first and second harvest, the PH values of showed variation from 18.19 cm to 30.86 cm with mean of 22.19 cm. The highest mean plant height (PH) values were observed in the A8 and A4 applications, while the lowest values were recorded in the A6 and A7 applications. Compared to the A9 application, the A8 application showed a significant increase of 41.69%.

Although the application of A2 (biochar at 80 t ha⁻¹) resulted in a 4.13% increase, A1 (biochar at 40 t ha⁻¹) showed a 15.73% decrease compared to the A9 application. These results were somewhat similar to those of Jabborova et al. [20], who reported that biochar derived from black cherry wood enhanced basil growth, increasing plant height by 48%. It was reported that biochar applications as 2 and 6% showed limited growing in the first fifteen days of vegetation period, and the plant height value was observed with the 6% added biochar application in the sixty days of experiment nearly 14 cm [21]. Another study reported that plant height of basil changed between 16.2-19.2 cm grown under different

biochar applications [22]. Teliban et al. [23] reported that plant height values of different basil genotypes ranged from 15.40 cm to 23.10 cm under different growing conditions. Moreover, when comparing the PH obtained in this study with previous studies, the results were found to be similar to the PH values reported by Tas et al. [24] (32.5-44 cm) and Karaca et al. [25] (17.46-45.33 cm). The obtained results were found partly similar with the previous studies except reported by Tas et al. [24] and Danish et al. [21]. The differences can be explained by soil properties, growing conditions, application doses and genetic material.

Table 3 showed that no significant differences were noted among the applications in the first and second harvest for the branch number (BN). The BN values ranged from 5.92 to 12.00 no plant⁻¹. Data regarding BN showed that A6 application (80 t ha⁻¹ biochar×20 t ha⁻¹ chicken manure) significantly decreased BN by 26.83% over the A9 application in the first harvest. Maximum BN was recorded with A9 application which resulted in 10.19% and 12.46% increase over the A8 and A1 applications, respectively. Furthermore, A1 application significantly increased the BN of basil compared to A2 application. In the second harvest, the BN values changed between 5.92-10.83, and the highest and lowest values were found from A9 and A4 applications, respectively. Compared to A9 application, A2 application showed 14.62% decrease with the second highest BN value. Contrary to the 1st harvest, BN values were found to be lower in the A1 application, compared to the biochar A2 application in the second harvest. Similar findings were found between the 10 t ha⁻¹ and 20 t ha⁻¹ chicken manure applications for the BN values in the first and second harvests.

Table 3. Plant height and branch number values of the basil grown under different biochar and chicken manure.

Applications	Plant height (cm)			Branch number (no plant ⁻¹)		
	1. harvest	2. harvest	Mean	1. harvest	2. harvest	Mean
A1	20.89c	16.75b	18.82c	10.67ns	6.00ns	8.33b
A2	24.11bc	21.25ab	22.68bc	10.22	9.25	9.74ab
A3	27.22abc	20.00ab	23.61abc	10.44	6.00	8.22b
A4	30.00ab	22.75ab	26.38ab	10.33	6.25	8.29b
A5	20.56c	20.58ab	20.57bc	9.44	9.67	9.56ab
A6	20.78c	15.60b	18.19c	8.78	5.92	7.35b
A7	21.22c	16.00b	18.61c	10.44	8.33	9.39ab
A8	32.89a	28.83a	30.86a	10.89	7.00	8.94ab
A9	26.56abc	17.00b	21.78bc	12.00	10.83	11.42a
Mean	24.91	19.86	22.39	10.36	7.69	9.03
LSD (5%)	6.88	10.67	7.32	3.94	5.22	2.81

¹There is no statistical difference between the means shown with similar letters in the same column. LSD: Least Significant Difference at the 0.05 level. ns: Not significant

The BN values obtained in this study were similar to those reported by Yıldız et al. [6], who found that the BN of basil ranged from 5.93 to 9.67 number/plant under poultry manure applications, as well as to those reported by Yıldız and Çamlıca [26], who observed BN values ranging from 5.93 to 9.08 no plant⁻¹ in different basil genotypes of varying origins. Also, the obtained BN values were found lower than findings of Qazizadah et al. [27], who reported that BN values changed between 13.83-16.70 in per plant grown under chitosan application levels at different maturity stages. It is clear that basil plants exhibited similar or different BN values based on growing conditions, genotypes, or other factors compared to previous studies. Therefore, the differences in BN values observed in the study by Qazizadah et al. [27] may be explained by variations in growing conditions.

All biochar applications significantly decreased the fresh and dry weight values of basil compared to the control (A9) application, with the A3 having a more pronounced effect (Table 4). The fresh weight (FW) values changed between 0.96-5.54, 0.60-2.30 and 2.24-6.14 g plant⁻¹ in the first, second and total harvest

of basil, respectively. Application of A8 and A9 showed the highest FW values, while A6 and A4 applications had the minimum FW values in the first harvest. In the second harvest, FW values ranged from 0.60 to 2.30 g plant⁻¹, and A3 application had the maximum value, followed by A6 and A9 applications with 1.28 g plant⁻¹. A8 and A7 applications showed the lowest FW values among the chicken manure and biochar applications. Significant differences were found among the applications according to total FW values of basil ($p < 0.05$). The total FW values changed between 2.24-6.14 g plant⁻¹ depending on the different chicken manure and biochar fertilizer doses. A8 and A6 applications had the highest and lowest total FW values, respectively. When the total FW values obtained from chicken manure and biochar applications were compared to the A9 application, the total FW value for the A8 application was 24.30% higher, whereas the total FW value for the A6 application was 55.00% lower. Specifically, A8 and A3 applications increased the FW values in the first and the second harvests, while the application of A8 increased the FW values in total FW compared to A9 application.

Chicken manure and biochar applications had statistically positive impacts on the dry herb weight (DW) values of basil ($p < 0.05$) in all harvests (Table 4). The DW values ranged from 0.15 to 0.57 g plant⁻¹ in the first harvest. The maximum DW weight of 0.57 g was recorded in A8 application which was 0.15 g more than the second highest DW in application of A3 ($p < 0.05$) and 0.17 g higher than the control (A9)- a weight increase of more than 42%. In the second harvest, different observations were found for the DW of basil grown under chicken manure and biochar applications. The maximum value for DW was found from A6 application, and A7 application had the next highest increase, but other applications except A8 were found statistically similar to A7 application. The lowest DW values were noted in A8 application with 0.06 g plant⁻¹, although it had maximum value in the first harvest. In the total DW values, statistically significant differences were found among the applications. The values ranged from 0.30 to 0.72 g plant⁻¹, and the highest values showed difference in the applications according to the first and second harvests. A3 application had the highest DW value, and compared to A9 application, it was higher with the increasing 14.29%.

Table 4. Impact of applications on the yield of basil.

Applications	Fresh weight (g plant ⁻¹)			Dry weight (g plant ⁻¹)		
	1. harvest	2. harvest	Total	1. harvest	2. harvest	Total
A1	1.80cde	0.81bc	2.61c	0.19cde	0.11ab	0.30c
A2	1.62cde	1.13bc	2.75c	0.20cde	0.22ab	0.42abc
A3	2.49bc	2.30a	4.79ab	0.42b	0.30ab	0.72a
A4	1.32de	0.96bc	2.28c	0.33bc	0.21ab	0.39bc
A5	2.56bc	0.88bc	3.44bc	0.15e	0.21ab	0.54abc
A6	0.96e	1.28b	2.24c	0.18de	0.37a	0.51abc
A7	2.42cd	0.78bc	3.20c	0.31bcd	0.24ab	0.55abc
A8	5.54a	0.60c	6.14a	0.57a	0.06b	0.63ab
A9	3.66b	1.28b	4.94a	0.40b	0.23ab	0.63ab
Mean	2.49	1.11	3.60	0.31	0.22	0.52
LSD (5%)	1.17	0.60	1.44	0.15	0.26	0.33

¹There is no statistical difference between the means shown with similar letters in the same column. LSD: Least Significant Difference at the 0.05 level.

The positive impact of biochar on plant growth is generally attributed to its improvement of soil physical, chemical, and biological properties, including nutrient availability and water retention [28]. When the obtained results were compared with previous studies, FW values were found to be lower than the values reported by Chang et al. [29] (29.2-35.3 g), while FW values showed partly similarities with the values reported by Jadczyk et al. [30] (4.19-28.35 g). In another study, Abdipour et al. [31] reported that cow manure biochar (CBM) was applied to basil at levels of 0%, 1%, 2%, and 3%. The results

showed that a 3% CBM application significantly increased both the fresh (about 0.5-4 g plant⁻¹) and dry herb (about 0.2-0.9 g plant⁻¹) values of basil. These differences can be explained by genotype differences, cultivation conditions, and the effects of genotype characteristics.

A study by Amin et al. [32] found that basil plants grown in soil amended with chicken manure exhibited higher dry weight compared to control plants. This was attributed to the higher nutrient availability in the soil, especially nitrogen, which promotes leaf and stem growth, and phosphorus, which is critical for root development. Gomez et al. [33] reported that plants grown with chicken manure had well-developed root systems, which in turn contributed to increased dry weight due to improved water and nutrient absorption.

In a climate chamber experiment by Zhang et al. [34], basil plants grown in soil amended with biochar at a rate of 5% showed a significant increase in dry weight compared to those grown without biochar, suggesting that biochar enhances growth under controlled conditions. Similarly, a study by Cheng and Lehmann [8] indicated that moderate biochar application improved basil dry weight, with better results observed when the biochar was combined with organic fertilizers, further enhancing soil fertility and promoting plant growth. In a study by Atkinson et al. [35], it was found that biochar application led to improved soil pH and nutrient availability, contributing to the increased dry weight of basil plants. Moreover, the slow-release nature of nutrients from biochar could sustain plant growth over time, enhancing biomass production.

There have also been studies reporting that biochar applications promoted plant growth [36] depending on the raw material used in production, production temperature, and the characteristics of the soil-applied, as well as studies reporting that it was ineffective [37] and even had a negative effect [38]. The obtained DW values results were lower than the values reported by Chang et al. [29] (3.4-5.4 g). These differences can be explained by genotype differences and cultivation conditions.

In the present study, 9 different applications on basil were analyzed for the crude protein content (PC) values grown under chicken manure and biochar applications, and showed significant differences at $p < 0.05$ level (Table 5). In the first harvest, the crude PC values ranged from 6.91 to 20.11%. The highest PC was found from the A7 application and followed by A9 and A5 applications. The lowest crude PC was noted in A6 and A2 applications. The control application (A9) had the higher values with the biochar and biochar×chicken manure applications with the 20 t ha⁻¹ chicken manure application (A8) in the first harvest. Significant differences were found among the applications based on the crude PCs of basil in the second harvest. The PCs values ranged from 10.80% to 20.28%, and the highest and lowest values were obtained from applications of A1 and A9, respectively (Table 5). Alone biochar and biochar×chicken manure applications increased the PCs of basil, except A5 application. The crude PC values according to mean of the harvests changed between 10.83-18.69% among the applications. A7 application had the highest crude PC content and followed by A1 (16.73%) and A5 (16.67%) applications. A4 application had the minimum crude PC values and followed by A2 (11.38%) and A6 (12.33%) among the applications (Table 4). It is clearly noted that increasing chicken manure and biochar applications decreased the PCs of basil in the first and second harvest. Compared to A9 application, A7, A1 and A5 applications increased the crude PC of basil as 26.54, 13.27 and 12.86%, respectively.

Table 5. Crude protein content values of basil grown under chicken manure and biochar applications in different harvests.

Applications	Protein content (%)		
	1. harvest	2. harvest	Mean
A1	13.18d	20.28a	16.73b
A2	8.07g	14.69d	11.38ef
A3	11.08e	17.65b	14.37c
A4	9.12f	12.54e	10.83f

Table 5 (cont). Crude protein content values of basil grown under chicken manure and biochar applications in different harvests.

A5	17.44c	15.90cd	16.67b
A6	6.91h	17.75b	12.33de
A7	20.11a	17.27bc	18.69a
A8	13.1d	12.64e	12.87d
A9	18.74b	10.80f	14.77c
Mean	13.08	15.5	14.29
LSD (5%)	0.43	1.65	0.97

¹There is no statistical difference between the means shown with similar letters in the same column. LSD: Least Significant Difference at the 0.05 level.

The previous studies revealed that genetic variability, growing conditions and chemical or organic applications caused the chemical properties of basil. Siti Mahirah et al. [39] and Yilmaz and Alibaş [40] reported that protein contents of basil in different drying methods ranged from 3.22 to 18.72% and from 19.21 to 31.50%. In another study, Nurzyńska-Wierdak et al. [41] noted that protein contents of herbs in different basil cultivars changed between 8.20-20.00%. The obtained protein contents (6.91-20.28%) from this study were found partly similar with the previous studies.

Antioxidant activities of different chicken manure and biochar applications on basil were evaluated as DPPH and FRAP in the first and second harvests (Table 6). In the first harvest, the first antioxidant activity was DPPH and its values showed statistically differences in the first harvest and the values changed between 20.98-98.44%. The highest DPPH value was observed from application of A3 and followed by A2 (92.66%) and A1 (73.68%). The lowest DPPH values were found from A4 and A8 applications. Compared to A9 condition, while A3 and A2 applications increased the DPPH values with 80.59% and 69.99%, A4 and A8 applications decreased the DPPH values by 61.51% and 49.77% in the first harvest. In the second harvest, DPPH values showed high variability and changed between 26.73-69.37%. A2 application had the maximum DPPH values and A4 application had the minimum DPPH value. As in the 1st harvest, it was determined that A2 had the highest value, while A4 application had the lowest value. The results showed that alone biochar and biochar×10 t ha⁻¹ chicken manure applications had positive impact on DPPH values of basil in the first harvest (Table 6). The highest biochar and chicken manure applications had the positive effect on the DPPH values of the basil in the second harvest. However, interaction of the highest biochar and chicken manure application revealed the lowest DPPH value in both harvests. The mean DPPH values of the basil grown under different chicken manure and biochar applications ranged from 23.85 to 81.02% with an average of 54.88%. The highest and lowest DPPH values according to mean values of the first and second harvest were found from A2 and A4 applications.

The second antioxidant activity was FRAP and it showed wide variations in the first and second harvests. In the first harvest, the FRAP values changed between 46.88-106.12 mg TE g⁻¹ (Table 6). The highest FRAP value was found from A5 application with 106.12 mg TE g⁻¹, and followed by A6 application with 104.99 mg TE g⁻¹ and A2 application with 74.32 mg TE g⁻¹. The lowest FRAP values were seen in A3 and A7 applications. In the second harvest, the FRAP values of the basil grown under different chicken manure and biochar applications ranged from 24.84 to 115.95 mg TE g⁻¹, and the highest and lowest FRAP values were obtained from A9 and A1 applications, respectively. Although the highest dose of biochar application proved effective, the highest FRAP value for basil in the second harvest was observed in the control (A9) treatment. This value was 27.00% higher than that of the next highest application. The FRAP values, based on the means of both harvests, showed statistically significant differences, ranging from 37.13 mg TE g⁻¹ to 92.35 mg TE g⁻¹. Similar with the second harvest, A9 application had the highest FRAP value, while A7 application had the lowest value.

Table 6. Antioxidant activities of the basil grown under chicken manure and biochar applications.

Applications	DPPH (%)			FRAP (mg TE g ⁻¹)		
	1. harvest	2. harvest	Mean	1. harvest	2. harvest	Mean
A1	73.68b	52.97bc	63.32b	62.88e	24.84h	43.86e
A2	92.66a	69.37a	81.02a	74.32c	91.15b	82.74c
A3	98.44a	46.68c	72.56a	42.49h	33.49e	37.99f
A4	20.98d	26.73d	23.85f	94.66b	30.12f	62.39d
A5	31.33d	52.25bc	41.79e	106.12a	67.33d	86.72b
A6	64.65bc	51.16c	57.91bc	104.99a	71.78c	88.39b
A7	64.31bc	45.61c	54.96bcd	46.88g	27.39g	37.13f
A8	27.38d	65.46ab	46.42de	57.22f	30.40f	43.81e
A9	54.51c	49.62c	52.06cd	68.74d	115.95a	92.35a
Mean	58.66	51.09	54.88	73.14	54.77	63.93
LSD (%)	12.09	14.14	9.13	3.85	1.91	2.11

[†]There is no statistical difference between the means shown with similar letters in the same column. LSD: Least Significant Difference at the 0.05 level.

Antioxidants help reduce the risk of chronic diseases, including cancer and heart disease. The primary sources of naturally occurring antioxidants are whole fruits, grains, and vegetables [42]. It has been reported that there is a relationship between the content of total phenolic compounds and their antioxidant capacity [43,44]. Previous studies reported that DPPH values of basil changed depending on the applications, genetic variation, growing conditions and environmental differences. Nadeem et al. [45] reported that DPPH value of basil leaves cultivated in Pakistan was found between 32.4-82.4%. Yaldiz and Camlica [42] was found the DPPH values of different origin basil genotypes between 8.14-54.69%. In a separate study, Ma and Le [46] reported that the antioxidant capacity of Thai basil leaves was measured at 39.06%. Uyoh et al. [47] reported that the DPPH value for *Ocimum basilicum* leaf extract was 92.37%, and that the DPPH values of various concentrations of *Ocimum* extracts and reference compounds ranged from 83.53% to 87.59%. The obtained DPPH values from this study were in accordance with the previous studies.

Total phenolic contents of basil showed statistically significant differences among the chicken manure and biochar applications for basil in both harvests (Table 7). The TPC values ranged from 14.66 to 104.93 mg GAE g⁻¹, and the highest TPC values were found in A9 and A4 applications. Applications of A2 and A8 had the minimum TPC with 14.66 and 56.88 mg GAE g⁻¹. While the TPC values of alone biochar applications were found closest, alone chicken manure applications showed high differences. In the second harvest, TPC values changed between 6.10-104.75 mg GAE g⁻¹, and A6 and A5 applications had the highest and lowest values, respectively. It was seen that the highest biochar and the lowest chicken manure applications had positive effect on TPC values of basil in the second harvest. However, combination of biochar and chicken manure applications showed opposite impact on the TPC values compared to pure applications. The mean TPC values of the harvests ranged from 16.38 to 86.10 mg GAE g⁻¹, and A6 and A7 applications had the highest values. A8 and A5 applications had the minimum TPC values in basil. The A9 application decreased the TPC values by 33.14%, and 13.15% compared to A6 and A7 applications, respectively.

Chicken manure and biochar applications had significant impacts on the total flavonoid contents (TFC) of basil in both harvest. In the first harvest, the highest TFC values were observed in A6 and A1 applications, while the lowest TFC values were found in A8 and A9 applications (Table 7). Pure applications of biochar showed differences as well as chicken manure applications, and the highest TFC values were found in the lower applications in the first harvest. The greatest reduction in TFC occurred in the A8 application, compared to A9 application. In the second harvest, the TFC values ranged from 1.06 to 22.39 mg QE g⁻¹, and the highest and lowest values were found from the applications of A4 and

A3, respectively. A9 application exhibited the higher rises in TFC values compared to A4 (63.15%) and A5 (31.48%) applications in the second harvest. In contrast, the highest TFC values were found in the higher applications in the second harvest. The mean TFC values according to harvest results showed statistically significant differences among the applications. The highest and lowest TFC values were found in A8 and A4 applications according to mean values of the both harvests, respectively.

Table 7. Total phenolic and flavonoid contents of basil grown under chicken manure and biochar applications.

Applications	Total phenolic (mg GAE g ⁻¹)			Total flavonoid (mg QE g ⁻¹)		
	1. harvest	2. harvest	Mean	1. harvest	2. harvest	Mean
A1	57.66d	19.66d	38.66ef	39.36b	3.36de	21.36d
A2	56.84d	56.69b	56.76c	15.09de	9.46c	12.28e
A3	60.32d	30.36c	45.34de	27.42c	1.06f	14.24e
A4	77.48b	18.03d	47.75d	49.35a	22.39a	35.87a
A5	69.13c	6.10e	37.61f	37.09b	12.04b	24.56c
A6	67.46c	104.75a	86.10a	51.12a	4.74d	27.93b
A7	66.52c	66.06b	66.29b	12.41ef	2.14ef	7.27f
A8	14.66e	18.09d	16.38g	9.61f	2.47ef	6.04f
A9	104.93a	10.22de	57.57c	18.03d	8.25c	13.14e
Mean	63.87	36.66	50.27	28.83	7.32	18.08
LSD (%)	5.25	10.09	6.69	4.15	2.18	2.60

[†]There is no statistical difference between the means shown with similar letters in the same column. LSD: Least Significant Difference at the 0.05 level.

Phenolic compounds with bioactive properties are known to contribute to the nutritional value of plants and play a crucial role in their environmental adaptation and stress resistance. Additionally, the cultivation system has been reported to influence the phenolic content of plants, along with various other factors [48]. It has been suggested that biochar amendment, as an alternative cultivation system, could alter the phenolic compound content of plants by modifying nutrient availability in the growing medium [49]. For example, Jabborova et al. [20] found that biochar produced from cherry tree wood increased basil's total flavonoid content and antioxidant activity. These differing findings highlight that effect of biochar on phenolic content may depend on its source material. Total phenolic and flavonoid contents of basil showed differences based on the genetic variability, growing conditions, extraction methods, environmental factors. A study conducted by Uyoh et al. [47] reported that total phenolic content of *Ocimum basilicum* grown in Nigeria extracts was found as 27.41 mg GAE g⁻¹ DW and the total flavonoid content was noted as 22.88 µg RE mg⁻¹. In another study conducted by Elmas et al. [50] reported that total phenolic and flavonoid contents of basil grown under different bio and chemical fertilizer ranged from 14.99 to 32.90 mg GAE g⁻¹ and from 4.44 to 26.29 mg QE g⁻¹, respectively. Yaldiz et al. [1] reported that total phenolic and total flavonoid contents were noted between 11.95-47.38 mg GAE g⁻¹ and between 4.29-18.08 mg QE g⁻¹, respectively. The total phenolic and flavonoid contents obtained in this study were consistent with those reported in previous studies.

B. PRINCIPAL COORDINATE ANALYSIS (PCA)

The first eight factors in the scree plot, derived from the original data, accounted for 100% of the total variation (Figure 1a, b). Principal component analysis (PCA) revealed that the first six principal components (PC1 to PC6) had eigenvalues greater than 1.0 and collectively explained 94.58% of the total variation. Specifically, PC1 accounted for 32.43%, and PC2 explained 19.80% of the total variation (Figure 1a, b).

The high variability observed across all four PC axes indicates considerable diversity among the twelve traits. Within the first principal component (PC1), traits with larger absolute values, closer to unity, had

a stronger influence on clustering compared to traits with values closer to zero. The major contributing traits to PC1 included the presence of FW-1, DW-1, FW-M, PH-M and PH-1 properties. The positive and negative correlations between the components and variables are indicated by the corresponding positive and negative loadings.

For the second principal component (PC2), the primary contributors were TFC-2, DPPH-M and DPPH-1. In PC3, BN-2 emerged as the principal contributor to variation, while the PC-M was the key factor for PC4. Traits with higher coefficients in PC1 and PC2 were of particular significance, as these two components together accounted for 52.23% of the overall variation. Positive and significant correlations were found among the eight traits such as FW-1, FW-M, DW-1, DW-M, BN-1, BN-2, BN-M, PC-1. Plant height traits as PH-1, PH-2 and PH-M were found at the same axis, and the significant correlations were observed among them (Figure 1). FRAP-M was correlated with TFC-1, TFC-2, TFC-M and FRAP-1, and rest of traits were correlated with each other. A8 application had positive effect on the PH-1, PH-2 and PH-M, A4 application showed significant effect on TFC in PCA.

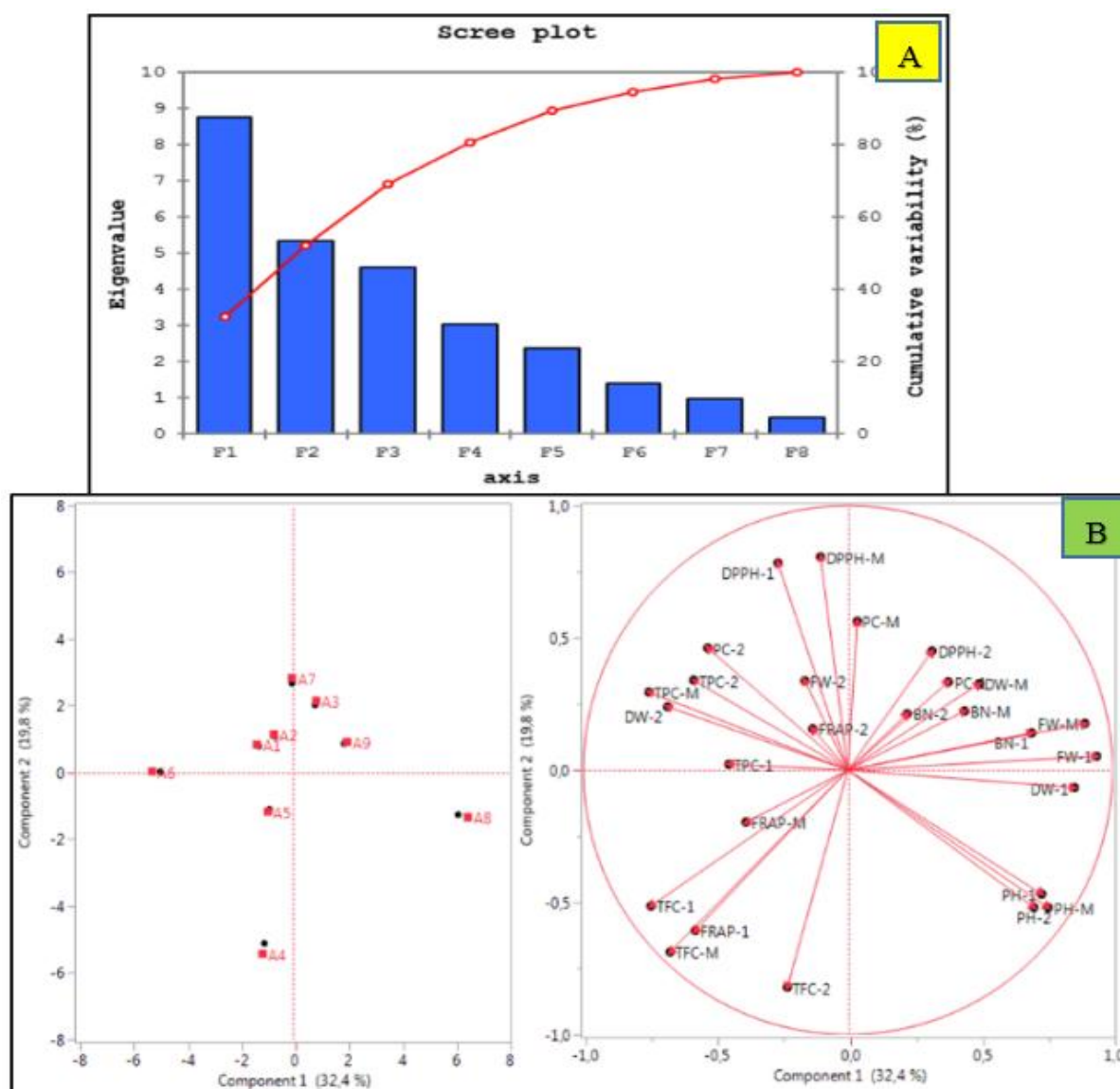


Figure 1. Scree plot (A) and PCA (B) of the study depending on the examined properties. PH: Plant height, BN: Branch number, FW: Fresh weight, DW: Dry weight, PC: Protein content, DPPH: 1,1-diphenyl-2-picrylhydrazyl, FRAP: Ferric reducing antioxidant power, TPC: Total phenolic content, TFC: Total flavonoid content.

The PCA results obtained from this study was found similar with Amato et al. [51], who reported that the variables contributed most to PC1 were those related to the morphology and yield of oregano, including stem height, inflorescence height, total fresh yield, and the dry yield of inflorescences and leaves.

C. HEAT MAP ANALYSIS

The heat map analysis (Figure 2) revealed two main clusters: one corresponding to the A3 and A8 applications and the other to all the applications. A3 and A4 applications (main group A) divided into two subgroups as A1 and A2, and separated with the values of plant height with dry and fresh weight except DW-2.

The main group B divided into two subgroups as B1 and B2, and B1 group separated from other group depending on the DW-2, TPC-M and TPC-2. Notably, the plant height values (PH-1, PH-2 and PH-M) and branch number values (BN-1, BN-2 and BN-M) clustered in the same group, while the other properties showed differences. Applications of A6, A4 and A9 exhibited the highest values of TPC-2, TFC-2 and BN-M in the main group B, respectively. In particular, the A9 application clustered separately because of its lower values of BN-1, BN-2, BN-M, FRAP-2, FRAP-M and TPC-1 traits. The applications A3, A4 and A6 showed the highest DPPH-1, TFC-2 and TPC-2 values, respectively. It was clearly noted that the traits about plant heights (PH-1, PH-2 and PH-M) were separated from other traits depending on the A8 application (20 t ha⁻¹ chicken manure). As a result, the heat map clearly highlighted which application contributes to the increase in each trait's value.

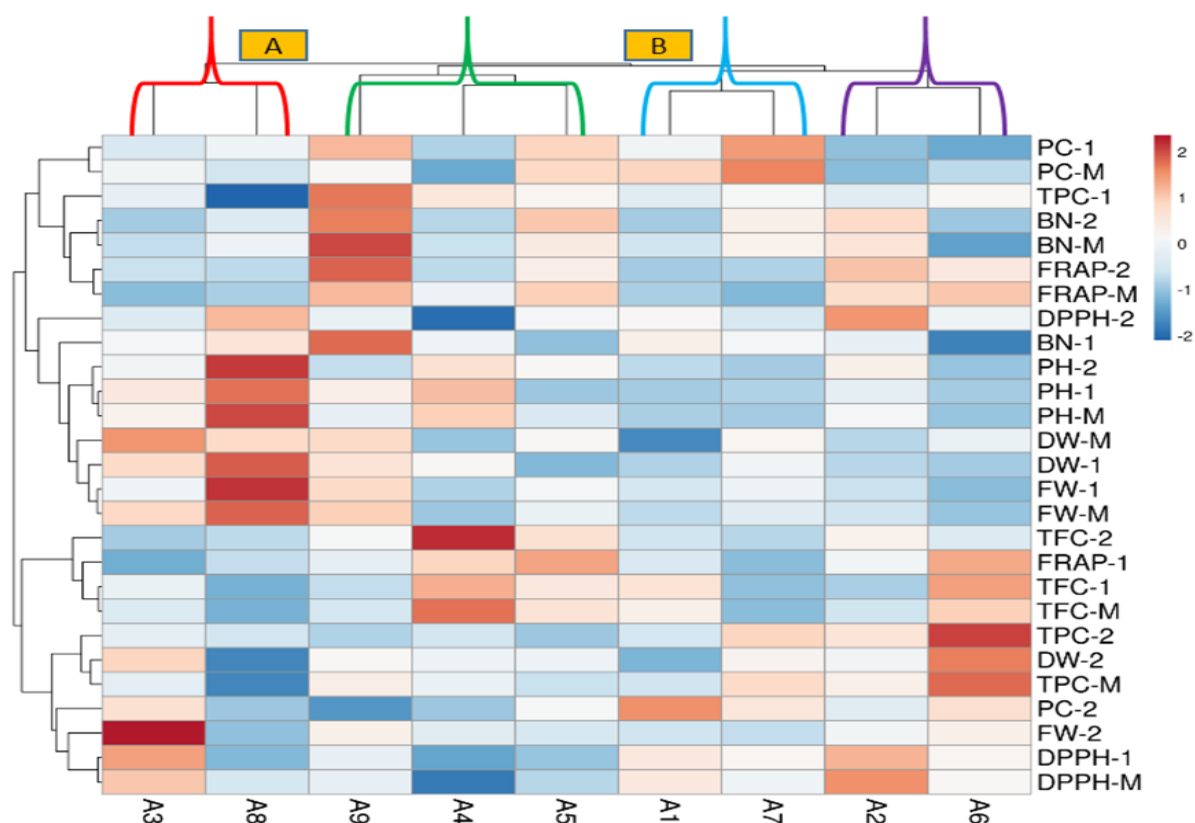


Figure 2. Heat map analysis summarizing oregano responses to chicken manure and biochar applications (from A1 to A9). PH: Plant height, BN: Branch number, FW: Fresh weight, DW: Dry weight, PC: Protein content, DPPH: 1,1-diphenyl-2-picrylhydrazyl, FRAP: Ferric reducing antioxidant power, TPC: Total phenolic content, TFC: Total flavonoid content

The heat map analysis results showed similarity with the previous study reported by Amato et al. [51].

IV. CONCLUSION

Biochar and chicken manure applications had a significantly positive impact on plant height, branch number, fresh and dry weights, as well as on antioxidant activity and protein content of basil grown in a climate room conditions. Chicken manure and biochar application promoted the development of morphological, yield, and antioxidant activity properties and thus production availability for basil. Furthermore, increasing biochar applications caused an increase of DPPH content, while the increasing chicken manure application enhanced the plant height and total fresh weight. The PCA and heat map analysis showed important results according to applications.

Chicken manure and biochar applications increased basil production and some quality properties with a significant increase. These results showed that the impacts of used materials as growth-promotings are related to the increase in nutrient intake besides its other properties, such as developing the soil physical properties and increasing the water holding capacity according to results of the present study, both chicken manure and biochar applications can be used to improve the productivity of basil.

In conclusion, the positive effects are attributed to the ability of chicken manure and biochar to improve soil structure, support microbial activity, and enhance nutrient availability. These benefits make chicken manure and biochar valuable amendments for sustainable agriculture.

V. REFERENCES

- [1] G. Yaldiz, M. Camlica, and F. Ozen, "Biological value and chemical components of essential oils of sweet basil (*Ocimum basilicum* L.) grown with organic fertilization sources," *Journal of the Science of Food and Agriculture*, vol. 99, no. 4, pp. 2005-2013, 2019.
- [2] E. O. Adeleye, L. S. Ayeni, and S. O. Ojeniyi, "Effect of poultry manure on soil physico-chemical properties, leaf nutrient contents and yield of yam (*Dioscorea rotundata*) on Alfisol in Southwestern Nigeria," *Journal of American Science*, vol. 6, no. 10, pp. 871-878, 2010.
- [3] G. E. Boyhan, R. J. Hicks, R. L. Torrance, C. M. Riner, and C. R. Hill. "Evaluation of poultry litter and organic fertilizer rate and source for production of organic short-day onions," *HortTechnology*, vol. 20, no. 2, pp. 304-7, 2010.
- [4] P. K. Srivastava, M. Gupta, R. K. Upadhyay, S. Sharma, N. Singh, S. K. Tewari, and B. Singh, "Effects of combined application of vermicompost and mineral fertilizer on the growth of *Allium cepa* L. and soil fertility," *Journal of Plant Nutrition and Soil Science*, vol. 175 no. 1, pp. 101-7.
- [5] K. Yohanne, D. Belew, and A. Debela, "Effect of farmyard manure and nitrogen fertilizer rates on growth, yield and yield components of onion (*Allium cepa* L.) at Jimma, Southwest Ethiopia," *Asian Journal of Plant Sciences*, vol. 12, no. 6-8, pp. 228-34, 2013.
- [6] G. Yaldız, M. Çamlıca, F. Özen, and S. A. Eratalar "Effect of poultry manure on yield and nutrient composition of sweet basil (*Ocimum basilicum* L.)," *Communications in Soil Science and Plant Analysis*, vol. 50, no. 7, pp. 838-852, 2019.
- [7] G. Yaldiz, M. Camlica, and D. Dasdemir, "Poultry manure application enhances the phytochemical contents, antioxidant, and fixed oil of *Momordica charantia* L.," *South African Journal of Botany*, vol. 175, pp. 103-114, 2024.
- [8] C. H. Cheng, and J. Lehmann, "Biochar effects on soil fertility and plant growth," *Biological and Fertilizer Soils*, vol. 44, no. 4, pp. 555-566, 2008.

- [9] J. Lehmann, P. da Silva, C. Steiner, T. Nehls, W. Zech, and B. Glaser, "Nutrient availability and leaching in an archaeological Anthrosol and a Ferralsol of the Central Amazon basin: fertilizer, manure and charcoal amendments," *Plant and Soil*, vol. 249, pp. 343-357, 2003.
- [10] K. Karhu, T. Mattila, I. Bergström, and K. Regina, "Biochar addition to agricultural soil increased CH₄ uptake and water holding capacity-results from a short-term pilot field study," *Agriculture, Ecosystems and Environment*, vol. 140, no. (1-2), pp. 309-313, 2011.
- [11] P. Conte, V. Marsala, C. De Pasquale, S. Bubici, M. Valagussa, A. Pozzi, and G. Alonzo, "Nature of water-biochar interface interactions," *GCB Bioenergy*, vol. 5, no. 2, 116-121, 2013.
- [12] Y. Wang, R. Yin, and R. Liu, "Characterization of biochar from fast pyrolysis and its effect on chemical properties of the tea garden soil," *Journal of Analytical and Applied Pyrolysis*, vol. 110, pp. 375-381, 2014.
- [13] S. Sadeghi, A. Rahnavard, and Z. Y. Ashrafi, "The effect of plant density and sowing date on yield of basil (*Ocimum basilicum* L.) in Iran," *International Journal of Agricultural Technology*, vol. 5, no. 2, 413-422, 2009.
- [14] G. W. Arendash, T. Mori, M. Dorsey, R. Gonzalez, N. Tajiri, and C. Borlongan, "Electromagnetic treatment to old Alzheimer's mice reverses beta-amyloid deposition, modifies cerebral blood flow, and provides selected cognitive benefit," *PLoS One*, vol. 7, no. 4, e35751, 2012.
- [15] K. Chandrasekaran, and M. Senthilkumar, "Synergic antibacterial effect of *Curcuma aromatic* Salisb and *Ocimum tenuiflorum* Linn herbal extract combinations on treated cotton knitted fabrics against selective bacterial strains," *Indian Journal of Fibre and Textile Research*, vol. 44, pp. 344-351, 2019.
- [16] B. Neeharika, K. G. Vijayalaxmi, and S. Shamshad Begum, "Traditional processing methods for quality enhancement of indigenous basil seeds and formulation of functional flours," *Indian Journal of Traditional Knowledge*, vol. 22, no. 4, 798-804, 2023.
- [17] G. Yaldiz, M. Camlica, A. Cetinkaya, and S. E. Duzcu, "Evaluating the effects of basil (*Ocimum basilicum*) in the experimental model of Alzheimer's disease in rats," *Indian Journal of Traditional Knowledge*, vol. 23, no. 10, pp. 929-938, 2024.
- [18] M. Camlica, G. Yaldiz, and H. Askın, "Deciphering the genetic diversity of different fenugreek genotypes based on the morphology, yield, UPOV criteria and some quality properties," *Genetic Resources and Crop Evolution*, 2024. <https://doi.org/10.1007/s10722-024-02207-9>
- [19] M. Camlica, and G. Yaldiz, "Comparison of twenty selected fenugreek genotypes grown under irrigated and dryland conditions: Morphology, yield, quality properties and antioxidant activities," *Agronomy*, vol. 14, no. 4, p. 713, 2024.
- [20] D. Jabborova, H. Ma, S. D. Bellingrath-Kimura, and S. Wirth, "Impacts of biochar on basil (*Ocimum basilicum*) growth, root morphological traits, plant biochemical and physiological properties and soil enzymatic activities," *Scientia Horticulturae*, vol. 290, no. 110518, 2021.
- [21] M. Danish, S. Pradhan, G. McKay, T. Al-Ansari, S. Mansour, and H. R. Mackey, "Effect of biochar, potting mixture and their blends to improve *Ocimum basilicum* growth in sandy soil," *Journal of Soil Science and Plant Nutrition*, vol. 24, pp. 1952-1967, 2024.
- [22] G. Yilmaz, H. Karadağ, O. Saraçoğlu, O. N. Öcalan, "Effects of biochar applications on growth, nutrient content and biochemical properties of *Ocimum basilicum* L.," *Acta Scientiarum Polonorum Hortorum Cultus*, vol. 22, no. 5, pp. 55-62, 2023.

- [23] G. C. Teliban, L. D. Popa, M. Burducea, C. Precupeanu, T. Stan, A. Agapie, M. Naie, I. Dumitru, and V. Stoleru, "Research on the obtaining basil in pots, in greenhouse conditions", *International Symposium, Isb-Inma Teh' 2021*, 2022, pp. 868-873.
- [24] I. Tas, T. Yeter, F. Ozkay, B. Cosge, and C. Gorgisen, "Effects of high boron containing irrigation waters on plant characteristics of basil (*Ocimum basilicum* L.)", *Journal of Agricultural Faculty of Gaziosmanpaşa University (JAFAG)*, vol. 33, no. 3, pp. 46-54, 2016.
- [25] M. Karaca, Ş. M. Kara ve M. Muharrem Özcan, "Bazı fesleğen (*Ocimum basilicum* L.) popülasyonlarının herba verimi ve uçucu yağ oranının belirlenmesi," *Ordu Üniversitesi Bilim ve Teknoloji Dergisi*, vol. 7, no. 2, pp. 160-169, 2017.
- [26] G. Yaldiz, and M. Camlica, "Genetic diversity of selected basil (*Ocimum basilicum* L.) genotypes based on morphological, yield, and leaf color parameters," *Journal of Crop Improvement*, vol. 38, no. 3, pp. 240-256, 2024.
- [27] A. Z. Qazizadah, J. J. Nakasha, U. R. Sinniah, and P. E. M. Wahap, "Improvement of growth and development of sweet basil (*Ocimum basilicum* L.) through the application of chitosan at different plant maturity stages," *Pertanika Tropical Agricultural Science*, vol. 46, no. 2, pp. 647-670, 2023.
- [28] J. Lehmann, M. C. Rillig, J. Thies, C. A. Masiello, W. C. Hockaday, and D. Crowley, "Biochar effects on soil biota-a review," *Soil Biology and Biochemistry*, vol. 43, no. 9, pp. 1812-1836, 2011.
- [29] X. Chang, P. Alderson, P., C. J. Wright, "Effect of temperature integration on the growth and volatile oil content of basil (*Ocimum basilicum* L.)," *The Journal of Horticultural Science and Biotechnology*, vol. 80, no. 5, pp. 593-598, 2005.
- [30] D. Jadcak, K. Bojko, M. Berova, and M. Kaymakanova, "Effects of salinity stress on growth and photosynthetic activity of common basil plants (*Ocimum basilicum* L.)," *Journal of Central European Agriculture*, vol. 22, no. 3, pp. 546-556, 2021.
- [31] M. Abdipour, M. Hosseinfarahi, and S. Najafian, "Effects of humic acid and cow manure biochar (CMB) in culture medium on growth and mineral concentrations of basil plant," *International Journal of Horticultural Science and Technology*, vol. 6, no. 1, pp. 27-38, 2019.
- [32] M. H. G. Amin, and M. A. Kader, "Effect of organic fertilizers on the growth and yield of basil under greenhouse conditions," *Journal of Agricultural Science and Technology*, vol. 18, no. 4, pp. 1223-1233, 2016.
- [33] K. A. Gomez, and A. A. Gomez, "Effects of organic and inorganic fertilizers on the growth and yield of basil in greenhouse conditions," *HortScience*, vol. 49, no. 5, pp. 631-635, 2014.
- [34] A. Zhang, Y. Liu, and X. Zhang, "Effect of biochar on basil growth under controlled conditions," *Environmental Science and Pollution Research*, vol. 23, no. 14, pp. 14585-14593, 2016.
- [35] C. J. Atkinson, J. D. Fitzgerald, and N. A. Hipps, "Potential mechanisms for achieving agricultural benefits from biochar application to temperate soils: A review," *Plant and Soil*, vol. 337, no. 1-2, pp. 1-18, 2010.
- [36] X. W. Lin, Z. Xie, J. Y. Zheng, Q. Liu, Q. C. Bei, and J. G. Zhu, "Effects of biochar application on greenhouse gas emissions, carbon sequestration and crop growth in coastal saline soil," *European Journal of Soil Science*, vol. 66, no. 2, pp. 329-338, 2015.

- [37] R. Subedi, N. Taupe, S. Pelissetti, L. Petruzzelli, C. Bertora, J. J. Leahy, and C. Grignani, "Greenhouse gas emissions and soil properties following amendment with manure-derived biochars: influence of pyrolysis temperature and feedstock type," *Journal of Environmental Management*, vol. 166, pp. 73-83, 2016.
- [38] V. Nelissen, G. Ruyschaert, D. Manka'Abusi, T. D'Hose, K. De Beuf, B. Al-Barri, and P. Boeckx, "Impact of a woody biochar on properties of a sandy loam soil and spring barley during a two-year field experiment," *European Journal of Agronomy*, vol. 62, pp. 65-78, 2015.
- [39] Y. Siti Mahirah, M. S. Rabeta, and R. A. Antora, "Effects of different drying methods on the proximate composition and antioxidant activities of *Ocimum basilicum* leaves," *Food Research*, vol. 2, no. 5, pp. 421-428, 2018.
- [40] A. Yilmaz, and I. Alibaş, "The impact of drying methods on quality parameters of purple basil leaves," *Journal of Food Processing and Preservation*, vol. 45 no. 7, e15638, 2021.
- [41] R. Nurzyńska-Wierdak, B. Borowski, and K. Dzida, "Yield and chemical composition of basil herb depending on cultivar and foliar feeding with nitrogen," *Acta Scientiarum Polonorum Hortorum Cultus*, vol. 10, no. 1, pp. 207-219, 2011.
- [42] G. Yaldiz, and M. Camlica, "Essential oils content, composition and antioxidant activity of selected basil (*Ocimum basilicum* L.) genotypes," *South African Journal of Botany*, vol. 151, no. Part A, pp. 675-694, 2022.
- [43] T. Katsube, H. Tabata, Y. Ohta, Y. Yamasaki, E. Anuurad, and K. Shiwaku, "Screening for antioxidant activity in edible plant products: Comparison of low density lipoprotein oxidation assay, DPPH radical scavenging assay, and Folin-Ciocalteu assay," *Journal of the Agricultural and Food Chemistry*, vol. 52, pp. 2391-2396, 2004.
- [44] V. Katalinic, M. Milos, and M. Jukic, "Screening of 70 medicinal plant extracts for antioxidant capacity and total phenols," *Food Chemistry*, vol. 94, pp. 550-557, 2006.
- [45] H. R. Nadeem, S. Akhtar, P. Sestili, T. Ismail, S. Neugart, M. Qamar, and T. Esatbeyoglu, "Toxicity, antioxidant activity, and phytochemicals of basil (*Ocimum basilicum* L.) leaves cultivated in Southern Punjab, Pakistan," *Foods*, vol. 11, no. 9, 1239, 2022.
- [46] N. B. Ma, and N. L. Le. "Extraction optimization of total phenolics from Thai basil (*Ocimum basilicum* Var. *Thyrsiflora*) leaves and bioactivities of the extract", In: *Proceedings of the AIP Conference proceedings*, vol. 2406, no. 1, 2021, 050002.
- [47] E. A. Uyoh, P. N. Chukwurah, I. A. David, and A. C. Bassey, "Evaluation of antioxidant capacity of two ocimum species consumed locally as spices in Nigeria as a justification for increased domestication," *American Journal of Plant Sciences*, vol. 4, pp. 222-230, 2013.
- [48] R. G. Borguini, D. H. M. Bastos, J. M. Moita-Neto, F. S. Capasso, and E. A. F. da Silva Torres, "Antioxidant potential of tomatoes cultivated in organic and conventional systems," *Brazilian Archives of Biology and Technology*, vol. 56, pp. 521-529, 2013.
- [49] R. Petruccelli, A. Bonetti, M. L. Traversi, C. Faraloni, M. Valagussa, and A. Pozzi, "Influence of biochar application on nutritional quality of tomato (*Lycopersicon esculentum*)," *Crop and Pasture Science*, vol. 66, pp. 747-755, 2015.
- [50] M. Elmas, G. Yaldiz, and M. Camlica, "Impact of bio-fertilizers and bio-fertilizers with reduced rates of chemical fertilization on growth, yield, antioxidant activity, essential oil composition of basil (*Ocimum basilicum* L.) plant," *Russian Journal of Plant Physiology*, vol. 71, no. 4 (2024).

[51] G. Amato, L. Cardone, N. Cicco, M. Denora, M. Perniola, D. Casiello, L. De Maradona, V. De Feo, and V. Candido, "Morphological traits, yield, antioxidant activity and essential oil composition of oregano as affected by biostimulant foliar applications," *Industrial Crops and Products*, vol. 222, no. 2, 119702, 2024.



Düzce University Journal of Science & Technology

Research Article

Synthesis, Dielectric and Magnetic Characterization and Properties of Nano Magnetic Particles by using Microwave Technique

 Harun BAYRAKDAR ^{a,*}

^a Department of Mechanical Engineering, Faculty of Engineering, Düzce University, Düzce, TÜRKİYE

* Corresponding author's e-mail address: harunbayrakdar@duzce.edu.tr

DOI: 10.29130/dubited.1647176

ABSTRACT

A microwave-induced combustion method has been utilized to prepare nano-sized powders of hexagonal ferrites using urea and glycine as fuel. The dielectric and magnetic properties of these products were investigated experimentally, the dielectric properties were investigated with the RF LCR device, the magnetic properties were investigated with the Electron Spin Resonance (ESR) and Vibration Sample Magnetometer (VSM) spectrometer, and the crystalline structure was investigated with the X-ray diffraction (XRD) device.

Keywords: Nanoparticles, Hexagonal ferrites, Dielectric behavior, Magnetic behavior, Polarization

Mikrodalga Tekniğini Kullanarak Nano Manyetik Parçacıkların Sentezi, Dielektrik ve Manyetik Karakterizasyonu ve Özellikleri

ÖZ

Nano boyutta hekzagonal ferritlerin hazırlanması için üre ve glisin yakıt olarak kullanarak, mikrodalga kaynaklı yanma yöntemi kullanılmıştır. Bu ürünlerin dielektrik ve manyetik özellikleri deneysel olarak incelendi, dielektrik özellikleri RF LCR cihazı ile incelendi, manyetik özellikleri Elektron Spin Rezonans (ESR) ve Titreşim Numune Manyetometresi (VSM) spektrometresi ile incelendi ve kristalin yapısı X-ışını kırınımı (XRD) cihazı ile incelendi.

Anahtar Kelimeler: Nanopartiküller, Hekzagonal ferritler, Dielektrik davranış, Manyetik davranış, Polarizasyon

I. INTRODUCTION

As the needs of human beings change and develop, today's technologies change and develop in parallel with them. Unhealthy diet, developments in communication ways, wireless communications, developments in the defense industry, etc.. It has become a threat to us as if it was an invitation to diseases in human beings [1], biomedical applications [2], ferrites exhibit soft magnetic behavior due to their structural properties and are used in different applications such as contrast agents in MRI, magnetic fluids, drug delivery and gas sensors [3-7], Biocompatible nanosized magnetic particles (MNPs) based on iron oxide NPs are essential components for biomedical applications such as drug delivery systems [8-10], hyperthermia [11]. Magnetic recording systems and quantum processors can be made at room temperature [12].

There are three main categories of synthesizing magnetic NPs: biological, physical, and chemical methods [1]. In this study, we demonstrate the synthesis of hexagonal ferrite nanoparticles (NPs) by a microwave-assisted combustion method by using glycine and urea. They remove the water molecules in the cellulose before they reach the ignition temperature and prevent further combustion by covering the surface of the coal formed.

In this study, the dielectric and magnetic behavior of hexagonal ferrite nanoparticles (NPs) were studied using a LCR Meter for dielectric measurements and magnetic behaviors were measured using Electron Spin Resonance (ESR) and Vibrating Sample Magnetometer (VSM) spectrometers. Synthesized nano-crystalline samples were structure characterized by x-ray diffraction (XRD).

II. SYNTHESIS OF NANOPARTICLES

Nanoparticles of hexagonal ferrite were prepared by microwave-induced combustion with glycine ($\text{NH}_2\text{CH}_2\text{COOH}$) and urea ($\text{CO}(\text{NH}_2)_2$). These nanoparticles were prepared using the method described in refs [14] with some modifications. Sodium dodecyl sulfate (SDS), glycine and urea to be used as fuel were dissolved in deionized water and poured into a crucible, then placed in a microwave oven [15].

In the microwave process; with the interaction of microwaves with the material, heat is produced in the sample itself; this heat pushes the water and moisture in the samples, resulting in a more desired sample [14]. In this study, glycine and urea were used as the precipitating/reducing agent to prevent local precipitation and thus to provide a homogeneous shape that provides a wide particle size distribution.

III. EXPERIMENTAL

X-ray diffraction (XRD) measurements were performed using a Bruker D8 Advance diffractometer with Cu K α radiation.

For dielectric measurements, an Agilent 4287A RF LCR Meter was used in the frequency range of 1 MHz-3 GHz at room temperature. Both surfaces of the samples were coated with Ag-epoxy. In dielectric measurements, the cross-sectional area (A) and the stack thickness (distance between contacts) (d) were measured.

Quantum Design Vibrating Sample Magnetometer (VSM) Model 6000 was used for magnetic measurements. X-band ($f \approx 9.7$ GHz) Bruker EMX model spectrometer was used for ESR measurements.

IV. RESULTS AND DISCUSSION

A. XRD MEASUREMENTS

XRD results are shown in Figures 1. The pattern exhibits the diffraction peaks of powders which correspond to (110), (1013), (116), (119), (024), (300), (2113), (1025), and (220). The measurement results show that NPs. are the y type hexa-ferrite structure [15]. As seen from the XRD measurement results of the nanoparticles, the highest peak (1013) proves that these samples are Y-type hexagonal ferrite and was calculated by ref 12,15. The lattice parameters (a and c) and unit cell volume (V) for the single phase sample were calculated by the following formulas, respectively [12]; $\sin^2\theta = \lambda^2/3a^2 (h^2+hk+k^2) + \lambda^2/4c^2 (l^2)$ and $V = a^2c \sin 120^\circ$ where “hkl” are the Miller indices, λ is the wavelength, a and c are the lattice parameters. The observed values of the lattice parameters ($a = 7.76 \text{ \AA}$, $c = 38.85 \text{ \AA}$) and unit cell volume (1287.57 \AA^3) very close to the values stated for Y-type hexagonal ferrites [12,15]. With the Debye-Scherrer equations used for XRD measurements;

$$D = (0.9\lambda) / (B \cos \theta_B) \quad (1)$$

where λ , B and θ_B are the wavelength of the X-ray source and the full width at half maximum (FWHM) and the angle of Bragg diffraction. For XRD, the intensity is

$$D_{Xray} = \frac{8M}{Na^3} \quad (2)$$

where M is molecular weight of the sample, N is Avogadro's number, and a^3 is volume of unit cell [12].

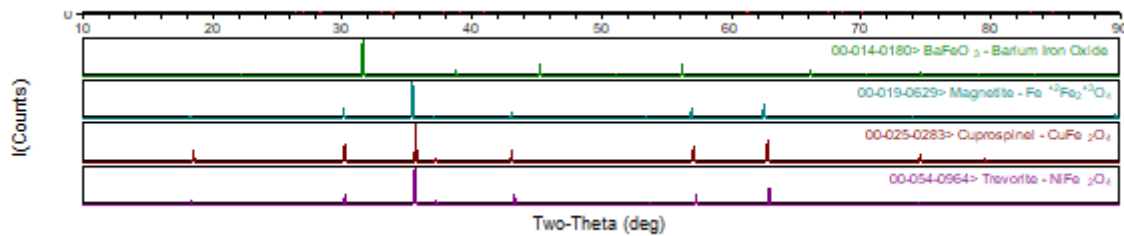


Figure 1. XRD results

B. DIELECTRIC MEASUREMENTS

B.1. Theory

In general, dielectric mechanisms are divided into relaxation and resonance processes. The most common are [16-18] electronic polarization, atomic polarization, dipole relaxation, and ionic relaxation. A theoretical study was conducted in ref [16,18].

From Clausius–Masotti equation,

$$\frac{\varepsilon' - 1}{\varepsilon'' + 2} = \frac{4\pi}{3} N \alpha$$

$$\alpha = \frac{e^2(\omega_0^2 - \omega^2 + i\omega\gamma)}{m[(\omega_0^2 - \omega^2)^2 + \gamma^2\omega^2]} = \frac{e^2(\omega_0^2 - \omega^2)}{m[(\omega_0^2 - \omega^2)^2 + \gamma^2\omega^2]} + i \frac{e^2\omega\gamma}{m[(\omega_0^2 - \omega^2)^2 + \gamma^2\omega^2]}$$

$$\varepsilon' = 1 - \frac{(4\pi e^2 N/m)(\omega_1^2 - \omega^2)}{(\omega_1^2 - \omega^2)^2 + \gamma^2\omega^2}$$

$$\varepsilon'' = \frac{(4\pi e^2 N/m)\gamma\omega}{(\omega_1^2 - \omega^2)^2 + \gamma^2\omega^2}$$

As can be seen, resonance phenomena can be observed in every frequency region. This is also consistent with the experimental results.

B.2. Dielectric Measurements Results

As we know the dielectric permittivity is, $\varepsilon = \varepsilon' - i\varepsilon''$, where ε' is the real part and ε'' is the imaginary part of the dielectric constant. As seen in Figure 2, it is clear that nanopowders in various compositions show almost the same trend and also both ε' and ε'' are sensitive to metallic behavior. The urea and glycine exhibits that the values of the real part of the ε' of complex permittivity increase with increasing frequency, with the exception of a resonance peak around 2.2 GHz [16].

The increase in both imaginary and real parts as the frequency increases and the transition to resonance is related to the high conductivity of the hexagonal ferrites of the samples. While it is stated in the literature that resonance can occur in the very high terrestrial voltage region, as can be seen from my previous publication, it has been proven both theoretically and experimentally that this resonance formation can occur in every region [16]. The resonance event is caused by atomic and electronic polarization.

In general, the resonance phenomenon, which is said to originate from vacancies or pores, is dominant in the low-frequency regions as long as the materials contain space charges. High-frequency resonances are attributed to the atomic and electronic polarizations mentioned earlier [16].

Therefore, the resonance phenomenon observed in the curves of both real and imaginary parts of the complex permittivity can be interpreted as different compositions of hexagonal ferrites using urea or glycine, which has an intrinsic property for the atomic polarization of the samples we synthesized [16].

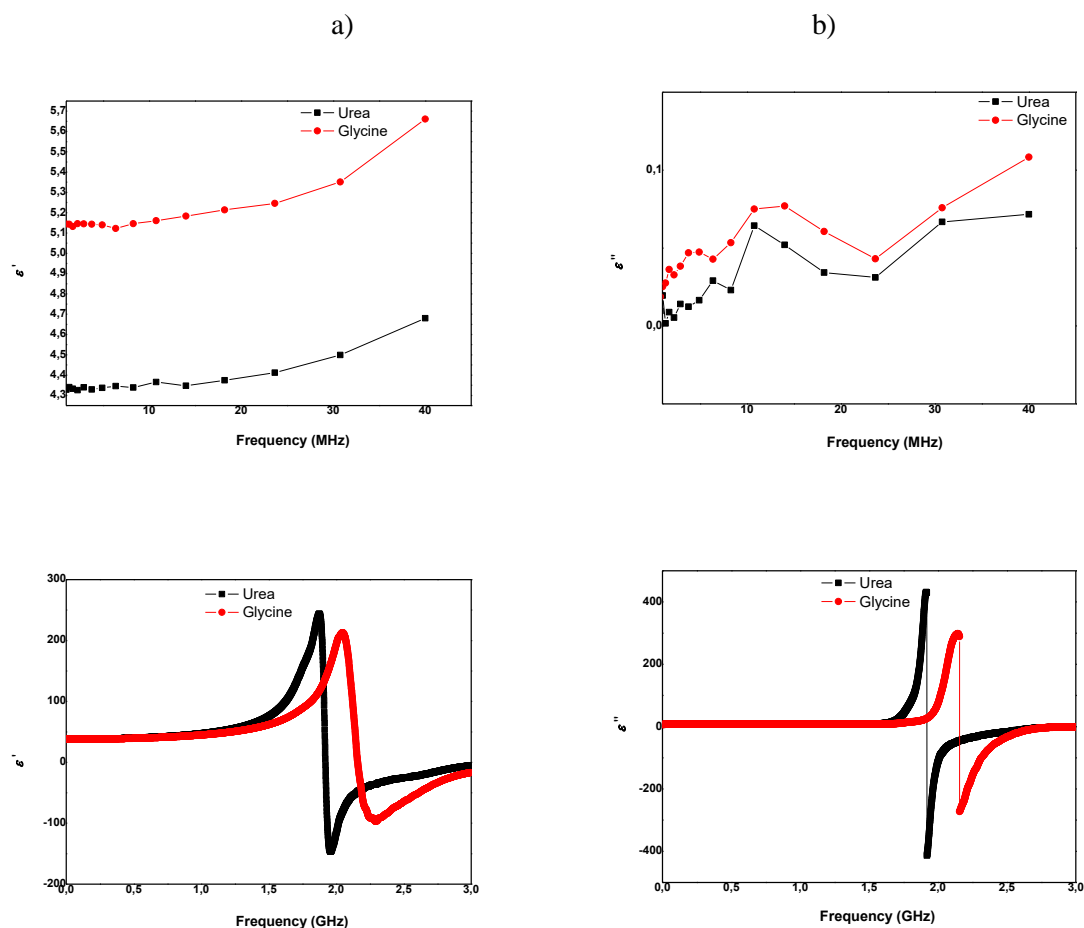


Figure 2. Dependency of real and imaginary part of permittivity on frequency for (a) and (b).

B. 3. Magnetic Measurements

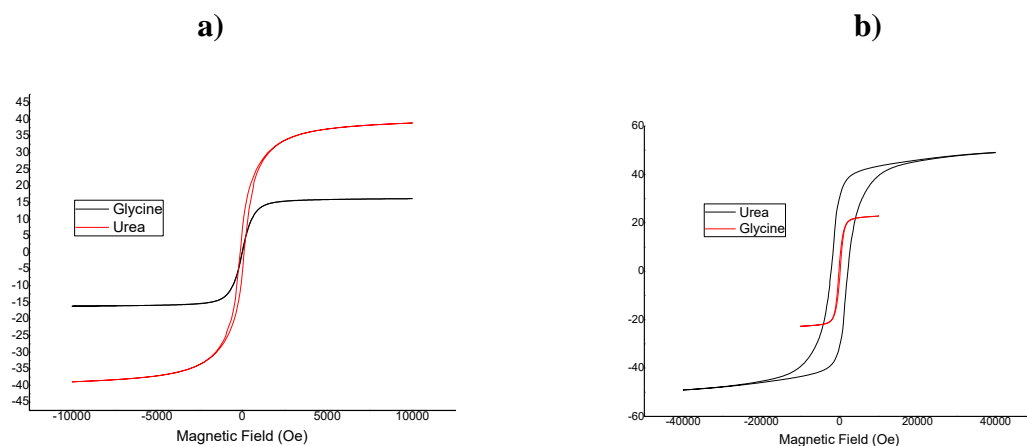


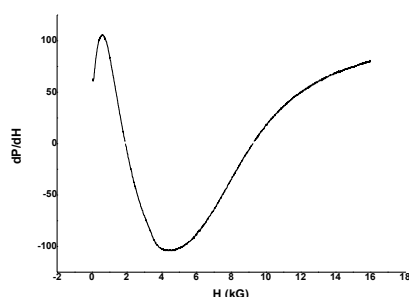
Figure 3. VSM measurements a) at room temperature b) 10 K temperature

Magnetization measurements of hexagonal ferrite nanoparticles were carried out using the VSM technique, and the results of the M-H curves of the sample are shown in Figure 3a) at room temperature and b) at 10 K temperature.

The coercivity (H_c) of magnetic materials is generally due to magneto-crystal anisotropy. We can see from the measurement results that the magnetic moment value of urea used for synthesis is higher than glycine. According to these results, we can say that the anisotropic properties of hexagonal ferrites produced with urea are higher than those produced with glycine. As can be seen, you can see that there is a typical super paramagnetic hysteresis loop shape.

It can be said that the reason for the increase in coercivity at low temperature is the exchange anisotropy. In magnetic materials, the coercive field increases as the temperature is lowered. It has the highest value at the lowest temperature. It can be seen that the coercivity and magnetization of hexagonal ferrites increase with decreasing temperature. In addition, coercivity and magnetization increase with increasing urea.

The asymmetric behavior of nano-sized hexagonal ferrites is shown in Figure 4. These measurements are associated with superparamagnetic behavior. Additionally, ESR spectrometer measurements of hexagonal ferrites were oriented from the magnetization field relative to the freezing field [12,17].



Figures 4. ESR spectrometer measurements

The very broad ESR spectra of NPs, that is, the asymmetric properties they exhibit, are due to the dipolar interactions between ions and hard magnetic materials [12].

ESR spectrometer measurements have been explained in detail in our previous studies [12,17]. As can be seen from the measurement results, a very successful study has been carried out. It has very useful results scientifically. There are very useful and useful results for biomedical and cancer applications used recently from ESR measurements [1,18].

We can say that these samples we synthesized can also be used quite successfully in magnetic recording, electromagnetic absorption, and electromagnetic interference suppression applications.

V. CONCLUSIONS

It can be seen that microwave method is very useful for powder technology. It has been shown that hexagonal ferrite nanoparticles obtained using this method can be obtained in a much faster, more reliable, cheaper and crystalline structure in nano size. The dielectric behavior of the NPs was studied at room temperature. Dielectric measurements showed that the complex permittivity of composites was significantly modified by the incorporation of nanoparticles with different hexagonal ferrites ratios. Dielectric measurements produce very interesting results. The resonance phenomenon occurring in both the real and imaginary parts of the complex permittivity can be interpreted as atomic polarization.

Magnetic measurements have shown that the coercivity of hexagonal ferrite nanoparticles increases at low temperatures and with the amount of urea used. We can say that the higher coercivity at low

temperatures is due to the exchange anisotropy resulting from the spin disorder of the particles. This method provides a rapid and reproducible route for the preparation of hexagonal ferrite using urea as fuel and offers a new route for the synthesis of similar magnetic materials.

These products can be used in magnetic recording media, electromagnetic absorption materials, radiofrequency coil manufacturing, transformer cores, biosensors, microwave devices, industrial and medical applications.

VI. REFERENCES

- [1] S.R. Mokhosi, W. Mdlalose, A. Nhlapo and M. Singh, "Advances in the synthesis and application of magnetic ferrite nanoparticles for cancer therapy", *Pharmaceutics*, vol. 14, pp. 937, 2022.
- [2] M. Irfan, N. Dogan, A. Bingolbali, F. Aliew, "Synthesis and characterization of NiFe₂O₄ magnetic nanoparticles with different coating materials for magnetic particle imaging (MPI)" *Journal of Magnetism and Magnetic Materials*, vol. 537, no. 1, pp. 168150, 2021.
- [3] C. Xiangfeng, J. Dongli, Z. Chenmou, "The preparation and gas-sensing properties of NiFe₂O₄ nanocubes and nanorods", *Sens. Actuators, B*, vol. 123 (2), pp. 793-797, 2007.
- [4] S. Rana, R.S. Srivastava, M.M. Sorensson, R.D.K. Verse, "Synthesis and characterization of nanoparticles with magnetic core and photocatalytic shell: Anatase TiO₂-NiFe₂O₄ system", *Mater. sci. Eng., B*, vol. 119 (2), pp. 144-151, 2005.
- [5] Raikher, V.I. Stepanov, J. Depeyrot, M.H. Sousa, F.A. Tourinho, E. Hasmonay, R. Perzynski, "Dynamic optical probing of the magnetic anisotropy of nickel-ferrite nanoparticles", *J. Appl. Phys.*, vol. 96 (9), pp. 5226-5233, 2004.
- [6] C.H. Cunningham, T. Arai, P. C. Yang, M.V. McConnell, J.M. Pauly, S.M. Conolly, "Positive contrast magnetic resonance imaging of cells labeled with magnetic nanoparticles", *Magn. reson. Med.*, vol. 53 (5), pp. 999-1005, 2005.
- [7] T.-J. Yoon, J.S. Kim, B.G. Kim, K.N. Yu, M.-H. Cho, J.-K. lee, "Multifunctional nanoparticles possessing a "magnetic motor effect" for drug or gene delivery", *Angew. chem. (International ed.)*, vol. 44 (7), pp. 1068-1071, 2005.
- [8] J. Dobson, "Magnetic nanoparticles for drug delivery", *Drug Dev. Res.*, vol. 67, pp. 55-60, 2006.
- [9] C. Sun, J.S.H. Lee, M. Zhang, "Magnetic nanoparticles in mr imaging and drug delivery", *Adv. Drug Deliv. Rev.*, vol. 60, pp. 1252-1265, 2008.
- [10] O. Veisesh, J.W. Gunn, M. Zhang, "Design and fabrication of magnetic nanoparticles for targeted drug delivery and imaging", *Adv. Drug Deliv. Rev.*, vol. 62, pp. 284-304, 2010.
- [11] A. Jordan, P. Wust, H. Fahling, W. John, A. Hinz, R. Felix, "Inductive heating of ferrimagnetic particles and magnetic fluids: physical evaluation of their potential for hyperthermia", *Int. J. Hyperth.*, vol. 9, pp. 51-68, 1993.
- [12] H. Bayrakdar, O. Yalçın, S. Özüm, U. Cengiz, "Synthesis and investigation of small g-values for smart spinel ferrite", *Journal of Alloys and Compounds*, vol. 869, pp. 159334, 2021.

- [13] N. Kasapoglu, A. Baykal, Y. Koseoglu and M.S. Toprak, "Microwave-assisted combustion synthesis of CoFe_2O_4 with urea, and its magnetic characterization", *Scripta Materialia*, vol. 57, pp. 441–444, 2007.
- [14] Harun Bayrakdar, "Microwave-Assisted hydrothermal synthesis of nanosheet layered hexagonal spinel ferrites for efficient electromagnetic wave absorbing", *Langmuir*, vol. 40, pp. 13716–13720, 2024.
- [15] Harun Bayrakdar, "Fabrication, magnetic and microwave absorbing properties of $\text{Ba}_2\text{Co}_2\text{Cr}_2\text{Fe}_{12}\text{O}_{22}$ hexagonal ferrites", *Journal of Alloys and Compounds*, vol. 674, pp. 185e188, 2016.
- [16] Harun Bayrakdar and Kadir Esmer, "Dielectric characterization of $\text{Ni}_x\text{Co}_{1-x}\text{Fe}_2\text{O}_4$ nanocrystals thin film over a broad frequency range 1 MHz–3 GHz", *J Appl Phys.*, vol. 107, pp. 044102, 2010.
- [17] H. Bayrakdar, O. Yalçın, U. Cengiz, S. Özüm, E. Anigi, O. Topel, "Comparison effects and electron spin resonance studies of $\alpha\text{-Fe}_2\text{O}_3$ spinel type ferrite nanoparticles", *Spectrochimica Acta Part A: Molecular and Biomolecular Spectroscopy*, vol. 132, pp. 160–164, 2014.
- [18] Priyank Purohit, Akanksha Bhatt, Shashank Kailkhura, Bibekananda Sarkar, Samir Kumar, Gaurav Joshi, "Biomedical applications of spinel ferrite nanoparticles", <https://www.researchgate.net/publication/374534261>



Düzce University Journal of Science & Technology

Research Article

The Relationship Between Sustainable Construction and Economic Growth for Reinforced Concrete Structures in Türkiye

 Esra DOBRUCALI ^{a,*}

^a Department of Civil Engineering, Faculty of Engineering, Sakarya University, Sakarya, TURKEY

* Corresponding author's e-mail address: eeken@sakarya.edu.tr

DOI: 10.29130/dubited.1612685

ABSTRACT

The construction sector is one of the key industries in terms of sustainable development. It plays a growing role in addressing issues such as sustainable cities, responsible production, and consumption, which are among the sustainable development goals set for Türkiye. Additionally, these goals aim to decouple economic growth from environmental degradation. The construction sector is also one of the industries contributing to environmental degradation. In order to reduce this degradation and ensure environmental sustainability, the vision of sustainable construction is emerging. Specifically, CO₂ emissions from building materials in the sector are considered one of the causes of environmental degradation. This study aims to determine the decoupling of economic growth from environmental degradation for reinforced concrete structures in the construction sector in line with Türkiye's sustainable development goals. By examining the relationship between embedded CO₂ emissions from the raw construction materials (concrete and reinforcement) used in the reinforced concrete structures built in Türkiye and economic growth, the study classifies the type of decoupling. It evaluates 12 statistical regions separately for the period from 2010 to 2019. As a result, weak decoupling was observed in four statistical regions, while strong decoupling was seen in the other regions. Weak decoupling was identified in the regions of Istanbul (TR1), East Marmara (TR4), Mediterranean (TR6), and Central Anatolia (TR7).

Keywords: Sustainable development, CO₂ emissions, Decoupling, Construction sector, Sustainable construction

Türkiye’de Betonarme Yapılar için Sürdürülebilir İnşaat ve Ekonomik Büyüme Arasındaki İlişki

ÖZ

İnşaat sektörü, sürdürülebilir kalkınma açısından önemli sektörlerden biridir. Türkiye için belirlenen sürdürülebilir kalkınma hedefleri arasında yer alan sürdürülebilir şehirler, sorumlu üretim ve tüketim gibi konuların ele alınmasında giderek artan bir rol oynamaktadır. Ayrıca bu hedefler ekonomik büyümeyi çevresel bozulmadan ayırmayı amaçlamaktadır. İnşaat sektörü de çevresel bozulmaya katkıda bulunan endüstrilerden biridir. Bu çevresel bozulmanın azalması ve çevresel sürdürülebilirliğin sağlanması amacı ile sürdürülebilir inşaat vizyonu oluşturulmuştur. Sektörde özellikle yapı malzemelerindeki CO₂ emisyonları çevresel bozulma sebepleri arasında gösterilmektedir. Bu çalışma Türkiye’deki betonarme yapılar için sürdürülebilir kalkınma amaçları doğrultusunda inşaat sektöründe ekonomik büyümenin çevresel bozulmadan ayrıklaştırma durumunu belirlemeyi hedeflenmektedir. Çalışma, Türkiye’deki inşa edilen betonarme yapıların kaba inşaat malzemelerindeki (beton ve donatı) gömülü CO₂ emisyonu ile ekonomik büyüme arasındaki ilişkiyi inceleyerek, ayrıklaştırma türünü sınıflandırmaktadır. Çalışmada 2010-2019 yılları arasında 12 istatistikî bölge için ayrı ayrı değerlendirme yapılmaktadır. Sonuç olarak dört istatistiksel bölgede zayıf ayrıklaştırma gözlemlenirken, diğer bölgelerde güçlü

ayırıklaştırma görülmüştür. Zayıf ayırıklaştırma; İstanbul (TR1), Doğu Marmara (TR4), Akdeniz (TR6) ve Orta Anadolu (TR7) bölgelerinde tespit edilmiştir.

Anahtar kelimeler: Sürdürülebilir kalkınma, CO₂ emisyonu, Ayırıştırma, İnşaat sektörü, Sürdürülebilir inşaat

I. INTRODUCTION

The construction sector supports environmental, economic, and social elements in terms of sustainable development. The construction sector plays a significant role in economic growth in terms of employment, due to its broad scope and diversity of inputs [1]. It also has significant social impacts by contributing to the construction of essential living and social spaces that enhance quality of life. Furthermore, its integration of structures and the environment as parts of a whole underscores its importance for environmental sustainability [2,3]. The concept of "sustainable construction" has also come to the forefront in the sector alongside the principles of sustainable development [2].

Sustainable construction is defined as "the creation of an environment where resources are used efficiently, based on ecological principles, and managed responsibly" [4,5]. Globally, sustainable construction encompasses a socioeconomic and environmental perspective while also possessing a national and regional vision [5,6]. It plays a significant role in addressing sustainability-related challenges [7].

With the increase in industrialization in developing countries, rapid urbanization is occurring, leading to a growing demand for buildings and infrastructure [8,9]. This demand results in significant resource consumption in the construction sector. Since many of these resources include emission-intensive materials such as cement, steel, and concrete, the construction sector is a major contributor to CO₂ emissions [9-15]. In 2019, global greenhouse gas emissions from buildings accounted for 21% of total global emissions. Furthermore, 18% of greenhouse gas emissions were attributed to the production of cement and steel used in building construction [16].

The majority of greenhouse gas emissions from the construction sector are CO₂ emissions, with approximately 40% of global annual emissions stemming from buildings and infrastructure [16,17]. Among embedded CO₂ emissions in the sector, concrete (30%) and steel (25%) rank as the top contributors [17]. If necessary measures are not taken by 2050, global concrete usage could result in 3.8 billion tons of CO₂ emissions [18].

The Paris Agreement, which came into effect in 2020, places the responsibility for reducing emissions on participating nations and aims to limit global warming to below 2°C compared to pre-industrial levels [19,20]. The cement and concrete sectors play a critical role in achieving this target [21]. Resource efficiency in structural materials such as steel and cement are declining, particularly in developing economies, where structural material resources are being rapidly depleted [22].

According to the United Nations Sustainable Development Goals, global resource efficiency in consumption and production must be progressively improved by 2030, and efforts should be made to decouple economic growth from environmental degradation [23]. Decoupling is defined by the European Union as "reducing the adverse effects arising from the use of natural resources in a growing economy" [24-25].

Today, the relationship between economic growth and environmental degradation has been extensively studied across various industrial sectors for sustainable production and development. In the literature, there are studies focusing on environmental pollution in the construction sector [26-31] and sustainable construction [3, 32-34]. Yılmaz et al. [32] examined the threats and opportunities for a sustainable construction sector. The authors emphasized the importance of designing integrated technological roadmaps involving all stakeholders for sustainable buildings [32]. Gökçe et al. [3] analyzed national

legal regulations and standards developed specifically for sustainable construction in Türkiye, incorporating internationally recognized standards as well. The result of the study emphasizes the need for training and incentive programs aimed at sustainable construction in the industry [3]. Hwang et al. [33] investigated the barriers and solutions for the adoption of sustainable construction practices by small contractors. The greatest barrier identified was the need for additional investment [33]. The study also explored the economic challenges in sustainable construction, concluding that market-driven measures in construction economics are strategically more effective [34].

According to Osuizugbo et al. [35], adopting sustainable construction practices in the construction industry significantly reduces the greenhouse gas emissions generated by the sector. In this context, the researchers have explored the variables that hinder the effective adoption of sustainable construction practices in the Nigerian construction sector and the possible solutions. As a result, they have stated that the government should take a larger role in promoting the sustainability of the sector. [35].

Tapio [26] examined the relationship between GDP, traffic volumes, and CO₂ emissions from transportation in the EU15 countries. As a result of the study, it was determined that in Finland, CO₂ emissions from road traffic were strongly decoupled from road traffic volume, while GDP was weakly decoupled from road traffic volume [26]. Du et al. [27] investigated the relationship between economic growth and carbon emissions caused by the construction industry in China, while Su et al. [28] focused on the supply chain, and Ogungbile et al. [29] included various sectors in their analysis. In the Su et al. [28] study, non-competitive input-output models at comparable prices for different years and the Structural Production Layer Difference (SPLD) method have been used. As a result, it has been determined that the direct impact of other service sectors and transportation-storage on carbon emissions in the construction sector was not highlighted by the structural decomposition analysis [28]. According to the results of the study conducted by Ogungbile et al. [29], it has been determined that the construction sector in Gansu, Xinjiang, Ningxia, and Inner Mongolia has significant CO₂ emission interactions compared to other provinces, and the construction sector is identified as the critical sector for these regions [29]. In a study by Artekin [30], the relationship between the construction sector, employment, and economic growth in Türkiye from 2005 to 2023 was analyzed. Zivot-Andrews (ZA) unit root, Phillips-Perron (PP) unit root, and GMM tests have been applied in the analysis. A bidirectional relationship was observed between the construction sector and economic growth [30]. Wang et al. [36] conducted research on the decoupling of economic growth and construction waste production. This study, which offered a comparative analysis between the China and EU, aimed to develop construction waste management theories and promote sustainable development. In this study, the Tapio, Kaya, and LMDI methods have been used. They have determined that the construction waste generation in China is in a weak decoupling situation [36]. Wong et al. [10] explored the adoption of carbon reduction strategies by Australian construction contractors. In this study, an evaluation based on a survey has been conducted [10]. Wu et al. [12] determined the type of decoupling between carbon emissions and economic output in the Chinese construction sector. This study has examined decoupling relationships at both national and state levels from 2005 to 2015 using the Tapio decoupling model [12]. Dobrucali [31] analyzed the relationship between embedded CO₂ emissions from ready-mix concrete production, environmental pollution, and economic growth. The decoupling method used by Tapio has been applied in the study. This study, conducted for 20 OECD countries, identified the types of decoupling during the Kyoto Protocol commitment periods. According to the results of the study, absolute decoupling between environmental degradation and economic growth has been observed in Switzerland and Belgium [31].

Overall, when a literature review is conducted, it can be observed that there are a few studies examining the relationship between environmental pollution and economic growth. It has been determined that studies specifically focusing on Türkiye's construction sector in this context are almost non-existent. According to the author's knowledge, there are very few studies in the literature on decoupling economic growth from environmental degradation in the construction sector. This study has been conducted to contribute to the literature and investigate the situation of decoupling economic growth from environmental degradation in the construction sector.

This study investigates the relationship between embedded CO₂ emissions from the primary construction materials (concrete and reinforcement) used in reinforced concrete structures in Türkiye and economic growth. It examines a 10-year period (2010–2019) prior to the Paris Agreement, providing an overview of the state of the construction sector before the agreement and contributing to sustainable construction and sustainable development.

II. MATERIAL AND METHODS

This study examines the relationship between embedded CO₂ emissions from primary construction materials (concrete and reinforcement) used in reinforced concrete structures and economic growth across 12 statistical regions in Türkiye. The study consists of four main stages. The first stage involves defining the analysis region and period, the second stage focuses on compiling the analysis data, the third stage applies the decoupling analysis method to determine the type of decoupling, and the final stage evaluates the analysis results. The methodology of the study is illustrated in Figure 1.

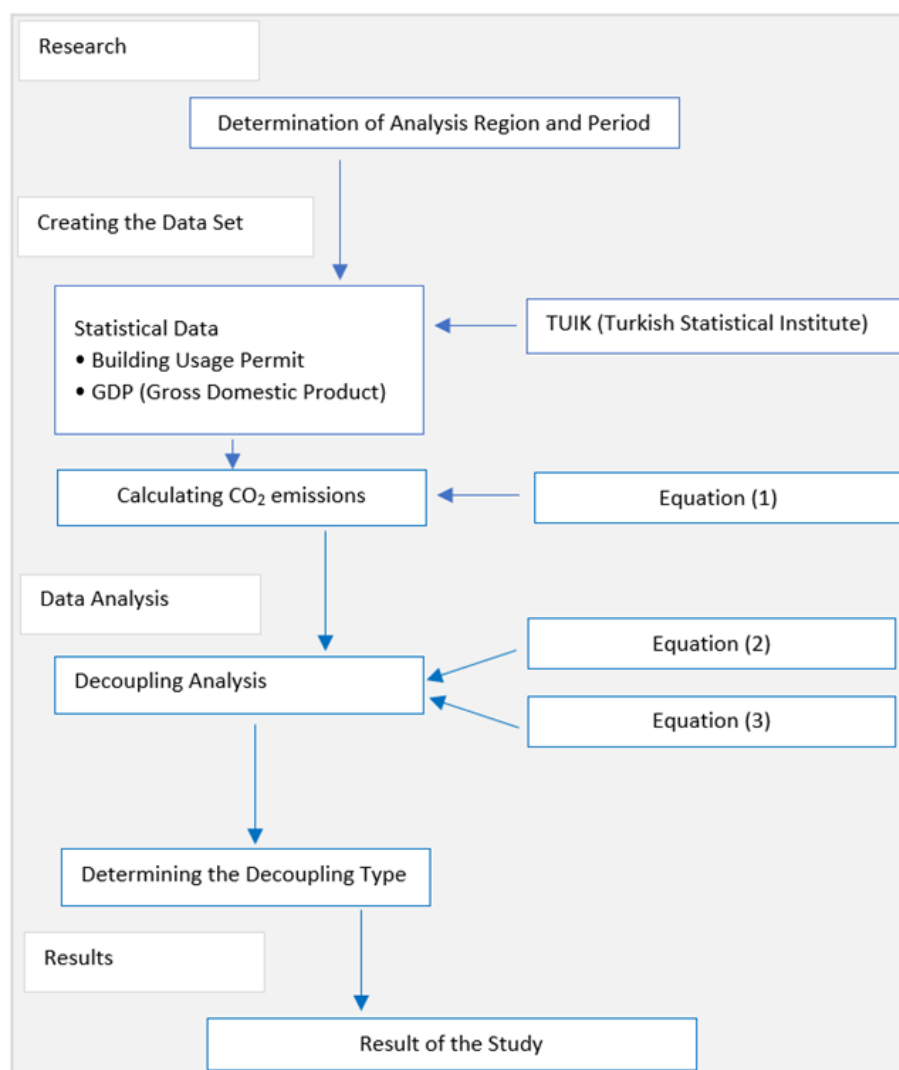


Figure 1. Study Methodology

A. DETERMINING THE ANALYSIS REGION AND PERIOD

The study focuses on 12 regions, selected based on the classification of Statistical Regional Units for Development Planning in Türkiye, coordinated by the State Planning Organization (DPT) and the Turkish Statistical Institute (TUIK) [37]. This classification includes:

TR1 (Istanbul): Istanbul;
TR2 (Western Marmara): Tekirdağ, Balıkesir, Kırklareli, Çanakkale, Edirne;
TR3 (Aegean): İzmir, Denizli, Aydın, Muğla, Afyonkarahisar, Kütahya, Manisa, Uşak;
TR4 (Eastern Marmara): Bursa, Bilecik, Eskişehir, Kocaeli, Sakarya, Bolu, Düzce, Yalova;
TR5 (Western Anatolia): Ankara, Karaman, Konya;
TR6 (Mediterranean): Antalya, Burdur, Isparta, Mersin, Adana, Kahramanmaraş, Hatay, Osmaniye;
TR7 (Central Anatolia): Kırıkkale, Niğde, Aksaray, Kırşehir, Nevşehir, Sivas, Kayseri, Yozgat;
TR8 (Western Black Sea): Zonguldak, Bartın, Karabük, Çankırı, Kastamonu, Samsun, Sinop, Çorum, Tokat, Amasya;
TR9 (Eastern Black Sea): Trabzon, Giresun, Ordu, Artvin, Rize, Gümüşhane;
TRA (North eastern Anatolia): Erzurum, Erzincan, Ağrı, Bayburt, Iğdır, Kars, Ardahan;
TRB (Central Eastern Anatolia): Malatya, Bingöl, Elazığ, Tunceli, Muş, Van, Bitlis, Hakkari;
TRC (South eastern Anatolia): Gaziantep, Kilis, Adıyaman, Şanlıurfa, Mardin, Diyarbakır, Şırnak, Batman, Siirt.

These regions are used with the abbreviations mentioned above. The study covers the period between 2010 and 2019, prior to the Paris Agreement. While the Paris Agreement applies to data from 2020 onwards, the year 2020 was not included in this study. This is due to the fact that the COVID-19 pandemic, which began in 2020, caused restrictions that had a significant impact on the construction sector.

B. CREATION OF ANALYSIS DATA

In this study, the embedded CO₂ emissions in the primary construction materials (concrete and reinforcement) of reinforced concrete structures were calculated based on building use permit data. These data include all construction type classifications, excluding industrial buildings. Industrial buildings were excluded from the analysis because steel construction is used much more extensively in these buildings compared to other construction types. Economic growth was correlated with GDP (Gross Domestic Product). The building use permit and GDP data for the study years and regions were obtained from the TUIK database [38]. The study covers 12 regions defined by the Statistical Region Units Classification for Development Planning in Türkiye, established under the coordination of the State Planning Organization (DPT) and the Turkish Statistical Institute (TUIK) [37].

For the study, it was assumed that the buildings with building use permits used C25 concrete and S420 steel in their construction. In the literature, there are coefficient values for floor area and measurement calculation (0.38 m³/m² for concrete; 0.034 tons/m² for steel) [39]. Using the total floor area values and these coefficients, the amounts of concrete and reinforcement were calculated. Additionally, the CO₂ values for C25 concrete and S420 steel were calculated based on studies from the literature. The unit CO₂ value for C25 concrete was taken as an average of 226 kg/m³ [40, 41] (The average value from the studies by Mergos [40] and de Medeiros & Kripka [41] was used.), and for S420 steel, it was taken as an average of 352 kg/ton [42]. The total CO₂ values for the years 2010–2019 were calculated using Equation (1) and are shown in Table 1 and Figure 2.

$$T = Y_N(M_c \times C + M_s \times S) \quad (1)$$

In Equation (1), T represents the total CO₂ amount, M_c is the measurement coefficient for concrete, C is the unit CO₂ amount for concrete (C25), M_s is the measurement coefficient for reinforcement steel, and S is the unit CO₂ amount for steel (S420).

Table 1. CO₂ amount and GDP for statistical regions

Region	Year	Building use permit (m ²)	Total CO ₂ (ton)	GDP (Based on 2009) (Thousand TRY)	GDP (Based on 2009) (Thousand USD)
TR1	2010	11,135,446	1,099,035.37	340,511,117.00	221,456,241.55
	2011	18,008,976	1,773,810.56	414,109,741.00	219,233,279.16
	2012	17,170,770	1,693,066.79	474,537,629.00	266,954,111.72
	2013	23,532,507	2,315,820.99	556,694,426.00	261,309,813.18
	2014	26,654,231	2,622,559.10	631,564,008.00	271,418,629.08
	2015	24,747,279	2,428,149.50	727,311,453.00	249,241,442.38
	2016	27,304,475	2,682,312.51	811,518,936.00	230,597,560.81
	2017	27,659,178	2,716,244.58	973,837,089.00	258,182,106.90
	2018	27,915,281	2,743,173.42	1,159,274,030.00	219,517,900.02
	2019	24,660,811	2,423,875.98	1,325,199,566.00	223,097,570.03
TR2	2010	7,270,110	717,000.40	53,923,382.00	35,069,837.41
	2011	7,095,831	700,530.46	63,412,142.00	33,570,936.52
	2012	7,315,466	721,521.64	70,296,672.00	39,545,832.58
	2013	7,551,350	744,866.26	77,758,672.00	36,499,564.40
	2014	8,586,869	846,167.69	89,527,539.00	38,475,026.43
	2015	8,072,678	794,327.29	101,535,098.00	34,794,934.38
	2016	10,134,373	995,001.51	115,785,133.00	32,900,981.19
	2017	13,162,990	1,293,696.64	138,404,151.00	36,693,483.66
	2018	8,760,697	862,316.26	168,995,702.00	32,000,701.00
	2019	3,304,882	325,658.81	195,678,907.00	32,942,576.94
TR3	2010	17,323,334	1,706,184.04	151,624,734.00	98,611,299.43
	2011	13,034,020	1,286,604.12	181,536,129.00	96,106,797.08
	2012	17,267,410	1,703,866.11	201,550,675.00	113,383,593.05
	2013	18,308,681	1,807,477.20	227,113,998.00	106,606,270.18
	2014	22,223,756	2,189,959.81	256,554,011.00	110,255,709.74
	2015	20,249,599	1,994,570.53	289,322,103.00	99,147,425.72
	2016	24,852,167	2,445,381.80	328,582,522.00	93,368,527.51
	2017	35,286,561	3,466,263.38	393,779,805.00	104,398,262.15
	2018	20,241,173	1,991,949.96	481,686,561.00	91,211,240.48
	2019	7,803,779	769,293.21	545,635,472.00	91,857,823.57
TR4	2010	9,332,759	923,649.26	129,250,396.00	84,059,830.91
	2011	11,815,418	1,170,772.18	159,689,985.00	84,541,259.46
	2012	12,815,253	1,268,532.12	177,108,473.00	99,633,479.41
	2013	15,039,781	1,490,107.26	205,083,616.00	96,265,309.80
	2014	16,071,590	1,591,194.79	232,237,852.00	99,805,686.54
	2015	14,703,945	1,452,357.29	267,592,002.00	91,700,764.88
	2016	16,055,451	1,587,143.50	296,276,028.00	84,188,459.88
	2017	18,819,933	1,854,176.06	363,023,993.00	96,244,331.24
	2018	21,764,699	2,150,216.07	448,760,465.00	84,976,418.29
	2019	16,696,825	1,649,158.08	496,345,678.00	83,559,878.45

Table 1 (cont). CO₂ amount and GDP for statistical regions

TR5	2010	20,793,585	2,044,492.46	136,501,751.00	88,775,852.63
	2011	20,039,160	1,970,157.92	163,975,572.00	86,810,086.29
	2012	22,461,037	2,211,236.63	184,144,943.00	103,591,889.63
	2013	25,507,821	2,509,060.89	218,674,158.00	102,644,647.95
	2014	30,892,463	3,041,942.21	241,103,632.00	103,615,811.59
	2015	23,718,681	2,333,225.53	273,437,161.00	93,703,835.03
	2016	25,471,244	2,507,785.80	313,169,029.00	88,988,698.85
	2017	40,892,797	4,020,330.43	361,369,604.00	95,805,722.32
	2018	16,006,244	1,582,684.28	425,587,933.00	80,588,512.21
	2019	8,029,738	797,941.52	502,764,108.00	84,640,422.22
TR6	2010	8,915,274	879,540.22	123,664,680.00	80,427,081.17
	2011	10,478,339	1,035,122.77	146,879,306.00	77,759,175.18
	2012	10,855,329	1,076,473.87	162,921,957.00	91,652,766.09
	2013	15,564,454	1,536,407.71	185,892,368.00	87,257,025.91
	2014	19,828,272	1,949,750.57	210,369,405.00	90,407,583.05
	2015	16,785,351	1,646,648.03	238,930,681.00	81,878,853.02
	2016	17,574,181	1,726,800.71	259,985,618.00	73,876,340.65
	2017	19,863,060	1,949,120.50	309,964,536.00	82,177,294.20
	2018	19,020,136	1,868,342.19	383,155,143.00	72,553,520.73
	2019	17,806,823	1,749,077.47	447,092,638.00	75,268,120.88
TR7	2010	5,150,119	506,496.95	46,073,924.00	29,964,830.91
	2011	6,024,045	591,070.45	54,584,204.00	28,897,349.78
	2012	5,137,753	505,271.77	60,228,650.00	33,882,003.83
	2013	6,399,509	628,437.81	68,161,782.00	31,994,828.20
	2014	7,021,171	690,751.01	77,133,354.00	33,148,546.99
	2015	8,268,997	811,359.19	87,871,986.00	30,112,739.80
	2016	8,157,567	802,901.11	97,594,250.00	27,731,941.92
	2017	10,370,407	1,016,458.56	114,346,051.00	30,315,239.27
	2018	11,418,879	1,120,713.91	135,288,255.00	25,617,923.69
	2019	9,926,153	973,960.26	154,098,680.00	25,942,538.72
TR8	2010	12,937,147	1,284,250.43	50,907,437.00	33,108,376.74
	2011	4,435,414	436,537.49	59,780,509.00	31,648,318.60
	2012	7,170,475	704,477.66	65,074,916.00	36,608,301.08
	2013	7,543,257	740,204.29	72,432,728.00	33,999,590.69
	2014	9,436,086	927,224.26	81,866,302.00	35,182,561.35
	2015	7,912,211	777,060.37	92,825,892.00	31,810,387.58
	2016	10,055,018	987,048.18	103,102,956.00	29,297,270.97
	2017	15,744,983	1,542,623.69	120,936,784.00	32,062,563.69
	2018	8,796,934	865,741.73	140,558,516.00	26,615,890.17
	2019	3,289,491	323,859.90	158,970,449.00	26,762,701.85

Table 1 (cont). CO₂ amount and GDP for statistical regions

TR9	2010	9,371,187	918,114.05	28,034,398.00	18,232,568.94
	2011	2,490,075	244,380.98	32,687,789.00	17,305,198.26
	2012	4,591,992	450,156.63	37,025,186.00	20,828,750.00
	2013	5,671,780	556,325.68	41,047,946.00	19,267,717.80
	2014	7,620,040	747,010.86	46,081,737.00	19,803,918.09
	2015	5,045,865	496,842.94	55,953,238.00	19,174,544.40
	2016	5,949,183	584,006.28	58,859,489.00	16,725,246.93
	2017	8,018,212	786,506.69	68,630,098.00	18,195,100.08
	2018	5,639,125	553,407.89	79,029,556.00	14,964,884.68
	2019	2,760,144	270,706.35	94,610,423.00	15,927,680.64
TRA	2010	3,579,616	351,790.25	19,696,844.00	12,810,122.27
	2011	1,689,693	165,567.80	22,605,262.00	11,967,421.25
	2012	2,079,604	203,706.38	26,006,101.00	14,629,894.80
	2013	2,981,670	292,335.13	28,685,208.00	13,464,705.22
	2014	3,639,420	356,788.66	30,714,581.00	13,199,785.55
	2015	3,573,482	350,495.56	35,093,081.00	12,026,003.56
	2016	4,374,570	428,605.68	40,173,851.00	11,415,620.31
	2017	4,314,151	423,177.83	47,262,817.00	12,530,241.26
	2018	3,956,203	387,608.14	53,992,237.00	10,223,866.12
	2019	2,487,760	244,187.93	62,220,210.00	10,474,782.83
TRB	2010	10,076,075	987,669.14	28,279,260.00	18,398,998.05
	2011	2,962,922	290,670.42	33,977,193.00	17,987,819.90
	2012	5,701,821	558,719.87	39,985,569.00	22,494,131.98
	2013	5,578,413	547,394.25	43,880,355.00	20,597,237.61
	2014	5,313,343	521,129.65	48,289,155.00	20,752,569.94
	2015	6,190,717	606,524.34	54,416,244.00	18,647,833.86
	2016	6,921,920	678,020.03	61,789,897.00	17,557,938.45
	2017	8,685,845	852,279.47	73,613,726.00	19,516,351.44
	2018	6,813,149	667,746.82	86,628,713.00	16,403,846.43
	2019	4,281,631	419,777.81	101,419,632.00	17,074,012.12
TRC	2010	13,899,831	1,364,484.45	59,196,554.00	38,499,319.72
	2011	6,900,899	677,533.26	71,689,784.00	37,953,191.80
	2012	12,134,268	1,190,616.03	82,598,480.00	46,466,291.63
	2013	13,796,119	1,353,688.73	98,002,057.00	46,001,716.58
	2014	18,822,132	1,846,771.54	109,456,252.00	47,039,516.95
	2015	14,878,574	1,458,059.48	126,652,406.00	43,402,352.90
	2016	13,412,320	1,316,615.58	139,722,001.00	39,702,773.64
	2017	18,737,144	1,837,104.61	168,535,614.00	44,681,888.17
	2018	13,096,768	1,286,856.74	198,208,447.00	37,532,370.20
	2019	7,068,252	696,033.28	233,774,062.00	39,355,902.69

Note: The building use permit and GDP data in the table were obtained from TUIK [38]. The total CO₂ values were calculated by the author. Dollar accounts for GDP were calculated by the author, considering the Central Bank of the Republic of Türkiye [43-52] dollar exchange rate on the last day of the relevant year. (TRY: Turkish

Lira, USD: American dollar)

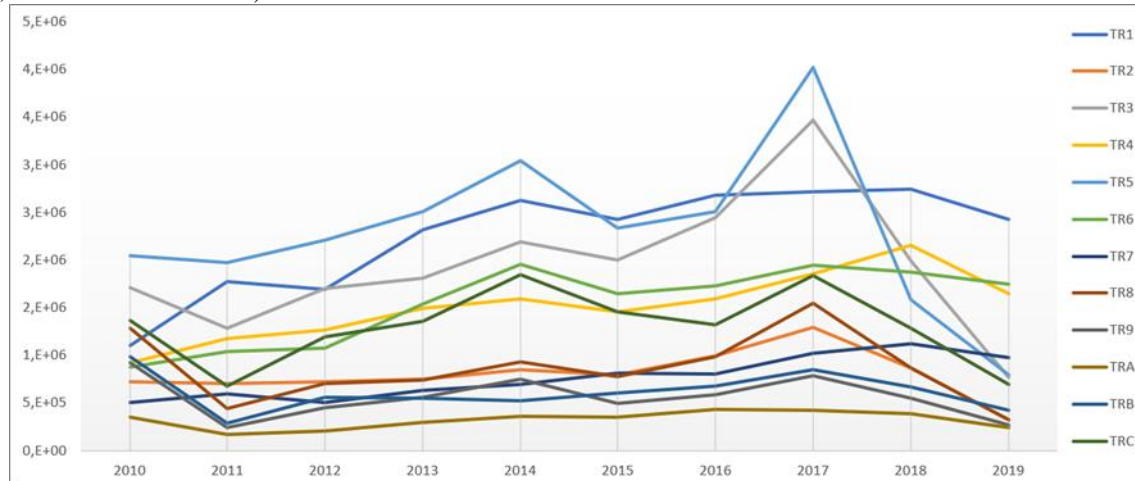


Figure 2. Total CO₂ Emission (tons)

In this study, to determine the relationship between environmental degradation caused by embedded CO₂ emissions in the primary construction materials (concrete and reinforcement) of reinforced concrete structures and economic growth, the ΔCO_2 and ΔGDP values were calculated separately for each statistical region. Equations (2) and (3) were used to calculate these values [26,31,53, 54]. The calculated values are presented in Table 2.

$$\Delta\text{CO}_2 = \left(\frac{\text{CO}_2(2019) - \text{CO}_2(2010)}{\text{CO}_2(2010)} \right) \times 100 \quad (2)$$

In Equation 2, ΔCO_2 represents the CO₂ value for the analysis period, CO₂ (2019) represents the CO₂ value for the year 2019, and CO₂ (2010) represents the CO₂ value for the year 2010.

$$\Delta\text{GDP} = \left(\frac{\text{GDP}_{(2019)} - \text{GDP}_{(2010)}}{\text{GDP}_{(2010)}} \right) \times 100 \quad (3)$$

In Equation 3, ΔGDP represents the GDP value for the analysis period, GDP (2019) represents the GDP value for the year 2019, and GDP (2010) represents the GDP value for the year 2010.

Table 2. ΔCO_2 and ΔGDP values for statistical regions.

Region	ΔCO_2 (%)	ΔGDP (%)	$\Delta\text{CO}_2/\Delta\text{GDP}$
TR1	120.55	289.18	0.42
TR2	-54.58	262.88	-0.21
TR3	-54.91	259.86	-0.21
TR4	78.55	284.02	0.28
TR5	-60.97	268.32	-0.23
TR6	98.86	261.54	0.38
TR7	92.29	234.46	0.39
TR8	-74.78	212.27	-0.35
TR9	-70.51	237.48	-0.30
TRA	-30.59	215.89	-0.14
TRB	-57.50	258.64	-0.22
TRC	-48.99	294.91	-0.17

Note: TRY values were used in ΔGDP calculations. Negative values in this table

indicate that the 2010 values are higher than the 2019 values.

In this study, the relationship between CO₂ emissions and GDP was evaluated considering the decoupling categories defined by Tapio [26]. The reason for using the method applied by Tapio is its simpler understanding compared to other analysis methods and its greater suitability for the dataset. Tapio (2005) identified eight types of decoupling. These decoupling types are detailed in Table 3.

Table 3. Types of decoupling [26]

ΔCO_2	ΔGDP	$\Delta\text{CO}_2/\Delta\text{GDP}$	Types of decoupling
>0	<0	<0	Strong negative decoupling
	>0	0-0.8	Weak decoupling
	>0	0,8-1,2	Recessive coupling
	>0	>1,2	Expansive negative decoupling
<0	>0	<0	Strong decoupling
	<0	0-0.8	Weak negative decoupling
	<0	0,8-1,2	Expansive coupling
	<0	>1,2	Recessive decoupling

III. FINDINGS AND DISCUSSION

The study consists of the following stages: determining the region and period, generating analytical data, and defining the disaggregation analysis method and type. In the Material and Method section, the study's boundaries, scope, dataset creation, and analysis methods were described, and Tables 2 and 3 were created to determine the types of disaggregation.

In this section, based on Tables 2 and 3, the type of disaggregation between environmental degradation caused by embedded CO₂ emissions in the primary construction materials (concrete and reinforcement) of reinforced concrete buildings constructed during the analysis period (2010–2019) and economic growth linked to GDP is determined. The analysis results for 12 statistical regions are presented in Table 4.

According to these results, strong decoupling was observed in 8 regions, while weak decoupling was noted in 4 regions. Strong decoupling was observed in the following regions: TR2 (West Marmara), TR3 (Aegean), TR5 (West Anatolia), TR8 (West Black Sea), TR9 (East Black Sea), TRA (Northeast Anatolia), TRB (Central Anatolia), TRC (Southeast Anatolia). Weak decoupling was observed in the following regions: TR1 (Istanbul), TR4 (East Marmara), TR6 (Mediterranean), TR7 (Central Anatolia).

Table 4. Analysis results

Region	ΔCO_2 (%)	ΔGDP (%)	$\Delta\text{CO}_2/\Delta\text{GDP}$	Types of decoupling
TR1	120.55>0	289.18>0	0.42>0	Weak decoupling
TR2	-54.58<0	262.88>0	-0.21<0	Strong decoupling
TR3	-54.91<0	259.86>0	-0.21<0	Strong decoupling
TR4	78.55>0	284.02>0	0.28>0	Weak decoupling
TR5	-60.97<0	268.32>0	-0.23<0	Strong decoupling
TR6	98.86>0	261.54>0	0.38>0	Weak decoupling
TR7	92.29>0	234.46>0	0.39>0	Weak decoupling
TR8	-74.78<0	212.27>0	-0.35<0	Strong decoupling
TR9	-70.51<0	237.48>0	-0.30<0	Strong decoupling
TRA	-30.59<0	215.89>0	-0.14<0	Strong decoupling

<i>TRB</i>	<i>-57.50<0</i>	<i>258.64>0</i>	<i>-0.22<0</i>	<i>Strong decoupling</i>
<i>TRC</i>	<i>-48.99<0</i>	<i>294.91>0</i>	<i>-0.17<0</i>	<i>Strong decoupling</i>

IV CONCLUSION

The construction sector, in addition to being one of the leading sectors of the national economy, holds a significant position in terms of sustainable development. Its multi-stakeholder structure influences numerous other sectors. In other words, any step taken towards economic and sustainability issues in the construction sector will have ripple effects across other sectors. Many of Türkiye's sustainable development goals, such as sustainable cities and responsible production and consumption, are directly or indirectly related to the construction sector. One of these goals, decoupling economic growth from environmental degradation, is particularly relevant to the sector.

The Paris Agreement, which Türkiye is a party to, highlights the increasing temperatures caused by environmental degradation, especially greenhouse gas (CO₂ and others) emissions. The construction sector is one of the industries contributing to this degradation. To mitigate this and ensure environmental sustainability, a vision for sustainable construction has been developed. Specifically, CO₂ emissions from construction materials in the sector are considered one of the causes of environmental degradation. This study aims to determine the decoupling state of economic growth from environmental degradation in the construction sector, aligning with Türkiye's sustainable construction and development objectives. It examines the relationship between embedded CO₂ emissions from primary construction materials (concrete and reinforcement) in reinforced concrete buildings and economic growth in Türkiye, classifying the type of decoupling observed.

The study covers 12 regions defined by the Statistical Region Units Classification for Development Planning in Türkiye [37], established under the coordination of the State Planning Organization (DPT) and the Turkish Statistical Institute (TUIK). The study period spans the decade preceding the Paris Agreement (2010–2019). The decoupling analysis and type determination were conducted using the method applied by Tapio (2005).

The results of the analysis indicate the presence of only two types of decoupling: strong and weak decoupling. In strong decoupling, both ΔCO_2 and $\Delta\text{CO}_2/\Delta\text{GDP}$ have negative values, while ΔGDP has a positive value. In weak decoupling, ΔCO_2 and ΔGDP have positive values, while $\Delta\text{CO}_2/\Delta\text{GDP}$ falls between 0 and 0.8. In other words, in strong decoupling, GDP has increased while CO₂ has decreased during the analysis period. In weak decoupling, both GDP and CO₂ have increased, but the rate of increase has not exceeded 0.8 (Table 3). Strong decoupling was observed in 8 regions: TR2 (West Marmara), TR3 (Aegean), TR5 (West Anatolia), TR8 (West Black Sea), TR9 (East Black Sea), TRA (Northeast Anatolia), TRB (Central Anatolia), TRC (Southeast Anatolia). Weak decoupling was observed in 4 regions: TR1 (Istanbul), TR4 (East Marmara), TR6 (Mediterranean), TR7 (Central Anatolia).

In the 8 regions with strong decoupling, the total GDP was 1,895,073,263 TL, and CO₂ emissions amounted to 3,847,458.81 tons. In the 4 regions with weak decoupling, the total GDP was 2,422,736,562 TL, and CO₂ emissions were 6,796,071.79 tons. These results indicate that the CO₂ emissions and GDP values in regions with weak decoupling are significantly higher than those in regions with strong decoupling, negatively impacting Türkiye's overall decoupling status.

An examination of the regions with weak decoupling reveals a concentration of industrial zones. It is estimated that the increased need for buildings driven by employment opportunities in these industrial zones has contributed to this outcome. The building use permit statistics in 2019 also support this finding, with 69,090,612 m² in regions with weak decoupling compared to 39,025,677 m² in regions with strong decoupling in 2019. The increased use of sustainable materials, such as low-carbon concrete, in the construction sector will contribute to reducing CO₂ emissions, thus helping to minimize

environmental degradation. As economic growth increases and environmental degradation decreases, strong decoupling can be achieved in all regions.

The results of this study reflect the situation of the construction sector's reinforced concrete building production before the Paris Agreement, in line with Sustainable Development Goal 8.4. The key constraint of this study is that the data from statistical regions specifically pertains to reinforced concrete buildings. Other types of structures, aside from reinforced concrete buildings, have not been included in this study. According to these results, decoupling has occurred in all regions, but in regions with weak decoupling, measures need to be taken. It also indicates that more work is needed in the construction sector to decouple economic growth from environmental degradation. In the future, analyses can be conducted for periods under the Paris Agreement, allowing for a comparison with the results of this study. This way, the construction sector's contribution to Sustainable Development Goal 8.4 can be determined.

V. REFERENCES

- [1] A. E. Alper, “İnşaat sektörünün ekonomik büyümedeki rolü: Türkiye örneği,” *Ç.Ü. Sosyal Bilimler Enstitüsü Dergisi*, c. 26, s. 2, ss 239-252, 2017,
- [2] E. Hoşkara and Y. Şey, “Ülkesel koşullar bağlamında sürdürülebilir yapım,” *itiüdergisi/a*, c. 7, s. 1, ss. 50-61, 2008.
- [3] Ş. Gökçe, O. Aytekin, H. Kuşan and I. Zorluer, “Türkiye’de mevzuatlar ve standartlar açısından Sürdürülebilir yapım,” *Uludağ Üniversitesi Mühendislik Fakültesi Dergisi*, c. 23, s. 3, 2018.
- [4] C. J. Kibert, “Establishing principles and a model for sustainable construction, University of Florida,” *Proceedings of the First International Conference on Sustainable Construction*, Florida, USA, 1994.
- [5] R. Akbıyıklı and S. Koç, “Charles Joseph Kibert' in sürdürülebilir kalkınma modeli ile günümüz inşaat sektörünün karşılaştırılması – Sakarya ili incelemesi,” *İleri Teknoloji Bilimleri Dergisi*, c. 5, s. 2, 2016.
- [6] L. Bourdeau and S. Nibel, “A European thematic network on construction and city related sustainability indicators,” The European Commission Community Research, Energy, Environment and Sustainable Development, France, Rap. Final, 2004.
- [7] M. W. Khan and Y. Ali, "Sustainable construction: Lessons learned from life cycle assessment (LCA) and life cycle cost analysis (LCCA)", *Construction Innovation*, vol. 20, no. 2, pp. 191-207, 2020.
- [8] S. Zhang, Z. Li, X. Ning and L. Li, “Gauging the Impacts of Urbanization on CO₂ Emissions from the Construction Industry: Evidence from China,” *Journal of Environmental Management*, vol. 28, 2021.
- [9] J. Chen, X. Song, J. You, “Structural paths of changes in CO₂ emissions in the Chinese construction industry,” *Journal of Environmental Planning and Management*, vol. 66, no 5, 1108–1126, 2022.
- [10] P. S. P. Wong, A. Owczarek, M. Murison, Z. Kefalianos and J. Spinozzi, “Driving construction contractors to adopt carbon reduction strategies: an Australian approach,” *Journal of Environmental Planning and Management*, vol. 57, no 10, pp. 1465–1483. 2014.

- [11] E. C. Mpakati-Gama, A. Brown and B. Sloan, “Embodied Energy and Carbon Analysis of Urban Residential Buildings in Malawi,” *International Journal of Construction Management*, vol. 16, no 1, pp. 1–12, 2016.
- [12] Y. Wu, K. Chau, W. Lu, L. Shen, C. Shuai and J. Chen, “Decoupling relationship between economic output and carbon emission in the Chinese construction industry,” *Environmental Impact Assessment Review*, vol. 71, pp. 60–69, 2018.
- [13] B. Z. Wang, Z. H. Zhu, E. Yang, Z. Chen and X. H. Wang, “Assessment and management of air emissions and environmental impacts from the construction industry,” *Journal of Environmental Planning and Management*, vol. 61, no 14, pp. 2421–2444, 2018.
- [14] P. Zhang, J. You, G. Jia, J. Chen and A. Yu, “Estimation of carbon efficiency decomposition in materials and potential material savings for China’s construction industry,” *Resources Policy*, Vol. 59 pp. 48–159, 2018.
- [15] M. Z. Tufan and C. Özel, “Sürdürülebilirlik kavramı ve yapı malzemeleri için sürdürülebilirlik kriterleri,” *Uluslararası Sürdürülebilir Mühendislik ve Teknoloji Dergisi*, vol. 2, no 1, pp. 9-13, 2018.
- [16] Intergovernmental Panel on Climate Change (IPCC), “Climate change 2022, mitigation of climate change-technical summary,” Cambridge University, New York, USA, 2022.
- [17] World Economic Forum (WEF), “Scaling low-carbon design and construction with concrete: enabling the path to net-zero for buildings and infrastructure,” WEF, Geneva, Switzerland, 2023.
- [18] Global Cement and Concrete Association (GCCA), “Concrete future–roadmap to net zero”, GCCA, London, UK, 2021.
- [19] İklim Değişikliği Başkanlığı. Paris Anlaşması [Çevrimiçi]. Erişim: <https://iklim.gov.tr/paris-anlasmasi-i-34>
- [20] M. Boran and B. Kayacan, “The economic impact of the Paris agreement on sectoral outputs in Türkiye: an input-output approach,” *İstanbul İktisat Dergisi- Istanbul Journal of Economics*, vol. 73, no 1, pp. 419-452, 2023.
- [21] A. Favier, C. De Wolf, K. Scrivener and G. A. Habert, “Sustainable future for the European cement and concrete industry-technology assessment for full decarbonisation of the industry by 2050”, ETH Zurich, Zürich, Switzerland, 2018.
- [22] T. Jackson, “Prosperity without growth? The transition to a sustainable economy, sustainable development commission,” London, UK, 2005.
- [23] Türkiye Cumhuriyeti Cumhurbaşkanlığı Strateji ve Bütçe Başkanlığı, “Sürdürülebilir kalkınma amaçları değerlendirme raporu,” Türkiye Cumhuriyeti Cumhurbaşkanlığı, Türkiye, Rap. 102, 2019.
- [24] S. Mudgal, M. Fischer-Kowalski, F. Krausmann, B. Chenot, S. Lockwood, A. Mitsios, A. Schaffartzik, N. Eisenmenger, F. Cachia, J. Steinberger, U. Weisz, K. Kotsalainen, H. Reisinger and E. Labouze, “Preparatory Study for the Review of the Thematic strategy on the Sustainable Use of Natural Resources,” Paris, France, Rap. Final, 2010.
- [25] M. Ucal, N. An and L. Kurnaz, “İklim değişikliği sürecinde ekonomideki yeni kavramlar ve yaklaşımlar,” *Dokuz Eylül Üniversitesi Sosyal Bilimler Enstitüsü Dergisi*, c. 19, s. 3, ss. 373-402, 2017.
- [26] P. Tapio, “Towards a theory of decoupling: degrees of decoupling in the EU and the case of road traffic in Finland between 1970 and 2001,” *Transport Policy*, vol. 12, no 2, pp. 137-151, 2005.

- [27] Q. Du, J. Zhou, Pan, T., Q. Sun and M. Wu, "Relationship of carbon emissions and economic growth in China's construction industry," *Journal of Cleaner Production*, vol. 220, pp. 99-109, 2019.
- [28] Y. Su, Z. Zou, X. Ma and J. Ji, "Understanding the relationships between the development of the construction sector, carbon emissions, and economic growth in China: Supply-chain level analysis based on the structural production layer difference approach," *Sustainable Production and Consumption*, vol. 29, pp. 730-743, 2022.
- [29] A. J. Ogungbile, G. Q. Shen, J. Xue and T. M. Alabi, "A hypothetical extraction method decomposition of intersectoral and interprovincial CO₂ emission linkages of China's construction industry," *Sustainability*, vol. 13, pp. 13917, 2021.
- [30] A. Ö. Artekin, "Türkiye'de inşaat sektörü, istihdam ve ekonomik büyüme arasındaki ilişkinin incelenmesi: GMM yaklaşımı," *Selçuk Üniversitesi Sosyal Bilimler Meslek Yüksekokulu Dergisi*, c. 26, s. 2, 2023.
- [31] E. Dobrucali, "Relationship between CO₂ emissions from concrete production and economic growth in 20 OECD countries," *Buildings*, vol. 14, no 9, 2024.
- [32] M. Yılmaz, S. Yıldız and A. B. Gültekin, "Yıkıcı yeniliklerin belirlenmesi: sürdürülebilir inşaat sektöründe tehditler ve fırsatlar," *Balıkesir Üniversitesi Fen Bilimleri Enstitüsü Dergisi*, c. 18, s 2, ss. 25-36, 2016.
- [33] O. O. A. Davies, "Barriers to implementation of sustainable construction techniques" *MAYFEB Journal of Environmental Science*, vol. 2, pp. 1-9, 2017.
- [34] R. Bon and K. Hutchinson, "Sustainable construction: some economic challenges," *Building Research & Information*, vol. 28, no. 5-6, pp. 310-314, 2000.
- [35] I. C. Osuizugbo, O. Oyeyipo, A. Lahanmi, A. Morakinyo and O. Olaniyi, "Barriers to the adoption of sustainable construction" *European Journal of Sustainable Development*, vol. 9, no 2, pp. 150-162, 2020.
- [36] Z. Wang, T. Hu and J. Liu, "Decoupling economic growth from construction waste generation: Comparative analysis between the EU and China," *Journal of Environmental Management*, vol. 353, 2024.
- [37] T.C. Sanayi ve Teknoloji Bakanlığı, Kalkınma Ajansları, [Çevrimiçi]. Erişim: <https://ka.gov.tr/sayfalar/kalkinma-lanlamasinda-istatistiki-bolge-birimleri-siniflandirmasi--24>
- [38] Türkiye İstatistik Kurumu (TUIK). [Çevrimiçi]. Erişim: <https://www.tuik.gov.tr/>.
- [39] L. Uğur, "Yapı maliyetinin yapay sinir ağı ile analizi," Doktora Tezi, Gazi Üniversitesi, Fen Bilimleri Enstitüsü, Ankara, Türkiye, 2007.
- [40] P. E. Mergos, "Seismic design of reinforced concrete frames for minimum embodied CO₂ emissions," *Energy and Buildings*, vol. 162, pp. 77-186, 2018.
- [41] G. F. de Medeiros and M. Kripka, "Optimization of reinforced concrete columns according to different environmental impact assessment parameters," *Engineering Structures*, vol. 59, pp. 185-194, 2014.
- [42] D. H. Yeo and F. A. Potra, "Sustainable design of reinforced concrete structures through CO₂ emission optimization," *Journal of Structural Engineering*, vol. 141, pp. 3, 2015.

- [43] Central Bank of the Republic of Türkiye. (2010, 31 December). Indicative Exchange Rates Announced at 15:30 on 12/31/2010 by the Central Bank of Turkey, no: 2010/247 [Çevrimiçi]. Erişim: <https://www.tcmb.gov.tr/kurlar/201012/31122010.xml>
- [44] Central Bank of the Republic of Türkiye. (2011, 30 December). Indicative Exchange Rates Announced at 15:30 on 12/30/2011 by the Central Bank of Turkey, no: 2011/251 [Çevrimiçi]. Erişim: <https://www.tcmb.gov.tr/kurlar/201112/30122011.xml>
- [45] Central Bank of the Republic of Türkiye. (2012, 31 December). Indicative Exchange Rates Announced at 15:30 on 12/31/2012 by the Central Bank of Turkey, no: 2012/252 [Çevrimiçi]. Erişim: <https://www.tcmb.gov.tr/kurlar/201212/31122012.xml>
- [46] Central Bank of the Republic of Türkiye. (2013, 31 December). Indicative Exchange Rates Announced at 15:30 on 12/31/2013 by the Central Bank of Turkey, no: 2013/247 [Çevrimiçi]. Erişim: <https://www.tcmb.gov.tr/kurlar/201312/31122013.xml>
- [47] Central Bank of the Republic of Türkiye. (2014, 31 December). Indicative Exchange Rates Announced at 15:30 on 12/31/2014 by the Central Bank of Turkey, no: 2014/249 [Çevrimiçi]. Erişim: <https://www.tcmb.gov.tr/kurlar/201412/31122014.xml>
- [48] Central Bank of the Republic of Türkiye. (2015, 31 December). Indicative Exchange Rates Announced at 15:30 on 12/31/2015 by the Central Bank of Turkey, no: 2015/250 [Çevrimiçi]. Erişim: <https://www.tcmb.gov.tr/kurlar/201512/31122015.xml>
- [49] Central Bank of the Republic of Türkiye. (2016, 30 December). Indicative Exchange Rates Announced at 15:30 on 12/30/2016 by the Central Bank of Turkey, no: 2016/249 [Çevrimiçi]. Erişim: <https://www.tcmb.gov.tr/kurlar/201612/30122016.xml>
- [50] Central Bank of the Republic of Türkiye. (2017, 29 December). Indicative Exchange Rates Announced at 15:30 on 12/29/2017 by the Central Bank of Turkey, no: 2017/252 [Çevrimiçi]. Erişim: <https://www.tcmb.gov.tr/kurlar/201712/29122017.xml>
- [51] Central Bank of the Republic of Türkiye. (2018, 31 December). Indicative Exchange Rates Announced at 15:30 on 12/31/2018 by the Central Bank of Turkey, no: 2018/249 [Çevrimiçi]. Erişim: <https://www.tcmb.gov.tr/kurlar/201812/31122018.xml>
- [52] Central Bank of the Republic of Türkiye. (2019, 31 December). Indicative Exchange Rates Announced at 15:30 on 12/31/2019 by the Central Bank of Turkey, no: 2019/247 [Çevrimiçi]. Erişim: <https://www.tcmb.gov.tr/kurlar/201912/31122019.xml>
- [53] A. Naqvi and K. Zwickl, “Fifty shades of green: Revisiting decoupling by economic sectors and air pollutants,” *Ecol. Econ.*, vol. 133, pp. 111–126, 2017.
- [54] C. Cautisanu and M. A. Hatmanu, “Study of the decoupling of economic growth from CO₂ and HFCs Emissions in the EU27 Countries,” *Energies*, vol. 16, no.14, 2023.



Düzce University Journal of Science & Technology

Research Article

Evaluation of the Contribution of Model Factories to Productivity with Multi-Criteria Decision Making Method: Application of Learn & Transform Program

 Ali SEVİNÇ^a*

^a KOSGEB Ankara Sincan Müdürlüğü, Ankara, TÜRKİYE

*Corresponding author's e-mail address: ali.sevinc@kosgeb.gov.tr

DOI: 10.29130/dubited.1628405

ABSTRACT

Model factory offers a wide range of training and consultancy services, including experiential learning techniques on continuous improvement, lean production, and digital transformation for businesses in the manufacturing sector. The Industry 4.0 approach guides the design of these applied trainings and consultancy services, which aim to significantly boost enterprises' productivity levels. Ten provinces in Türkiye have established model factories since 2015. One of them is the Ankara Chamber of Industry (ACI) model factory. The aim of this study is to examine the benefits of the companies participating in Learn & Transform Program of the ACI model factory. To evaluate the benefit of the companies participating in the Learn & Transform Program, the number of employees, the production increase rate as a result of the Learn & Transform Program, and the return on investment periods were examined using the WASPAS method. I ranked the participating companies in the program from the highest benefit to the lowest. According to this ranking, F12 was the firm that provided the highest benefit, F2 ranked second, and F6 ranked third. The first-ranked company was determined to be the one that participated in the Learn & Transform Program, and provided the highest benefit among these companies. The last ranked firm, F18, was considered to be the least benefited firm. This analysis gives the model factory managers, experts, and business managers the opportunity to evaluate the Learn & Transform Program.

Keywords: WASPAS method, Multi-Criteria decision making, Model factory, Learn & Transform program

Model Fabrikaların Verimliliğe Katkısının Çok Kriterli Karar Verme Yöntemi ile Değerlendirilmesi: Öğren-Dönüş Programı Uygulaması

ÖZ

Model Fabrikalar, üretim sektöründeki işletmeler için sürekli iyileştirme, yalın üretim ve dijital dönüşüm konularında deneyimsel öğrenme tekniklerini içeren geniş kapsamlı eğitim ve danışmanlık hizmetleri sunmaktadır. Bu uygulamalı eğitimler ve danışmanlık hizmetleri, Endüstri 4.0 yaklaşımına uygun olarak tasarlanmış olup, işletmelerin verimlilik düzeylerini önemli ölçüde artırmayı hedeflemektedir. Türkiye’de 2015 yılından itibaren on ilde model fabrika kurulmuştur. Bunlardan biri Ankara Sanayi Odası (ASO) model fabrikadır. Bu çalışmanın amacı, Ankara Sanayi Odası (ASO) model fabrika Öğren-Dönüş programına katılan firmaların programdan elde ettikleri fayda durumunu incelemektir. Öğren-Dönüş programına katılan işletmelerin programdan fayda durumunu değerlendirmek amacıyla, çalışan sayısı, Öğren-Dönüş programı sonucundaki üretim artış oranı ve yatırımın geri dönüş süreleri WASPAS yöntemi kullanılarak incelenmiştir. Programa katılan firmalar arasında en yüksek faydayı

sağlayan firmadan en düşüğe doğru bir sıralama yapılmıştır. Bu sıralamaya göre en yüksek fayda sağlayan F12 firması, ikinci sırada F2 ve üçüncü sırada F6 firması yer almıştır. Birinci sıradaki firma, Öğren-Dönüş programına katılan ve bu firmalar arasında en fazla fayda sağlayan firma olarak belirlenmiştir. Son sıradaki firma ise F18 nolu firma, en az fayda gören firma olarak olduğu değerlendirilmiştir. Bu analiz, model fabrika yönetici, uzmanlarına ve işletme yöneticilerine Öğren-Dönüş programı hakkında değerlendirme yapma imkânı vermektedir.

Anahtar Kelimeler: WASPAS yöntemi, Çok kriterli karar verme, Model fabrika, Öğren-Dönüş programı

I. INTRODUCTION

Model factory is a simulation-based learning tool developed specifically for the industry. It allows company employees to gain new competencies in various areas, from lean production to digital technologies. Participants embark on a transformational learning journey through model factory and have an interactive and practical learning experience. In this way, model factory provide knowledge and competence in transforming this knowledge into practice, making learning outcomes tangible and valuable. The target audience of model factory includes for-profit companies and organizations as well as non-profit organizations. By interacting with the simulation-based learning tool, these organizations learn more effectively how to use the techniques in their daily practice routines. This allows the organization to focus on continuous improvement and success [1], [2], [3], [4], [5].

Model factory offers applied training and consultancy services to enterprises in Türkiye's manufacturing sector to boost productivity in production through Learn & Transform Program. Businesses can achieve their strategic goals with the help of these training and consultancy services. Guidance on critical issues such as productivity improvement, cost optimization, and quality control contributes to a more competitive position. In addition, Model Factories' sustainability-focused approach supports businesses in taking strategic steps to reduce their environmental impact and fulfill their social responsibilities. This strategy ensures not only short-term but also long-term success. The Learn & Transform Program and consultancy services offered by Model Factories significantly strengthen Turkish manufacturing businesses and build a sustainable and competitive future [6], [7].

In Türkiye, model factories are established under the leadership of the Ministry of Industry and Technology. These institutions provide practical training and consultancy services for a certain period of time within the scope of the Learn & Transform Program. Businesses participating in the program in the manufacturing sector aim to increase their productivity levels. Under the leadership of training coaches, enterprises evaluate their situation before and after participating in the program and determine the increase in production productivity. Model factory management records the productivity increase and return on investment periods for the enterprises [6], [7]. But there is no scientific analysis of the productivity increase and return on investment for the companies in the Learn & Transform Program, nor is there a tool to compare their utilization status. In addition, there is no study in the literature that compares the benefits of the program to the enterprises participating in the Learn & Transform Program.

The purpose of this study is to show that model factory managers, experts, and business officials have information about the benefits of the Learn & Transform Program for their businesses. But no tool can compare the benefits of this program to those of the Learn & Transform Program 's companies. The objective of this research is also to examine the benefits of the program for the companies participating in the Ankara Chamber of Industry (ACI) model factory, the Learn & Transform Program. In this context, It is used the WASPAS method to examine the number of employees, the production increase rate resulting from the Learn & Transform Program, and the return on investment periods. I ranked the participating companies in the program from the most beneficial to the least beneficial. With this analysis, it will be possible to compare the benefits of the companies participating in the Learn & Transform Program. Thus, It can be evaluated the top-ranked companies that derive sufficient benefits from the program and those that do not. This information can provide feedback on the Learn & Transform Program for model factory managers and experts.

II. LITERATURE

The problems of selecting a flexible production system, a machine in a flexible production cell, an automatic guided vehicle, an automatic control system, and an industrial robot were determined by the WASPAS method. It was determined that the method gave acceptable results [8]. The performance of the companies in the automotive sector traded in Borsa Istanbul was ranked by us using the MAUT (Multi-Attribute Utility Theory) and SAW (Simple Additive Weighting) methods. According to both methods, the same firms are ranked in the first three places [9]. In this study, a model factory was established to disseminate additive manufacturing technologies to be used in the production of mechatronic products in the industry. It enabled the participants to increase their knowledge of innovative production technologies and accelerate their industrial transformation [10]. The performances of banks were analyzed with the WASPAS method [11]. The quality of life of European Union countries was evaluated with ENTROPY, ARAS, and MOOSRA methods. It was determined that the most important criterion for quality of life is pollution. It was determined that Finland is the best country in terms of quality of life [12]. This study presents a transformation model encompassing value creation, value chain development, information and communication technology infrastructure enhancement, and the integration of cyber-physical systems to assist the shift. Industry 4.0 at EAFIT University aims to reform production engineering methodologies through the implementation of the learning factory idea inside engineering education [13]. The methodical design of a maturity model was resented for its purpose of evaluating the design and ongoing development of learning factories, as well as assessing the model's applicability in such environments [14]. In their study, they aim to design a teaching factory for engineering students based on the requirements expected by the industry. A model factory design suitable for developing the needs and abilities of mechanical engineering students was obtained [15]. The study employed ENTROPY and EDAS methods to analyze the performance of logistics companies. It was determined to be the "Mars" company with the best performance [16]. Designed and implemented a model factory in a public university in Brazil to ensure the implementation and dissemination of Industry 4.0 technologies. The model factory was designed and successfully implemented [17]. To facilitate the adoption of Industry 4.0, automation, and lean manufacturing technologies by small and medium-sized enterprises (SMEs), It is introduced a learning factory concept known as IdeaLab. This Lab offers a learning factory concept to provide solutions to the problems faced by SMEs [18]. The financial performance of logistics companies in the Fortune 500 list was evaluated. The study determined that exports significantly influenced the performance of logistics companies between 2015 and 2019 [19]. This study elucidates the design and implementation process of a learning factory aimed at facilitating Industry 4.0 training for students in Croatia. The factory commenced operations in 2022, promoting awareness of Industry 4.0 and the implementation of these technologies in Croatia [20]. Logistics performance of OECD member countries was analyzed with the ENTROPY and WASPAS methods. According to the ranking results, the top five countries are Germany, Sweden, Denmark, the Netherlands, and Austria [21]. The performance of the Serbian economy was analyzed according to the MEREC-WASPAS method. According to the WASPAS method, the Serbian economy showed the best performance in 2012 [22].

III. CONCEPTUAL FRAMEWORK

A. FUNCTION OF THE MODEL FACTORY

The first, second, and third industrial revolutions in the evolution of industrial revolutions symbolize the industrial transformation processes in which energy resources diversified and automation developed. The Third Industrial Revolution brought automation with the integration of information and communication technologies into production processes, paving the way for smart systems and robotic technologies, and Industry 4.0, which emerged after this evolution, aims to transform traditional machines into a learning structure, optimizing performance and maintenance management with environmental interaction. Industry 4.0 represents an industrial revolution that interacts with its environment by minimizing human intervention through the integration of smart production systems

and information technologies [23], [24], [25]. In these processes, each stage of the developments in the industry is referred to as a revolution. Model factories provide training and consultancy services that include theory and practice to achieve the goal of Industry 4.0 and its competitive advantage.

The Model Factory concept aims to adapt quickly to customer demands and offer flexible capacity. This structure makes it possible to set up new production lines around the world and increase capacity with minimal effort. This model accelerates the company's production processes and provides flexible capacity by working according to different customer requests and expectations, using the standard line setup while customizing the customers' product. Model factory aim to provide hands-on training for field workers, balance between efficiency and flexibility, and be responsive to local demands and the supply chain network [26].

Model factories adopt active learning methods, aiming to give participants experience in industrial projects. They simulate various Industry 4.0 application scenarios for use in education, research, and training and provide a learning environment that includes real-world experiences through modules such as "Inspection/Creation" and "Production Control." This learning model aims to increase collaboration between industry, academia, and professionals by promoting the adoption of Industry 4.0. However, especially in less developed countries, the importance of model factory is evident in efforts to overcome challenges such as the slow pace of technological progress, high costs, and lack of employee access to new technologies [13], [27], [17], [20]. These challenges can limit the implementation of Industry 4.0, making it difficult to keep pace with technological development. However, adopting various strategies to overcome them, such as international collaborations and resource sharing, can help these countries transition to Industry 4.0 more effectively.

Model factory, a concept that supports hands-on learning, aim to bridge the skills gap between industry needs and the theoretical knowledge provided in schools. This concept combines innovative learning technologies and effective practices to align student competencies with the needs of the industrial world. Model factory, based on the concept of digitalization, include free-designed virtual systems and virtual replicas of physical systems. This concept aims to offer an ever-expanding learning environment and enhance the personal learning experience by using realistic and modifiable production processes. It offers participants task-oriented learning opportunities, such as analyzing and optimizing processes. Covering various topics such as Industry 4.0, manufacturing efficiency, and sustainability, specialized learning factories have become common among industries and universities for practical training [15], [14], [28], [29], [18].

Model factories are clearly differentiated from other teaching and learning formats by providing the ability to effectively use realistic and modifiable production processes. Its main function is to offer different learning methods, such as analyzing and optimizing production systems through realistic simulations [2]. Model factories help participants gain practical skills beyond theoretical knowledge by allowing them to experience real industry practices [31].

People around the world understand the importance and benefits of model factory. In Türkiye, studies on model factory designs have begun, and efforts are underway to make them widespread. Model factories have been established in different cities, especially ACI, to contribute to manufacturers' productivity. It is observed that Model Factories have been established in Adana, Ankara, Bursa, Eskişehir, Gaziantep, İzmir, Kayseri, Konya, Mersin, and Samsun. Model Factories in Türkiye are established to enhance industrial efficiency and innovation [6].

The first model factory studies were initiated in 2015 under the coordination of the Ministry of Industry and Technology, and a total of 10 model factories were established and put into operation in Adana, Ankara, Bursa, Gaziantep, Izmir, Kayseri, Konya, Eskişehir, Samsun, and Mersin provinces through national and international funds. Model factories provide training and consultancy on lean production by guiding the transformation processes of enterprises and continue to develop infrastructure and human resources within the scope of Learn & Transform Program so that they can operate in the field of digital transformation [6].

A.1. Target Audience of the Ankara Chamber of Industry Model Factory

The ACI model factory appeals to companies in many different sectors operating in the manufacturing industry and producing various products and technologies. Machinery manufacturing companies, companies in the food sector, and companies in the textile sector are among the target audience of the model factory. There is no distinction between companies producing low- and high-technology products [7].

Model factory experts identify the productivity-related problems of the companies that apply for service. They provide applied training and consultancy services to companies in groups for three to four months. During this period, solutions are produced to the problems identified about productivity. At the end of the study, companies have a productivity report card. Each company participating in the Learn & Transform Program can prepare a road map for itself [7].

A.2. Fields of Activity of the Companies Included in the Study

The companies in this study are involved in the production of buildings, highways, tunnels, streets, recreation and sports areas lighting, plastic parts design, injection, grouping, mold production, paint, primer, coating, varnish, insulation materials, construction chemicals, buildings, shopping malls, stores, hospitals, schools, highways, street lighting, automatic doors, cabins and complete elevator systems, enamel coated hot water storage tanks, air and sediment separators, balance tanks and apartment entrance stations, porcelain insulator production, power plant infrastructure projects, structural steel manufacturing and assembly for skyscrapers and industrial buildings, earthquake isolation devices, compound feed production, microfiber cloth production, women's underwear and outerwear, medium voltage electrical equipment, home and office furniture, urban furniture, Tactical mini UAV systems, chocolate, cream, paste production, industrial kitchen equipment manufacturing.

A.3. Model Factory Activities and Learn & Transform Program

The ACI Model Factory offers an approach model that allows companies to make mistakes on actual production lines with learn-and-transform programs. These programs include theoretical teaching of "Lean Production" principles and methods, as well as workshops that provide participants with experience. Learn & Transform Program aim to train companies' own lean leaders. This approach demonstrates that businesses can implement scalable lean applications that yield cost-effective results within a short timeframe and budget. Learn & Transform Program: These programs include theoretical training, group workshops, and field coaching to train lean leaders. This program aim to reduce costs, increase productivity, and improve competitiveness. The program consists of sequential "Learn" and "Transform" themes. In the "Learn" phase, participants receive experiential training in the Model Factory, while in the "Transform" phase, they apply what they have learned in their own production sites, accompanied by field coaches [7].

The Learn & Transform Program forms the basis of model factory activities and aims to provide permanent competence to enterprises. In the learning phases of the program, participants are taught lean management theory and make their first applications in the model factory. One of the most essential activities of the program is the applications that the participants will carry out in their own companies. To achieve the targeted outputs, Model Factory trainers conduct transformation visits to the selected companies and implement lean transformation in the pilot area determined in the enterprise [6].

Within the scope of the Learn & Transform Program, in each period, a joint working group is formed with project leaders of two and four people for four months, with 4-8 enterprises coming together. These groups receive theoretical and practical training in 4 main sessions under diagnosis, design, implementation, and sustainability for 12 days. After each session, the methods they have learned and experienced in the model factory are repeated for 3 weeks in a pilot area selected in their enterprises [6], [7].

A.4. Participant Profile and Learn & Transform Program

Senior executives such as the chairman of the board of directors, members of the board of directors, factory managers, production managers, and new-generation management candidates can participate in the Learn & Transform Program. In addition, employees who have a good command of the work done in the pilot area, who are willing to participate in the program, who are open to innovations, who do not have a planned leave, and who can participate in training and coaching full-time can be included in the program. Firms from different sectors can also participate in the program [7].

B. METHOD

In this study, the ENTROPY method, a multi-criteria decision-making (MCDM) method, was used for weighting. The analysis used the WASPAS method, an MCDM method that takes benefits and costs into account.

B.1. ENTROPY Method

Claude E. Shannon developed the entropy method in 1948 within the context of information theory. It has been used in many fields of science and engineering, especially in problem-solving. It is used to solve problems to eliminate uncertainty. CRM prefers the entropy method because it makes mathematical calculations, is easy to understand, and doesn't require decision-making expertise. It is used the ENTROPY method, an objective weighting method, to determine the weights of the criteria in the analysis [32]. The ACI model factory provided the data for this study. We preferred the ENTROPY method in the weighting process due to the objective nature of the data.

The entropy method consists of five process steps [11], [21], [32] [38].

B.1.1. Creation of Decision Matrix

Entropy management creates a decision (D) matrix with the values of the priority criteria based on weighted alternatives.

In the decision matrix, m is the number of alternatives, n is the number of criteria, and is the value of the j criteria of alternative i .

$$D = \begin{matrix} & \begin{matrix} x_{11} & x_{12} & \dots & x_{1n} \\ x_{21} & x_{22} & \dots & x_{2n} \\ \dots & \dots & \dots & \dots \\ x_{i1} & x_{i2} & \dots & x_{in} \\ \dots & \dots & \dots & \dots \\ x_{m1} & x_{m2} & \dots & x_{mn} \end{matrix} \\ \begin{matrix} \\ \\ \\ \\ \\ \end{matrix} & \end{matrix} \quad (1)$$

B.1.2 Constructing the Normalized Decision Matrix

In order to eliminate the effects of different index dimensions in the decision matrix on incommensurability, the indices can be standardized by various methods. According to the benefit and cost indices, the criteria are normalized using Equation (2) and Equation (3).

$$r_{ij} = x_{ij} \frac{1}{\max_{ij}} \quad (i=1, \dots, m; j=1, \dots, n) \quad (2)$$

$$r_{ij} = x_{ij} \frac{1}{\min_{ij}} \quad (i=1, \dots, m; j=1, \dots, n) \quad (3)$$

Different units of measurement normalization to eliminate anomalies P_{ij} is calculated. with Equation (4).

$$p_{ij} = \frac{x_{ij}}{\sum_{i=1}^m x_{ij}}, \quad \forall i, j \quad (4)$$

B.1.3. Finding Entropy Values for Criteria

Entropy value of the criteria (E_j) is calculated by Equation (5).

$$E_j = -\sum_{i=1}^m p_{ij} \ln p_{ij}, \quad \forall j \quad (5)$$

B.1.4. Calculation Of The Degree Of Differentiation Of Knowledge

In this step, high values of the degree of differentiation of information (d_j) indicate that the distance or differentiation between alternative results regarding the criteria is high.

$$d_j = 1 - E_j, \quad \forall j \quad (6)$$

B.1.5. Calculation of Criterion Weights

In this step, if the decision maker prefers one criterion over the other, the best-expected weight value is calculated using Equation (7)

$$w_j = \frac{d_j}{\sum_{j=1}^n d_j} \quad (7)$$

The value w_j in the equation expresses the weight values, which are indicators of the importance levels of the criteria. The entropy probability value is 1. (Equation 8)

$$w_1 + w_2 + \dots + w_n = 1 \quad (8)$$

Despite its restricted application in the entropy technique, subjective weights can be derived using Equation (9), considering the weights acquired from Equation (8) and the decision maker's a priori context.

In this step, λ_j refers to the decision maker's relevant prior.

$$w_j^0 = \frac{\lambda_j w_j}{\sum_{j=1}^n \lambda_j w_j} \quad (9)$$

B.2. The WASPAS Method

The WASPAS method is a Multi-Criteria Decision Making (MCDM) approach developed by Chakraborty and Zavadskas (2014). This method combines the results of the "Weighted Sum Model" and "Weighted Multiplication Model." It uses the value of the combined optimality criterion calculated based on the results of these two models to determine the ranking of the alternatives. The WASPAS method can perform sensitivity analysis within its own functioning. This serves the purpose of checking the consistency in alternative rankings [33], [34], [35], [36], [37], [38]. Therefore, it can help decision-makers make more informed and reliable choices among alternatives.

In this study, the WASPAS method aims to rank the companies, facilitating performance comparison by evaluating the productivity increase resulting from the applied training and consultancy services received from the model factory. The WASPAS method ranks the companies based on the outcomes of the weighted multiplication method and the weighted sum method. Since the number of employees of the enterprises in the data obtained from the model factory is the cost, production increase, and return on investment benefit, this method was chosen because this method takes these two issues into account.

B.2.1. Defining the Problem

The Problem starts with the following decision matrix: It is determined that the alternatives and criteria in advance. The criteria are determined using information obtained from various sources such as historical data, expert opinions, and literature reviews, and the alternatives to be evaluated are decided. It is constructed the matrix using Equation (10).

$$X = \begin{matrix} & \begin{matrix} x_{11} & x_{12} & \dots & x_{1n} \end{matrix} \\ \begin{matrix} x_{21} \\ \vdots \\ \vdots \\ \vdots \\ x_{m1} \end{matrix} & \begin{matrix} x_{22} \\ \vdots \\ \vdots \\ \vdots \\ x_{m2} \end{matrix} & \begin{matrix} \dots \\ \vdots \\ \vdots \\ \vdots \\ \dots \end{matrix} & \begin{matrix} x_{2n} \\ \vdots \\ \vdots \\ \vdots \\ x_{mn} \end{matrix} \end{matrix} \quad (10)$$

In this framework, m represents the number of alternative candidates, while n is the number of evaluation criteria. x_{mn} denotes the performance of alternative m concerning criterion n .

B.2.2. Decision Matrix Normalisation

Normalization is used to eliminate the effect of unit differences in criterion values. Therefore, It is applied normalization based on whether each criterion in the decision matrix is benefit- or cost-oriented. If the criterion is benefit-based, the formula of Equation (11) comes into play. This formula aims to correct for differences in the range of values in the units of the criteria, making the decision matrix more consistent.

$$\text{For benefit-based: } \bar{x}_{ij} = \frac{x_{ij}}{\max_i x_{ij}} \quad (11)$$

For non- benefit-based criteria, normalization is performed using Equation (12).

$$\bar{x}_{ij} = \frac{\min_i x_{ij}}{x_{ij}} \quad (12)$$

Equation (11) and Equation (12) result in a normalized decision matrix. Equation (13) performs an additional operation on this matrix.

$$X = \begin{matrix} & \begin{matrix} \bar{x}_{11} & \bar{x}_{12} & \dots & \bar{x}_{1n} \end{matrix} \\ \begin{matrix} \bar{x}_{21} \\ \vdots \\ \vdots \\ \vdots \\ \bar{x}_{m1} \end{matrix} & \begin{matrix} \bar{x}_{22} \\ \vdots \\ \vdots \\ \vdots \\ \bar{x}_{m2} \end{matrix} & \begin{matrix} \dots \\ \vdots \\ \vdots \\ \vdots \\ \dots \end{matrix} & \begin{matrix} \bar{x}_{2n} \\ \vdots \\ \vdots \\ \vdots \\ \bar{x}_{mn} \end{matrix} \end{matrix} \quad i = 0,1,2, \dots, m \text{ ve } j: 1,2, \dots, n \quad (13)$$

B.2.3. Evaluation by Weighted Sum Method

According to the weighted sum method, the score of each alternative i is calculated using Equation (14). In this equation, w_j represents the weight value of the criterion and $Q^{(1)}$, i is the evaluation score of the alternative.

$$Q_i^{(1)} = \prod_{j=1}^n \bar{x}_{ij} w_j \quad (14)$$

B.2.4. Evaluation by the weighted Multiplication method

According to the weighted multiplication method, the total relative importance of the alternative is calculated using Equation (15). $Q_i^{(2)}$ refers to the evaluation score of alternatives based on the weighted multiplication method.

$$Q_i^{(2)} = \prod_{j=1}^n (\bar{x}_{ij})^{w_j} \quad (15)$$

B.2.5. Integration of Weighted Sum and Multiplication Results

The scores obtained by weighted sum and weighted multiplication methods are integrated to form a single value to facilitate decision making. The weighted common criterion value of alternative i is expressed as $Q(i)$ and is calculated using Equation (16).

$$Q_i = 0.5Q_i^{(1)} + 0.5Q_i^{(2)} = 0.5 \sum_{j=1}^n \bar{x}_{ij} w_j + 0.5 \prod_{j=1}^n (\bar{x}_{ij})^{w_j} \quad (16)$$

The model based on the assumption that the results obtained from the weighted sum and multiplication methods are of equal importance is expressed by Equation (17). However, this assumption is replaced by a generalized weighted common criterion score formula that expresses the importance of the weighted sum model in terms of λ . Here, λ can take values between 0 and 1.

$$Q_i = \lambda Q_i^{(1)} + (1 - \lambda) Q_i^{(2)} = \lambda \sum_{j=1}^n \bar{x}_{ij} w_j + (1 - \lambda) \prod_{j=1}^n (\bar{x}_{ij})^{w_j} \quad (17)$$

As the value of λ approaches 0, the method becomes more similar to the weighted multiplication model, while as it approaches 1, it becomes the weighted sum method.

B.2.6. Selection

The weighted common criterion score ranks the alternatives from high to low. The alternative with the highest score is the best. According to this score ranking, the order of alternatives is determined. In the implementation phase, the WASPAS method will analyze 19 companies in the Learn & Transform Program from the model factory based on the production increase rate as a percentage, the return on investment period, and the number of employees.

IV. RESULTS

The data were obtained from the Model Factory web page for 19 manufacturing companies participating in the Model Factory, Learn & Transform Program of the ACI. Three variables were used. The number of employees variable is the total number of blue and white-collar employees in each firm. The criterion for the increase in the amount of production expresses the increase in production as a percentage after the end of the Learn & Transform Program in the firm. The other benefit to the firm is the return on investment period, which is the number of days that the cost incurred by the firm for the Learn & Transform Program returns to the firm as profit. The total number of blue and white-collar employees is a cost-side criterion. The rate of increase in production and the return on investment are given in days. Two criteria are benefit-oriented.

The managers and experts of the model factory analyze the productivity problems of the companies applying to the Learn & Transform Program and determine the current situation. They analyze the issues that cause productivity problems: idle resources in terms of raw materials, equipment, and time spent in the company; inefficient situations related to labor; machinery and equipment problems; raw materials; product scraps and wastes, machine programming times, idle situations in production capacity, and cycle times of equipment. They prepare a report that determines the productivity status for each company. Work is carried out to solve the problems in the report. In the Learn & Transform Program company employees who participate in the training by providing with practical training work to produce solutions to company productivity problems. By providing solutions to the problems of the companies, many gains, such as increased labor productivity, increased capacity, reduction in the rates of poor-quality products, waste, and scrap products, reduction in additional shifts and savings in shift production, acquisition of new areas of use, savings in production time, and shortening product transportation times within the factory, are provided. Since these gains cause an increase in productivity in the company and are reflected in the increase in product production, they are calculated as “increase in production quantity.” Therefore, “productivity increase in production” represents a large number of variables. Therefore, the number of benefit-side criteria was limited. The number of employees was available as a cost-side criterion.

Table 1. Model Factory Decision Matrix of the Results of the Companies Participating in the Learn & Transform Program

Firms	Firms Number of Employees	Increase in Production Amount (%)	Return on investment (Days)
F1	250	124	14
F2	60	150	180
F3	40	83	90
F4	140	33	30
F5	250	47	180
F6	48	310	48
F7	175	200	10
F8	273	56	30
F9	603	10	45
F10	37	15,5	51
F11	60	15	30
F12	30	230	141
F13	273	14	120
F14	200	40	7,5
F15	450	211	11
F16	165	50	150
F17	78	400	8
F18	848	115	3
F19	182	162	36

The study uses data from firms named F1 to F19. All of these firms are in the manufacturing sector and produce in different fields. Firms produce office furniture, power plants, earthquake insulation materials, textiles, microfiber cloth, feed, electrical equipment, and security equipment. There are also companies in the ceramic, casting, chemical, and lighting sectors. Matrix of the results of the model factory participating in the Learn & Transform Program was created and given in Table 1.

Table 2. *Weighting of Criteria by ENTROPY Method*

Firms Number of Employees	Increase in Production Amount (%)	Return on investment (Days)
0,3135	0,3225	0,3640

The ENTROPY method calculated every step of the table's criteria and carried out the weighting process. ENTROPY weighting scores are presented in Table 2. The weighting sum of each criterion is equal to 1. I preferred the ENTROPY method because it is objective.

Table 3. *Decision Matrix Normalisation*

Firms	Firms Number of Employees	Increase in Production Amount (%)	Return on investment (Days)
F1	0,120	0,310	0,078
F2	0,500	0,375	1,000
F3	0,750	0,208	0,500
F4	0,214	0,083	0,167
F5	0,120	0,118	1,000
F6	0,625	0,775	0,267
F7	0,171	0,500	0,056
F8	0,110	0,140	0,167
F9	0,050	0,025	0,250
F10	0,811	0,039	0,283
F11	0,500	0,038	0,167
F12	1,000	0,575	0,783
F13	0,110	0,035	0,667
F14	0,150	0,100	0,042
F15	0,067	0,528	0,061
F16	0,182	0,125	0,833
F17	0,385	1,000	0,044
F18	0,035	0,288	0,017
F19	0,165	0,405	0,200

Table 4. *Evaluation of the Companies Participating in the Learn & Transform Program by Weighted Sum Method and Weighted Multiplication Method*

Firms	Ranking of Alternatives according to WSM	Ranking of Alternatives according to WPM
F1	0,166	0,326
F2	0,642	0,586
F3	0,484	0,428

Table 4. (continued) *Evaluation of the Companies Participating in the Learn & Transform Program by Weighted Sum Method and Weighted Multiplication Method*

F4	0,154	0,144
F5	0,440	0,258
F6	0,543	0,491
F7	0,235	0,161
F8	0,140	0,138
F9	0,115	0,072
F10	0,370	0,207
F11	0,230	0,145
F12	0,784	0,765
F13	0,288	0,146
F14	0,094	0,083
F15	0,213	0,126
F16	0,401	0,280
F17	0,459	0,239
F18	0,110	0,053
F19	0,255	0,236

The weighted sum and weighted multiplication determined the combined optimal value. Therefore, weights were determined by integrating the weighted values. I applied weightings based on WSM and WPM. It is presented in Table 4.

Table 5. *Integration of Weighted Sum Method and Weighted Multiplication Method Results and Ranking According to WASPAS Method*

Firms	Weights of Alternatives	Ranking of Alternatives
F12	0,775	1
F2	0,614	2
F6	0,517	3
F3	0,456	4
F17	0,349	5
F5	0,349	6
F16	0,341	7
F10	0,289	8
F1	0,246	9
F19	0,246	9
F13	0,217	10
F7	0,198	11
F11	0,187	11
F15	0,170	13

Table 5. (continued) *Integration of Weighted Sum Method and Weighted Multiplication Method Results and Ranking According to WASPAS Method*

F4	0,149	14
F8	0,139	15
F9	0,093	16
F14	0,089	17
F18	0,081	18

The level of importance was set at $\lambda=0.50$ in calculating the firms' score values based on the integrated weighted values. The combined optimum value was determined. The alternatives are ranked according to these values and given in Table 5. This ranking determined F12 as the firm with the highest efficiency score. F2 and F6 were ranked second and third, respectively. Company F3 ranked fourth, and company F17 ranked fifth. The first-ranked company was determined to be the company that benefited the most from the Learn & Transform Program, while the company that benefited the least was F18. It allows for a comparison between the companies that benefit the most and the companies that benefit the least from the Learn & Transform Program.

V. DISCUSSION

Restructuring manufacturing engineering practices with the learning factory concept in the context of engineering education [13]. Development of a maturity model for the design and continuous improvement of learning factories [14]. Design of a teaching factory for engineering students based on industry-expected requirements [15]. Designing and implementing a model factory in a public university in Brazil [17]. A learning factory called IdeaLab to enable small and medium-sized enterprises (SMEs) to adopt Industry 4.0, automation, and lean manufacturing technologies [18]. In Croatia, there are studies involving the design and establishment of a learning factory to facilitate Industry 4.0 training for students [20]. Generally, these studies focus on the design of model factories. The concept of model factories is new in Türkiye. There are no studies on model factories and their services in the Turkish literature. Furthermore, a study evaluating the services of model factories for firms in the international literature faces limitations. It may be a start for further academic studies on model factories and the program they offer in Türkiye. I used the ENTROPY method for the weighting process in this study. I conducted the analysis using the WASPAS method. The analysis was conducted starting from the company that provides the most benefit from the Learn & Transform Program to the company that provides the least.

VI. CONCLUSION

Model factories in Türkiye aim to increase the efficiency of businesses in production through the Learn & Transform Program. The programs provide participants with the opportunity to practice the key principles of Industry 4.0 through experiential trainings and then apply these gains in their businesses. The results of the Learn & Transform Program point to significant increases in the productivity levels of companies in a variety of sectors. Model factory Learn & Transform Program offer an effective way for businesses to improve their performance in critical areas such as sustainability, productivity, and competitiveness. By providing participants with experience in real production environments and the opportunity to apply theoretical knowledge in practice, Learn & Transform Program contribute to the transformation of Turkish businesses in line with Industry 4.0 principles.

The WASPAS method ranks the alternatives based on weighted values. It can be determined the rank of each alternative. This method allows comparison between alternatives. If a choice is desired, it can

be made with the WASPAS method. The ENTROPY method performs the weighting of objective data. These methods were found to be suitable for this study.

Within the scope of this study, using the WASPAS method, the production increase rate, return on investment period, and number of employees of 19 companies participating in the ACI model factory Learn & Transform Program was analyzed, and weights were revealed. Weights were ranked. According to this ranking, F12 was identified as the firm with the highest benefit. F6 ranked second, and F17 ranked third. The company in the first place was determined to be the company that benefited the most from the Learn & Transform Program among the companies, while the company that benefited the least was the company coded F9.

The ranking process of the results obtained by the firms from the Learn & Transform Program was evaluated as the ranking of the benefits obtained by the firms from this program. In other words, the top-ranked firm was considered the most beneficial, while the last-ranked firm was considered the least beneficial. The ranking of the outputs obtained by the firms from the Learn & Transform Program was made from the highest value to the lowest value. The ranking of the firms also allows for a comparison of the benefit status of the firms. These analyses can provide a basis for understanding the value of Learn-To-Transform programs to businesses and their overall efficiency for a more effective transformation process. By examining the most and least benefited companies, model factory managers can make evaluations to increase the benefit of the Learn & Transform Program. In other words, the feedback from the top and bottom-ranked companies can inform improvements to the program. Additional modules can be added to the program for companies that benefit less from the Learn & Transform Program. The sectors that provide the most and least benefit can be identified. Target sectors can be determined by the model factory management. In the ranking, the top, middle, and bottom-ranked companies can be grouped as A, B, and C, which means satisfactory, medium-level, or unsatisfactory, to give an idea about their benefit status. To increase the effectiveness of the model factory, further studies can be conducted to compare the companies that participated in the Learn & Transform Program with the companies that did not participate in this program.

Model factory management can present the work of the companies that provide the most benefits in the ranking made by the WASPAS method as an example to other enterprises; sharing these success stories with the business world can create a source of inspiration for other companies. Award programs can be organized, and prizes can be given to the companies that provide the most benefits, and the prizes to be given to the companies that rank high in the ranking can create a competitive environment among other businesses and encourage the emergence of innovative solutions. After this study, the performance evaluation of model factories in Türkiye can be carried out by using the methods of MCDM, such as TOPSIS, VIKOR, MOORA, and COPRAS.

VII. REFERENCES

- [1] M. Tisch, C. Hertle, E. Abele, J. Metternich, and R. Tenberg, "Learning Factory Design: A Competency-Oriented Approach Integrating Three Design Levels," *International Journal of Computer Integrated Manufacturing*, pp. 1–21, 2015.
- [2] E. Abele, J. Metternich, M. Tisch, G. Chryssolouris, W. Sihn, H. Elmaraghy, and F. Ranz, "Learning Factories For Research, Education, And Training", *Procedia Cirp*, 32, 1-6, 2015
- [3] J. Cachay, J. Wennemer, E. Abele, and R. Tenberg, "Study On Action-Oriented Learning With A Learning Factory Approach," *Procedia-Social And Behavioral Sciences*, vol. 55, pp. 1144–1153, 2012.

- [4] S. Kreitlein, A. Höft, S. Schwender, and J. Franke, “Green Factories Bavaria: A Network of Distributed Learning Factories for Energy Efficient Production,” *Procedia CIRP*, vol. 32, pp. 58–63, 2015.
- [5] L. Morell, and M. Trucco, “A Proven Model to Re-Engineer Engineering Education in Partnership with Industry,” in World Engineering Education Forum, *Buenos Aires, Argentina*, 2012
- [6] Sanayi ve Teknoloji Bakanlığı. (2024, 01 Ocak). Model Fabrika Yaklaşımı [çevrimiçi]. Erişim: <https://www.sanayi.gov.tr/merkez-birimi/92d9c73bddbb/model-fabrika>.
- [7] ASO Model Fabrika. (2023, 17 Aralık). Hizmetler [Çevrimiçi]. Erişim: <https://www.modelfabrika.org/ogrendonus-programi>.
- [8] S. Chakraborty, E. K. Zavadskas, and J. Antuchevičienė, “Applications Of WASPAS Method As A Multi-Criteria Decision-Making Tool”, *etalpykla.vilniustech.lt*, 2015.
- [9] N. Ömürbek, M. Karaatlı ve H. F. Balcı, “Entropi Temelli MAUT Ve SAW Yöntemleri ile Otomotiv Firmalarının Performans Değerlemesi”, *Dokuz Eylül Üniversitesi İktisadi İdari Bilimler Fakültesi Dergisi*, 31(1), 227-255, 2016.
- [10] I. S. Yoo, T. Braun, C. Kaestle, M. Spahr, J. Franke, P. Kestel, ve E. Feige, (2016). “Model Factory For Additive Manufacturing Of Mechatronic Products: Interconnecting World-Class Technology Partnerships With Leading AM Players”, *Procedia CIRP*, 54, 210-214, 2016.
- [11] Ö. Akçakanat, H. Eren, E. Aksoy, ve V. Ömürbek, “Bankacılık sektöründe ENTROPI ve WASPAS yöntemleri ile performans değerlendirmesi”, *Süleyman Demirel Üniversitesi İktisadi ve İdari Bilimler Fakültesi Dergisi*, 22(2), 285-300, 2017.
- [12] N. Ömürbek, H. Eren ve O. Dağ, “Entropi-Aras ve Entropi-Moosra yöntemleri ile yaşam kalitesi açısından AB ülkelerinin değerlendirilmesi”, *Ömer Halisdemir Üniversitesi İktisadi ve İdari Bilimler Fakültesi Dergisi*, 10(2), 29-48, 2017.
- [13] F. Baena, A. Guarín, J. Mora, J. Souza, and S. Retat, “Learning Factory: The Path To Industry 4.0.”, *Procedia Manufacturing*, 9, 73-80, 2017.
- [14] J. Enke, R. Glass, ve J. Metternich, “Introducing A Maturity Model For Learning Factories”, *Procedia Manufacturing*, 9, 1-8, 2017, 2017.
- [15] R. C. Putra, I. H. Kusumah, M. Komaro, Y. Rahayu, and E. P. Asfiyanur, “Design Learning of Teaching Factory in Mechanical Engineering”, In *IOP Conference Series: Materials Science and Engineering* (Vol. 306, No. 1, p. 012104). IOP Publishin, 2018, February.
- [16] A. Ulutaş, “Entropi Tabanlı Edas Yöntemi İle Lojistik Firmalarının Performans Analizi”, *Uluslararası İktisadi Ve İdari İncelemeler Dergisi*, (23), 53-66, 2018.
- [17] L. F. Leal, A. Fleury, and E. Zancul, “Starting up a Learning Factory focused on Industry 4.0.”, *Procedia Manufacturing*, 45, 436-441, 2020.
- [18] K. K. Vijayan, and O. J. Mork, “Idealab: A Learning Factory Concept For Norwegian Manufacturing SME”, *Procedia Manufacturing*, 45, 411-416, 2020.
- [19] H. H. Erdoğan ve G. Kırbaç, “Financial Performance Measurement Of Logistics Companies Based On Entropy And WASPAS Methods”, *İşletme Araştırmaları Dergisi*, 13(2), 1093-1106, 2021.

- [20] M. Hegedić, P. Gregurić, M. Gudlin, M. Golec, A. Đenadija, N. Tošanović, N. ve Štefanić, “Design and Establishment of a Learning Factory at the FMENA Zagreb”, *Tehnički glasnik*, 16(3), 426-431, 2022.
- [21] V. S. Arıkan Kargı, “Evaluation Of Logistics Performance Of The Oecd Member Countries With Integrated Entropy and Waspas Method”, *Journal of Management & Economics/Yönetim ve Ekonomi*, 29(4), 2022.
- [22] R. Lukić, “Analysis Of The Performance Of The Serbian Economy Based on the MEREC-WASPAS method”, *MARSONIA: Časopis za društvena i humanistička istraživanja*, 2(1), 39-52, 2023.
- [23] E. Gökalp, U. Şener ve P. E. Eren, “Development Of An Assessment Model For Industry 4.0: Industry 4.0-MM. In *Software Process Improvement And Capability Determination: 17th*, 2017.
- [24] S. Vaidya, P. Ambad, and S. Bhosle, “Industry 4.0–A Glimpse”, *Procedia Manufacturing*, 20, 233-238, 2018.
- [25] S. Khin, and D. M. H. Kee, “Factors Influencing Industry 4.0 Adoption”, *Journal of Manufacturing Technology Management*. 33(3), 448-467, 2022.
- [26] P. Kurttila, M. Shaw, and P. Helo, “Model Factory Concept–Enabler For Quick Manufacturing Capacity Ramp-Up. In *European Wind Energy*”, *Conference and Exhibition, EWEC* (Vol. 4), 2010.
- [27] C. Prinz, F. Morlock, S. Freith, N. Kreggenfeld, D. Kreimeier, and B. Kuhlenkötter, “Learning Factory Modules For Smart Factories In Industrie 4.0. “, *Procedia CiRp*, 54, 113-118, 2016.
- [28] C. Chau Khac Bao, and T. T. Tran, “Development of a Digital Learning Factory Toward Multi Objectives for Engineering Education: An Educational Concept Adopts the Application of Digital Twin. *Thanh Trung, Development of a Digital Learning Factory Toward Multi Objectives for Engineering Education: An Educational Concept Adopts the Application of Digital Twin (March 5, 2023)*.
- [29] E. Abele, C. J. Bauerdick, N. Strobel, and N. Panten, “ETA Learning Factory: A Holistic Concept For Teaching Energy Efficiency In Production”, *Procedia CIRP*, 54, 83-88, 2016.
- [30] D. T. Matt, E. Rauch, and P. Dallasega, “Mini-Factory–A Learning Factory Concept For Students And Small And Medium Sized Enterprises”, *Procedia CiRP*, 17, 178-183, 2014.
- [31] L. Mchauser, C. Schmitz, and M. Hammer, “Model-Factory-In-A-Box: A Portable Solution That Brings The Complexity Of A Real Factory And All The Benefits Of Experiential-Learning Environments Directly To Learners In Industry”, *Procedia Manufacturing*, 45, 246-252, 2020.
- [32] E. Aksakal ve E. Çalışkan, “Olimpiyatlara Aday Şehirlerin Seçim Sürecinde Dikkate Alınacak Kriterlerin Entropi Yöntemi ile Değerlendirilmesi”, *Çok Kriterli Karar Verme Yöntemleri MS Excel Çözüm Uygulamaları*, 1. Baskı, Ankara, Türkiye: Nobel Akademik Yayıncılık, M. Kabak, Y. Çınar, Editör, 2020, böl.10, 13, ss.169-179.
- [33] Chakraborty, S. and Zavadskas, E. K. (2014). Applications of WASPAS Method in Manufacturing Decision Making. *Informatica*, Vol. 25, No. 1, 1–20
- [34] P. H. Nguyen, T. T. Dang, K. A. Nguyen, and H. A Pham, “Spherical Fuzzy WASPAS-based Entropy Objective Weighting for International Payment Method Selection. *Computers, Materials & Continua*”, 72(1), 2022.

- [35] G. Stojić, Z. Stević, J. Antuchevičienė, D. Pamučar, and M. Vasiljević, “A Novel Rough WASPAS Approach For Supplier Selection In A Company Manufacturing PVC Carpentry Products”, *Information*, 9(5), 12, 2018.
- [36] S. K. Vaid, G. Vaid, S. Kaur, R. Kumar, and M.S. Sidhu, “Application Of Multi-Criteria Decision-Making Theory With VIKOR-WASPAS-Entropy Methods: A Case Study Of Silent Genset”, *Materials Today: Proceedings*, 50, 2416-2423, 2022.
- [37] E. K. Zavadskas, J. Antucheviciene, S. H. R. Hajiagha, and S.S. Hashemi, “Extension Of Weighted Aggregated Sum Product Assessment With Interval-Valued Intuitionistic Fuzzy Numbers (WASPAS-IVIF)” *Applied Soft Computing*, 24, 1013-1021, 2014.
- [38] B. Ecer, “ WASPAS Yöntemi ile Tedarikçi Seçimi”, *Çok Kriterli Karar Verme Yöntemleri MS Excel Çözüm Uygulamaları*, 1. Baskı, Ankara, Türkiye: Nobel Akademik Yayıncılık, M. Kabak, Y. Çınar, Editör, 2020, böl.13, ss.209-219.